

THREE-DIMENSIONAL NONLINEAR SEISMIC SOIL-
ABUTMENT-FOUNDATION-STRUCTURE INTERACTION
ANALYSIS OF SKEWED BRIDGES

by

Anooshirvan Shamsabadi

A Dissertation Presented to the
FACULTY OF THE GRADUATE SCHOOL
UNIVERSITY OF SOUTHERN CALIFORNIA
In Partial Fulfillment of the
Requirements for the Degree
DOCTOR OF PHILOSOPHY
(CIVIL ENGINEERING)

May 2007

Copyright 2007

Anooshirvan Shamsabadi

UMI Number: 3262688



UMI Microform 3262688

Copyright 2007 by ProQuest Information and Learning Company.
All rights reserved. This microform edition is protected against
unauthorized copying under Title 17, United States Code.

ProQuest Information and Learning Company
300 North Zeeb Road
P.O. Box 1346
Ann Arbor, MI 48106-1346

DEDICATION

To the memory of my parents for all their supports and sacrifices.

ACKNOWLEDGMENTS

The author would like to express his sincere and deepest thanks to his advisor, Professor Geoffrey R. Martin, for many hours he has spent with me for his research project and review of this dissertation.

The author is very grateful to the rest of his committee members: Professor Jean-Pierre Bardet, Professor Vincent Lee, and Professor Frank Crosetti.

I would like to thank Dr. Liping Yan of Arroya Geotechnical for the friendship, consultations, and review and very helpful suggestions for this dissertation.

In addition, I am very thankful to Mr. Po Lam of Earth Mechanics, Inc. for his intuition and insightful suggestions in implementation and practical application of this dissertation for bridge abutment design under seismic loading.

The comments and suggestions of my academic and professional colleagues are also greatly appreciated.

My utmost gratitude goes to my family members for their love, patience and understanding.

TABLE OF CONTENTS

DEDICATION	ii
ACKNOWLEDGMENTS	iii
LIST OF TABLES	viii
LIST OF FIGURES	ix
ABSTRACT	xxiii
CHAPTER ONE: INTRODUCTION	1
1.1 Background	1
1.2 Scope and Objectives	4
1.3 Organization of Dissertation	8
CHAPTER TWO: LITERATURE REVIEW	11
2.1 Introduction	11
2.2 Abutment Behavior during a Seismic Event	26
2.3 Caltrans Abutment Design Criteria	28
CHAPTER THREE: ABUTMENT LSH MODEL	36
3.1 Introduction	36
3.2 Types of Bridge Abutments.....	37
3.3 Seismic Behavior of Seat-Type Abutments	40
3.4 Seismic Behavior of Monolithic Abutments	41
3.5 Force-Displacement Capacity of Bridge Abutment	41
3.6 Mechanism of the Abutment Backfill Failure	44
3.7 Abutment Backfill Constitutive Model	49
3.8 Nonlinear Hyperbolic Model.....	52
3.9 Nonlinear Abutment Backfill Capacity	58
3.10 Verification of LSH Model	68
3.11 Full-Scaled Abutment Experiments	68
3.11.1 UCLA Abutment Experiment.....	68
3.11.2 UCD Abutment Experiment	72
3.12 Full-Scaled Pile Cap Experiment.....	72
3.12.1 Clean Sand.....	73
3.12.2 Silty Sand	73
3.12.3 Fine-grained Gravel.....	77
3.12.4 Coarse-grained Gravel.....	77

3.13	RPI Centrifuge Experiment in Nevada Sand	77
3.13.1	Seat-type abutment	80
3.13.2	Pile Cap	80
3.14	3.14 Small-Scaled Experiment of Wall in Loose Sand.....	81
3.15	Recommended Abutment Force-deformation Relationship.....	81
3.15.1	Application of HFD Model for other Height.....	90
3.15.2	Development of the Height Factors.....	93
3.15.3	HFD Height Validation	96
3.16	Conclusions	100

CHAPTER FOUR: ABUTMENT CONTINUUM FINITE ELEMENT

	MODEL.....	102
4.1	Introduction	102
4.2	Method of Analysis	103
4.2.1	Presumptive Values	103
4.2.2	Closed-Form Solution	106
4.2.3	Simplified Solution.....	107
4.2.4	Numerical Solution.....	107
4.3	Constitutive Models for Bridge Structures.....	108
4.4	Constitutive Model for Abutment Backfill	111
4.4.1	Primary Loading Stiffness.....	113
4.4.2	Unloading/Reloading Stiffness.....	115
4.4.3	Oedometer Stiffness	115
4.4.4	Dilatancy	117
4.5	Verification of the Constitutive Model	118
4.6	2-D Finite Element Model.....	123
4.6.1	Interface Elements	125
4.6.2	2-D Finite Element Simulations for Various Backfill.....	126
4.6.3	UCLA-CT Full-Scaled Abutment Experiment.....	127
4.6.4	Selection of Parameters Used in the Finite Element Model....	130
4.6.5	UCLA 2-D Abutment Finite Element Model.....	131
4.6.6	Sequence of the Events in the Model	133
4.7	UCD Abutment Field Experiment.....	136
4.7.1	UCD Abutment 2-D Finite Element Model	140
4.7.2	BYU Pile Cap Experiments 2-D Finite Element Model	144
4.7.3	Pile Cap Backfill Parameters.....	145
4.8	Backfill Behavior Using 3-D Finite Element Model.....	148
4.8.1	3-D Finite Element Simulation of UCLA Abutment Test.....	151
4.8.2	Testing Sequence.....	153
4.9	3-D Finite Element Simulation of UCD Abutment Test.....	158
4.9.1	Sequence of the Events.....	158
4.10	3-D Finite Element Simulation of BYU Pile Cap Experiments.....	163
4.10.1	3-D Finite Element Simulations Using Half Model	165
4.10.2	Testing Sequence.....	166

4.11	Comparisons of Various Models Versus Experimental Data	171
4.12	3-D Finite Element Model for Skewed Abutment	178
4.13	Summary	185

**CHAPTER FIVE: NONLINEAR SEISMIC RESPONSE OF
SKEWED BRIDGES..... 187**

5.1	Introduction	187
5.2	Impact of Ground Motion Characteristics.....	190
5.3	Selection of the Ground Motions	192
5.4	Model's Boundary Conditions	209
5.4.1	Abutment Soil-Structure Interaction	209
5.4.2	Abutment Gaps.....	210
5.4.3	Abutment Backwall-Backfill Longitudinal Response.....	210
5.4.4	Abutment Shear Key	212
5.4.5	Validation of Abutment Model	214
5.4.6	Bridge Deck Model	217
5.4.7	Bridge Columns.....	219
5.5	Bridge Models	220
5.6	Analytical Study	226
5.6.1	Bridges Types.....	226
5.6.2	Single-Span Bridge.....	227
5.6.3	Two-Span Bridge	228
5.6.4	Three-Span Bridge with a Single-Column Bent.....	229
5.6.5	Two-Span Bridge with Two-Column Bent	229
5.6.6	Three-Span Bridge with Two-Column Bents.....	230
5.7	Longitudinal and Transverse Abutment Response.....	240
5.7.1	Effects of Skew Angles on the Bridge Abutment	240
5.8	Response Due to Spectra-Compatible Time History Motions	248
5.8.1	Abutment Response.....	248
5.8.2	Rotation Due to Deck Flexibility	251
5.8.3	Rotation Due to Column Rigidity	251
5.9	Analytical Results of the Single-Column Two-Span Bridge	256
5.9.1	Abutment Behavior in the Longitudinal Direction.....	264
5.9.2	Abutment Behavior in the Transverse Direction.....	266
5.10	Results of the Analysis for All Bridge Models.....	271
5.10.1	Rotational Response	271
5.11	Conclusions	296

**CHAPTER SIX: CASE STUDY OF AN INSTRUMENTED SKEWED
BRIDGE..... 298**

6.1	Introduction	298
6.2	Bridge Description	300

6.3	Seismic Instrumentation and Input Ground Motion.....	304
6.4	Geotechnical Information.....	309
6.5	Idealized Soil Profile and Properties.....	312
6.6	Global Bridge Model.....	317
6.7	Global Bridge Modeling Using Direct Method.....	319
6.7.1	Pile Foundations.....	325
6.7.2	Abutment Soil-Structure Interaction.....	325
6.7.3	Global Bridge Displacement Response.....	330
6.7.4	Abutment Force and Displacement Response.....	343
6.8	Substructuring Technique.....	349
6.8.1	Procedures To Develop Stiffness Matrix.....	353
6.9	Bridge Response Using Substructuring Technique.....	354
6.10	Conclusions.....	364

CHAPTER SEVEN: CONCLUSIONS AND RECOMMENDATIONS 365

7.1	Summary and Conclusions.....	365
7.2	Recommendations.....	367
7.3	Further Research.....	368

REFERENCES 371

LIST OF TABLES

Table 3.1	Typical Values of ϵ_{50}	56
Table 3.2	Mobilized Earth Pressure Coefficients Using Three Methods	66
Table 3.3	Parameters for HFD Model.....	89
Table 3.4	Suggested HFD Parameters for Abutment Backfills	89
Table 3.5	Height factors to calculate abutment force-displacement	96
Table 4.1	Parameters of the HS model.....	115
Table 4.2	Input Parameters Used in the UCLA-Caltrans PLAXIS Model	130
Table 4.3	Input Parameters for UCD PLAXIS Model.....	140
Table 4.4	Input Parameters for BYU Pile Cap Analyses	145
Table 5.1	Selected Earthquake Records.....	193
Table 5.2	Input Ground Motion Characteristics	194
Table 6.1	Characteristics of the Input Motions of the Painter Street Bridge.....	304
Table 6.2	Idealized Soil Parameters for Painter Street Bridge Site	316
Table 6.3	Idealized Stiffness Parameters to Develop p-y Springs for Painter Street Bridge Site.....	316
Table 6.4	Bent Foundation Stiffness Matrix (kips, inch and radian).....	354

LIST OF FIGURES

Figure 2.1:	Linear Elastic Finite Element Model	12
Figure 2.2:	Idealized Spline Bridge Model	14
Figure 2.3:	3-D Continuum (Sweet and Morill, 1993).....	19
Figure 2.4:	3-D Continuum (Maroney,1995)	19
Figure 2.5:	Passive Earth Pressure Coefficient (Caquot and Kerisel 1948)....	23
Figure 2.6:	Stress-Strain Relationship (Shamsabadi et al., 2005)	26
Figure 2.7:	Backwall Shear Failure and Mobilized Passive Wedge.....	27
Figure 2.8:	UCD Test Setup (Maroney,1995)	29
Figure 2.9:	Estimated Bilinear Abutment Stiffness.....	30
Figure 2.10:	Effective Abutment Stiffness (SDC, 2004).....	34
Figure 2.11:	Effective Abutment Area (SDC, 2004).....	34
Figure 2.12:	Effective Abutment Width for Skewed Bridges (SDC, 2004).....	35
Figure 2.13:	Abutment Seat Width Requirements (SDC, 2004)	35
Figure 3.1:	Seat-Type Abutment and Foundation System	38
Figure 3.2:	Monolithic Abutment and Foundation System	39
Figure 3.3:	Example of Mobilized Passive Wedges.....	40
Figure 3.4:	Mobilization of Passive Resistance.....	45
Figure 3.5:	Mobilized Wedges During Seismic Event	48
Figure 3.6:	Various Types of Elastoplastic Soils Behavior (Bardet, 1997)	50
Figure 3.7:	Stress-Strain Relationship for Typical Abutment Backfill	51
Figure 3.8:	Hyperbolic Model	53

Figure 3.9:	Modified Hyperbolic Stress-Strain Relationship	55
Figure 3.10:	Mobilized Passive Wedge (Shamsabadi et al., 2005)	58
Figure 3.11:	Associated Mohr Circle and Soil Strain.....	61
Figure 3.12:	Flowchart of LSH Procedure	63
Figure 3.13:	Simple Wedge with Planar Failure	64
Figure 3.14:	Mobilized Earth Pressure Coefficients Using Three Methods	67
Figure 3.15:	LSH Model Failure Wedges Versus Experimental Failure Wedges (UCLA Test)	70
Figure 3.16:	LSH Prediction of UCLA Abutment Test.....	71
Figure 3.17:	LSH Prediction of UCD-CT Abutment test.....	74
Figure 3.18:	LSH Prediction of BYU Pile Cap Test in Clean Sand.....	75
Figure 3.19:	LSH Prediction of BYU Pile Cap Test in Silty Sand.....	76
Figure 3.20:	LSH Prediction of BYU Pile Cap Test in Fine Gravel	78
Figure 3.21:	LSH Prediction of BYU Pile Cap in Test Coarse Gravel	79
Figure 3.22:	LSH Prediction of RPI Abutment Test in Dense Sand	82
Figure 3.23:	LSH Prediction of RPI Pile Cap Test in Nevada Sand	83
Figure 3.24:	LSH Prediction of Wall Test in Loose Sand.....	84
Figure 3.25:	Hyperbolic Force-Displacement Formulation	85
Figure 3.26:	UCLA Abutment Experiment Compared with Various Models.....	88
Figure 3.27:	UCD Abutment Experiment Compared with Various Models	92
Figure 3.28:	Backbone Curves for Various Abutment Height (Silty Sand).....	94
Figure 3.29:	Backbone Curves for Various Abutment Height (Clay).....	95
Figure 3.30:	Comparisons of LSH and HFD Models for Cohesive Backfill.....	97
Figure 3.31:	Comparisons of LSH and HFD Models for Silty Sand.....	98

Figure 3.32:	HFD Validation Using BYU Silty Sand Backfill	99
Figure 4.1:	Abutment Force-Deformation Based on Presumptive Value.....	104
Figure 4.2:	Closed-Form Solution	107
Figure 4.3:	Hysteretic Behavior of Confined Concrete	110
Figure 4.4:	Behavior of Steel.....	110
Figure 4.5:	Hardening Soil (HS) Model	114
Figure 4.6:	HS Model in Stress Space	116
Figure 4.7:	PLAXIS Dilatancy Model.....	118
Figure 4.8:	Triaxial: (a) Specimen; (b) Finite Element Model.....	120
Figure 4.9:	Triaxial Test of the Cohesionless Backfill.....	121
Figure 4.10:	Triaxial Test of the Abutment Backfill for Cohesive Soil	122
Figure 4.11:	2-D Finite Element Mesh with Backwall Interface	124
Figure 4.12:	Mohr-Coulomb Interface Stress-Strain Relationship.....	126
Figure 4.13:	Seat-type Abutment and Foundation System.....	128
Figure 4.14:	UCLA-CT Full-Scaled Abutment Test with Sandy Backfill	129
Figure 4.15:	UCLA-CT Abutment Backfill Triaxial Test	131
Figure 4.16:	UCLA-CT Triaxial Test of the Abutment Backfill.....	132
Figure 4.17:	Limits of 2-D Finite Element Model.....	133
Figure 4.18:	2-D Finite Element Deformed Shape for UCLA Abutment Test.....	134
Figure 4.19:	2-D Finite Element Displacement Vectors for UCLA Abutment Test.....	134
Figure 4.20:	2-D Finite Element Displacement Contours for UCLA Abutment Test.....	134
Figure 4.21:	2-D Finite Element Failure Surfaces for UCLA Abutment Test.....	135

Figure 4.22:	2-D Finite Element Incremental Strains for UCLA Abutment Test.....	135
Figure 4.23:	2-D Cyclic UCLA Abutment Test versus Finite Element Model Predictions	137
Figure 4.24:	UCD Abutment Test Setup	138
Figure 4.25:	UCD 3-D Abutment Field Experiment	138
Figure 4.26:	Failure Mechanism of the UCD Abutment Test	139
Figure 4.27:	2-D Finite Element Deformed Shape for UCD Abutment Test.....	141
Figure 4.28:	2-D Finite Element Displacement Vectors for UCD Abutment Test.....	141
Figure 4.29:	2-D Finite Element Displacement Contours for UCD Abutment Test.....	141
Figure 4.30:	2-D Finite Element Failure Surfaces for UCD Abutment Test...	142
Figure 4.31:	2-D Finite Element Incremental Strains for UCD Abutment Test.....	142
Figure 4.32:	UCD Abutment Test versus Finite Element Model Prediction...	143
Figure 4.33:	Finite Element Model for BYU Clean Sand Backfill	144
Figure 4.34:	2-D Finite Element Deformed Mesh for BYU Clean Sand Backfill.....	146
Figure 4.35:	2-D Finite Element Displacement Vector Field for BYU Clean Sand Backfill	146
Figure 4.36:	2-D Finite Element Displacement Contours for BYU Clean Sand Backfill.....	147
Figure 4.37:	2-D Finite Element Mohr-Coulomb Failure Surface for BYU Clean Sand Backfill	147
Figure 4.38:	2-D Finite Element Incremental Strains for BYU Clean Sand Backfill.....	147

Figure 4.39:	BYU Pile Cap Test versus Finite Element Model Prediction For Clean Sand Backfill	150
Figure 4.40:	3-D Solid Element.....	151
Figure 4.41:	Section Through the Full 3-D Finite Element Model of the UCLA Abutment Experiment	152
Figure 4.42:	Full 3-D Finite Element Model of the Deformed Shape for UCLA Abutment Experiment	154
Figure 4.43:	Section Through Gypsum Columns for the Full 3-D Finite Element Model for UCLA Abutment Experiment.....	154
Figure 4.44:	Full 3-D Finite Element Model of the Displacement Vectors for UCLA Abutment Experiment.....	155
Figure 4.45:	Full 3-D Finite Element Model of the Displacement Contours of UCLA Abutment Experiment	155
Figure 4.46:	Full 3-D Finite Element Model of the Plastic Points Through Gypsum Columns for UCLA Abutment Experiment.....	156
Figure 4.47:	Full 3-D Finite Element Model of the Incremental Strains Through Gypsum Columns for UCLA Abutment Experiment...	156
Figure 4.48:	Measured Experimental Data Versus Finite Element Prediction for UCLA Abutment Experiment	157
Figure 4.49:	Finite Element Model of the of the Deformed Shape for UCD Abutment Experiment.....	158
Figure 4.50:	Full 3-D Finite Element Model of the Displacement Vectors for UCD Abutment Experiment	160
Figure 4.51:	Full 3-D Finite Element Model of the Displacement Contours for the UCD Abutment Experiment	160
Figure 4.52:	Full 3-D Finite Element Model of Mohr-Coulomb Plastic Points for UCD Abutment Experiment	161
Figure 4.53:	Full 3-D Finite Element Model of the Incremental Strains for UCD Abutment Experiment.....	161
Figure 4.54:	Measured Experimental Data Versus Finite Element Prediction for UCD Abutment Experiment.....	162

Figure 4.55:	Schematic of a Typical 3-D Wedge Failures and Cracking Patterns of BYU Pile Cap Experiments	163
Figure 4.56:	Full 3-D Finite Element Model Displacement Contours of BYU Pile Cap Experiment	164
Figure 4.57:	3-D Finite Element Using Half Model of BYU Pile Cap Experiment	165
Figure 4.58:	3-D Finite Element Model of the Displacement Contours for BYU Pile Cap Experiment	167
Figure 4.59:	3-D Finite Element Model of the Displacement Contours for BYU Pile Cap Experiment	168
Figure 4.60:	Full 3-D Finite Element Model of Mohr-Coulomb Plastic Points for BYU Pile Cap Experiment	168
Figure 4.61:	Full 3-D Finite Element Model of Mohr-Coulomb Incremental Strains for BYU Pile Cap Experiment	169
Figure 4.62:	Measured Experimental Data Versus Finite Element Prediction for BYU Silty Sand Backfill Experiment	170
Figure 4.63:	Measure Force-Deformation of the UCLA Abutment Test Versus Predictions by Various Methods	172
Figure 4.64:	Measure Force-Deformation of the UCD Abutment Test Versus Predictions by Various Methods	173
Figure 4.65:	Measure Force-Deformation of the BYU Pile Cap Test Versus Predictions by Various Methods for Silty Sand Backfill	174
Figure 4.66:	Measure Force-Deformation of the BYU Pile Cap Test Versus Predictions by Various Methods for Clean Sand Backfill	175
Figure 4.67:	Measure Force-Deformation of the BYU Pile Cap Test Versus Predictions by Various Methods for Fine Gravel Backfill	176
Figure 4.68:	Measure Force-Deformation of the BYU Pile Cap Test Versus Predictions by Various Methods for Coarse Gravel Backfill	177

Figure 4.69:	Clockwise Deck Rotation During a Seismic Event	178
Figure 4.70:	Non-uniform Passive wedge behind skewed abutment	179
Figure 4.71:	Passive Soil Wedge Plunging in Between Wingwalls	180
Figure 4.72:	Full 3-D Finite Element Model of the Passive Wedge Formation Behind Skewed Abutment.....	181
Figure 4.73:	Nonlinear Normal and Tangential Components of the Abutment-Backfill Resistance for a 30 Skew angle	183
Figure 4.74:	Impact of Skew Angles on Nonlinear Abutment Force- Deformation Relationship	184
Figure 5.1:	Components of Bridge System.....	189
Figure 5.2:	Measured Shaking Table Hysteretic Response of Bridge Column (Phan et al., 2005)	191
Figure 5.3:	Input Ground Motion 1 in Longitudinal Direction	195
Figure 5.4:	Input Ground Motion 1 in Transverse Direction	196
Figure 5.5:	Input Ground Motion 2 in Longitudinal Direction	197
Figure 5.6:	Input Ground Motion 2 in Transverse Direction	198
Figure 5.7:	Input Ground Motion 3 in Longitudinal Direction	199
Figure 5.8:	Input Ground Motion 3 in the Transverse Direction	200
Figure 5.9:	Input Ground Motion 4 in the Longitudinal Direction	201
Figure 5.10:	Input Ground Motion 4 in the Transverse Direction	202
Figure 5.11:	Input Ground Motion 5 in the Longitudinal Direction	203
Figure 5.12:	Input Ground Motion 5 in the Transverse Direction	204
Figure 5.13:	Input Ground Motion 6 in the Longitudinal Direction	205
Figure 5.14:	Input Ground Motion 6 in the transverse Direction.....	206
Figure 5.15:	Input Ground Motion 7 in the Longitudinal Direction	207
Figure 5.16:	Input Ground Motion 7 in the Transverse Direction	208

Figure 5.17:	Bridge Monolithic Abutment Model.....	211
Figure 5.18:	Abutment Shear Key Experiment (Bozorgzadeh et al., 2005)....	212
Figure 5.19:	Generic Model of the Exterior Shear Key Backbone Curve.....	213
Figure 5.20:	Displacement Cycles in the UCD Abutment Test (Romstad et al., 1995).....	215
Figure 5.21:	Measured Load-Deformation in the UCD Abutment Test (Romstad et al., 1995).....	215
Figure 5.22:	Simulated Longitudinal Response of the UCD Abutment Test.....	216
Figure 5.23:	Longitudinal and Transverse Backbone Curves Used in the Bridge Global Models.....	216
Figure 5.24:	Typical Bridge Model	218
Figure 5.25:	Column Moment-Curvature Relationship.....	219
Figure 5.26:	Single-Span Bridge	221
Figure 5.27:	Single-Column Two-Span Bridge.....	222
Figure 5.28:	Single-Column Three-Span Bridge.....	223
Figure 5.29:	Tow-Columns Two-Spans Bridge.....	224
Figure 5.30:	Tow-Columns Three-Spans Bent Bridge.....	225
Figure 5.31:	Transverse and Longitudinal Sections of the Single-Span Bridge.....	231
Figure 5.32:	Transverse Section of the Two-Span Single-Column Bridge.....	232
Figure 5.33:	Analytical Models of the Two-Span Single-Column Bridge.....	233
Figure 5.34:	Analytical Models of the Three-Span Single-Column Bridge....	234
Figure 5.35:	Transverse Section of the Two-Span Two-Column Bridge.....	235
Figure 5.36:	Analytical Models of the Two-Span Two-Column Bridge.....	236
Figure 5.37:	Transverse Section of the Three-Span Two-Column Bridge.....	237

Figure 5.38:	Analytical Models of the Three -Span Two-Column Bridge.....	238
Figure 5.39:	Columns Longitudinal and Transverse Moment Curvatures	239
Figure 5.40:	Single Span Bridge With 0o and 45o Skew Angles.....	241
Figure 5.41:	Recorded Renaldi Longitudinal Motion	244
Figure 5.42:	Recorded Renaldi Transverse Motion.....	245
Figure 5.43:	Variation of Normal Abutment Impact Forces For a Single Span-Bridge With 0o Skew Angle.....	246
Figure 5.44:	Variation of Normal Abutment Impact Forces For a Single Span-Bridge With 45o Skew Angle During the First 4 Seconds of Shaking.....	247
Figure 5.45:	Variation of Normal Abutment Impact Forces For a Single Span-Bridge With 45o Skew Angle Between 2 Seconds to 2.6 Seconds of Shaking.....	248
Figure 5.46:	Longitudinal Hysteretic Behavior of the Single-Span Bridge Abutment With 0o Skew Angle	250
Figure 5.47:	Longitudinal Hysteretic Behavior of the Single-Span Bridge Abutment With 45o Skew Angle	252
Figure 5.48:	Transverse Hysteretic Behavior of the Single-Span Bridge Abutment With 45o Skew Angle	253
Figure 5.49:	Average Rotation Due to Deck Flexibility of the Single-Span Bridge With 45o Skew Angle	254
Figure 5.50:	Average Rotation Due to Presence of the Number of Spans With 45o Skew Angle	255
Figure 5.51:	Transverse Displacement Due Motion 1 For a Two-Span Single-Column Bridge	257
Figure 5.52:	Transverse Displacement Due Motion 2 For a Two-Span Single-Column Bridge	258
Figure 5.53:	Transverse Displacement Due Motion 3 For a Two-Span Single-Column Bridge	259

Figure 5.54:	Transverse Displacement Due Motion 4 For a Two-Span Single-Column Bridge	260
Figure 5.55:	Transverse Displacement Due Motion 5 For a Two-Span Single-Column Bridge	261
Figure 5.56:	Transverse Displacement Due Motion 6 For a Two-Span Single-Column Bridge	262
Figure 5.57:	Transverse Displacement Due Motion 7 For a Two-Span Single-Column Bridge	263
Figure 5.58:	Hysteretic Abutment Backfill Response For a Two-Span Single-Column Bridge with 0o Skew Angle.....	264
Figure 5.59:	Hysteretic Abutment Backfill Response For a Two-Span Single-Column Bridge with 25o Skew Angle.....	265
Figure 5.60:	Hysteretic Abutment Backfill Response For a Two-Span Single-Column Bridge with 60o Skew Angle.....	265
Figure 5.61:	Shear Key Failure Due to Deck Rotation 1994 Northridge Earthquake	268
Figure 5.62:	Hysteretic Abutment Shear Key Response at the Acute Corners For a Two-Span Single-Column Bridge with 0o Skew Angle	269
Figure 5.63:	Hysteretic Abutment Shear Key Response at the Obtuse Corners For a Two-Span Single-Column Bridge with 45o Skew Angle	270
Figure 5.64:	Rotation Time History of Single Span Bridge With 25o Skew Angle (Length =102')	274
Figure 5.65:	Rotation Time History of Single Span Bridge With 45o Skew Angle (Length =102')	275
Figure 5.66:	Rotation Time History of Single Span Bridge With 60o Skew Angle (Length =102')	276
Figure 5.67:	Rotation Time History of Single Span Bridge With 25o Skew Angle (Length =204')	277
Figure 5.68:	Rotation Time History of Single Span Bridge With 45o Skew Angle (Length =204')	278

Figure 5.69:	Rotation Time History of Single Span Bridge With 60o Skew Angle (Length =204')	279
Figure 5.70:	Rotation Time History of Two- Span Single-column Bridge With 25o Skew Angle	280
Figure 5.71:	Rotation Time History of Two- Span Single-column Bridge With 45o Skew Angle	281
Figure 5.72:	Rotation Time History of Two- Span Single-column Bridge With 60o Skew Angle	282
Figure 5.73:	Rotation Time History of Three- Span Single-column Bridge With 25o Skew Angle	283
Figure 5.74:	Rotation Time History of Three- Span Single-column Bridge With 45o Skew Angle	284
Figure 5.75:	Rotation Time History of Three- Span Single-column Bridge With 60o Skew Angle	285
Figure 5.76:	Rotation Time History of Two- Span Two-column Bridge With 25o Skew Angle	286
Figure 5.77:	Rotation Time History of Two-Span Two-column Bridge With 45o Skew Angle	287
Figure 5.78:	Rotation Time History of Two-Span Two-column Bridge With 60o Skew Angle	288
Figure 5.79:	Rotation Time History of Three-Span Two-column Bridge With 25o Skew Angle	289
Figure 5.80:	Rotation Time History of Three-Span Two-column Bridge With 45o Skew Angle	290
Figure 5.81:	Rotation Time History of Three-Span Two-column Bridge With 60o Skew Angle	291
Figure 5.82:	Maximum Deck Rotations	292
Figure 5.83:	Average Residual Deck Rotations	293
Figure 5.84:	Two-Span Bridge Maximum Residual Deck Rotations.....	294
Figure 5.85:	Three-Span Bridge Maximum Residual Deck Rotations.....	295

Figure 6.1:	3-D View of the Painter Street Bridge	301
Figure 6.2:	Elevation and Plan Views of the Painter Street Bridge	302
Figure 6.3:	Cross Section of Superstructure and Pile Foundation of the Painter Street Bridge	303
Figure 6.4:	Seismic Instrumentation at the Painter Street Bridge	305
Figure 6.5:	Input Motion in Longitudinal Direction (Channel 12)	306
Figure 6.6:	Input Motion in Vertical Direction (Channel 13)	307
Figure 6.7:	Input Motion in Transverse Direction (Channel 14).....	308
Figure 6.8:	Layout of Abutment Backfill Borings at the Painter Street Bridge Site.....	310
Figure 6.9:	Geometry and Idealized Soil Profile at the Painter Street Bridge Site.....	313
Figure 6.10:	Total System Versus Substructure System	318
Figure 6.11:	Painter Street Bridge Model for Direct Method	320
Figure 6.12:	Bent and columns Sections for Painter Street Bridge	322
Figure 6.13:	Moment Curvature Relationship for Painter Street Bridge.....	323
Figure 6.14:	Shear Key Capacities at West Abutment for Painter Street Bridge.....	324
Figure 6.15:	Bridge Pile Foundation Model.....	328
Figure 6.16:	Longitudinal Abutment-Soil Loading-Unloading Curves	329
Figure 6.17:	Bridge Monolithic Abutment Model.....	329
Figure 6.18:	Recorded Response Versus Analytical Response of the Direct Method (Channel 18)	331
Figure 6.19:	Recorded Response Versus Analytical Response of the Direct Method (Channel 11)	332
Figure 6.20:	Recorded Response Versus Analytical Response of the Direct Method (Channel 17)	333

Figure 6.21:	Recorded Response Versus Analytical Response of the Direct Method (Channel 4)	334
Figure 6.22:	Recorded Response Versus Analytical Response of the Direct Method (Channel 3)	335
Figure 6.23:	Recorded Response Versus Analytical Response of the Direct Method (Channel 9)	336
Figure 6.24:	Recorded Response Versus Analytical Response of the Direct Method (Channel 5)	337
Figure 6.25:	Recorded Response Versus Analytical Response of the Direct Method (Channel 8)	338
Figure 6.26:	Recorded Response Versus Analytical Response of the Direct Method (Channel 2)	339
Figure 6.27:	Channel 1 Transverse at Column base of the Direct Method	340
Figure 6.28:	Comparisons of the Northwest and Southeast Corners Displacement Response in the Transverse Directions Using Direct Method	341
Figure 6.29:	Deck Rotational Response Using Direct method.....	342
Figure 6.30:	Force-Displacement Response at The West Abutments Using Direct method.....	344
Figure 6.31:	Force-Displacement Response at The East Abutments Using Direct method.....	345
Figure 6.32:	Displacement response at the West Abutment Seat Using Direct method.....	346
Figure 6.33:	Force-Displacement Capacity of Shear Key at West Abutment Using Direct method	347
Figure 6.34:	Force-Displacement Capacity of Shear Key at West Abutment Using Direct method	348
Figure 6.35:	Schematic of soil-pile interaction	349
Figure 6.36:	Dynamic Impedance Versus frequency	352
Figure 6.37:	Substructuring Approach For Abutments and Bent.....	355

Figure 6.38:	Soil-Pile Interaction	356
Figure 6.39:	Recorded Response Versus Analytical Response Using Substructure Method (Channel 1)	357
Figure 6.40:	Recorded Response Versus Analytical Response Using Substructure Method (Channel 3)	358
Figure 6.41:	Recorded Response Versus Analytical Response Using Substructure Method (Channel 4)	359
Figure 6.42:	Recorded Response Versus Analytical Response Using Substructure Method (Channel 7)	360
Figure 6.43:	Recorded Response Versus Analytical Response Using Substructure Method (Channel 9)	361
Figure 6.44:	Recorded Response Versus Analytical Response Using Substructure Method (Channel 5)	362
Figure 6.45:	Recorded Response Versus Analytical Response Using Substructure Method (Channel 11)	363
Figure 7.1:	Abutment Seat Width Requirements.....	368

ABSTRACT

The purpose of this thesis is to investigate the nonlinear global seismic soil-abutment-foundation-structure interaction behavior of typical highway skewed-bridge structures subjected to near-fault ground motions with high velocity pulses.

Three-dimensional nonlinear finite element models of typical bridges with various skew angles were developed. The bridge deck was modeled using shell elements referred as “shell models” and beam elements referred as “spline models”. The validity of the spline models was established by comparing results obtained from shell models. There is a very good agreement between the shell and the spline models. The bridge columns were modeled as beam elements with cracked sectional properties. The abutment-backfill and the transverse shear keys were simulated using nonlinear springs. The structural models were excited using seven sets of bilateral ground motions with the near fault effects.

The limit-equilibrium methods using mobilized Logarithmic-Spiral failure surfaces coupled with a modified Hyperbolic soil stress-strain behavior referred here as the “LSH” model is employed to capture the nonlinear abutment-backfill force-displacement relationship. The validity of the LSH model was established using experimental data and nonlinear continuum finite element models. The predicted results obtained using the LSH model is in good agreement with the experimental force-displacement capacity and the finite element model.

A nonlinear Hyperbolic Force-Deformation relationship referred here as the “HFD” model is developed as a powerful and effective tool for practicing bridge engineers to develop nonlinear abutment backbone curves for typical abutment backfill.

Case study based on the recorded response of a skewed-two-span reinforced concrete box girder under strong shaking was performed. The bridge system was subjected to the three-component recorded free-field earthquake motions. The resulting dynamic response of the bridge model was found to be in good agreement with most of the motions recorded at various locations of the bridge. This validates the practical application and the methodology developed in this dissertation for evaluating the seismic response of other skewed bridges that is realistic, repeatable and reliable.

CHAPTER ONE

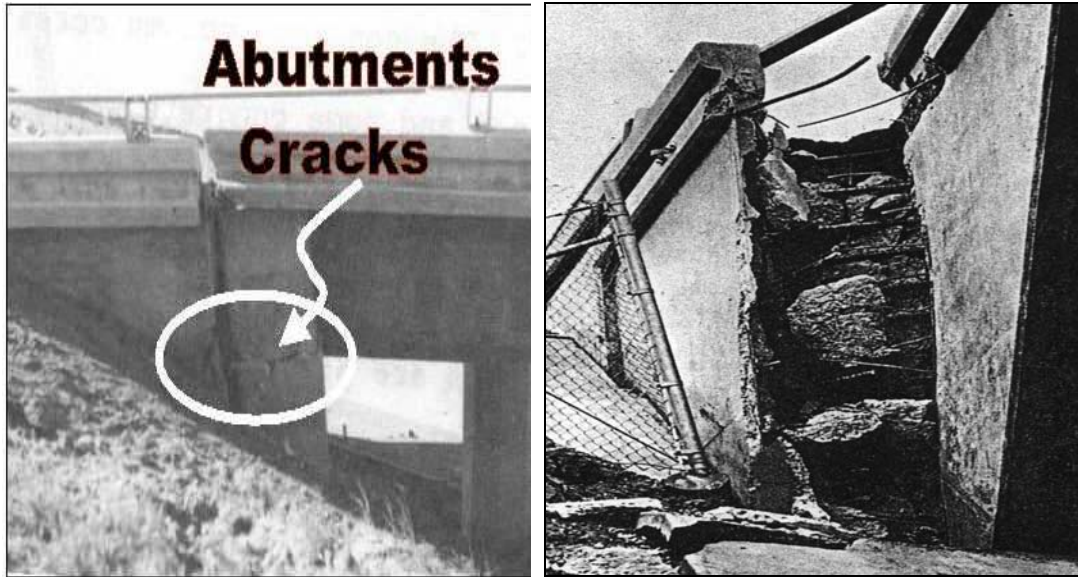
INTRODUCTION

1.1 Background

Earthquake records with near-source ground motion characteristics, such as those of the 1994 Northridge earthquake (U.S.A.), the 1995 Kobe earthquake (Japan), the 1999 Izmit and Duzce earthquake (Turkey), and 1999 Chi-Chi earthquake (Taiwan), have increased the awareness of importance of nonlinear seismic analyses employing soil-foundation-structure-interaction on bridge structures. It has been long recognized that the short-span highway bridges and in particular skewed-bridges are highly influenced by characteristics of bridge abutments during a strong seismic excitation. During the 1971 San Fernando earthquake (magnitude 6.7), many bridges in particular bridge structures with high skew angles such as Northbound Truck Route Undercrossing and Roxford Street Undercrossing, concrete box-girder bridges both built in 1969, resulted in significant amount of rotation and translation of the superstructure as shown in Figure 1.1.

Northbound Truck Route Undercrossing was a curved-three-span bridge with high skew angle. As a result of in-plane rotation and longitudinal translation the abutments end diaphragm and the wingwalls sheared off approximately at the bottom of the deck elevation. The end diaphragm abutments were pinned at the bottom and supported on spread footings, allowing it to immediately engage the soil as a result of the earthquake movement. Roxford Street Undercrossing was a two-parallel-

single-span bridge with integral abutments supported on pile foundation. During the earthquake, the bridge moved about three feet transversely, shearing off all eight wingwall connections to the abutments. The fill around the abutment settled several feet, exposing the abutment piles which were tilted in the transverse direction.



(a) Northbound Truck Route

(b) Roxford Street

Figure 1.1: Abutment Failure During 1971 San Fernando Earthquake

The research conducted by Chen and Penzin (1977) on the effect of poundings between the bridge deck and the abutments during the 1971 San Fernando earthquake has motivated challenges and the needs to further study and understand the seismic behavior of skewed bridges.

During the 1994 Northridge earthquake, Route 14/I5 Separation and Overhead (Bridge #53-1960F) collapsed primarily as consequence of high horizontal ground motion and subsequent rotational response of the bridge. This ten-span

curved box-girder bridge connected westbound traffic on SR14 to southbound I-5. The bridge was constructed as five frames separated by expansion hinges. Prestressed concrete box girders were used in the frames at each end of the bridge and in the central frame. The east wingwall at Abutment 1 was severely damaged, presumably by impact of the bridge deck. The bridge deck lost seat support and moved about 5 feet north of the abutment face as shown in Figure 1.2.



Figure 1.2: Abutment Shear Key Failure Due to Deck Rotation

During a seismic event the bridge deck undergoes significant amount of rotations about the vertical axis due to the effect of bilateral seismic excitations. In

particular when the center of the mass and the center of stiffness of the global bridge system are not coincident, the inertia loading on the bridge tends to create torsional bridge response about the vertical axis. As a consequence of superstructure rotations about the vertical axis, excessive transverse movement can result in unseating of the superstructure and pounding on the abutment wall.

Global seismic behavior of a skewed bridge is affected by a number of factors, including bridge skew angle, bridge width, deck flexibility, number of spans, the ratio of spans length to bridge length, number of columns per bent, columns ductility, soil-abutment-superstructure interaction, abutment shear keys, abutment bearing pads soil-bent foundation-structure interaction and characteristics of the seismic source.

In this dissertation, the bridge elements considered include the nonlinear abutment-backfill, bridge deck, bent cap and a pier column. The bridge deck is modeled using full 3-dimensional (3-D) shell elements to account for the realistic flexibility of the superstructure. The computational efficiency is achieved in the three-dimensional finite element model by converting the shell model to three-dimensional stick models for practicing bridge engineers.

1.2 Scope and Objectives

Significant difficulties have been encountered for design of short span skewed bridges as observations from the past earthquakes suggest strong coupling behavior between longitudinal and transverse movements. In-plane rotation of the bridge superstructure about the vertical axis is a contributing factor leading to some

of bridge damages and current design practice does not explicitly address how to handle such a mechanism. The lateral response of the abutment-embankment during strong shaking is highly nonlinear. Therefore, it is not suitable to represent the lateral stiffness of the abutment-backfill with an elastic element during strong shaking. In most cases, bridge engineers ignore the contributions of the abutment resistance in seismic design of bridge structures due to complexity of the problem.

In recent decades, however, Performance-Based Earthquake Engineering (PBEE) has been identified as a quantitative means for design of the bridge structures to provide life safety for the public. PBEE involves the design of ductile bridge structures that will resist earthquake loads in a predictable manner. Therefore, new bridge designs with ductile columns will impose large displacements on abutments and this may cause more damage to the abutments than the damage levels that have been observed in the past earthquakes. Proper evaluation and design of the bridge abutment reduces the columns displacement demand during earthquake shaking, this leads to a more efficient and economical design. Modeling assumptions made for nonlinear abutment-embankment stiffness as well as hysteretic and geometrical damping of the abutment can have significant effects on the global seismic response characteristics of the short span skewed-bridges. Large-scaled field experiments, observation following the major seismic event and system identification techniques on the instrument bridges have identified that:

- (1) The abutment-soil-structure-interaction plays a significant role in the global response of this class of bridges.

- (2) Stiffness and strength of the abutment-backfill depends on the level of shaking and exhibits significant degradation at the large deformation.
- (3) The abutment-backfill undergoes well into inelastic range and dissipate significant amount of energy through the soil hysteretic action as a result of abutment damage during strong seismic event.
- (4) The abutment-backfill not only can provide significant lateral resistance but also is a good source of energy dissipation at large deformation due to nonlinear hysteretic behavior of the abutment-soil system.

The overall objective of the research presented in this dissertation is to evaluate and understand the global seismic response of actual skewed-bridges employing soil-abutment-foundation-structure interaction models subjected to seismic bilateral excitations with near-source response-spectra-compatible ground motion characteristics. The abutment-backfill enclosed in between the abutment wingwalls provides significant resistance to the bridge deck motions during a seismic event for single-span, two-span and three-span bridges, but becomes less effective as the number of spans and columns increased. However, for multi-span bridges with continuous deck and small diameter column-pile-extension the bridge engineers can transfer the lateral seismic load to the bridge abutment. Therefore, in the present research the global response of continuous single-span, two-spans-single-column bent, two-spans-two-column bent, three-spans-single-column bents and three-spans-two-column bents reinforced bridge structures with various skewed angles is investigated. In most cases, the pier columns are supported by a pinned

connection at the base of the column, and thus the need to explicitly model the pier foundations is not required. Since the primary objective of this research is to understand the effect of the abutment-soil-structure interaction on the global behavior of the bridge structures for the first part of the dissertation only this class of bridge structure is selected. The second part of the dissertation is focused on the skewed-bridge models including the pile foundations for the bents and the abutments. The findings from this research can be used to improve the current bridge design practice for seismic design of skewed bridges. To achieve this objective the following tasks were undertaken:

- A practical and simplified design tool was developed and calibrated with all available experimental data to predict the nonlinear force displacement capacity of the abutment backfill.
- Full three-dimensional nonlinear finite element models were developed to simulate the skew abutment-backfill nonlinear behavior and to understand the mechanism of the problem.
- A nonlinear closed form hyperbolic force-deformation relationship which takes the backfill stiffness and ultimate capacity of the backfill into account is developed as a powerful and effective tool for practicing bridge engineers to calculate a realistic non-linear load versus displacement relationship for abutment-backfill without tedious finite element analysis.
- Using the nonlinear abutment springs developed above, three-dimensional nonlinear finite element models for wide ranges of bilateral ground motions and

bridges with various skewed angles were carried out to quantify the global seismic response for this class of bridge structures.

- Parametric studies on all bridge models were carried out to better understand the mechanics of skewed bridge behavior. The parameters included nonlinear wide ranges of skew angle, bridge width, span length, number of columns per bent, number of actual earthquakes recorded motions and response spectra-compatible time history ground motions. All the motions have near-source ground motion characteristics with high velocity pulses.
- Case study based on the recorded response of a skewed-two-span reinforced concrete box girder under strong shaking was performed to validate the modeling techniques developed in this dissertation. The bridge system was subjected to the three-component recorded free-field earthquake motions at the bridge site.

1.3 Organization of Dissertation

Chapter 2 presents a comprehensive review of seismic behavior of skew bridges and the issues regarding nonlinear longitudinal abutment-backfill force-deformation, nonlinear transverse abutment-shear-keys force-deformation and their implementations in the current Caltrans seismic design criteria for the global bridge behavior analysis.

Chapter 3 describes the proposed plane-strain two-dimensional (2-D) model to evaluate abutment stiffness. The limit-equilibrium methods using mobilized Logarithmic-Spiral failure surfaces coupled with a modified Hyperbolic soil stress-strain behavior (referred here as the “LSH” model) is employed to capture the

nonlinear abutment-backfill force-displacement relationship. A nonlinear closed-form hyperbolic force-deformation relationship which takes the backfill stiffness and ultimate capacity of the backfill into account is developed to be a powerful and effective tool for practicing bridge engineers.

Chapter 4 uses 2-D and 3-D finite element models to validate the LSH model. The computer program Plaxis (Brinkgreve, 2006) was used to perform finite-element analyses to evaluate the development of passive resistance of the bridge abutment-backfill based on experimental data. The constitutive Hardening Soil (HS) model (Schanz et al., 1999) available in Plaxis was used to model the nonlinear abutment backfill behavior. This material model defines the soil stiffness moduli that reduce with strain according to a hyperbolic relationship modified from the well-known Duncan-Chang hyperbolic model (Duncan et al., 1970).

Chapter 5 discusses the three-dimensional dynamic behavior of bridges with wide ranges of skew angles, implementation of the nonlinear abutment-structure interaction into the global bridge model, parametric studies and discussion regarding the impact of ground motions with high velocity pulses.

Chapter 6 deals with validation of the modeling technique applied in this dissertation to investigate the behavior of an instrumented Painter Street Overpass in Humboldt County, California. A three-dimensional nonlinear finite-element model of bridge was developed. Direct method and substructure method of analysis were considered. The direct model includes the superstructure, the nonlinear abutment springs, and pile foundations with full coupling between structure and foundation

soils. For the substructure model, the pile foundations are represented by a condensed foundation matrices. Realistic geotechnical soil properties obtained from a geotechnical field exploration were used to represent the nonlinear soil support provided by the abutment backfill and the pile foundations. The bridge system was subjected to the three-component Cape Mendocino/Petrolia 1992 free-field earthquake motions. The model was calibrated and verified using the recorded data from the Painter Street Bridge.

Chapter 7 provides a critical discussion of the research results and the conclusion.

CHAPTER TWO

LITERATURE REVIEW

2.1 Introduction

The literature review presented herein focuses on analytical research as well as experimental studies on the bridge abutment-backfill behavior and the response of instrumented ordinary box girder bridges during a seismic event.

The dynamic behavior of the skew bridges following the 1971 San Fernando earthquake (magnitude-6.7) has received considerable attention and has motivated challenges and the needs to further study and understand the seismic behavior of skewed bridges. Chen and Penzin (1977) studied the effect of seismic soil-foundation-structure interaction on the global behavior of skew bridges using a finite element model. Their model included linear elastic beam to represent the bridge deck and the bridge columns, linear springs were used to represent the foundation flexibility. A three-dimensional linear continuum finite element was used to represent the backfill and the abutment wall as shown in Figure 2.1. The elastic perfectly-plastic Mohr-Coulomb yield criterion was used to represent the nonlinear abutment-backfill interface interaction. They concluded that the foundation flexibility and in particular the poundings between the bridge deck and the abutments have significant influence on the global response of the bridge structures and should be included in the bridge model.

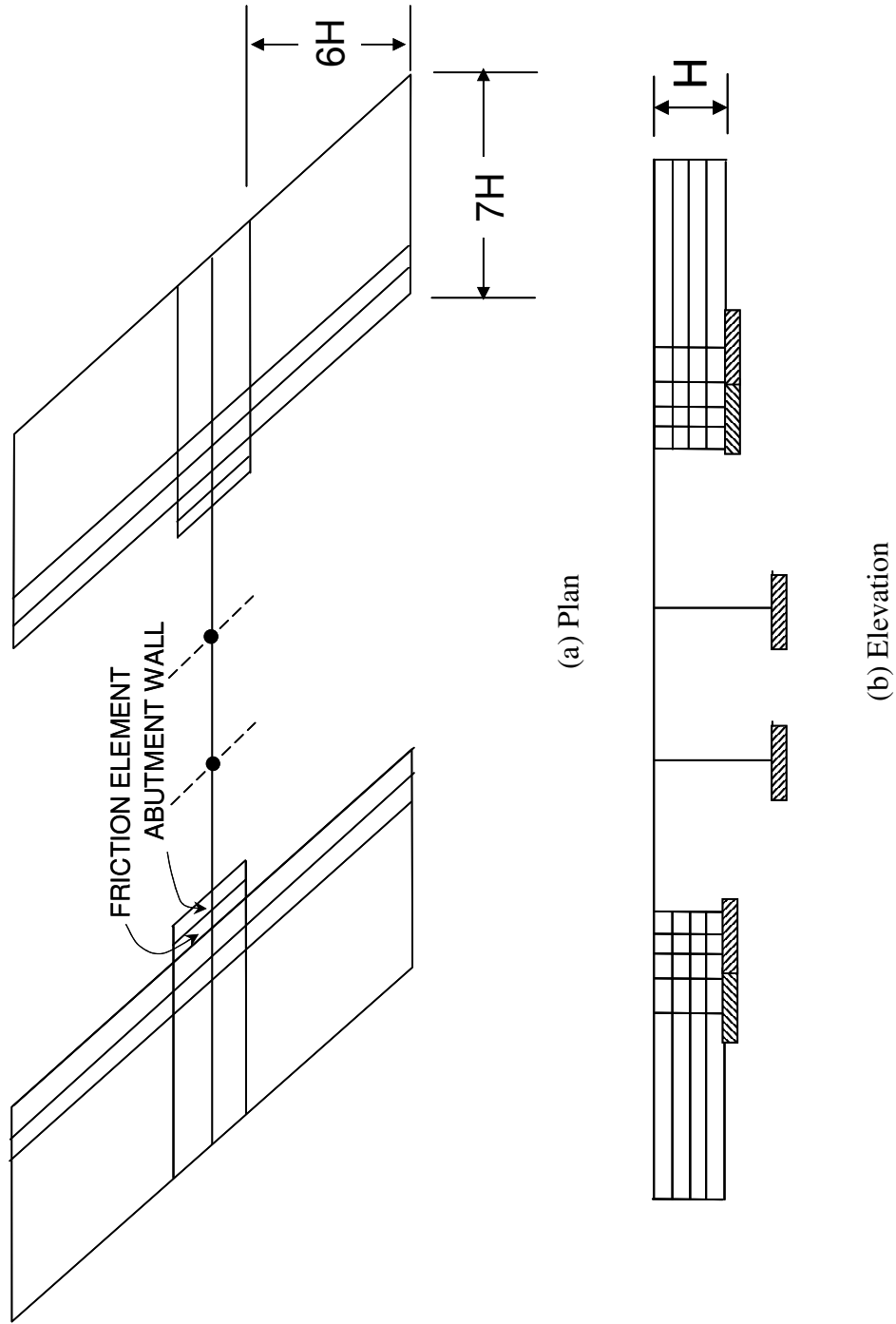


Figure 2.1: Linear Elastic Finite Element Model

Traditional bridge design practice evaluates dynamic performance of skewed bridges using spline models. The spline model is a collection of beam elements with cross section properties adjusted from geometric data as shown in Figure 2.2.

Researchers have used both the simple spline models and the detail continuum finite element models. Maragakis and Jennings (1987) used a rigid beam element to model the bridge deck.

Wilson and Tan (1990) used elastic spline model to analyze the seismic response of the Meloland Road Overcrossing (MRO). The MRO is a single column bent concrete box-girder bridge with a monolithic abutment located near El Centro in a high seismic region in the southern California. They carried out time history analysis and high damping values were used to match the computed response of the model to the recorded response of the structure. They concluded that, due to the softening effect of the abutment backfill, the frequency of the vibration of the abutment system decreased during the strong portion of the shaking and increased near initial value after the strong shaking decreased.

Werner et al. (1994) also applied system identification technique for the MRO to identify parameters for implementation of a simple elastic spline model. They concluded that high modal damping ratios and low abutment stiffness were necessary to replicate the recorded response of the bridge. They attribute this observation to evidence of nonlinear behavior of the abutment-backfill system during the seismic event.

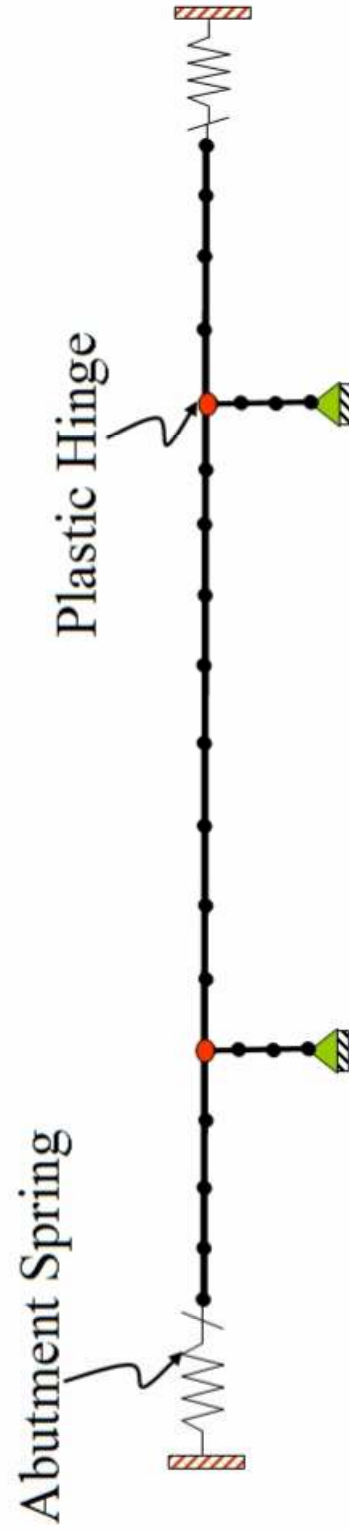
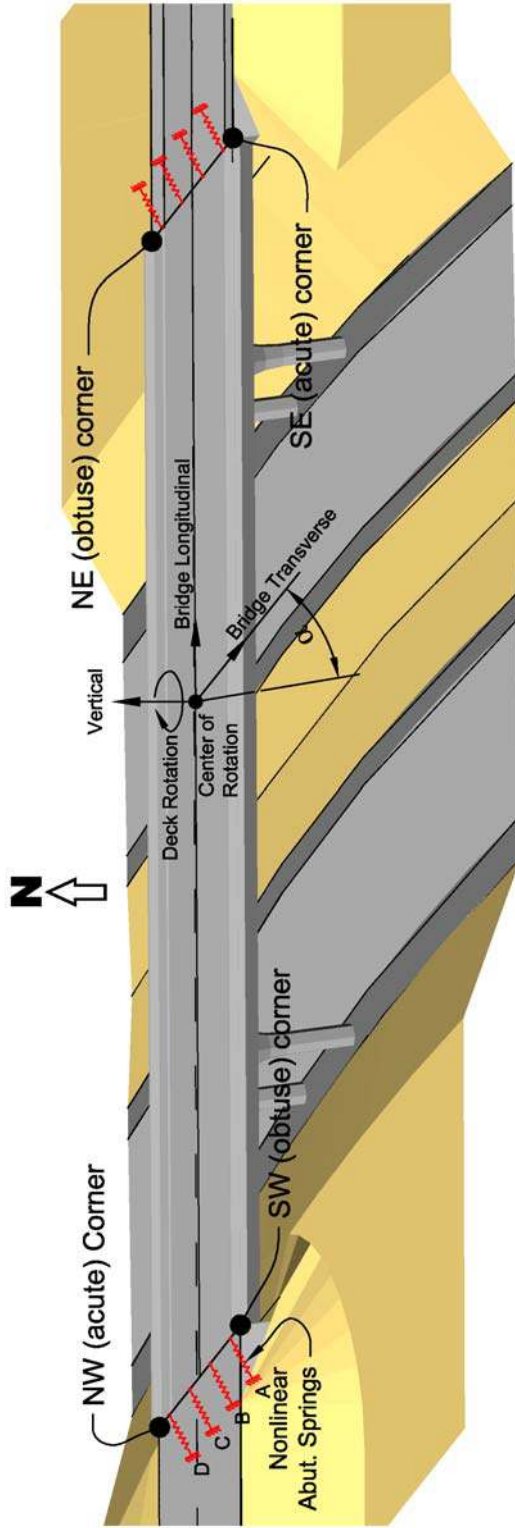


Figure 2.2: Idealized Spline Bridge Model

Their evaluation also indicated that the wingwalls behave as a flexible plate rather than a rigid retaining wall, and do not appear to have the capacity to mobilized resistance of the soil between the wing walls in the transverse direction. However, shearing resistance of the soil along the abutment end walls may carry some fraction of the seismic load.

Wakefield et al. (1991) used beam elements to model concrete box girder bridge deck, supporting columns, and the bent cap. McCallen and Romstad (1994) simulated the bent cap using a beam element and the bridge deck was modeled by flexible beam along the bridge length and a series of transverse rigid bars.

Tirasit, Kazuhiko and Kaeashima (2005) used spline model to investigate the torsional response of skewed bridge columns during a seismic event. Watanabe and Kaeashima (2004) used spline model to study the effect of the seismic cable restrainers for the retrofit of skewed bridges.

Sweet and Morril (1993) and MaCallen and Romstad (1994) developed a large three-dimensional finite element model including large volume of soil to include abutment embankment and surrounding soil around the pile foundations for the Painter Street Overcrossing to back calculate response of the structure during the past earthquake.

The lateral response of the bridge abutments has been investigated through theoretical models, half scale load tests on abutments, small-amplitude field vibration tests, centrifuge tests, and analyses of recorded motions of actual bridges during earthquakes. Wilson and Tan (1990), Levine and Scott (1989), and Wilson

(1988) proposed theoretical models for determining abutment stiffness based on the soil properties and abutment dimensions. However, these models do not include the significant effects of nonlinear soil behavior (Shamsabadi et al., 2005, 1998; Siddharthan et al., 1995). Martin and Yan (1998) conducted research on load-deformation characteristics of bridge abutments under cyclic loading. In their research, they used a large-strain finite difference computer program, *FLAC* yielding highly nonlinear abutment response.

Several researchers have attempted to determine abutment stiffness and/or vibration properties from field vibration tests on highway bridges (Crouse et al., 1987; Gates and Smith, 1982; Douglas et al., 1990; Ventura et al., 1995). However, such small amplitude tests lead to results that are not useful in design for intense earthquake motions, because the stiffness of abutment depends on level of shaking. Recognizing this limitation of small-amplitude tests, several investigations to estimate abutment stiffness from motions of bridges recorded during earthquakes have been reported (Maroney et al., 1990; McCallen and Romstad, 1994; Werner et al., 1994; Goel and Chopra, 1997). Maroney et al. (1994) described the results of a half scale load test on a monolithic abutment tested to failure.

It is evident that from the abutment backfill experimental studies (Romstad et al. 1995), system identifications techniques (Wilson et al., 1990; Werner et al., 1994; Goel et al., 1997) and theoretical studies (Shamsabadi et al., 2005; Martin et al., 1999; and Sidharthan et al., 1997) that the behavior of the bridge abutment-backfill system is increasing nonlinear as displacement increases. Experiments conducted by

Thomson and Lutenegger (1998), Fang and Ishibashi (1994), Sherif et al. (1992), Row (1954), and Terzaghi (1936) show that both the deformation mode and magnitude of the deformation affect the magnitude and distribution of the earth pressure. Results from the full-scale cyclic tests (Duncan and Mokwa, 2001; Rollins and Sparks, 2002; and Rollins and Cole, 2005) to measure a lateral resistance of a pile cap with a various backfill soils suggest that the force-displacement relationship of the backfill is highly nonlinear and it is a function of backfill properties, formation of the gap between the backfill and the pile cap at each loading cycle and the level of pile cap displacement. Gadre (1997) performed centrifuge tests on model pile cap and seat type abutment in dry Nevada sand. The most prominent feature in the mobilized passive force response was the large reduction of the backfill stiffness as a function of displacement after unloading or reloading occurs. There was a large drop-off on the load due to the formation of the gap between the backfill and the structure under cyclic loading. Similar to the Rollins' pile cap test, upon gap closure and structure contact with the backfill the load started to build up. The experimental results also indicate that limiting equilibrium analysis using a logarithmic spiral failure surface may be more appropriate to compute the ultimate passive earth pressure.

Several researchers have attempted to capture seismic response of the instrumented short span highway bridges (i.e., Painter Street Overpass, a skewed-bridge and Meloland Overpass, a non-skewed-bridge) using field vibration test records or earthquake seismic records and using spline models or more complicated

finite element models. Very high modal damping and discrete elastic abutment stiffness values were selected as they lead to a good match between the elastic earthquake response of the models and the motions recorded during the earthquake. These may not be valid assumptions because the global system will behave in a nonlinear manner during strong shaking (Goel and Chopra, 1997). Zhang and Markis (2001) adopted a substructure approach where the kinematic motions and linear elastic foundations and abutments stiffness were computed separately and subsequently incorporated in the dynamic model for the Meloland and Painter Street Models. Substructuring system is a matrix reduction technique that has been used efficiently for seismic analysis linear systems. However, as mentioned above the bridge abutment is highly nonlinear and substructuring technique is not suitable to represent bridge abutments.

Sweet and Morill (1993) presented a three-dimensional continuum finite element analyses which included large volume of, surrounding embankment soil and the structure system for the Painter Street Overcrossing as shown in Figure 2.3. However, the soil properties were based on numerous assumptions that are not valid based on a recent investigation conducted at the bridge site. Furthermore, the analysis approach is not suited for typical bridge design applications.

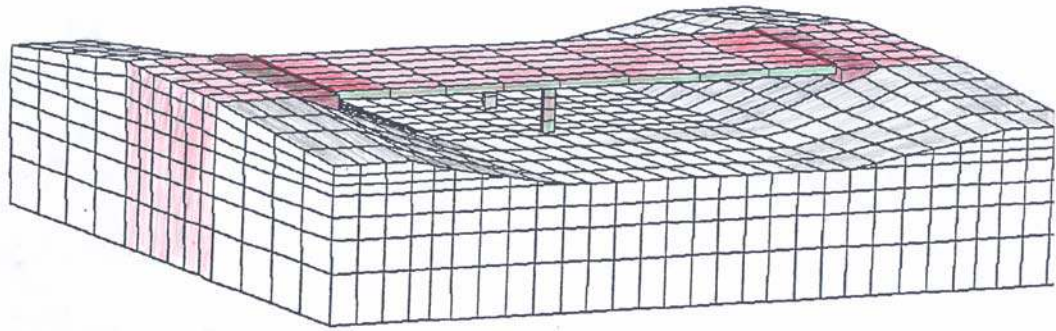


Figure 2.3: 3-D Continuum (Sweet and Morill, 1993)

MaCallen and Romstad (1994) also developed a large three-dimensional finite element model for the Painter Street as shown in Figure 2.4.

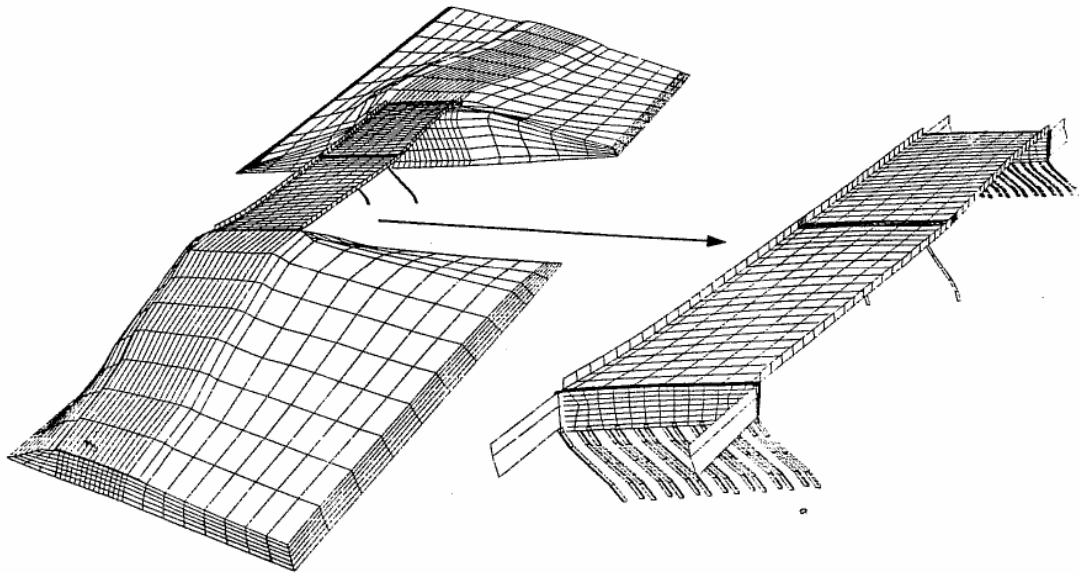


Figure 2.4 : 3-D Continuum (Maroney,1995)

These types of simulations require the use of rigorous three-dimensional finite element models. The three-dimensional finite element computational is very expensive and time consuming. The models require the use of appropriate boundary

conditions, advanced nonlinear constitute models with a robust interface element between the abutment-backfill, abutment backwall, bridge deck and the pile foundations and surrounding soils. For these types of large models if coarse mesh is selected the level of accuracy will be lost. Therefore, these types of models with high complexity are unrealistic and should not be used in engineering practice. As an alternative to the three-dimensional finite element models, simple and practical nonlinear soil springs connected to the beam elements representing the pile foundations. Nonlinear springs should be used to connect abutment-backfill to bridge deck.

The impact of the bridge abutment on the overall response of a bridge structure depends on many factors including bridge displacement, abutment skew angle, and backfill strength and stress-strain properties. The nonlinear force displacement capacity of the bridge abutment in a seismic event is developed mainly from the mobilized passive pressure behind the abutment wall. From the time of the French scientist Coulomb (1776) to the present, the analysis of lateral earth pressure evaluation has been of prime interest to civil engineers. Literature on the subject of earth pressure computation is rather abundant; however, most of it involves certain simplifying assumptions. Coulomb (1776) presented a theory to evaluate the lateral earth pressure against retaining structures based on the concept of limiting equilibrium for cohesionless backfill. He assumed that the slip surface is a plane and passes through the heel of the wall at a certain angle. The friction between the wall and the adjacent soil is taken into account.

Rankine (1857) considered the equilibrium of a soil element within a semi-finite soil mass bounded by a plane surface. Rankine's theory is the same as Coulomb's theory except in his assumption no shearing stress exist along the wall, and therefore, the friction between the wall and the soil does not exist. However, frictional forces do exist specially during earthquake the behavior of the soil is governed by compression forces induced by the abutment tending to push into the soil. Thus the basic assumption used by Rankine is not valid. Tschbotarioff (1951), in his book Soil Mechanics Foundation and Earth Structure, quotes Terzaghi, "*The fundamental assumptions of Rankine in earth pressure theory are incompatible with the known relation between stress and strain in soils, including sand. Therefore, the use of this theory should be discontinued.*"

All of the methods now in common use are based on these theories. The limiting equilibrium approach originating with Coulomb is statically indeterminate along the straight line failure plane. However, it is statically determinate along a curved failure plane. Developments since 1920, largely due to the influence of Terzaghi, have led to a better understanding of the limitations and appropriate applications of the classical earth pressure theories. Many experiments have been conducted to prove the validity of the wedge theory and it has been found that the sliding surface is not a plane, but a combination of a curve and straight line. Furthermore these experiments have shown that the classical earth pressure theories for cohesionless soil lead to quite accurate results for backfill of clean dry sand for

low wall-backfill friction angle. However, realistically most structural backfill materials possess cohesion and a structure soil interface friction angle.

Kerry (1936) developed the friction circle method using trial and error procedures. In this method the lower portion of the slip surface is assumed to be curved in the form of arc of a circle which joins continuously to the upper portion of the slip surface which is a straight line.

Caquot and Kerisel (1948) provided tables for passive earth pressure coefficients only for cohesionless soil using the arc of an ellipse for the failure plane as shown in Figure 2.5.

Sokolovski (1960) developed the Method of Characteristic by using finite difference technique. Rosenfard and Chen (1972) applied plasticity theory and their results compared very well with those of Sokolovski. Lambe and Whitman (1969) reported that Sokolovski's method is an alternative which may be used to evaluate soil passive resistance. However this method gives the same solution as that proposed by Terzaghi (1943) using a trial curved failure surface.

Janbu (1957) proposed the use of method of slices and bearing capacity calculation techniques for evaluating passive earth pressure coefficients.

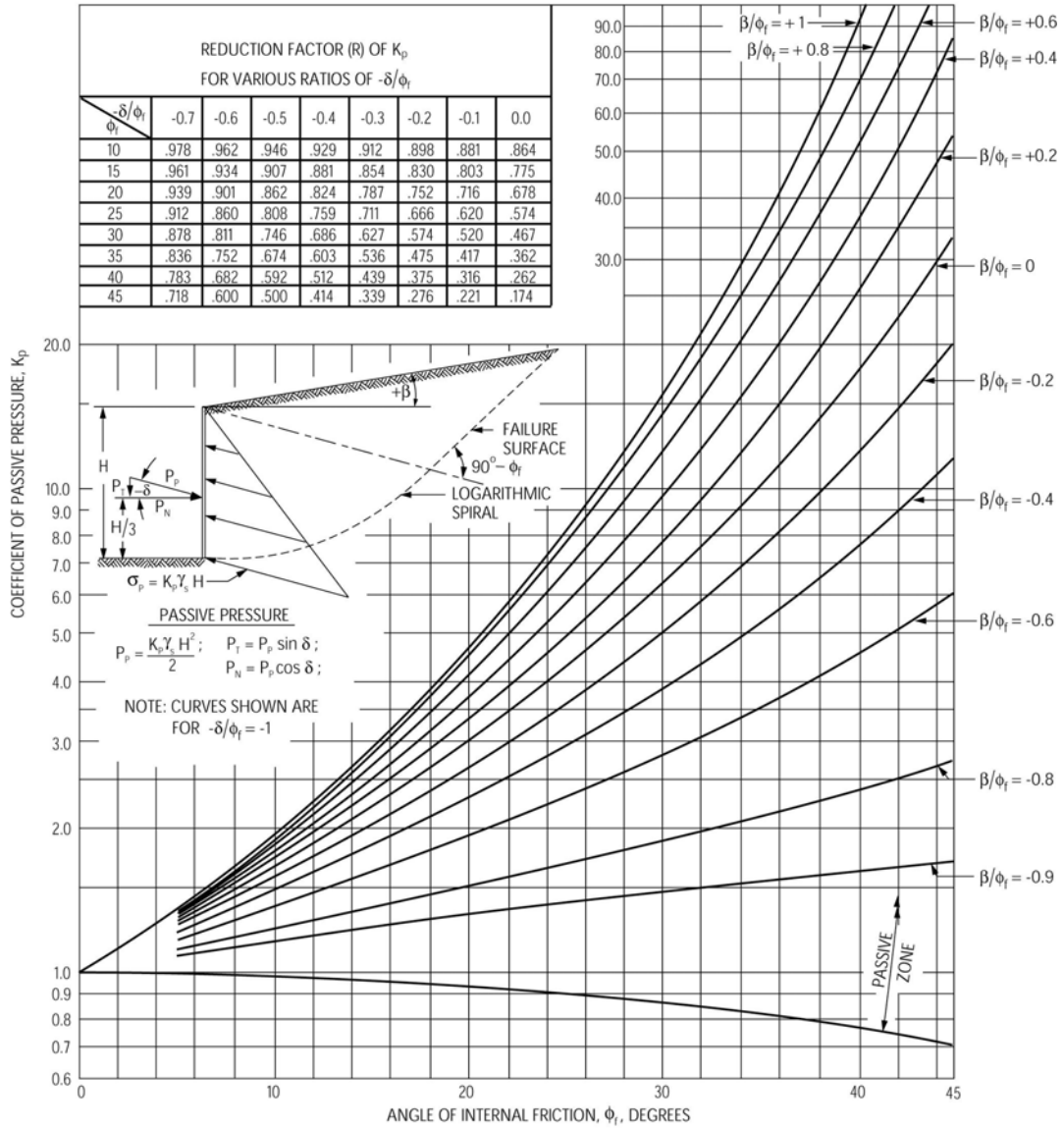


Figure 2.5: Passive Earth Pressure Coefficient (Caquot and Kerisel 1948)

Rowe and Peaker (1965) conducted several laboratory tests on rigid walls and concluded that the peak values of the soil friction angle ϕ and the wall friction angle δ should not be used in theoretical expressions for earth pressure computations without a reduction factor.

Narain, Saran and Nandakunran (1969) have conducted several laboratory tests with a rough wall having a vertical face and horizontal backfill. Passive pressure at various depths of the wall was measured when the wall was subjected to rotation about its bottom, its top and horizontal translation. They concluded that none of the more common theories including Terzaghi's were found to give the passive earth resistance or the size and shape of the rupture wedge correctly.

Shields and Tolunay (1973) used simplified Bishop's method of slices and logarithmic failure surface to predict passive earth pressure coefficients. They assumed no interslice shear force developed along the slice boundary. This indicates that there is only a large shear force at the first slice (face of the wall) compare to other slices. They concluded that for dense sand ($\phi = 40^\circ$) the method of slices gives earth pressure coefficient K_p values which are in better agreement with experimental values than other theories. For loose sand ($\phi = 34^\circ$) the other theoretical values of K_p are closer to the experimental values, but the slice method values are lower and, therefore, more conservative. However, recent experimental test results conducted by various universities and institutions indicated that using simplified Bishop's method of slices under predict the passive earth pressure capacity for dense sand since the effect of vertical interslice forces are being ignored.

In the derivation of the classical earth pressure formulation, no wall movement was specified. Dubrova (1963) recognized this fact and assumed that the backfill material mobilizes its strength to a certain extent that is in proportion to the corresponding wall movement and that the strength varies along the height of the wall. The extensive experimental work conducted by James and Bransby (1970, 1971) remarkably showed that wall movement is a function of backfill shear strain and mobilized shear strength.

Prakash and Rafnsson (1991) used a simplified method to estimate the backfill stiffness as a function of three variables which are displacement, at-rest earth force and ultimate earth forces. Because stiffness by definition is the ratio of change in force to change in displacement, they used the following relationship to estimate the passive stiffness of the backfill.

$$K = (F_p - F_o) / d_p \quad (2.1)$$

Rahardjo, Fredlund, and Fan (1995) used the method of slices and two-dimensional finite element analysis to compute lateral earth pressure for dry sand. They concluded that the interslice shear forces occur as a result of soil displacement, the magnitude of mobilized wall-soil interface friction angle δ and the shear forces dissipate from the maximum at wall to zero at some distance away from the wall and the selection of proper interslice force function is essential for an accurate passive earth pressure computation.

Martin, Yan, and Lam (1997) conducted advanced theoretical studies at the University of Southern California using the two-dimensional explicit finite

difference computer program *FLAC* (ITASCA, 1995) for improved seismic design of bridge abutment. They used a simple elastoplastic constitutive modeling in a numerical analysis to evaluate passive earth pressure capacity of several abutment-soil combinations. Based on this study it can also be concluded that all of the acceptable common theories for passive earth pressure computation over predict the bridge abutment capacity for competent embankment approach fills.

Shamsabadi et al. (2005) developed nonlinear abutment force-deformation based on the exponential empirical stress-strain relationship (Norris, 1998, 1979) shown in Figure 2.6.

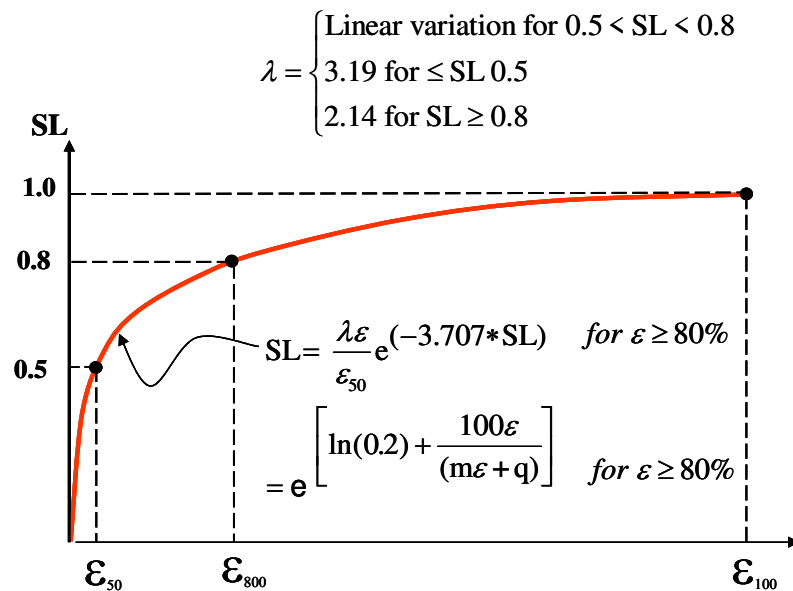


Figure 2.6: Stress-Strain Relationship (Shamsabadi et al., 2005)

2.2 Abutment Behavior During a Seismic Event

Reconnaissance reports after a number of earthquakes around the world all indicated that approach embankment failure resulted in many bridge closures. During a seismic event, depending on its magnitude, the abutment structural

capacity, and the pile-abutment connection details different types of damage will occur. For instance, the backwall shear failure and formation of the mobilized passive wedge (shown in Figure 2.7) are the result of the bridge cyclic displacement of the bridge deck in the longitudinal direction.



Figure 2.7: Backwall Shear Failure and Mobilized Passive Wedge

The top of the abutment is pushed back by the impact from the superstructure. Since there is no longer sufficient lateral embankment resistance, as a result of abutment displacement and rotation the bottom of the abutments moves forward, pushing out the slope paving and imposing high flexural as well as shear demand on the abutment piles. During the June 2001 Atica earthquake in Peru, the

north abutment of the Puente Los Banos bridge (a three-span continuous RC box girder structure supported on two-column bents and seat-type abutments) experienced significant displacement and rotation.

2.3 Caltrans Abutment Design Criteria

Field experiment from the full scale abutment testing conducted at the University of California, Davis forms the basis for development of abutment springs in longitudinal direction to simulate bridge-abutment-backfill interaction during a seismic event. The experimental set up is shown in Figure 2.8. The wall height and width were 5.5 feet and 10 feet, respectively. The soil used to construct the embankment in this abutment test was Yolo Loam-compacted clay with an undrained shear strength of about 2 ksf and unit weight of 120 pcf. The abutment-embankment interface friction angle (δ) was estimated to be 22 degrees. The horizontal force versus displacement curve measured from the test is shown in Figure 2.9 indicating highly nonlinear behavior. The ultimate abutment backfill capacity was approximately 312 kips. The abutment experienced over 6 inches of longitudinal displacement and 2 degrees of rotation.



Figure 2.8: UC-D Test Setup (Maroney, 1995)

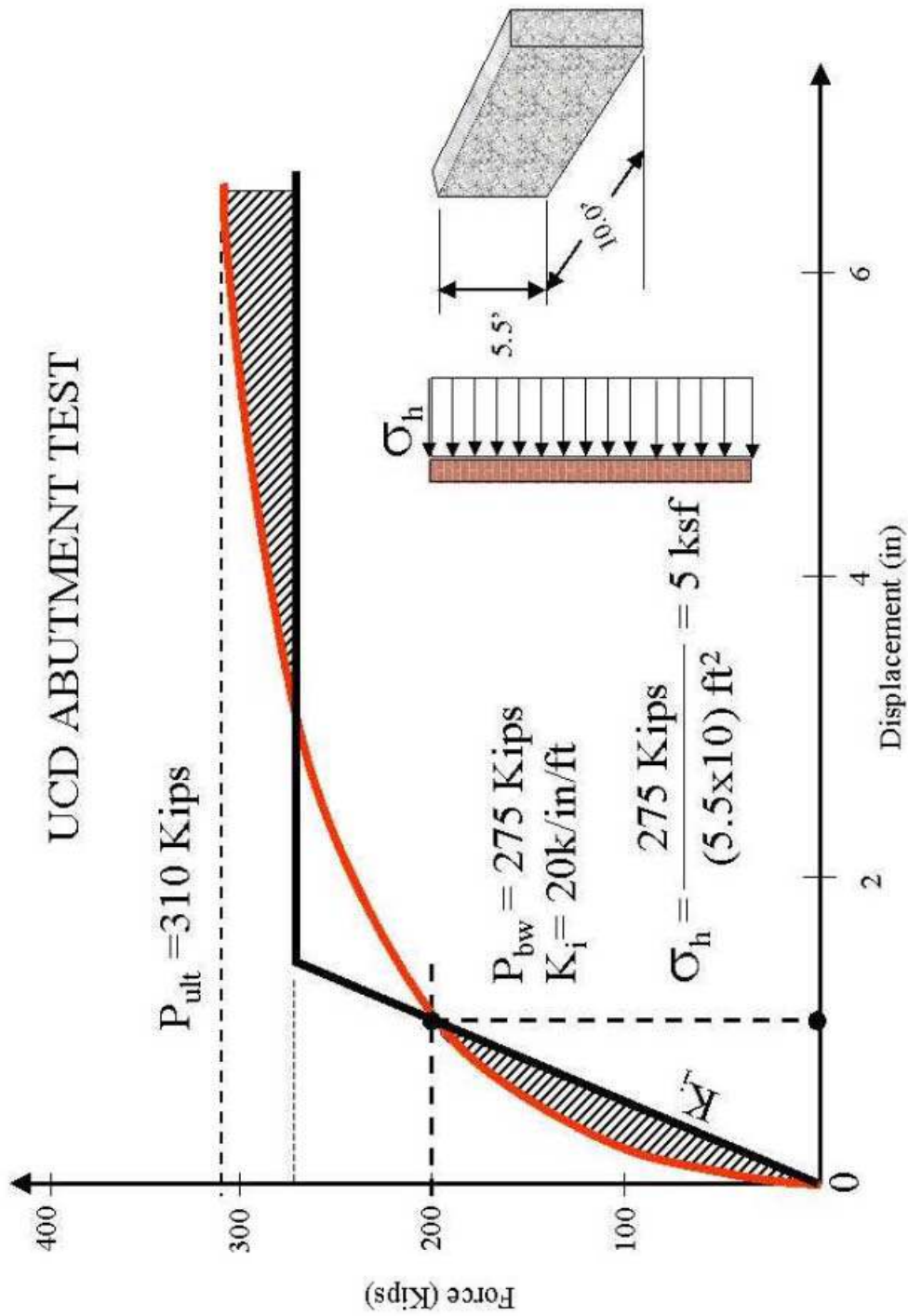


Figure 2.9 : Estimated Bilinear Abutment Stiffness

The nonlinear force-deformation relationship and the idealized bilinear curve per Caltrans recommendation is also shown in Figure 2.9. This idealization resulted ultimate abutment pressure of 5 ksf and an average stiffness of 20 kips per inch per foot of abutment. For the longitudinal abutment response currently per Caltrans Seismic Design Criteria (SDC, 2004), acceptable design procedure for the seismic design of the bridge abutment is the idealized bilinear force deformation relationship shown in Figures 2.9 and 2.10.

Adjustment height factor based on the height of the UC Davis abutment is considered according to the following equations for other wall heights.

The initial stiffness and the maximum passive capacity provide by the abutment backfill are adjusted proportional to the abutment backwall height as shown in Equations (2.2) and (2.3).

$$K_{abut} = K_i * W * \alpha \quad (2.2)$$

$$F_{abut} = A_e * 5.0 * \alpha \quad (2.3)$$

Where

$$\alpha = \left(\frac{h}{5.5} \right) \quad (2.4)$$

W is the width of the backwall and A_e is the effective width of the backwall.

Regarding the seat-type abutment shown in Figure 2.11b, for the linear elastic demand model effective abutment stiffness, K_{eff} that accounts for expansion gaps, and incorporates a realistic value for the abutment backfill response is used.

For diaphragm abutments shown in Figure 2.11a, the entire diaphragm above and below the soffit is typically designed to engage the backfill immediately when the bridge is displaced longitudinally. Therefore, the effective abutment area is equal to the entire area of the diaphragm. If the diaphragm has not been designed to resist the passive earth pressure exerted by the abutment backfill, the effective abutment area is limited to the portion of the diaphragm above the soffit of the deck.

$$\begin{aligned}
 A_e &= h_{bw} W_{bw} && \text{Seat Abutment} \\
 A_e &= h_{dia} W_{dia} && \text{Diaphragm Abutment}
 \end{aligned}
 \tag{2.5}$$

$h_{dia} = h_{dia}^*$ = Effective height if the diaphragm is not designed for full soil pressure (see Figure 2.11: Effective Abutment Area).

$h_{dia} = h_{dia}^{**}$ = Effective height if the diaphragm is designed for full soil pressure (see Figure 2.11: Effective Abutment Area).

Per current Caltrans SDC, typically abutment shear keys are expected to transmit the lateral shear forces generated by small earthquakes and service loads. Determining the earthquake force demand on shear keys is difficult. The forces generated with elastic demand assessment models should not be used to size the abutment shear keys. Per SDC 2004, shear key capacity for seat abutments shall be limited to the smaller of the following:

$$F_{sk} \leq \begin{cases} .75 \times \sum V_{pile} \\ 0.3 \times P_{dl}^{sup} \end{cases}
 \tag{2.6}$$

$\sum V_{pile}$ = Sum of the lateral pile capacity

P_{dl}^{sup} = Axial dead load reaction at the abutment

For abutments supported on spread footings the shear keys are only designed to 0.3P. Wide bridges may require internal shear keys to insure adequate lateral resistance is available for service load and moderate earthquakes. Internal shear keys should be avoided whenever possible because of maintenance problems associated with premature failure caused by binding due to the superstructure rotation or shortening. Sufficient abutment seat width shall be available to accommodate the anticipated thermal movement, prestress shortening, creep, shrinkage, and the relative longitudinal earthquake displacement. Per SDC 2004, the seat width normal to the centerline of bearing shall be calculated by equation 2.7 but not less than 30 inches as shown in Figure 2.13.

$$N_A \geq \left(\Delta_{p/s} + \Delta_{cr+sh} + \Delta_{temp} + \Delta_{eq} + 4 \right) \quad (2.7)$$

Where

N_A = Abutment seat width normal to the centerline of bearing

$\Delta_{p/s}$ = Displacement attributed to pre-stress shortening

Δ_{cr+sh} = Displacement attributed to creep and shrinkage

Δ_{temp} = Displacement attributed to thermal expansion and contraction

Δ_{eq} = The largest relative earthquake displacement between the superstructure and the abutment calculated by global or stand-alone analysis

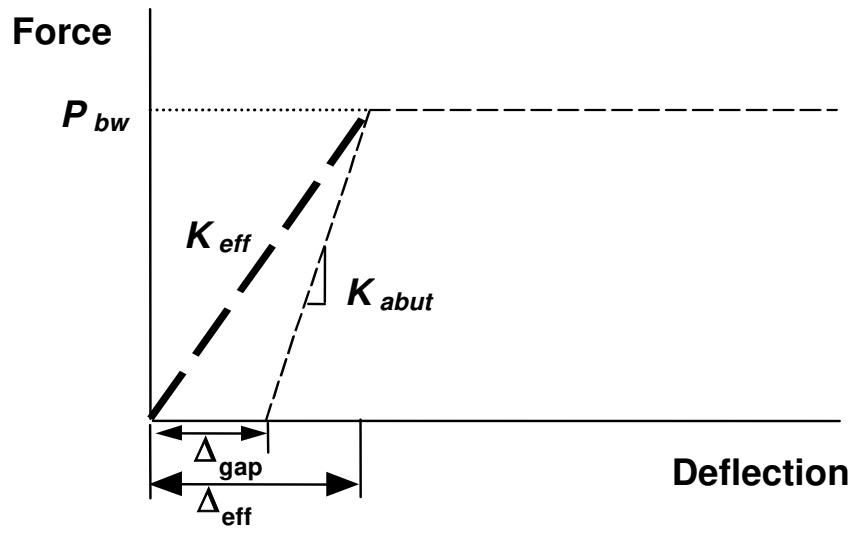


Figure 2.10: Effective Abutment Stiffness (SDC, 2004)

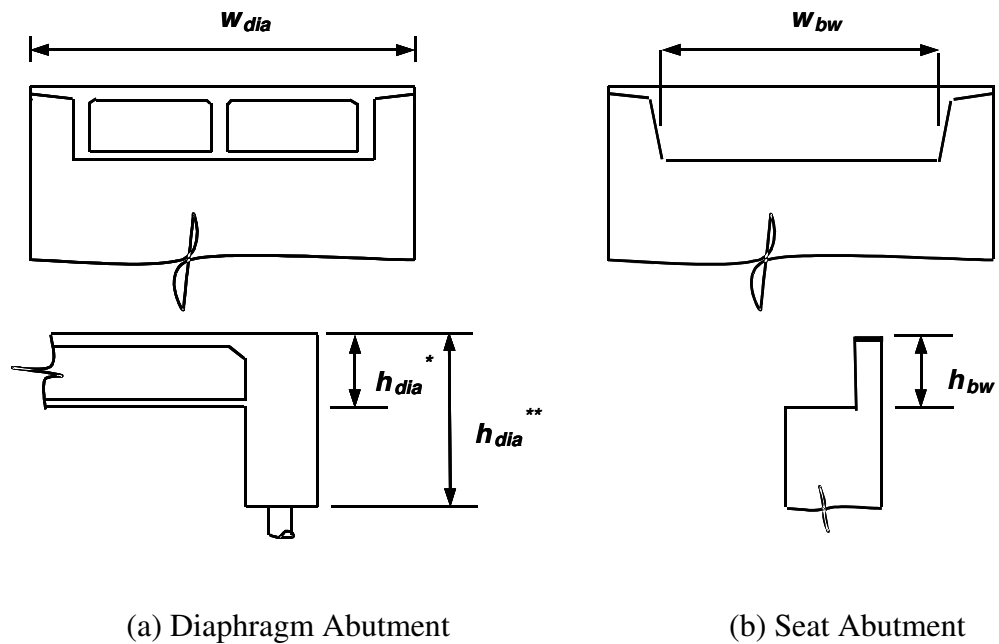


Figure 2.11: Effective Abutment Area (SDC, 2004)

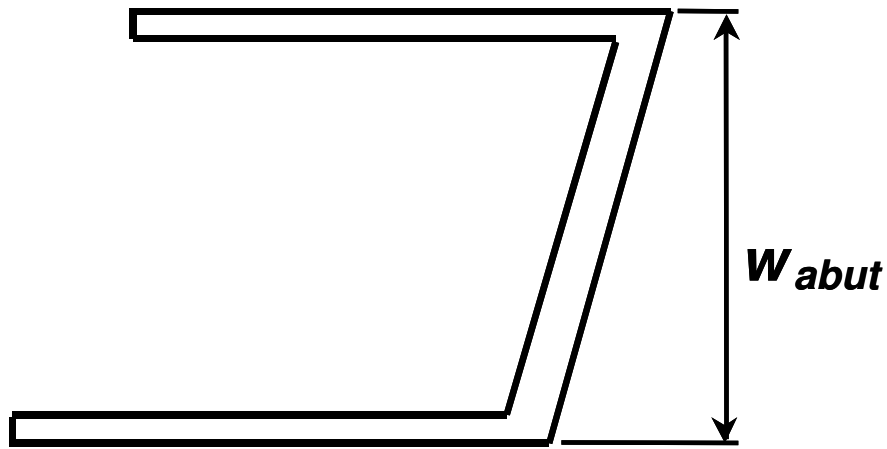


Figure 2.12: Effective Abutment Width for Skewed Bridges (SDC, 2004)

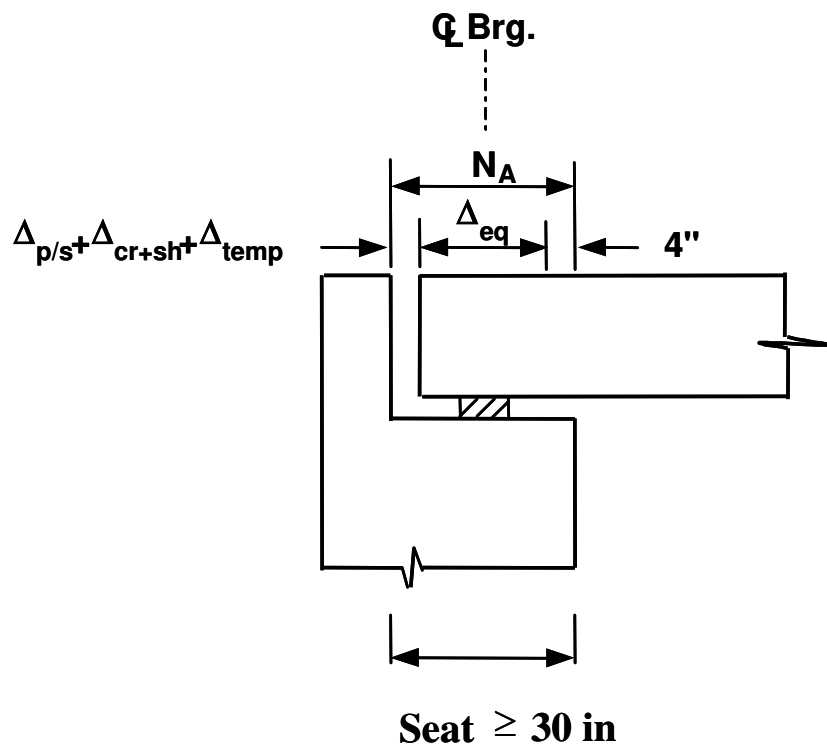


Figure 2.13: Abutment Seat Width Requirements (SDC, 2004)

CHAPTER THREE

ABUTMENT LSH MODEL

3.1 Introduction

Current seismic design of bridges is based on a displacement performance philosophy. This type of bridge design necessitates that geotechnical engineers predict the resistance of the abutment backfill soils, which is inherently nonlinear with respect to the displacement between soil backfill and the bridge structure. Usually bridge engineers ignore the contributions of the abutment resistance in seismic design of bridge structures due to complexity of the abutment soil-structure interaction.

The objective of this chapter is to apply a limit-equilibrium method using mobilized Logarithmic-Spiral failure surfaces coupled with a modified Hyperbolic soil stress-strain behavior (the “LSH” model) to capture the nonlinear abutment force-displacement relationship. The LSH model is developed to estimate abutment nonlinear force-displacement capacity as a function of wall displacement and soil backfill properties. The predicted results obtained using the LSH model are compared with the results obtained from a total of nine experiments conducted on various typical structure backfills. The predicted capacities calculated from the LSH model are in good agreement with the measured capacities from the experiments. The LSH model can also be expressed directly as a function of average soil stiffness

and ultimate soil capacity that can be used as a powerful and effective tool for performance-based bridge design.

3.2 Types of Bridge Abutments

A bridge abutment consists of stem walls to support the bridge deck. The footing to support the stem and the wingwalls attached at the end of each abutment to retain the abutment-backfill in between the wingwalls. Abutments are basically classified into two types: (1) seat-type-abutments, and (2) monolithic abutments.

Seat-type-abutments are located at or near the top of approach fills, with a backwall depth sufficient to accommodate the structure depth. The seat-type abutment is constructed separately from the bridge deck. The bridge deck rests on the abutment seat through bearings pads as shown in Figure 3.1.

Monolithic abutments are cast integrally with the superstructure and are supported on either spread footings or pile foundations as shown in Figure 3.2. For monolithic abutments, the entire backwall is typically designed to engage the backfill immediately when the bridge is displaced longitudinally. If the backwall has not been designed to resist the passive earth pressure exerted by the abutment backfill, the effective abutment height is limited to the depth of the bridge deck.

Figure 3.3 shows an example of the abutment damage occurred in the June 2001 Attica earthquake in Peru. The north abutment of the Puente Los Banos Bridge (a three-span continuous RC box girder structure supported on two-column bents and seat-type abutments) experienced significant displacement and rotation.

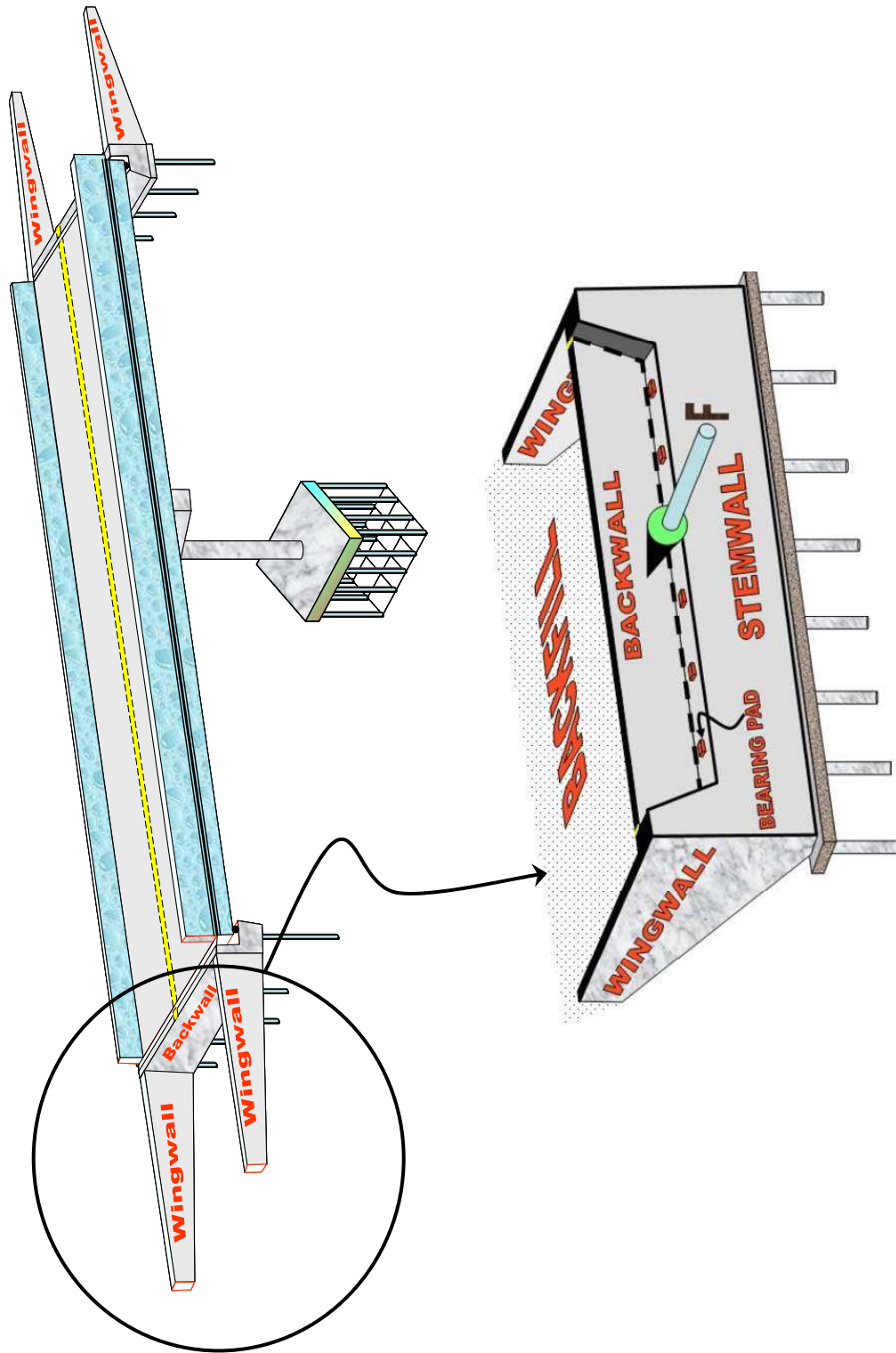


Figure 3.1: Seat-Type Abutment and Foundation System

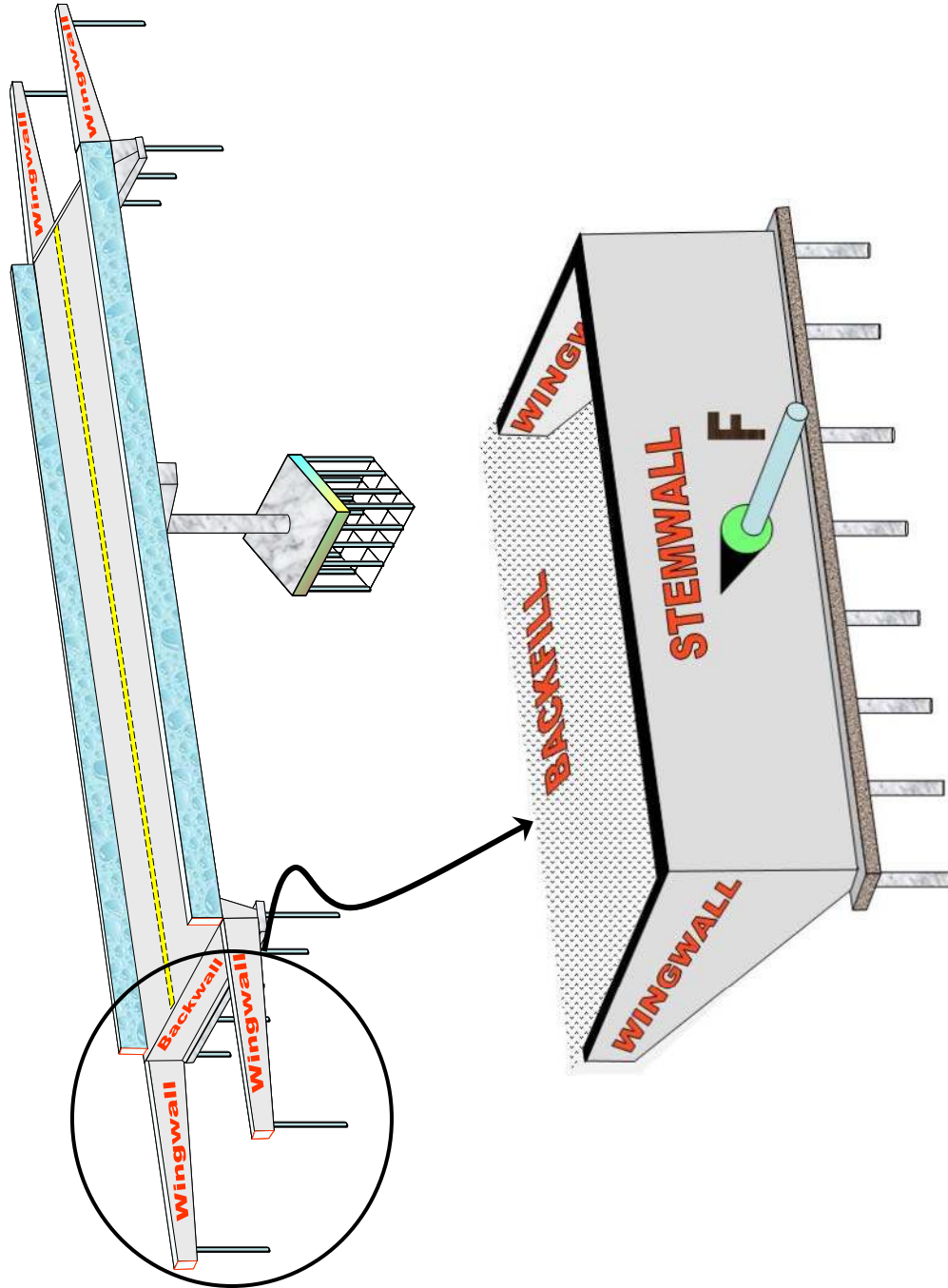


Figure 3.2 : Monolithic Abutment and Foundation System



Figure 3.3: Example of Mobilized Passive Wedges

The top of the abutment was pushed back by the impact from the superstructure. Since there was no sufficient lateral embankment resistance as a result of abutment displacement and rotation, the bottom of the abutments moves forward, pushing out the slope paving and imposing high flexural as well as shear demand on the abutment piles.

3.3 Seismic Behavior of Seat-Type Abutments

During a seismic event, the bridge moves laterally and collides with the abutment backwall in between the wingwalls. The backwall is designed to break off as a result of seismic force F in order to protect the foundation from inelastic action

as a result of backwall displacement. This type of abutment allows the bridge engineers to control the amount bridge deck forces and or displacement that are to be transferred to the abutment backfill.

The abutment force-deformation capacity is provided by the passive resistance of the abutment backfill. A typical highway bridge is wide and has a moderate back wall height, often 5 to 6 feet. The earth pressure problem is then a plane strain problem and 2-D simulations may be sufficient to simulate the abutment-backfill response.

3.4 Seismic Behavior of Monolithic Abutments

Contrary to the seat-type abutment, the monolithic abutment has the potential for heavy damage during a major seismic event. There is no relative displacement allowed between the superstructure and abutment. All the superstructure forces at the bridge ends are transferred to the abutment backwall and then to the abutment backfill and foundations. The lateral force-deformation capacity of the monolithic abutment is a function of abutment backfill properties as well as foundation and structural capacity of the abutment backwall.

3.5 Force-Displacement Capacity of Bridge Abutment

Bridges are one of the most crucial parts of the transportation network which have been struck by earthquakes in the past. It is generally recognized that when the bridge deck moves laterally towards the abutment during a seismic event, the bridge structure applies a lateral compressive force to the abutment which mobilizes passive resistance in the soil backfill and results in permanent soil displacement. When the

bridge moves away from the abutment, a gap can form between the bridge deck and the abutment backfill.

When bridges are subjected to small earthquake-induced lateral forces, they generally remain in the elastic range. When subjected to strong earthquake shaking, however, the dynamic response of the bridge becomes nonlinear and is largely dependent on the nonlinear soil-structure interaction effects between the abutments and the backfill soils. The nonlinear force-displacement-capacity of the bridge abutment in a seismic event is developed mainly from the mobilized passive pressure behind the abutment backwall. Proper modeling of the abutment-backfill system is therefore critical and the assumptions made for the nonlinear stiffness as well as the hysteretic of the abutment have been shown to have a profound effect on the global seismic response and performance of the bridge (Shamsabadi et al., 2005; Shamsabadi et al., 2007; Faraji et al., 2001; El-Gamal and Siddharthan, 1998).

There are many bridges with seat-type abutments in which the bridge deck is supported by the abutments on bearings and the columns are supported by a pinned connection at the base of the column to the pile caps or spread footings. The performance of these bridges during seismic shaking is profoundly affected by the interaction between the backfill soil and the abutment structure which involves relative displacement and soil stress-strain behavior.

Earth pressure theories are developed based on different assumptions and employ various methods to predict lateral soil-abutment capacity. As a result, the capacities they predict can vary drastically from each other. The distribution and the

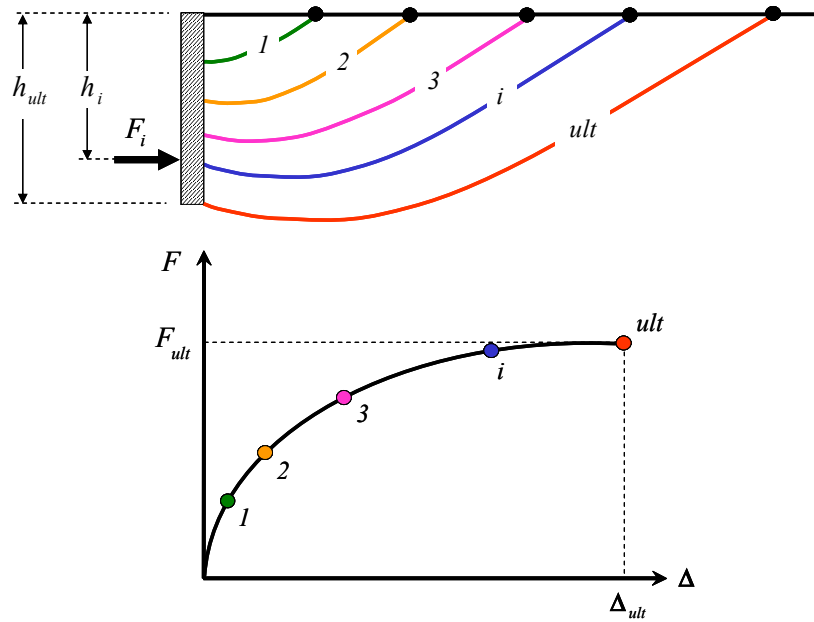
magnitude of the lateral soil-abutment resistance are highly dependent on the abutment displacement. In spite of this, classical earth pressure theories give no information about the wall movement. In order to calculate the wall passive pressure as a function of wall movement, advanced analytical model such as finite element (Shamsabadi et al., 2006) or finite difference (Martin et al., 1997) models should be used. The analyses using these types of models are very expensive and time consuming. They are also complex because they require the use of appropriate boundary conditions, advanced nonlinear constitute models with a robust interface element between the abutment-backfill and the abutment backwall. Therefore, they are not feasible to be used in day- to-day bridge design.

The purpose of this chapter is to present a new model to predict the realistic nonlinear lateral force-displacement capacity of a regular bridge abutment as a function of common backfill properties and structural configurations. The basic framework of the formulation is based on the mobilized Logarithmic Spiral (LS) failure coupled with modified Hyperbolic (H) abutment-backfill stress-strain behavior.

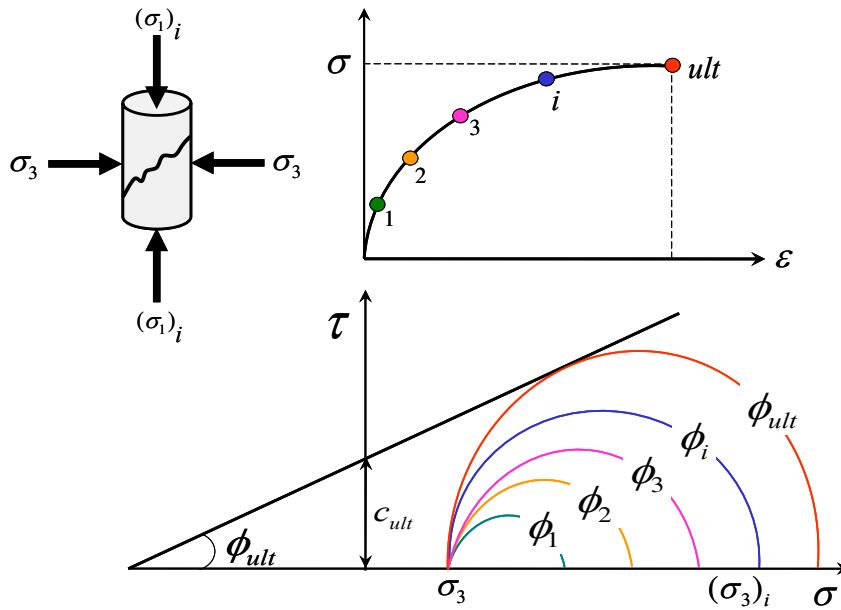
The LSH relationship which was developed from evaluation of a large number of experimental test data can used to calculate the backfill capacity. The LSH model can be used by geotechnical and bridge engineers to calculate the backfill capacity as a function of soil stress-strain and strength characteristics, and therefore it requires an understanding of soil mechanics.

3.6 Mechanism of the Abutment Backfill Failure

In the derivation of the classical earth pressure formulation, no wall movement was specified. Dubrova (1963) recognized this fact and assumed that the backfill material mobilizes its strength to a certain extent that is in proportion to the corresponding wall movement and that the strength varies along the height of the wall. The extensive experimental work conducted by James and Bransby (1970, 1971) remarkably showed that wall movement is a function of backfill shear strain and mobilized shear strength. Therefore, when an abutment wall is loaded monotonically by a horizontal force F , the wall is resisted by the mobilized passive resistance of the abutment backfill as a function of relative displacement Δ between the wall and the backfill. For intermediate levels of displacement ($\Delta < \Delta_{ult}$), the shear strength of the backfill can not be fully mobilized and therefore, the final passive wedge can not be formed behind the abutment-wall. It is assumed that at each level of displacement, Δ , a mobilized passive wedge is formed and as a result, an intermediate passive resistance force F is developed. When the displacement becomes large enough ($\Delta = \Delta_{ult}$), the shear strength of the backfill will be fully mobilized and the ultimate passive backfill capacity F_{ult} develops as shown in Figure 3.4.



(a) Force-Displacement Relationship



(b) Stress-Strain Relationship

Figure 3.4: Mobilization of Passive Resistance

The formation of these wedges is primarily a function of the stress-strain behavior of the backfill. The intermediate levels of displacement are associated with intermediate states of strain (ϵ) and stress (τ). The ultimate wedge forms at maximum level of strain (ϵ_{ult}). This stress-strain relationship will be used to calculate the “mobilized” shear strain levels (γ_i) and shear strength parameters of the backfill soil in order to predict the nonlinear passive force as a function of wall-soil displacement.

The abutment-backfill failure mechanism has been observed to occur for both wall rotations about the toe as well as translations during major seismic events (Kosa et al., 2001), small-scaled laboratory experiments (Maciejewski et al., 2004; Bransby, 1971)) and large-scaled field experiments (UCLA, 2006; Rollins et al., 2006).

Bransby (1970, 1971) observed in rigid wall load tests that the failure surfaces in dense sand progress from the top down for both failure modes. Maciejewski and Jarzebowski (2004) made similar observations in load tests of a rigid wall pushed into silty sand for translation.

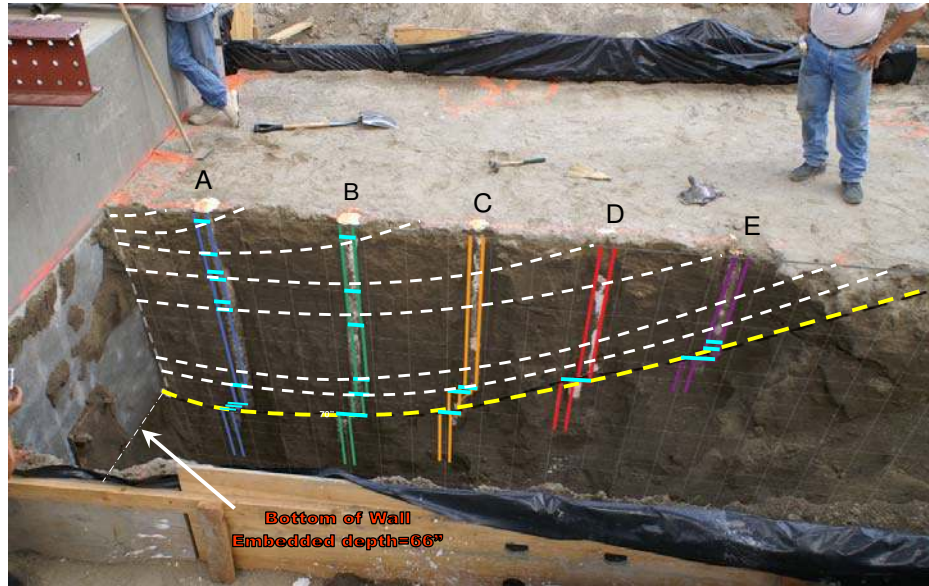
Rollins (2006) showed the traces of multiple passive wedges in cracking patterns behind a pile cap progressing with increasing distance from the pile cap.

As part of UCLA-Caltrans research program, a full-scale cyclic load tests was conducted to develop abutment nonlinear force-deformation relationship for a typical backfill (2006). Before the test, 3-inch diameter vertical holes were drilled along the longitudinal centerline of the abutment into the abutment backfill and filled

with brittle gypsum columns to map the failure mechanism of the abutment backfill placed behind the backwall as shown in Figure 3.5a. After the completion of the test, a longitudinal trench was excavated and the failure mechanism of the backfill was carefully investigated by mapping the deformation and cracks of the gypsum columns. The pattern of the cracks developed in the gypsum columns illustrates the development of successive plane-strain failure surfaces that mobilize as a function of lateral displacement and backfill properties. The deformed wedges started to develop within the upper soil layer and progress deeper down and away from the backwall.

Observations and post earthquake investigations have also indicated that during a major seismic event mobilized passive wedges will form within the abutment backfill. The effect of an actual earthquake pushing a bridge deck into the abutment-backfill is shown in Figure 3.5b. This is an example of the mobilized passive wedge formation when a bridge superstructure has been pushed into the abutment-backfill due to longitudinal seismic excitation. The surface cracks were developed in the roadway pavement behind the northern (77-foot wide, near-normal 5° skew) abutment of the Shiwei Bridge in Taiwan during the Chi-Chi earthquake (Kosa et al., 2001).

The LSH model is developed to simulate such a failure mechanism as a function of abutment height and abutment backfill strength and stress-strain properties. Similar failure mechanism has been observed using two-dimensional and three-dimensional nonlinear finite element models. The finite element models are presented in the next chapter.



(a) UCLA Abutment Field Experiment



(b) Shiwei Bridge after Chi-Chi earthquake (Kosa et al., 2001)

Figure 3.5: Mobilized Wedges During Seismic Event

3.7 Abutment Backfill Constitutive Model

When soils are subjected to stress changes in the laboratory and in the field, they deform in complicated ways, which can be represented in terms of stress-strain relationship (Bardet, 1997). Stress-strain characteristics of the soils are extremely complex, highly nonlinear and inelastic. Bardet (1983) has shown several types of stress-strain behavior that have been observed for various soils as shown in Figure 3.6. In all cases, the soil undergoes both elastic and plastic deformation. The yield stress σ^* marks the transition between elastic and plastic soils behavior. Determination of σ^* is not always trivial and may be subjected to interpretations (Bardet, 1997). This above statement is also true based on all the small-scaled and full-scaled abutment experimental nonlinear force-deformation backbone curves. This is the main reason that the current Caltrans Seismic Design Criteria (SDC, 2006) suggests an average stiffness rather than the initial stiffness should be used to calculate a bilinear force-deformation relationship to model the nonlinear behavior of the backfill as a set of independent horizontal springs based on large-scaled abutment and pile cap field experiments.

The realistic constitutive model must be able to distinguish between the elastic and plastic deformation of the soil behavior up to and beyond the failure.

As part of Caltrans seismic research program, Earth Mechanic Inc. (EMI) conducted State-wide field exploration and cyclic triaxial tests on the in-situ soil samples to characterize strength properties and stress-strain behavior of abutment backfills.

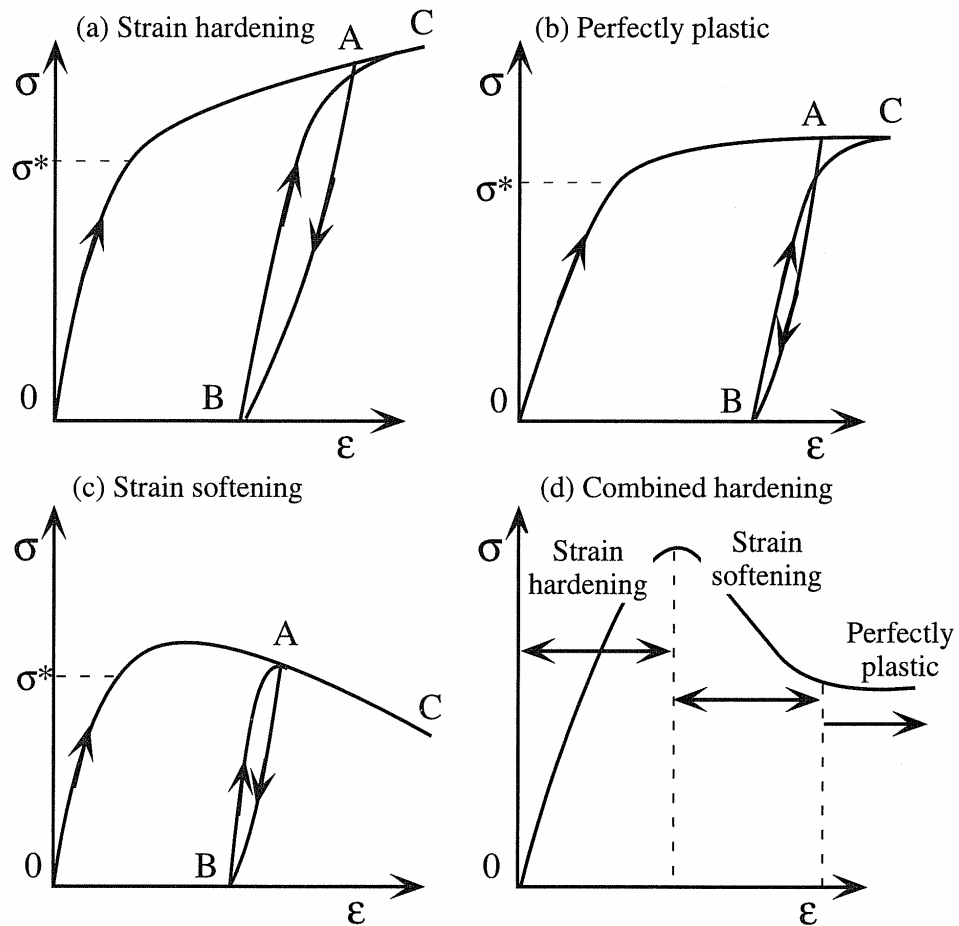


Figure 3.6: Various Types of Elastoplastic Soils Behavior (Bardet, 1997)

The results of the EMI's laboratory cyclic triaxial experiments indicate that the stress-strain behavior of the backfill is highly plastic and nonlinear from the very early stages of the loading as shown in Figure 3.7. The decreasing stiffness and simultaneously irreversible plastic strain were present for all the backfills. Typical abutment-backfill triaxial experimental stress-strain data and the triaxial finite element simulations will be presented in the next chapter.

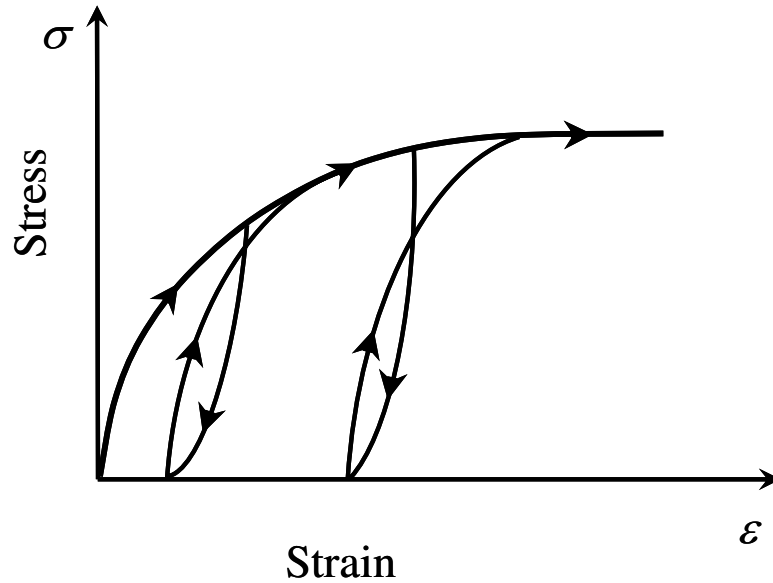


Figure 3.7: Stress-Strain Relationship for Typical Abutment Backfill

Constitutive modeling of the backfill soil mass behavior is an essential component for prediction of abutment force-displacement relationships. It requires an understanding of the shear strength parameters and stress-strain characteristics of the abutment-backfill material. The backfill material model is described by a set of equations that define a nonlinear relationship between the stress and strain. Norris (1998, 1979) developed the basic idea for the formulation of the intermediate mobilized passive wedge coupled with an exponential stress-strain relationship based on triaxial test data to capture the behavior of pile foundations subjected to lateral loading. Shamsabadi et al. (2005) used this relationship to calculate the nonlinear passive force-displacement capacity for cohesionless ($c = 0$) and purely cohesive ($\phi = 0$) abutment backfills.

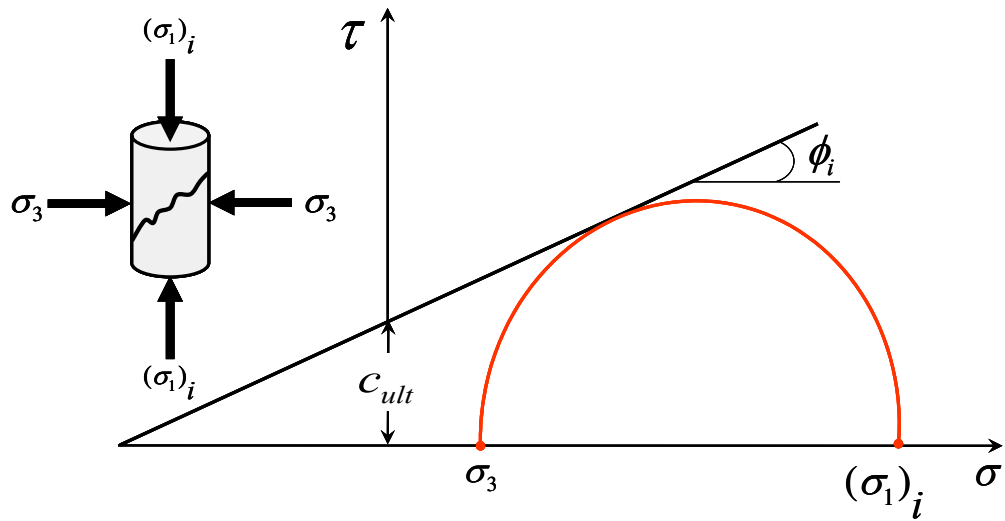
Kondner et al. (1963) have shown that the stress-strain behavior of various soil types can be approximated by a hyperbolic relationship. Duncan and Chang (1970) developed a widely used nonlinear material model which employs this hyperbolic relationship to capture the soil stress-strain behavior. In this chapter, the hyperbolic stress-strain relationship is modified to develop the mobilized backfill shear strength parameters ($\phi-c$) as a function of strain. The modified hyperbolic model consists of one expression compared to the exponential model which consists of three equations. The hyperbolic stress-strain model is found to have better quality and to be easier in matching load test data compared to the exponential relationship.

3.8 Nonlinear Hyperbolic Model

The basic idea for the formulation of the intermediate mobilized passive wedge formation is based on the hyperbolic relationship between the vertical strain ε and deviatoric stress $(\sigma_1 - \sigma_3)$ during triaxial loading. The hyperbolic model described by Duncan and Chang (1970) is shown in Figure 3.8 and defined as follows:

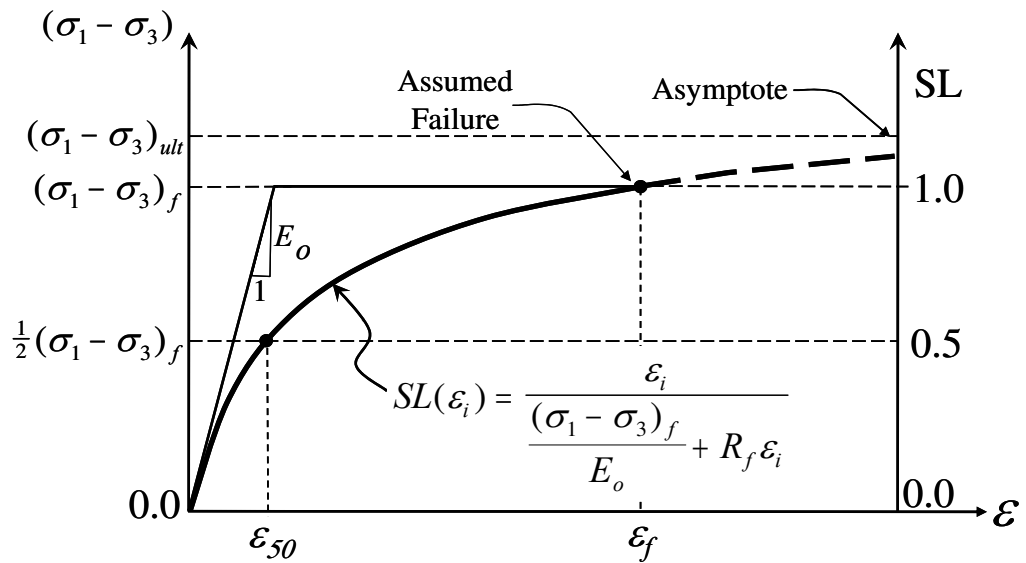
$$(\sigma_1 - \sigma_3)_i = \frac{\varepsilon_i}{\frac{1}{E_o} + \frac{\varepsilon_i}{(\sigma_1 - \sigma_3)_{ult}}} \quad (3.1)$$

In the hyperbolic relationship, the deviatoric stresses increase towards an asymptotic value of $(\sigma_1 - \sigma_3)_i$ and a stress level of $(\sigma_1 - \sigma_3)_f$ must be defined at which the soil is postulated to fail. The failure ratio R_f is introduced that specifies the stress level at failure as follows:



$$(\sigma_1 - \sigma_3)_i = \sigma_3 \left(\tan^2 \left(45^\circ + \frac{\phi_i}{2} \right) - 1 \right) + 2c_i \tan \left(45^\circ + \frac{\phi_i}{2} \right)$$

(a) Stresses



(b) Stress-Strain Relationship

Figure 3.8: Hyperbolic Model

$$R_f = \frac{(\sigma_1 - \sigma_3)_f}{(\sigma_1 - \sigma_3)_{ult}} \quad (3.2)$$

The hyperbolic relationship then can be expressed as:

$$(\sigma_1 - \sigma_3)_i = \frac{\varepsilon_i}{\frac{1}{E_o} + \frac{R_f \varepsilon_i}{(\sigma_1 - \sigma_3)_f}} \quad (3.3)$$

By normalizing the stresses to the stress at failure, the hyperbolic relationship can be expressed in terms of the deviatoric stress ratio $SL(\varepsilon_i)$:

$$SL(\varepsilon_i) = \frac{(\sigma_1 - \sigma_3)_i}{(\sigma_1 - \sigma_3)_f} = \frac{\varepsilon_i}{\frac{(\sigma_1 - \sigma_3)_f}{E_o} + R_f \varepsilon_i} = \frac{\varepsilon_i}{\varepsilon_o + R_f \varepsilon_i} \quad (3.4)$$

The modulus E_o is determined from the slope at the departure of the nonlinear stress-strain curve and is typically difficult to obtain due to the nonlinear nature of curve as was discussed earlier. For practical purposes, the secant modulus E_{50} associated with ε_{50} is used instead (Schanz et al., 1999), where ε_{50} is the strain at which 50% of the failure strength is achieved as illustrated in Figure 3.8.

Figure 3.8 shows three following boundary conditions that the hyperbolic relationship should satisfy:

$$\left. \begin{array}{l} (I) \quad SL = \text{at } \varepsilon_i = 0 \\ (II) \quad SL = 0.5 \text{ at } \varepsilon_i = \varepsilon_{50} \\ (III) \quad SL = 1.0 \text{ at } \varepsilon_i = \varepsilon_f \end{array} \right\} \quad (3.5)$$

Eq. (3.4) satisfies boundary condition (I). It is found that Eq. (3.4) satisfies boundary condition (II) only if the R_f factor is set to 1 and the strain $\varepsilon_{50} = \varepsilon_o$. However, in that

case the equation does not converge as shown in Figure 3.8 and as a result, the hyperbolic function must be modified as shown in Figure 3.9. The hyperbolic equation in a more general form is as follows:

$$SL(\varepsilon_i) = \frac{\varepsilon_i}{A + B\varepsilon_i} \quad (3.6)$$

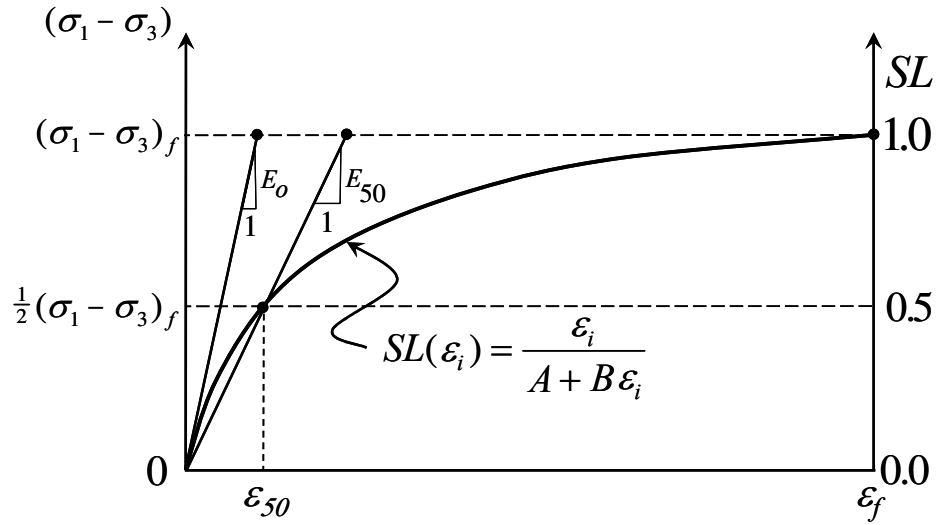


Figure 3.9 Modified Hyperbolic Stress-Strain Relationship

A and B are constants that can be found by applying the same boundary conditions in Eq. (3.5) shown in Figure 3.9. The resulting constants are:

$$A = \frac{\varepsilon_x \varepsilon_{50}}{\varepsilon_x - \varepsilon_{50}} \quad \text{and} \quad B = \left(\frac{\varepsilon_x - 2\varepsilon_{50}}{\varepsilon_x - \varepsilon_{50}} \right) \quad (3.7)$$

The modified hyperbolic relationship of Eq. (3.6) satisfying the boundary conditions then becomes

$$SL(\varepsilon_i) = \frac{\varepsilon_i}{\frac{\varepsilon_f \varepsilon_{50}}{\varepsilon_f - \varepsilon_{50}} + \left(\frac{\varepsilon_f - 2\varepsilon_{50}}{\varepsilon_f - \varepsilon_{50}} \right) \varepsilon_i} \quad (3.8)$$

This modified relationship was used in subsequent LSH applications presented later and requires parameters ε_{50} and ε_f to be defined. The ε_{50} can be determined from geotechnical laboratory testing of a sample from the backfill. The sample needs to be tested to failure and the stress-strain curve is recorded. When there is a lack of laboratory test data, typical values of ε_{50} are recommended to be selected from Table 3.1, which was developed by matching LSH model fittings with field data and from correlation with published values. For sand, ε_{50} is a function of relative density (D_r), grain size distribution (coefficient uniformity C_u), grain shape, and confinement (σ_3). For clay, ε_{50} is a function of undrained shear strength (S_u) and plasticity index (PI).

Table 3.1 Typical Values of ε_{50}

<i>Predominant Soil Type</i>	<i>ε_{50}</i>	
	<i>Range</i>	<i>Presumptive Value</i>
Gravel	0.001 to 0.005	0.0035
Clean Sand (0-12% Fines*)	0.002 to 0.003	
Silty Sands (12-50% Fines*)	0.003 to 0.005	
Silt	0.005 to 0.007	0.007
Clay	0.0075	
<u>Note:</u> *) "Fines" is the percentage by weight of soil grain sizes smaller than 0.075 mm.		

From the evaluation of 144 triaxial tests (Norris, 1979), it was back calculated that the strain at failure ε_f is approximately 31 times larger than ε_{50} :

$$\varepsilon_f \cong 31 \cdot \varepsilon_{50} \quad (3.9)$$

From comparison of this relationship with the original relationship of Eq. (3.4), it is found that

$$\varepsilon_f = \frac{\varepsilon_{50}}{1 - R_f} \quad (3.10)$$

From Eq. (3.9) and Eq. (3.10), the corresponding R_f value would be approximately 0.97. Typical R_f values between 0.94 and 0.98 were obtained for various soil types from backfitting of load test data presented in the next section.

By substituting Eq. (3.10) into Eq. (3.8), the *modified hyperbolic stress-strain relationship* can be expressed in terms of R_f and ε_{50} :

$$SL(\varepsilon_i) = \frac{\varepsilon_i}{\frac{\varepsilon_{50}}{R_f} + (2 - \frac{1}{R_f}) \varepsilon_i} \quad (3.11)$$

Based on the concepts of triaxial tests, the stress level SL can be also expressed in terms of shear strength as the ratio of incremental deviatoric stress $(\sigma_1 - \sigma_3)_i$ to deviatoric stress at failure $(\sigma_1 - \sigma_3)_f$ for the stress level $SL = 1$ as shown in Figures 3.8 and 3.9:

$$SL(\phi_i, c_i) = \frac{(\sigma_1 - \sigma_3)_i}{(\sigma_1 - \sigma_3)_f} = \frac{\sigma_3 \left(\tan^2(45^\circ + \frac{1}{2} \phi_i) - 1 \right) + 2 c_i \tan(45^\circ + \frac{1}{2} \phi_i)}{\sigma_3 \left(\tan^2(45^\circ + \frac{1}{2} \phi) - 1 \right) + 2 c \tan(45^\circ + \frac{1}{2} \phi)} \quad (3.12)$$

where

$$c_i = \frac{c \tan \phi_i}{\tan \phi} \quad (3.13)$$

Eq. (3.12) can be also expressed in terms of Rankine earth pressure coefficients:

$$SL(K_{pi}) = \frac{\sigma_3(K_{pi} - 1) + 2c_i\sqrt{K_{pi}}}{\sigma_3(K_p - 1) + 2c\sqrt{K_p}} \quad (3.14)$$

where K_{pi} is the intermediate mobilized passive earth pressure coefficient develops as a function of soil strain ε_i during triaxial tests, and K_p is the ultimate passive earth pressure coefficient of the soil at failure.

3.9 Nonlinear Abutment Backfill Capacity

Figure 3.10 shows the geometry and forces acting on a mobilized logarithmic-spiral failure surface (Shamsabadi et al., 2005).

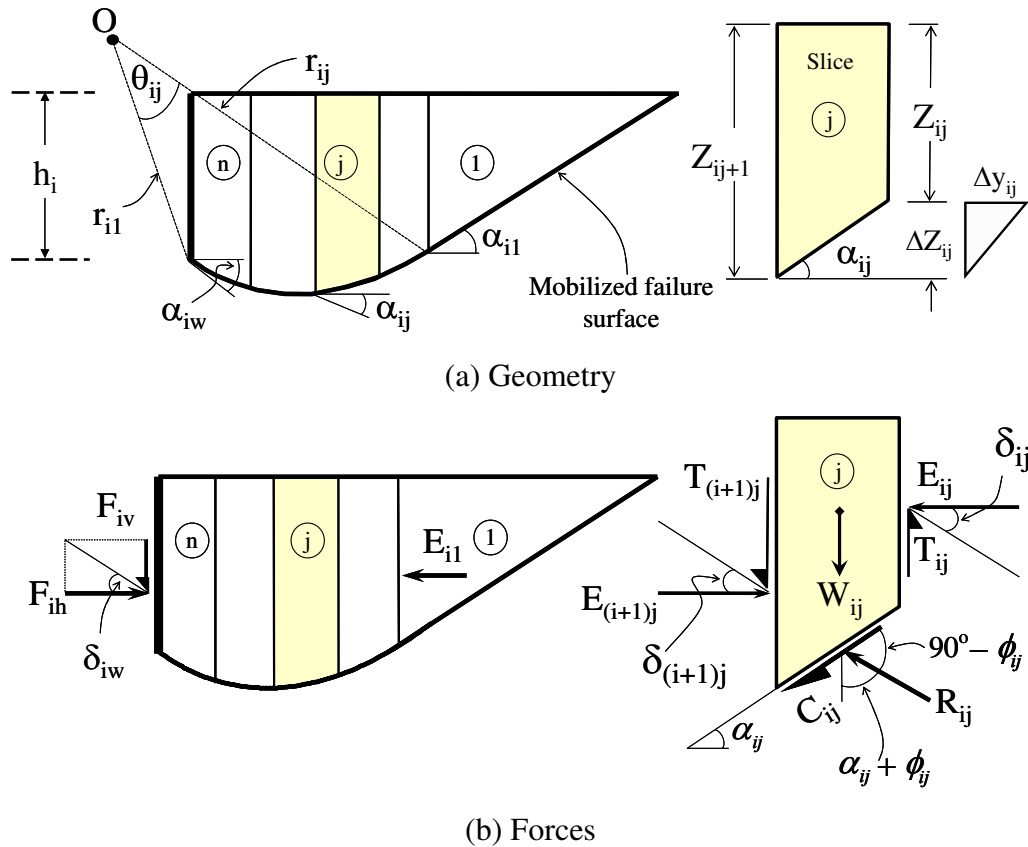


Figure 3.10 Mobilized Passive Wedge (Shamsabadi et al., 2005)

Where

i = subscript denoting a quantity associated with intermediate mobilized failure surface i ,

j = subscript denoting a quantity associated with the slice j ,

W_{ij} = intermediate mobilized total weight of slice,

L_{ij} = intermediate mobilized length of failure plane of slice,

α_{ij} = intermediate mobilized inclination of the failure plane at the slice base (with respect to horizontal),

ϕ_{ij} = intermediate mobilized soil interface friction angle,

R_{ij} = intermediate mobilized resultant friction force at mid point of slice failure surface,

C_{ij} = intermediate mobilized resultant cohesion force along failure surface of a slice,

δ_{ij} = intermediate mobilized friction angle between slices (with respect to horizontal).

E_{ij} = intermediate mobilized force of slice,

h_i = intermediate mobilized wall height Figure 3.9, and

δ_{iw} = intermediate mobilized wall-soil interface friction angle.

The mobilized logarithmic-spiral failure surface is defined as follows:

$$r_{ij} = r_{il} e^{\theta_{ij} \tan \phi_{ij}} \quad (3.14)$$

where

$$\theta_{ij} = \frac{1}{2} \tan^{-1} \frac{2K \tan \delta_{ij}}{K-1}$$

$$K = \frac{A_1 + A_2}{A_3}$$

$$A_1 = 1 + \sin^2 \phi_{ij} + \frac{c_{ij}}{h_{ij}} \sin 2\phi_{ij}$$

$$A_2 = 2(\cos \phi_{ij}) \sqrt{(\tan \phi_{ij} + \frac{c_{ij}}{\gamma z_{ij}})^2 + \tan^2 \delta_{ij} [4(\frac{c_{ij}}{\gamma z_{ij}})^2 + 4\frac{c_{ij}}{z_{ij}} \tan \phi_{ij} - 1]}$$

$$A_3 = \cos^2 \phi_{ij} + 4 \tan^2 \delta_{ij}$$

Here, K is a ratio of horizontal to vertical stresses in the slice (Shamsabadi et al., 2005). For the mobilized logarithmic-spiral failure surface shown in Figure 3.9, the horizontal component ΔE_{ij} resulting from the interslice forces E_{ij} and $E_{(i+1)j}$ acting at the sides of slice j can be expressed as (Shamsabadi et al., 2005):

$$\Delta E_{ij} = \frac{W_{ij} \tan(\alpha_{ij} + \phi_{ij}) + c_{ij} L_{ij} [\sin \alpha_{ij} \tan(\alpha_{ij} + \phi_{ij}) + \cos \alpha_{ij}]}{1 - \tan \delta_{ij} \tan(\alpha_{ij} + \phi_{ij})} \quad (3.16)$$

Summation of the ΔE_{ij} forces yields the mobilized horizontal passive capacity F_{ih} associated with the mobilized failure surface i and mobilized displacement:

$$F_{ih} = \frac{\sum_{j=1}^n \Delta E_{ij}}{1 - \tan \delta_{iw} \tan(\alpha_{iw} + \phi_i)} \quad (3.17)$$

where

$$\alpha_{iw} = \theta_{i1} + \alpha_{i1}$$

as shown in Figure 3.10. The local horizontal displacement of slice j as shown in Figure 3.11 associated with the mobilized failure surface i is as follows (Shamsabadi et al., 2005):

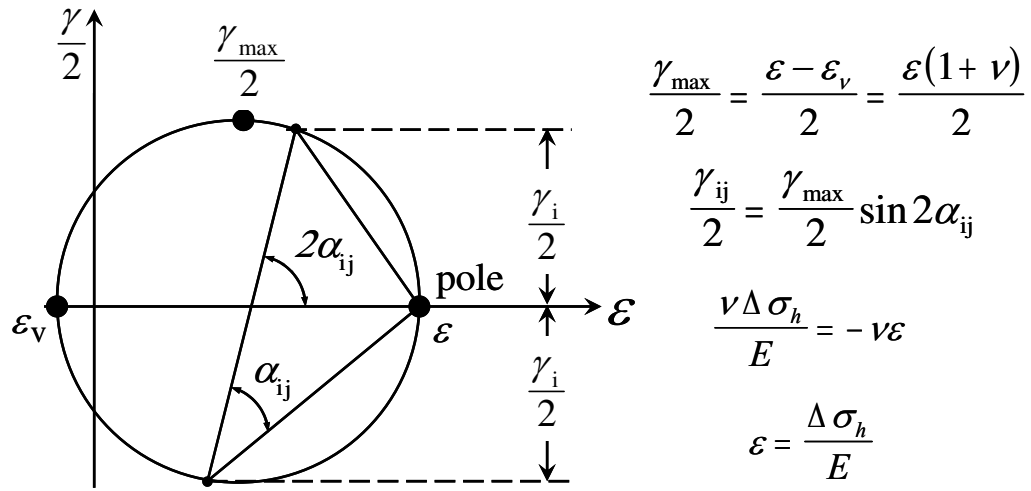


Figure 3.11: Associated Mohr Circle and Soil Strain

$$\Delta y_{ij} = \Delta z_{ij} \frac{\gamma_{ij}}{2} = \Delta z_{ij} \frac{1}{2} \epsilon_{ij} (1 + \nu) \sin 2\alpha_{ij} \quad (3.18)$$

where

ν = Poisson's ratio of the soil,

ϵ_{ij} = axial strain in the slice, and

γ_{ij} = shear strain in the slice.

The Mohr circle associated with failure surface i (see Figure 3.11) demonstrates the relationship between the normal strain ε and shear strain $\gamma/2$ in the soil (Shamsabadi et al., 2005).

The displacement of the entire mobilized logarithmic-spiral failure surface is then obtained by summation of the displacements Δy_{ij} of all slices (Shamsabadi et al., 2005):

$$y_i = \sum_{j=1}^n \Delta y_{ij} \quad (3.19)$$

The entire LSH procedure to develop the nonlinear abutment force-displacement curve using the modified hyperbolic soil model is illustrated in Figure 3.12.

For the simple wedge with planar failure surface shown in Figure 3.13, the mobilized horizontal passive force F_{ih} associated with each stress level $SL(\varepsilon_i)$ can be calculated as follows:

$$F_{ih} = \frac{W_i \tan(\alpha_i + \phi_i) + c_i L_i (\sin \alpha_i \tan(\alpha_i + \phi_i) + \cos \alpha_i)}{1 - \tan \delta_{iw} \tan(\alpha_i + \phi_i)} \quad (3.20)$$

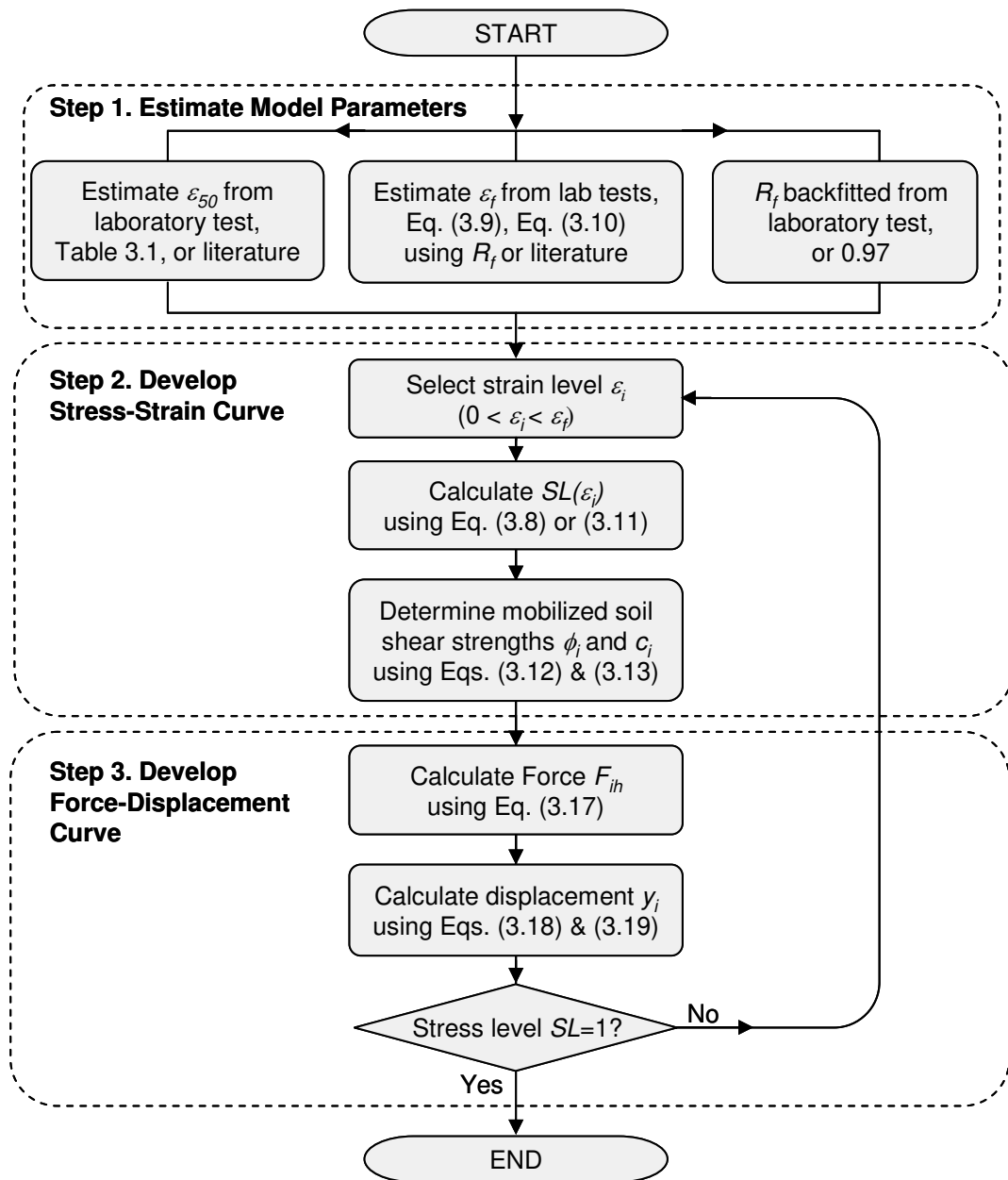
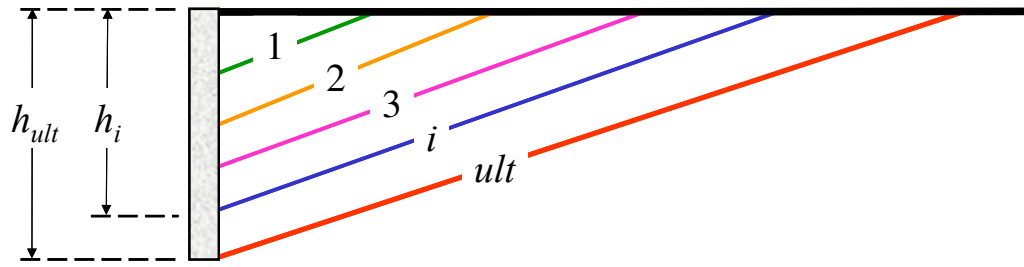
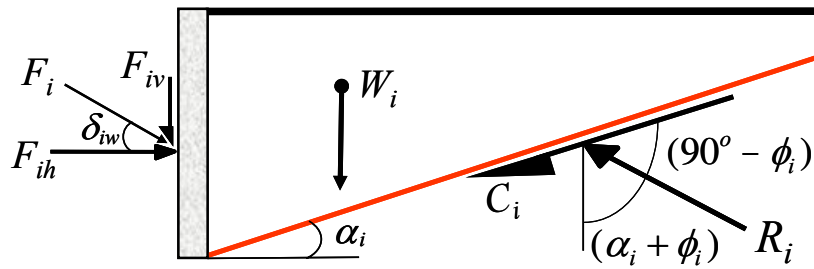


Figure 3.12: Flowchart of LSH Procedure



(a) Mobilized Failure Surfaces



(b) Forces acting on the simple wedge

Figure 3.13: Simple Wedge with Planar Failure

For a given wall interface friction angle δ_{iw} and a given mobilized failure surface angle α_i , Eq. (3.20) yields the exact same value as Coulomb's equation. If the wall interface friction angle $\delta_{iw}=0$ and the mobilized failure surface angle $\alpha_i=45^\circ-\phi/2$, then Eq. (3.20) yields the exact same value per Rankine's equation. Therefore, once the mobilized backfill properties as a function of stress-strain is determined, both Rankine's and Coulomb's equations can be used to determine the nonlinear passive earth pressure as a function of wall displacement. The mobilized displacement for the planar failure surface i can be calculated as follows:

$$\Delta y_i = h_i \frac{\gamma}{2} = \frac{1}{2} h_i \varepsilon_i (1 + \nu) \sin 2\alpha_i \quad (3.21)$$

where

h_i = the intermediate mobilized wall height, and

α_i = inclination of intermediate mobilized failure surface of a planar Rankine's or Coulomb's wedge (with respect to horizontal).

The mobilized soil strength parameters coupled with soil hyperbolic stress-strain relationship (the "LSH procedure") can be used with any earth pressure theory. Table 3.2 compares the capacities obtained using the LSH procedure with two limit-equilibrium methods for a 10-foot high wall. The material properties and LSH model parameters used are also given in Table 3.2. The resulting coefficients are shown in Table 3.2 and plotted in Figure 3.14.

It can be seen that (1) Coulomb's nonlinear earth pressure coefficient is very stiff, (2) Coulomb ultimate earth pressure coefficient is more than 5 times larger than Rankine's coefficient and about 2 times larger than the Log Spiral earth pressure coefficient, and (3) Coulomb reaches the ultimate failure at lower displacement because the mobilized wedge is larger. There is a large spread of the coefficients at larger displacement. For displacement performance-based design, it is important to select the earth pressure theory that is most suitable to a particular application in terms of acceptable displacement criteria.

Table 3.2 Mobilized Earth Pressure Coefficients Using Three Methods

SL	ε_i	Mobilized ϕ_i	Mobilized δ_i	Earth Pressure Coefficient, K_{pi}		
				Rankine	LSH	Coulomb
0.0008	0.0000	0.00	0.0	0.00	0.00	0.00
0.027	0.0001	2.61	0.80	1.10	1.13	1.13
0.233	0.0011	17.17	6.98	1.84	2.32	2.45
0.468	0.0031	27.21	14.05	2.69	4.16	4.95
0.645	0.0061	32.48	19.34	3.32	5.91	8.04
0.762	0.0101	35.33	22.86	3.74	7.27	11.07
0.839	0.0151	36.99	25.18	4.02	8.26	13.68
0.891	0.0211	38.02	26.74	4.21	8.96	15.82
0.927	0.0281	38.70	27.82	4.34	9.47	17.51
0.953	0.0361	39.17	28.59	4.43	9.85	18.84
0.972	0.0451	39.51	29.15	4.50	10.13	19.89
0.986	0.0551	39.76	29.58	4.55	10.35	20.74
0.997	0.0661	39.95	29.91	4.59	10.51	21.41
1.000	0.0781	40.00	30.00	4.60	10.56	21.59

Notes: Wall height: $h_{ult} = 10$ ft
 Soil parameters: $\phi = 40^\circ$, $\delta = 30^\circ$
 LSH model parameters: $\nu = 0.35$, $R_f = 0.95$, $\varepsilon_{50} = 0.0035$

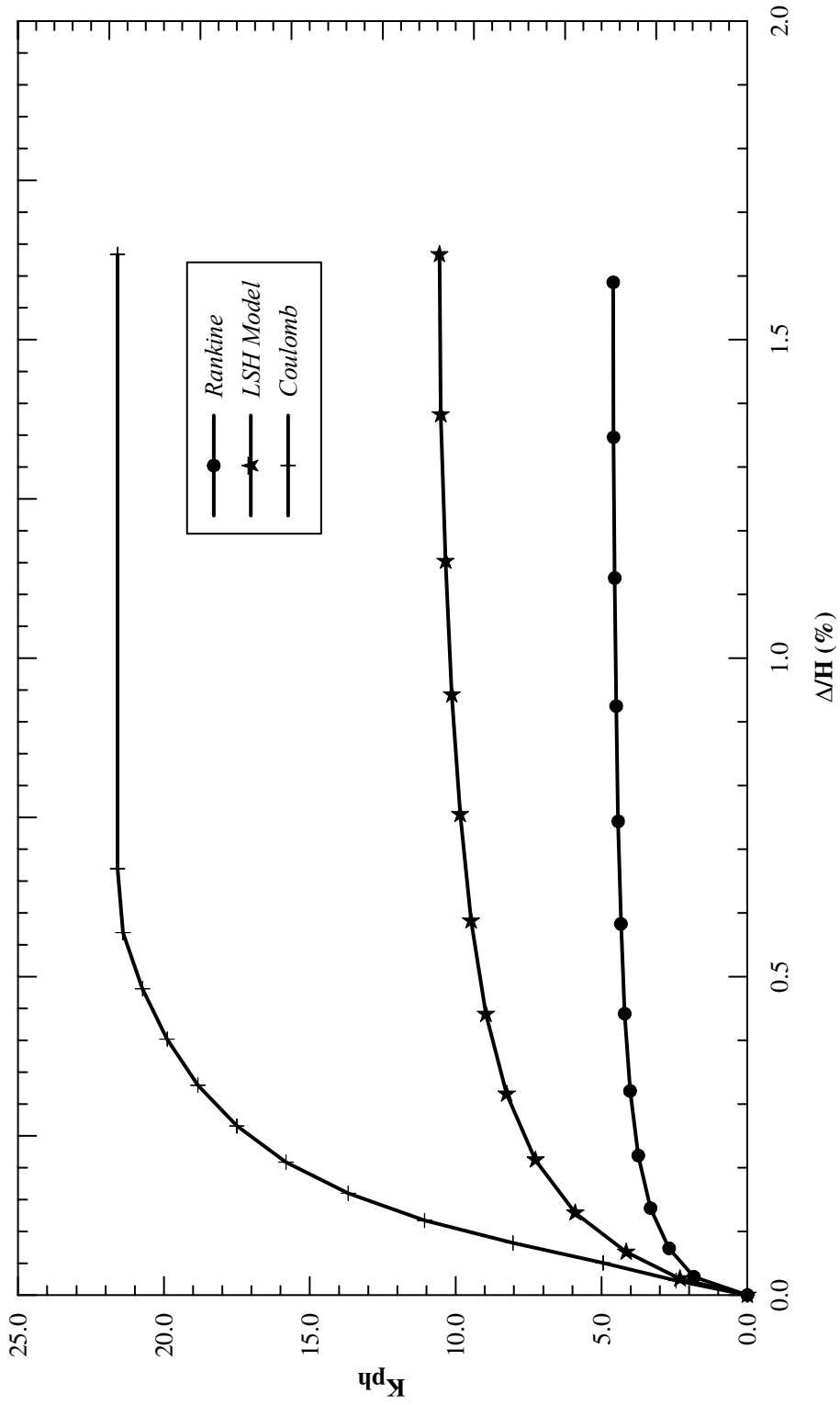


Figure 3.14 : Mobilized Earth Pressure Coefficients Using Three Methods

3.10 Verification of LSH Model

The passive resistance of the backfill has been studied by various researchers in lateral centrifuge experiments, small-scale laboratory experiments and full-scale field experiments on walls and pile caps subjected to monotonic and cyclic lateral loadings. Analytical models have been developed to better understand the nonlinear response of the bridge abutment as a function of displacement (Shamsabadi et al., 2005; Martin et al., 1996; Siddharthan et al., 1997).

For the present study, the nonlinear backfill force-displacement capacity curves from selected tests on various soil types are summarized. The results are compared with the LSH model predictions.

3.11 Full-Scaled Abutment Experiments

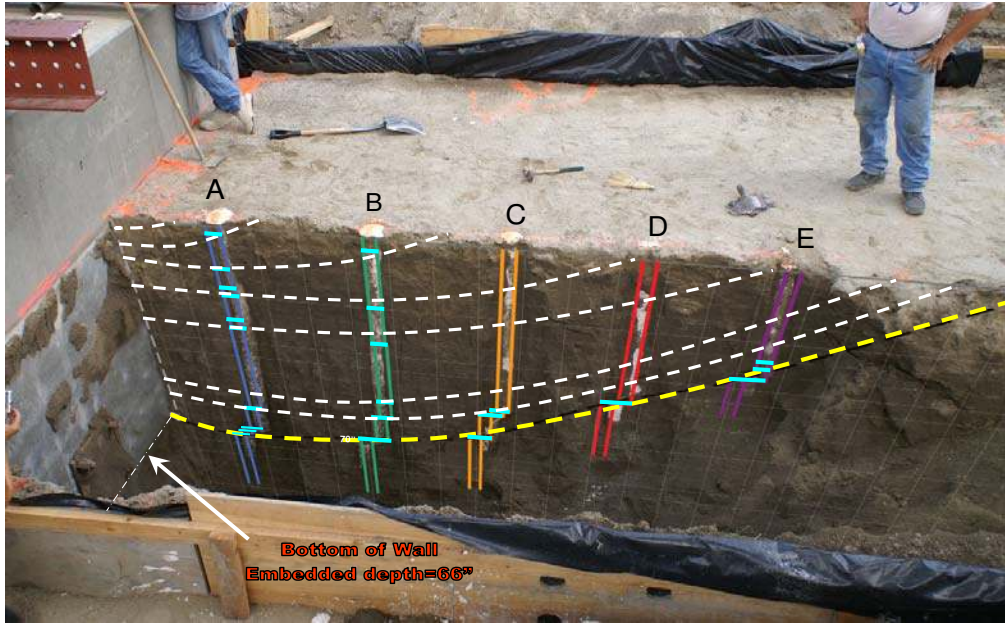
As part of the Caltrans seismic research program, full-scale abutment field experiments were conducted at University of California, Los Angeles (2006) and University of California, Davis (Romstad et al., 1995; Maroney et al., 1994). A brief description of the abutment experiments and the LSH prediction is described herein.

3.11.1 UCLA Abutment Experiment

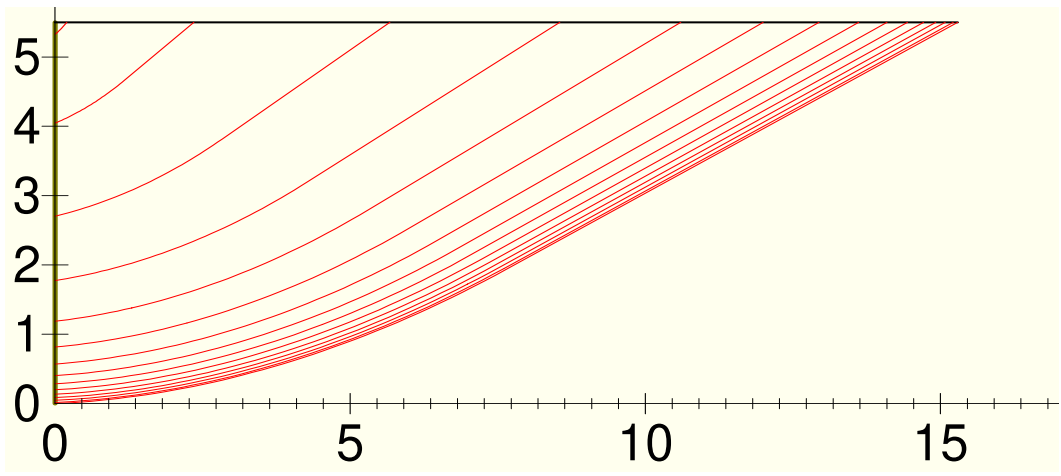
A full-scale cyclic load test was performed by UCLA research team on a 15 feet by 3 feet abutment wall with a height of 5.5 feet having a silty sand backfill. The purpose of the test was to simulate the seat-type abutment shown in Figure 3.1. The backfill was placed in layers and compacted to over 95% Modified Proctor density behind the wall and was extended about 3 times the backwall height in the longitudinal direction. The backwall was pushed horizontally in between the

abutment wingwalls without any vertical movement. The abutment wingwalls were constructed using smooth plywood. Plastic sheeting was placed at the interior face of the plywood to minimize the friction along the wingwalls in order to simulate a plane strain condition.

After the completion of the test, a longitudinal trench was excavated and the failure mechanism of the backfill was carefully investigated by mapping the mobilized deformed passive wedges along the abutment backfill. The deformed wedges started to develop within the upper soil layer and progress deeper down and away from the abutment backwall. The final failure surface extended from the bottom of the abutment backwall and intersected the backfill surface at about 3 times the height of the backwall. The mobilized deformed wedges and the final failure surface which were mapped after the completion of the experiment is shown in Figure 3.15a. The mobilized passive wedges predicted by the LSH model are shown in Figure 3.15b. The final logarithmic spiral failure surface predicted by the LSH model intersected the abutment backfill at about 16 feet behind the abutment backwall, which remarkably matches the experimental failure surface mapped in the field. The backfill properties, the LSH parameters and the measured data and predicted capacity curves are shown in Figure 3.16. The backfill properties are based on the triaxial test results conducted by EMI. The curve predicted by the LSH model is in good agreement with the experimental data.



(a)



(b)

Figure 3.15: LSH Model Failure Wedges Versus Experimental Failure Wedges (UCLA Test)

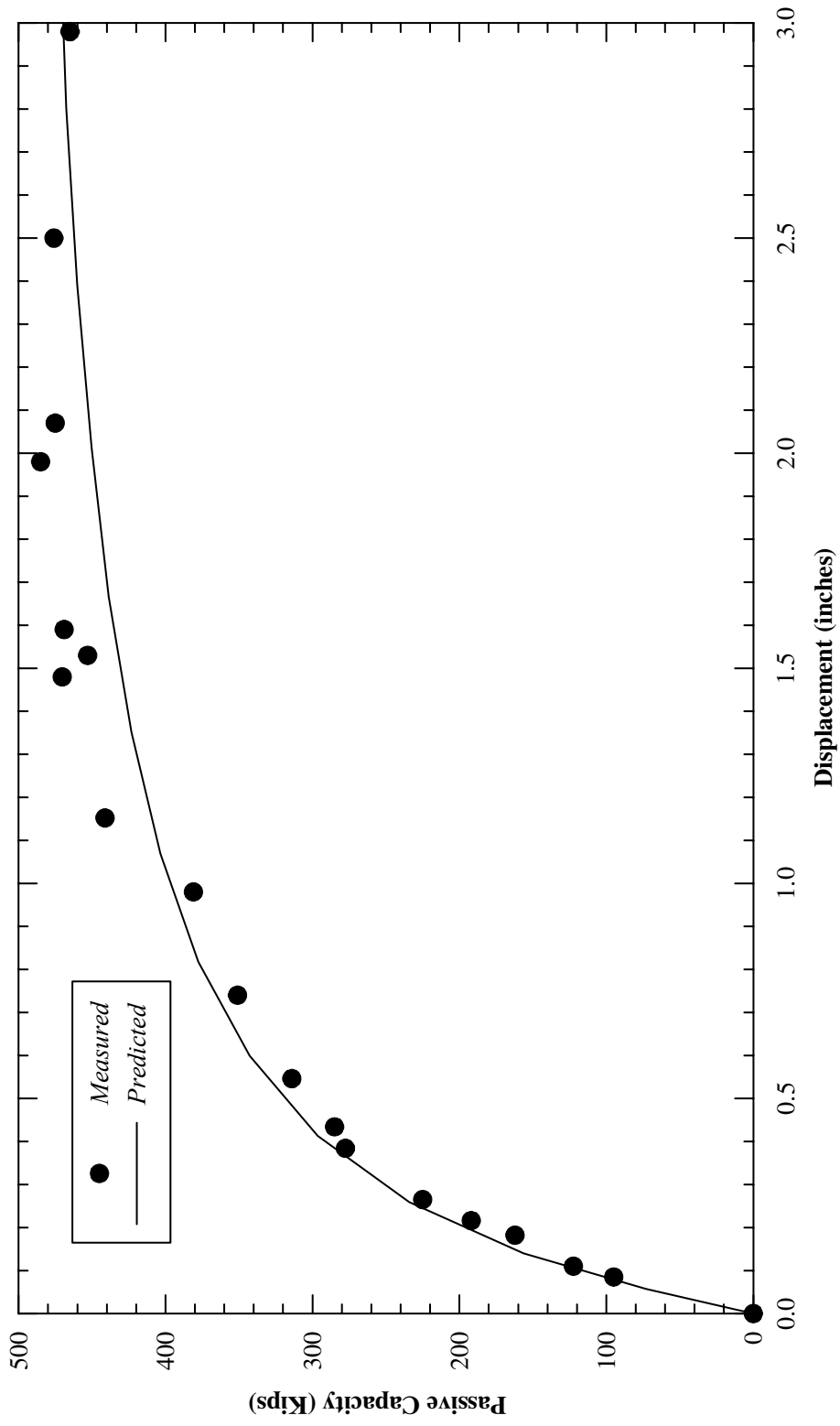


Figure 3.16: LSH Prediction of UCLA Abutment Test

3.11.2 UCD Abutment Experiment

A full-scale test was conducted on a monolithic abutment in University of California, Davis by applying cyclic longitudinal loading to ultimate failure (Romstad et al., 1995, Maroney et al., 1994). The backfill consisted of compacted Yolo Loam clay. The soil properties and the measured force-displacement response of the abutment wall are shown in Figure 3.17. The predicted force-displacement response using the LSH model and the LSH model parameters are also shown in Figure 3.17. The predicted abutment wall capacity using the LSH model is in good agreement with the experimental data. UCD abutment experiment will be explained in more details in the next chapter as part of the advanced analytical modeling.

3.12 Full-Scaled Pile Cap Experiment

A series of full-scale static load tests were performed by Rollins and Cole (2006) on a 17-foot by a 10-foot pile cap with a height of 3.67 feet. The pile cap was placed on a 3 by 4 group of 12-inch diameter steel pipe piles driven in saturated low-plasticity silts and clays. The passive resistance of the backfill against the side of pile cap was determined to be about 40% of the total load resistance. The tests were designed to differentiate the passive resistance of the pile cap in four different types of backfill: clean sand with small amount of silt, silty sand, fine-grained gravel, and coarse-grained gravel. The sand was compacted to approximately 95% of modified Proctor density per ASTM D-1557 (ASTM, 2003). Adjustment factors were applied to the structure width in the LSH model to account for the three-dimensional wedge observed in the field. The factors were based on measurements of observed surface

cracking patterns in Rollins' field tests (2006) and are similar to Ovesen-Brinch Hansen correction factors based on field tests (Ovesen, 1964).

3.12.1 Clean Sand

The clean sand (SP) backfill was fine to coarse-grained, poorly-graded with less than 2% fines and no gravel. The soil strength properties, the LSH parameters and measured capacity of the pile cap are shown in Figure 3.18. For the LSH model, a small apparent cohesion of 80 psf due to the presence of silt was applied. Rollins et al. (2006) found that the maximum width of the 3-dimensional passive wedge observed from cracking patterns at the ground surface was 40% larger than the width of the pile cap. To account for three-dimensional effects, the pile cap width was increased by 1.4 in the LSH model. The nonlinear response of the pile cap predicted by the LSH model is in good agreement with the measured data.

3.12.2 Silty Sand

The silty sand (SM) backfill had a maximum particle size of 12.5 mm with approximately 90% passing the No. 40 sieve and 45% non-plastic fines. The C_u and C_c coefficients were 14.8 and 2.8, respectively. The pile cap width was increased by 1.2 in the LSH model for three-dimensional effects based on findings by Rollins et al. (2006) from the field data. Figure 3.19 shows the key soil properties, the LSH model parameters and the measured and predicted pile cap capacity. The computed curve obtained by the LSH model is close to the measured data.

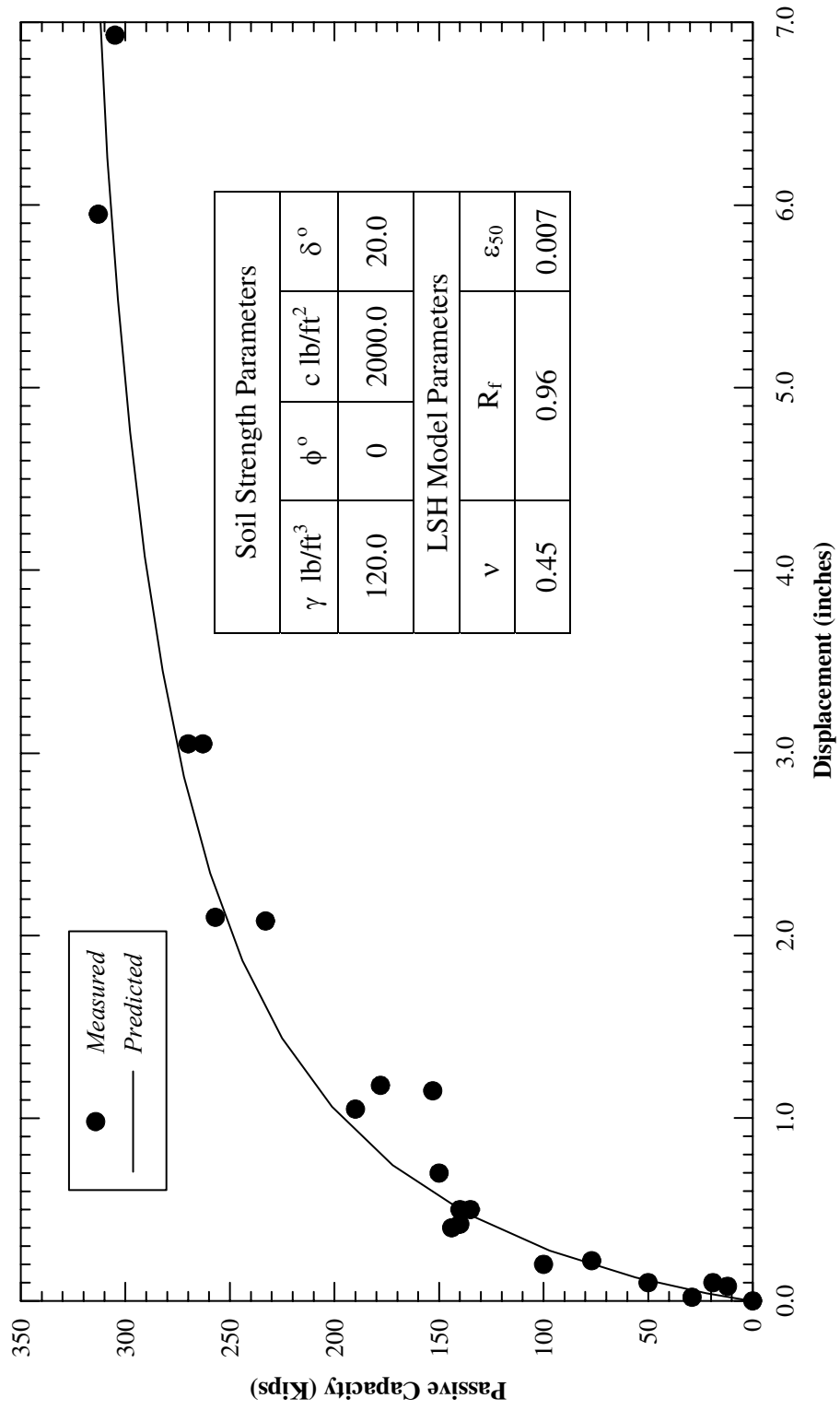


Figure 3.17: LSH Prediction of UCDD-CT Abutment test

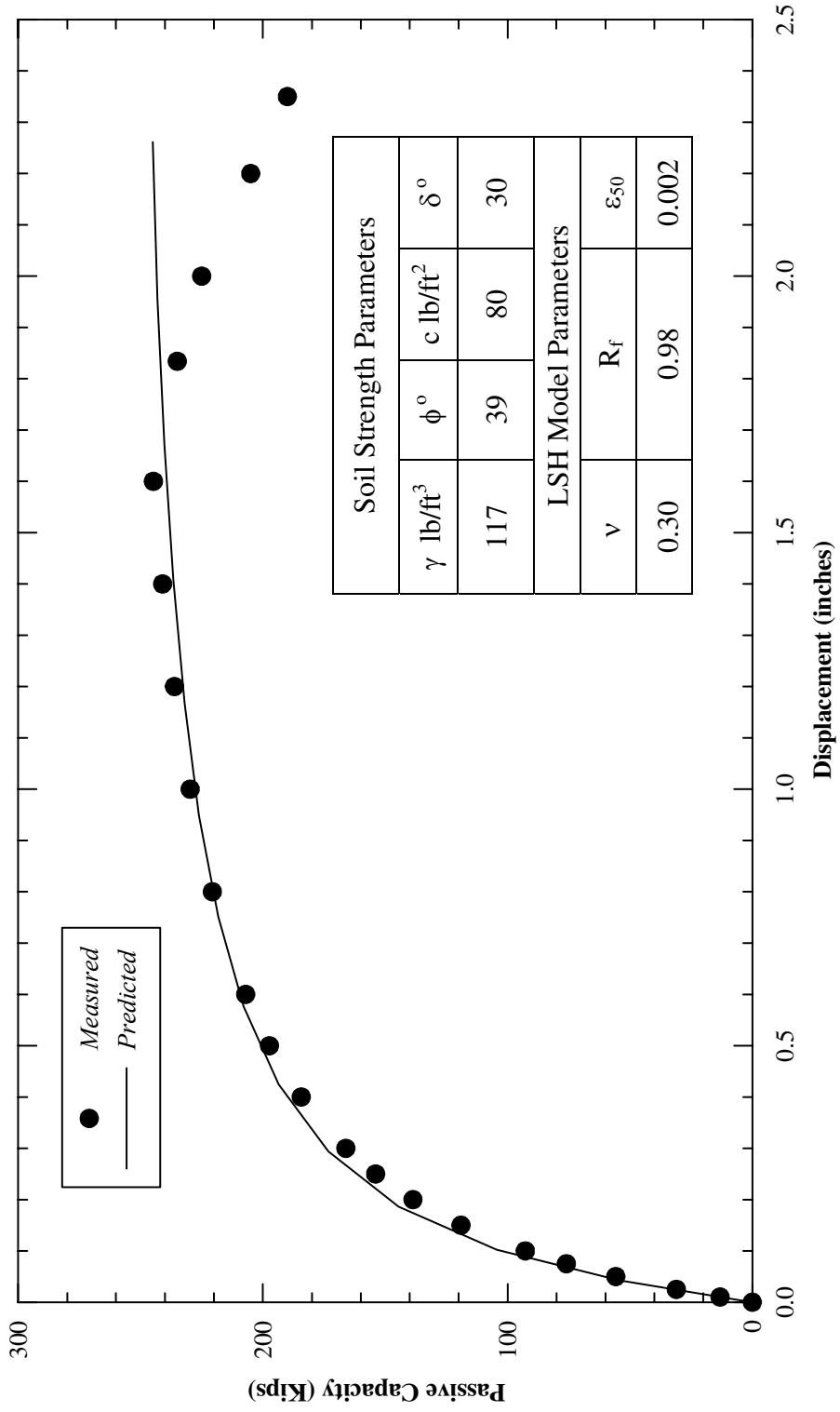


Figure 3.18: LSH Prediction of BYU Pile Cap Test in Clean Sand

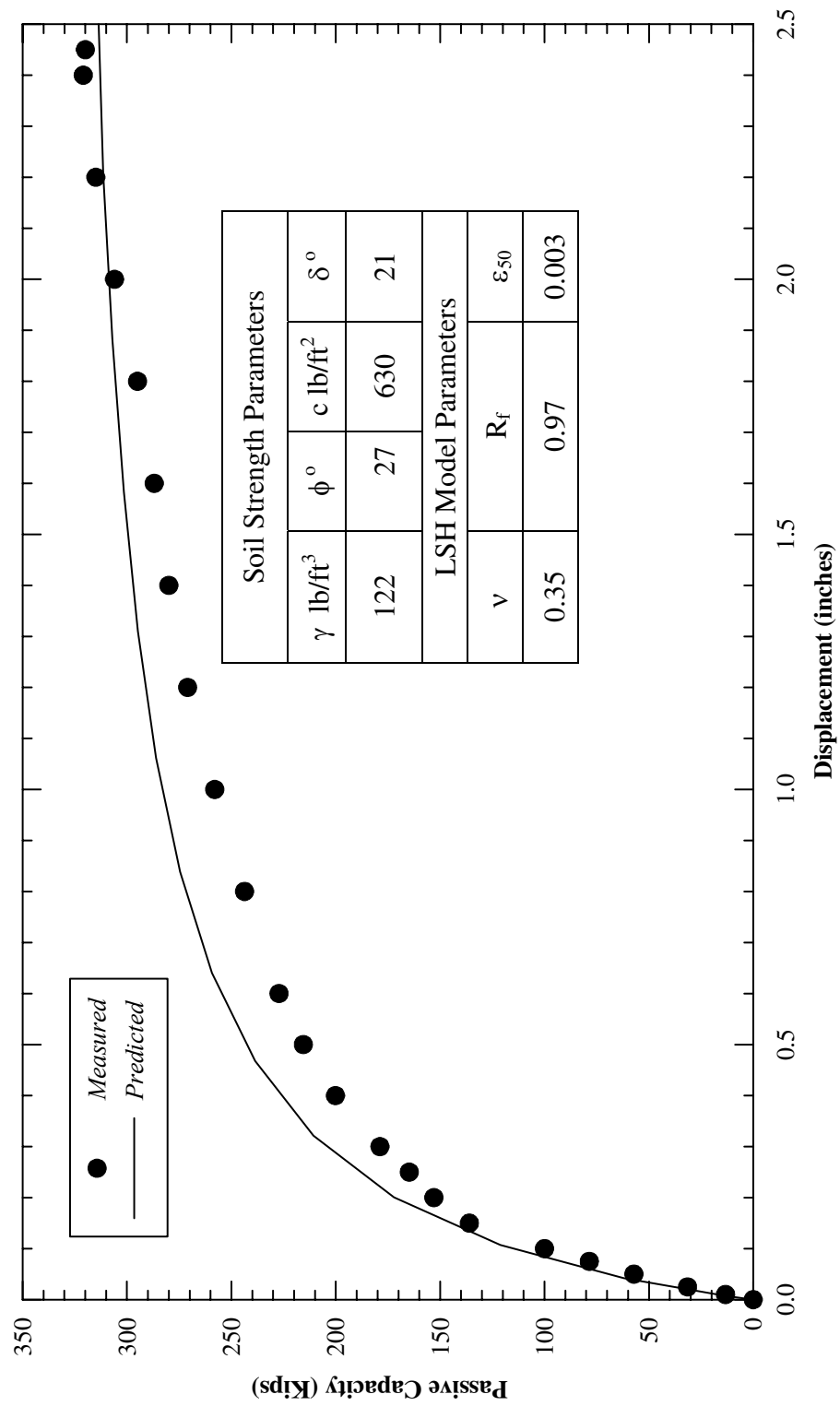


Figure 3.19: LSH Prediction of BYU Pile Cap Test in Silty Sand

3.12.3 Fine-grained Gravel

The fine-grained gravel backfill was poorly graded and had a maximum particle size of 19 mm with approximately 50% gravel, 30% sand, and 20% fines. The soil properties, the LSH model parameters, and the measured nonlinear pile cap capacity are shown in Figure 3.20. The pile cap width was increased by 1.4 for three-dimensional effects based on Rollins et al. (2006) field data. The LSH prediction matched the measured load-displacement curve well as shown in Figure 3.20.

3.12.4 Coarse-grained Gravel

The coarse-grained gravel backfill was poorly graded and had a maximum particle size of 100 mm with approximately 36% gravel, 15% sand, and 20% non-plastic fines. The soil properties, the LSH model parameters and the measured pile cap resistance are shown in Figure 3.21. The pile cap width was again increased by 1.4 for three-dimensional effects based on Rollins et al. (2006) field data. The predicted capacity from the LSH model captures the rising trend of the measured data.

3.13 RPI Centrifuge Experiment in Nevada Sand

Nonlinear abutment and pile cap backfill behavior under large amplitude displacement has been investigated using centrifuge experiments. Scaled-centrifuge abutment and pile cap experiments conducted at RPI has also provided a unique opportunity to validate the LSH model.

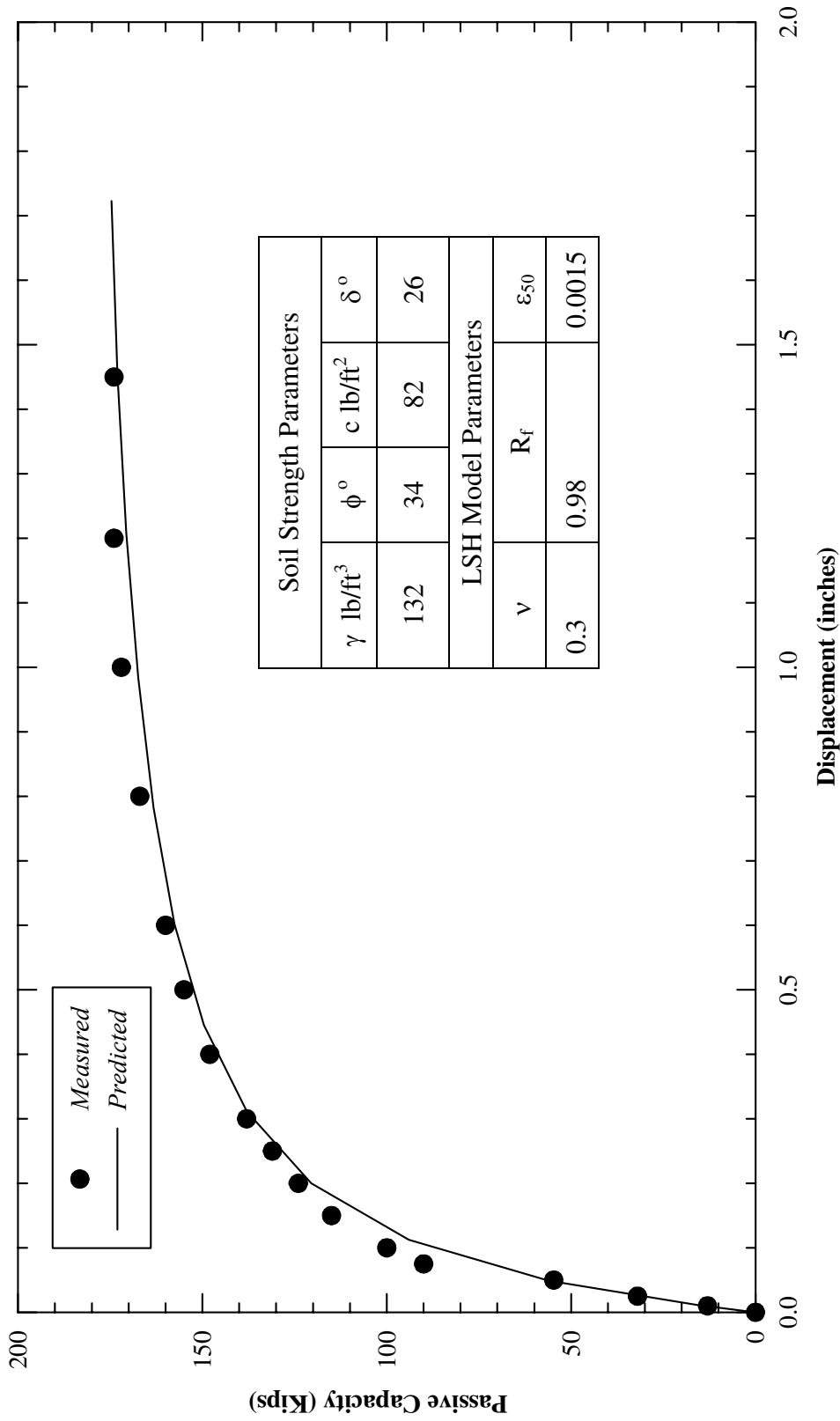


Figure 3.20 : LSH Prediction of BYU Pile Cap Test in Fine Gravel

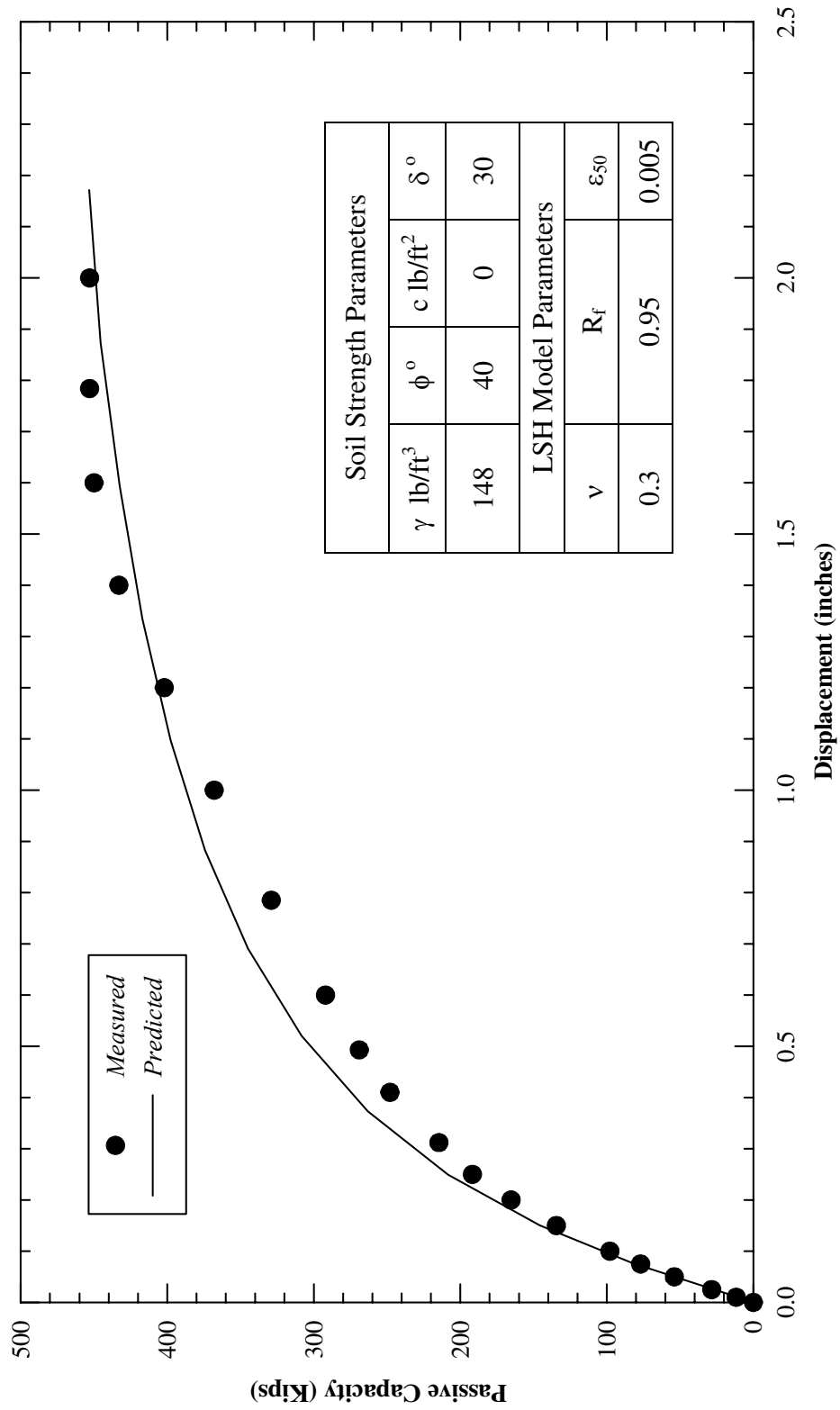


Figure 3.21: LSH Prediction of BYU Pile Cap in Test Course Gravel

3.13.1 Seat-Type Abutment

Gadre and Dobry (1998) conducted a number of cyclic load tests in the centrifuge on a seat-type bridge abutment prototype using dry dense Nevada sand. The prototype represented a bridge abutment 5 feet high and 18.77 feet long. A three-dimensional correction factor of 1.25 was applied to the abutment width (Gadre, 1997). The soil properties, the LSH model parameters and the measured force-displacement capacity of the abutment wall are shown in Figure 3.22. The sand was glued to the back face of the wall to simulate a rough concrete surface ($\delta = \phi = 39^\circ$). The predicted curve using the LSH model is in good agreement with the experimental data.

3.13.2 Pile Cap

Gadre and Dobry (1998) also conducted a number of cyclic load tests in the centrifuge on a pile cap prototype model embedded in dry dense Nevada sand. The soil properties are shown in Figure 3.23. The prototype represented a pile cap with a width of 3.74 feet and a height of 2.76 feet. An equivalent surcharge load of about 12 inches was also imposed on the pile cap. Since the contribution of the side and the base friction of the pile cap were subtracted from the total measured resistance, no correction for three-dimensional effects per Ovesen and Stromann (1972) was applied in the model. The sand was again glued to the back face of the Pile Cap ($\delta = \phi = 39^\circ$). The soil properties, the LSH model parameters and the measured force-displacement curve for the pile cap are shown in Figure 3.23. The predicted curve using the LSH model is in good agreement with the experimental data.

3.14 3.14 Small-Scaled Experiment of Wall in Loose Sand

Fang et al. (1994) conducted a small-scale laboratory test on a rigid vertical retaining wall about 1.64 feet high by 3.28 feet wide. The wall was backfilled with dry loose sand and subjected to slow monotonic, lateral loading. The soil properties and LSH model parameters are given in Figure 3.24. The figure shows the horizontal force-displacement response from strain gage measurements at four wall locations. The curve predicted by the LSH model reasonably matches the experimental results.

3.15 Recommended Abutment Force-deformation Relationship

The relationship used in Eq. (3.8) and Eq. (3.11) was expressed in terms of stress and strain. In seismic bridge design practice, however, abutment soil capacity is typically based on an average soil stiffness K and the maximum abutment force F_{ult} developed at a maximum displacement y_{max} . All three quantities are typically provided by the geotechnical engineer. This abutment force-displacement relationship (“backbone curve”) is shown in Figure 3.25 with the average stiffness defined as:

$$K = \frac{\frac{1}{2} F_{ult}}{y_{ave}} \quad (3.22)$$

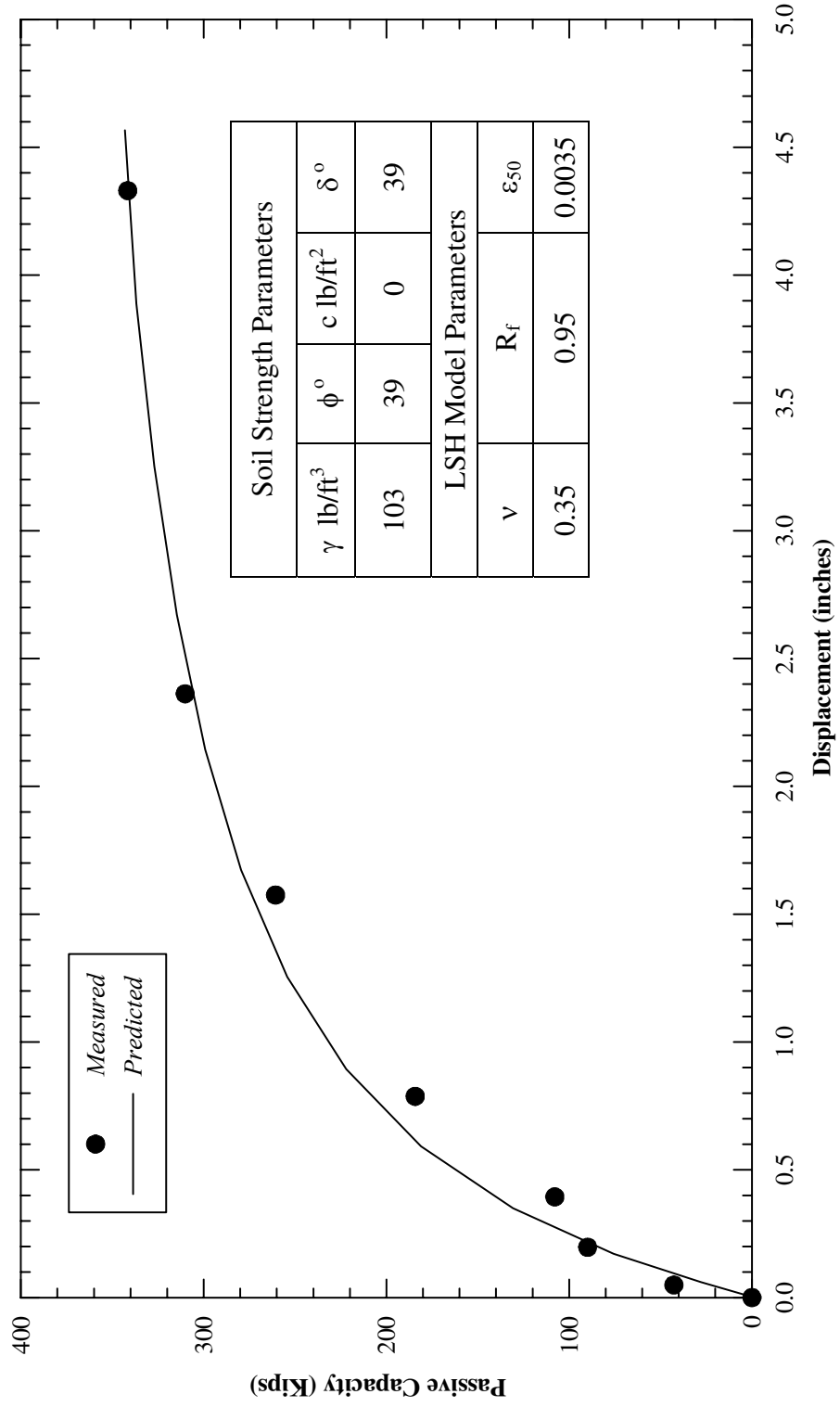


Figure 3.22: LSH Prediction of RPI Abutment Test in Dense Sand

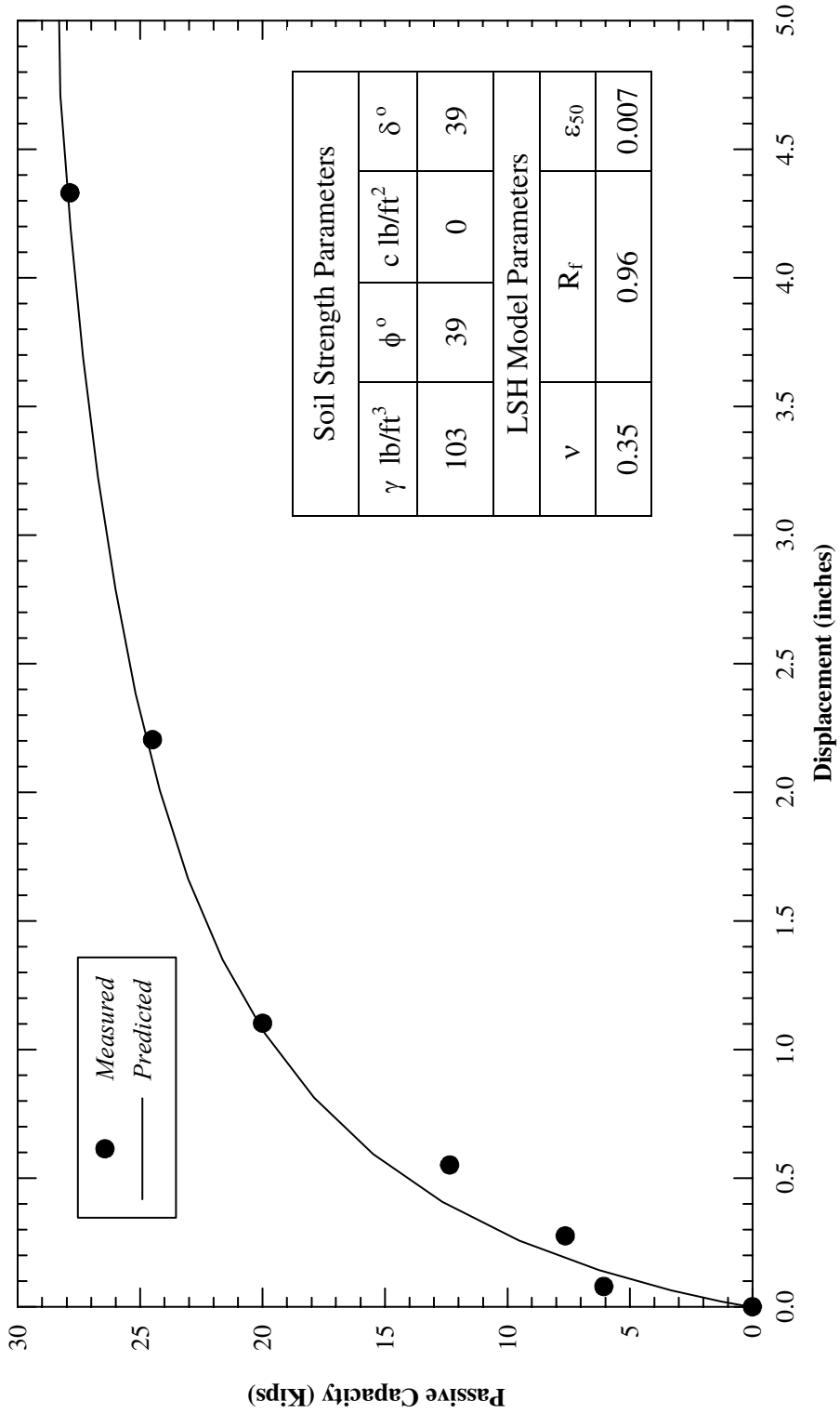


Figure 3.23: LSH Prediction of RPI Pile Cap Test in Nevada Sand

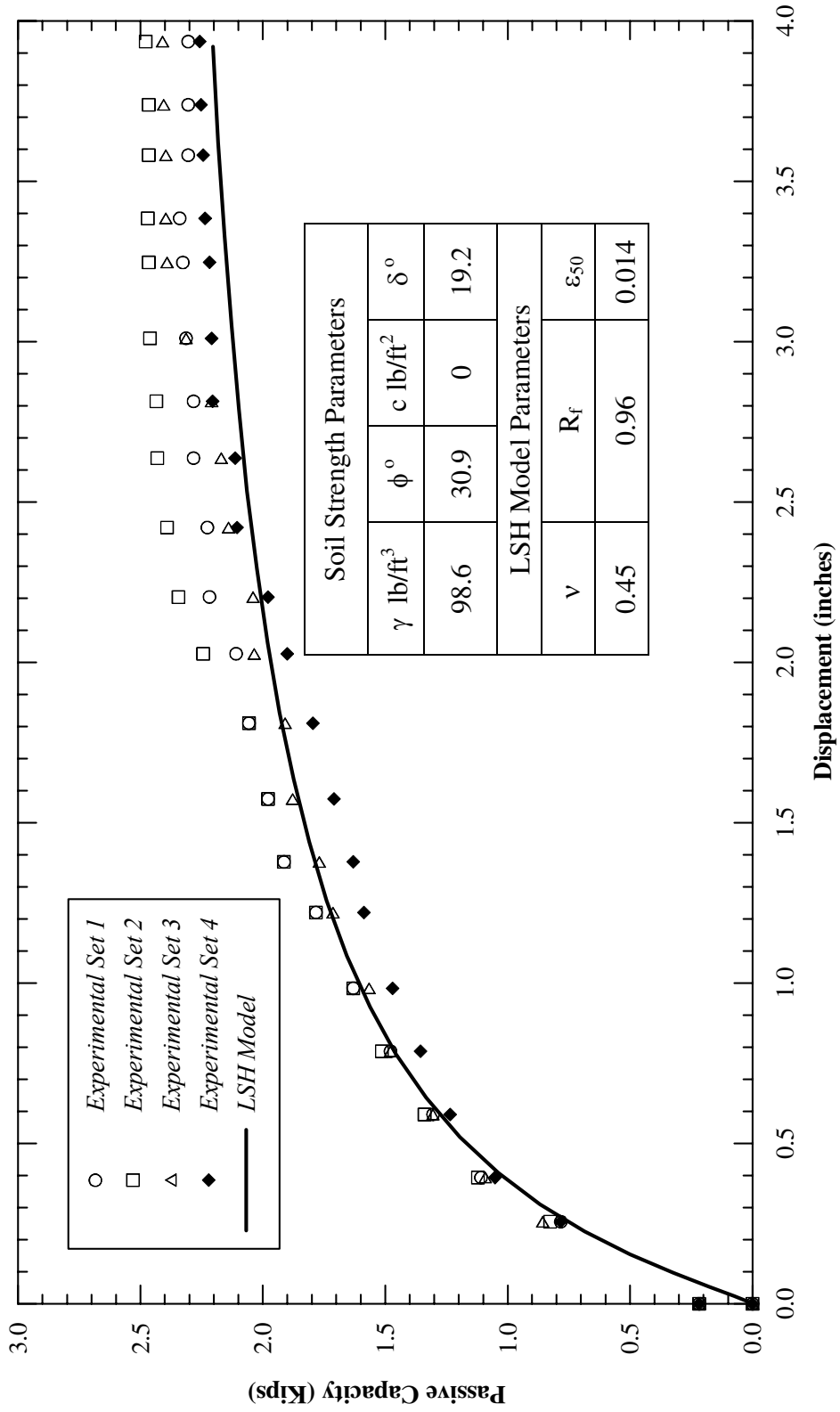


Figure 3.24: LSH Prediction of Wall Test in Loose Sand

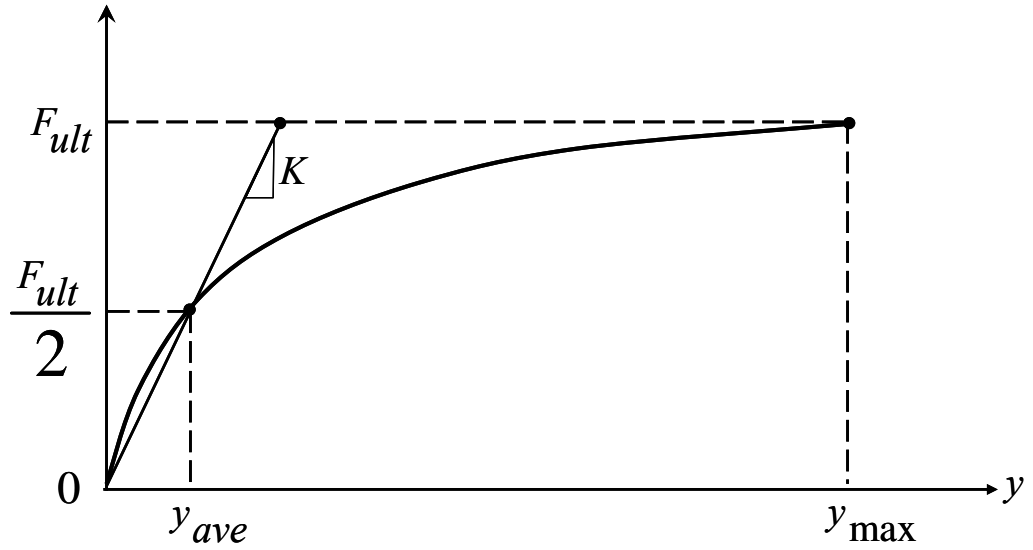


Figure 3.25: Hyperbolic Force-Displacement Formulation

The force-displacement relationship in general hyperbolic form is:

$$F(y) = \frac{y}{A + By} \quad (3.23)$$

The constants A and B can be found by applying the following boundary conditions as shown Figure 3.25:

$$\left. \begin{array}{l} (I) \quad FL = 0 \quad \text{at} \quad y_i = 0 \\ (II) \quad FL = \frac{1}{2} F_{ult} \quad \text{at} \quad y_i = y_{ave} \\ (III) \quad FL = F_{ult} \quad \text{at} \quad y_i = y_{max} \end{array} \right\} \quad (3.24)$$

The resulting constants are:

$$A = \frac{y_{max}}{2Ky_{max} - F_{ult}} \quad \text{and} \quad B = \frac{2(Ky_{max} - F_{ult})}{F_{ult}(2Ky_{max} - F_{ult})} \quad (3.25)$$

Therefore, the hyperbolic force-displacement (“HFD”) relationship is:

$$F(y) = \frac{y}{\frac{y_{\max}}{2Ky_{\max} - F_{ult}} + \frac{2(Ky_{\max} - F_{ult})}{F_{ult}(2Ky_{\max} - F_{ult})}y} \quad (3.26)$$

which can also be expressed as

$$F(y) = \frac{F_{ult}(2Ky_{\max} - F_{ult})y}{F_{ult}y_{\max} + 2(Ky_{\max} - F_{ult})y} \quad (3.27)$$

Current Caltrans Seismic Design Criteria (SDC, 2006) uses a bilinear force-deformation relationship to model the nonlinear behavior of the bridge abutment. It is based on an average abutment-backfill capacity of 5 kips per square foot of effective abutment backwall area and an average abutment backwall stiffness of 20 K/in per foot of wall length obtained from UCD’s field experiment (Maroney, 1994) of a 5.5-ft high wall in cohesive soil. Eq. (3.28) is used to adjust for various abutment heights:

$$\begin{aligned} K_{Abut} &= 20 \text{ K / in / ft} \cdot f \\ F_{ult} &= 5 \text{ ksf} \cdot A_e \cdot f \end{aligned} \quad (3.28)$$

where

$$f = \frac{H}{5.5 \text{ ft}}$$

H is the wall height, and f is the height adjustment factor.

The average stiffness (K) based on the UCD data shown in Figure 3.27 is about 25 K/in/ft and the ultimate capacity (F_{ult}) is about 5.5 K/ft² at approximately 6.6 inches of displacement.

Based on the recent UCLA abutment field experiment (2006) performed on a 5.5-ft high wall on compacted silty sand, the average abutment backwall stiffness is about double that of UCD abutment experiment. However, the measured ultimate capacity F_{ult} is about the same as the UCD abutment experiment at approximately 3.3 inches of displacement as shown in Figure 3.26.

Table 3.3 summarizes the average stiffness, and the predicted maximum capacity and displacement for each of the nine case studies presented in the prior section. The y_{max}/H ratio was based on the maximum passive force. For any of the cases studies, the predicted HFD curves using Eq. (3.27) based on the stiffness and maximum capacity and displacement parameters shown in Table 3.3 is nearly the same as predicted using the LSH approach.

For a typical concrete highway bridge when no geotechnical data is available, the following presumptive HFD parameters shown in Table 3.4 can be used to develop the nonlinear force-displacement curve for engineered abutment backfill based on the full-scale experimental test results and the author's experience.

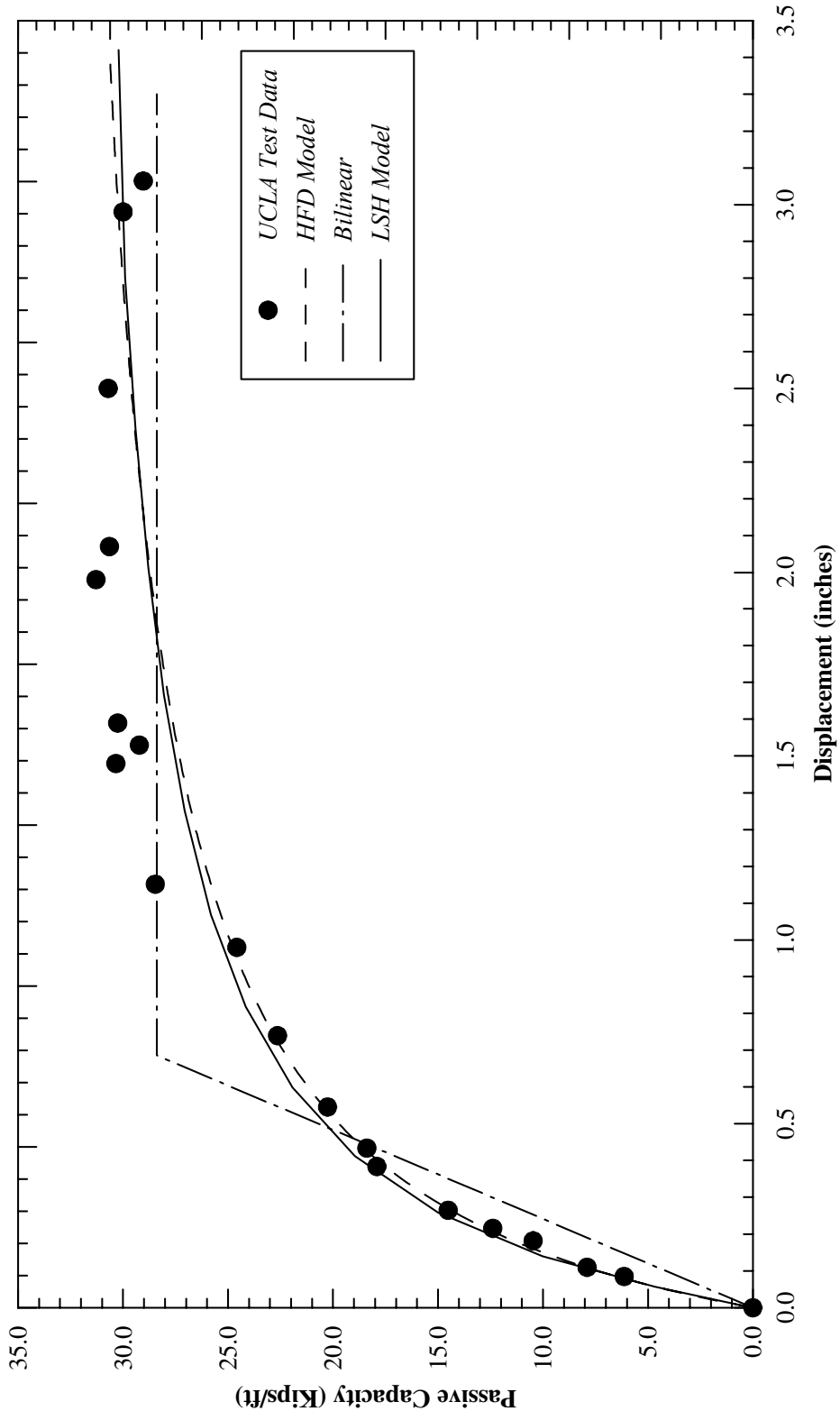


Figure 3.26 : UCLA Abutment Experiment Compared with Various Models

Table 3.3 Parameters for HFD Model

Case Study (Ref.)	F_{ult} (Kips)	y_{max} (in)	y_{max}/H	K (K/in/ft)
Silty Sand (UCLA, 2006)	455.0	3.3	0.05	54
Clean Sand (BYU, 2005)	245.0	2.2	0.05	51
Silty Sand (BYU, 2005)	414.0	2.2	0.05	53
Fine Gravel (BYU, 2005)	175.0	1.8	0.04	51
Coarse Gravel (BYU, 2005)	453.0	2.6	0.06	46
Sand (BYU, 2002)	345.0	1.30	0.03	42
Sand/Abutment (RPI, 1998)	343.0	4.3	0.06	17
Sand/Pile cap (RPI, 1998)	28.30	4.3	0.10	7.5
Clay (UCD, 1994)	312.0	6.6	0.10	25
Sand (Fang, 1994)	2.20	4.3	0.20	2.4

Table 3.4 Suggested HFD Parameters for Abutment Backfills

Abutment Backfill Type	Pressure (ksf)	Ave. Soil Stiffness (K/in/ft)	y_{max} / H
Granular*	5.5	50	0.05
Cohesive*	5.5	25	0.10
Note: * Compacted to at least 95% relative compaction per ASTM D-1557 Abutment Backwall Height = 5.5 ft			

The constants A and B in Eq. (3.25) can be found by substituting the values give in Table 3.4 as follows.

For a granular backfill:

$$H = 5.5 \text{ ft}$$

$$F_{ult} = 5.5 \text{ ft} \bullet 5.5 \text{ ksf} = 30.25 \text{ k / ft}$$

$$K_{Abut} = 50 \text{ K / in / ft}$$

Solve for A and B then:

$$A = 0.011$$

$$B = 0.030$$

Substitute A and B into Eq. (3.23), then

$$F(y) = \frac{y}{.011 + .03y} \quad (y \text{ in inches, } F_{ult} \text{ in K per ft of wall}) \quad (3.29)$$

For a cohesive backfill

$$H = 5.5 \text{ ft}$$

$$F_{ult} = 5.5 \text{ ft} \bullet 5.5 \text{ ksf} = 30.25 \text{ k / ft}$$

$$K_{Abut} = 25 \text{ K / in / ft}$$

Solve for A and B then

$$A = 0.022$$

$$B = 0.030$$

Substitute A and B into Eq. (3.23), then

$$F(y) = \frac{y}{.022 + .03y} \quad (y \text{ in inches, } F_{ult} \text{ in K per ft of wall}) \quad (3.30)$$

Comparisons of the experimental data, LSH model, bilinear model and HFD model using Eq. (3.29) and Eq. (3.30) are shown in Figure 3.26 and Figure 3.27. The results of the LSH model and HFD model are remarkably close.

3.15.1 Application of HFD Model for other Height

The experimental data and the LSH model were used to develop Eq. (3.29) and Eq. (3.30) to calculate nonlinear force-deformation relationship for a 5.5 feet high abutment-backwall. In order to develop nonlinear abutment force-deformation

relationship for other wall height, Eq. (3.29) and Eq. (3.30) are multiplied by the height adjustment factors as shown in Eq. (3.31) and Eq. (3.32) for granular and cohesive backfills, respectively.

For the granular backfill:

$$F(y) = \frac{f_s \cdot y}{.011 + .03y} \quad (y \text{ in inches, } F_{ult} \text{ in K per ft of wall}) \quad (3.31)$$

For the cohesive backfill:

$$F(y) = \frac{f_c \cdot y}{.022 + .03y} \quad (y \text{ in inches, } F \text{ in K per ft of wall}) \quad (3.32)$$

The height factors f_s and f_c are defined as follows

$$f_s = \left(\frac{H}{5.5}\right)^{1.5} \quad (3.33)$$

$$f_c = \left(\frac{H}{5.5}\right) \quad (3.34)$$

Substitute Eq.(3.33) and Eq.(3.34) into Eq.(3.31) and Eq.(3.32), then following force-displacement relationship per foot of abutment-backwall is recommended for granular backfill:

$$F(y) = \frac{y}{.14 + .38y} H^{1.5} \quad (y \text{ in inches, } F \text{ in kips per ft of wall}) \quad (3.35a)$$

$$F(y) = \frac{y}{1 + \frac{.38}{.14}y} H^{1.5} = \frac{7.143y}{1 + 2.714y} H^{1.5} = \frac{7.89y}{1 + 3y} H^{1.5} \quad (3.35b)$$

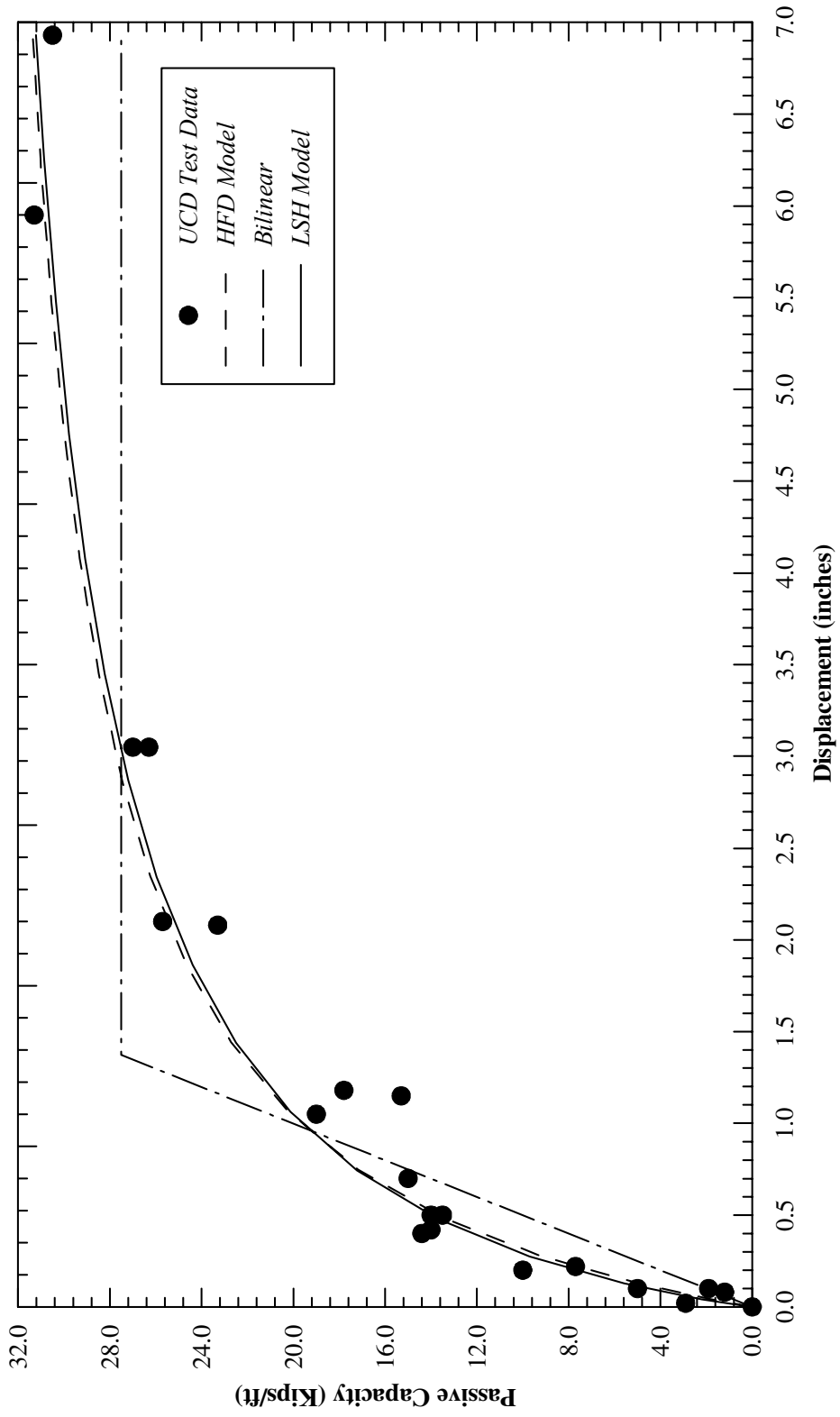


Figure 3.27 : UCDA Abutment Experiment Compared with Various Models

For all practical purposes Eq.(3.35b) can be simplified to Eq.(3.36):

$$F(y) \approx \frac{8y}{1+3y} H^{1.5} \quad (y \text{ in inches, } F \text{ in kips per ft of wall}) \quad (3.36)$$

For the cohesive backfill, the force-displacement relationship is given in Eq.(3.37).

$$F(y) = \frac{y}{.12+.16y} H \quad (y \text{ in inches, } F \text{ in kips per ft of wall}) \quad (3.37a)$$

$$F(y) = \frac{\frac{y}{.12}}{1+\frac{.16}{.12}y} H = \frac{8.33y}{1+1.33y} H = \frac{8y}{1+1.28y} H \quad (3.37b)$$

Eq.(3.37) can be simplified to Eq.(3.38)

$$F(y) \approx \frac{8y}{1+1.3y} H \quad (y \text{ in inches, } F \text{ in kips per ft of wall}) \quad (3.38)$$

3.15.2 Development of the Height Factors.

To develop the height adjustment factors, the following steps were followed:

- Developed nonlinear force-deformation relationship for various abutment heights using the LSH model, as shown in Figures 3.28 and 3.29.
- Normalized ultimate capacity of various wall heights to the ultimate capacity of the 5.5-foot wall as shown in Table 3.5:

$$f_r = \frac{F_{Hult}}{F_{5.5ult}} \quad (3.39)$$

where F_{Hult} is the ultimate calculate capacity for various abutment height and $F_{5.5ult}$ is the ultimate capacity of the experimental abutment height.

Use Eq.(3.33) and Eq.(3.34) the value of f_c and f_s listed in Table 3.5.

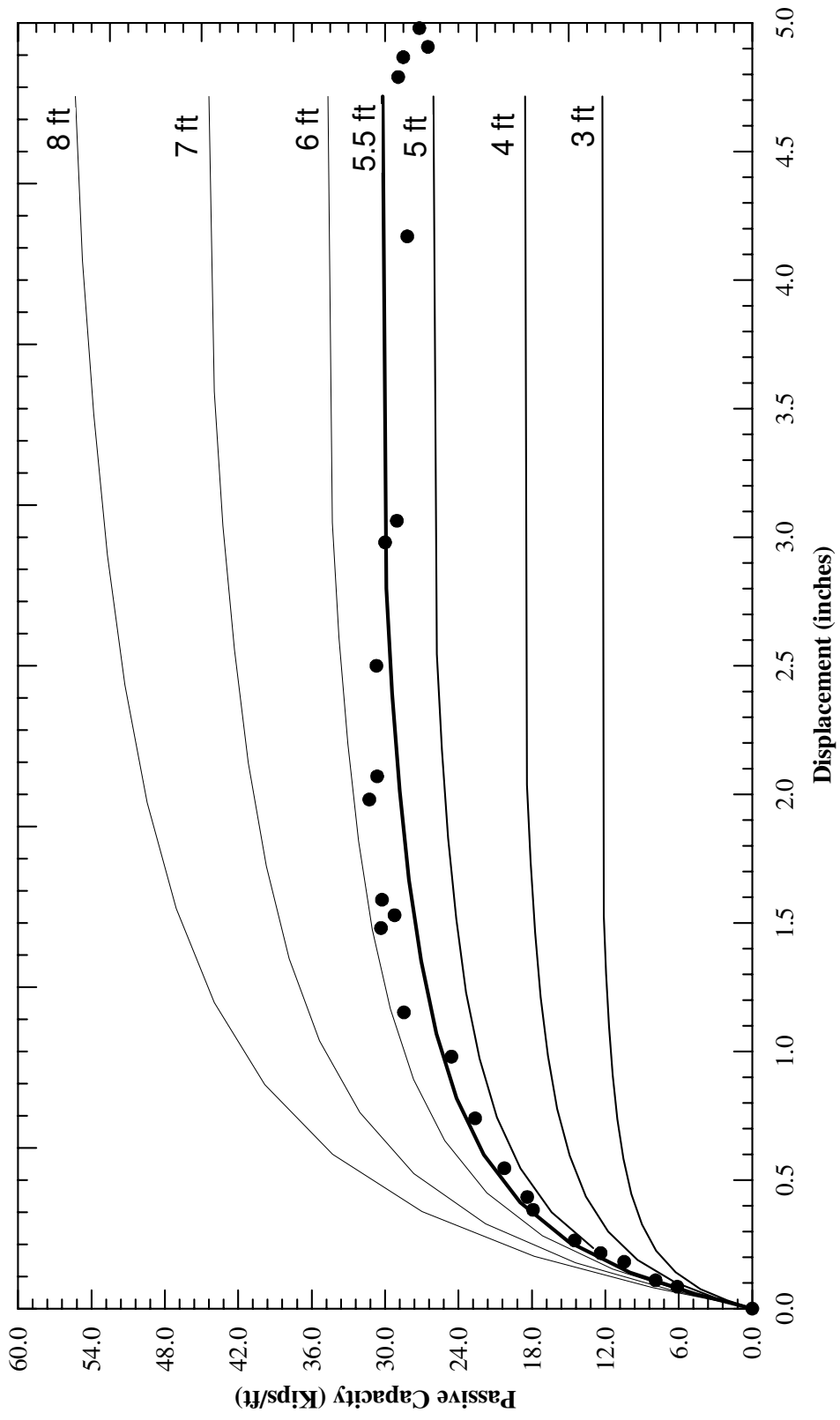


Figure 3.28: Backbone Curves for Various Abutment Height (Silty Sand)

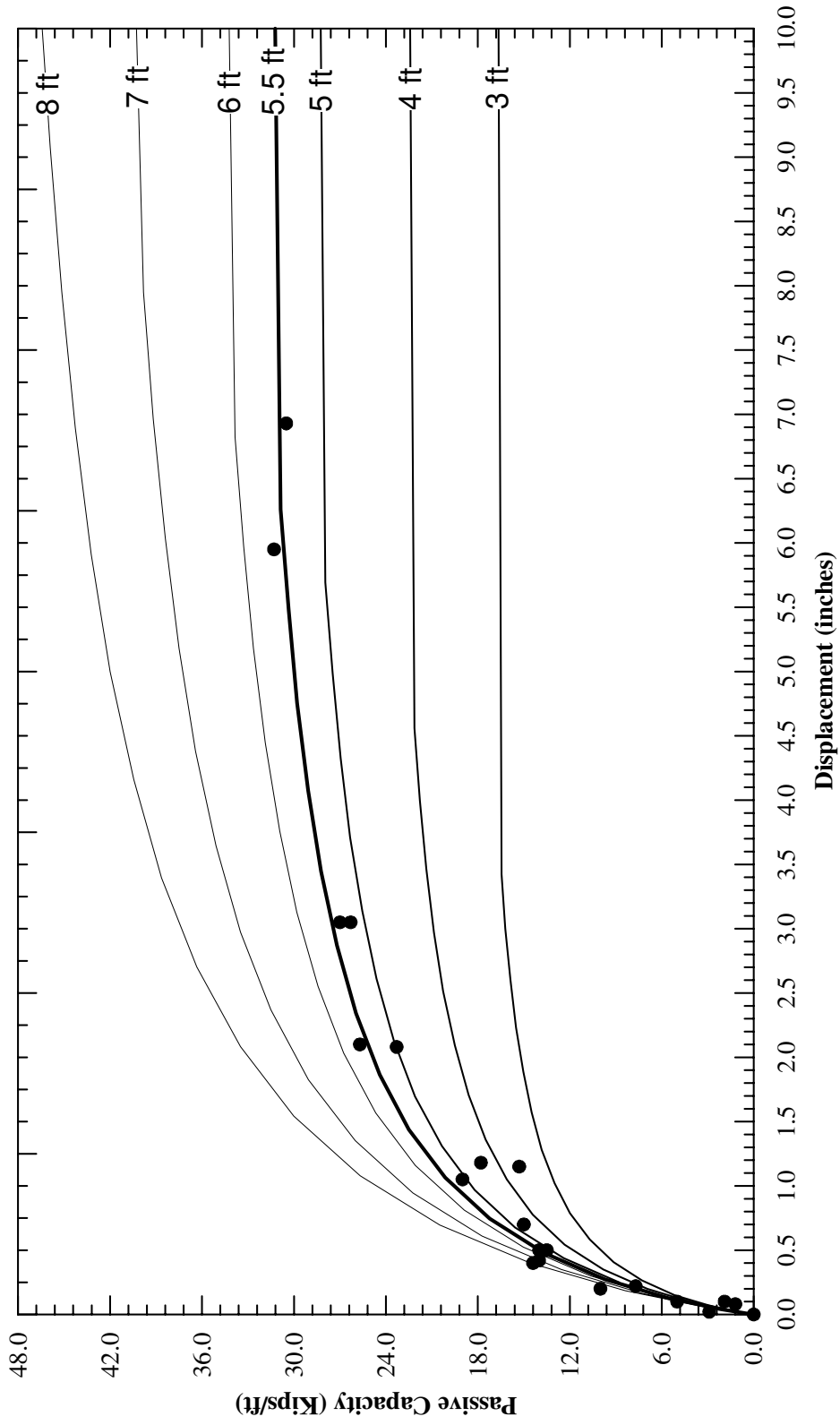


Figure 3.29: Backbone Curves for Various Abutment Height (Clay)

Table 3.5 Height factors to calculate abutment force-displacement

Height H (feet)	3	4	5	5.5	6	7	8
Granular Backfill							
f_r	0.41	0.61	0.86	1.0	1.15	1.47	1.83
f_s	0.41	0.62	0.87	1.0	1.14	1.44	1.75
Cohesive Backfill							
f_r	0.53	0.72	0.90	1.0	1.10	1.29	1.49
f_c	0.55	0.73	0.91	1.0	1.09	1.27	1.45

Figures 3.30 and 3.31 show comparisons of the nonlinear abutment force-deformation relationship predicted using the LSH model and the HFD model with Eq.(3.35) and Eq.(3.37).

3.15.3 HFD Height Validation

Experimental result of the full-scale static load test performed by Rollins and Cole (2006) at Brigham Young University (BYU) using a silty sand backfill discussed in section 3.12.2 was selected to examine the validity of Eq.(3.36). The Ovesen-Brinch Hansen 3-D correction factor (Ovesen, 1964) of 1.2 was applied to the pile cap width in the Eq.(3.36) to account for the three-dimensional wedge effect similar to the LSH model. Substituting the pile cap dimensions:

$$Height = 3.67 \text{ ft} ; Width = 17 \text{ ft} ; 3D \text{ Factor} = 1.2$$

and the adjustment factor into Eq.(3.36), we obtain

$$F(y) = 17 \left[\frac{8y}{1+3y} (3.67)^{1.5} \right] 1.2 \quad (y \text{ in inches, } F \text{ in kips}) \quad (3.36)$$

The force-displacement relationship using Eq.(3.36) is shown in Figure 3.32.

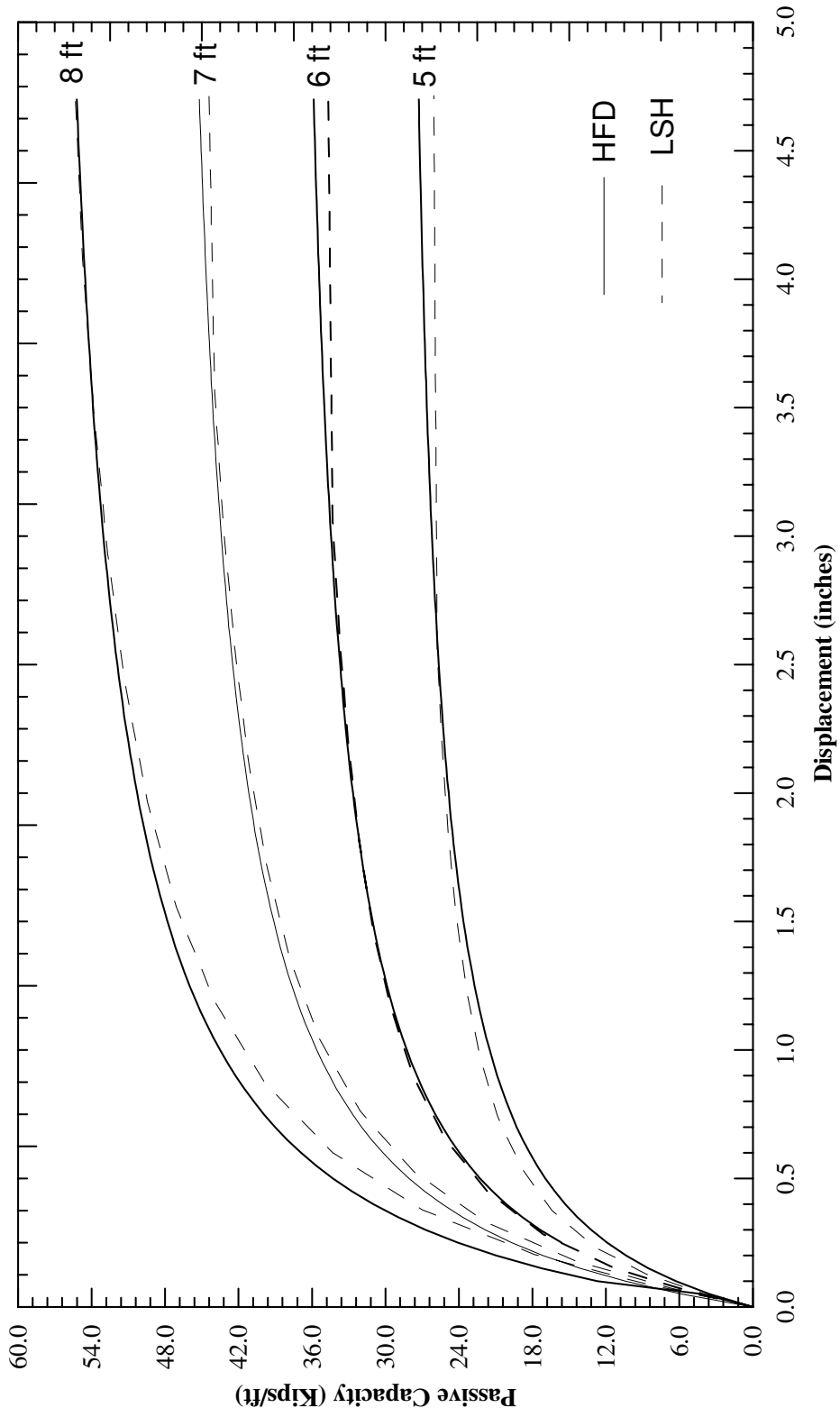


Figure 3.30: Comparisons of LSH and HFD Models for Cohesive Backfill

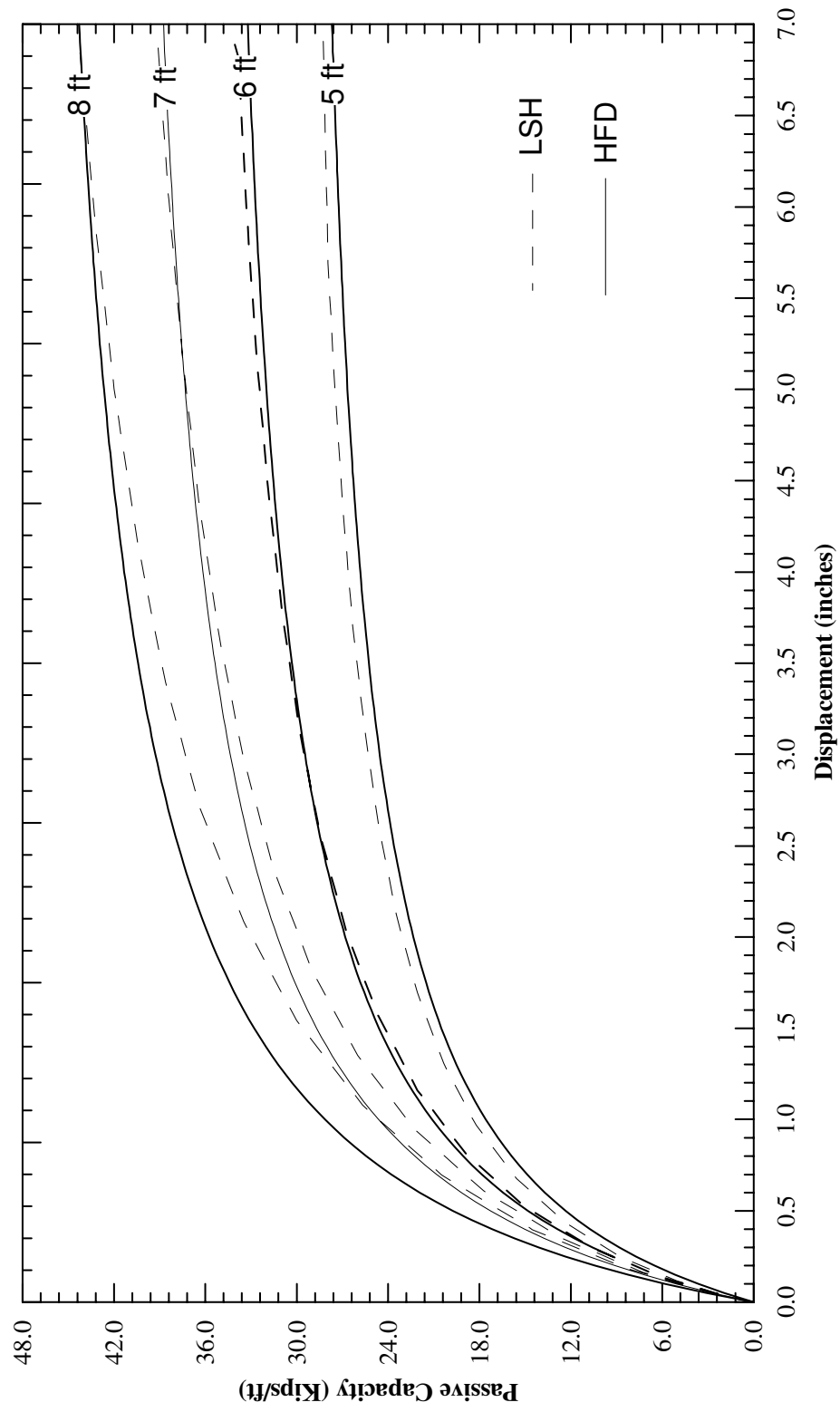


Figure 3.31: Comparisons of LSH and HFD Models for Silty Sand

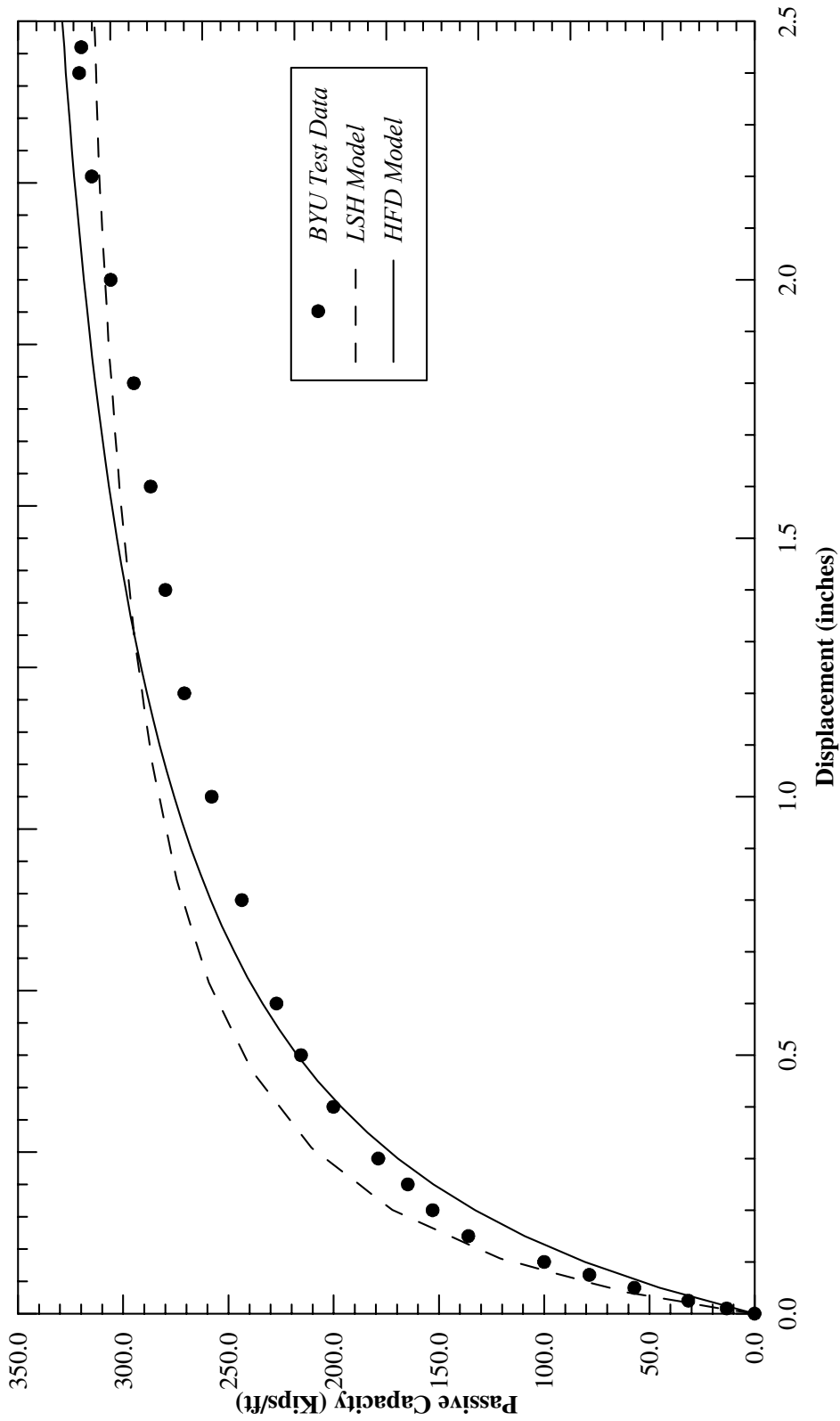


Figure 3.32: HFD Validation Using BYU Silty Sand Backfill

3.16 Conclusions

The LSH model was developed to provide a simplified means to estimate nonlinear abutment backfill force-displacement capacity. The model employs a full-length logarithmic-spiral failure wedge mechanism coupled with a modified hyperbolic stress-strain relationship. The model has seven model parameters, five of which characterize the soil properties (total unit weight γ , shear strength parameters ϕ and c , Poisson's ratio ν , and a parameter ε_{50} relating to the low-strain Young's modulus), which may be determined from field or laboratory testing or estimated. The ε_{50} parameter can be determined from testing of soil samples in a geotechnical laboratory to failure and recording of the stress-strain curve. When there is a lack of laboratory test data, the presumptive values of ε_{50} (0.0035 for granular soils and 0.007 for cohesive soils) are recommended. The sixth parameter δ is the structure-soil interface friction angle and experimental values are given in the literature. The last model parameter R_f describes the theoretical ultimate capacity of the soil in the hyperbolic stress-strain relationship and typical values are between 0.94 and 0.98 for all soil types considered. When no capacity data is available for calibrating the LSH model, it is found that a value of 0.97 is reasonable.

The LSH model is applicable to all soil types that can be reasonably characterized by these seven parameters. The validity of the LSH model is established by comparison with experimental nonlinear force-deformation results from full-scale tests, centrifuge model tests and small-scale laboratory tests of abutments and pile caps in a variety of structure backfills.

A modified hyperbolic force-displacement (HFD) equation was developed, which requires only three parameters: average soil stiffness K , and the ultimate passive capacity F_{ult} , and the maximum displacement y_{max} at which F_{ult} is mobilized. The first parameter can be readily determined using presumptive soil stiffnesses, such as used in Caltrans seismic design of bridge abutments (SDC, 2004). The latter two parameters can be estimated from available experimental test data (such as Caltrans SDC, 2006) or by the geotechnical engineer using a selected earth pressure theory depending on the application. Using the HFD parameters derived directly from the nine experimental test data, the HFD model is found to match all test data well (nearly the same as the LSH predicted curves). Nonlinear closed-form solutions are to develop the nonlinear force-displacement curve for compacted abutment backfills when no geotechnical data is available. The LSH and HFD models are practical and versatile tools that can be used by structural and geotechnical engineers in seismic analysis for bridge design.

CHAPTER FOUR

ABUTMENT CONTINUUM FINITE ELEMENT MODEL

4.1 Introduction

The finite element method (FEM) is the most powerful numerical technique to solve soil-abutment-structure interaction problems for seismic analysis of bridge structures. The FEM can provide insight into the behavior and cause of abutment-backfill failure during a seismic event. Before using FEM, at least a preliminary solution should be obtained using previously available solutions or experimental data. In common practice, bridge engineers use presumptive value to calculate a bilinear force-deformation relationship to model the nonlinear behavior of the abutment backfill.

Depending on the complexity of the bridge abutment system, there is more than one method of analysis to develop nonlinear abutment-backfill springs. The purpose of this chapter is to carry out a displacement finite element analysis to capture the nonlinear force-deformation capacity of the abutment backfill and to investigate the mechanism of the backfill failure in particular the bridge abutments with high skew angles. PLAXIS, a finite element code that is capable of performing both two-dimensional and three-dimensional analysis is used to calculate backfill backbone curves for both skewed and nonskewed abutments. The results of the finite element analysis is compared with results from full-scale experiments, presumptive values, a closed-form solution and a simplified solution. It is assumed that the

abutment backwall is loaded very gradually such that it remains in a state of static equilibrium, for which the static action of the backwall and reaction of the backfill equilibrate each other and time has no influence on the results.

4.2 Method of Analysis

For exact theoretical solution of bridge abutment backfill behavior, the requirements for equilibrium, compatibility, and constitutive stress-strain relationship with the proper boundary conditions must all be satisfied. Nonlinear force-deformation relationship for seismic design and analysis of bridge abutment-backfill interaction can be calculated using the following methodologies: (1) Presumptive values, (2) closed-form solution, (3) simplified solution and (4) numerical solution.

4.2.1 Presumptive Values

In bridge engineering practice, it is common to use a presumptive value to calculate abutment bilinear force-deformation relationship for seismic design and analysis of bridge structures. Bilinear force-deformation relationship in longitudinal direction of the bridge superstructure is developed using Eq.(4.1) (SDC, 2004).

$$\begin{aligned} K_{Abut} &= K_{Exp} * f \\ F_{Ult} &= A_e * \sigma_{Exp} * f \end{aligned} \tag{4.1}$$

The allowable presumptive value is calibrated based on full-scale abutment field experiments. Bilinear abutment force-deformation relationship assumes linear elasticity for all stress states below the yield point. Once idealized backfill passive

capacity is reached, the ultimate abutment force-capacity remains constant with increasing displacement as shown in Figure 4.1

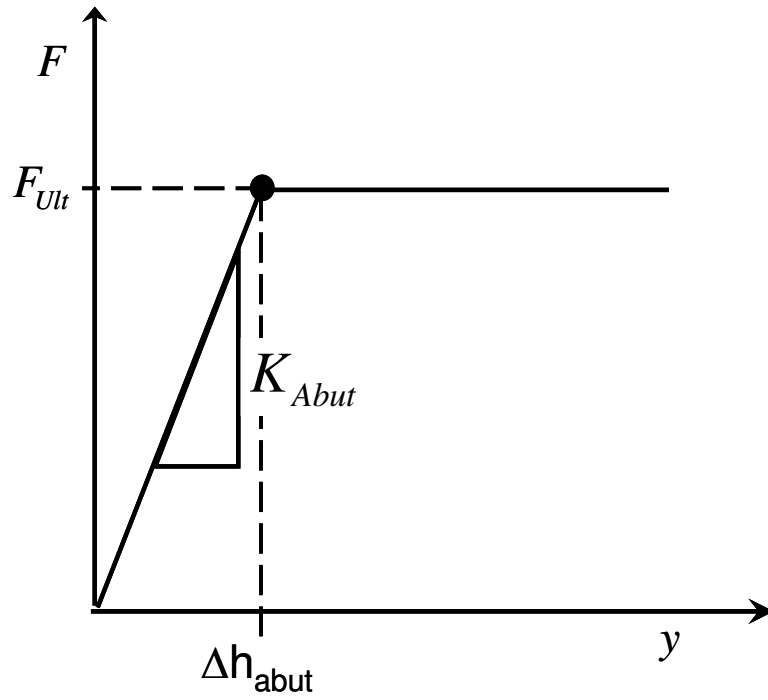


Figure 4.1: Abutment Force-Deformation Based on Presumptive Value

The parameters in Eq.(4.1) and Figure 4.1 are defined as follows:

K_{abut} is the average abutment stiffness in the longitudinal direction,

F_{ult} is the ultimate allowable passive resistance provided by the abutment backfill,

σ_{exp} is the ultimate allowable stress resistance provided by the abutment backfill,

f is the width and height adjustment factor,

h_{abut} is the height of abutment backwall,

Δ is a factor as a function of backfill properties to define the yield point, and h_{exp} is the height of field experiment abutment backwall height,

The current Federal Highway Administration's Seismic Retrofit Manual for Highway Structures (MCEER, 2006) suggests for integral or monolithic abutments, an initial secant stiffness (K_{abut}) shown in Eq.(4.2) may be used to calculate bilinear abutment backbone curve as shown in Figure 4.1.

$$K_{Abut} = \frac{F_{ult}}{0.02h} \quad (4.2)$$

where

$\Delta = 0.02h$ which defines the yield point shown in Figure 4.1.

For the seat-type abutments, the expansion gap should be included in the calculation of the secant stiffness as follows:

$$K_{Abut} = \frac{F_{ult}}{(0.02h + D_g)} \quad (4.3)$$

where

D_g is the gap width.

Current Caltrans Seismic Design Criteria (SDC, 2006) suggests presumptive value for the abutment stiffness (K_{abut}) of 20 k/in per foot of wall and a presumptive value of 5 kips per square foot of abutment backwall should be used to calculate the yield plateau of the bilinear abutment force-deformation relationship. Per current Caltrans criteria, the adjustment factor f used in Eq.(4.1) should be set equal to the

ratio $h_{\text{abut}}/5.5$ (5.5 is wall height in feet based on the UCD abutment test). The abutment stiffness should be modified to account for the expansion gap.

4.2.2 Closed-Form Solution

Simple nonlinear closed-form solution is the ultimate goal for bridge engineers to develop discrete abutment springs for various backfill. In order to get a solution for more realistic abutment-backfill behavior, good engineering judgment and approximations must be introduced. As shown in the previous chapter, for the engineered abutment backfill it is possible to establish a realistic closed form solution as shown in Figure 4.2 to develop an abutment-backfill nonlinear force-deformation relationship.

As discussed in Chapter 3, based on experimental data and parametric studies using the LSH model, the hyperbolic force-displacement (HFD) relationships per foot of abutment-backwall for cohesionless and cohesive backfills, respectively, are expressed below:

$$F(y) = \frac{8y}{1+3y} H^{1.5} \quad (y \text{ in inches, } F \text{ in kips per ft of wall}) \quad (4.4a)$$

$$F(y) = \frac{8y}{1+1.3y} H \quad (y \text{ in inches, } F \text{ in kips per ft of wall}) \quad (4.4b)$$

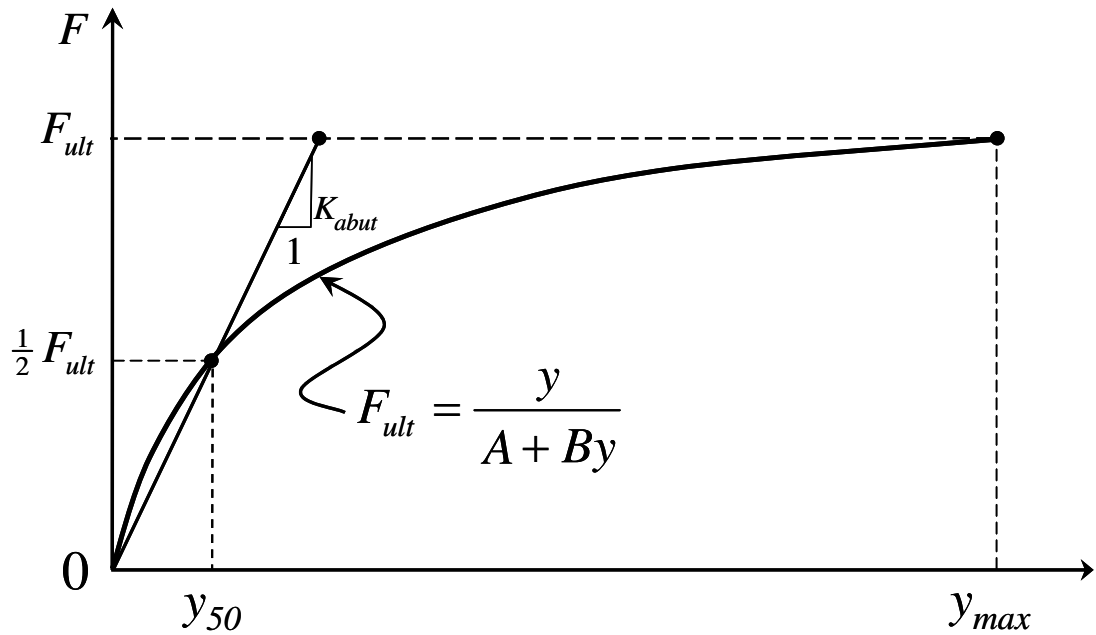


Figure 4.2: Closed-Form Solution

4.2.3 Simplified Solution

As shown in the previous chapter, the LSH model can capture the abutment behavior fairly accurately. The method can be used by both geotechnical and bridge engineers to calculate the nonlinear abutment backbone curves based on strength and stress-strain behavior of the backfill. The requirements of equilibrium, stress-strain and deformation compatibility are all satisfied.

4.2.4 Numerical Solution

The most common numerical method used in the geotechnical engineering to solve complicated soil-structure interaction problems is the finite element method. Unlike the classical analysis methods (e.g., limit equilibrium, limit analysis, etc), it is

capable of satisfying all four basis requirements for a complete theoretical solution. The requirements of limiting equilibrium, compatibility of displacement, material constitutive behavior, boundary conditions and stage constructions are all satisfied. The geometry of the abutment-backfill system, loading conditions, nonlinear material properties and boundary are absolute necessary to be accurately modeled. The accuracy of displacement finite element method is dependent on the realistic stress-strain characteristics of the abutment backfill. The intent of this section is to:

- Develop a finite element model to validate the constitutive soil model based on realistic triaxial test data for existing bridge abutment-backfill;
- Develop 2-D finite element models to simulate full-scaled abutment and pile cap experiments conducted at UCLA, UCD and BYU;
- Develop 3-D finite element models to simulate full-scaled experiments and investigate the mechanism of the skewed abutment failure; and
- Compare the results of the experimental data versus closed-form solution, simplified solution and the 2-D and 3-D finite element solutions.

4.3 Constitutive Models for Bridge Structures

Bridge structures considered herein are constructed from reinforced concrete. Steel reinforcement is to provide tensile capacity and concrete is to provide compressive capacity. A brief description of the constitutive models for the reinforced concrete is given below. Extensive experimental and analytical research has resulted in significant advances and the development of reinforced accurate

concrete constitutive relationships. However, in the bridge community, there is not a well define stress-strain relationship for the bridge abutment backfill.

Figure 4.3 shows the constitutive stress-strain model including unloading and reloading branches for a confined concrete section which is used in the analysis to determine the capacity of the ductile concrete members. The envelope for the model is the monotonic stress-strain curve based on Mander et al. (1988) confined concrete model. Where (f'_{cc}) is expected concrete compressive strength, (ϵ_{cc}) is the concrete confined compressive strain and (ϵ_{cu}) is the concrete ultimate compressive strain.

The tensile stress-strain relationship for typical reinforcing steel used in bridge structures is shown in Figure 4.4. The steel stress-strain relationship exhibits an initial linear elastic portion up to point A, a yield plateau AB, and a strain hardening range in which the stress increases with strain. The yield point is defined by the expected yield stress of the steel f_{ys} . The length of the yield plateau is a function of the steel strength and bar size. The strain-hardening portion is nonlinear and is terminated at the ultimate tensile strain ϵ_{su} .

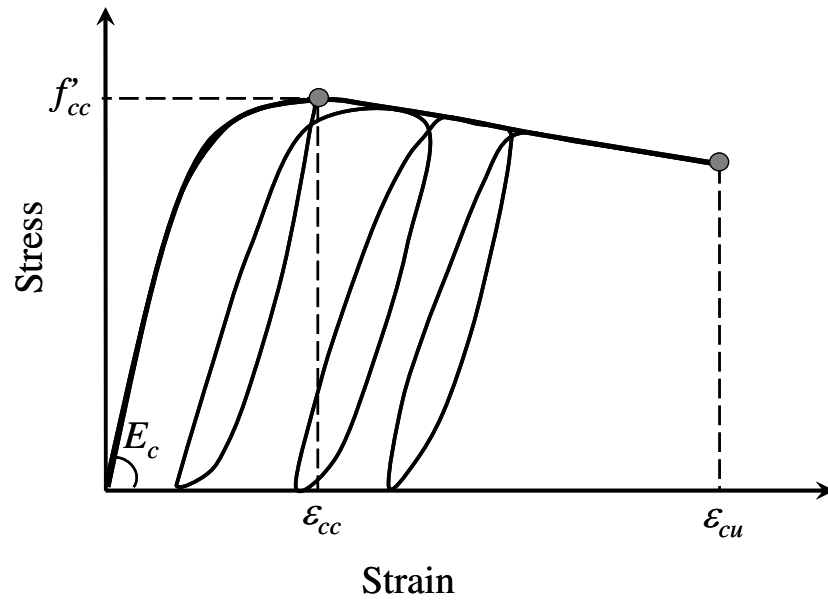


Figure 4.3: Hysteretic Behavior of Confined Concrete

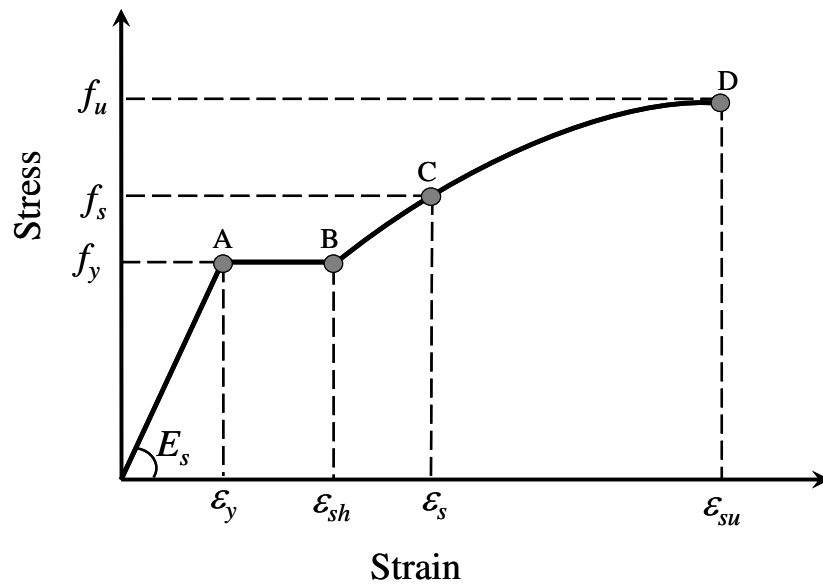


Figure 4.4: Behavior of Steel

4.4 Constitutive Model for Abutment Backfill

A detailed description of the abutment backfill stress-strain relationship was given in the previous chapter. Based on the data of triaxial tests conducted on state-wide abutment-backfill using both in-situ and remolded samples, the decreasing stiffness and simultaneously irreversible plastic strain were characteristics of all the abutment backfill. Advanced constitutive modeling such as bounding surface plasticity model (Bardet, 1986) has been developed to simulate the nonlinear soil behavior. When these constitutive models are implemented in finite element computer programs, they can be used to solve difficult geotechnical engineering problems (Bardet, 1997). For the seismic analysis of bridge abutment, a constitutive model should be selected such that it would be possible to obtain the model parameter values in a simple manner from conventional geotechnical field exploration and laboratory test data.

The purpose of this section is to use a finite element model which not only can simulate the stress-strain behavior of the abutment backfill up to and beyond the failure, but also can capture the nonlinear force-deformation of the abutment-backfill. The application of finite element method for abutment-backfill interaction requires not only knowledge of the fundamentals of the method, but also understanding of the material properties used for abutment backfill. A hardening soil model, Hardening Soil (HS), which is an advanced double stiffness model available in the finite element code, PLAXIS, is selected for the simulation of the nonlinear abutment backfill behavior. The model captures the abutment backfill behavior in a

tractable manner on the basis of only two stiffness parameters and is very much appreciated by the practicing geotechnical engineers due to its simplicity. The stiffness moduli are stress-dependent, which are reduced with the strain according to a hyperbolic relationship. This model represents an updated version of the well-known Duncan-Chang hyperbolic model (Duncan et al., 1980), however, it supersedes the Duncan-Chang model by: (1) using theory of plasticity rather than elasticity, (2) including soil dilatancy, and (3) introducing a yield cap.

The full explanation and derivation of this model is described by Schantz (1999) and Brinkgreve (2006). A brief description of the model formulation and parameters are given below. More detailed explanation of nonlinear soil behavior and application of plasticity theory to soil behavior are described by Bardet (1983).

The basic idea for the formulation of the HS model is the Hyperbolic relationship between the deviatoric stress (q_i) and the vertical strain (ε_i) in primary triaxial loading as shown in the following equation.

$$q_i = \frac{\varepsilon_i}{\frac{1}{2E_{50}} + \frac{R_f \varepsilon_i}{q_f}} \quad (4.5)$$

where

$$q_f = (c \cot \phi - \sigma_3) \frac{2 \sin \phi}{1 - \sin \phi} \quad (4.6)$$

The value of q_f is the ultimate value of the deviatoric stress which can be express as

$$q_f = (\sigma_1 - \sigma_3) R_f \quad (4.7)$$

There are two types of hardening, namely shear hardening and compression hardening in the HS model. The shear hardening controls the irreversible shear strains and the shear yield surface of the HS model. The compression hardening controls the irreversible plastic straining of the HS model due to compressional loading. The limiting states of stress are described by means of conventional Mohr-Coulomb parameters (soil friction angle, ϕ ; the cohesion, c ; and the dilatancy angle, ψ).

The nonlinear stress-strain behavior in loading is represented by the hyperbolic function as shown in Figure 4.5. The HS model enables a realistic description of the stiffness. The model is consisted of three stiffnesses: (1) primary loading stiffness, (2) unloading/reloading stiffness and (3) oedometer stiffness.

4.4.1 Primary Loading Stiffness

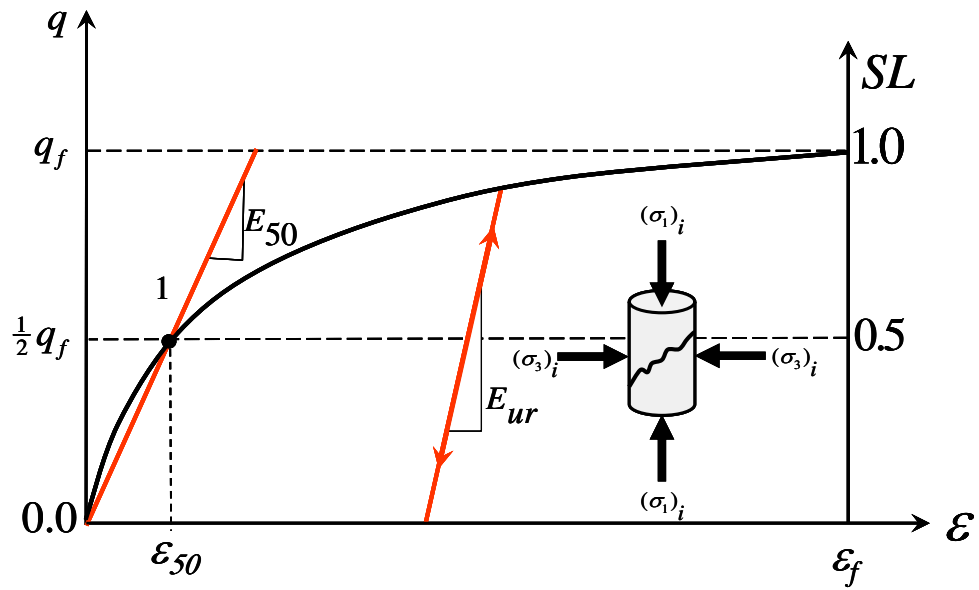
The primary loading stiffness (E_{50}) is an average secant modulus and is the confining stress dependent. The value of the parameter E_{50} is calculated using Eq.(4.8).

$$E_{50} = E_{50}^{ref} \left(\frac{a + \sigma_3}{a + p^{ref}} \right)^m \quad (4.8)$$

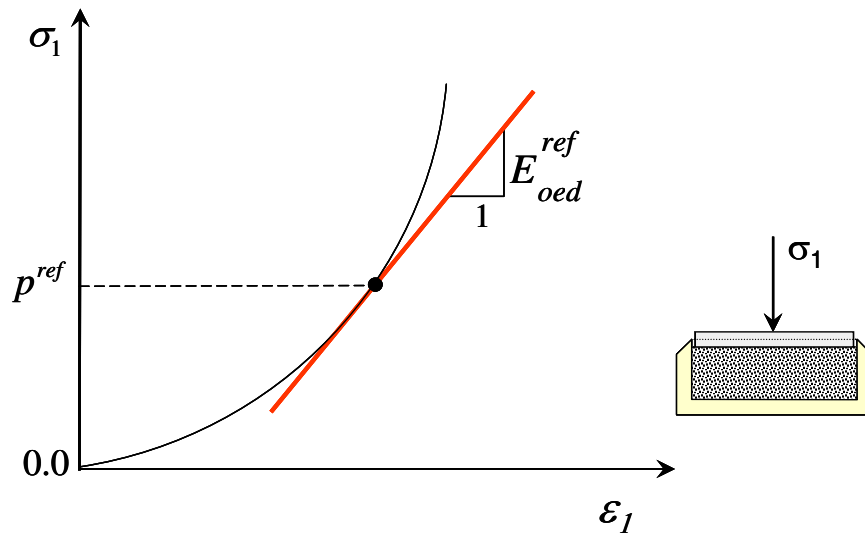
where

$$a = c / \tan \phi$$

The shear hardening is used to model irreversible strains due to primary deviatoric loading. The triaxial modulus controls the shear yield surface of the HS model. The parameters used in the HS model are summarized in Table 4.1.



(a) Triaxial Test



(b) Oedometer Test

Figure 4.5: Hardening Soil (HS) Model

Table 4.1 Parameters of the HS model

Parameters	Expression	Description
Deformation	E_{50}^{ref}	Primary loading reference modulus in drained triaxial test
	E_{oed}^{ref}	Reference modulus for primary loading in oedometer test
	E_{eur}^{ref}	Unloading/reloading reference modulus in drained triaxial test
	M	Modulus exponent for stress dependency
	V_{ur}	Poisson's ratio for loading/unloading
Strength	C	Effective cohesion at failure
	ϕ	Effective friction angle at failure
	ψ	Dilatancy angle at failure

4.4.2 Unloading/Reloading Stiffness

For unloading and reloading stress path, a much stiffer linear response in unloading is described by the parameter, E_{ur} . The value of the parameter E_{ur} is calculated using Eq.(4.9).

$$E_{ur} = E_{ur}^{ref} \left(\frac{a + \sigma_3}{a + p^{ref}} \right)^m \quad (4.9)$$

4.4.3 Oedometer Stiffness

The oedometer modulus (E_{oed}) controls the cap yield surface. It is a compression hardening which is used to model irreversible plastic straining due to primary compression in oedometer loading and isotropic loading as shown in Figure 4.5. The value of the parameter E_{oed} is calculated using Eq.(4.10).

$$E_{oed} = E_{oed}^{ref} \left(\frac{a + \sigma_1}{a + p^{ref}} \right)^m \quad (4.10)$$

The parameter m used in Eq. (4.8), Eq. (4.9) and Eq. (4.10) controls variation of stiffness with confining pressure. The value of the parameter m for sand varies from 0.40 to 0.70; for highly overconsolidated clays it varies from 0.50 to 0.90; and for normally consolidated clays it is about 1.0 (PLAXIS, 2006 Manual).

The plastic behavior is defined through the yield/failure surfaces. In contrast to the elastic perfectly-plastic model, the yield surface of the HS is not fixed in principal stress space, but will expand due to plastic straining as shown in Figure 4.6 .

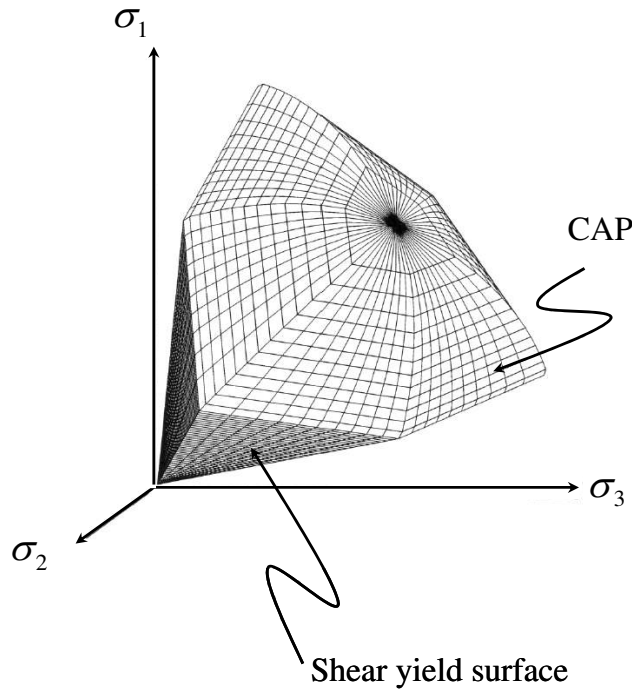


Figure 4.6: HS Model in Stress Space

4.4.4 Dilatancy

Dilatancy Ψ is defined as the volume change associated with the application of shear stresses. An increase in volume, or expansion, is known as positive dilation, while a decrease in volume, or contraction, is known as negative dilation. The stress-dilatancy theory is able to explain qualitatively and quantitatively how sandy soils dilate when subjected to shearing stresses (Bardet, 1983). The amount of dilatancy that an abutment-backfill can experience is dependent on particle interlocking, which relates to the fabric of the material. Dilatancy can be estimated from the volumetric strain versus axial strain curve (Figure 4.7) of a material subjected to shearing with the following expression as stated by Bolton (1986) for plane-strain conditions and later derived by Schanz and Vermeer (1996) for triaxial test conditions.

$$\sin \psi_m = \frac{\sin \phi_m - \sin \phi_{cv}}{1 - \sin \phi_m \sin \phi_{cv}} \quad \text{for } e < e_{cv} \quad (4.11)$$

where:

$$\sin \phi_{cv} = \frac{\sin \phi_m - \sin \psi}{1 - \sin \phi_m \sin \psi} \quad (4.12)$$

$$\sin \psi_m = 0 \quad \text{for } e \geq e_{cv} \quad (4.13)$$

ϕ_m is the mobilized friction angle, and

ϕ_{cv} is the critical friction angle at the maximum void ratio.

The void ratio is related to the volumetric strain, ε_v by the relationship given in Eq.(4.14):

$$\varepsilon_{vo} - \varepsilon_v = \ln\left(\frac{1+e}{1-e_o}\right) \quad (4.14)$$

where an increment of ε_v is negative for dilatancy.

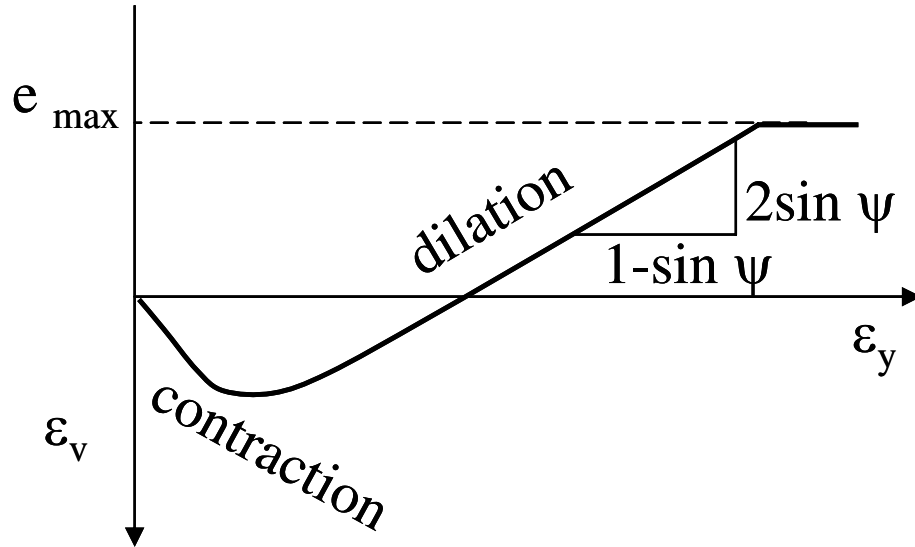


Figure 4.7: PLAXIS Dilatancy Model

The initial void ratio, e_o , is the in-situ void ratio of the abutment backfill. The maximum void ratio, ε_{cv} is the void ratio of the material in a state of critical void (critical state). Critical state is an asymptotic state eventually reached during loading characterized by volume change, no stress change and infinite deviatoric stain: “It is as material has melted under stress.” (Bardet, 1983).

4.5 Verification of the Constitutive Model

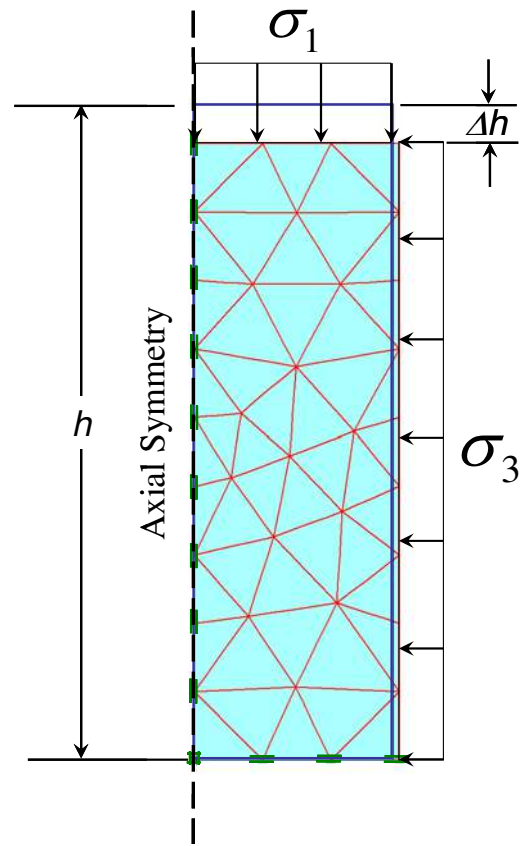
A seismic soil-structure interaction analysis of the bridge abutment generally requires knowledge of both the shear strength and nonlinear stress-strain behavior of the abutment backfill. In particular for the deformation analysis of the abutment, description of the stress-strain behavior is necessary, as the overall performance of

the abutment is defined mostly within the range of nonlinear stress-strain behavior of the abutment backfill. To describe the abutment nonlinear behavior using a finite element model, the modified hyperbolic stress-strain relationship in the PLAXIS code is proposed herein. In this section, the verification of the constitutive soil model selected for the abutment backfill is utilized using triaxial test data conducted by Earth Mechanics In. (EMI, 2005) to characterize representative bridge abutment backfill properties as part of a Caltrans seismic research program. Finite element analysis of the triaxial tests was performed and compared with the measured stress-strain response for the Painter Street Overcrossing abutment backfill. In the finite element analysis, the PLAXIS HS model was used to simulate the triaxial tests. Figure 4.8 shows the test specimen and axisymmetric finite element analysis of the triaxial test.

The left hand side and the bottom of the model are axes of symmetry. At these boundaries, the displacements normal to the boundary are fixed and tangential displacements are free for move. Two representatives of the in-situ samples from the bridge abutment backfill are selected to validate the constitutive model used in the finite element analysis: one predominantly cohesive soil and one predominantly cohesionless soil. The triaxial test specimens were run at three confining pressures and three deviatoric stresses to obtain cyclic stress-strain relationships, friction angle and cohesion values of the abutment backfill at the failure.



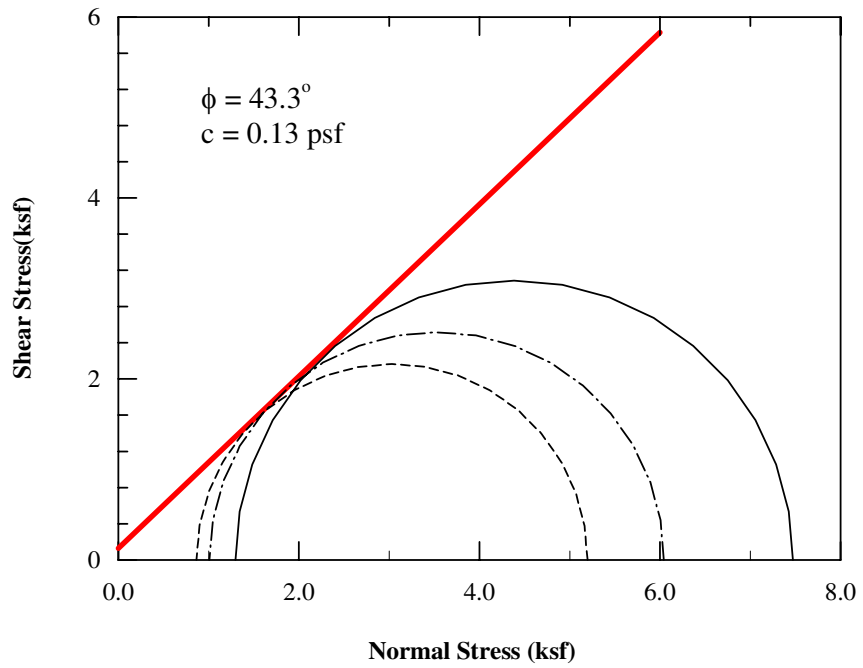
(a)



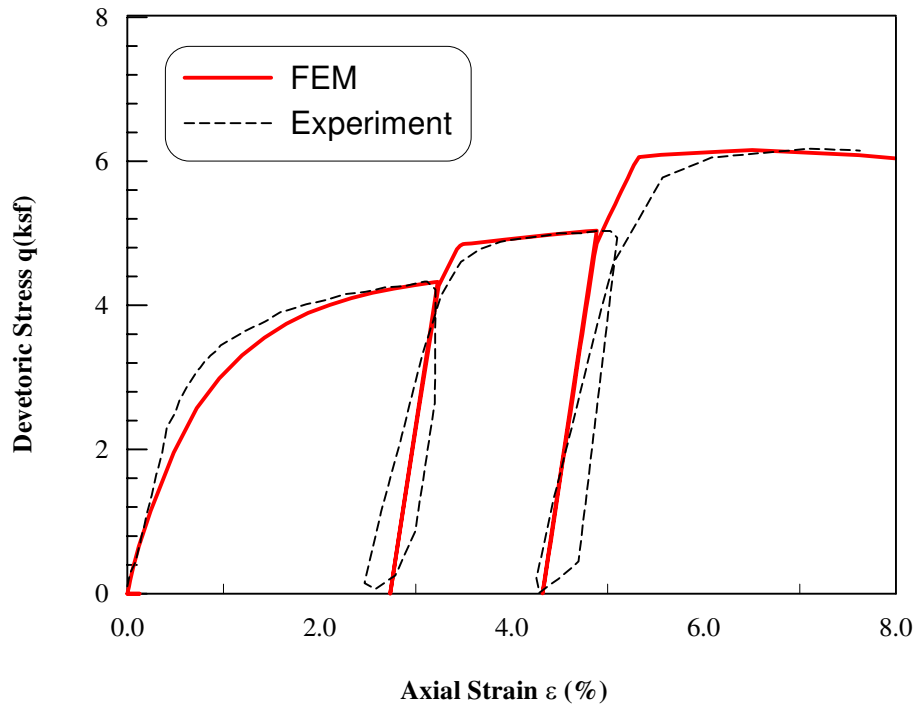
(b)

Figure 4.8: Triaxial: (a) Specimen; (b) Finite Element Model

The cyclic stress-strain relationships measured and predicted from the finite element analysis are plotted in Figure 4.10 and Figure 4.11 showing three unloading and reloading cycles. The plots include the three associated Mohr circles, the shear strength parameters at the failure the nonlinear stress-strain behavior of the backfill. Figure 4.9 and Figure 4.10 demonstrate that the measured and calculated stress-strain curves show a good match for both triaxial tests. Therefore, the HS model available in PLAXIS is capable of capturing the nonlinear stress-strain behavior of both cohesive and cohesionless abutment backfills.

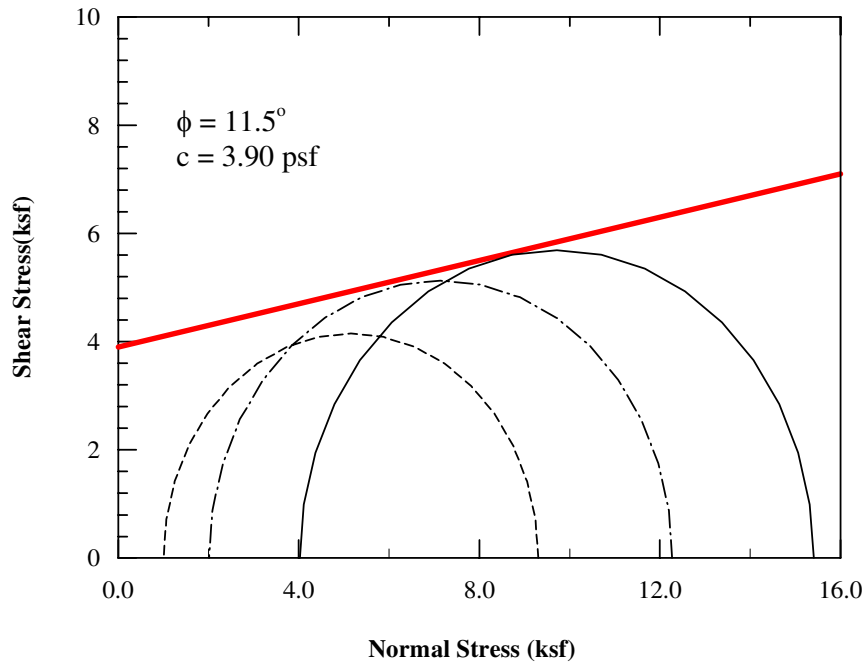


(a) Mohr Circles

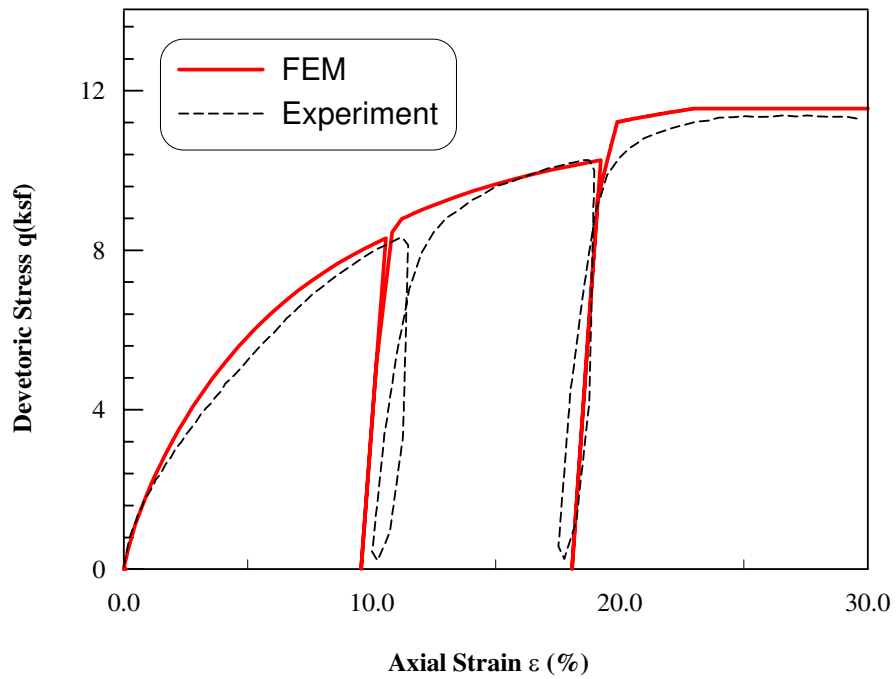


(b) Stress-strain Behavior

Figure 4.9: Triaxial Test of the Cohesionless Backfill



(a) Mohr Circles



(b) Stress-strain Behavior

Figure 4.10: Triaxial Test of the Abutment Backfill for Cohesive Soil

4.6 2-D Finite Element Model

A series of two-dimensional (2-D) displacement-controlled finite element (FE) simulations using PLAXIS have been carried out to calculate the nonlinear backbone curves for full-scaled abutments and pile cap experiments. Detail description of these experiments were presented in the previous chapter. The finite element mesh used in the simulations is shown in Figure 4.11. For each simulation, a geometry model was first created. The geometry model is a representation of the real problem and consists of points, lines and clusters (elements), which includes a representative abutment backfill, construction stages and loading. The model was sufficiently large so that the boundaries did not influence the results. The points were used to position the point of fixities and local refinement of the finite element mesh. The lines were used to define the physical boundaries of the geometry and the backfill for staged construction. Clusters are the areas that are fully enclosed by lines. The finite element model was generated based on the composition of the clusters and lines in the geometry model.

During the generation of the mesh, the clusters were divided into 15-noded triangular elements. The distribution of nodes over the elements are shown in Figure 4.11. During the finite element calculation, displacements are calculated at the nodes. In contrast to displacements, stresses are calculated at individual Gaussian integration points (stress points) rather than at the nodes.

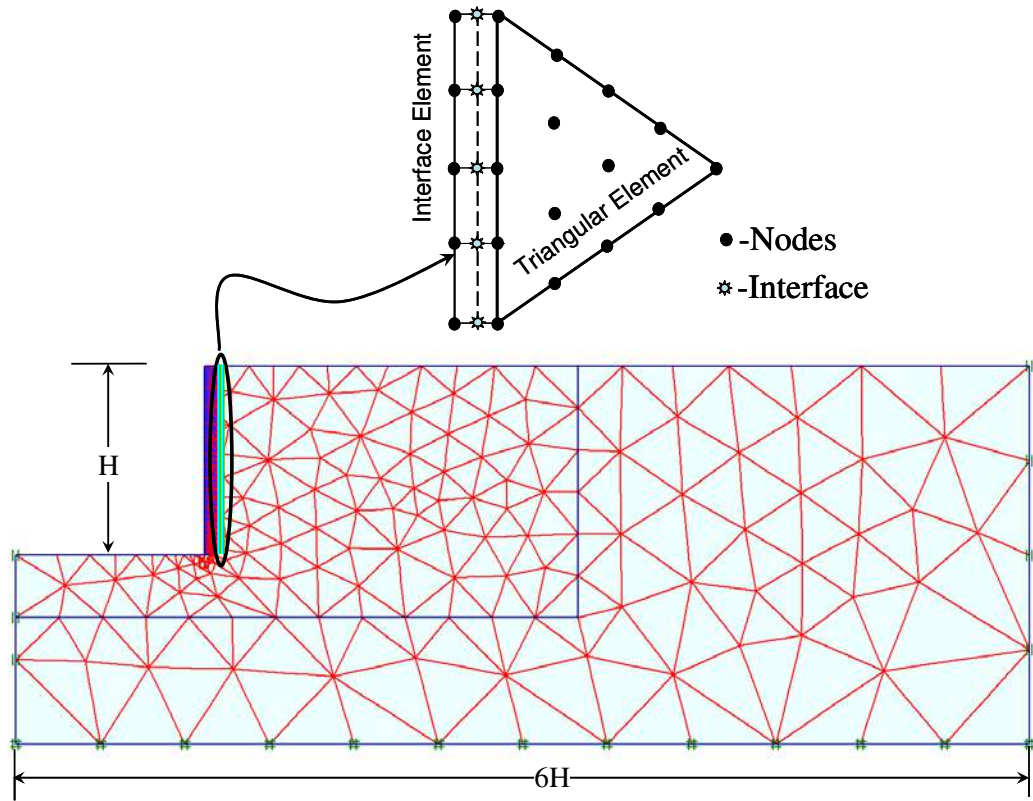


Figure 4.11: 2-D Finite Element Mesh with Backwall Interface

The right vertical boundary was placed over a distance of $6H$, the left boundary was placed $1H$ away from the abutment backwall and the bottom boundary was placed $1H$ below the bottom of the backwall, which were similar to those used by Martin et al. (1997). Numerical simulation of the experiments involved two steps of analysis: the first step was to establish the geostatic state by applying gravity load and the second step was to push the wall by prescribing either cyclic displacements or monotonic displacement until the backfill failed and the passive wedge was formed.

4.6.1 Interface Elements

The abutment backwall-backfill interaction is modeled with the interface elements. Figure 4.11 shows how the abutment backwall interface elements are connected to backfill elements. When using 15-node soil elements, the corresponding interface elements are defined by five pairs of nodes. In Figure 4.11 the interface elements are shown to have a finite thickness, but in the finite element formulation the coordinates of each node pair are identical, which means that the element has a zero thickness.

A bilinear model is used to describe the behavior of interfaces for modeling backfill-abutment interaction. The Coulomb criterion is used to distinguish between elastic behavior (where small displacements can occur within the interface) and plastic interface behavior (slip).

For the interface to remain elastic, the shear stress τ is given by:

$$|\tau| < \sigma_n \tan \phi + c \quad (4.15)$$

For plastic behavior, shear stress τ is given by:

$$|\tau| = \sigma_n \tan \phi + c \quad (4.16)$$

where ϕ and c are the friction angle and cohesion of the interface and σ_n and τ are the normal stress and shear stress acting in the interface. The strength properties of interfaces are linked to the strength properties of the abutment-backfill using a

strength reduction factor (R_{inter}). The interface properties are calculated using the following relationships:

$$c = R_{inter} c_{soil} \quad (4.17)$$

$$|\tau| = R_{inter} \tan \phi_{soil} \leq \tan \phi_{soil} \quad (4.18)$$

Figure 4.12 shows stress-strength and stress-strain relationship of the classical Mohr-Coulomb model applied to the interface elements. Once the specified shear stress is reached, the shear stress is assumed to remain constant with increasing slip.

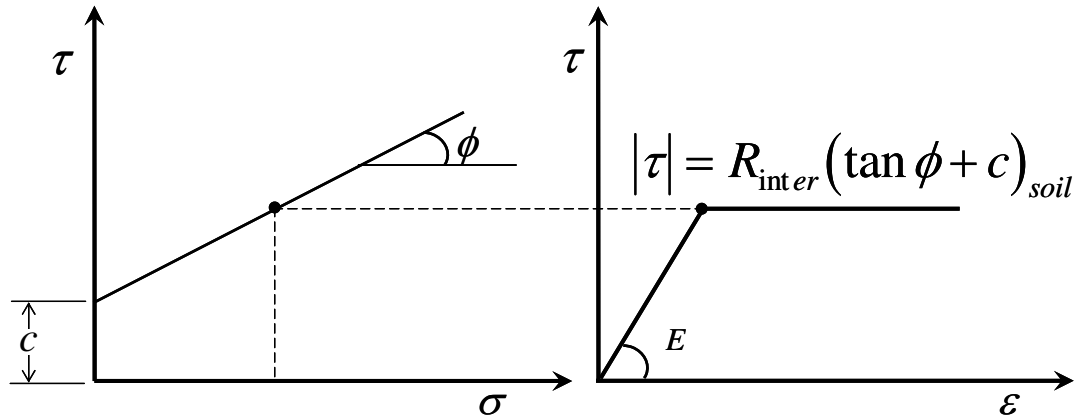


Figure 4.12: Mohr-Coulomb Interface Stress-Strain Relationship

4.6.2 2-D Finite Element Simulations for Various Backfill

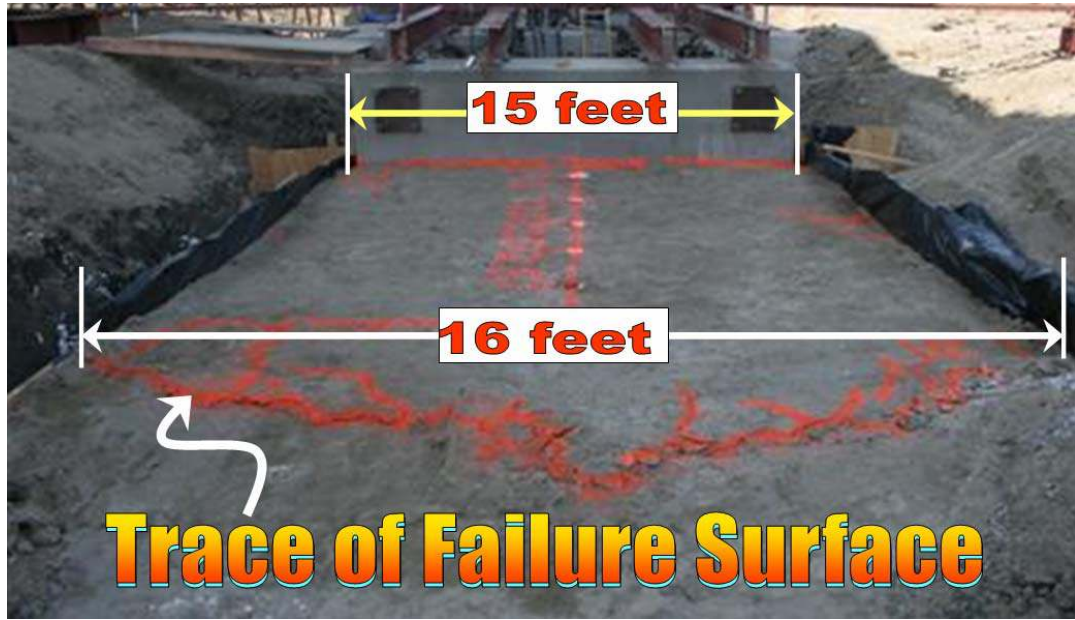
The previous chapter has dealt with LSH model for full-scale abutment backwall, full-scale pile cap, small-scale laboratory for retaining wall and centrifuge experiments for abutment backwall and pile cap. This section presents simulations

using finite element models only for the full-scale experiments, which include UCLA and UCD abutment test and BYU pile cap experiments.

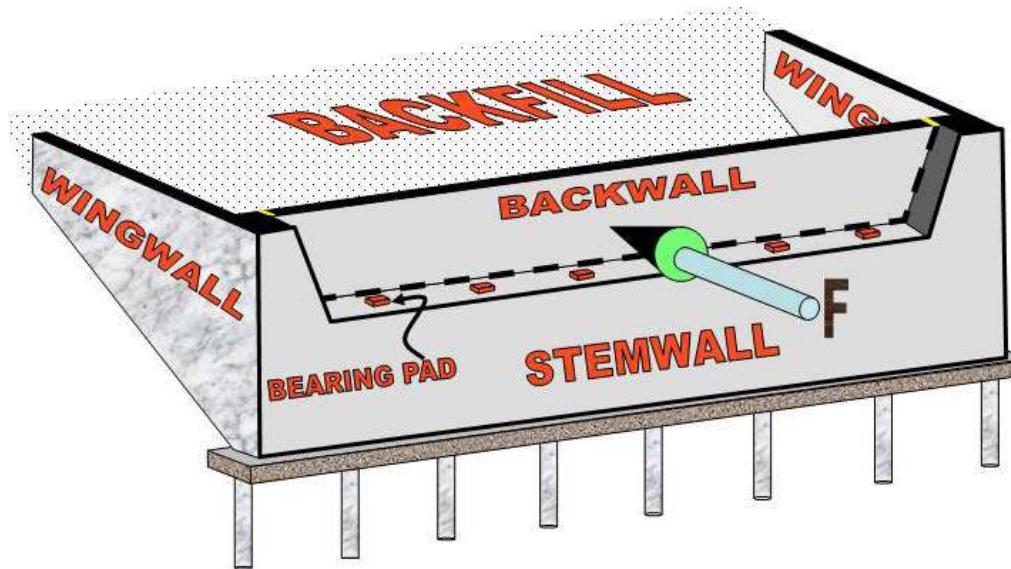
4.6.3 UCLA-CT Full-Scaled Abutment Experiment

A detailed description of the abutment experiment was given in Chapter 3. A brief description of the test related to the analytical model is given herein. As shown in Figure 4.13a, the rigid abutment-backwall was constructed to be 15 feet wide but the backfill was constructed to be 16 feet wide. Figure 4.13b shows a typical seat type bridge abutment, indicating how the bridge may move in the longitudinal direction and collide with the abutment backwall during a seismic event. Per Caltrans Seismic Design Criteria (SDC, 2004), the backwall is designed to break away when the bridge deck jolts against it during a seismic event, pushing the backwall into the backfill and forming a passive wedge between the wingwalls. Therefore, the width of the abutment-backwall was constructed to be less than the width of the backfill to simulate the real seat-type abutment. Figure 4.14a shows the schematics of the abutment field experiment with the three-dimensional mobilized passive wedges bounded by a logarithmic-spiral type failure surface within the abutment backfill in-between the wingwalls.

Figure 4.14b shows observed crack patterns in the brittle gypsum columns within the abutment backfill. The patterns of the cracks developed in the gypsum columns illustrates the development of successive failure surfaces that mobilize as a function of lateral displacement and backfill properties.

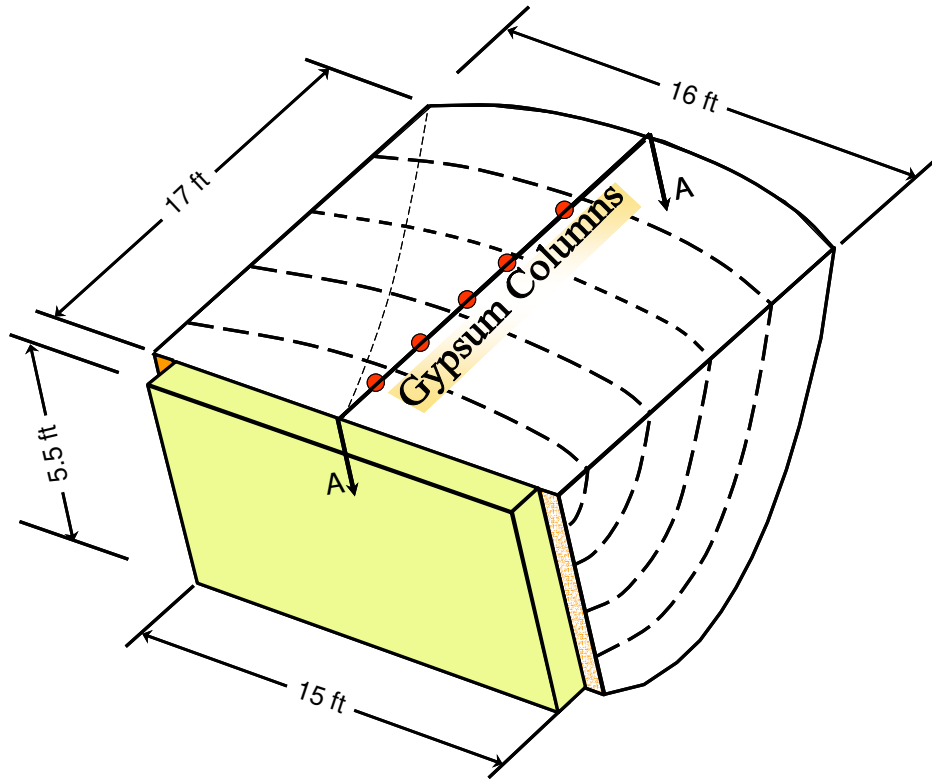


(a) Field Experiment

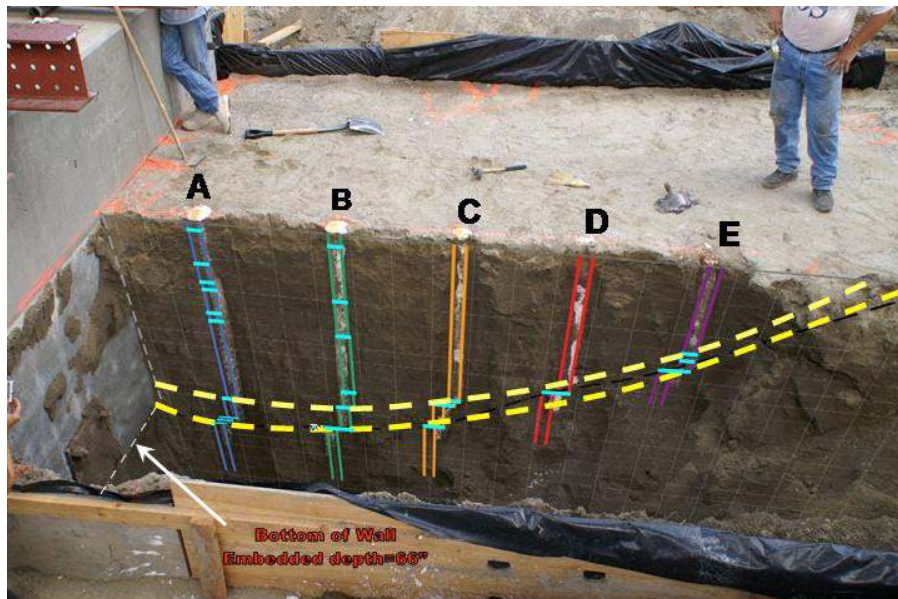


(b) Plunging Action

Figure 4.13: Seat-type Abutment and Foundation System



(a) Schematic of Mobilized Failure Surfaces



(b) Section A-A Mapped Mobilized Final Failure Surface

Figure 4.14: UCLA-CT Full-Scaled Abutment Test with Sandy Backfill

The deformed wedges started to develop within the upper soil layer and progress deeper down and away from the abutment backwall. This failure mechanism was observed using the LSH model and field observation which was described in Chapter 3.

The failure surface started from the bottom of the abutment backwall and extended upward with a log spiral shape intercepting the backfill surface at about 3 times the height of the backwall. The height of the rupture zone of the gypsum columns along the logarithmic failure surface indicates that the final failure was not a distinct line but it manifested a shear band, a zone of intense shearing to form the log spiral failure surface. The numerical simulations and formations of the shear band in geomaterials have been well demonstrated by Bardet (1992) and are beyond the scope of this dissertation.

4.6.4 Selection of Parameters Used in the Finite Element Model

The cyclic triaxial laboratory test was conducted on the remolded samples to obtain the stiffness and strength properties of the abutment backfill as shown in Figure 4.15. The plot of the stress-strain behavior and the associated Mohr circles are shown in Figure 4.16. The backfill strength values and the stiffness parameters obtained from the laboratory test are listed in Table 4.2.

Table 4.2 Input Parameters Used in the UCLA-Caltrans PLAXIS Model

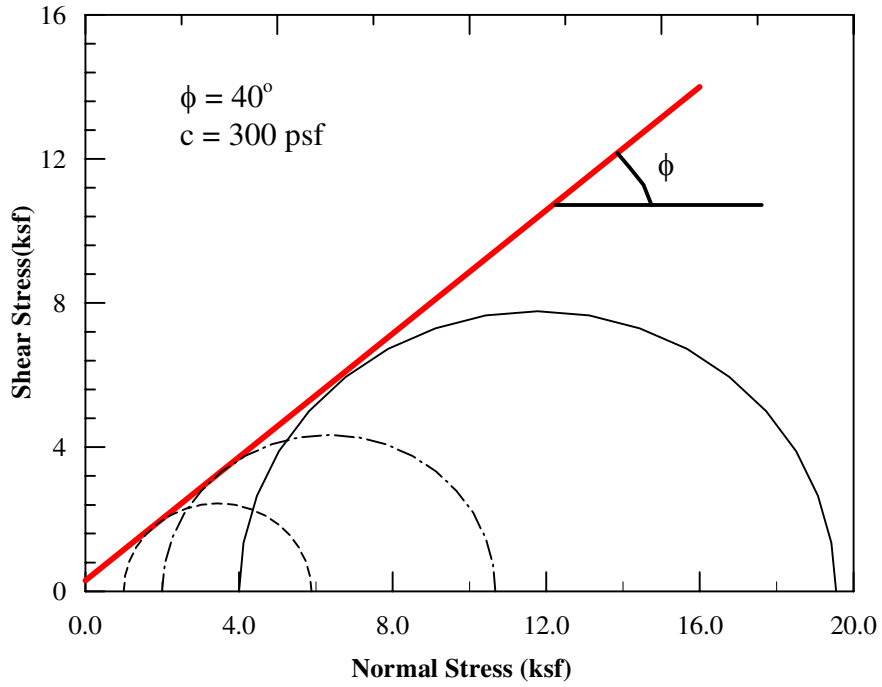
Backfill Type	γ [lb/ft ³]	ϕ Friction	c [psf]	ψ Dilatancy	R_{inter} Wall interface	R_f	E_{50}^{ref} [psf]	E_{ur}^{ref} [psf]
Sand/UCLA	130	40 ⁰	300	0 ⁰	0.70	0.97	1.4E5	2.8E5



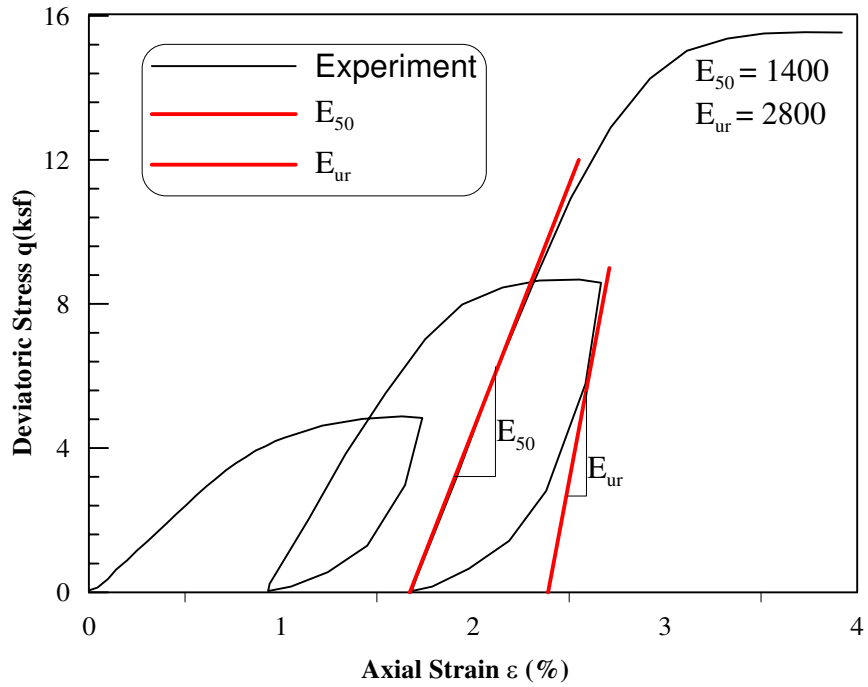
Figure 4.15: UCLA-CT Abutment Backfill Triaxial Test

4.6.5 UCLA 2-D Abutment Finite Element Model

The finite element model used in the simulation of the UCLA-CT abutment experiment is shown in Figure 4.17. The height of the abutment backwall is 5.5 feet. The right vertical boundary of the model was placed a distance of about 28 feet from the face of the backwall and the left vertical is placed about 5 feet from the wall face. The bottom boundary is set about 5.5 feet below the bottom of the backwall. Control horizontal cyclic displacements were applied at the face of the backwall, while displacement of the bottom and vertical boundaries were constrained in both horizontal and vertical directions.



(a) Stress-strain Behavior



(b) Mohr Circles

Figure 4.16: UCLA-CT Triaxial Test of the Abutment Backfill

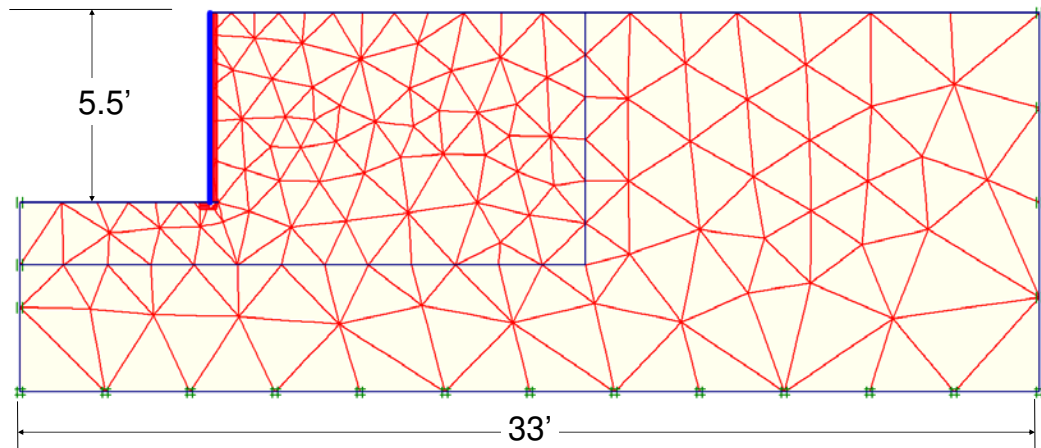


Figure 4.17: Limits of 2-D Finite Element Model

4.6.6 Sequence of the Events in the Model

The analysis was performed in steps to simulate sequence of the real events during the field experiment. The backfill was placed and compacted behind the wall and was extended more than 3 times the abutment wall height behind the backwall laterally. No backfill was placed at the exterior sides of abutment wingwalls. The computations were performed using the following steps:

- (1) Starting with a level ground the initial stresses were calculated.
- (2) Excavation was performed by deactivating 5.5 feet of clusters of elements in the front of the abutment face.
- (3) Both cyclic displacement history and monotonic displacement were applied to the abutment vertical face.

The deformed mesh, displacement vectors and contours of the FE model at the final stage of the backfill failure are shown in Figure 4.18 through Figure 4.20, respectively.

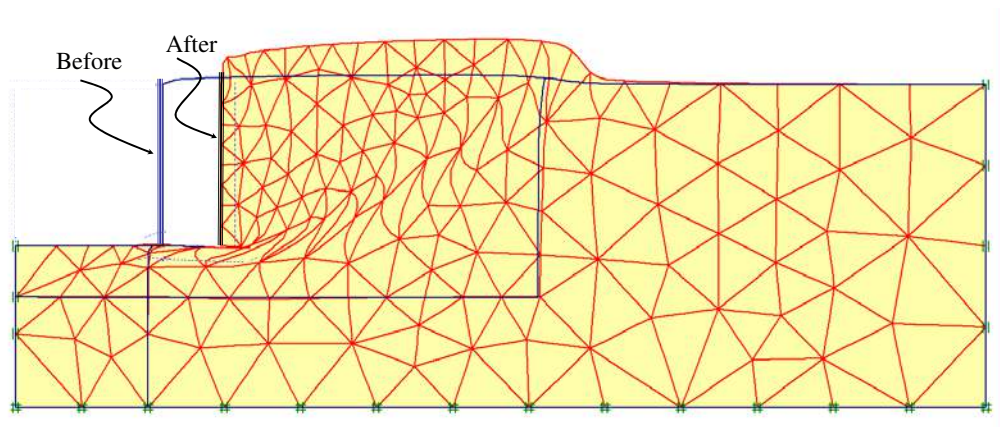


Figure 4.18: 2-D Finite Element Deformed Shape for UCLA Abutment Test

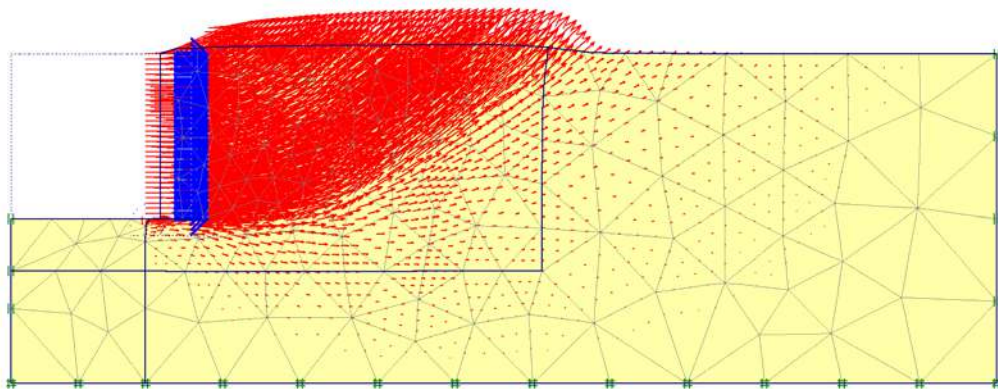


Figure 4.19: 2-D Finite Element Displacement Vectors for UCLA Abutment Test

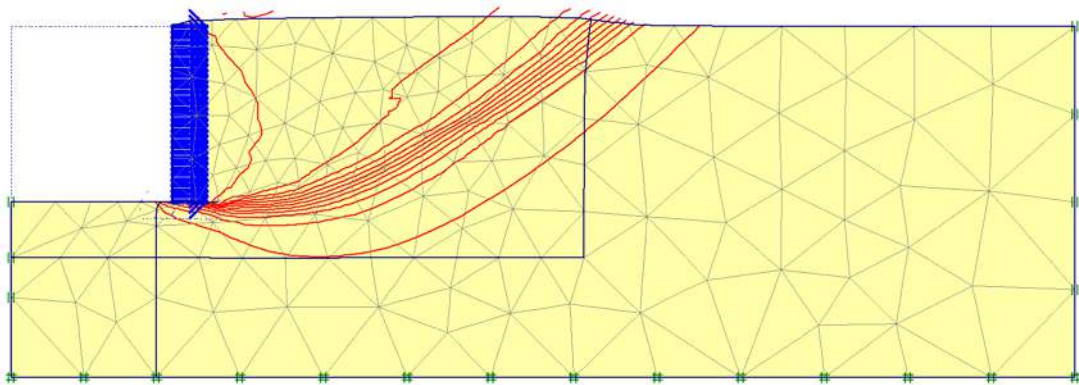


Figure 4.20: 2-D Finite Element Displacement Contours for UCLA Abutment Test

The formation of the plastic points is shown in Figure 4.21. The plastic points are stress points in plastic state, displayed on undeformed model geometry. The plastic points shown by open squares indicate the stresses that lie on the surface of the Coulomb failure envelope within the shear zone. The incremental strain of the backfill shown in Figure 4.22 is also a very good indication of the most critical failure surface and formation of the shear zone. The failure surface predicted by the analytical model remarkably resembles the experimental failure surface which was mapped in the field.

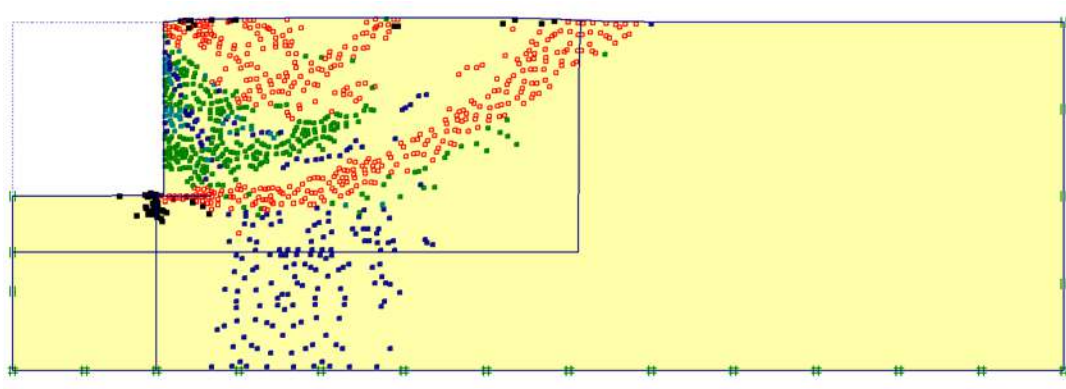


Figure 4.21: 2-D Finite Element Failure Surfaces for UCLA Abutment Test

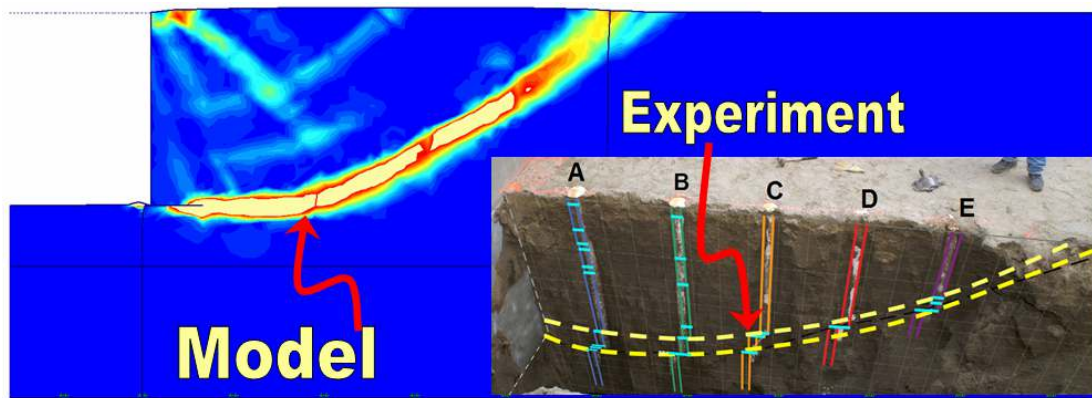


Figure 4.22: 2-D Finite Element Incremental Strains for UCLA Abutment Test

The load-displacement curves predicted by the finite element model applying cyclic displacements and monotonic displacement versus experimental data are shown in Figure 4.23. There is good agreement between the experimental data and the model prediction. The backbone curve predicted by applying monotonic displacement is slightly higher than the backbone curve predicted by the cyclic displacement at higher displacement. For all practical purposes, the difference between the two models is insignificant.

4.7 UCD Abutment Field Experiment

The simulation using the displacement controlled finite element model for the UCD-Caltrans abutment experiment conducted by Maroney et al. (1994) is presented herein. Figure 4.24 illustrates the abutment test setup. This is an example of the monolithic abutment which was described in detail in Chapter 3.

Before the test, 3-inch diameter vertical holes were drilled along the longitudinal centerline of the abutment into the abutment backfill and filled with liquid styrofoam columns as shown in Figure 4.25 and Figure 4.26. After the completion of the test, a longitudinal trench was excavated and the failure mechanism of the backfill was carefully investigated by mapping the deformation of the styrofoam columns. The longitudinal failure features exposed by trenching behind the abutment wall is shown in Figure 4.26. The center of the deformed shape of the styrofoam columns were mapped in the field (Romstad et al., 1995) as shown in Figure 4.26b.

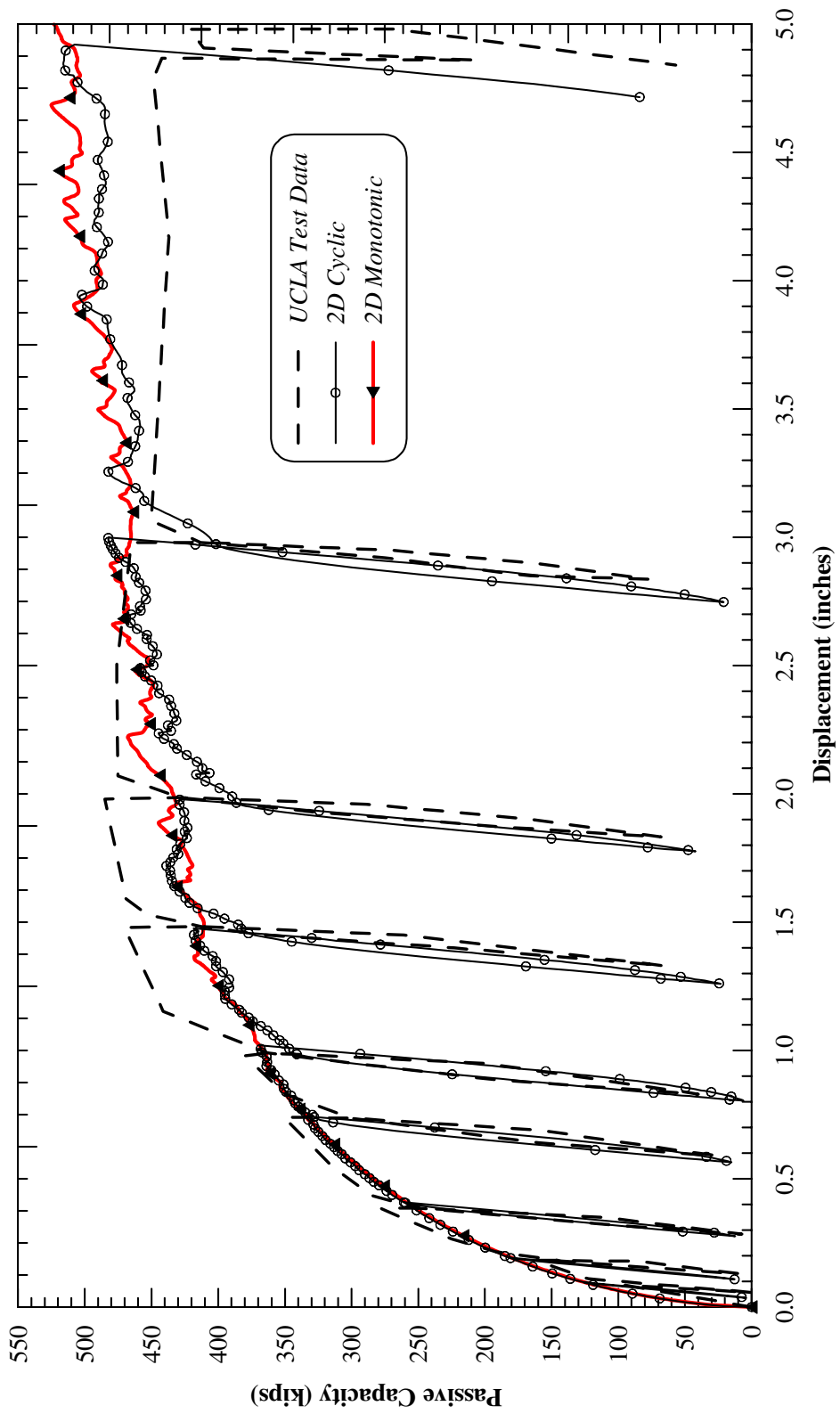


Figure 4.23 : 2-D Cyclic UCLA Abutment Test versus Finite Element Model Predictions



Figure 4.24: UCD Abutment Test Setup

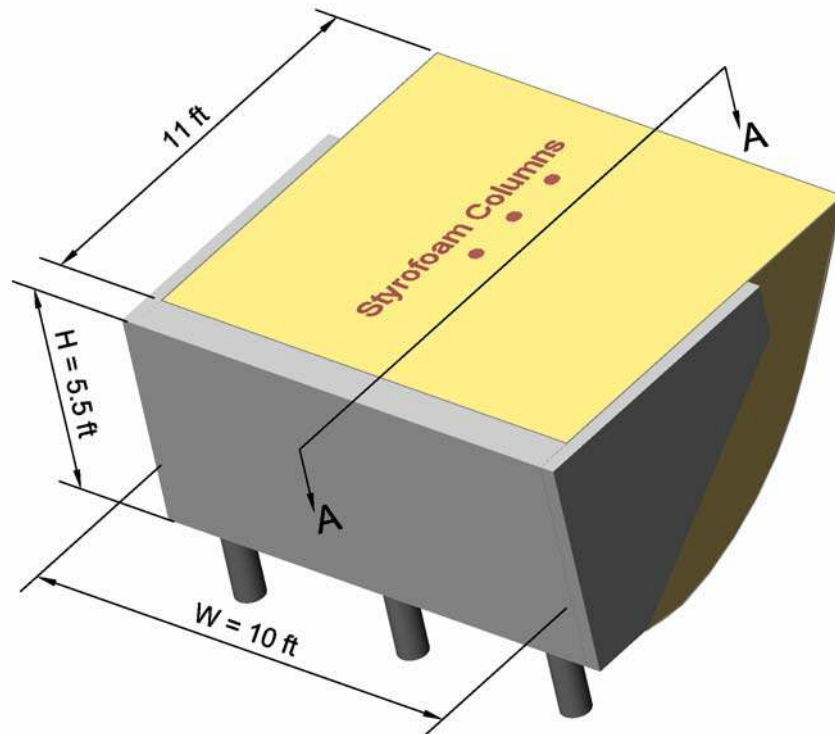
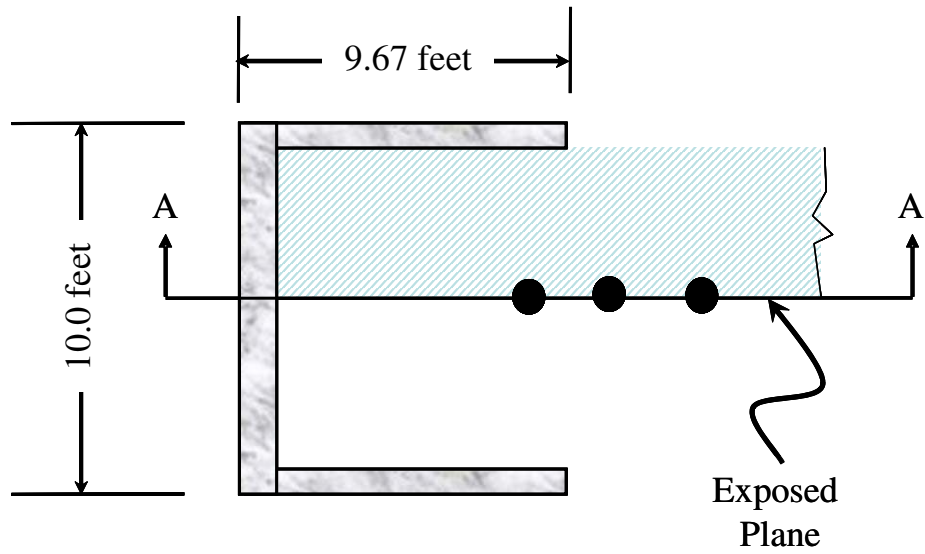
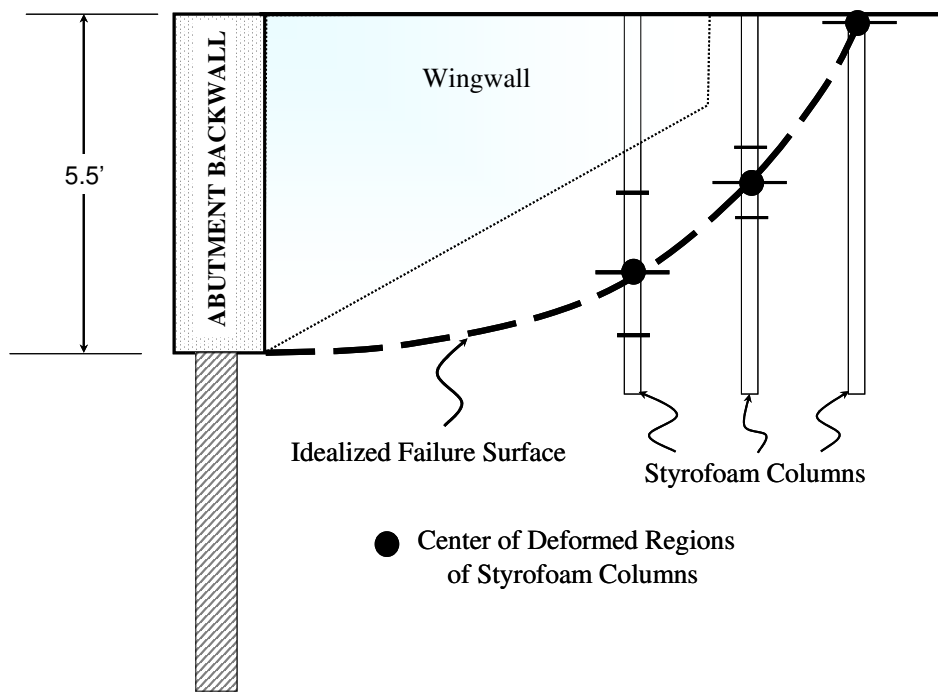


Figure 4.25: UCD 3-D Abutment Field Experiment



(a) Plan



(b) A-A Elevation

Figure 4.26: Failure Mechanism of the UCD Abutment Test

The approximate idealized failure surface is shown through the center of deformed regions of the styrofoam columns. Maroney (1995) reported that the failure surface extended from the bottom of the abutment backwall at initially a zero slope and upward to the embankment surface with increasing slope and intercepting embankment surface at near by twice the height of the backwall.

4.7.1 UCD Abutment 2-D Finite Element Model

The geometry and the boundary conditions of the finite element model used in the simulation is the same as shown in Figure 4.17. The backfill strength values and the stiffness parameters are listed in Table 4.3.

Table 4.3 Input Parameters for UCD PLAXIS Model

Backfill Type	γ (lb/ft ³)	ϕ Friction	c (psf)	ψ Dilatancy	R_{inter} Wall interface	R_f	E_{50}^{ref} (psf)	E_{ur}^{ref} (psf)
Clay/UCD	120	0 ⁰	2000	0 ⁰	0.70	0.95	3.0E5	9.0E5

The deformed mesh of the finite element model at the final stage of the backfill failure is shown in Figure 4.27. The analytical model indicates that the failure surface extended from the bottom of the abutment backwall at initially a zero slope and intersected the abutment backfill at surface near twice the height of the backwall. The displacement vectors of the deformed model and are shown in Figure 4.28. The displacement contours are shown in Figure 4.29. The Mohr-Coulomb failure surface of the model is shown in Figure 4.30 and the incremental strain is shown in Figure 4.31.

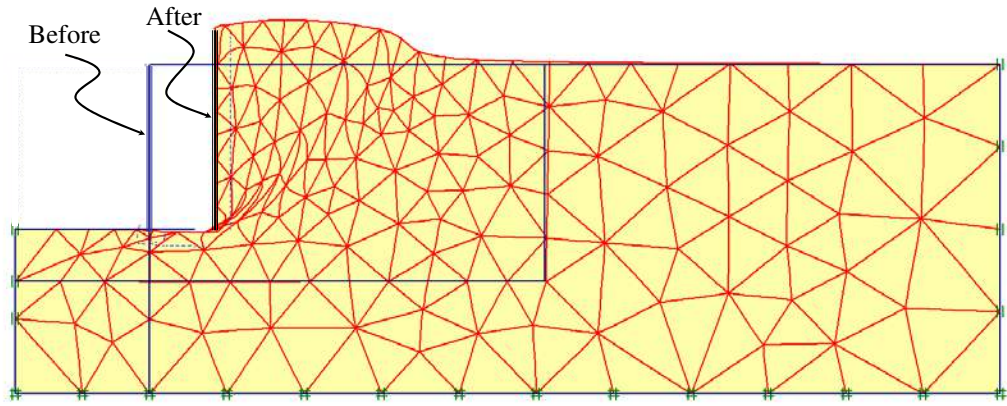


Figure 4.27: 2-D Finite Element Deformed Shape for UCD Abutment Test

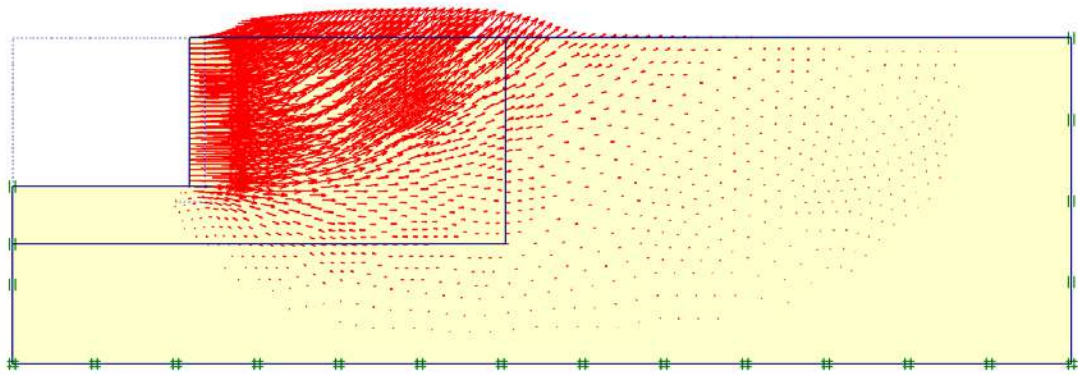


Figure 4.28: 2-D Finite Element Displacement Vectors for UCD Abutment Test

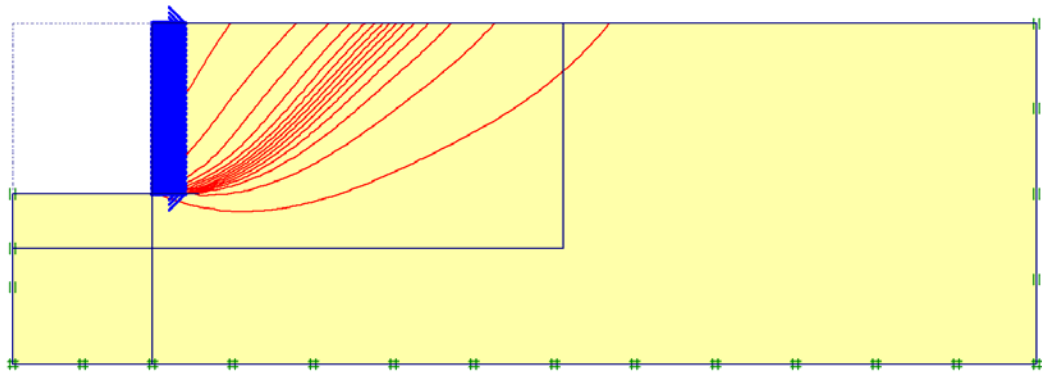


Figure 4.29: 2-D Finite Element Displacement Contours for UCD Abutment Test

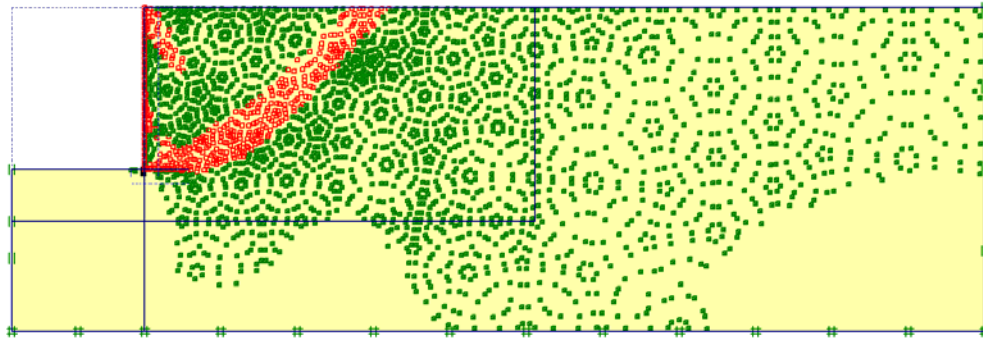


Figure 4.30: 2-D Finite Element Failure Surfaces for UCD Abutment Test

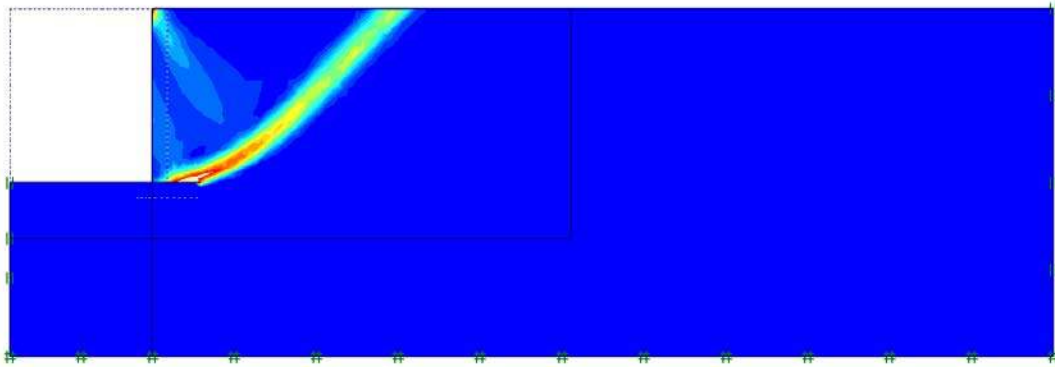


Figure 4.31: 2-D Finite Element Incremental Strains for UCD Abutment Test

The failure mechanism of the backfill is similar to the UCLA experiment which was discussed in the previous section. However, the extent of the failure surface within the backfill is quite different. The UCLA abutment experiment intersected the backfill surface at about three times the height of the backwall due to presence of the cohesionless backfill. As shown in Figure 4.21 and Figure 4.30, it appears that there are more mobilized failure surfaces present in the cohesionless abutment backfill than in the cohesive backfill. The plastic points are mostly concentrated in a single shear zones for the cohesive backfill. The load-displacement curve of the model and the experimental data are shown in Figure 4.32. There is a good agreement between the experimental data and the model prediction.

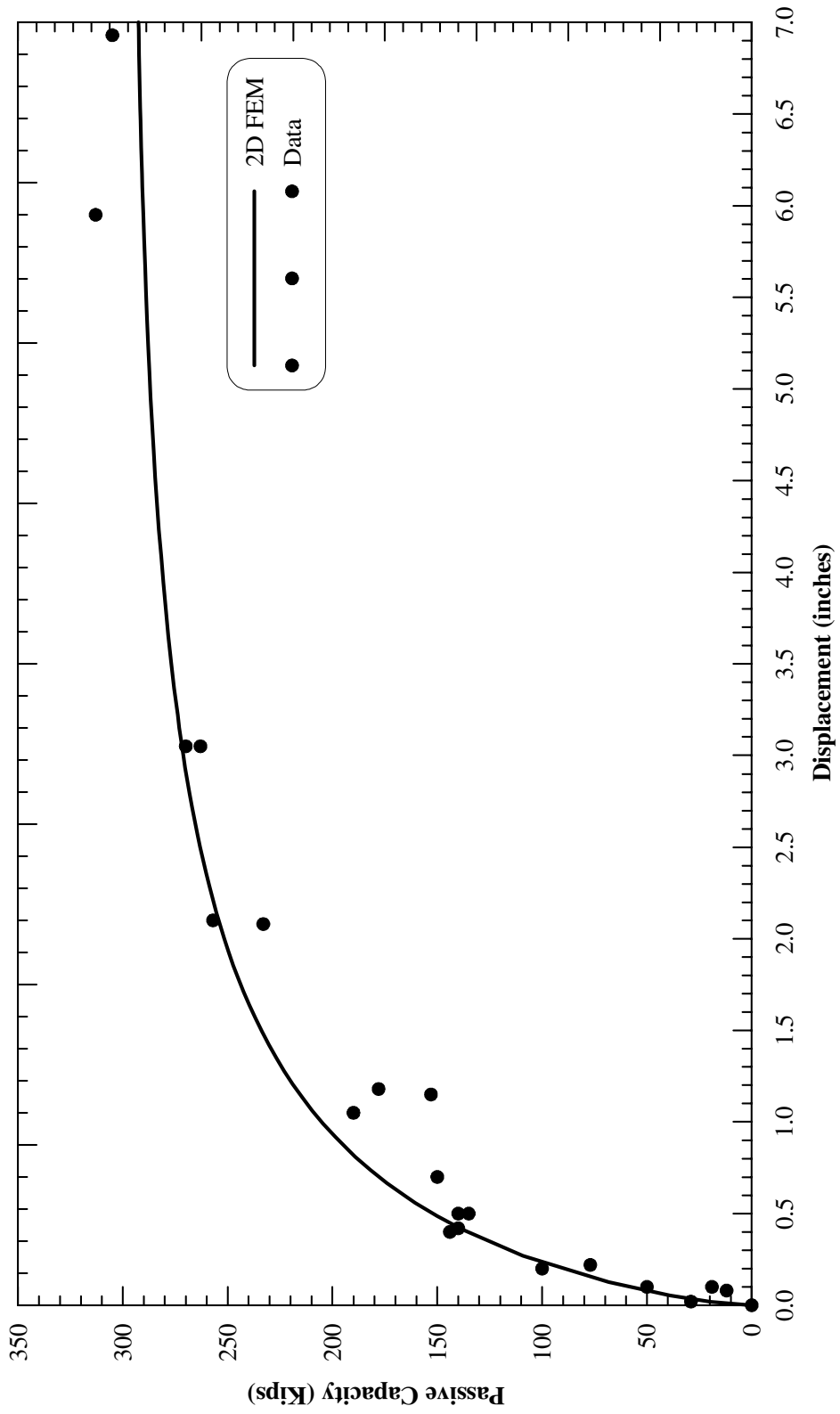


Figure 4.32: UCSD Abutment Test versus Finite Element Model Prediction

4.7.2 BYU Pile Cap Experiments 2-D Finite Element Model

The geometry of all the finite element models for all BYU pile cap experiment are identical. Therefore, only a typical finite element model for one case is presented in this section. The load-displacement curves calculated by LSH, HFD, 2-D and 3-D finite element models for all cases will be presented later in this chapter.

The 2-D finite element model of the BYU pile cap with clean sand backfill is shown in Figure 4.33. The height of the wall is 3.67 feet. The right vertical boundary of the model is place about 20 feet from the wall face and the left vertical is placed about 4 feet from the wall face. The bottom boundary is set about 4 feet below the bottom of the wall. A controlled horizontal displacement was applied at the face of the wall, while the bottom and vertical boundaries were constrained in both horizontal and vertical directions.

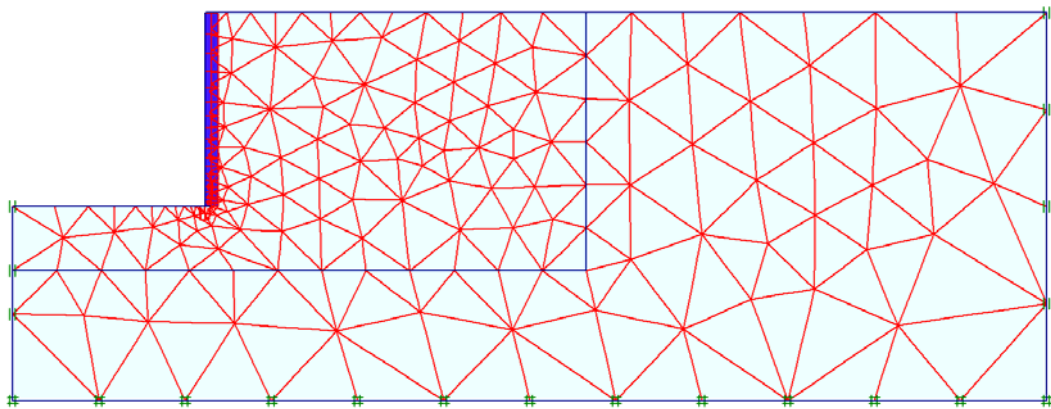


Figure 4.33: Finite Element Model for BYU Clean Sand Backfill

4.7.3 Pile Cap Backfill Parameters

The backfill strength values and the stiffness parameters used for the Hardening Soil model available in PLAXIS are shown in **Table 4.4**. Because the stress-strain measurements for the BYU experiments were not available, the stiffness parameters used in the finite element models for the backfill were back-calculated. It is important to mention that the purpose of the validation was not to obtain a perfect match between the measured structural-backfill force-displacement and the results from the finite element model, but rather to establish a set of reasonable stiffness parameters to be used by the practicing engineers. Perfect match could have been obtained if strength and stiffness variation were utilized for every separate test. The recommended stiffness parameters listed in Table 4.4 provides a good estimate for practicing geotechnical and bridge engineers to develop nonlinear force-displacement relationships of the bridge abutment-backfill using the PLAXIS HS model.

Table 4.4 Input Parameters for BYU Pile Cap Analyses

Backfill Type	γ (lb/ft ³)	ϕ Friction	c (psf)	ψ Dilatancy	R_{inter} Wall interface	R_f	E_{50}^{ref} (psf)	E_{ur}^{ref} (psf)
Clean Sand	117	39°	80	9°	0.70	0.97	2.0E6	4.0E6
Fine Gravel	132	34°	80	4°	0.70	0.97	2.0E6	4.0E6
Coarse Gravel	148	40°	250	10°	0.70	0.97	2.0E6	4.0E6
Silty Sand	122	27°	648	0°	0.70	0.97	1.0E6	2.0E6

The strength parameters used in the Hardening Soil model are identical to the parameters used in the “LSH” model presented in the previous chapter. The Hyperbola cut-off parameter, R_f , was set equal to 0.97. This gives a better match

with the measured nonlinear force-displacement than the default value of 0.90 proposed in the PLAXIS User Manual (2006). The deformed mesh, displacement vector, displacement contours, Mohr-Coulomb plastic points and the incremental strains of the model are shown in Figure 4.34 through Figure 4.38. The Mohr-Coulomb failure surface of the model is also shown in Figure 4.38.

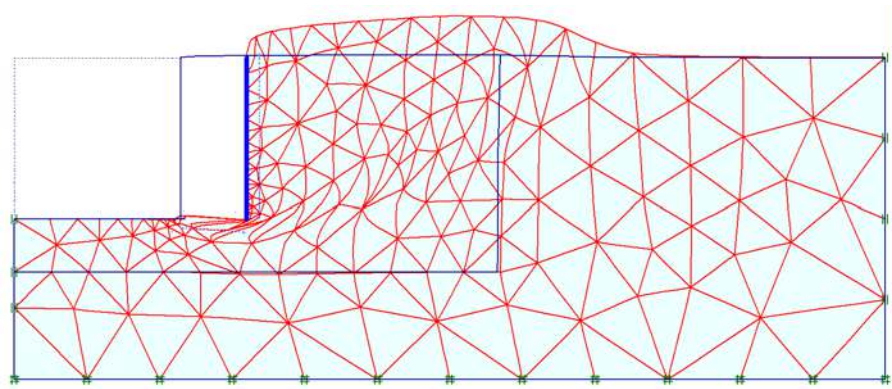


Figure 4.34: 2-D Finite Element Deformed Mesh for BYU Clean Sand Backfill

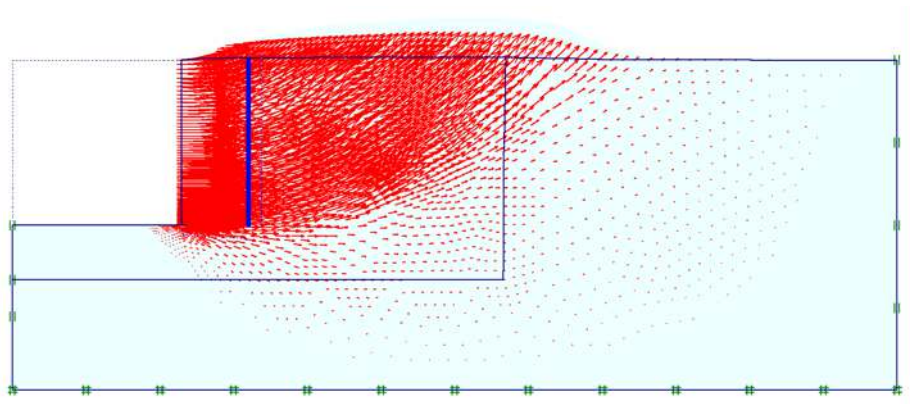


Figure 4.35: 2-D Finite Element Displacement Vector Field for BYU Clean Sand Backfill

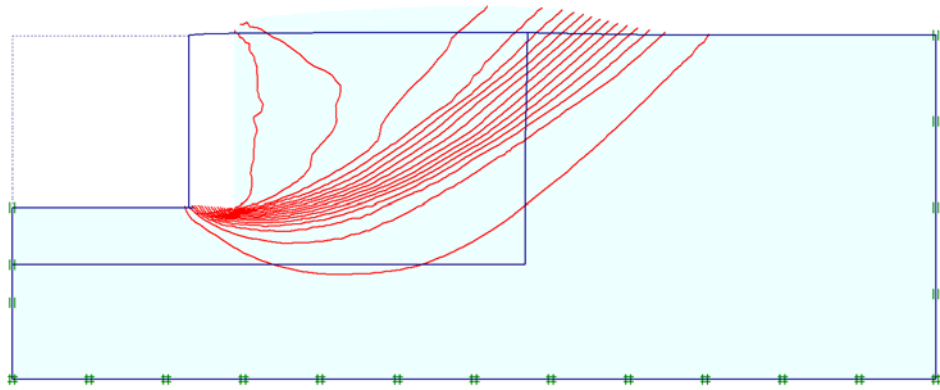


Figure 4.36: 2-D Finite Element Displacement Contours for BYU Clean Sand Backfill

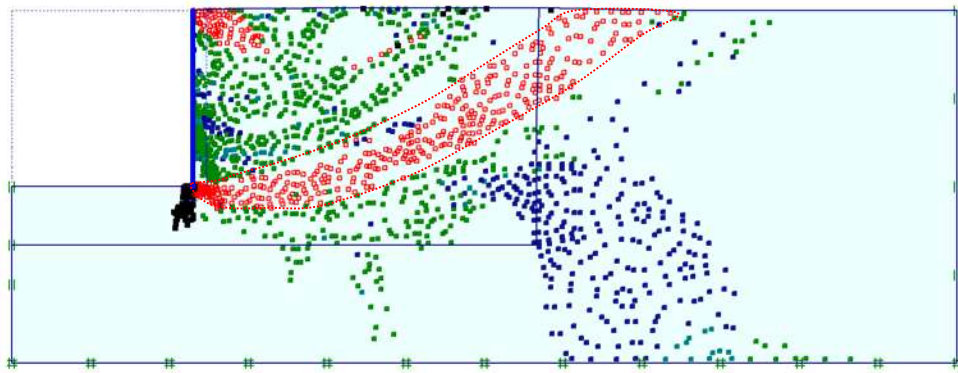


Figure 4.37: 2-D Finite Element Mohr-Coulomb Failure Surface for BYU Clean Sand Backfill

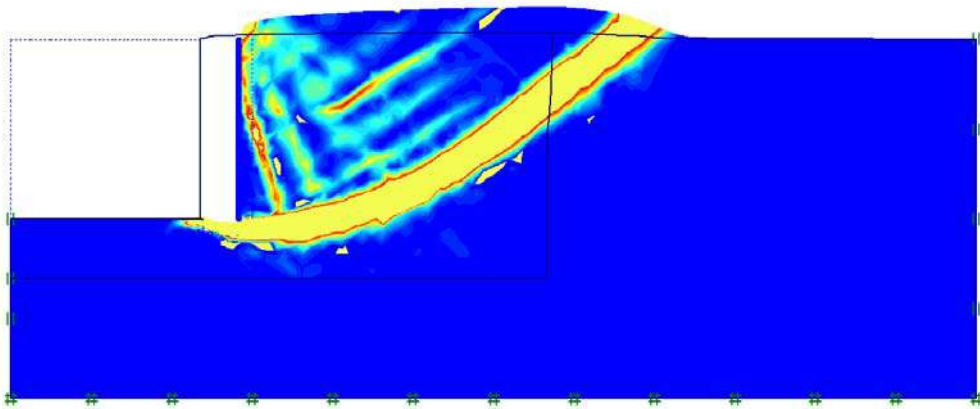


Figure 4.38: 2-D Finite Element Incremental Strains for BYU Clean Sand Backfill

The failure surface remarkably resembles the logarithmic spiral failure surface which was mapped in the field (Rollins et al., 2006). The Mohr-Coulomb plastic points and the incremental shear strain contours illustrating the progressive logarithmic-spiral shear surfaces similar to the LSH model and the experimental data.

As shown in Figure 4.36 through Figure 4.38, the failure surface initiated from the bottom of the abutment backwall at a negative slope. This was referred to as “take off angle” using the LSH model in the previous chapter. The failure surface then extended upward to the backfill free surface with increasing slope, intercepting backfill surface at about three times the height of the backwall similar to the UCLA abutment experiment. The finite element model demonstrates a good match between the simulated deformed shapes of the passive wedges and the slip surfaces mapped in the field (Rollins et al., 2006).

The load-displacement curve of the model and the experimental data are shown in Figure 4.39. The calculated load-displacement curve was multiply by the same adjustment factor explained in the previous chapter to account for the 3-D effect. There is a good agreement between the experimental data and the model prediction only after applying an adjustment factors which were discussed in the previous chapter.

4.8 Backfill Behavior Using 3-D Finite Element Model

In this section, a three-dimensional continuum finite element model is presented to investigate the abutment-backfill behavior. In the previous section, it

was shown that a two-dimensional plane-strain finite element model is capable of modeling the behavior of the bridge abutment. However, a three-dimensional finite element model must be used to simulate the soil-structure behavior of bridge abutments with high skewed angles due to significant out-of-plane rotation during a seismic event since axisymmetric condition does not exist anymore. Using a three-dimensional finite element model, bridge engineers are able to develop nonlinear abutment force-deformation and understand the mechanism of the abutment failure. At the present time, there is no experimental data available for skewed abutments. Therefore, full-three-dimensional finite element models of the abutments and pile cap experiments mentioned in the previous sections are used to calibrate the three-dimensional finite element models for skewed abutments. A realistic bridge abutment with typical bridge abutment backfill is used to examine the mechanism of the skewed-abutment-backfill behavior which will be presented later in this chapter.

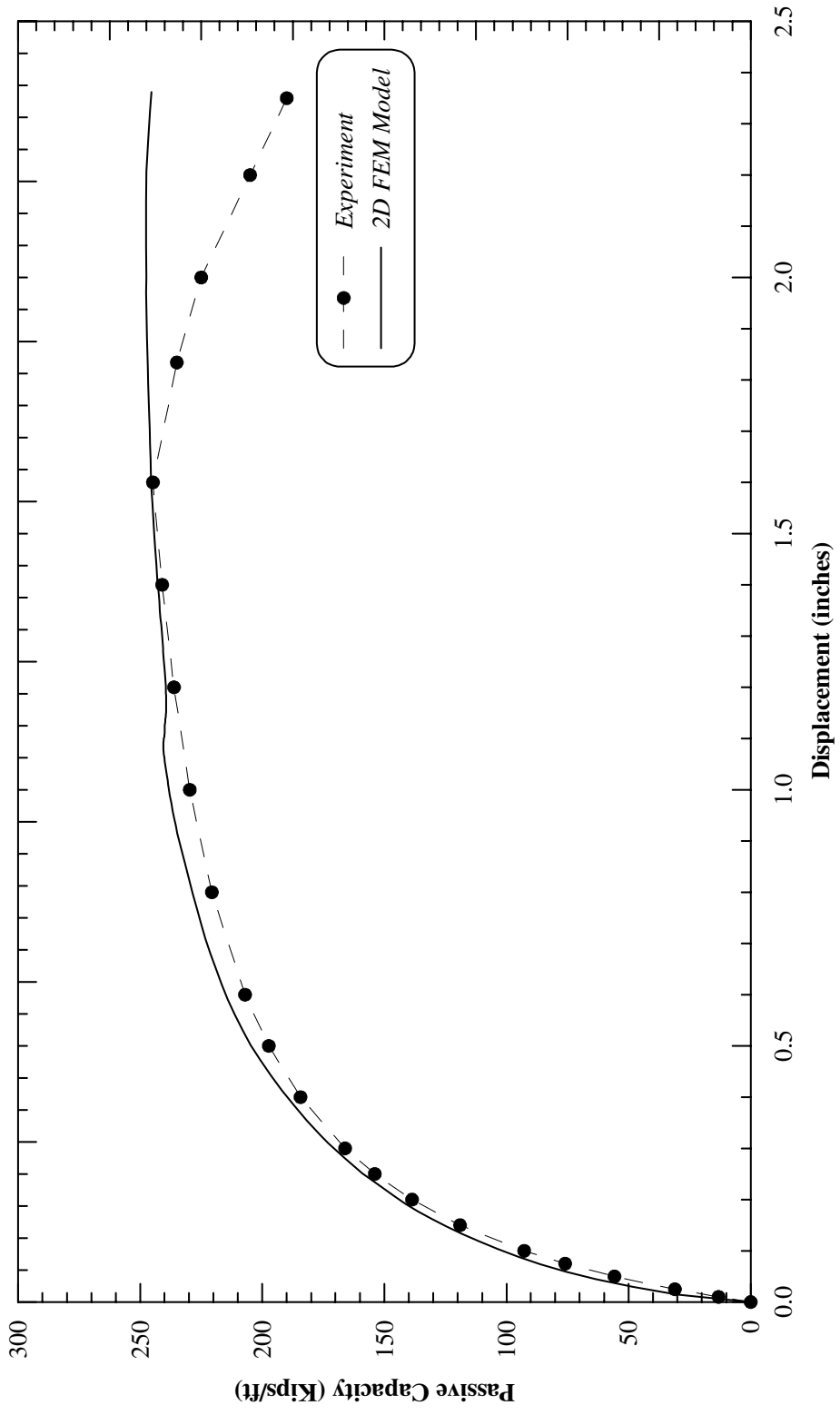


Figure 4.39: BYU Pile Cap Test versus Finite Element Model Prediction For Clean Sand Backfill

4.8.1 3-D Finite Element Simulation of UCLA Abutment Test

Simulation using a full 3-D finite element model for the UCLA Abutment field experiment is presented herein. The abutment backfill is modeled using a 15-node solid element. These elements are composed of 6-node triangular at each face as is shown in Figure 4.40.

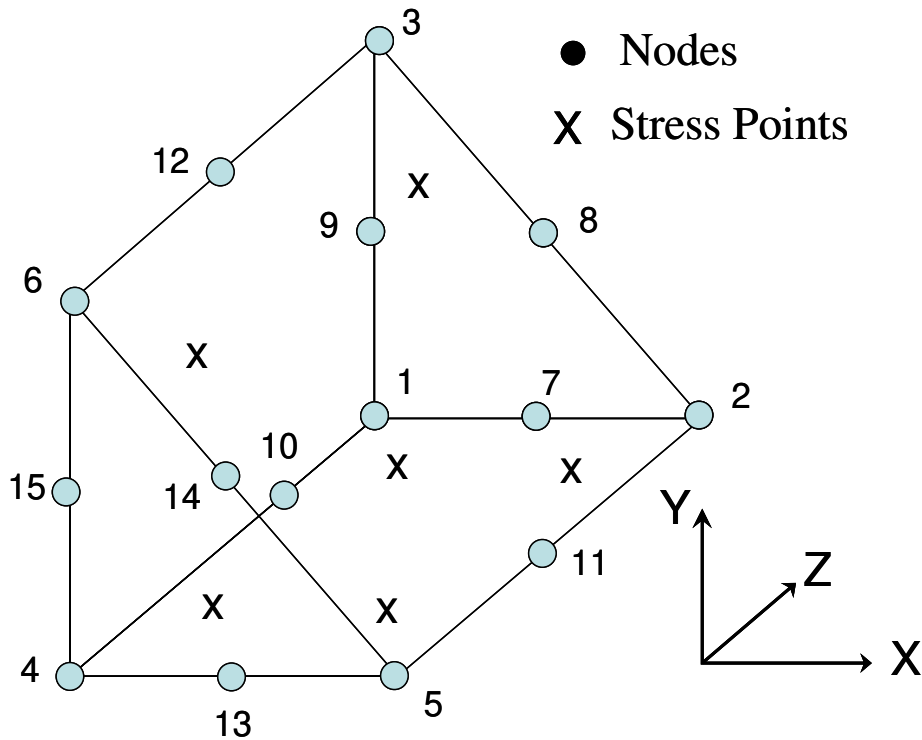
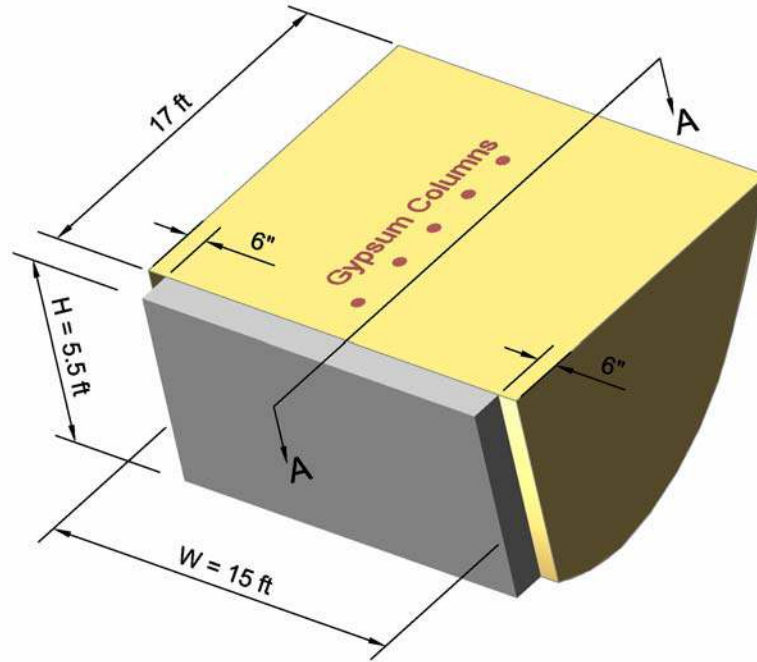


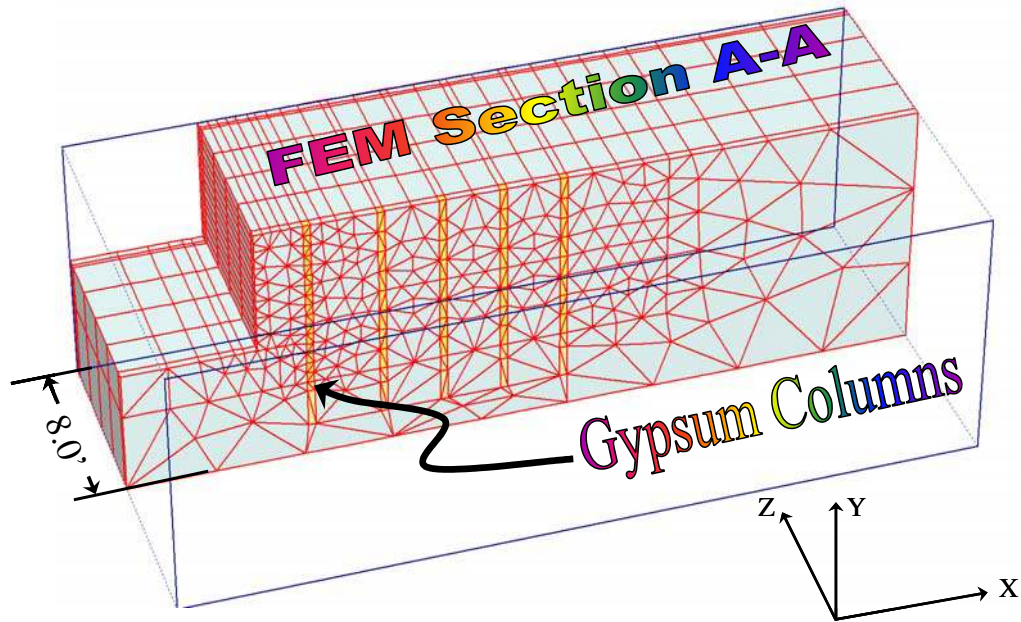
Figure 4.40: 3-D Solid Element

The 3-D passive wedge with gypsum columns and section A-A of the 3-D finite element model are shown in Figure 4.41. Low strength properties were assigned to the gypsum columns. The left, right and bottom boundaries of the 3-D finite element model are the same as the 2-D model. The 2-D finite element model

was extruded 16 feet in the z direction. The constitutive Hardening Soil (HS) model was used to simulate the abutment-backfill stress-strain behavior.



(a) Schematic of UCLA 3D Abutment Passive Wedge Formation



(b) Section A-A of the Backfill

Figure 4.41: Section Through the Full 3-D Finite Element Model of the UCLA Abutment Experiment

4.8.2 Testing Sequence

Similar to the 2-D analysis, the analysis was performed in steps to simulate the sequence of actual events that occurred during the field experiments.

The width of the abutment backwall was set to be 15 feet and the backfill width was set to 16 feet to simulate the field experiment and the backfill behind the shear keys in the longitudinal direction. A uniform displacement of 3.5 inches was applied only to the 15 feet of abutment-backfill. Zero displacement was applied to the remaining 6-inch of backfill at each side of the backwall as shown in Figure 4.42 and Figure 4.43. The computations were performed using the following steps:

- (1) Starting with a level ground, the initial stresses were calculated.
- (2) Excavation was performed by deactivating entire 16 feet of clusters of elements in the front of the abutment face.
- (3) A 3.5 inches of monotonic uniform horizontal displacement was applied at the 5.5-foot by 15-foot of vertical abutment-backfill.
- (4) Zero displacement was applied at the vertical backfill face at each side of the abutment-backwall as shown in Figure 4.43 and Figure 4.44.

The deformed mesh, displacement vector, displacement contours, Mohr-Coulomb plastic points and the incremental strains of the model are shown in Figure 4.43 through Figure 4.47. The calculated force-displacement relationship of the 3-D finite element model is shown in Figure 4.48. The results are very close to the 2-D finite element model shown in Figure 4.23 and the LSH model presented in the previous

chapter, demonstrating that the force-displacement relationship of the bridge abutment can be simulated using a simple 2-D plane-strain analysis.

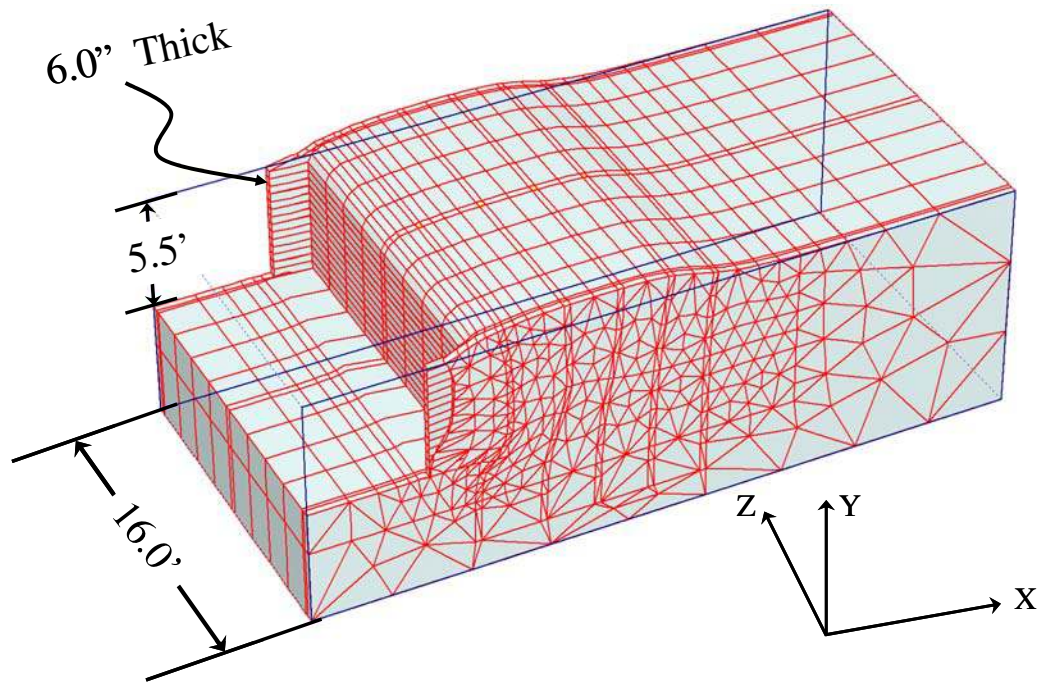


Figure 4.42: Full 3-D Finite Element Model of the Deformed Shape for UCLA Abutment Experiment

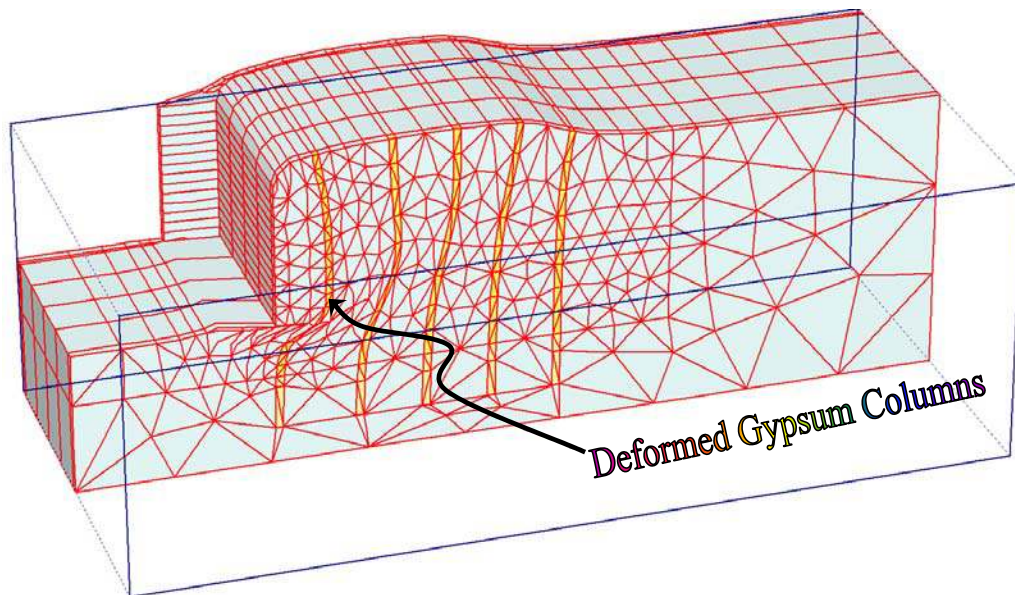


Figure 4.43: Section Through Gypsum Columns for the Full 3-D Finite Element Model for UCLA Abutment Experiment

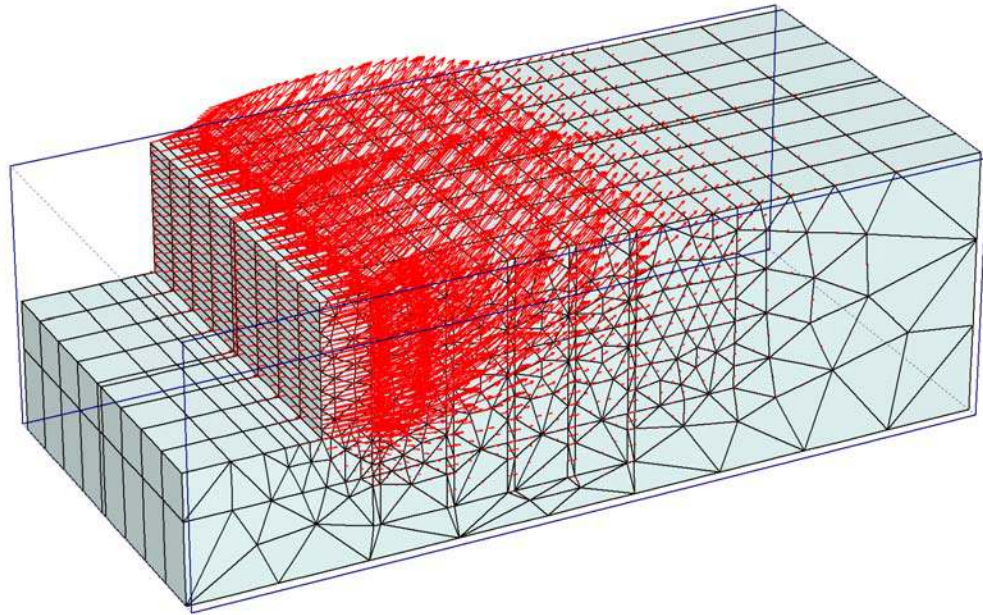


Figure 4.44: Full 3-D Finite Element Model of the Displacement Vectors for UCLA Abutment Experiment

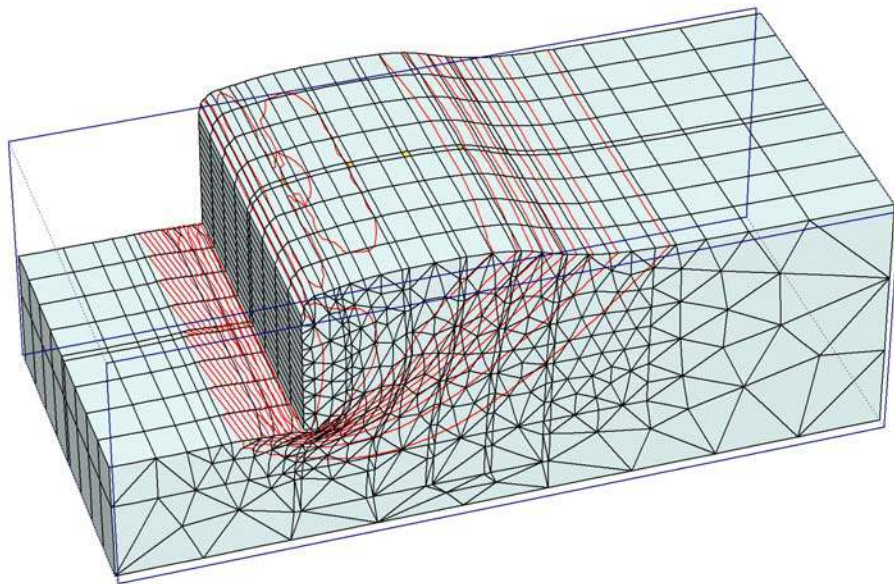


Figure 4.45: Full 3-D Finite Element Model of the Displacement Contours of UCLA Abutment Experiment

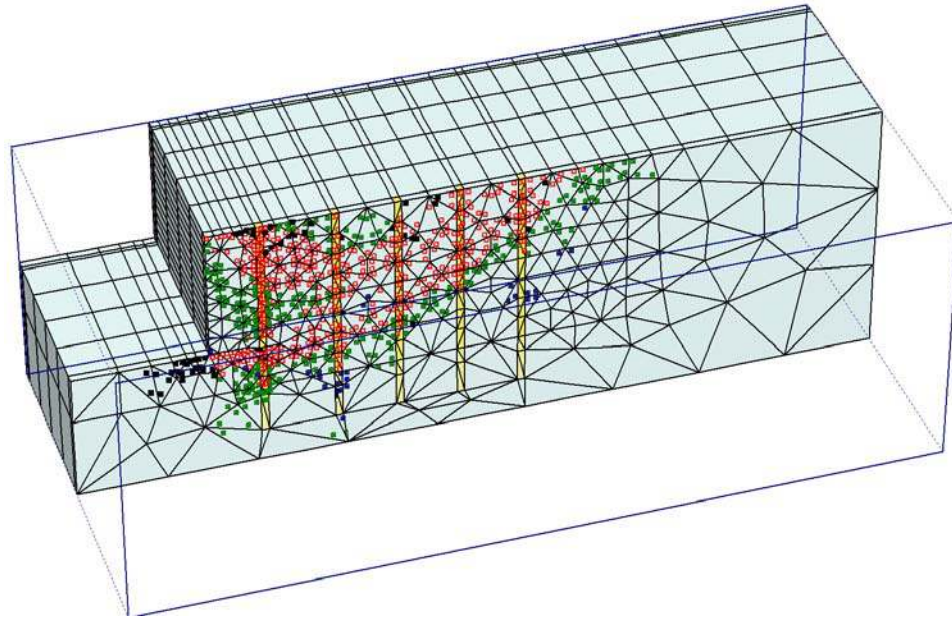


Figure 4.46: Full 3-D Finite Element Model of the Plastic Points Through Gypsum Columns for UCLA Abutment Experiment

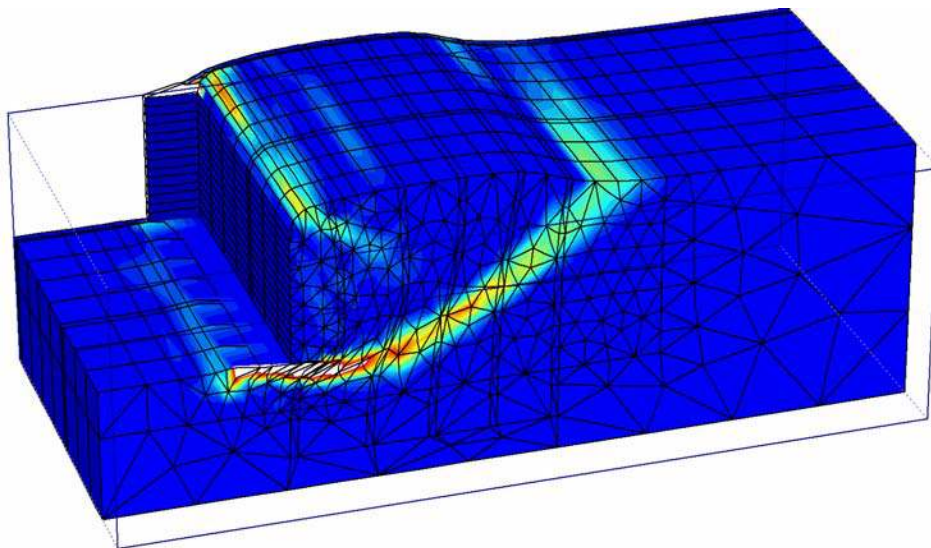


Figure 4.47: Full 3-D Finite Element Model of the Incremental Strains Through Gypsum Columns for UCLA Abutment Experiment

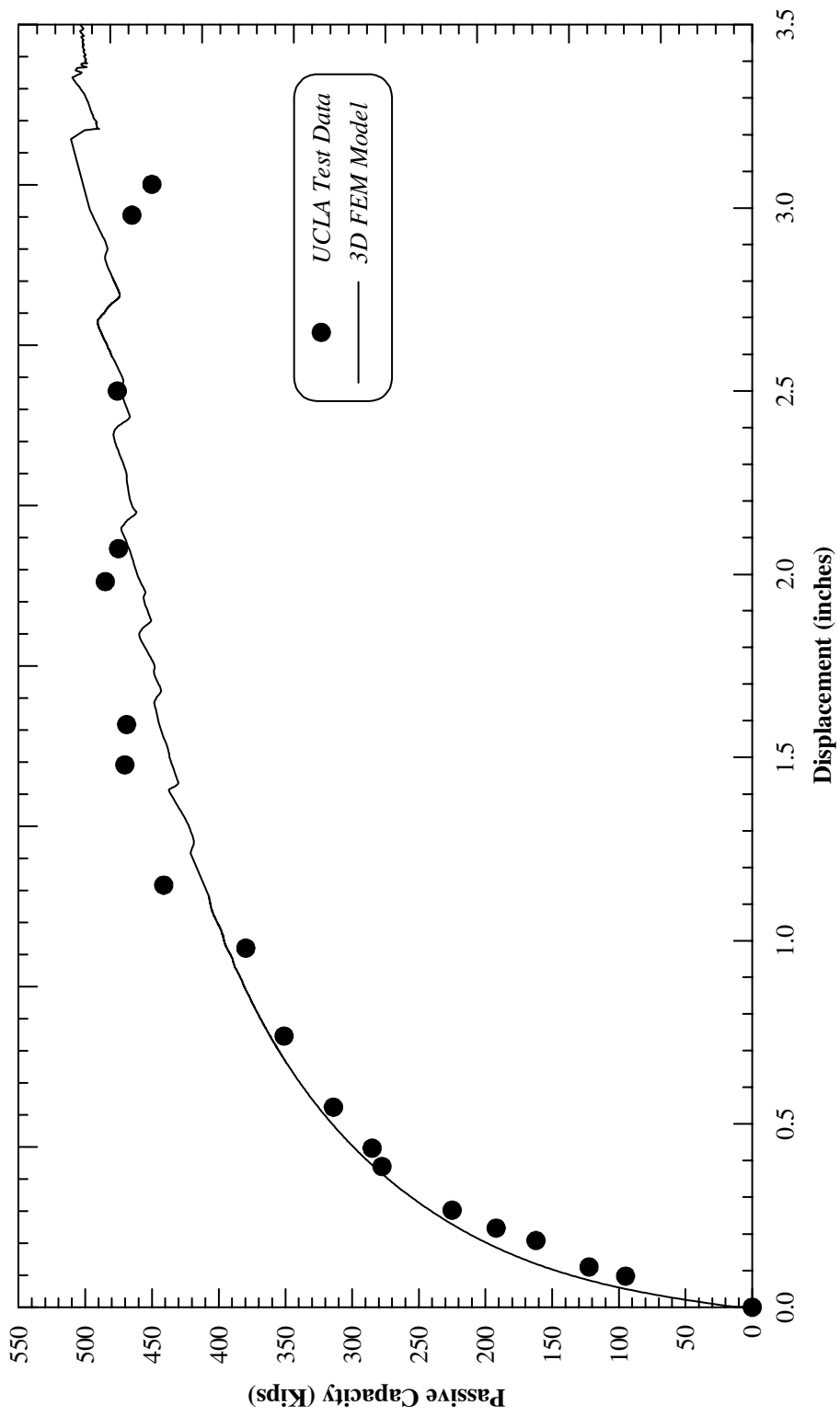


Figure 4.48.: Measured Experimental Data Versus Finite Element Prediction for UCLA Abutment Experiment

4.9 3-D Finite Element Simulation of UCD Abutment Test

Full 3-D finite element model simulation for the UCD Abutment field experiment is presented herein. The dimensions and 3-D deformed mesh of the finite element model is shown in Figure 4.49. The left, right and bottom boundaries of the 3-D finite element model are the same as the 2-D model. The 2-D finite element model was extruded 10 feet in the z direction. The constitutive Hardening Soil (HS) model was used to model the nonlinear abutment backfill behavior.

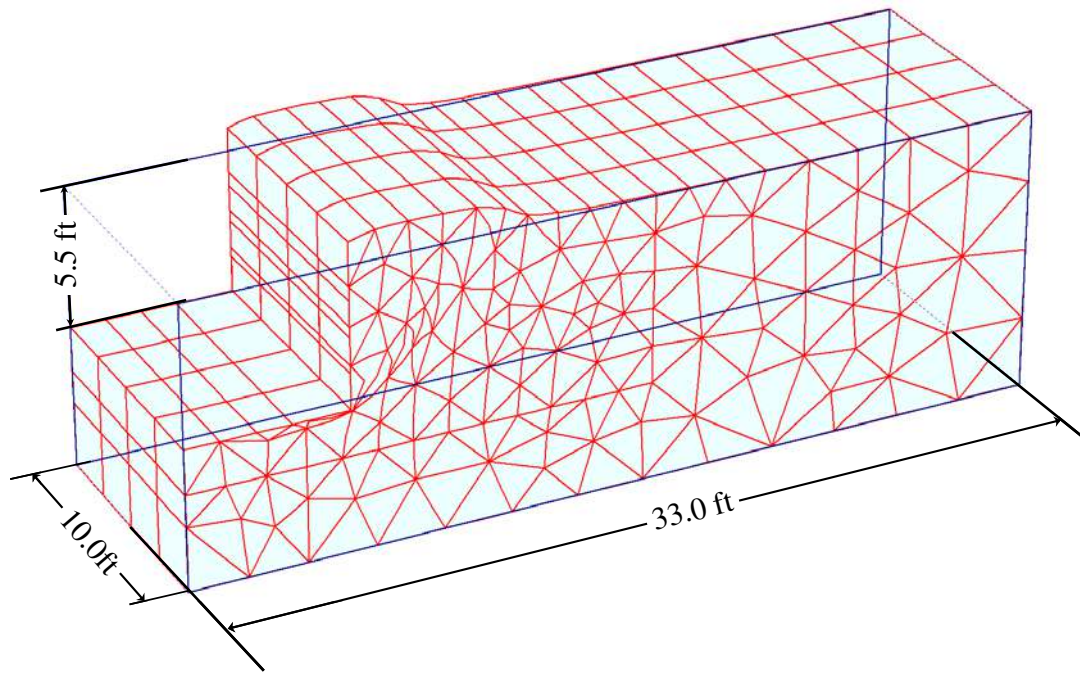


Figure 4.49: Finite Element Model of the of the Deformed Shape for UCD Abutment Experiment

4.9.1 Sequence of the Events

The analysis was performed in steps to simulate sequence of the real events during the field experiments, where the backfill was placed and compacted behind

the wall and was extended some distance behind the back wall laterally. The width of the backfill and the abutment wall were identical, therefore there was no 3-D effect. The computations were performed using the following steps:

- (1) Starting with a level ground the initial stresses were calculated.
- (2) Excavation was performed by deactivating clusters of elements in the front of the abutment face.
- (3) The entire 5.5 feet of vertical abutment face was pushed up to backfill failure using a uniform displacement.

The deformed mesh, displacement vector and contours, Mohr-Coulomb plastic points and the incremental strains of the model are shown in Figure 4.49 through Figure 4.53. The three-dimensional finite element analysis also indicates that the failure surface does not extend more than twice the height of the backwall.

The calculated force-displacement relationship predicted by the model is shown in Figure 4.54. There is a good agreement between the experimental data and the model prediction. The results are very close to the 2-D finite element model and the LSH model. This shows that the force-displacement relationship of the bridge abutment can be simulated using a simple 2-D plane strain analysis.

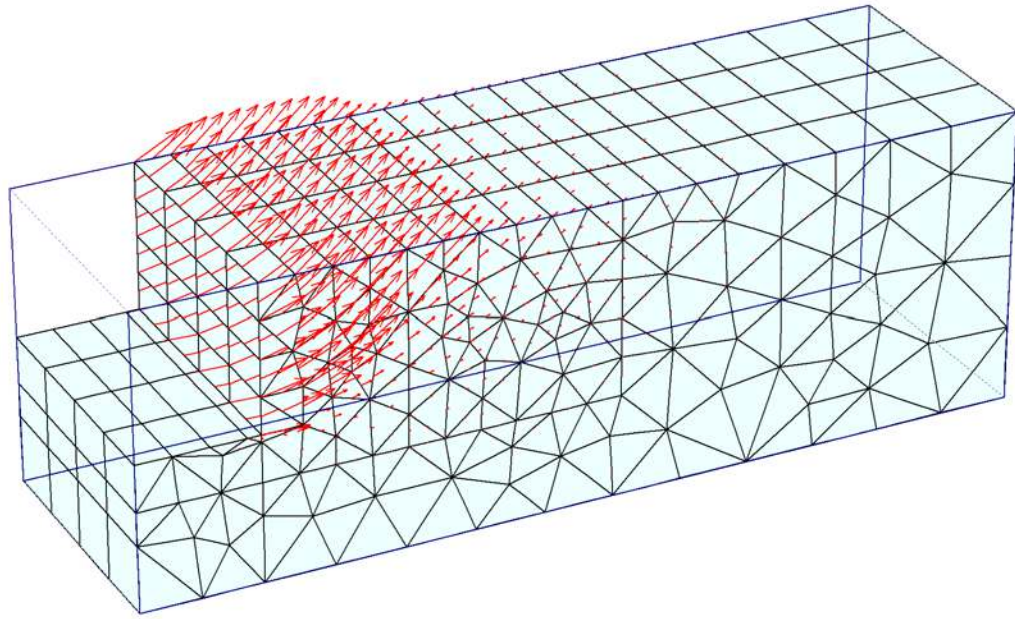


Figure 4.50: Full 3-D Finite Element Model of the Displacement Vectors for UCD Abutment Experiment

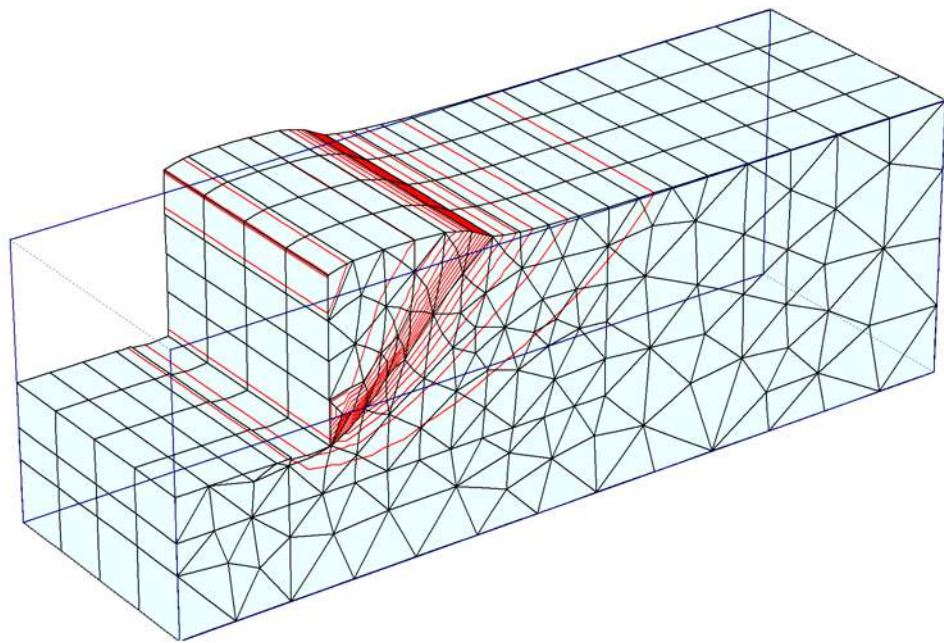


Figure 4.51: Full 3-D Finite Element Model of the Displacement Contours for the UCD Abutment Experiment

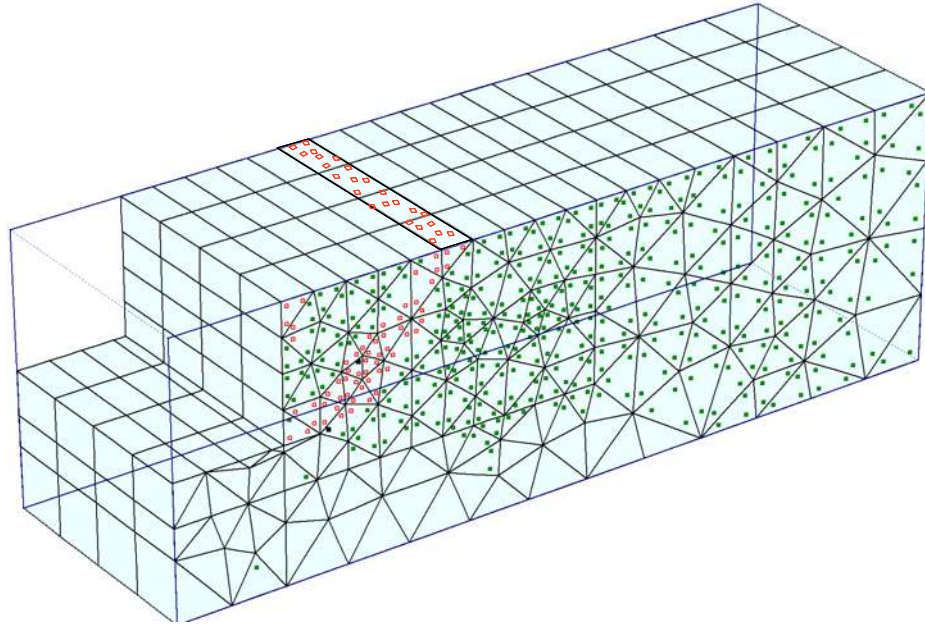


Figure 4.52: Full 3-D Finite Element Model of Mohr-Coulomb Plastic Points for UCD Abutment Experiment

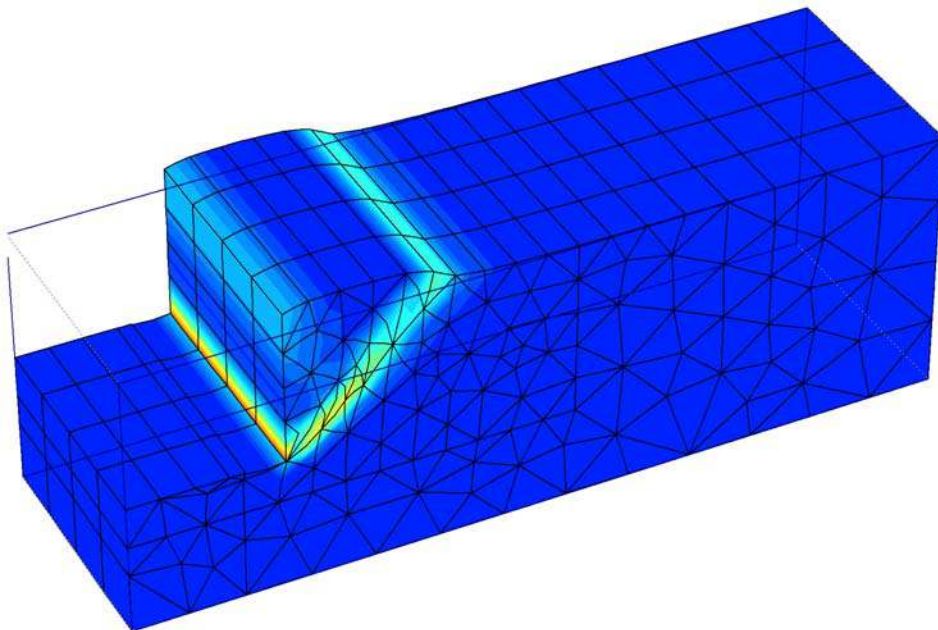


Figure 4.53: Full 3-D Finite Element Model of the Incremental Strains for UCD Abutment Experiment

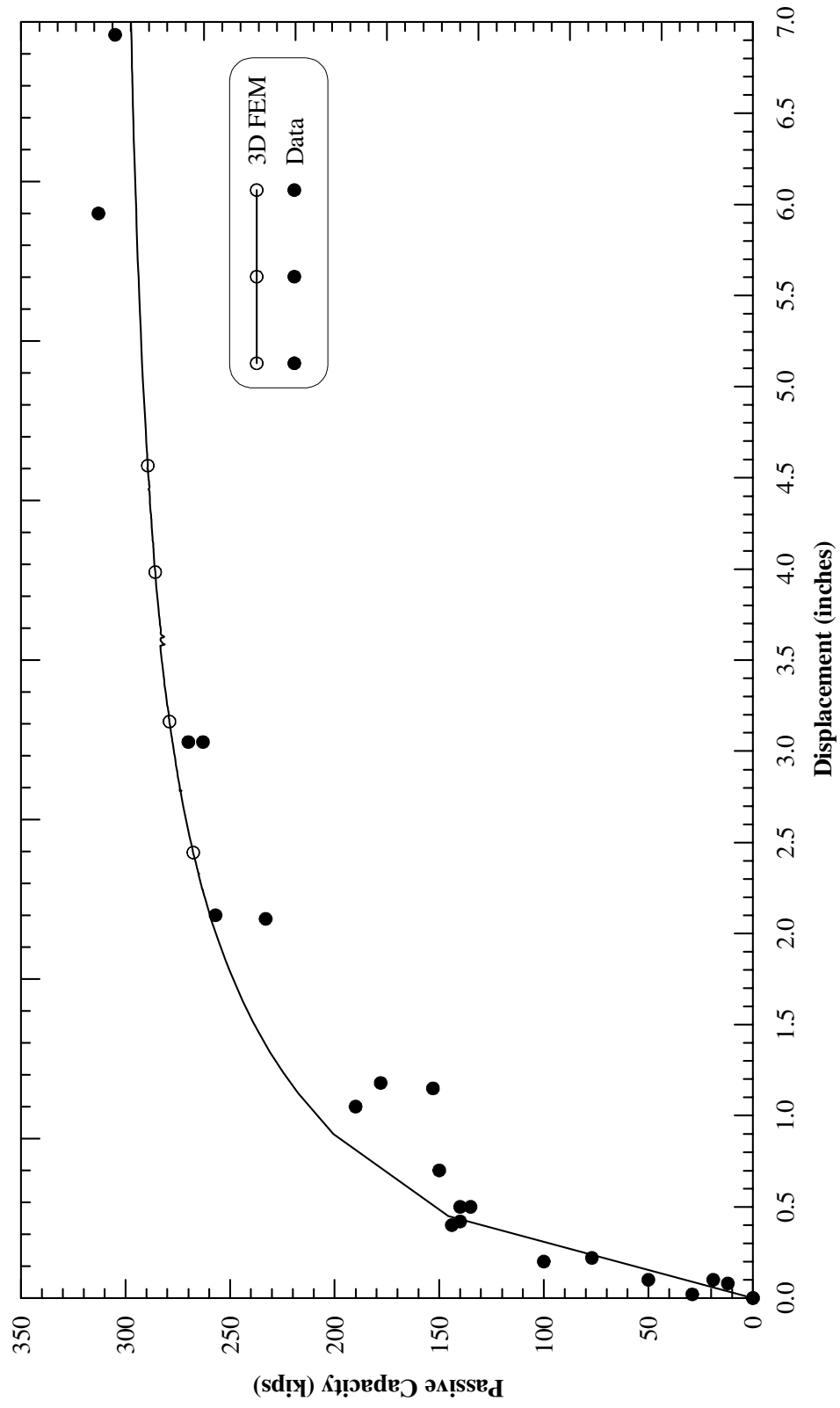


Figure 4.54: Measured Experimental Data Versus Finite Element Prediction for UCD Abutment Experiment

4.10 3-D Finite Element Simulation of BYU Pile Cap Experiments

The pile cap experiments conducted by Kyle et al. (2006) were described in the previous chapter. Cracking pattern of the pile cap backfill for each experiment was measured. The surface cracking for all experiments were extended beyond the edges of the pile caps in the longitudinal as well as transverse direction. Figure 4.55 shows the schematics of a typical BYU pile cap field experiment with the three-dimensional passive wedges bounded by a logarithmic-spiral type failure surface, based on field measurements of observed cracking patterns and wedge deformations by Rollins and Cole (2006).

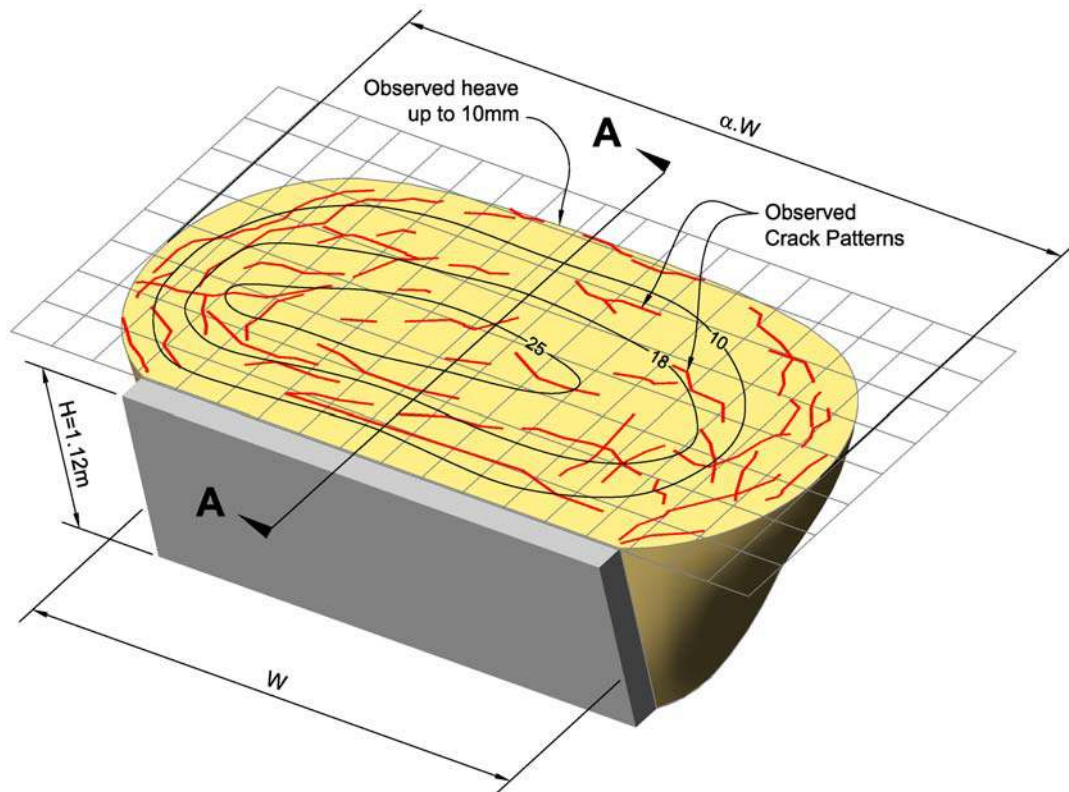


Figure 4.55: Schematic of a Typical 3-D Wedge Failures and Cracking Patterns of BYU Pile Cap Experiments

The 3-D finite element model simulations were performed using both full-wall-width model and half-wall-width model due to symmetry of the problem as shown in Figure 4.56 and Figure 4.57. The deformed finite element mesh of the full model with displacement contours is also shown in Figure 4.57 to illustrate the capability of the model and to examine the mechanism of the failure mode. The backfill material was extended 11.5 feet in the lateral directions at each side of the wall to account for the three-dimensional effect of the backfill. A 2.5-inch uniform monotonic displacement was applied at across the wall (3.67 feet by 17 feet). A zero displacement was applied at the vertical face of the soil each side of the wall (3.67 feet' by 11.5 feet).

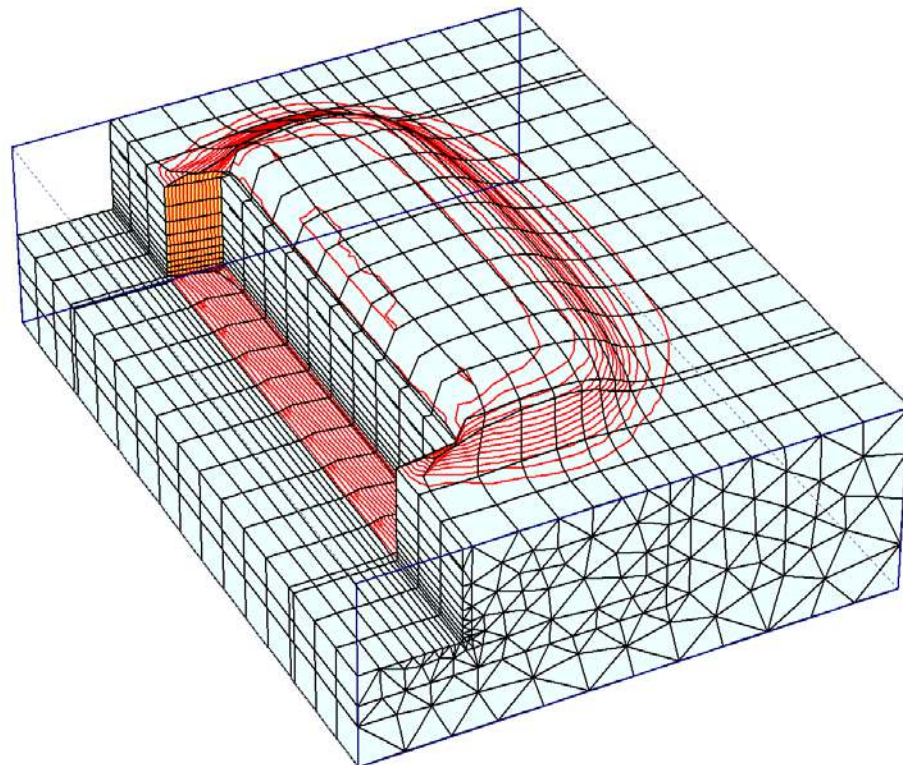


Figure 4.56: Full 3-D Finite Element Model Displacement Contours of BYU Pile Cap Experiment

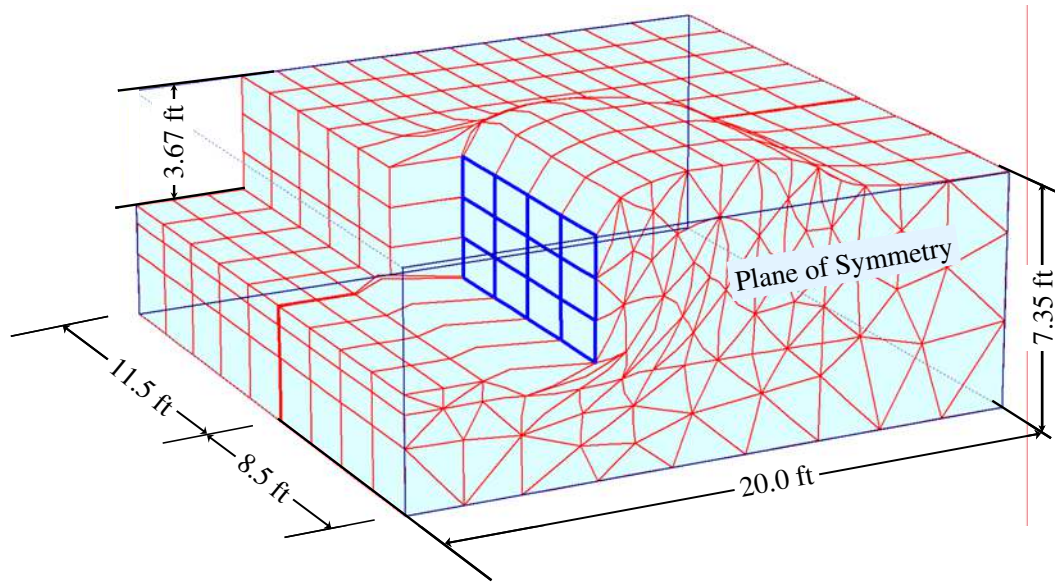


Figure 4.57: 3-D Finite Element Using Half Model of BYU Pile Cap Experiment

The testing sequence for the analytical model will be presented in Section 4.10.2. Since the full three-dimensional finite element model is relatively large and computationally expensive, only half models were developed for all BYU pile cap experiments. The result of the half models and the full models were identical. The three-dimensional finite element model demonstrates a good match between the simulated deformed shapes of the passive wedges and the slip surfaces mapped in the field (Rollins et al., 2006).

4.10.1 3-D Finite Element Simulations Using Half Model

The 3-D finite element model simulations were performed using half-wall-width model due to symmetry of the problem as shown in Figure 4.57. The constitutive Hardening Soil (HS) model was used to simulate the nonlinear pile cap backfill stress-strain behavior.

4.10.2 Testing Sequence

The analysis was performed in steps to simulate sequence of actual events during the field experiments, where the backfill was placed and compacted behind the pile cap and was extended some distance behind the pile cap laterally. No backfill was placed at the sides of the pile cap, therefore the simulations were performed only with a vertical face of the backfill. The 2-D finite element model was extruded in the z direction as shown in Figure 4.57. The computations were performed using the following steps:

- (1) Starting with a level ground the initial stresses were calculated.
- (2) Excavation was performed by deactivating clusters of elements in the entire front face of the pile cap and the vertical face in the lateral direction.
- (3) A 2.5-inch uniform displacement was applied to the 8.5 feet of the pile cap. A zero displacement was applied to the remaining 11.5 feet of the model shown in Figure 4.57.

The extent of the deformed mesh and the displacement contours in the longitudinal and transverse direction of the pile cap backfill is shown in Figure 4.57. This illustrates the realistic three-dimensional simulation of the backfill as shown in Figure 4.55. The computed load-displacement components using the “LSH” model and 2-D finite element model were multiplied by an adjustment factor α varying between 1.2 and 1.4 to account for the three-dimensional effect of the mobilized passive wedge in the backfill. However, the force-deformation relationships calculated using 3-D finite element model were compared against experimental data

without any adjustment factor. Figure 4.56 and Figure 4.55 show the formation of the three-dimensional passive wedge using half-wall-width. Figure 4.58 through Figure 4.61 show the total displacement contours, displacement vectors Mohr-Column plastic points and incremental shear strains reflecting the location of the failure surface.

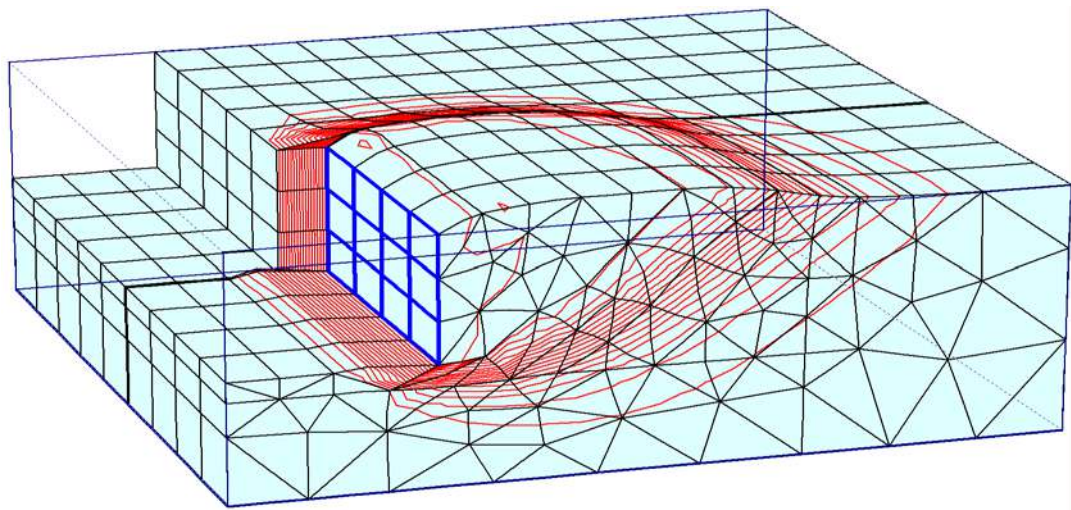


Figure 4.58: 3-D Finite Element Model of the Displacement Contours for BYU Pile Cap Experiment

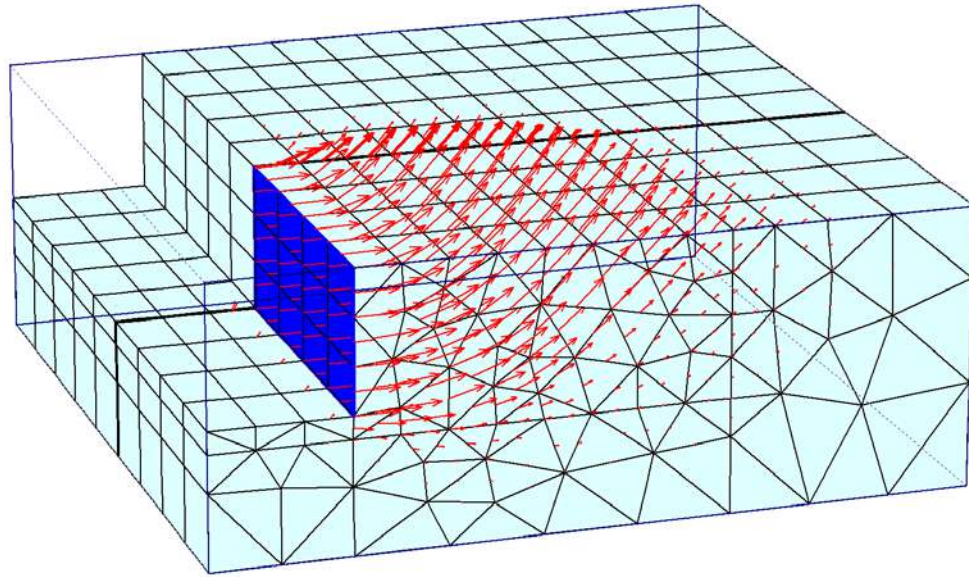


Figure 4.59: 3-D Finite Element Model of the Displacement Contours for BYU Pile Cap Experiment

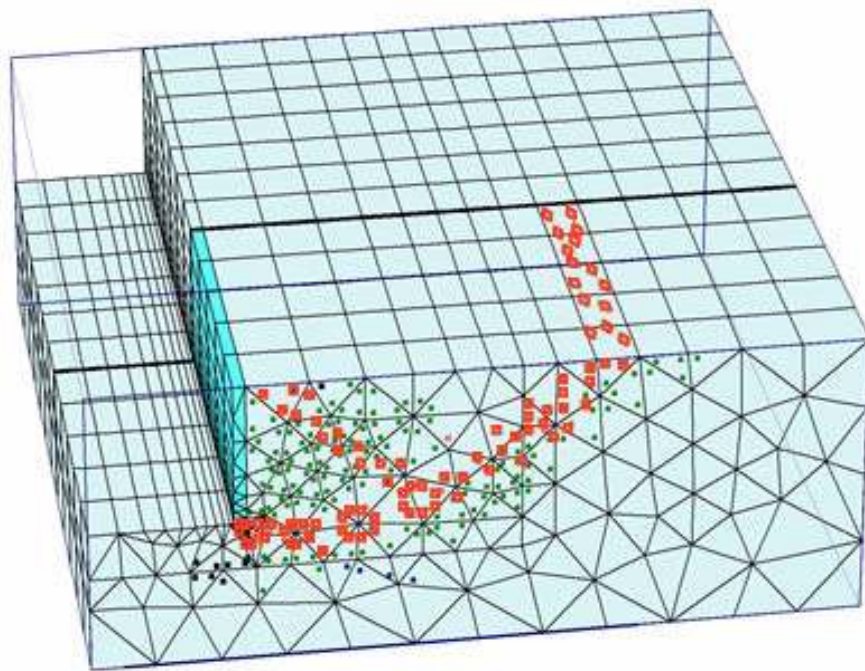


Figure 4.60: Full 3-D Finite Element Model of Mohr-Coulomb Plastic Points for BYU Pile Cap Experiment

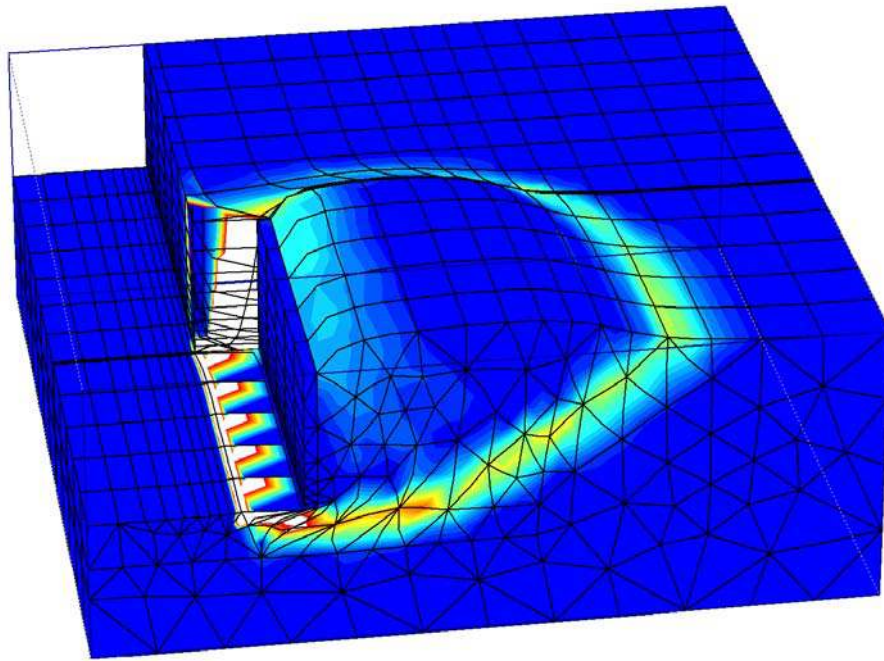


Figure 4.61: Full 3-D Finite Element Model of Mohr-Coulomb Incremental Strains for BYU Pile Cap Experiment

The load-displacement curve of the model and the experimental data for the pile cap with the silty sand backfill is shown in Figure 4.62. In contrast to the 2-D model, the calculated coordinates of the load- displacement curve are the direct results of the three-dimensional finite element without any adjustment factor. There is a good agreement between the experimental data and the model prediction.

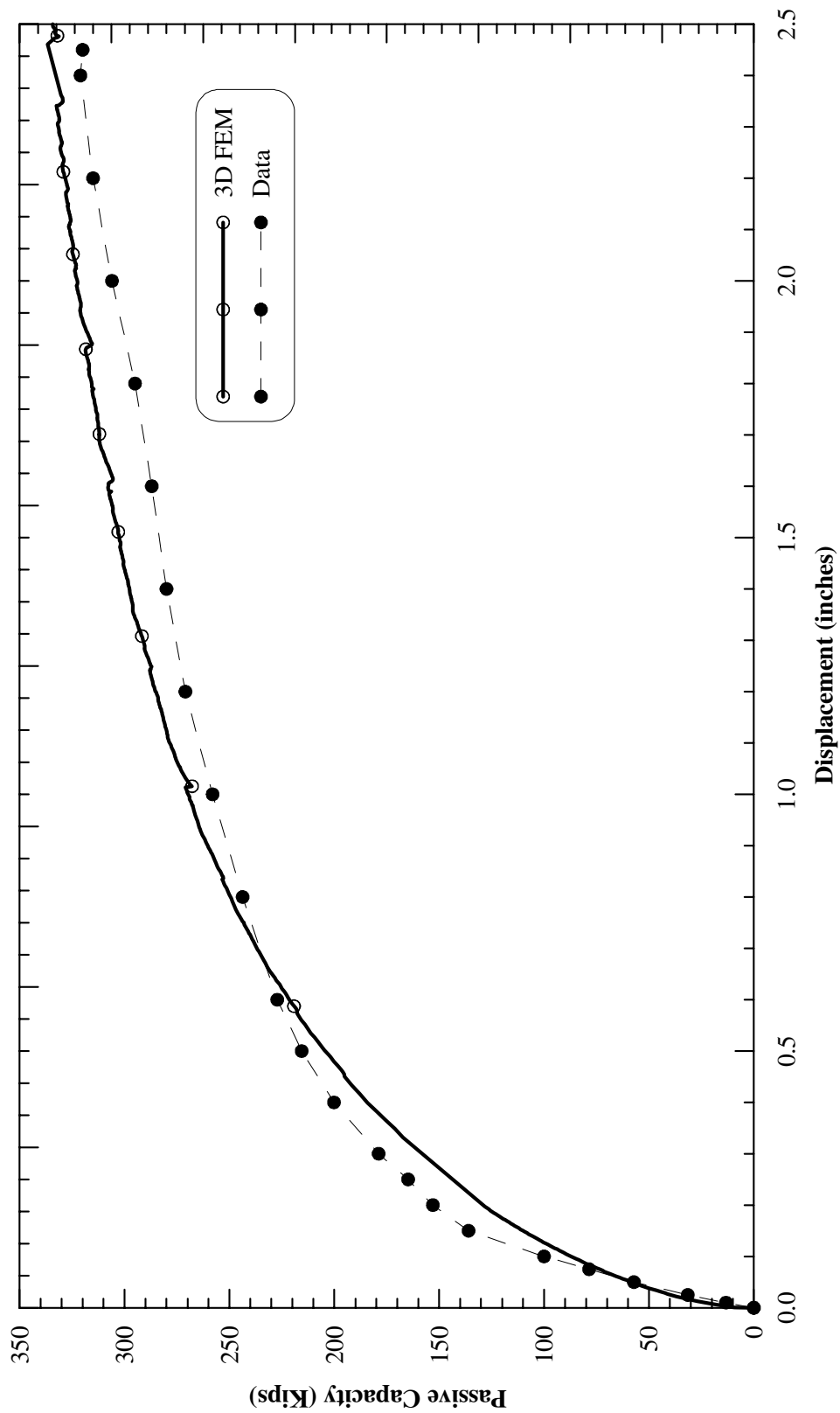


Figure 4.62: Measured Experimental Data Versus Finite Element Prediction for BYU Silty Sand Backfill Experiment

4.11 Comparisons of Various Models Versus Experimental Data

Numerical results are compared with the measurements by means of set of load-displacement curves that show backfill capacity as a function of displacement. The comparisons of the load- displacement curves resulted from the closed-form solution (HFD model), simplified solution (LSH model) and the numerical solution (2-D and 3-D finite element models) for all the full-scale abutments and pile cap experiments are presented herein. The comparisons of the abutment backbone curves predicted by all methods presented are nearly the same for all practical purposes. Therefore, typical bridge abutments behavior is a 2-D plane-strain problem. However, for the pile caps, the coordinate of the backbones developed by the LSH or 2-D finite element model were multiplied by an adjustment factor to account for the three-dimensional effect. The pile cap backbone curves predicted using the 3-D finite element model need not to be multiplied by an adjustment factor. The comparisons the analytical models versus the experimental data are shown in Figure 4.63 through Figure 4.68.

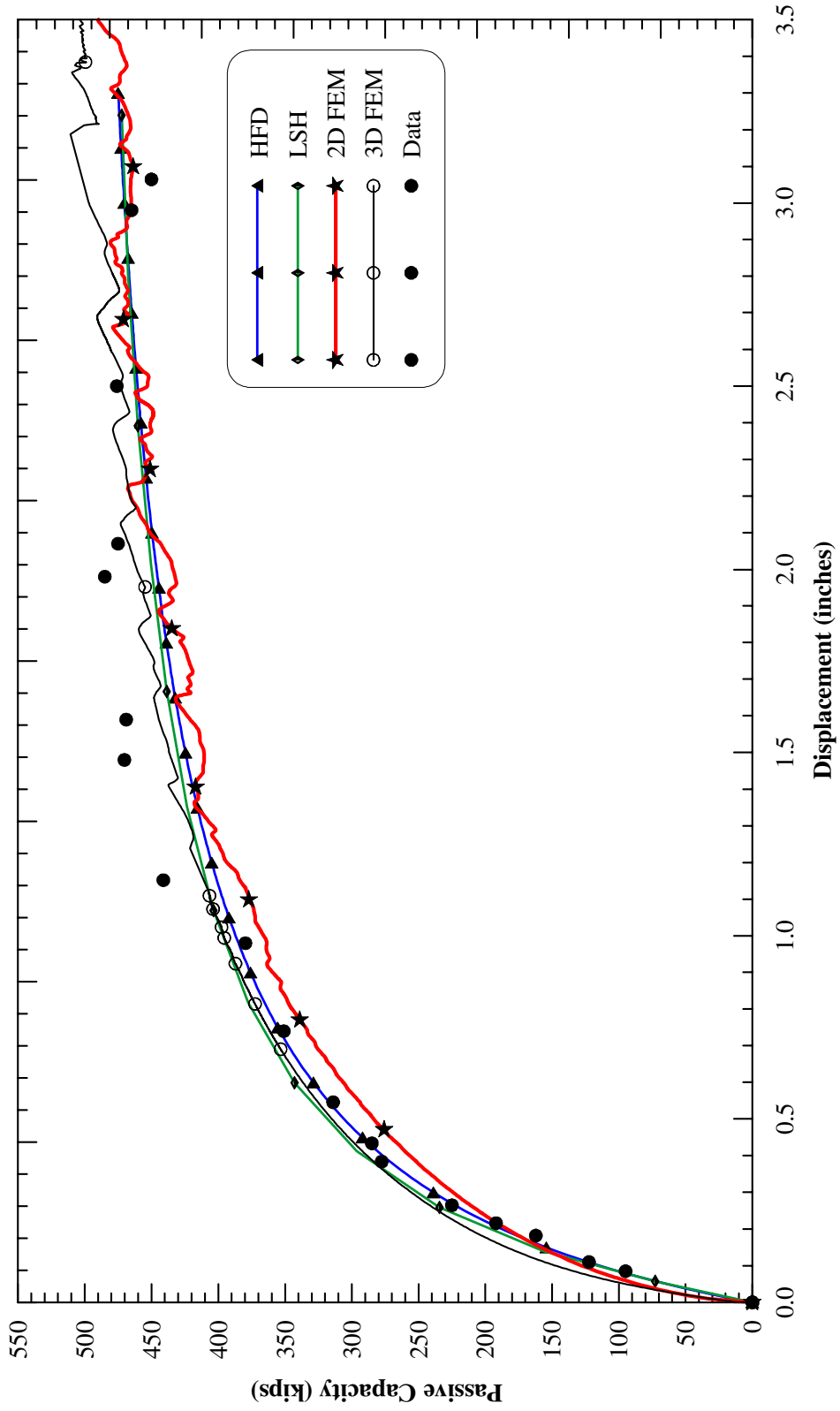


Figure 4.63: Measure Force-Deformation of the UCLA Abutment Test Versus Predictions by Various Methods

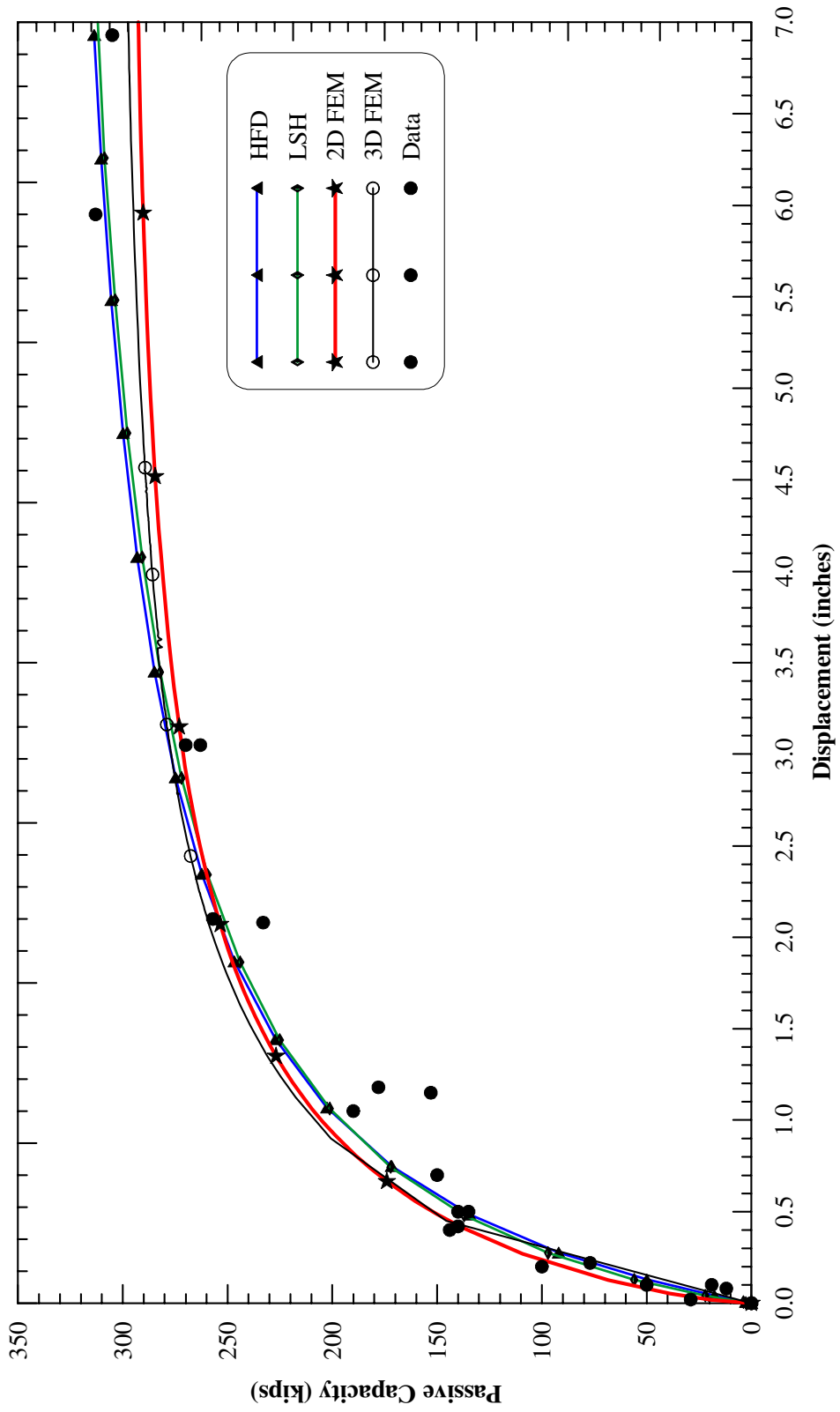


Figure 4.64: Measure Force-Deformation of the UCD Abutment Test Versus Predictions by Various Methods

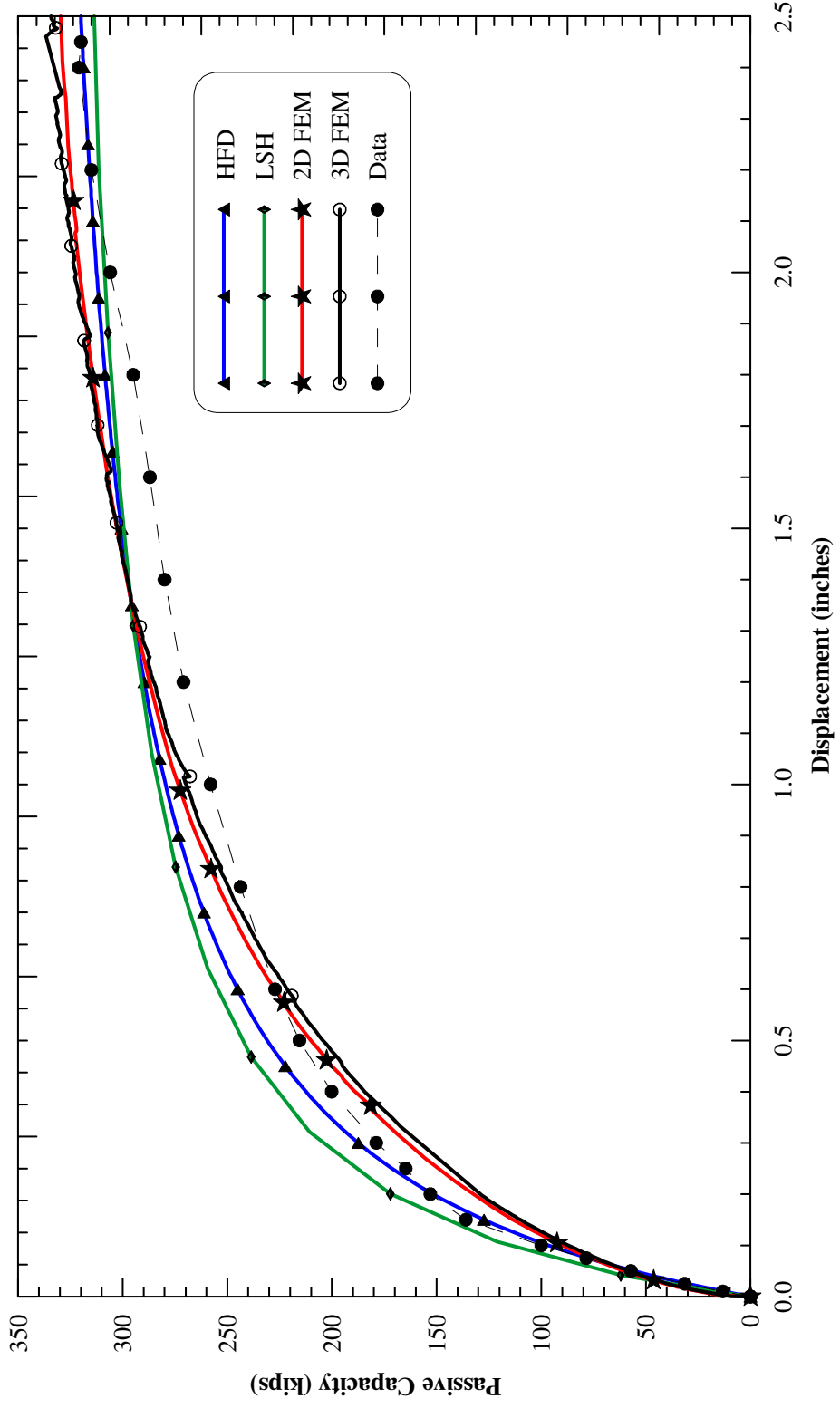


Figure 4.65: Measure Force-Deformation of the BYU Pile Cap Test Versus Predictions by Various Methods for Silty Sand Backfill

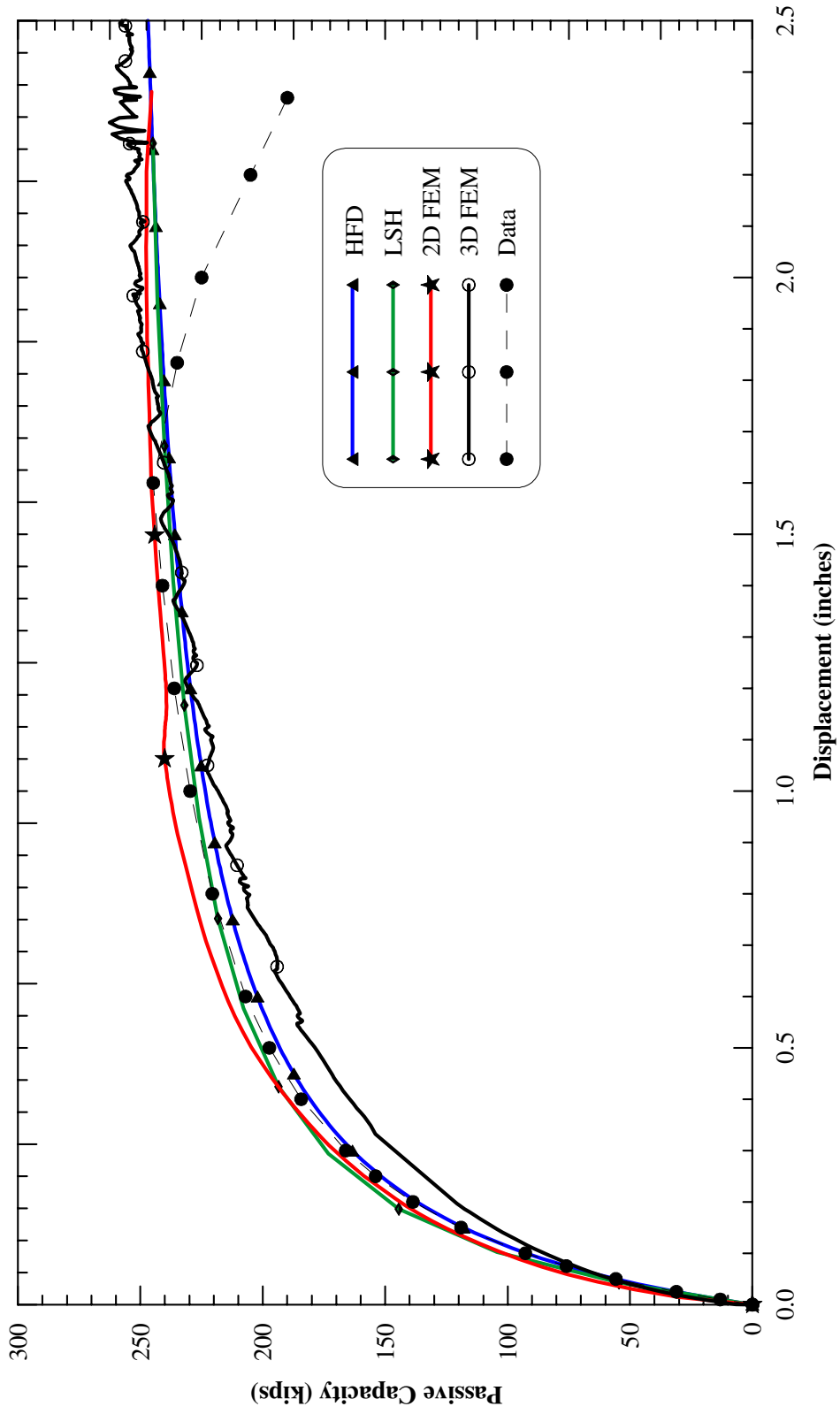


Figure 4.66 : Measure Force-Deformation of the BYU Pile Cap Test Versus Predictions by Various Methods for Clean Sand Backfill

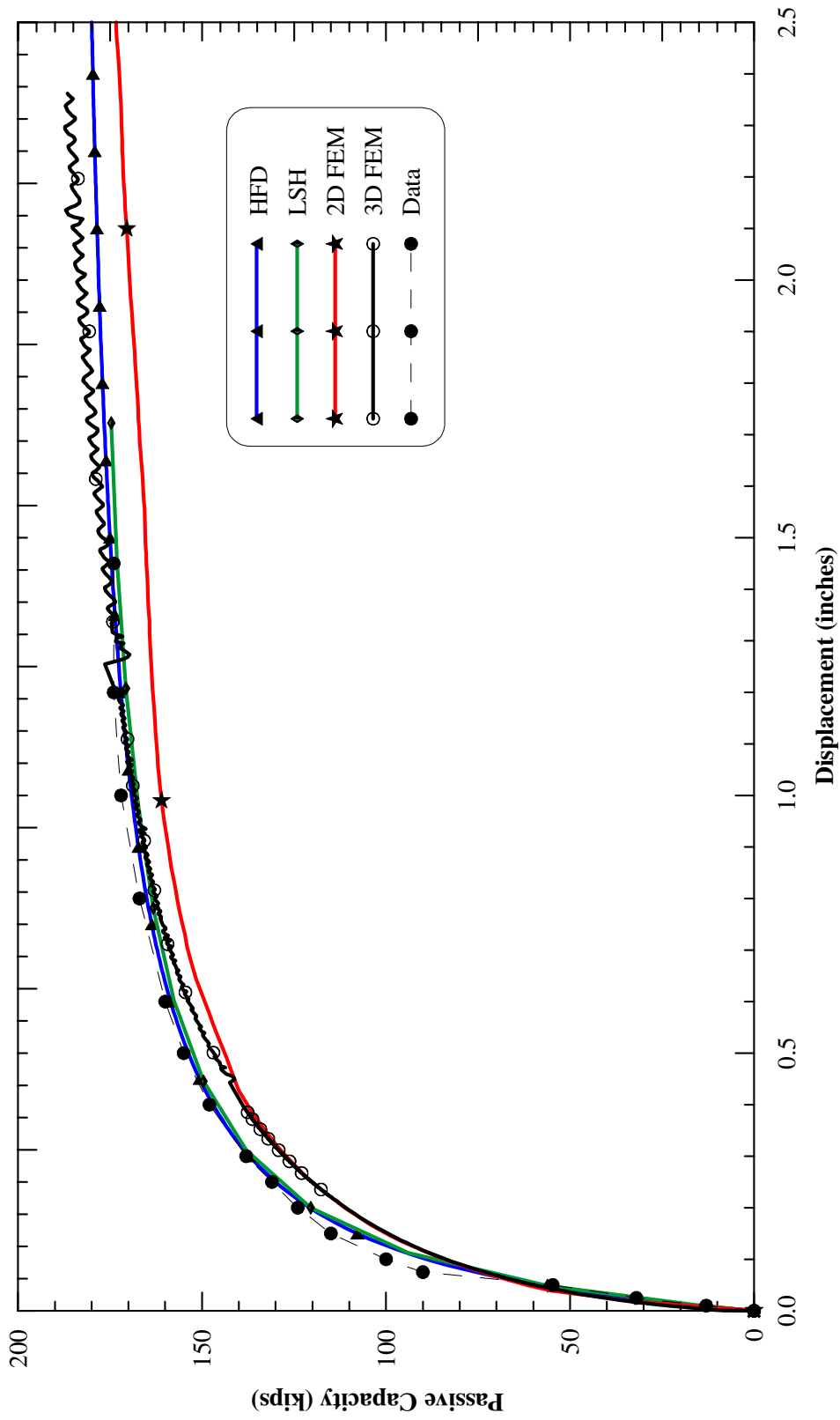


Figure 4.67: Measure Force-Deformation of the BYU Pile Cap Test Versus Predictions by Various Methods for Fine Gravel Backfill

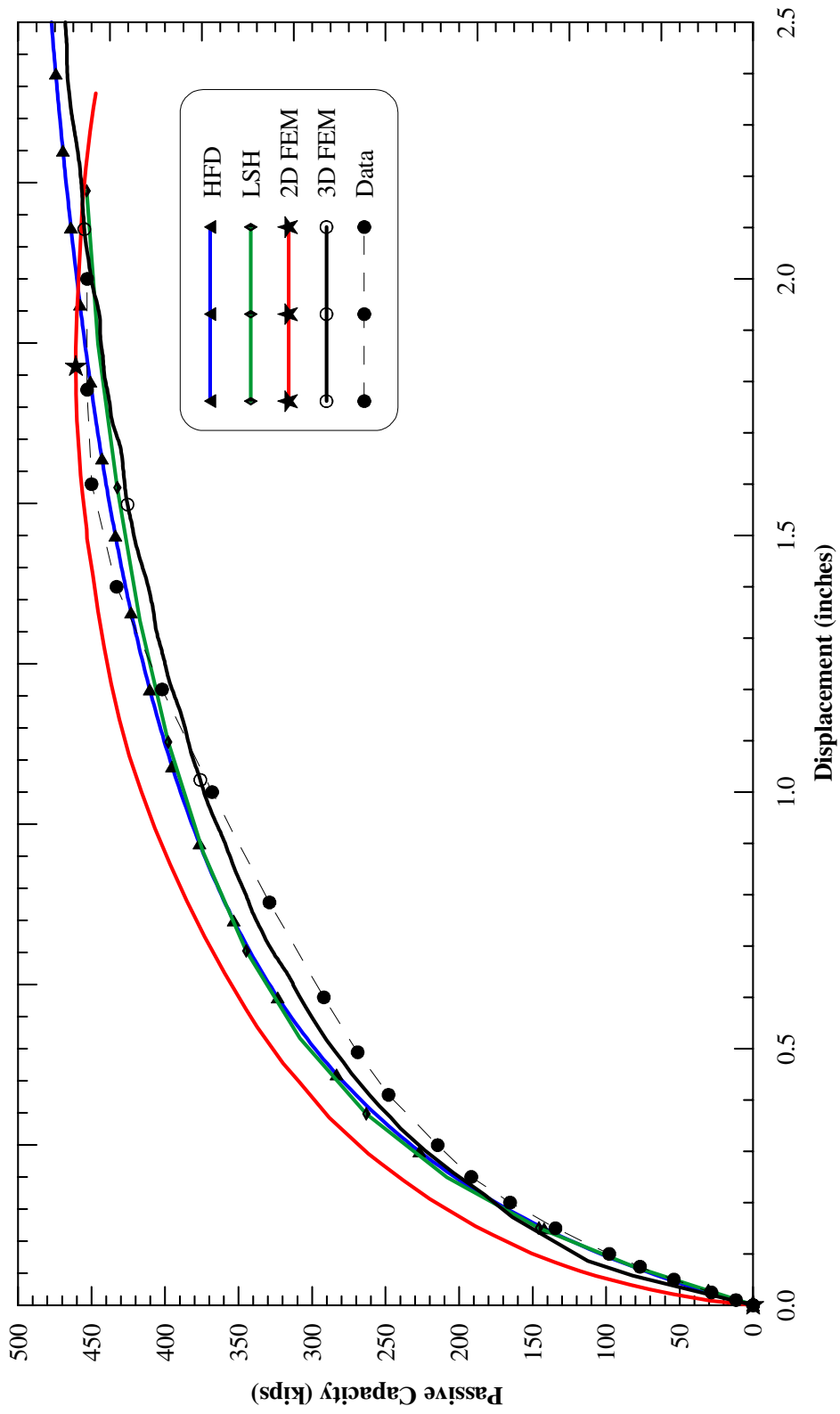


Figure 4.68: Measure Force-Deformation of the BYU Pile Cap Test Versus Predictions by Various Methods for Coarse Gravel Backfill

4.12 3-D Finite Element Model for Skewed Abutment

During seismic events, the bridge deck experiences significant rotational motions about its vertical axis. As a result, the deck first collides with the abutment–backfill system. The collision continues for some times and then the clockwise rotation of the deck as shown in Figure 4.69 results in the separation of the deck from the abutment.

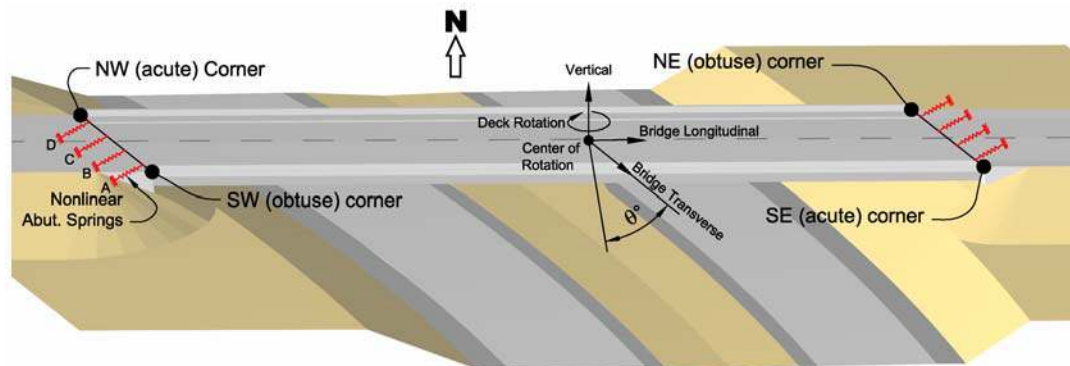


Figure 4.69: Clockwise Deck Rotation During a Seismic Event

The photograph of Figure 4.70 shows manifestation of the asymmetric passive wedge and ground heave in the west half of the roadway for more than 2 feet, adjacent to the obtuse corner of the bridge deck. This river bridge crosses the Chelongpu reverse-thrust Fault that generated slip movements causing incremental collapse of the southern two deck spans and driving the northern span into the skewed abutment backfill a distance of 7.25 feet.

Inspection of existing skewed abutments after recent earthquakes indicates that the passive wedges that form behind the skewed walls tend to be asymmetric along the abutment backwall due to deck rotation as shown in Figure 4.71. Such

behavior was observed at the northern abutment of the skewed Wushi highway bridge in Taiwan that was severely damaged during the recent Chi-Chi earthquake as shown in Figure 4.70.

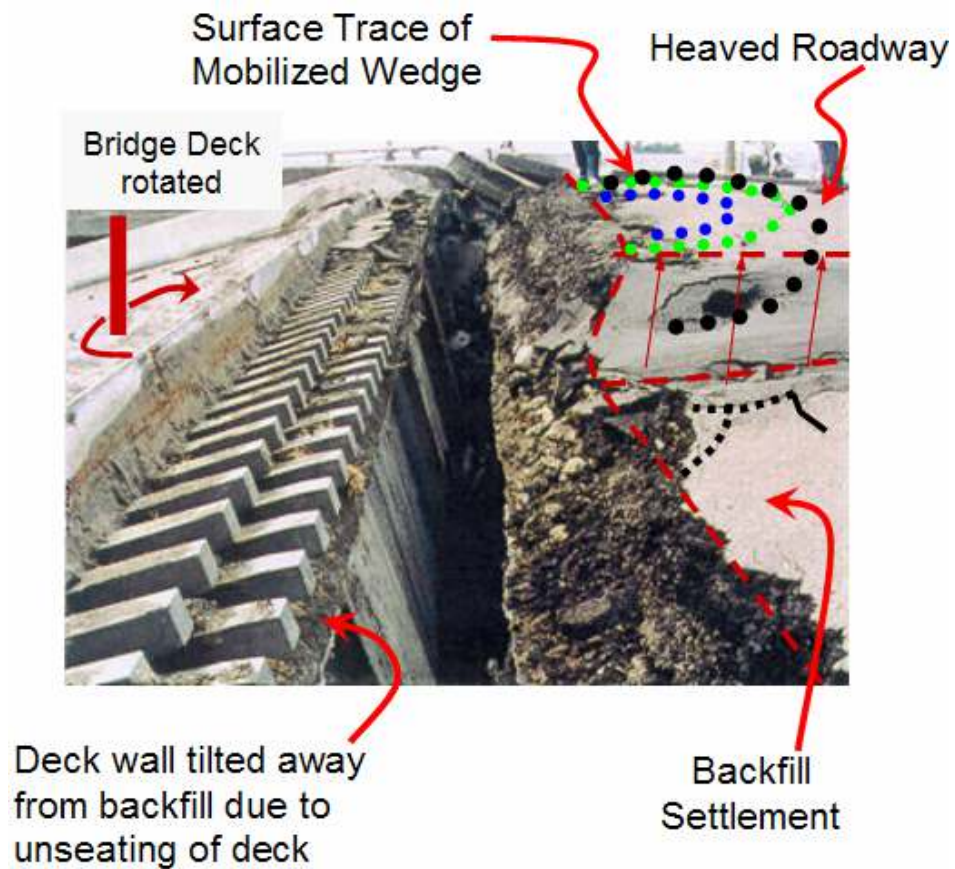


Figure 4.70: Non-uniform Passive wedge behind skewed abutment

A set of 3-D finite-element analyses using PLAXIS was performed to evaluate the development of passive resistance behind a 75-foot wide abutment with a 5.5-foot high backwall of varying skew angles. First, the soil in the front of the abutment backwall was excavated and then the abutment backwall was loaded

monotonically using a displacement control normal to the abutment backfill to simulate the non-skewed abutment failure mechanism as shown in Figure 4.71. It was assumed that the bridge deck will be pushed between the wingwalls in a plunging mode during a seismic event. The wingwalls were kept in stationary in the analytical model. The PLAXIS HS model was used to simulate the nonlinear abutment backfill. Linear elastic material properties were assigned to the abutment wingwalls. The formation of the mobilized passive wedge and the displacement contours are shown in Figure 4.71.

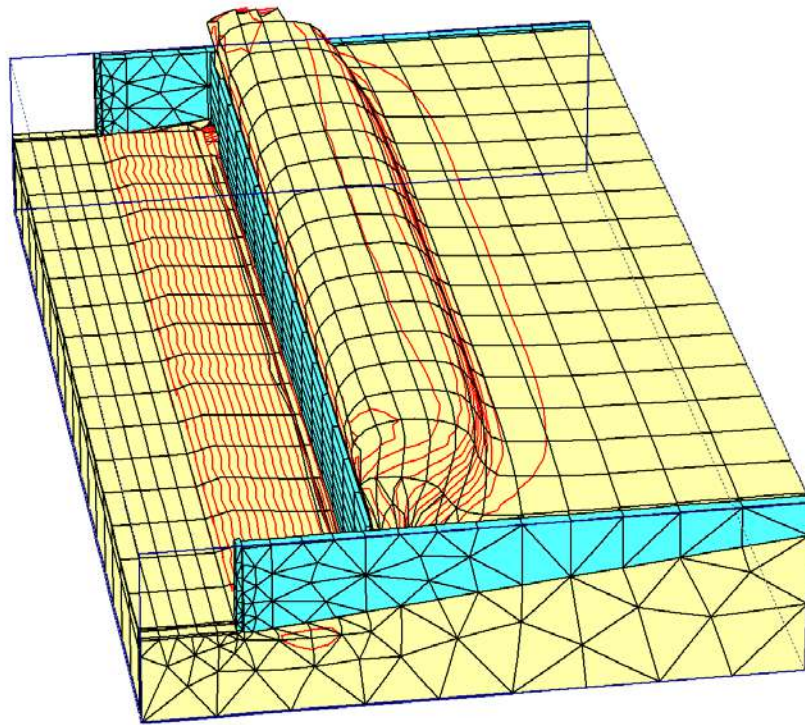
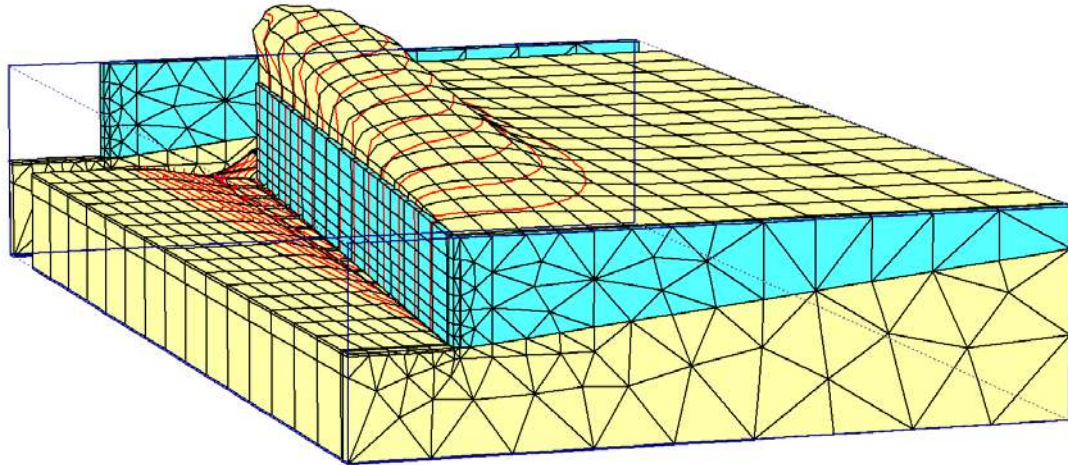


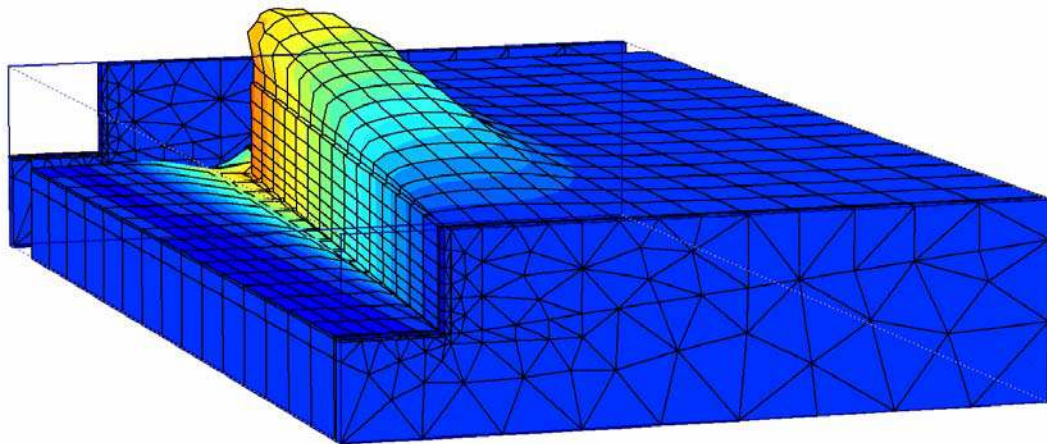
Figure 4.71: Passive Soil Wedge Plunging in Between Wingwalls

The same 3-D displacement control finite element model was used to investigate the failure mechanism of the skewed-abutment with various skewed

angles. Figure 4.72 shows the shape of the fully formed 3-D passive wedge formed between the wingwalls of the abutment with 45° skew.



(a) Deformed Mesh and Displacement Contours



(b) Total Displacement Contours

Figure 4.72: Full 3-D Finite Element Model of the Passive Wedge Formation Behind Skewed Abutment

As a result of deck clockwise rotation, the abutment backwalls tend to be pushed primarily in the obtuse corners of the deck, causing asymmetric passive wedges to form behind the abutment backwall. In skewed abutments, the non-

uniform loading of the abutment backwall can result in a reduced mobilized soil capacity as compared to ordinary non-skewed abutments. The ground heave at the far half of the wall width (see Figure 4.72) illustrates the overstress and breakdown of the passive wedge, resulting in the reduction of soil resistance.

Due to in-plane motions and induced pounding forces (compression) of the bridge deck, the abutment-backfill response consists of normal and tangential passive resistance. Figure 4.73 shows example of the nonlinear tangential and normal components of 30° skewed-abutment-backfill backbone curves. Therefore, for the global seismic analysis of the skew bridges both tangential and normal components of the abutment backfill should be considered. The tangential component of passive resistance about one third of the normal component.

The normal components of the abutment passive resistance for various skew angles are shown in Figure 4.74. The results indicate that the mobilized passive capacity might decrease as a function of skew angles at large displacement levels.

At very high-skew abutments, the passive capacity can decrease significantly, which is a result of separation of the deck at the acute corners and “disintegration” of the passive wedge after significant plastic ground deformation and heave has occurred near the obtuse corners of the deck. These findings raise the possibility that a skew abutment may develop a considerably reduced soil resistance in comparison to a similar normal abutment, affecting overall bridge response.

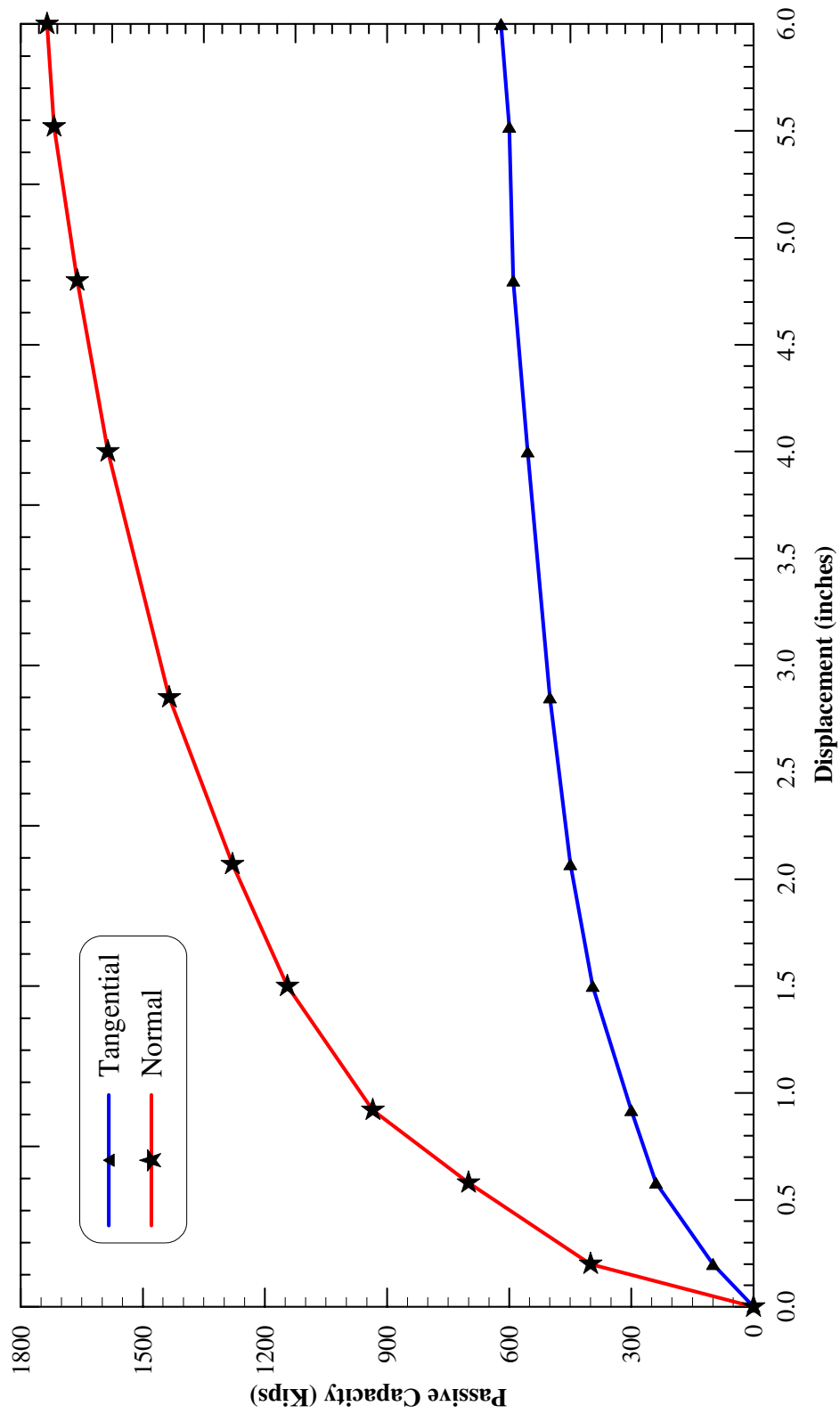


Figure 4.73: Nonlinear Normal and Tangential Components of the Abutment-Backfill Resistance for a 30 Skew angle

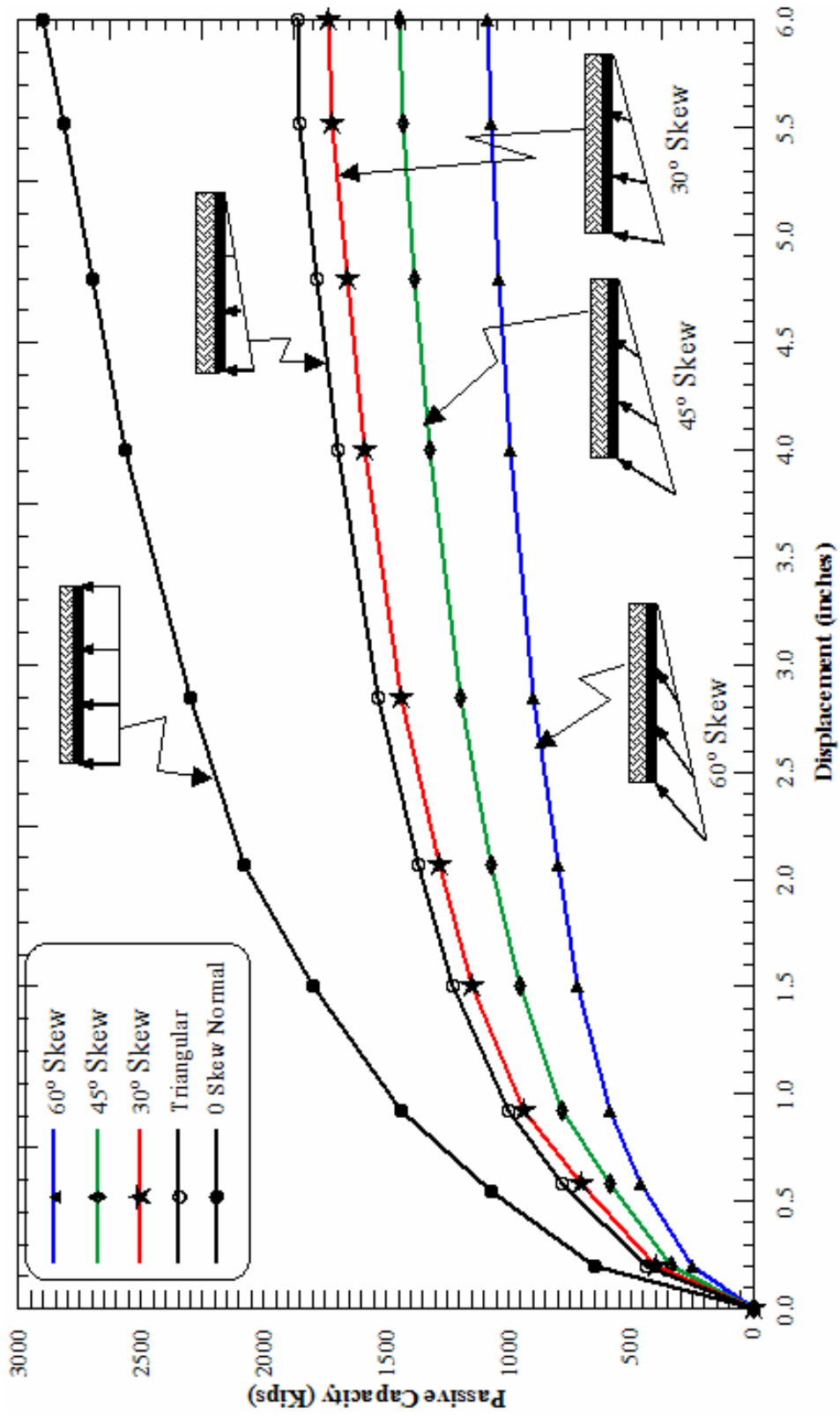


Figure 4.74: Impact of Skew Angles on Nonlinear Abutment Force-Deformation Relationship

4.13 Summary

The full-scale field experiments conducted on the abutments backwall and pile caps provide the opportunity to compare actual recorded measurements with the results from Hyperbolic Force-Displacement (HFD model) relationship, the limiting equilibrium using Log Spiral combined with modified Hyperbolic backfill stress-strain relationship (LSH model), 2-D and 3-D finite element model. The 3-D finite element models were calibrated against the experimental data and was used to investigate the failure mechanism and the response of the skew abutments.

From comparison of field observations after a seismic event and computer simulations, it is clear that the skewed abutment tend to develop an asymmetric passive soil wedge that is less wide and generates less soil resistance than the normal passive wedge behind a non-skewed abutment. The size (width) and capacity of this passive wedge depends on abutment width and skew angle. These factors affect the interaction of the bridge deck with the abutment. Soil resistance does not increase with increasing skew angle as could be expected from a combination of passive resistance normal to the wall and additional soil traction developed along the back face of the abutment wall. Current analyses indicate that the width and total resistance of the mobilized passive wedge is maximum for zero skew and decreases as the magnitude of skew angles is increased.

It is assumed that the abutment wingwalls are expected to yield or fail during a seismic event because they is designed to retain the abutment backfills in sloped ground and not to provide passive resistance in the transverse directions. The

transverse capacity of the abutment is provided by the abutment shear keys which will be described in the following chapter.

CHAPTER FIVE

NONLINEAR SEISMIC RESPONSE OF SKEWED BRIDGES

5.1 Introduction

Global seismic behavior of skewed bridges is affected by a number of factors, including bridge skew angle, deck width, deck flexibility, number of spans, number of columns per bent, column ductility, soil-abutment-superstructure interaction, abutment shear keys, soil-bent foundation-structure interaction, abutment bearing pads, and characteristics of the seismic source. The objective of this chapter is to evaluate the dynamic nonlinear soil-abutment-structure interaction (SASI) behavior of typical straight, concrete box girder highway bridges at several skew angles subjected to a suit of ground motions with the near fault effect. Skewed bridges tend to rotate during a seismic event, which can cause excessive transverse movement and unseating of the superstructure and pounding to the abutment backwall.

A number of SASI studies have been performed on skewed bridges. Traditional bridge design practice evaluates dynamic performance of skewed bridges using two dimensional stick models with lumped springs to represent the abutment structure and foundation. However, when a bridge has a skew abutment, the longitudinal bridge response is affected by transverse loading due to the coupling nature of the two horizontal directions. Full three-dimensional bridge models which include bridge deck, bent caps, and ductile columns, seat-type abutments with

abutment-backfill and abutment shear keys are developed to perform nonlinear dynamic time history analysis for various typical bridge structures.

Figure 5.1 shows various components of a bridge system and the modeling assumptions used in this chapter. The bridge deck is model either using shell elements (referred to as shell model) and or beam elements (referred to as spline model). The cracked moment of inertia obtained from the moment-curvature analysis of the column cross section is used to model the bridge columns. Nonlinear frame elements with the moment-curvature properties are used to model the top of columns to allow plastic hinge formations during a major seismic event. Pinned connections are assumed at the base of the columns. Abutment-soil interaction was modeled by an expansion gaps and nonlinear normal springs skewed to the principal bridge axis. Abutment shear keys were modeled using nonlinear springs and an expansion gaps in the skewed transverse direction. Nonlinear response-spectra-compatible time history analyses were performed using seven sets of ground motions with two lateral components incorporating near-fault effects. The analyses show that the superstructure undergoes significant rotations about the vertical axis, this result in permanent lateral deck offset at the abutments.

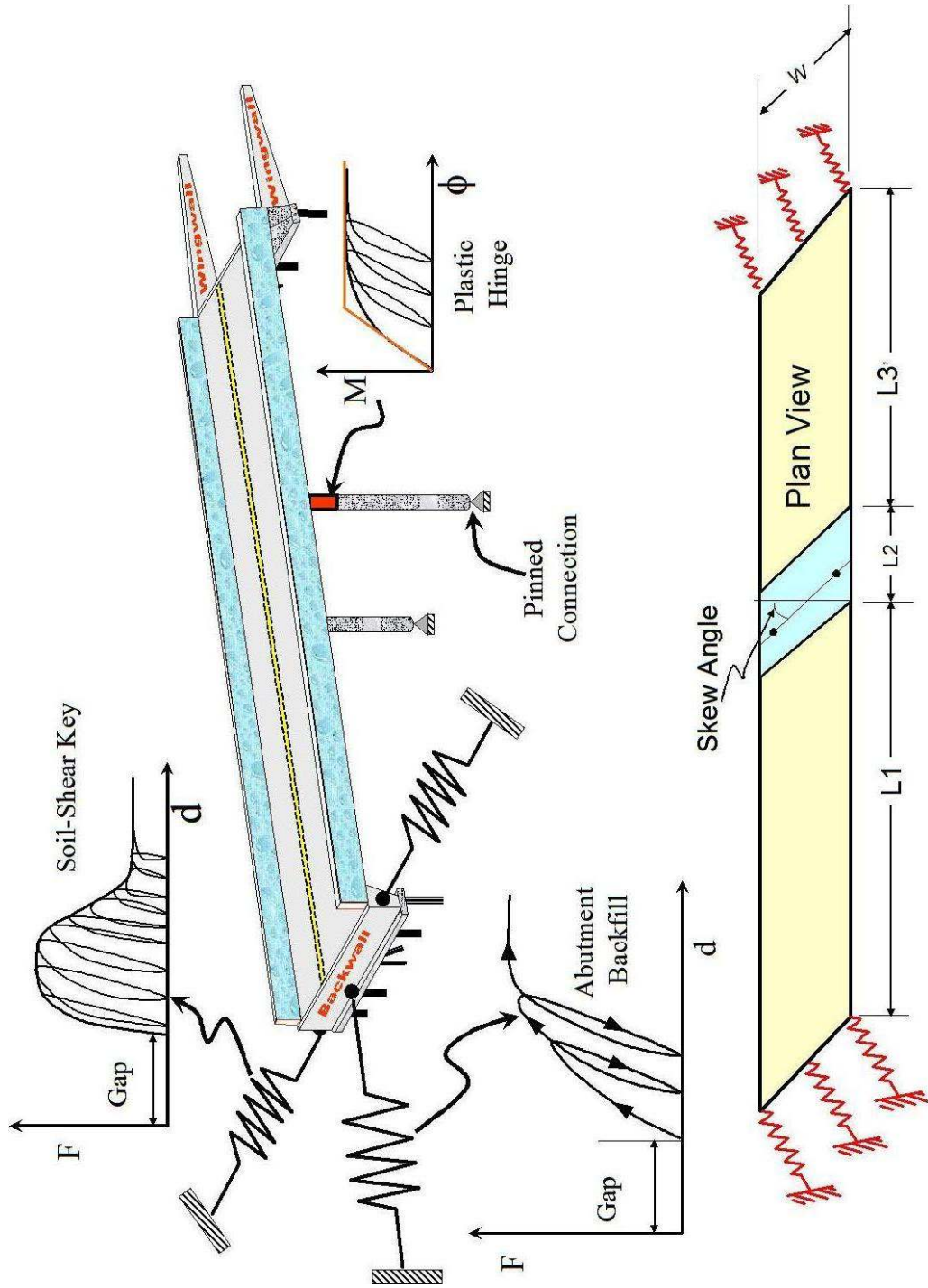


Figure 5.1: Components of Bridge System

5.2 Impact of Ground Motion Characteristics

The effects of rupture directivity on near-fault ground motions have been recognized by engineering seismologists for several decades. The propagation of fault rupture toward a site at a velocity close to the shear wave velocity causes most of the seismic energy from the rupture to arrive in a single large long-period pulse of motion that occurs at the beginning of the record (Somerville et al., 1997). Current seismic design of ordinary bridges is based on the response spectrum approach. However, the response spectrum does not provide an adequate characterization of the ground motions with the near-fault effect. Current trends for seismic response of bridge structures have embraced the concept of performance based design. The validity of performance-based design depends on realistic specification of ground motion inputs, realistic models of the bridge structure and realistic boundary conditions of the bridge model. Therefore, time history input ground motions should be used instead of a response spectrum to adequately characterize the nonlinear response of the bridge models due to near-fault ground motions.

Ground motions with an asymmetrical and high amplitude velocity pulse characteristic have the tendency of producing a biased, one-sided response of the bridge structures. Asymmetrical impulsive loading generates large displacements in one direction leading to a significant residual displacement. As part of the FHW seismic research program, the effect of near-fault motions on bridge columns was studied using shake table tests at the University of Nevada, Reno (Phan et al., 2005). The asymmetry in the directivity pulse generated an asymmetric response in column

specimens. The measured results revealed the important role of ground motion characteristics on the bridge column hysteretic behavior. The most unique aspect of the measured response was the presence of high residual displacements. The measured force displacement hysteretic behavior of the column specimen is shown in Figure 5.2. The one-sided high velocity pulse of the input ground motion caused the hysteretic response of the column to be biased in one direction.

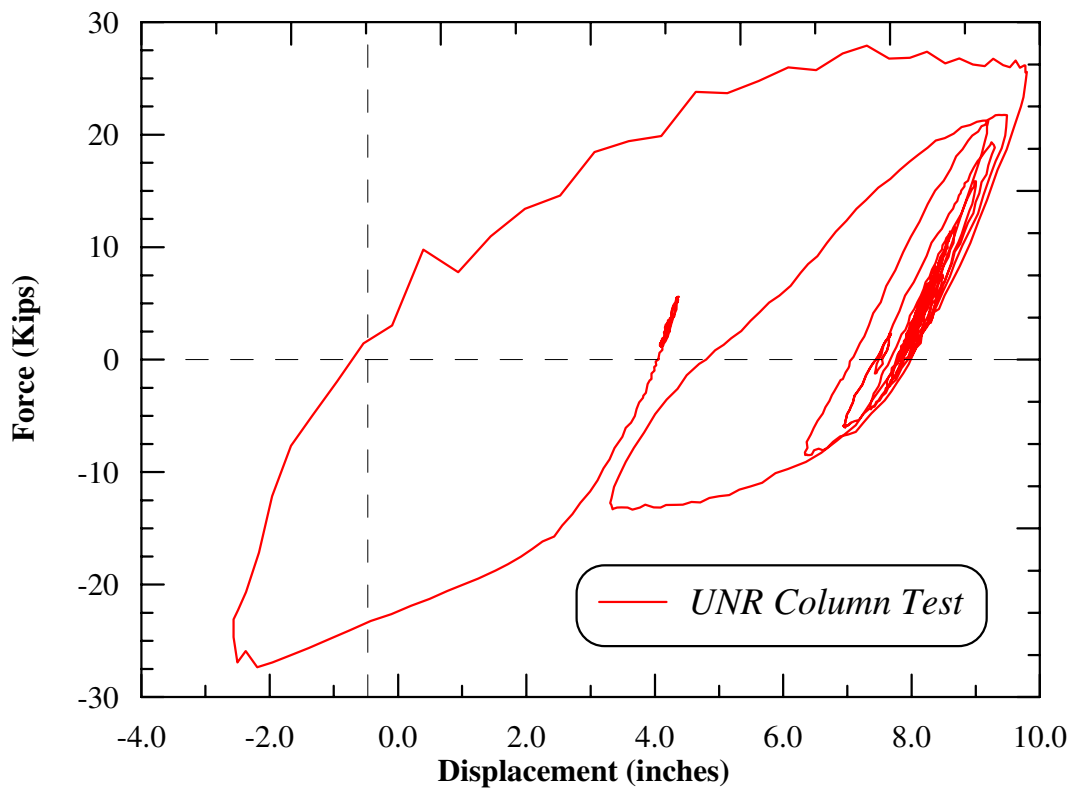


Figure 5.2: Measured Shaking Table Hysteretic Response of Bridge Column (Phan et al., 2005)

In this chapter, in addition to the seven response-spectra-compatible time history ground motions, the two-components recorded Renaldi ground motion was used to investigate the response of skew bridges in particular the abutment response

due to the asymmetrical impulse loading of the ground motions with near-fault effect.

5.3 Selection of the Ground Motions

Many toll bridge designs require a minimum of three sets of spectrum-compatible time history ground motions. However, three sets of time histories are still not sufficient to cover aleatory variability in ground motion parameters; as a result, envelop of the results is used for the design of all toll bridges. If one wishes to use average structural response (rather than envelop), the number of time histories needs to be significantly more than three. The requirement of number of time histories has been discussed in several literatures and in many project meetings for Caltrans Toll Bridge projects. The consensus has been to employ seven spectrum-compatible time histories to be eligible for averaging. Same number or more has been recommended in UBC 1997 and IBC 2000.

For this research project, it is more important to obtain statistically stable mean values in order to make reasonable conclusions of bridge abutment response under general conditions. Since the conclusion must be applicable for a wide range of seismological considerations including near fault directivity effects, seven spectrum-compatible time histories with the near-fault effects are used.

The time histories were developed to match the Caltrans standard SDC curve having a Magnitude 8 with a peak ground acceleration of 0.7 g on Soil Type D (stiff soil with shear wave velocity $600 < V_s < 1200$ ft/s). All seven sets of start-up motions are modified to represent time history motions that are response spectrum compatible

with the target SDC curve. All the time histories have been baseline corrected. The earthquake records with high velocity pulses selected for this research are listed in Table 5.1

Table 5.1 Selected Earthquake Records

No.	Startup Motion
1	1979 Imperial Valley, Array 7
2	1994 Northridge, Slymar Record
3	1992 Landers, Lucerne Record
4	1994 Northridge, Renaldi Record
5	1989 Loma Prieta, Los Gatos Record
6	1995 Kobe, Takatori Record
7	1992 Turkey Erzincan Record

Since the purpose of the research is to investigate the in plane motion of the bridge deck, the vertical components of the ground motions were ignored. The two components were applied in the longitudinal and transverse directions of the bridge. All input motions exhibit high-velocity pulses; the components with the largest velocity pulses were applied in the longitudinal direction. The peak accelerations, velocities and displacements including the time of the velocity pulses for both components are listed in Table 5.2. The largest velocity pulses occurred between 4.9 to 12.9 seconds. Figure 5.3 to Figure 5.16 show the response spectra compatible acceleration, velocity and displacement time histories of all seven input motions applied in the longitudinal and transverse bridge directions of the bridge models.

Table 5.2 Input Ground Motion Characteristics

Motion No	Bridge Longitudinal Direction				Bridge Transverse Direction			
	PGA	PGV	PGD	t_p	PGA	PGV	PGD	t_p
1	0.7	56	38	8.3	0.7	51	40	8.8
2	0.7	68	21	7.9	0.7	47	30	10.6
3	0.7	53	23	12.6	0.7	43	23	11.0
4	0.7	79	23	4.0	0.7	52	25	7.3
5	0.7	51	36	9.9	0.7	51	27	9.9
6	0.7	44	32	7.7	0.7	43	28	10.5
7	0.7	58	36	4.9	0.7	39	39	6.0

Note:

PGA- Peak Ground Acceleration (g)

PGV-Peak Ground Velocity (in/sec)

PGD-Peak Ground Displacement (in)

t_p -Time of the peak (sec)

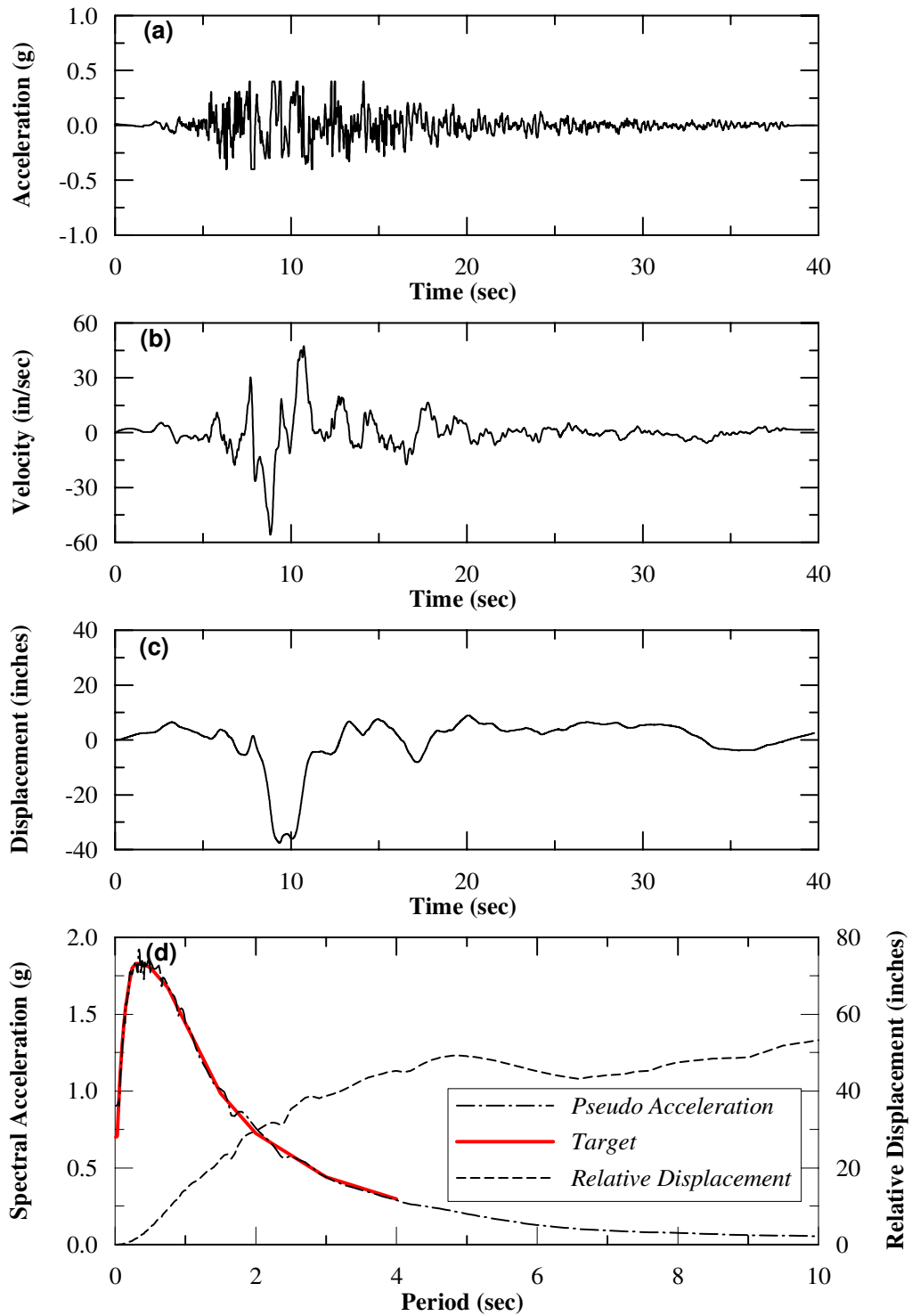


Figure 5.3: Input Ground Motion 1 in Longitudinal Direction

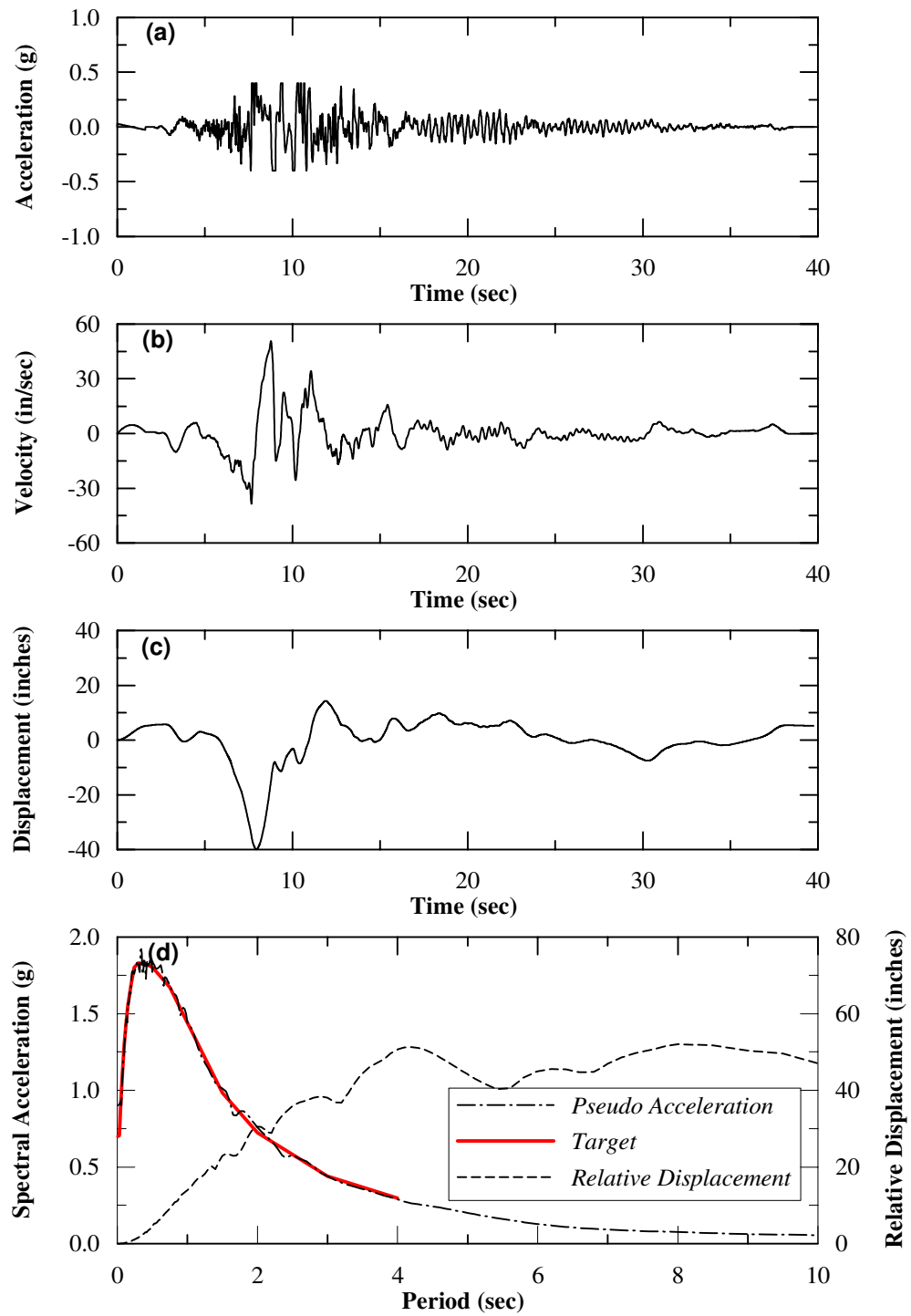


Figure 5.4: Input Ground Motion 1 in Transverse Direction

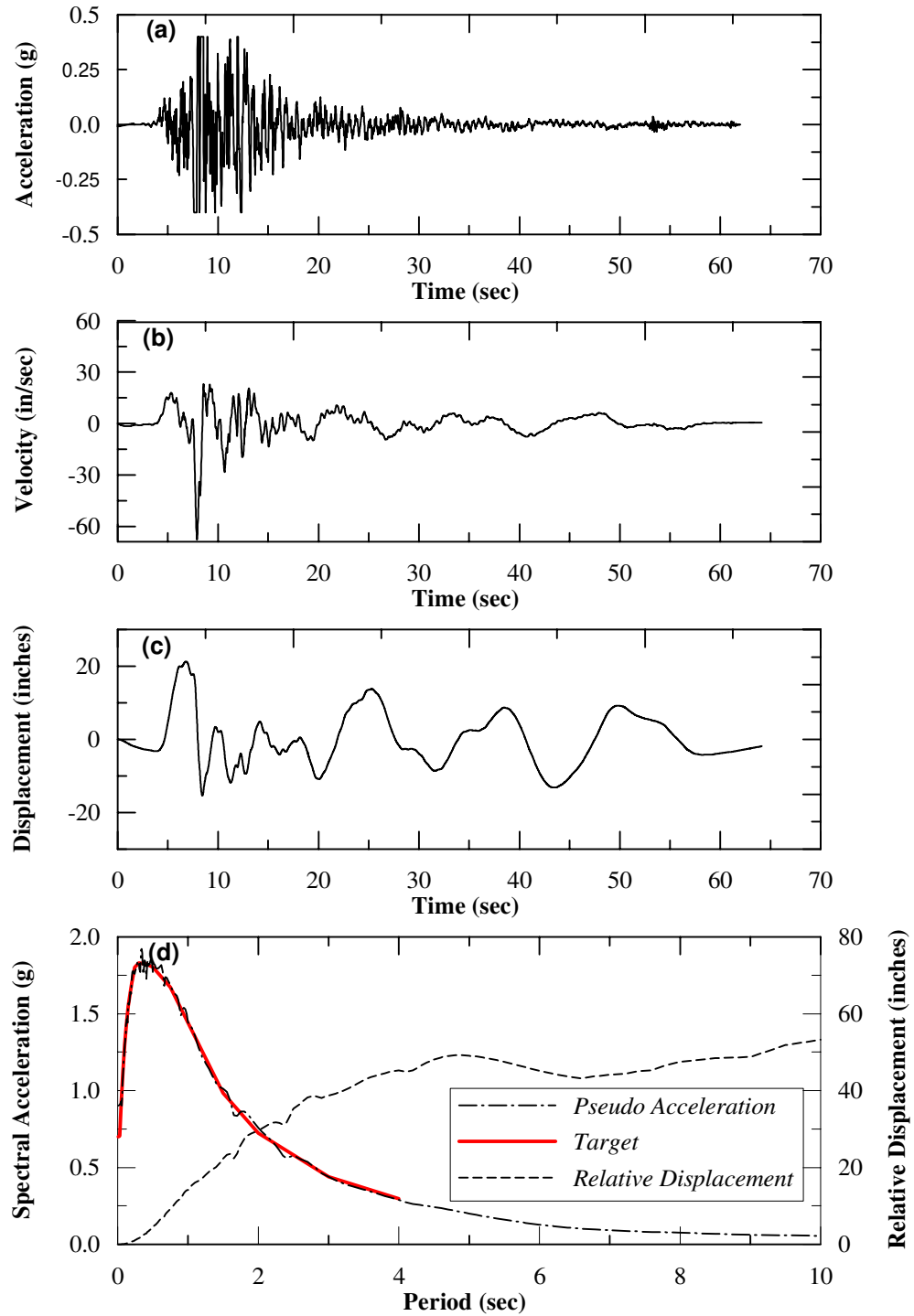


Figure 5.5: Input Ground Motion 2 in Longitudinal Direction

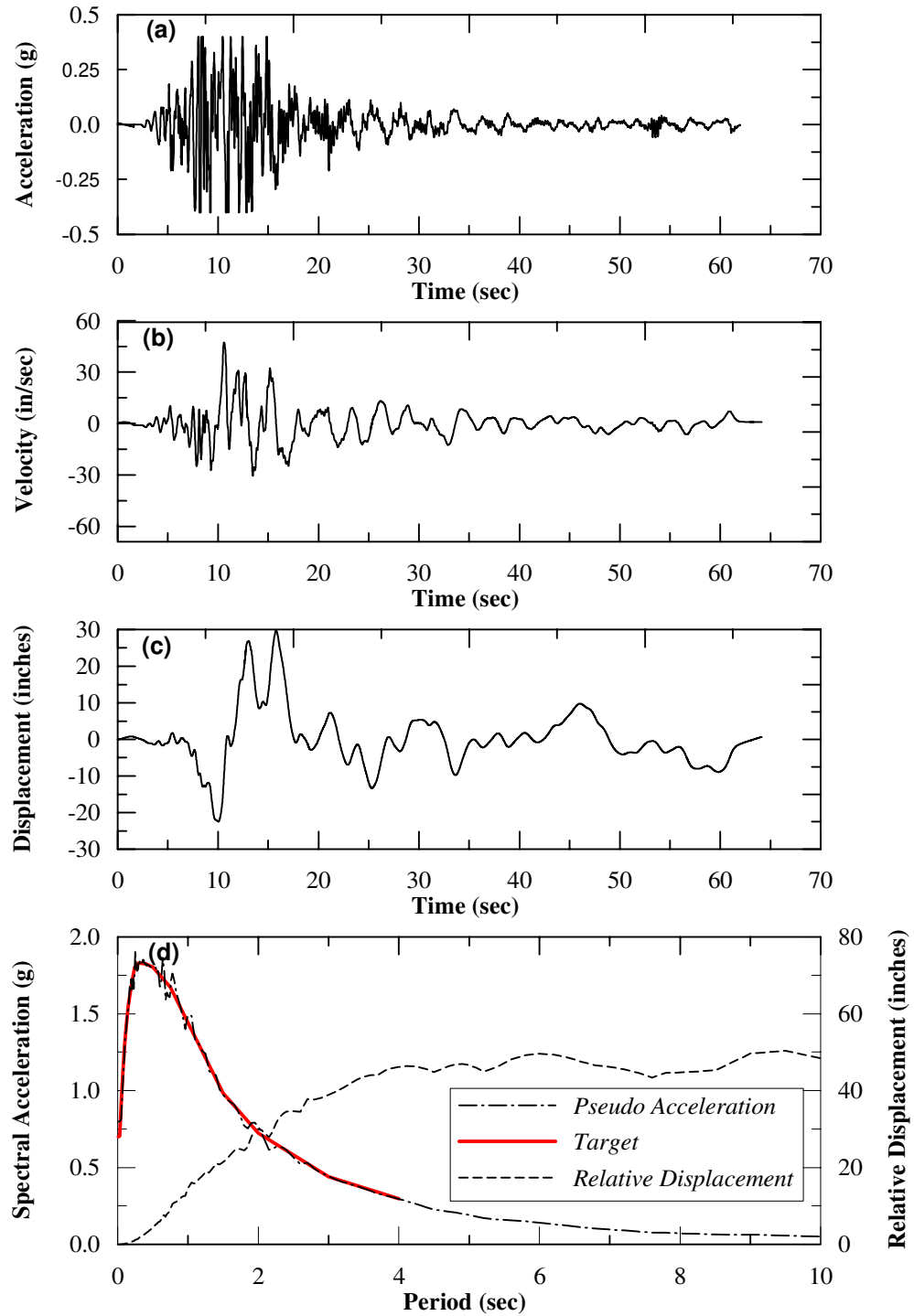


Figure 5.6: Input Ground Motion 2 in Transverse Direction

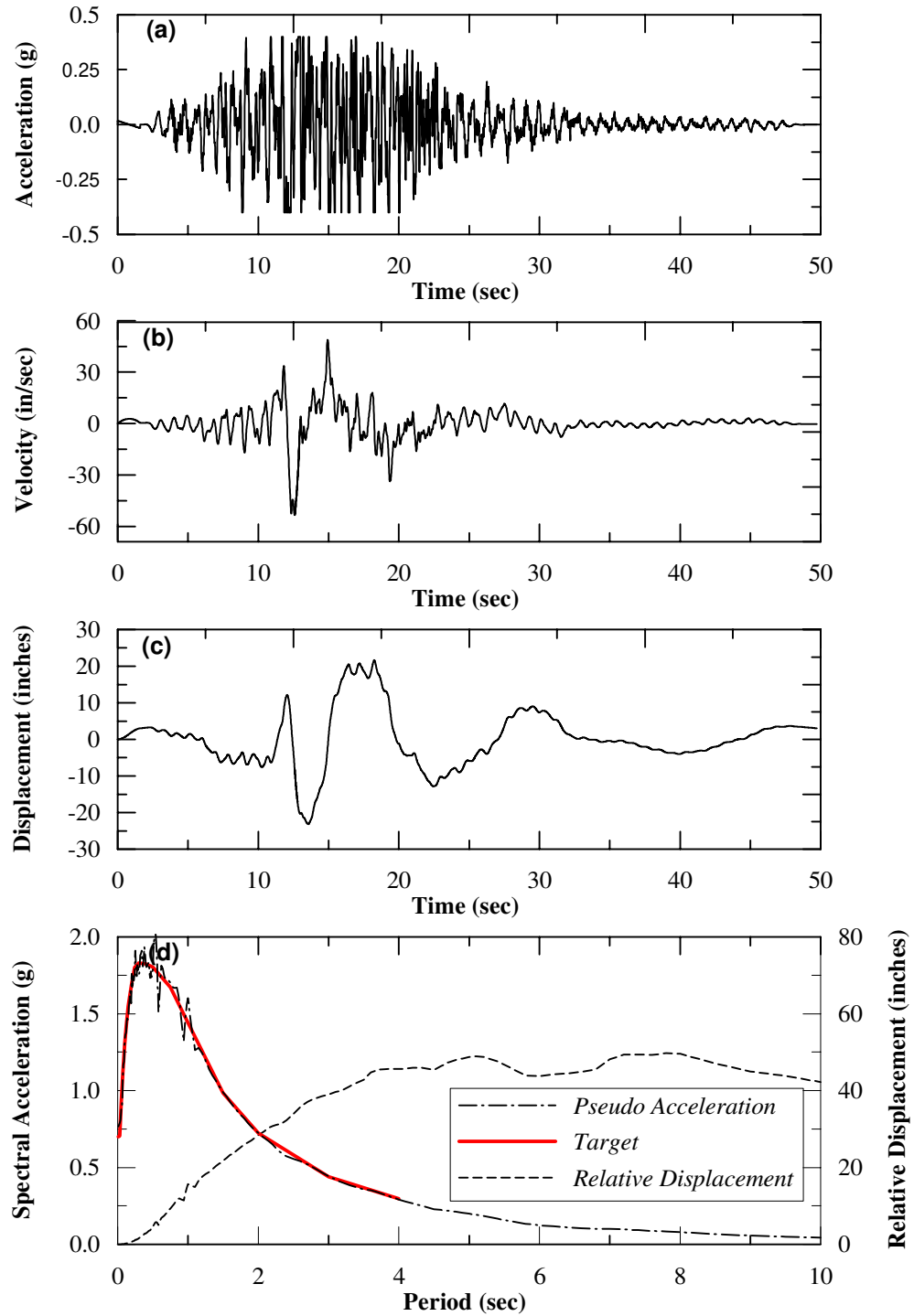


Figure 5.7: Input Ground Motion 3 in Longitudinal Direction

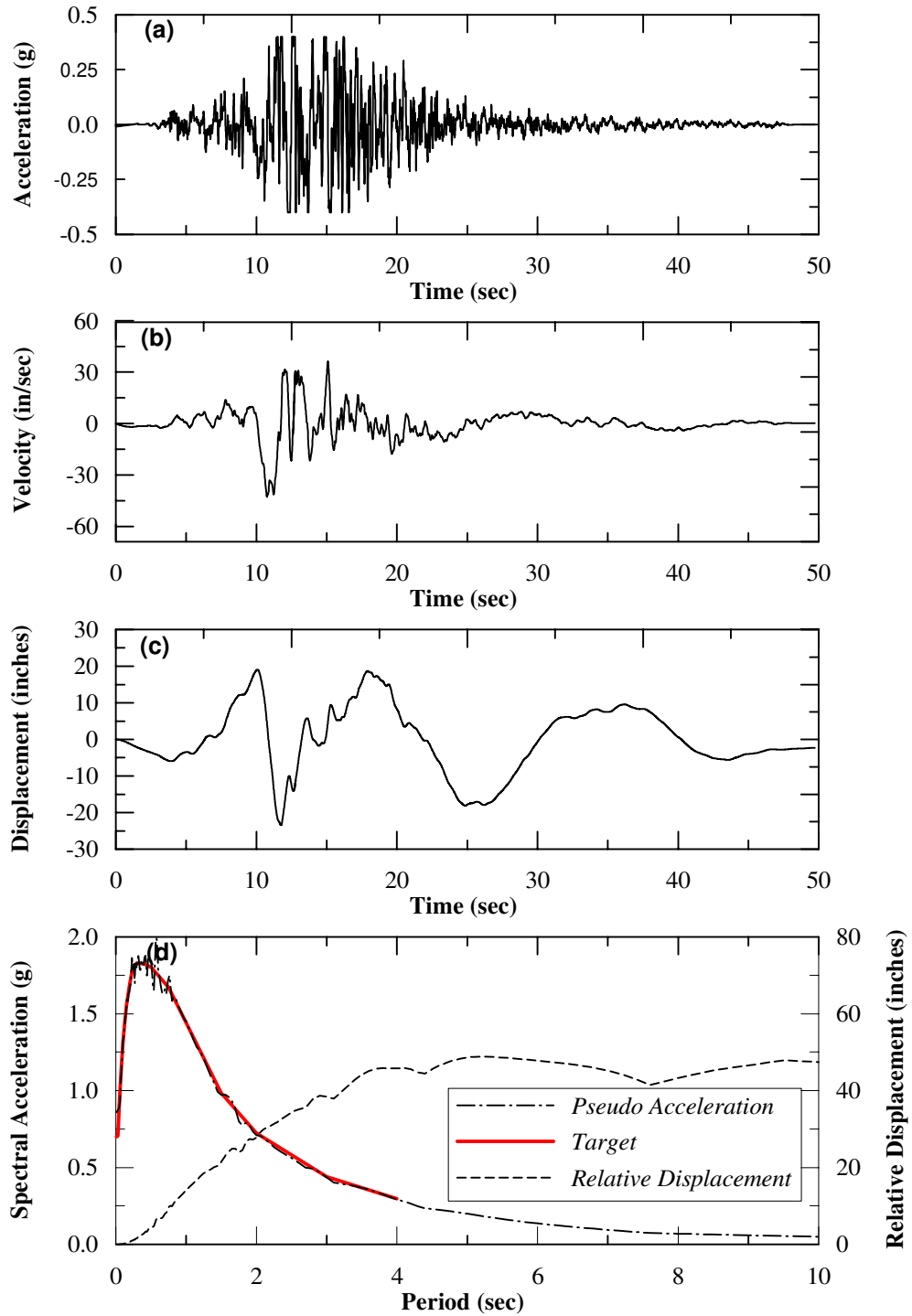


Figure 5.8: Input Ground Motion 3 in the Transverse Direction

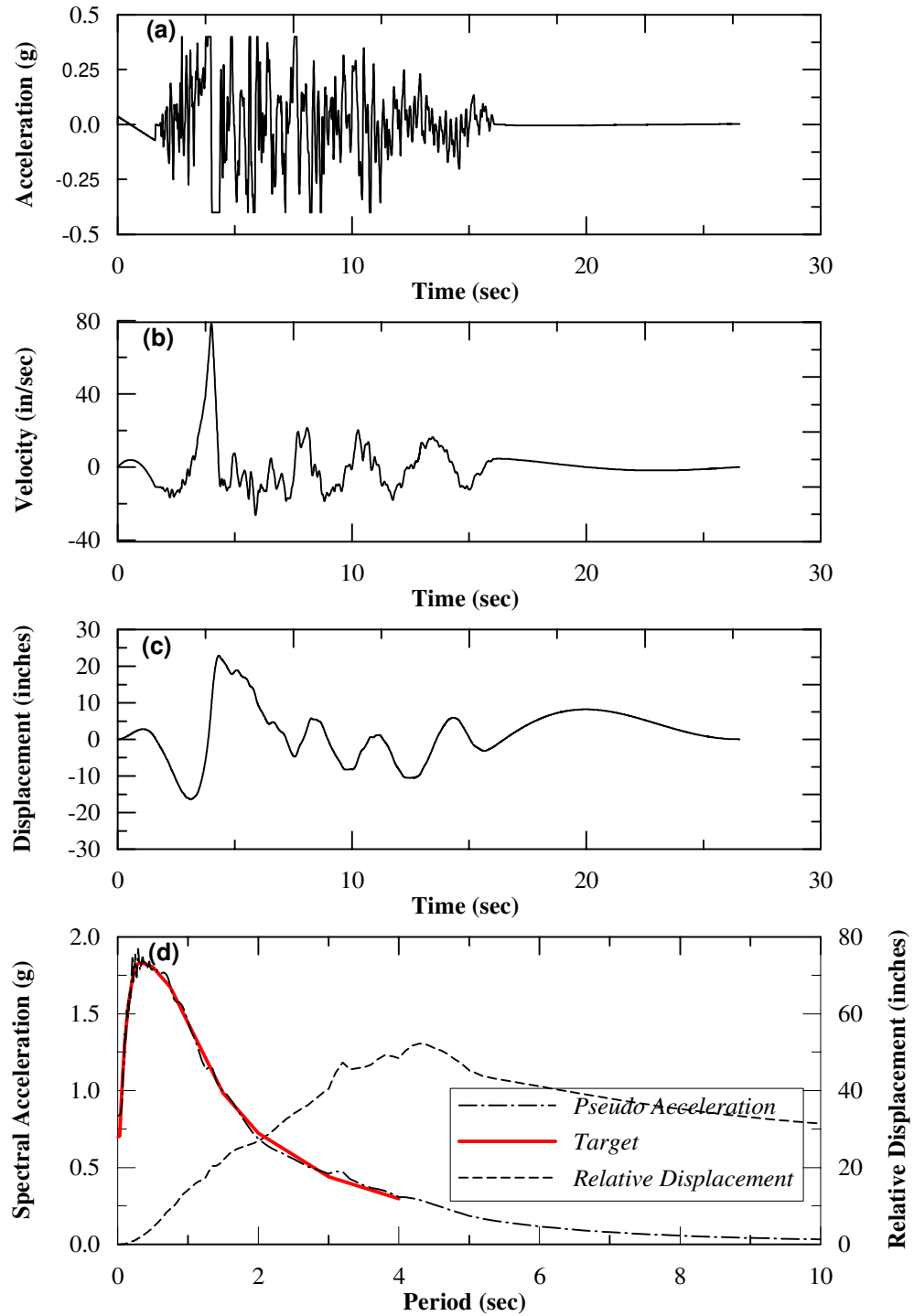


Figure 5.9: Input Ground Motion 4 in the Longitudinal Direction

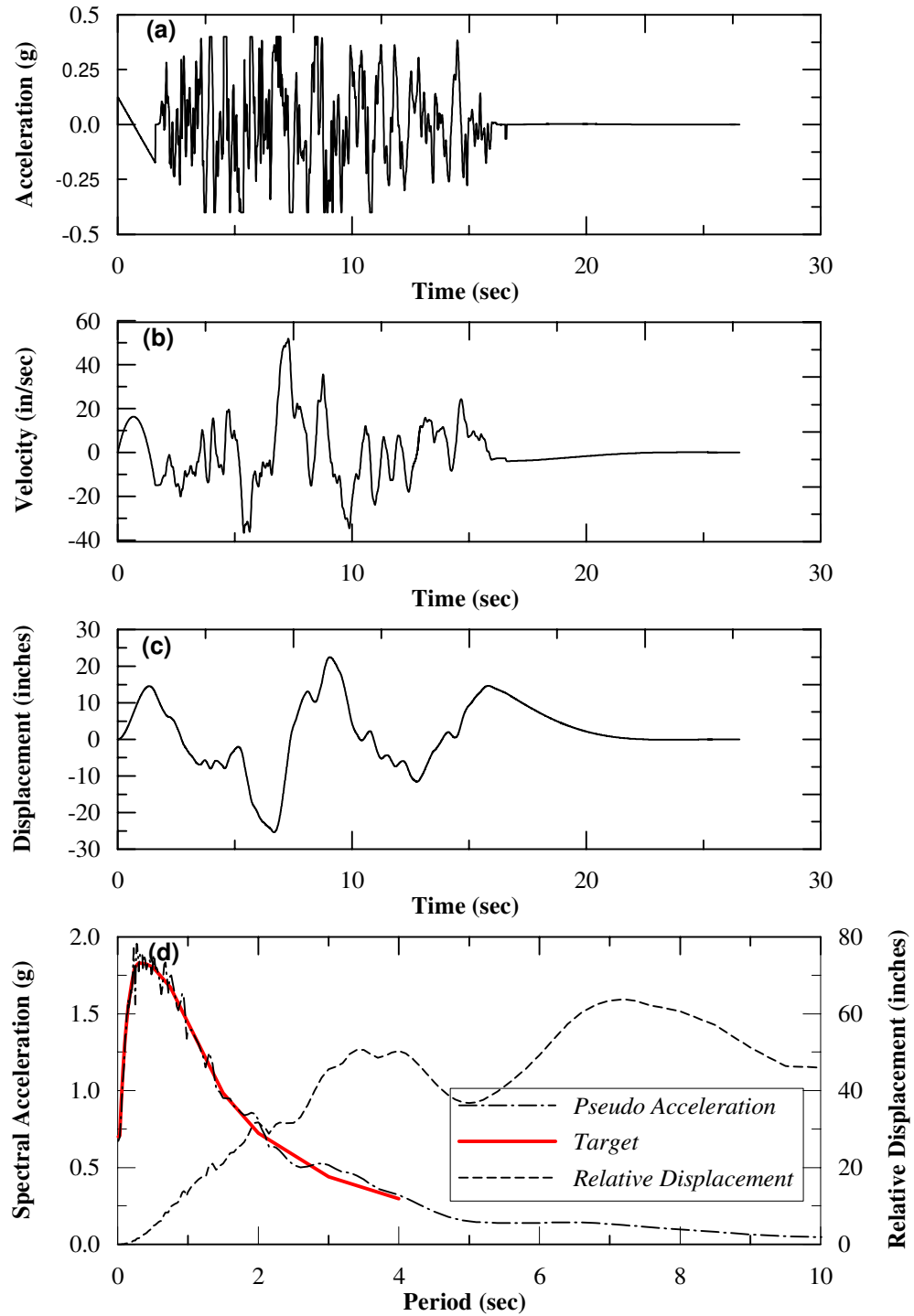


Figure 5.10: Input Ground Motion 4 in the Transverse Direction

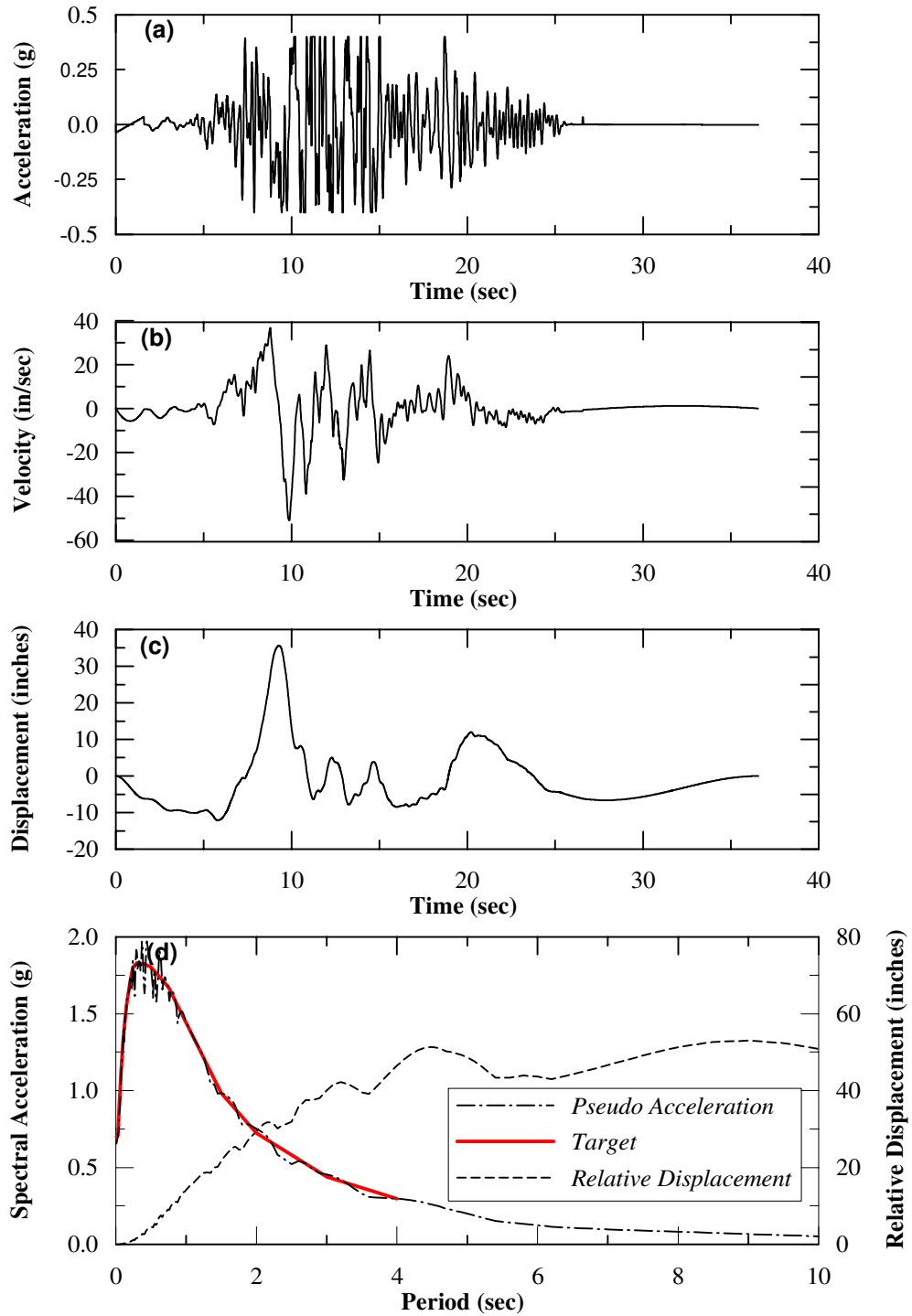


Figure 5.11: Input Ground Motion 5 in the Longitudinal Direction

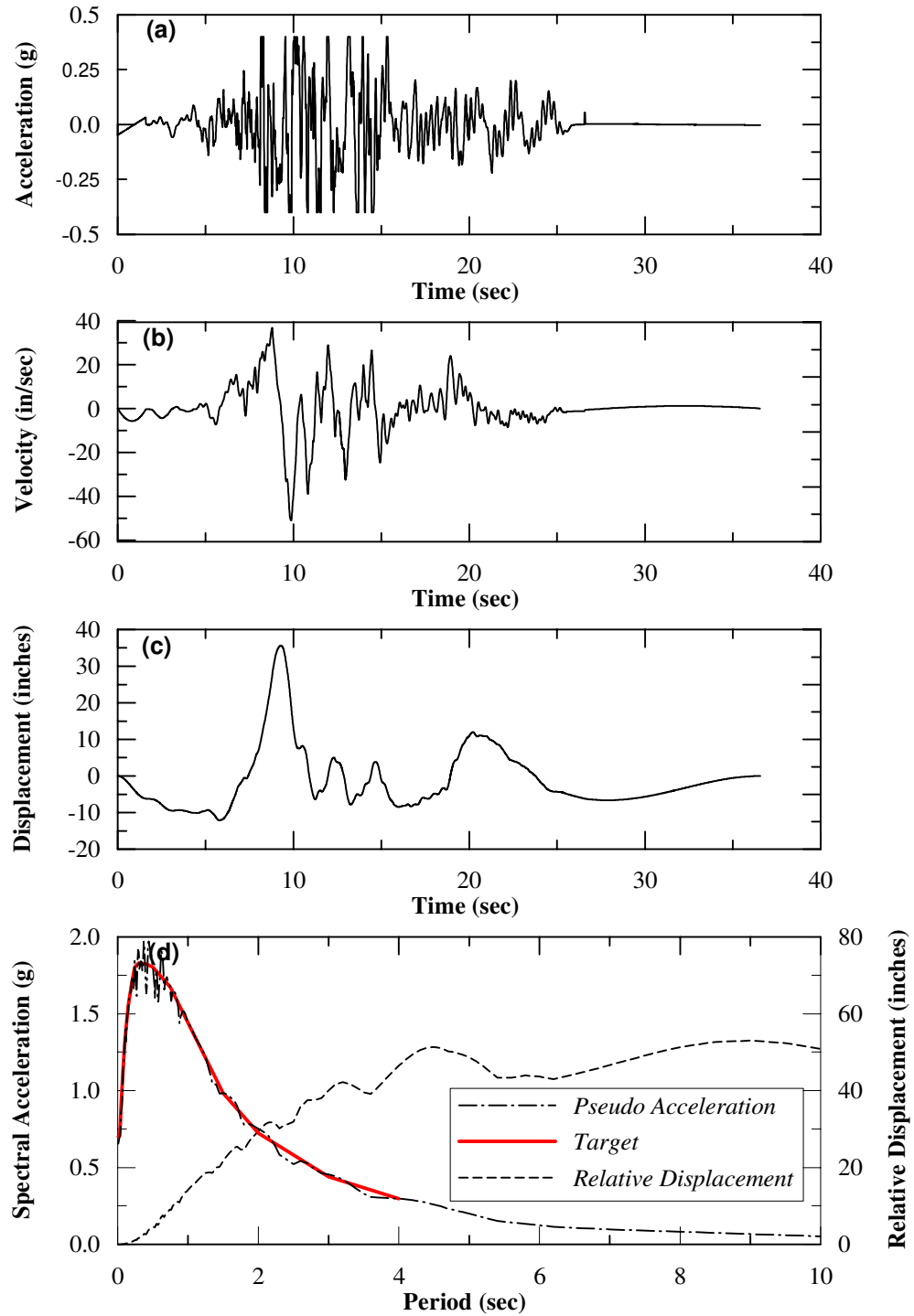


Figure 5.12: Input Ground Motion 5 in the Transverse Direction

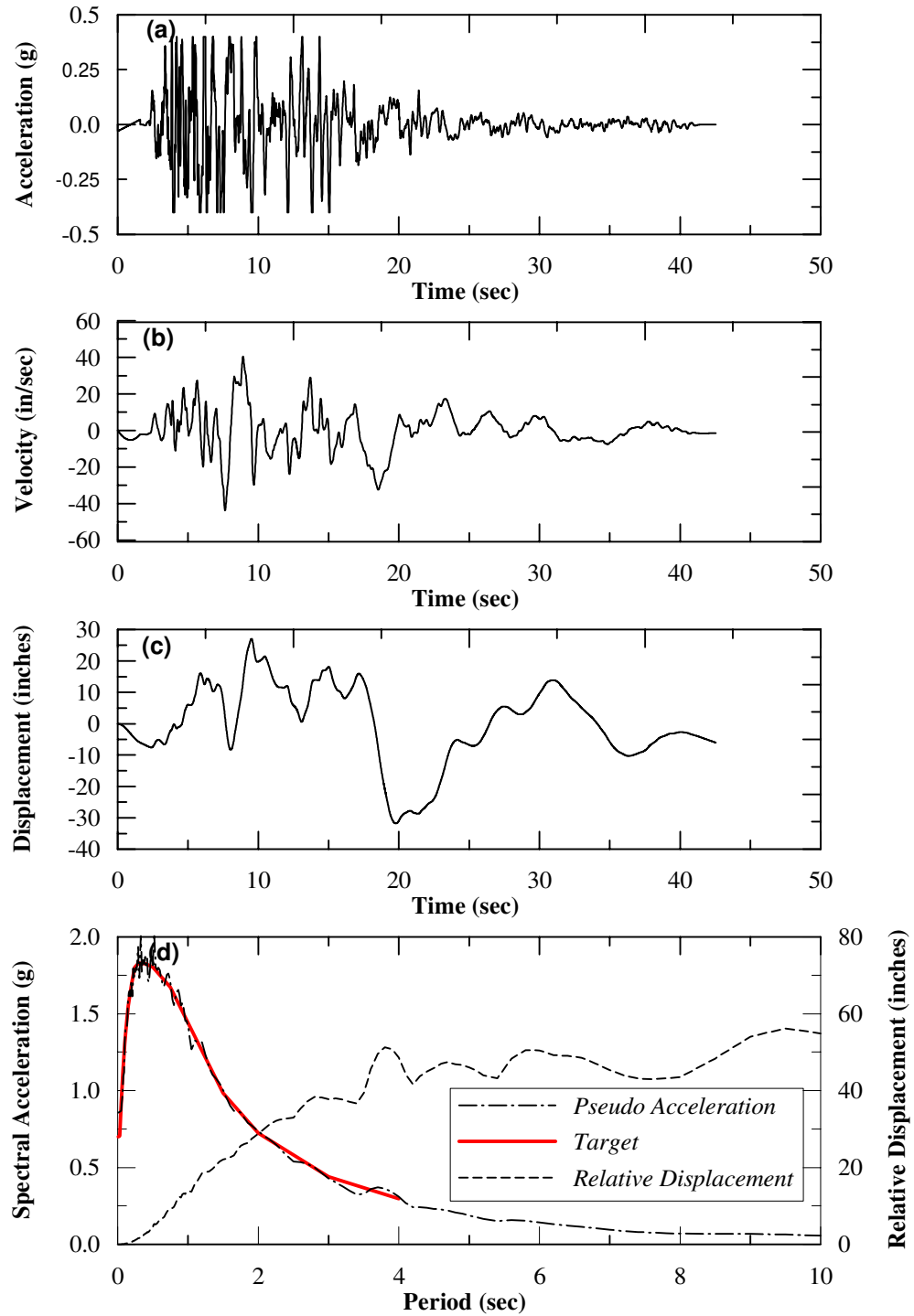


Figure 5.13: Input Ground Motion 6 in the Longitudinal Direction

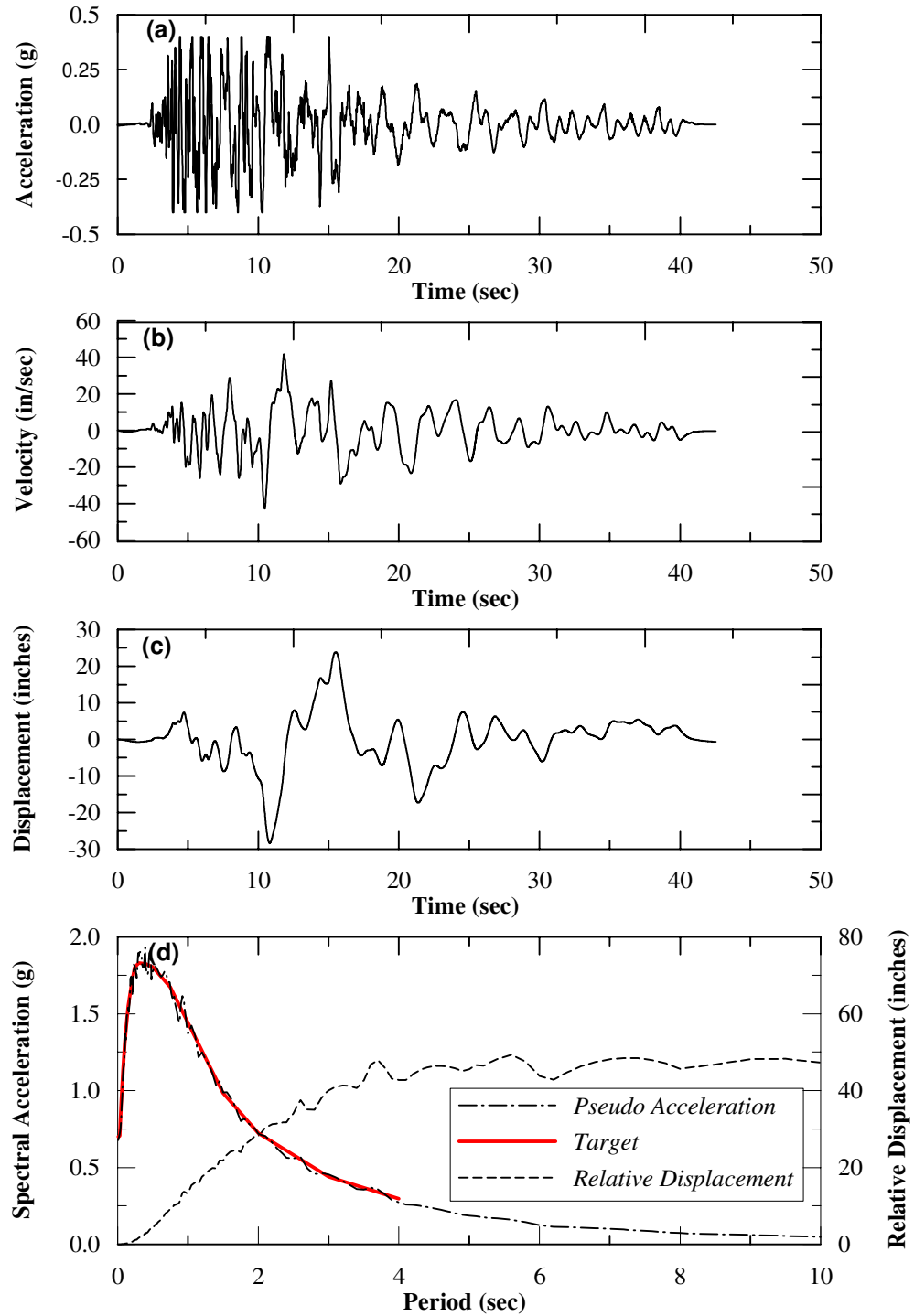


Figure 5.14: Input Ground Motion 6 in the transverse Direction

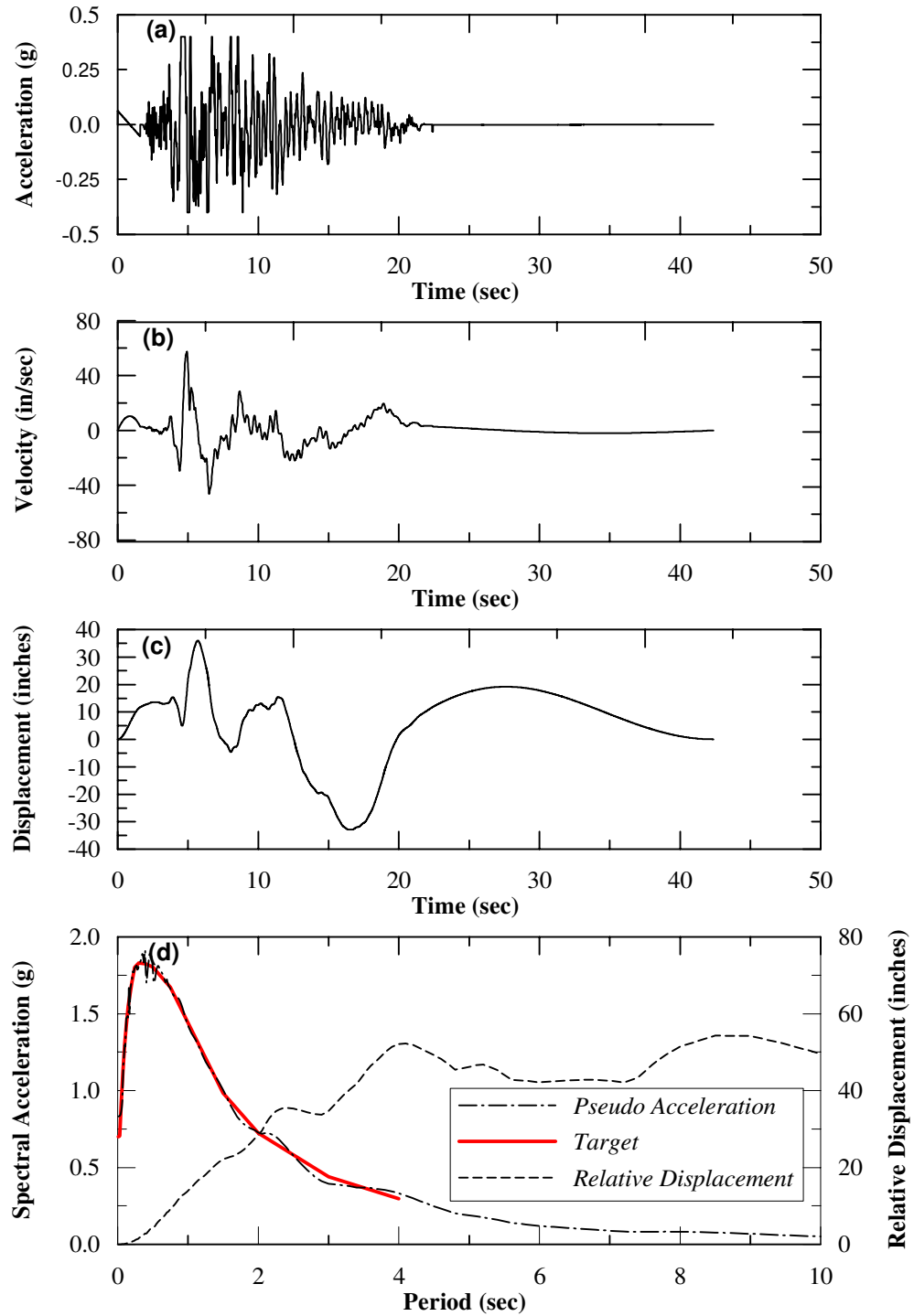


Figure 5.15: Input Ground Motion 7 in the Longitudinal Direction

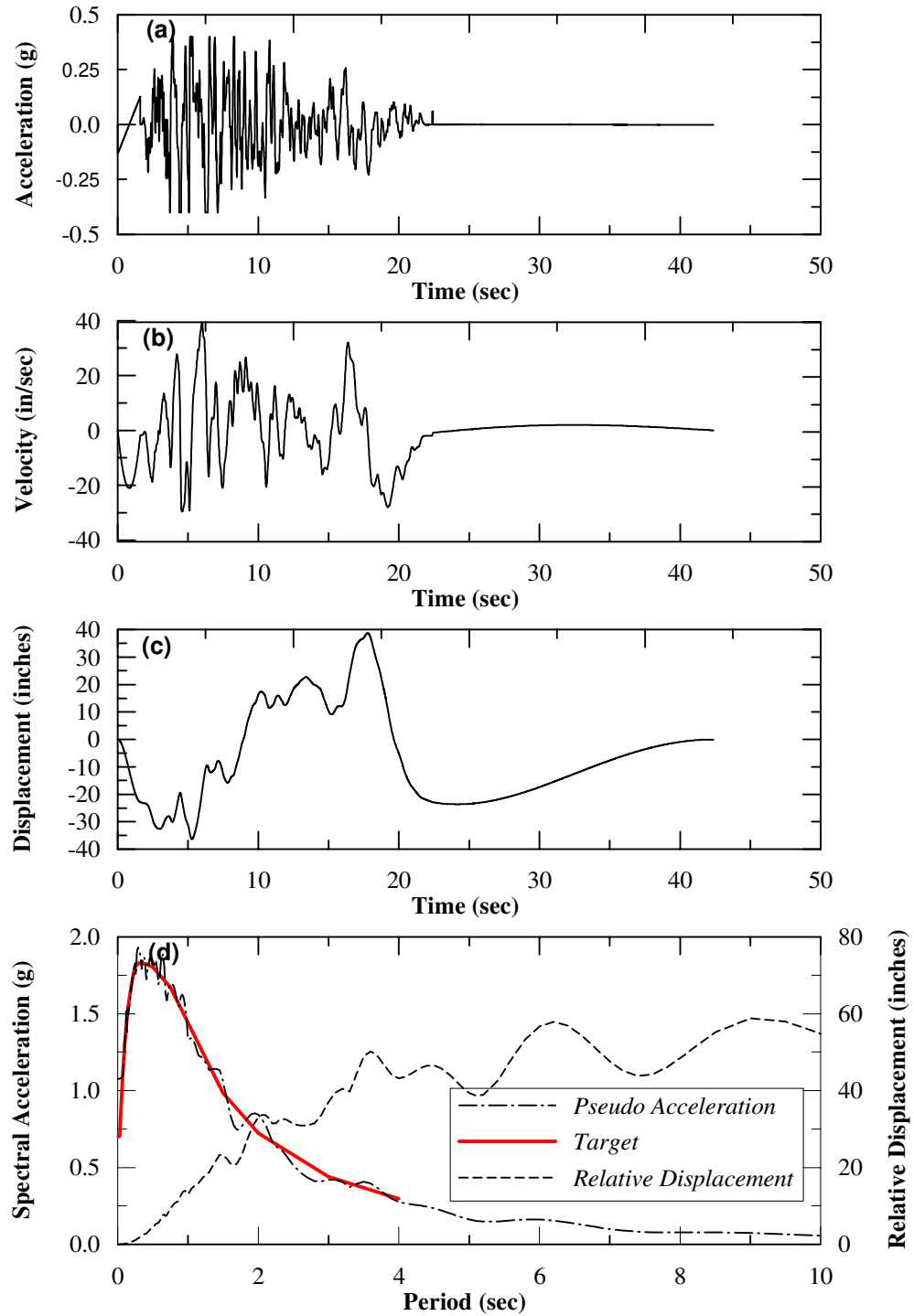


Figure 5.16: Input Ground Motion 7 in the Transverse Direction

5.4 Model's Boundary Conditions

Three-dimensional analytical finite element models are developed as a computational representation of various bridge structures. In order for the analytical models to accurately predict bridge-structure response, realistic boundary conditions are essential part of models. For the single-span bridge structures, the dynamic behavior of the structural system is completely dominated by the boundary conditions at the beginning and end of the analytical model. These boundary conditions for a single-span bridge are the nonlinear abutment-backfill and nonlinear abutment shear keys in the longitudinal and transverse directions respectively. For the multi-span bridge structures, in addition to boundary conditions at the beginning and end of the bridge system, nonlinear boundary conditions of the deck-column-soil-structure-foundation must be modeled accurately. For the dynamic analysis of bridge systems considered in this chapter, the beginning and ending boundary conditions (bridge abutments) are modeled as a set of nonlinear springs in both transverse and longitudinal directions. Pinned connections are used at the base of the columns. Descriptions of the boundary conditions for various bridge models are given later in this chapter.

5.4.1 Abutment Soil-Structure Interaction

The longitudinal abutment-backfill-structure interaction model is shown in Figure 5.17. The dynamic interaction between the deck, abutment backwall in the longitudinal direction and the abutment shear keys in the transverse direction were modeled by, gap elements between the bridge deck and the abutment backfill, gap

elements between the bridge deck and the abutment shear keys, nonlinear springs in the longitudinal direction representing the abutment backfill and nonlinear springs in the transverse direction representing the abutment shear keys. The bridge abutments are constrained in the vertical direction, while free to move in the horizontal longitudinal and transverse direction. However, once the relative motion of the bridge deck exhausts the abutment gap the bridge deck starts pounding on the abutment backfill.

5.4.2 Abutment Gaps

At each abutment, a one-inch structural expansion gap exists between the bridge deck and the abutment-backwall in the longitudinal direction as well as between the bridge deck and the abutment shear key in the transverse direction. Two methods were used to simulate the expansion gaps, (1) the gap elements in series with nonlinear backfill link elements, (2) only one nonlinear link element which includes the abutments expansion gaps as part of the nonlinear abutment-backfill backbone curve as shown in Figure 5.17 and Figure 5.19. The second nonlinear abutment model is more efficient and computationally less expensive.

5.4.3 Abutment Backwall-Backfill Longitudinal Response

The nonlinear spring represents the near-field load-deformation behavior at the longitudinal abutment-embankment soil interface. The hysteretic behavior of the backbone curve is modeled using the multi-linear plasticity model with the tension

side of the curve set to zero. The behavior is essentially that of a gap element in series with a compressive plastic spring s shown in Figure 5.17.

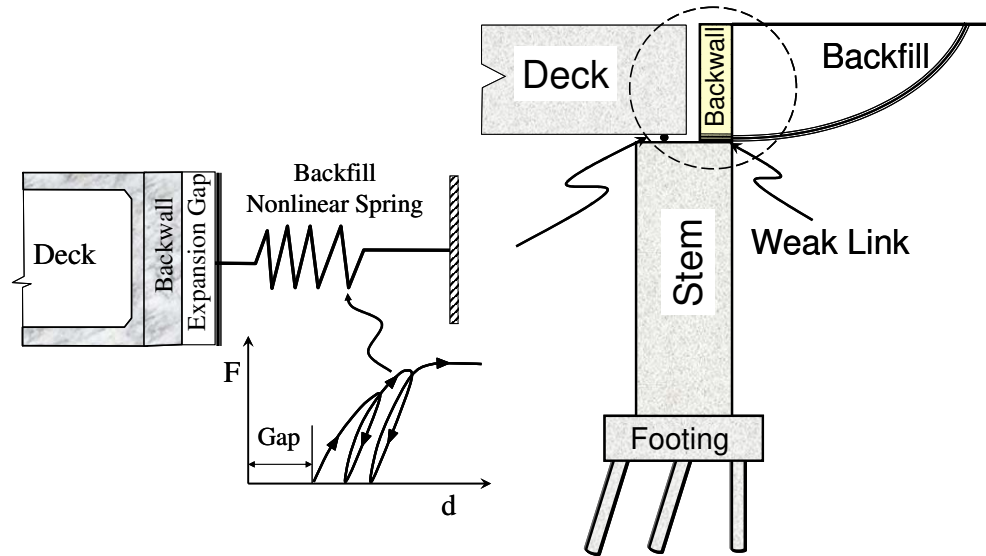


Figure 5.17: Bridge Monolithic Abutment Model

Upon load reversal, the spring unloads elastically until zero force is reached, with net permanent deformation present. Further loading in the tension direction acts as an open gap, with no force exhibited. Reloading in the compressive direction remains at zero force until the gap is closed at a deformation equal to the permanent plastic deformation. The spring loads elastically until the backbone curve is reached, then follows the backbone with increasing plastic deformation. A series of two nonlinear longitudinal abutment springs was used at the top and bottom of each girder.

5.4.4 Abutment Shear Key

The abutment shear keys are designed to support the bridge deck in the transverse direction and to act as a fuse in order to protect the abutment piles failure during a seismic event. As part of Caltrans seismic research program a large-scale experiment was conducted at USCD to investigate the seismic behavior of the abutment exterior shear key. The experimental nonlinear force deformation of the abutment exterior shear key is shown in Figure 5.18 (Bozorgzadeh et al., 2005).

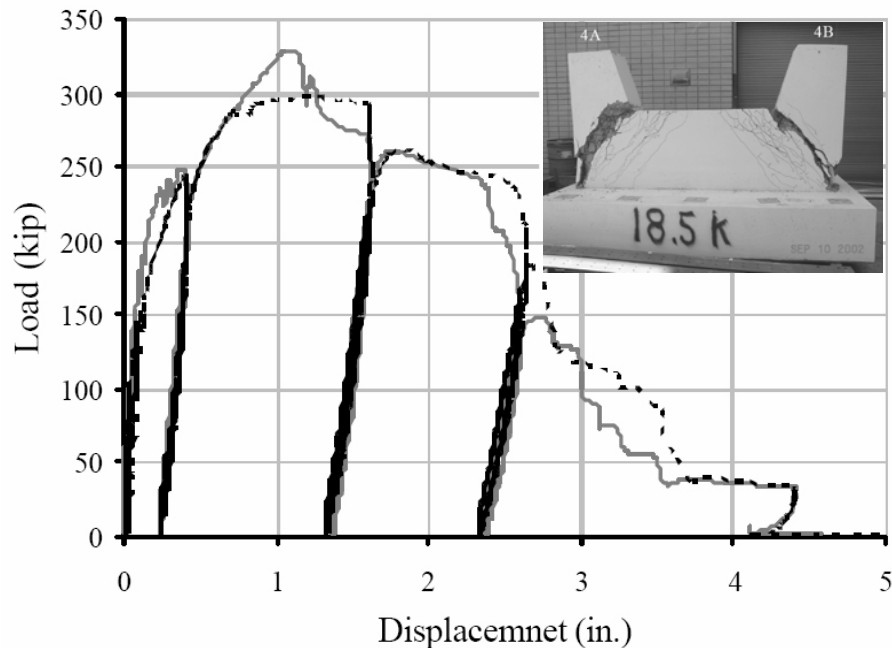


Figure 5.18: Abutment Shear Key Experiment (Bozorgzadeh et al., 2005).

In the present study the abutment transverse shear key behavior was simulated using a multi-linear plasticity model that addresses the structural capacity of the shear key as well as contribution of passive resistance of the abutment

embankment in the transverse direction as a function of relative displacement between bridge deck and abutment. The model included the 1-inch expansion gap between shear key and deck, and the limiting passive capacity of the embankment soil in the transverse direction. The generic nonlinear force-deformation relationship of the shear key backbone curve based on the USCD experiment used in the present study is shown in Figure 5.19.

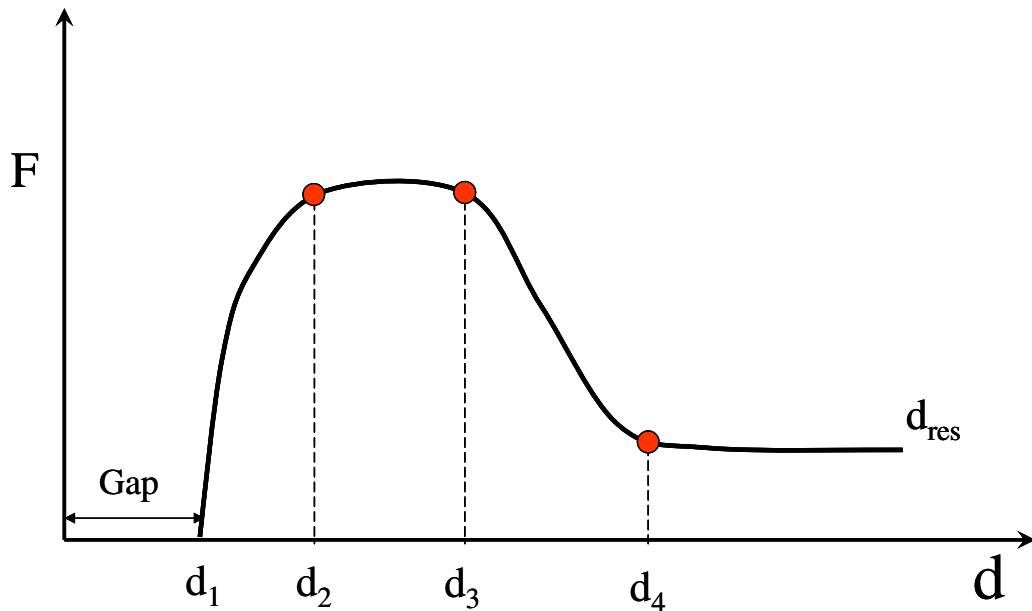


Figure 5.19: Generic Model of the Exterior Shear Key Backbone Curve

The curve has one inch gap, a nonlinear ascending branch from d_1 to d_2 , a yield plateau from d_2 to d_3 at the combined ultimate force deformation capacity of the shear key and transverse-abutment-soil capacity, a descending branch from d_3 to d_4 and residual branch d_{res} .

5.4.5 Validation of Abutment Model

Nonlinear link element available in SAP2000 computer program was used to model the abutment backfill and the shear keys. The UCD abutment test which was subjected to a series of longitudinal displacement cycles as shown in Figure 5.20. Figure 5.21 was used to validate the cyclic behavior of the nonlinear link element. The link element was model using the nonlinear backbone curve predicted using LSH model. The link element was subjected to the experimental UCD cyclic loading shown in Figure 5.20. Figure 5.22 shows the simulated load-displacement response of the abutment backfill using the cyclic displacement history of the test specimen. The simulated results from SAP2000 agree reasonably well with the measured results for the displacement controlled longitudinal abutment field experiment. Therefore, link elements available in SAP2000 are capable of simulating the dynamic behavior of the bridge abutment subjected to earthquake loading. The longitudinal and transverse abutment backbone curves including one inch expansion gap used in all the global models presented in this chapter are shown in Figure 5.23.

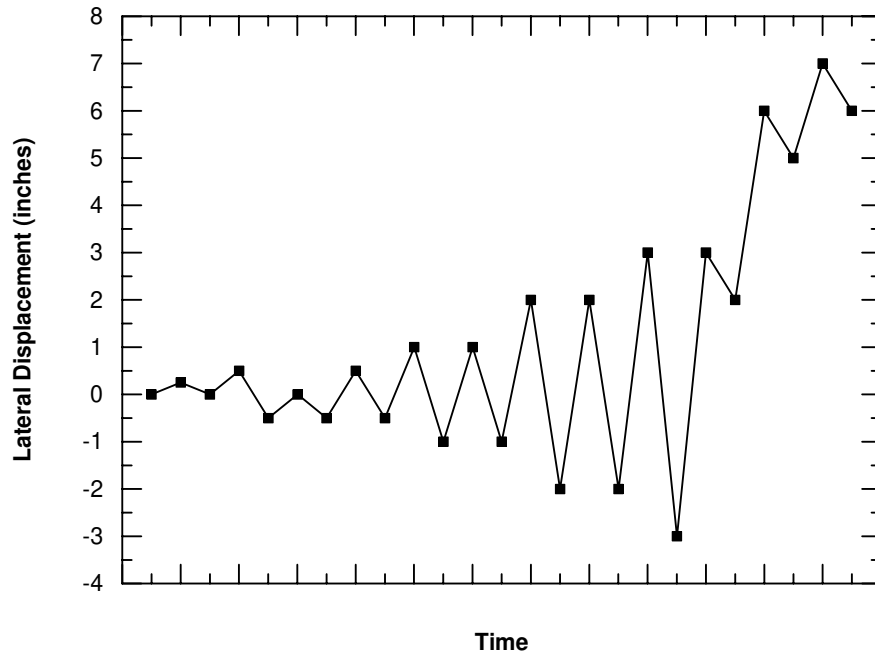


Figure 5.20: Displacement Cycles in the UCD Abutment Test (Romstad et al., 1995)

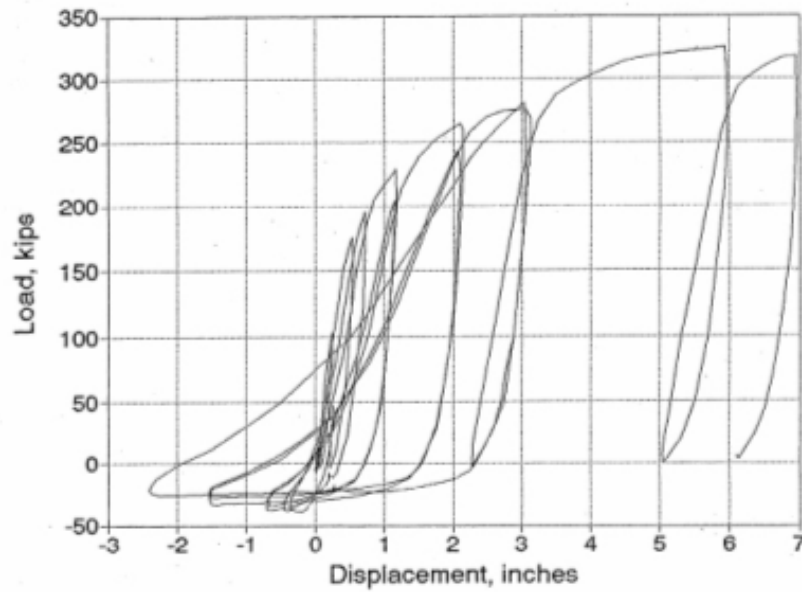


Figure 5.21: Measured Load-Deformation in the UCD Abutment Test (Romstad et al., 1995)

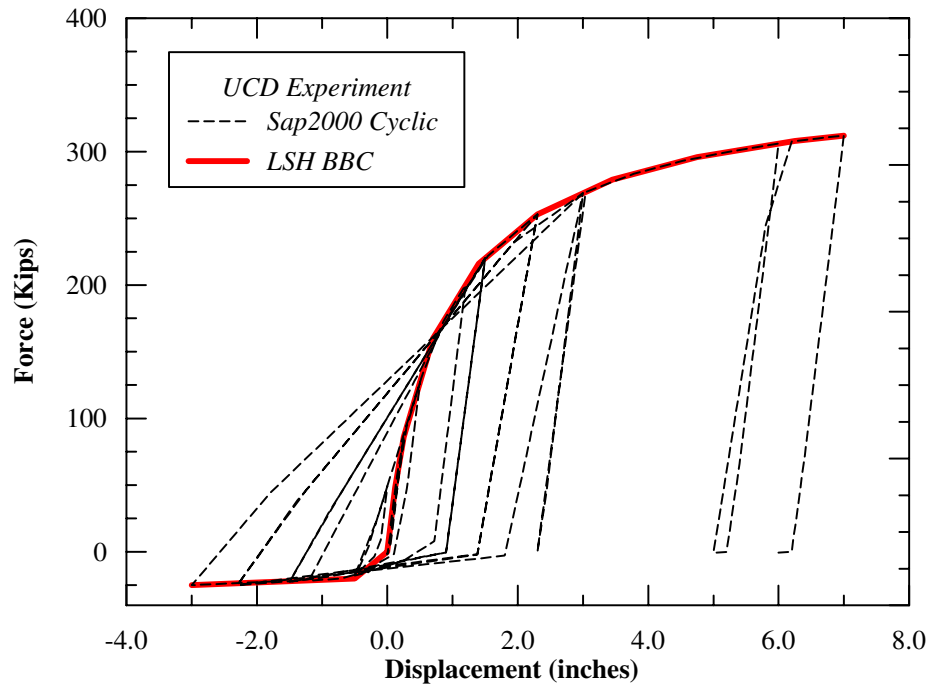


Figure 5.22: Simulated Longitudinal Response of the UCD Abutment Test

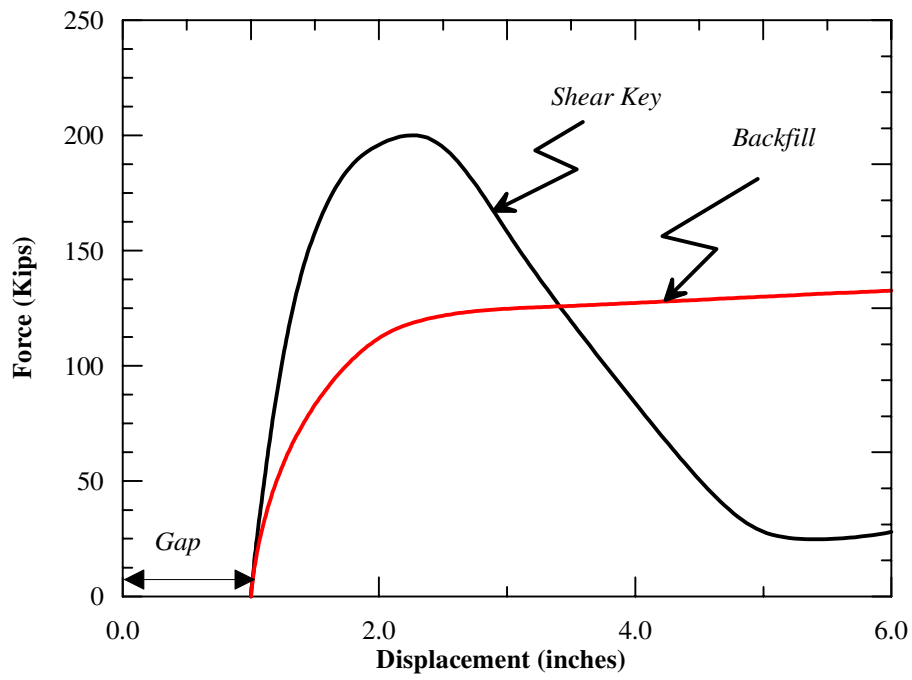
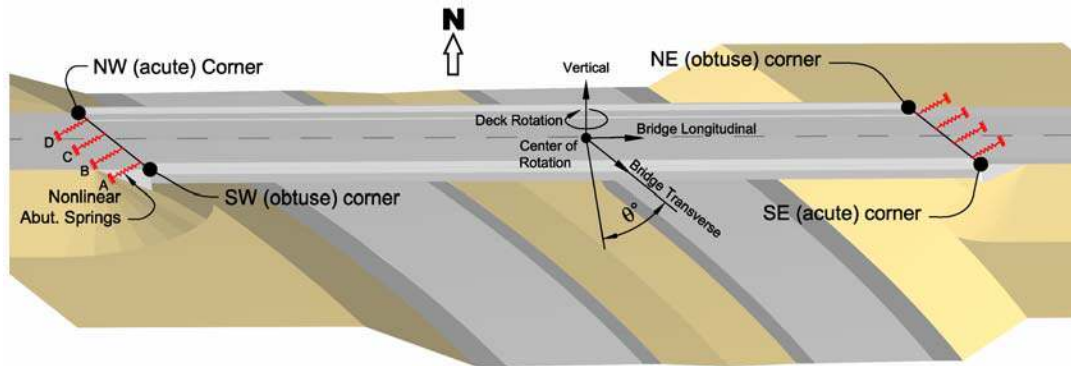


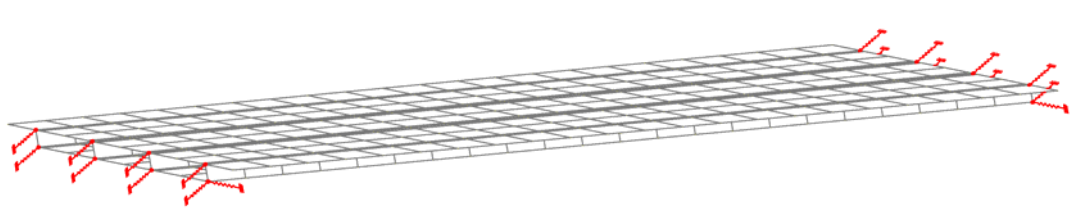
Figure 5.23: Longitudinal and Transverse Backbone Curves Used in the Bridge Global Models

5.4.6 Bridge Deck Model

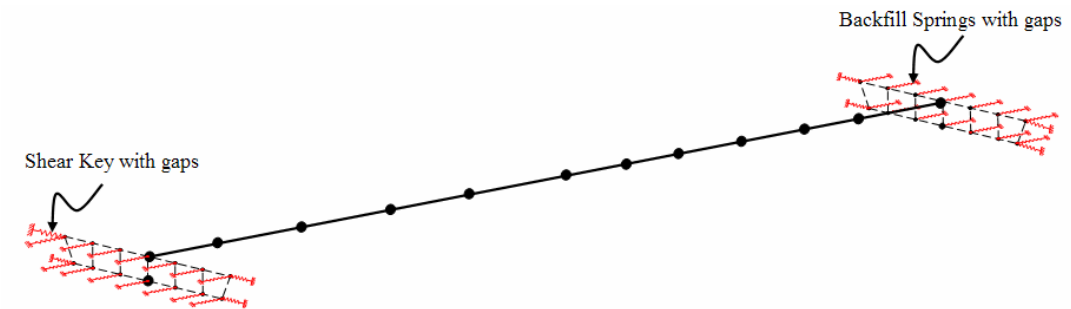
Since the bridge decks are extremely stiff and strong in compression with supporting columns and abutments, the bridge response during a major seismic event is primarily dominated by the inelastic deformation of the columns and bridge abutment backfill. The deck will remain elastic and, therefore, can be modeled by linear elastic elements. Both shell elements and frame elements with superstructure properties can be used to model the bridge deck. Shell and frame elements have their advantages and disadvantages. Since the global seismic behavior of skewed bridges is affected not only by skew angle but also by the deck width, the deck flexibility and the deck mass distribution, shell elements are more appropriate to represent the bridge deck. However, the shell elements are computationally expensive. In this respect, first the bridge deck is modeled using full three-dimensional shell elements (shell model) to account for the realistic properties of the bridge deck. On the other hand the bridge deck modeled with beam elements (spline model) can represent effective stiffness characterization very well but it is not a good representation of bridge width and the mass distribution of the bridge deck. Therefore, first the models were developed using shell elements to represent the bridge deck model. Figure 5.24 shows the 3D view for the shell and spline models of a single-span bridge structure. The seismic response of shell and spline models was found to be comparable. The simpler spline models were much less computationally intensive than the shell models.



(a) Bridge Geometry



(b) Shell Model



(c) Spline Model

Figure 5.24: Typical Bridge Model

5.4.7 Bridge Columns

Per Caltrans SDC, moment-curvature of the column cross sections for a range of strain values were calculated to develop an idealized moment-curvature relationship and plastic moment capacity of the column as shown in Figure 5.25.

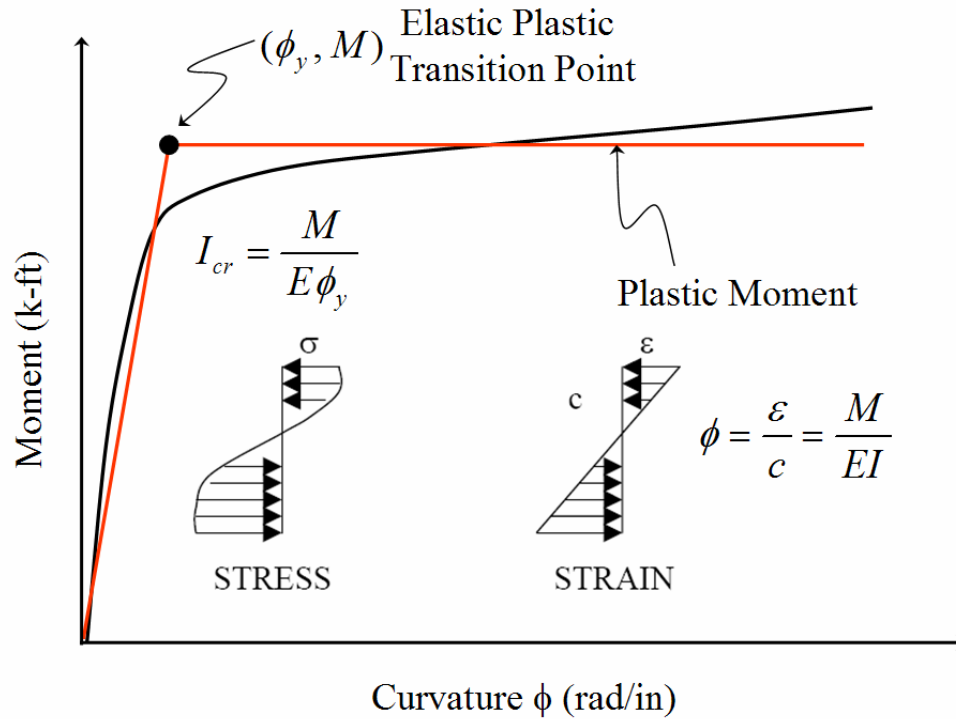


Figure 5.25: Column Moment-Curvature Relationship

The calculated plastic moment was used at the top of the column to simulate the plastic hinge action during a seismic event. Pinned connections were used at the base of the column. SAP2000 was used to develop the moment-curvature relationship of the column cross-section.

5.5 Bridge Models

In the present research, the longitudinal and transverse response of continuous reinforced concrete box girder bridge structures of 1, 2 and 3 spans as shown in Figure 5.26 to Figure 5.30 are investigated. All bridge models are subjected to the same seismic ground motions with high velocity pulses. The bridge decks were supported by bearing pads on seat-type abutments and rigidly connected to reinforced concrete columns. The following classes of bridge structures are investigated.

1. Bridge No. 1 - A typical single-span bridge,
2. Bridge No. 2 - A two-span with a single-column center bent,
3. Bridge No. 3 - A two-span bridge with a dual-column at the center bent,
4. Bridge No. 4 - A three-span bridge with single-column bents, and
5. Bridge No. 5 - A three-span bridge on two bents supported by two columns per bent based.

In order to determine a meaning full seismic analysis of the above bridge configurations, typical existing bridge structures with well defined traffic lanes, shoulders as well as span length were selected. These bridges were based on actual bridge plans from a single-span Meloland Road Bridge in Imperial County, a two-span LaVeta Avenue Bridge and a three-span Redhill Avenue Bridge both located in Orange County. Three-dimensional finite-element models of various bridge structures were developed using SAP2000 (2006). Descriptions of bridge components used in the three-dimensional models are given bellow.

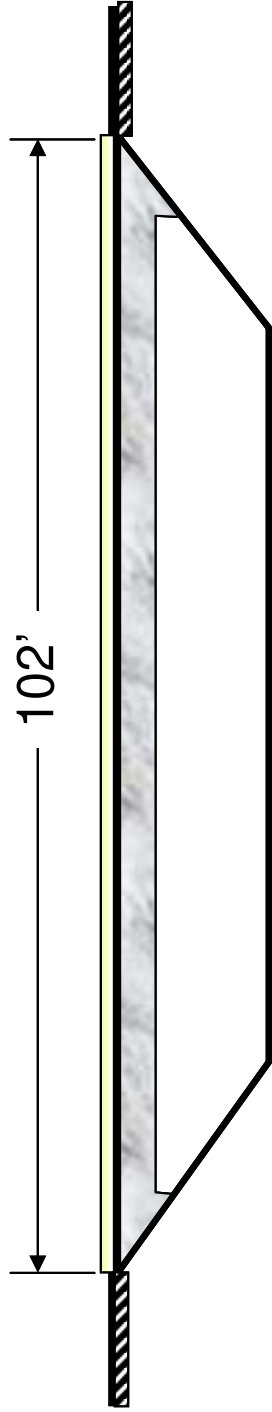


Figure 5.26: Single-Span Bridge

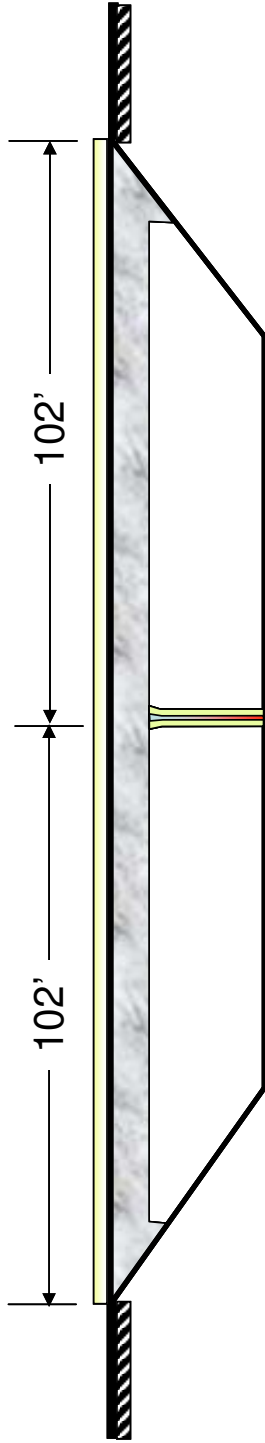


Figure 5.27: Single-Column Two-Span Bridge

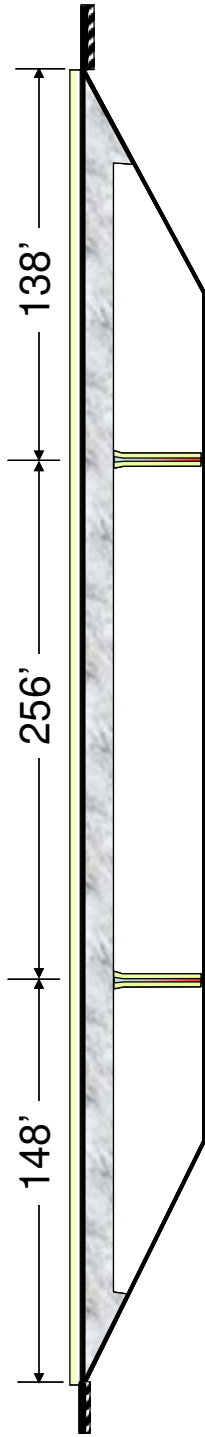


Figure 5.28: Single-Column Three-Span Bridge

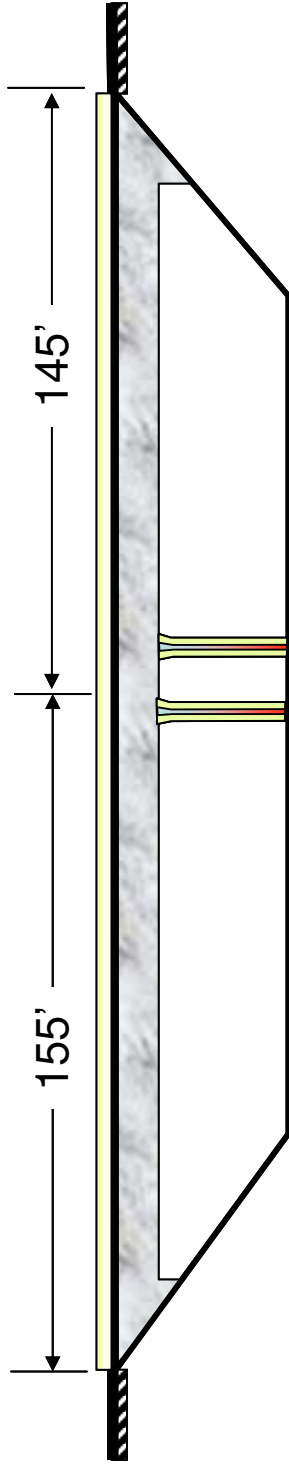


Figure 5.29: Tow-Columns Two-Spans Bridge

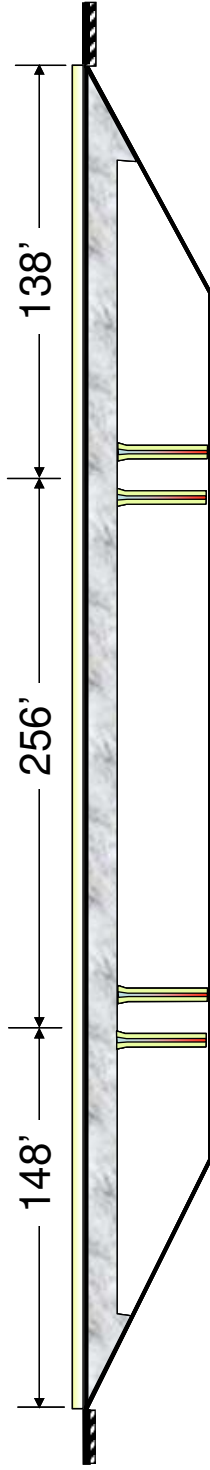


Figure 5.30: Tow-Columns Three-Spans Bent Bridge

5.6 Analytical Study

The investigation is limited to single-span, two-span and three-span ordinary bridge structures. The following are some of the criteria used in selection of bridges for this study:

Bridge alignment has no horizontal or vertical curves

- Original models started with no skew angle
- Bridge models with 25, 45 and 60 degree skew angle were developed from the original models
- The bridge is constructed very recently with modern design and construction techniques

Three-dimensional finite-element models of various bridge structures were developed using both shell and frame elements with appropriate superstructure properties. Frame elements with moment curvature and cracked sectional properties were used to model bridge columns. Nonlinear springs were used to model the bridge abutments. A total of five typical bridge configurations were modeled. The bridge structures selected for this study are described in the following sections.

5.6.1 Bridges Types

The investigation was limited to single-span, two-span and three-span ordinary standard bridges. The bridge alignments have no horizontal or vertical curves, but the skew angles vary from 0 to 60 degrees. Full 3D nonlinear finite element model of the soil-abutment-structure interaction (SASI) for all bridge structures were developed. The purpose of the first three analytical models is to

study the impact of the skew angles on the dynamic behavior of ordinary bridge structures. The Meloland Road Overpass, located near El Centro in southern California was selected for the first three analytical models.

The Meloland Road Overpass is a very simple non-skewed two-span cast-in-place reinforced concrete box girder bridge structure with monolithic abutments. The bridge was strongly shaken by the October 1979 Imperial Valley Earthquake of magnitude 6.4. However, even bridge was shaken by such strong earthquake virtually no damage was observed in the bridge. Since the purpose of this chapter is to investigate the nonlinear SASI, it was assumed that all bridge structures have set-type abutment for the analytical models.

5.6.2 Single-Span Bridge

The longitudinal and transverse sections of the model are shown in Figure 5.31. It is assumed that the deck is supported at the two-ends on abutment bearing pads resting on the set-type abutment with one-inch expansion gap. The length and width of the bridge is assumed approximately 102 feet long and 34 feet wide respectively. The depth of the superstructure is 5.5 feet. The bridge model is constrained at each abutment in the vertical direction but free to move in the horizontal direction. In the analyses, the ground motion is prescribed at the end of the nonlinear abutment springs. Since there is no bridge column, during a seismic event upon the abutments gap closure the bridge deck will impose time varying pounding forces and displacement directly to the bridge abutment in the transverse

and longitudinal directions. Three-dimensional shell and spline finite element models of the bridge are shown in Figure 5.24.

5.6.3 Two-Span Bridge

Only the deck cross section and the column cross section of this model was developed based on the Meloland Road Overpass. However, for the analytical model a two-span cast-in-place reinforced concrete box girder bridge with a continuous deck which is supported by bearing pads on the seat-type abutments with one-inch expansion gap was considered. The bridge deck is rigidly connected to a single reinforced concrete column at the bent cap as shown in Figure 5.27.

The geometry of the model was exactly the same as that of Meloland Road Overpass. The model bridge is approximately 204 feet long and 34 feet wide. The depth of the superstructure is about 5.5 feet. The bridge column is 35 feet tall and 5 feet in diameter as shown in Figure 5.32. The bridge deck is constrained in all degrees of freedom at the bent cap but it is constrained at each abutment only in the vertical. In the analyses, the ground motion is prescribed at the bottom of the column and the end of the nonlinear abutment springs. First the three-dimensional finite-element models of bridge deck was developed using shell elements. The shell model was converted to the spline model.

The frame element with moment curvature and cracked sectional properties was used to model bridge column. Plastic hinge was used at the top and pinned connections at the base of the column. The plastic hinge was calculated using an idealized bilinear moment-curvature relationship taking bridge axial load as well as

confinement effect into account. Cross section and idealized moment-curvature of the column is shown in Figure 5.33.

5.6.4 Three-Span Bridge with a Single-Column Bent

The third bridge considered in the analysis is a continuous three-span cast-in-place reinforced concrete box girder bridge which is supported by bearing pads on the seat-type abutments with one-inch expansion gap and rigidly connected to a single reinforced concrete column at the bent caps. The bridge has a total length of 642 feet as shown in Figure 5.28. The cross section of the deck, the cross section of the columns and the height of the columns are identical to the two-span bridge structure shown in Figure 5.32. The analytical models of the bridge are shown in Figure 5.34.

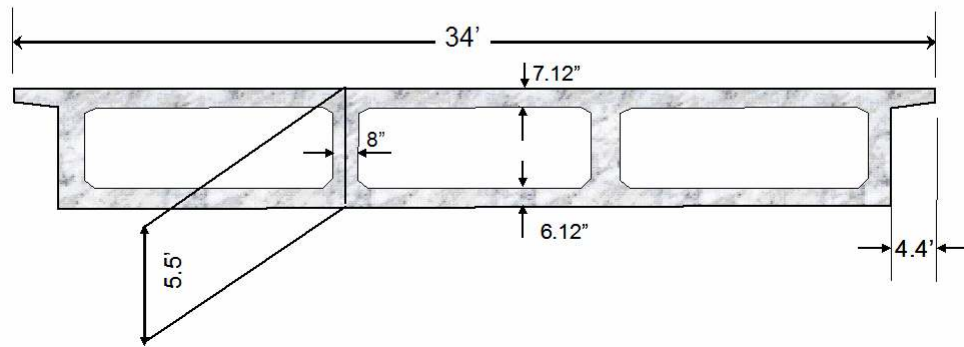
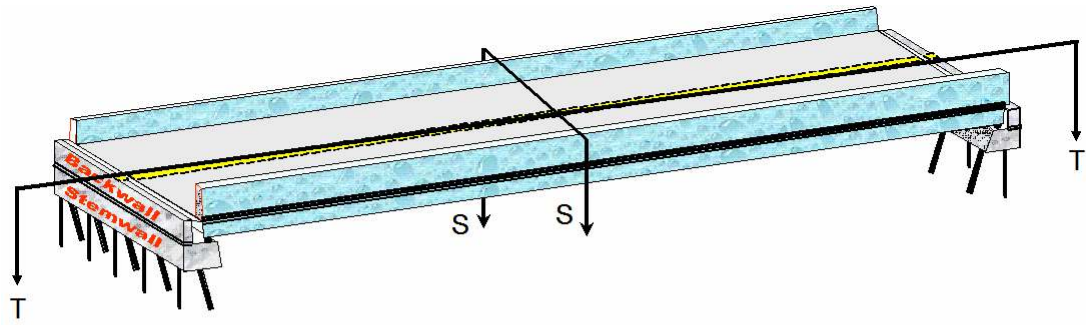
5.6.5 Two-Span Bridge with Two-Column Bent

The analytical model was developed based on the As-Built plan for the LaVeta Avenue Overcrossing bridge structure. The existing bridge structure is approximately 286 feet long and 75.5 feet wide. The deck is a 6.25 feet thick box girder supported on two-column bents, each 25.5 feet high. The span lengths are 155 and 145 feet, respectively. The bridge deck is continuous and is rigidly connected to the reinforced concrete columns at the bent cap and is supported by bearing pads on the seat-type abutments with one-inch expansion gap. There is pin connection at the bottom of the flared columns to the pile cap. The longitudinal and transverse

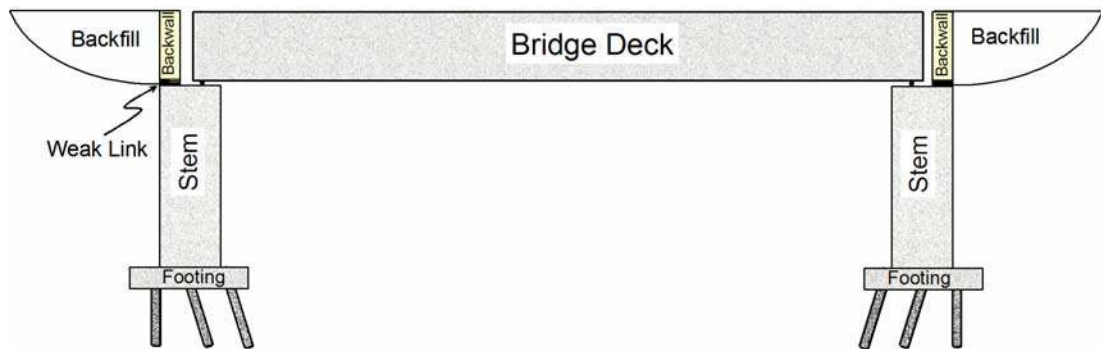
sections of the model are shown in Figure 5.35. Cross section and idealized moment-curvature of the column is shown in Figure 5.36.

5.6.6 Three-Span Bridge with Tow-Column Bents

The analytical model is based on Redhill Avenue Over Crossing. The bridge site is located in the southern end of the Los Angeles physiographic basin, at the San Diego freeway (I-405) adjacent to the John Wayne Airport. The Red Hill Avenue Over Crossing is a three-span haunch cast-in-place prestressed reinforced concrete box girder bridge supported on dual-column bents and seat type abutments with a 25 degree skewed angle. The average height of the columns is approximately 40 feet. The bridge is approximately 642 feet long and 72 feet wide with spans measuring 148, 256, and 138 feet. The depth of the deck varies from minimum of 6.5 feet (at each abutment and at the midpoint of each span) to a maximum of 13 feet (at the bent caps). There is pin connection at the bottom of the flared columns to the pile cap. The reinforced concrete columns with interlocking spiral reinforcements were used to construct the bridge columns. The longitudinal and transverse sections of the model are shown in Figure 5.37. The analytical shell and spline model are shown in Figure 5.38. The interlocking spirals provide confinement to enhance ductility of the columns. The idealized moment-curvature of the columns in the longitudinal and transverse direction of the bridge alignment are shown in Figure 5.39.

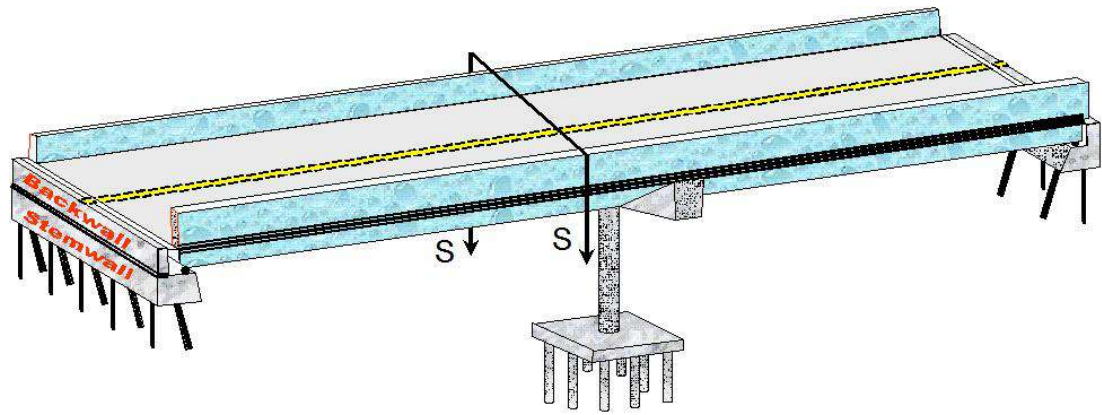


(a) Section S-S

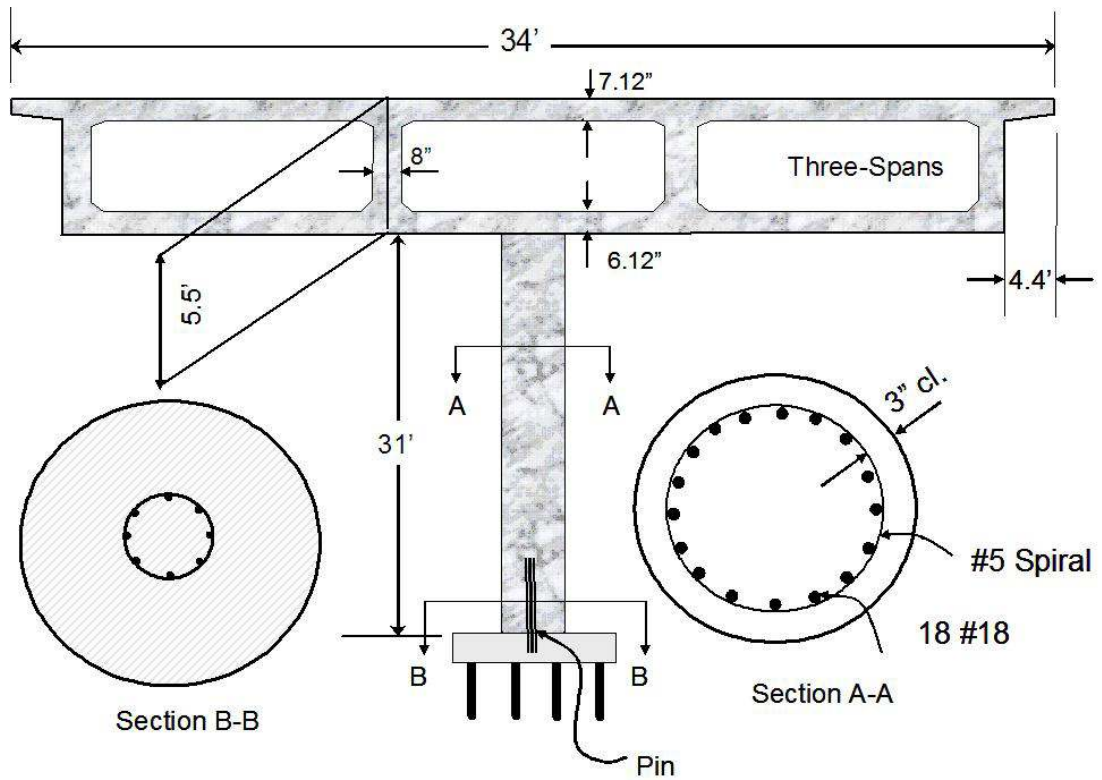


(b) Section T-T

Figure 5.31: Transverse and Longitudinal Sections of the Single-Span Bridge

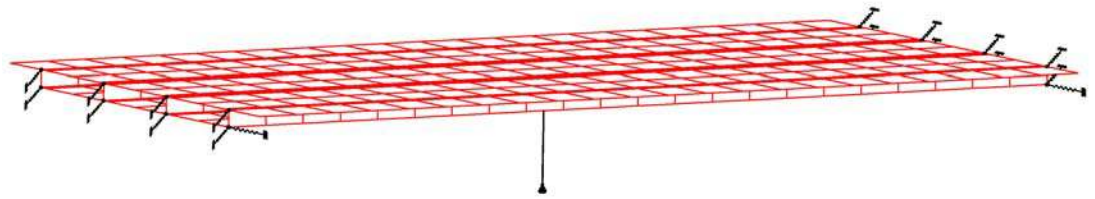


(a) 3D View

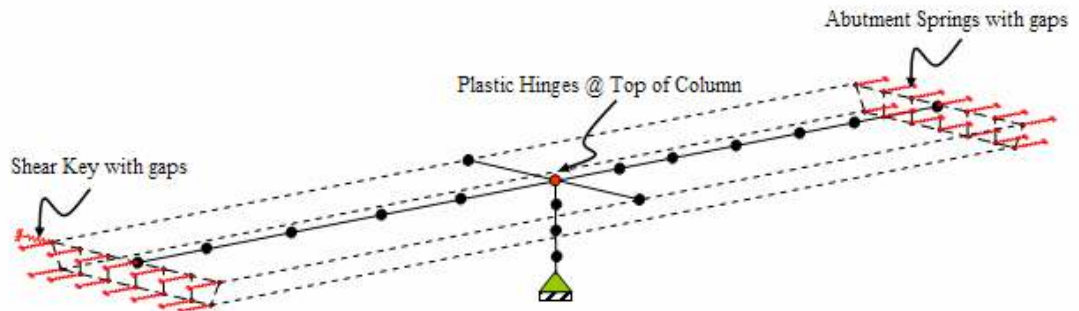


(b) Section s-s

Figure 5.32: Transverse Section of the Two-Span Single-Column Bridge



(a) 3D Shell Model



(b) 3D Spline Model

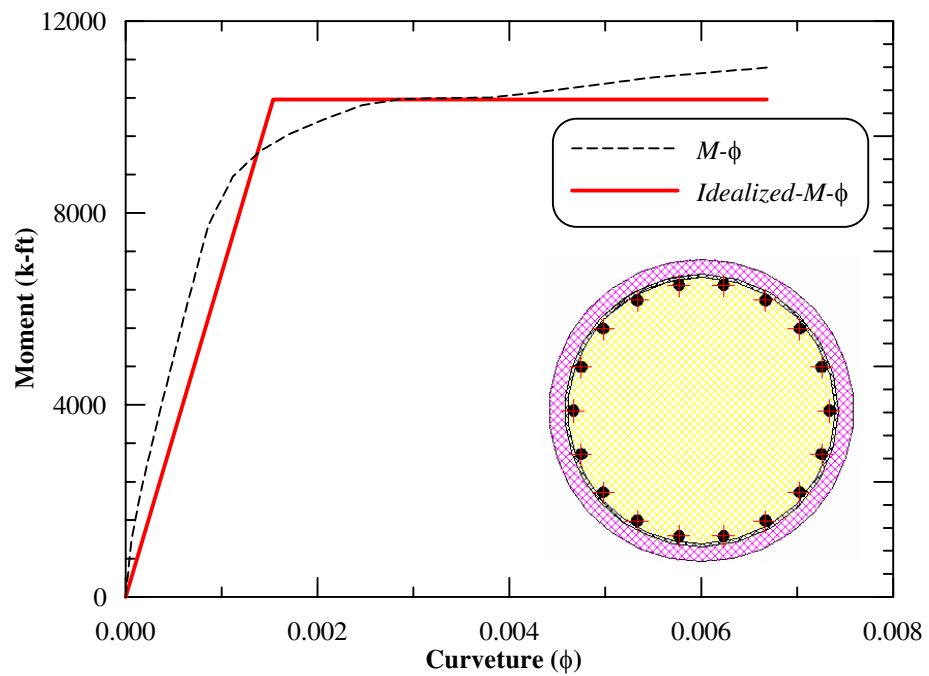
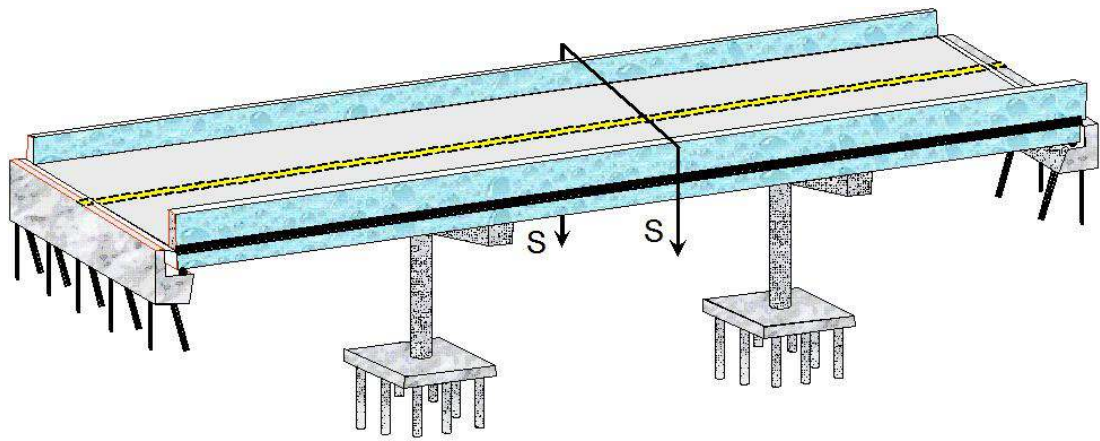
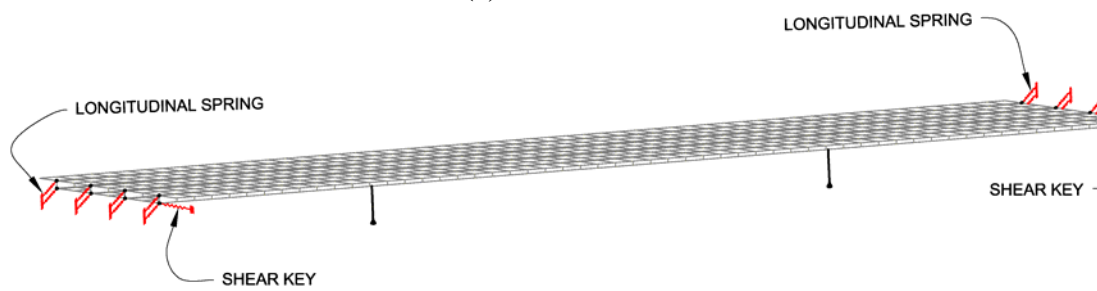


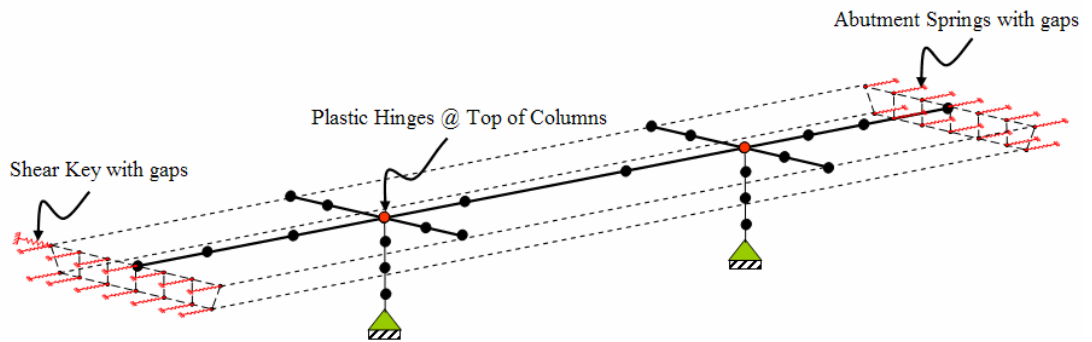
Figure 5.33: Analytical Models of the Two-Span Single-Column Bridge



(a) 3D View

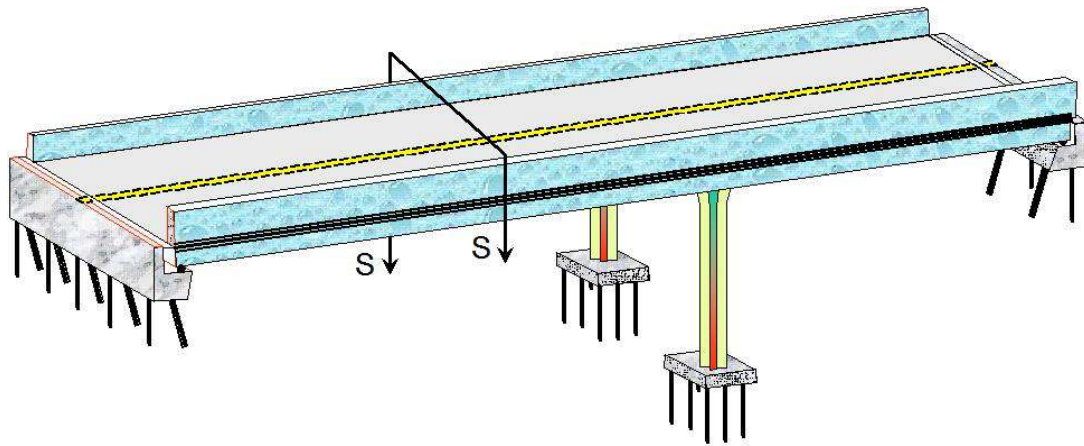


(b) Shell Model

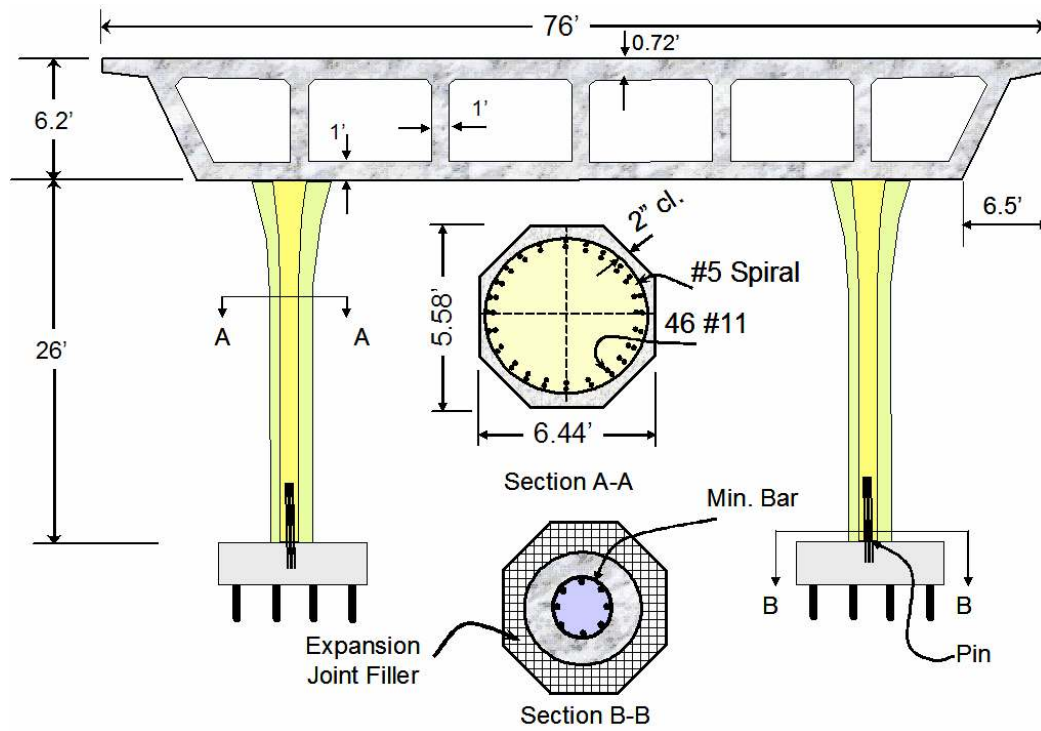


(c) Spline Model

Figure 5.34: Analytical Models of the Three-Span Single-Column Bridge

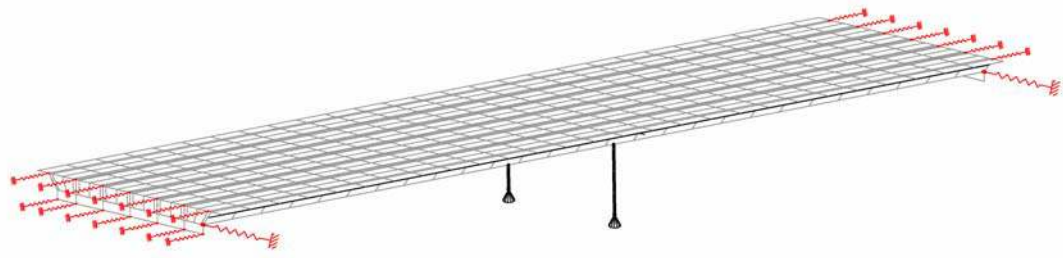


(a) 3D View

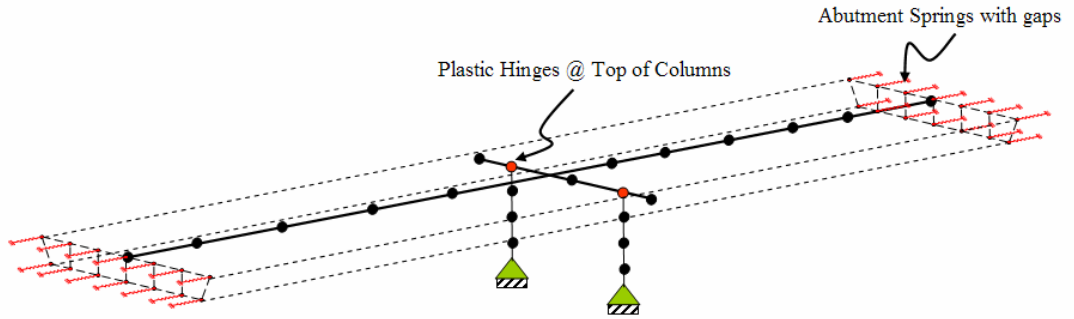


(c) Section S-S

Figure 5.35 Transverse Section of the Two-Span Two-Column Bridge



(a) Shell Model



(b) Spline Model

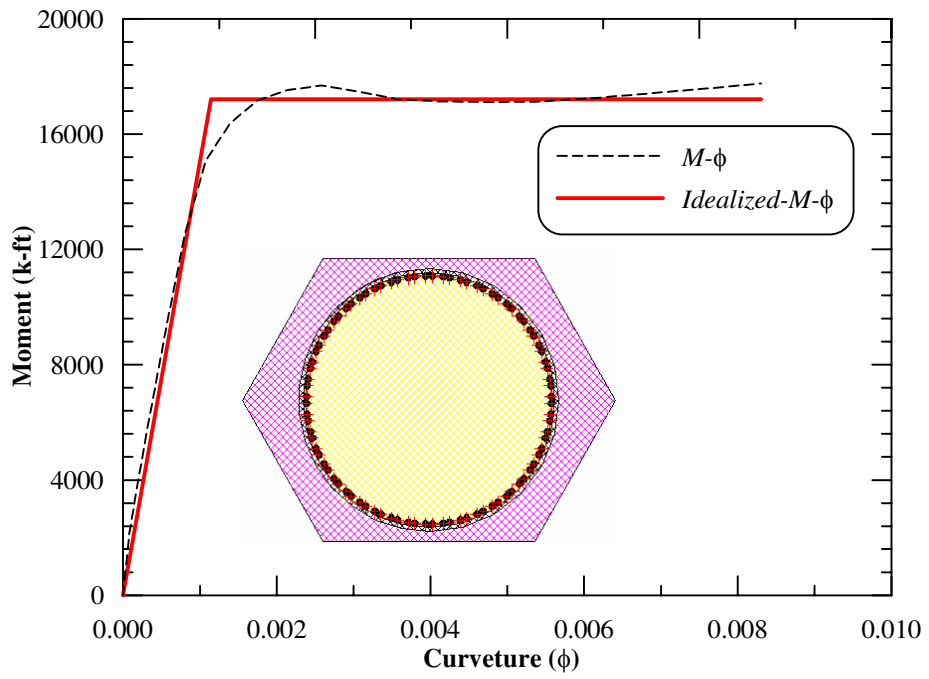
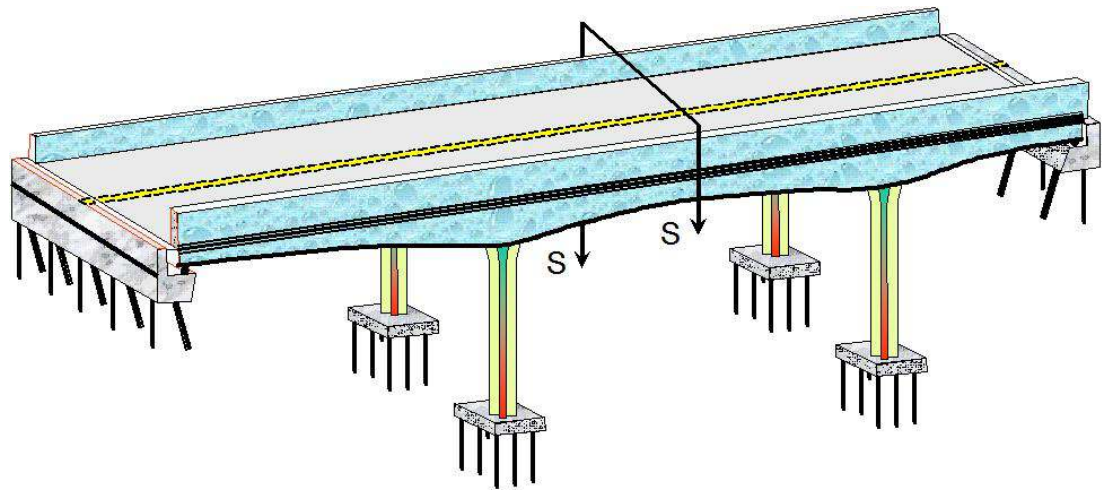
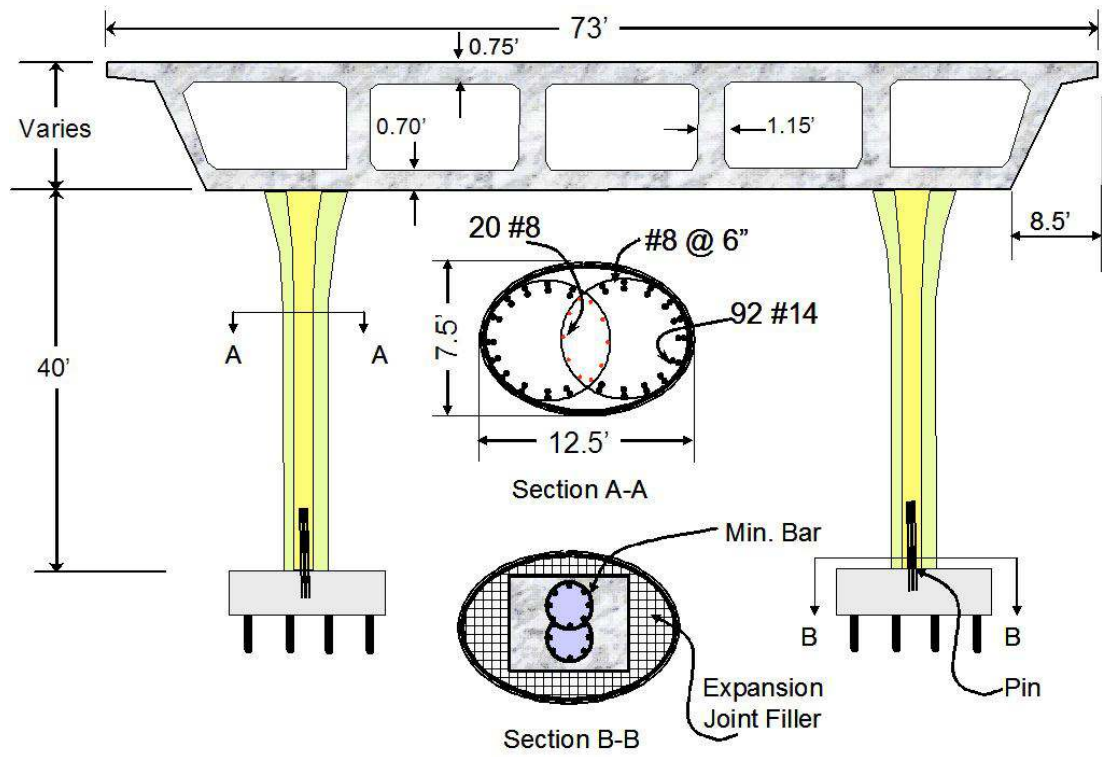


Figure 5.36: Analytical Models of the Two-Span Two-Column Bridge

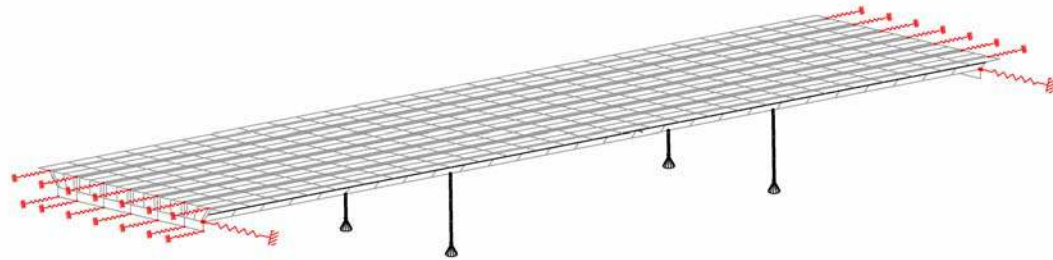


(a) 3D View

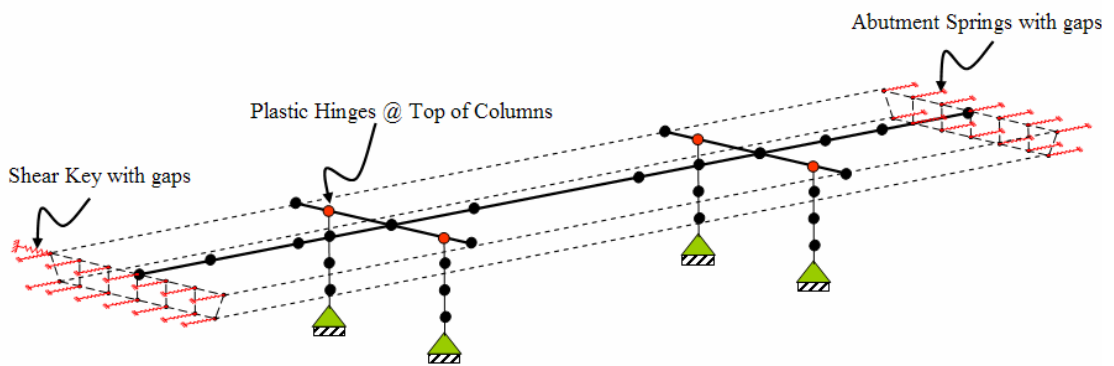


(b) Section S-S

Figure 5.37: T Transverse Section of the Three-Span Two-Column Bridge

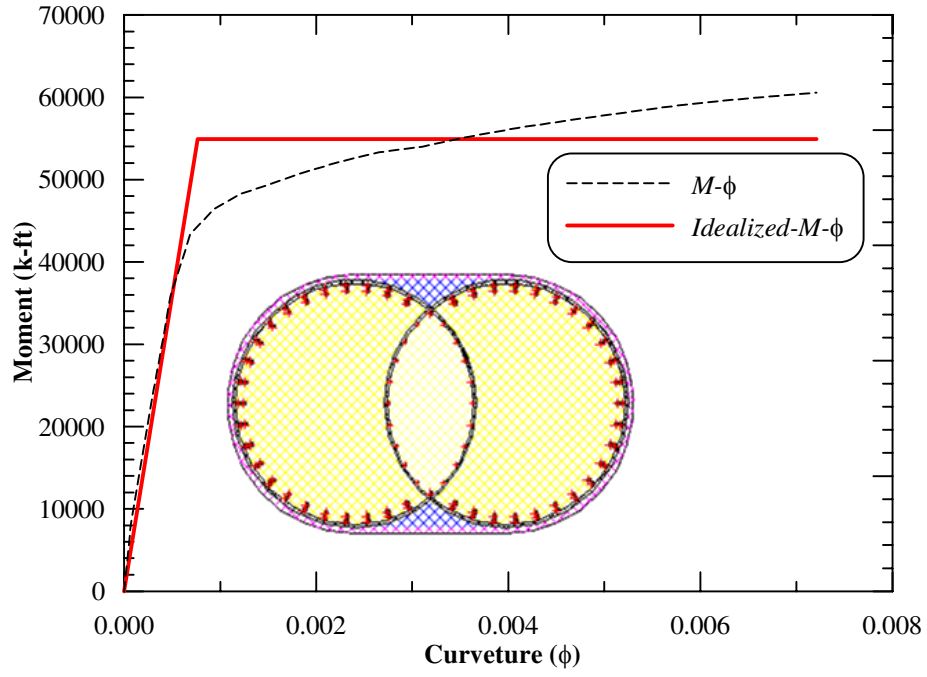


(a) 3-D Shell Model

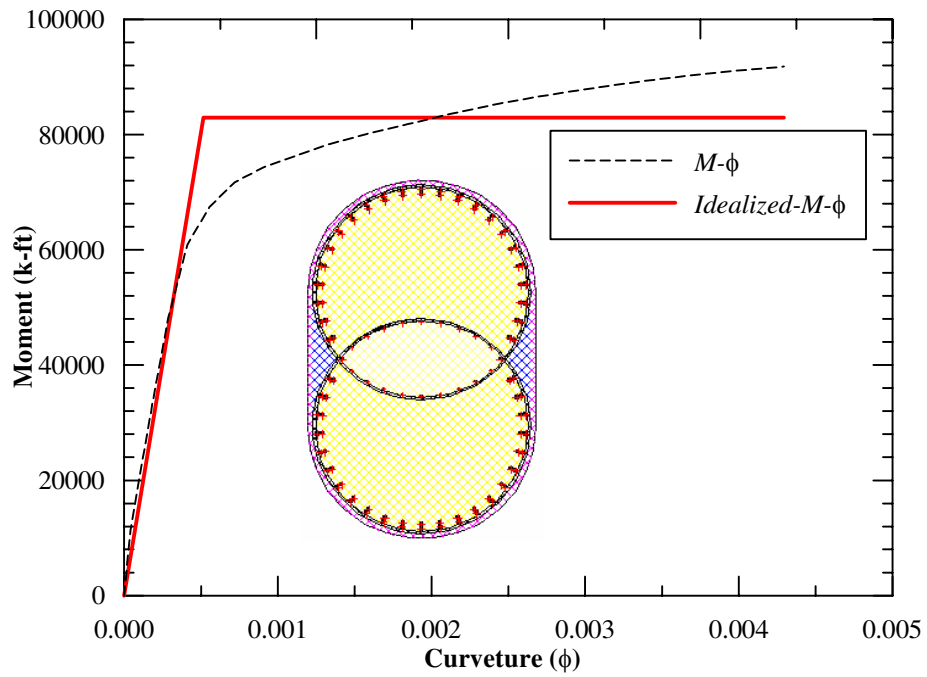


(b) 3-D Spline Model

Figure 5.38: Analytical Models of the Three -Span Two-Column Bridge



(a) Longitudinal



(b) Transverse

Figure 5.39: Columns Longitudinal and Transverse Moment Curvatures

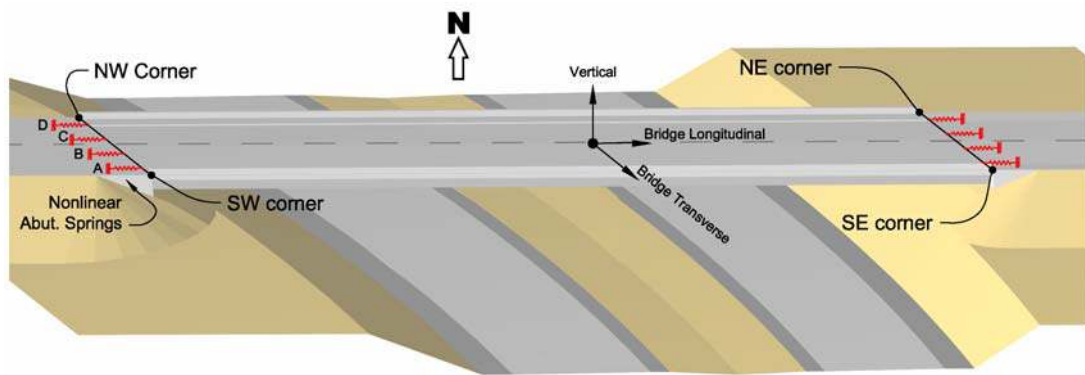
5.7 Longitudinal and Transverse Abutment Response

In order to understand the impact of the ground motions on the bridge abutment the soil-abutment interaction of a single span bridge structure is first investigated without the complexity of the bridge columns.

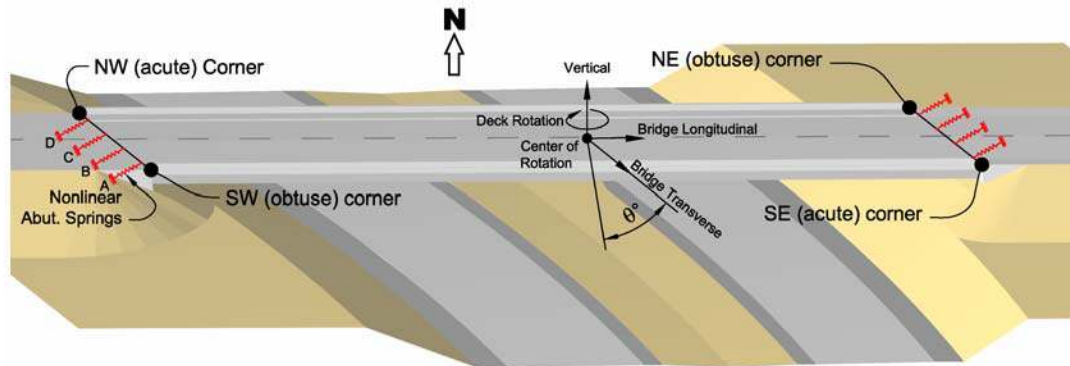
5.7.1 Effects of Skew Angles on the Bridge Abutment

As indicated earlier, the ground motions with an asymmetrical and high amplitude velocity pulse characteristics have the tendency of producing a biased, one-sided response of the bridge structures. Asymmetrical impulsive loading generates large displacements in one direction leading to a significant rotation and residual displacement on the bridges with skew-abutment. To evaluate the interaction behavior of a skewed bridge deck with a skewed abutment, a global three-dimensional nonlinear dynamic model of a concrete box-girder bridge shown in Figure 5.40 was performed using a zero skew angle and a 45 degree skew angle.

The interaction between abutments and backfill was modeled by two rows of four nonlinear soil springs denoted A, B, C and D (Figure 5.40) at each abutment, oriented normal to the backwall. Each spring was modeled by a nonlinear plasticity link element using the coordinate of the backbone curve shown in Figure 5.23. The model was excited by the two-horizontal-component earthquake motion with high-velocity pulses from the Renaldi record of the 1994 Northridge earthquake.



(a) Zero Skew Angle



(b) 45 Degree Skew Angle

Figure 5.40: Single Span Bridge With 0° and 45° Skew Angles

Two components of the recorded motion at the Renaldi station are shown in Figure 5.41 and Figure 5.42. The southwest direction motion has peak velocity pulse amplitude of 62 in/s in one direction and peak velocity pulse amplitude of 31 inch/s in the other direction. The northwest direction motion has peak velocity pulse amplitude of 25 inch/s in one direction and peak velocity pulse amplitude of 22 inch/s in the other direction. The recorded motion in the southwest direction has

biased (residual) acceleration, velocity, and displacement in one direction. Therefore, both components must be considered when conducting shake table experiments or performing nonlinear analytical models.

Figure 5.43 shows the abutment-backfill response due to deformation and compressive pounding force time histories of the bridge deck along the abutment-backwall. Despite the presence of the biased velocity pulse in the longitudinal direction of the model, the normal passive forces are distributed uniformly along the width of the abutment backwall. The abutment backfill provided resistance during the entire shaking without any significant bridge rotation. The first impact between the abutment-backfill and the bridge deck took place at about 2 seconds from the beginning of the excitation and continued pounding on the abutment-backfill up to about 11 seconds of the earthquake duration. The results of the analysis indicate that the bridge deck stopped pounding on springs A, B and C after about 9 second of the earthquake. However, the acute corner of the bridge deck continued pounding spring D up to 11 seconds of the shaking. This is an indication of slight counterclock wise rotation of the bridge deck. The residual displacement of the abutment-backfill is about 2.5 inches including the 1-inch expansion gap (net displacement about 1.5 inches).

Variation of normal passive forces and abutment deformation during the shaking of the single-span bridge with a 45 degree skew angle are shown in Figure 5.44. The first impact between the abutment-backfill and the bridge deck took place at about 2.17 seconds from the beginning of the excitation and continued pounding

on the abutment-backfill only up to about 2.6 seconds of the earthquake duration. The dynamic response of the abutment-backfill indicates that, the superstructure underwent significant clockwise rotations about the vertical axis and was permanently displaced from its original position by approximately 20 inches of the end of ground shaking. Figure 5.44 also illustrates the variation of abutment impact forces as a function of time across the abutment backwall. The passive forces were developed in each of the four normal springs from acute corner (NW) to obtuse (SW) corner at the abutment during initial shaking of the earthquake. It is interesting to note that the normal passive forces are distributed non-uniformly along the width of the abutment walls due to bridge deck rotation. It can also be observed that this non-uniform loading of the abutment backwalls resulted in a smaller magnitude of total soil resisting force in the acute corners of the deck as compared to non-skewed abutments. As the bridge deck is pushed into the abutment during ground shaking, the abutment backwall generates asymmetric passive soil resistances that cause the ends of the deck to “bounce” off the abutment seat in the bridge transverse direction, resulting in deck rotation. The width and capacity of this passive wedge depends on abutment (embankment) width, skew angle and ground motion characteristics. Therefore, for the bridge structures with high skew angles ground motions with high velocity pulse plays significant which can not be capture using response spectra analysis.

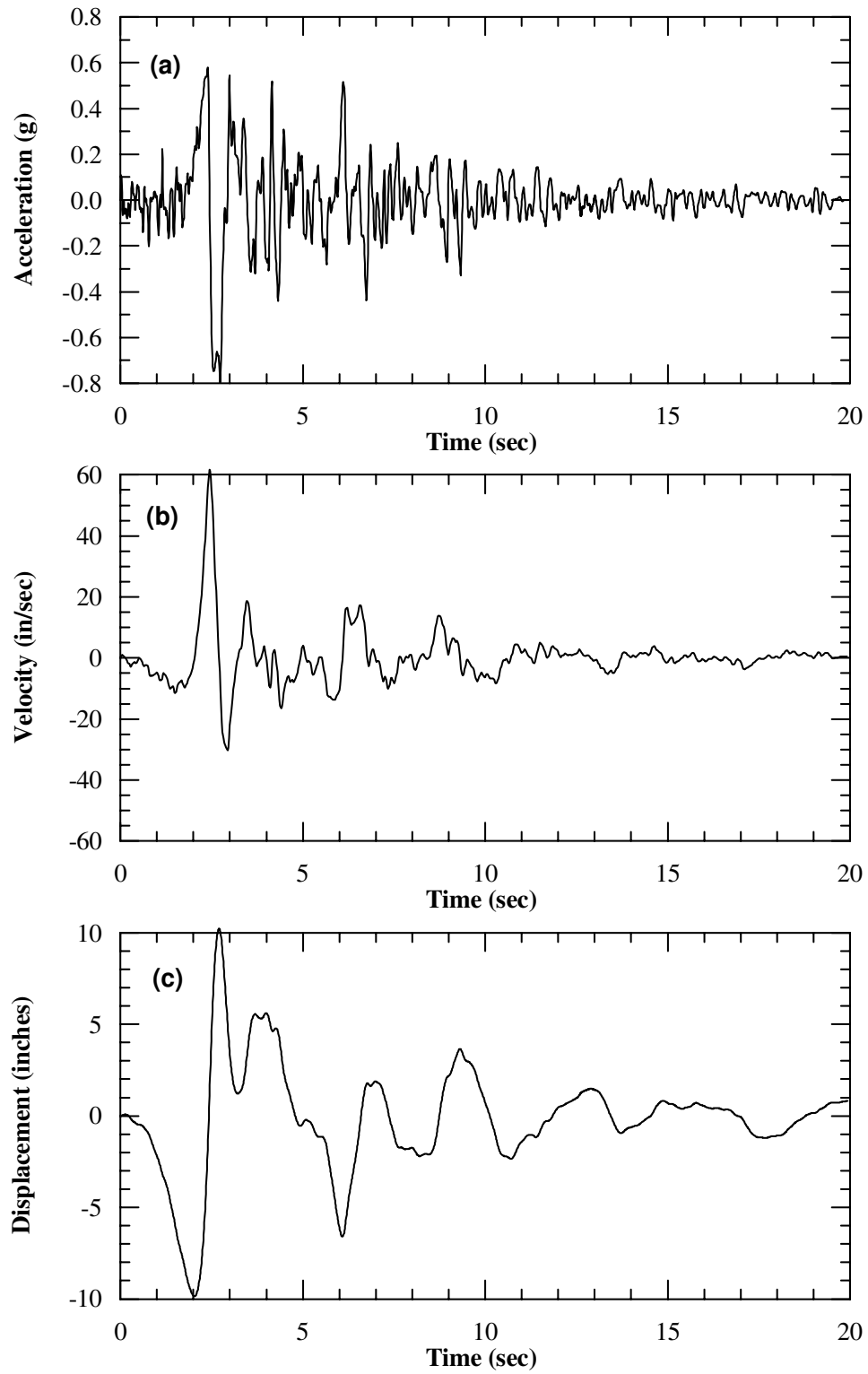


Figure 5.41: Recorded Renaldi Longitudinal Motion

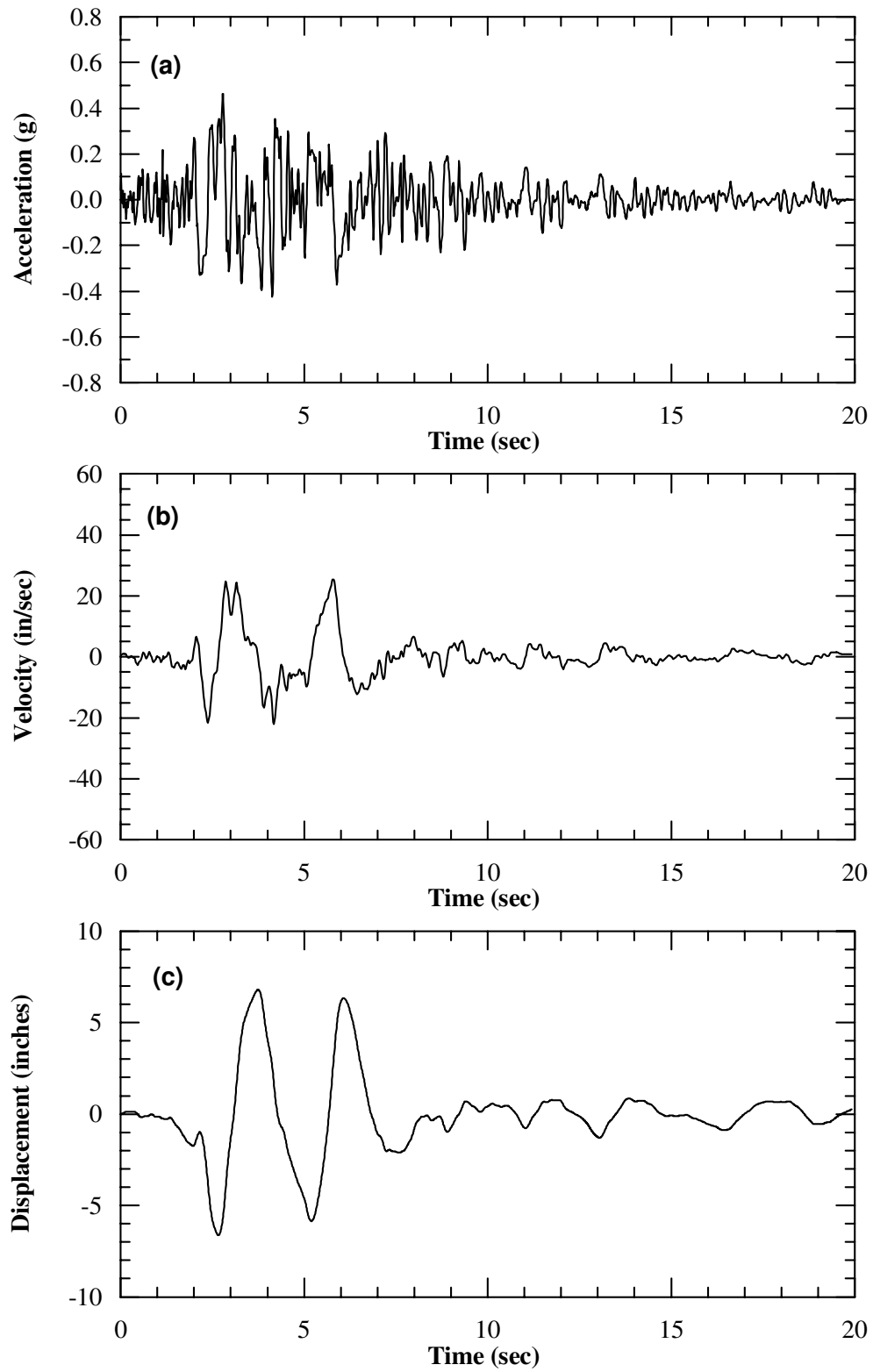
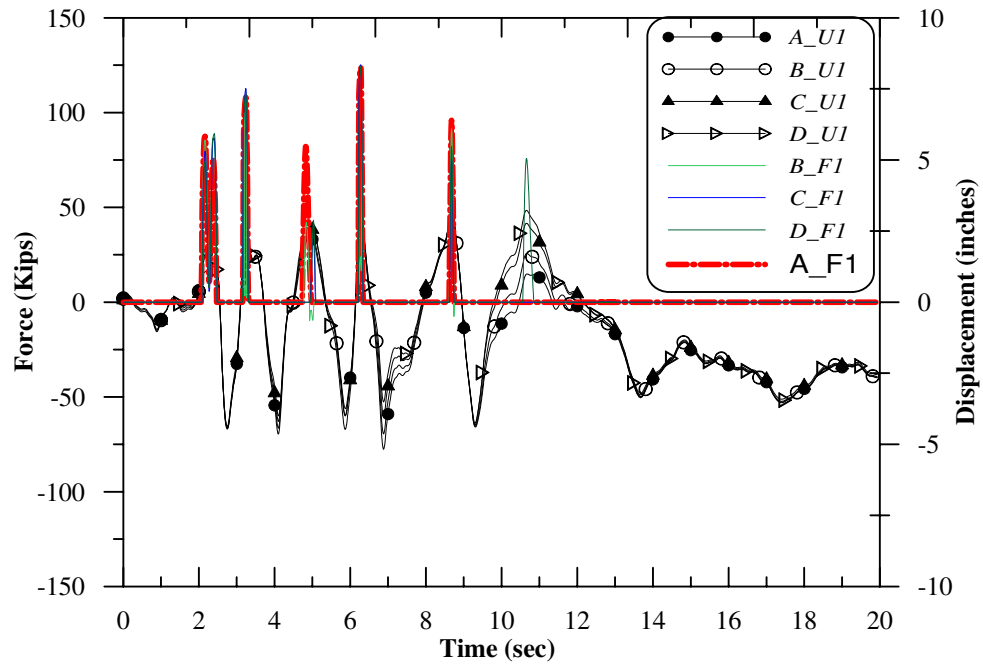
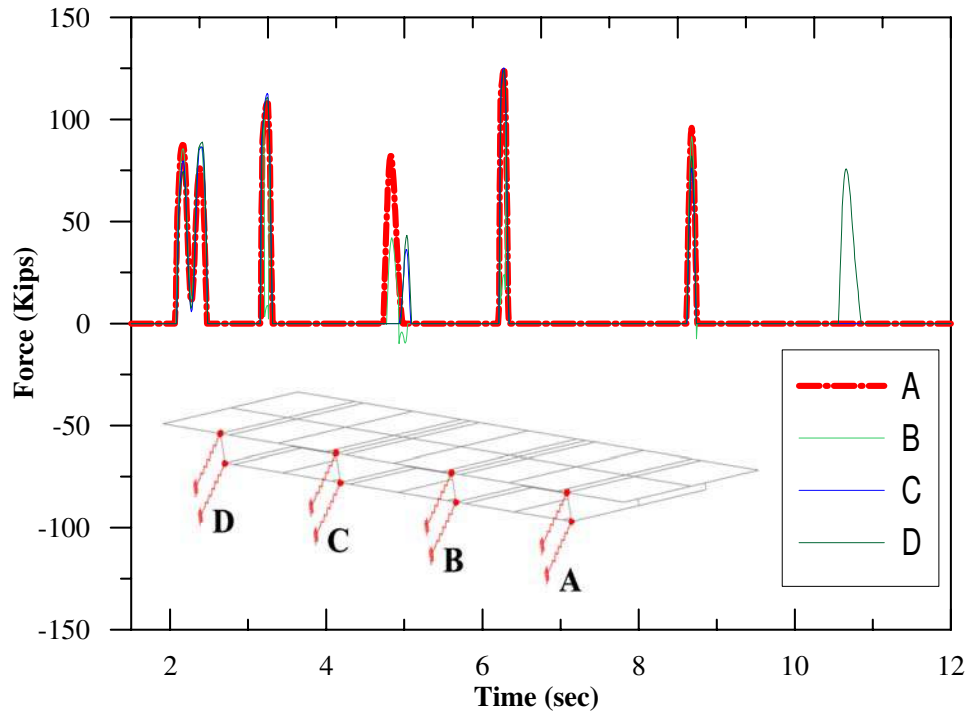


Figure 5.42: Recorded Renaldi Transverse Motion



(a)



(b)

Figure 5.43: Variation of Normal Abutment Impact Forces For a Single Span-Bridge With 0° Skew Angle

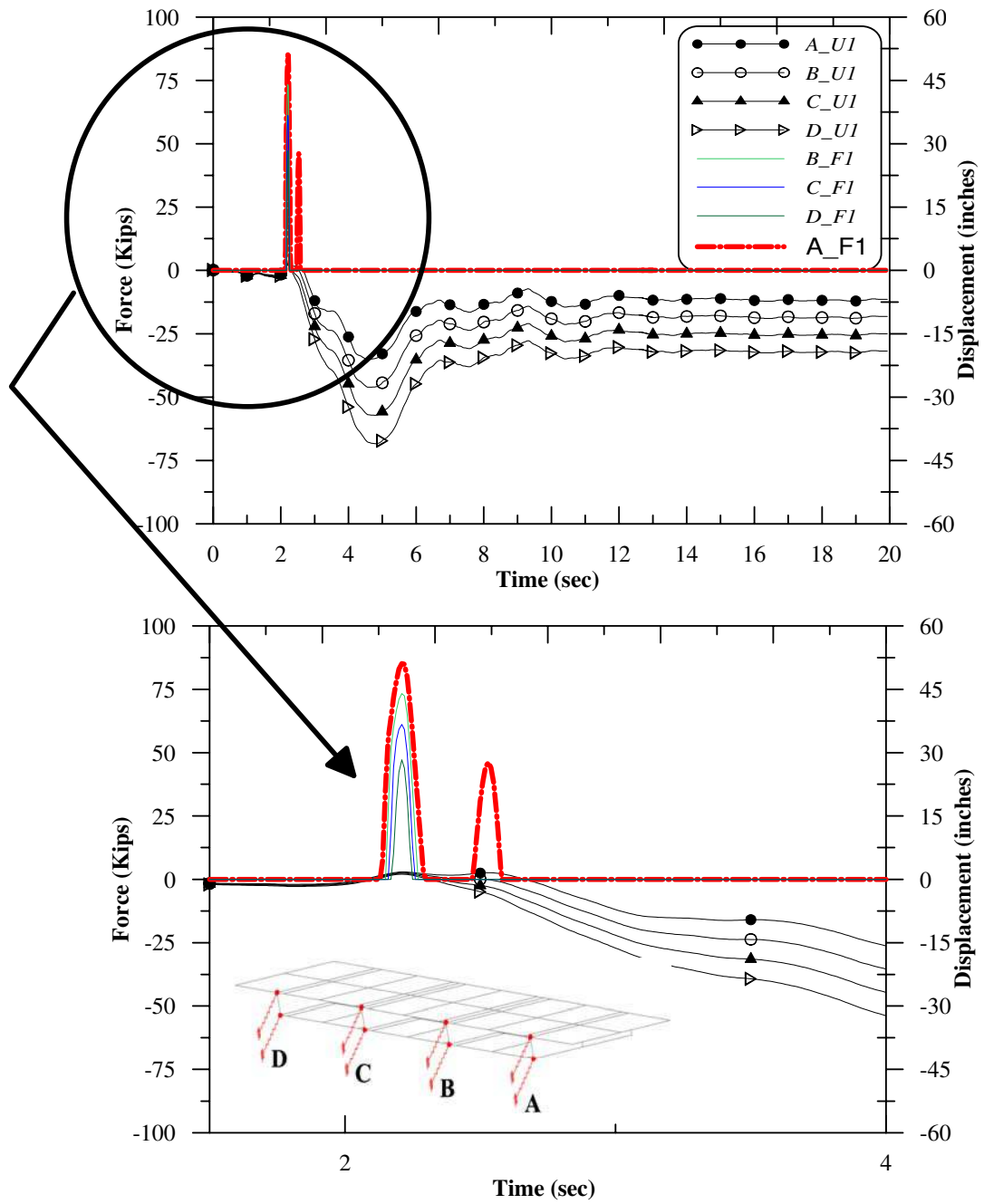


Figure 5.44: Variation of Normal Abutment Impact Forces For a Single Span-Bridge With 45° Skew Angle During the First 4 Seconds of Shaking

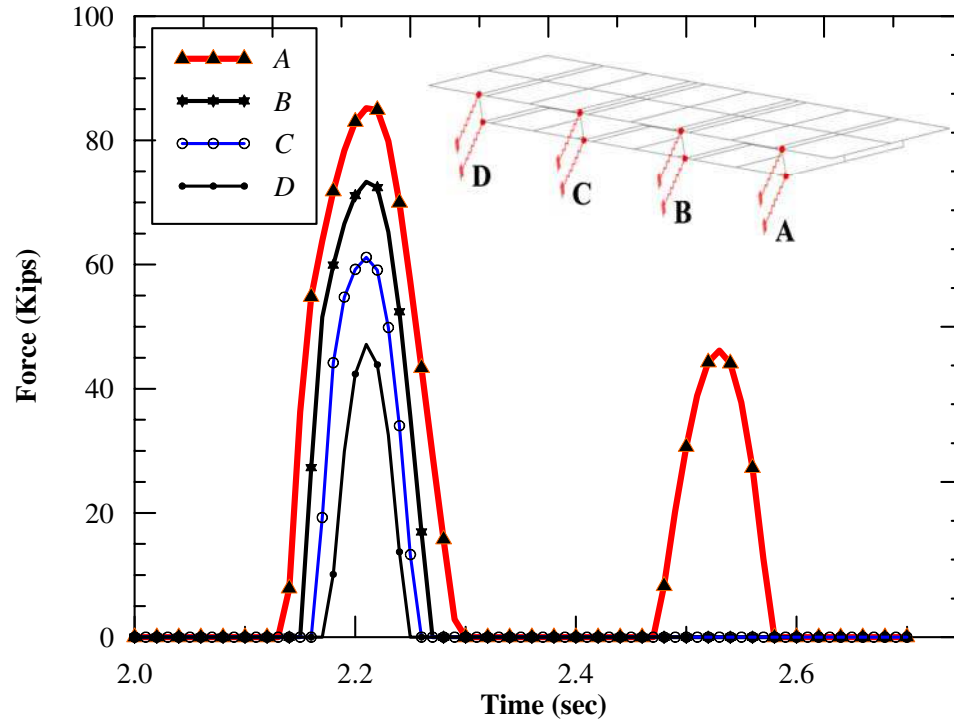


Figure 5.45: Variation of Normal Abutment Impact Forces For a Single Span-Bridge With 45° Skew Angle Between 2 Seconds to 2.6 Seconds of Shaking

5.8 Response Due to Spectra-Compatible Time History Motions

The global response and the abutment response of various bridge configurations using seven sets of the Response-Spectra-Compatible Time History Ground Motions with high velocity pulses are discussed in this section.

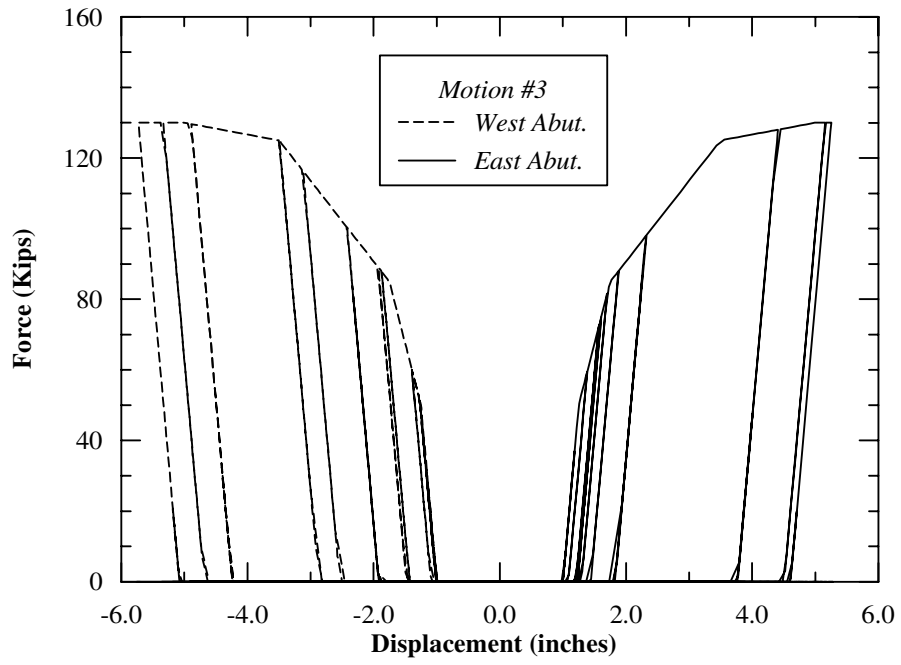
5.8.1 Abutment Response

Figure 5.46 shows the result of the abutment hysteretic behavior for a single-span bridge structure subjected to motion number 3 and number 5 motions. It can observe that the ultimate abutment passive force developed in the abutment-backfill is almost the same for both input ground motions. However, the loop of the

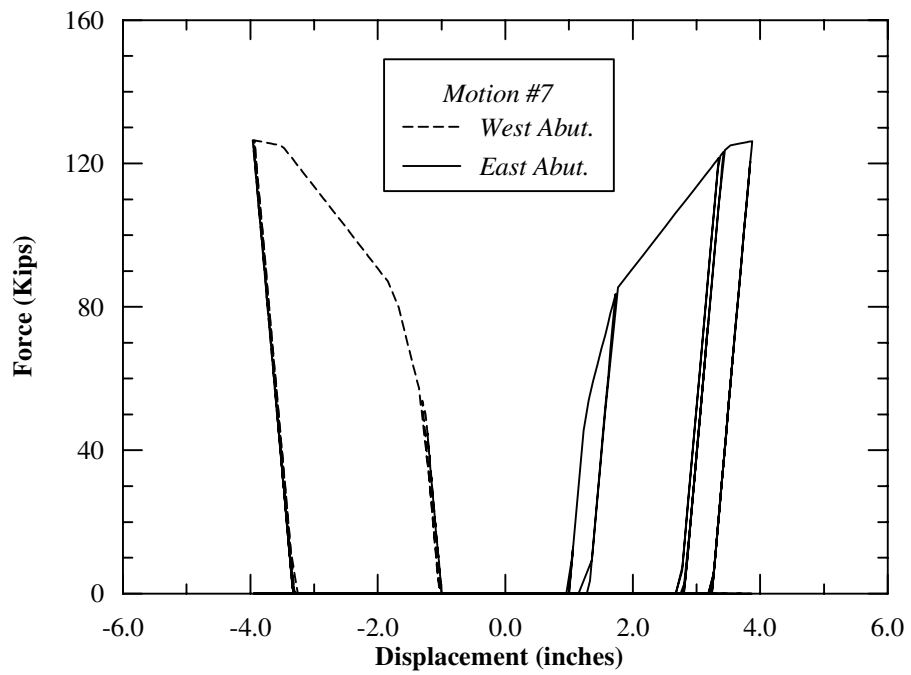
abutment force-displacement curve and loading and unloading features of the hysteretic response differ from one input ground motion to another, which reflects the influenced of different dynamic characteristics of input ground motions on the bridge abutment.

Figure 5.47 shows the hysteretic behavior of the abutment backfill at the obtuse corner (south west) and acute corner (south east) of the 45 degree skewed-bridge abutment due to input motion number 3 and number 7. From Figure 5.47 it can be observed that in addition to the characteristics of the ground motion the abutment-backfill hysteretic force-displacement response differs for the skewed abutments due to clockwise rotation versus non-skewed abutment. As the result of bridge rotation, the obtuse corners of the bridge deck have been pushed into the abutment backfill and the passive force is fully mobilized, while the acute corners have moved away from the abutment backfill and the passive wedge has been mobilized only partially. More discussion of the abutment-bridge interaction will be presented later on in this chapter.

Figure 5.48 shows example of the hysteretic abutment shear keys force-displacement response at the obtuse corner and acute corner of the 45 degree skewed-bridge abutment due to input motion number 3. The shear keys at the acute corners are observed to approach their ultimate soil-structural capacities. This result suggests that these keys at the acute corners of the bridge deck failed and the deck become unseated due to deck rotation and lateral movement.



(a)



(b)

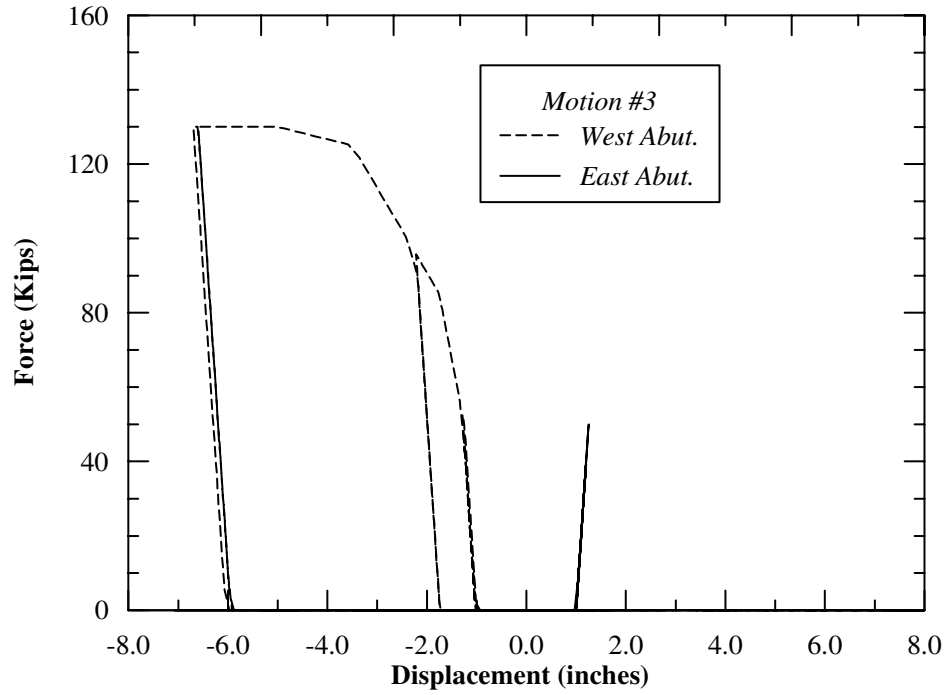
Figure 5.46: Longitudinal Hysteretic Behavior of the Single-Span Bridge Abutment With 0° Skew Angle

5.8.2 Rotation Due to Deck Flexibility

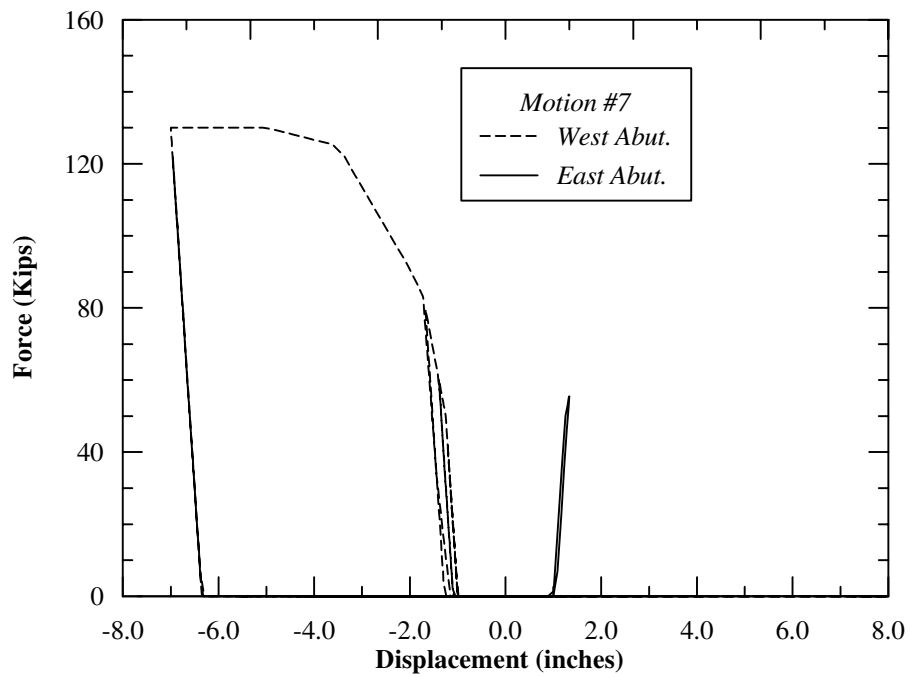
Global seismic behavior of skewed bridges is dominated not only by the abutment springs, number of spans and skew angles but also by the deck flexibility. The more the bridge deck is flexible the less rotation occurs during a seismic event. In order to investigate the impact of the deck flexibility, a 102-foot long single-span bridge and a 204-foot single-span bridge with a 45 degree skew angle were excited using seven sets of response-spectra-compatible time history input motions. Figure 5.49 shows the average rotational response of both bridges subjected to seven sets of response-spectra-compatible time history ground motion. Since the 204-foot long bridge is more flexible it has experienced less rotation than the 102-foot long bridge. Bridge rotation will be discussed in more detail later in this chapter.

5.8.3 Rotation Due to Column Rigidity

In order to investigate the impact of the bridge column a two-span bridge (204-foot long) and a single-span bridge (102-foot long) were excited using seven sets of time history input motions. The average rotational response of both bridges subjected to seven sets of response-spectra-compatible time history ground motion is shown in Figure 5.50. Even though both bridges have the same span length, the presence of the column causes the rotational response of the two-span bridge to drop more than half.

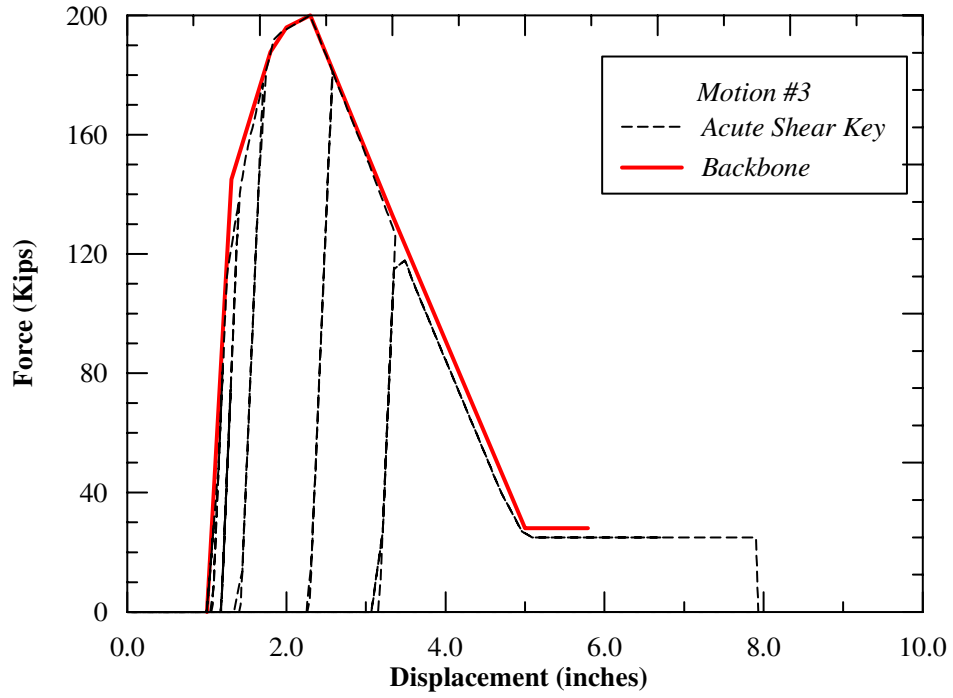


(a)

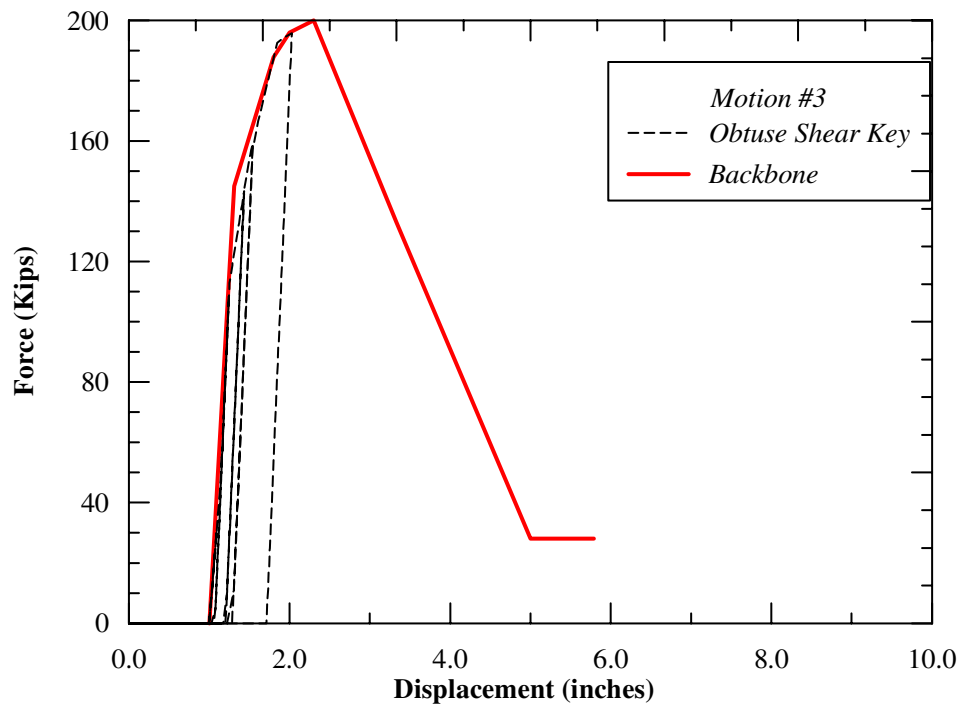


(b)

Figure 5.47: Longitudinal Hysteretic Behavior of the Single-Span Bridge Abutment With 45° Skew Angle



(a)



(b)

Figure 5.48: Transverse Hysteretic Behavior of the Single-Span Bridge Abutment With 45° Skew Angle

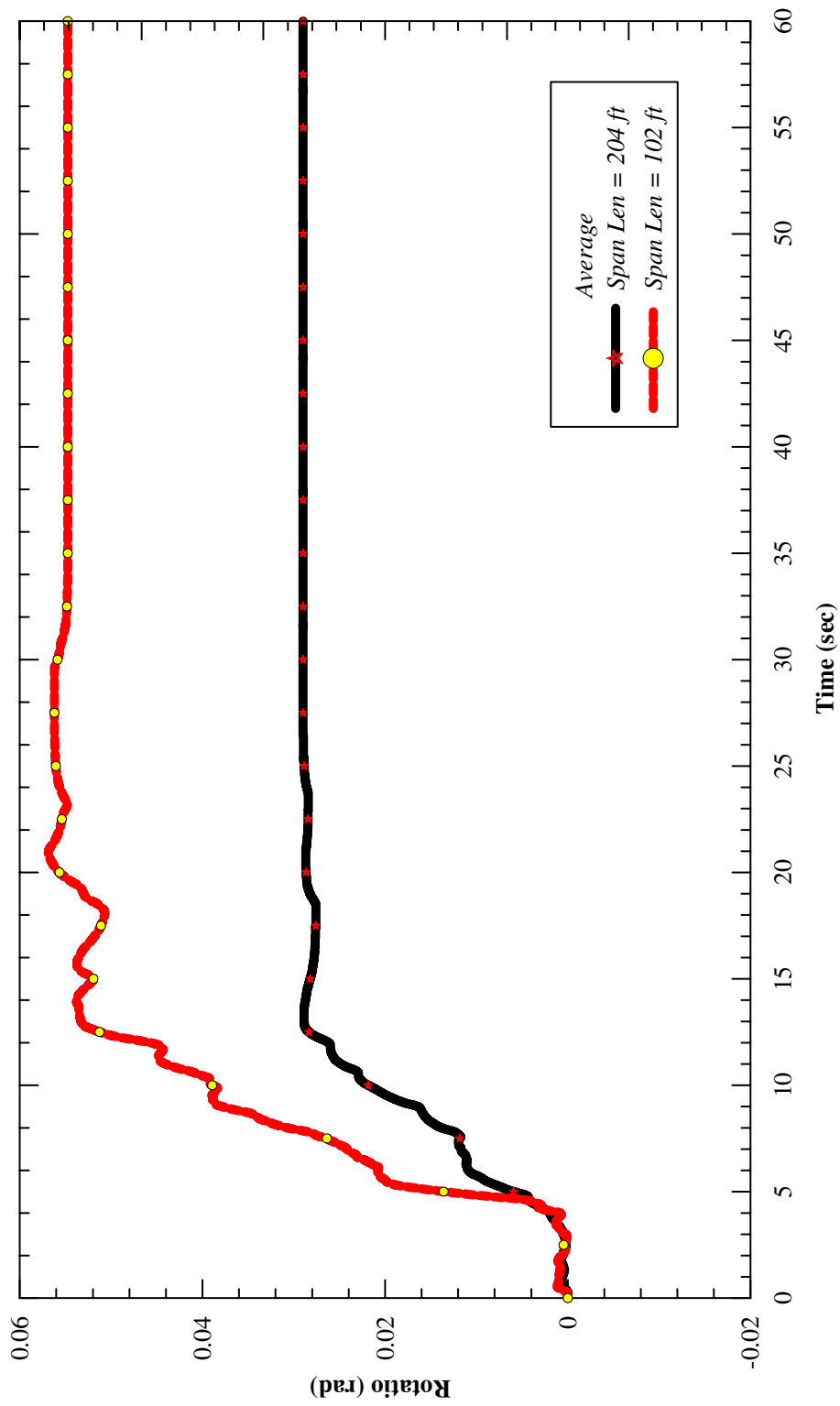


Figure 5.49: Average Rotation Due to Deck Flexibility of the Single-Span Bridge With 45° Skew Angle

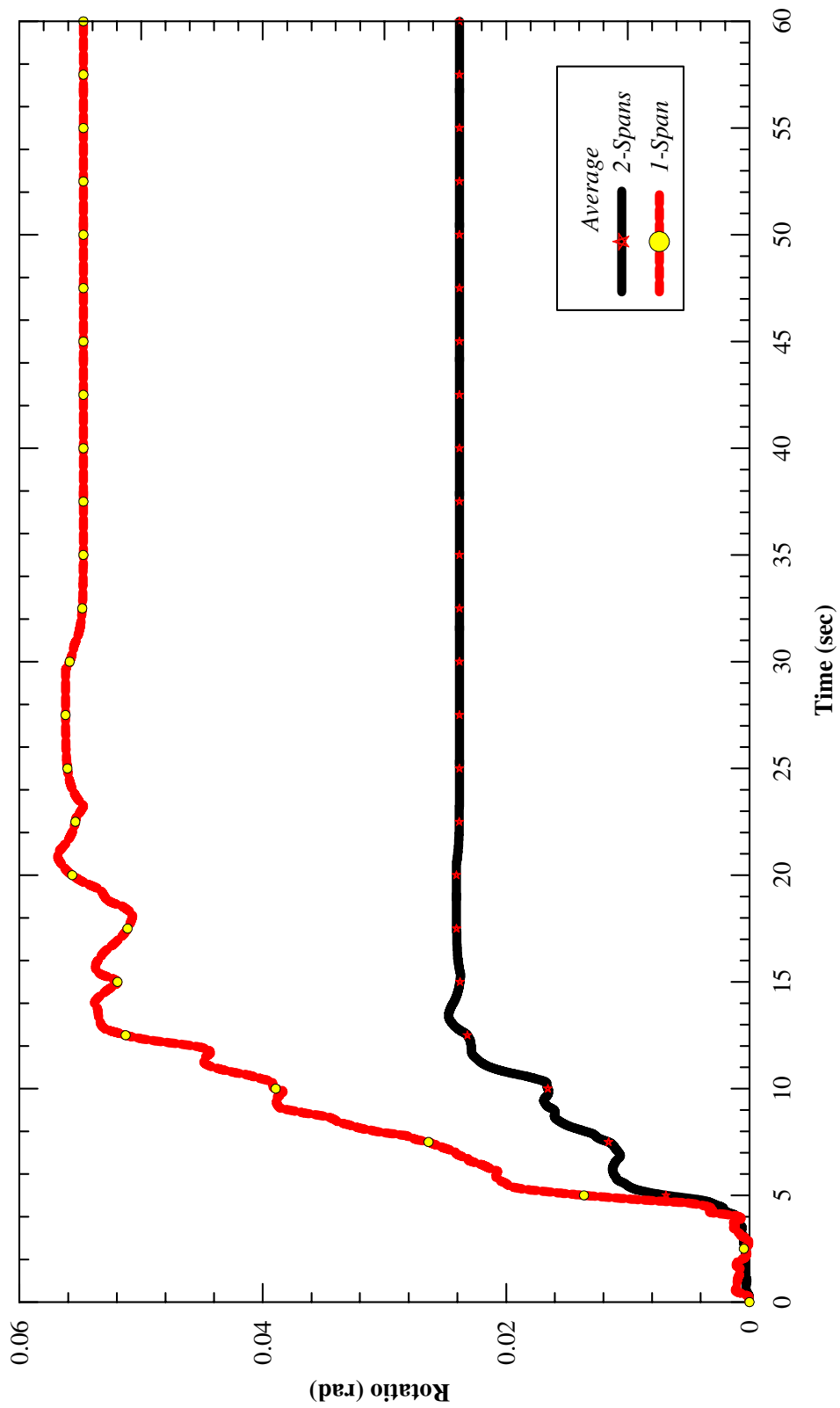


Figure 5.50: Average Rotation Due to Presence of the Number of Spans With 45° Skew Angle

5.9 Analytical Results of the Single-Column Two-Span Bridge

In order to investigate a realistic global behavior of skew bridges, first the global response of a simple two-span bridge will be discussed. Figure 5.51 through Figure 5.57 show examples of the transverse displacement time history response at the acute corners (northwest and southeast) of the bridge deck for all seven input motions used in the analysis. The abutment interaction in the longitudinal direction was modeled as a set of 4 nonlinear springs shown in Figure 5.23. The bridge column was modeled using a frame element with a bi-linear moment curvature shown in Figure 5.33. The response time histories demonstrate that the bridge decks experienced significant amounts of transverse displacement and rotation about the vertical axis during seismic ground shaking when the abutments are skewed, whereas the non-skewed bridge showed little or no rotation. Since the two span lengths are the same for all models, the center of mass and the center of rigidity of the bridge system coincides at the top of the bent.

The transverse displacement results of the analyses show that the bridge dynamic behavior is dependent on the characteristics of the input ground motions. The permanent residual displacements of the acute deck corners at end of shaking. The magnitude of permanent residual displacements (deck rotation) varies among all seven input motions and all three skew angles.

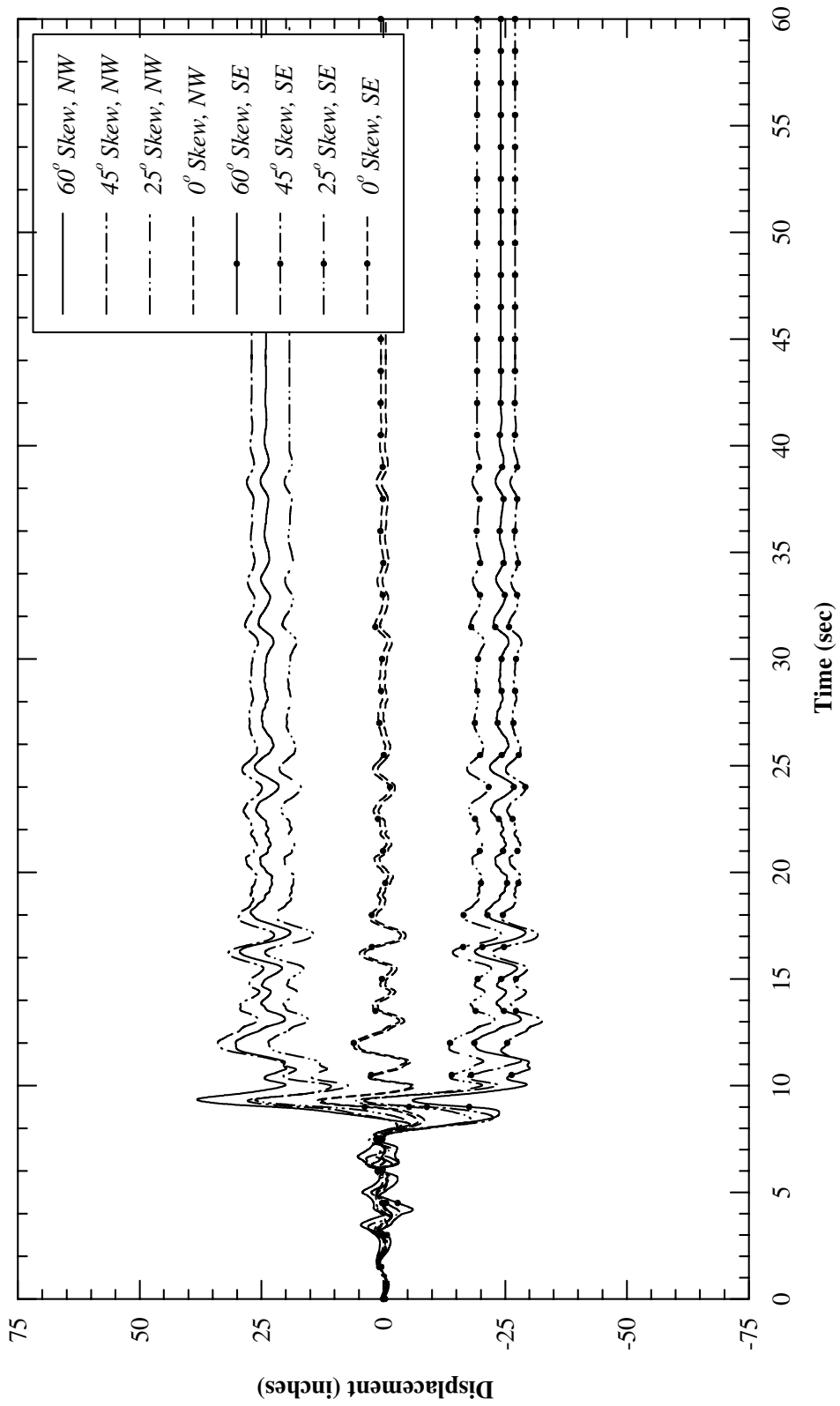


Figure 5.51: Transverse Displacement Due Motion 1 For a Two-Span Single-Column Bridge

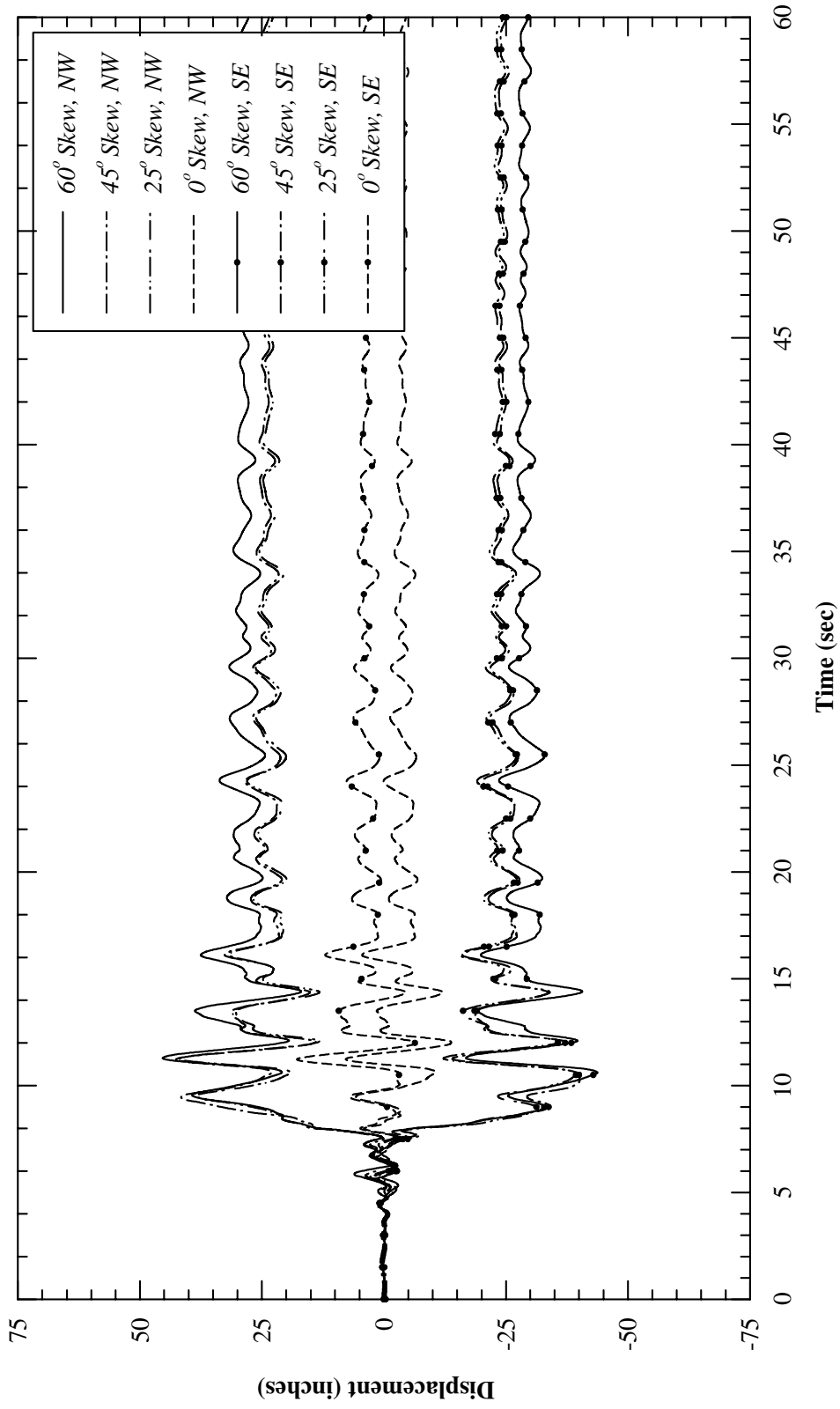


Figure 5.52 : Transverse Displacement Due Motion 2 For a Two-Span Single-Column Bridge

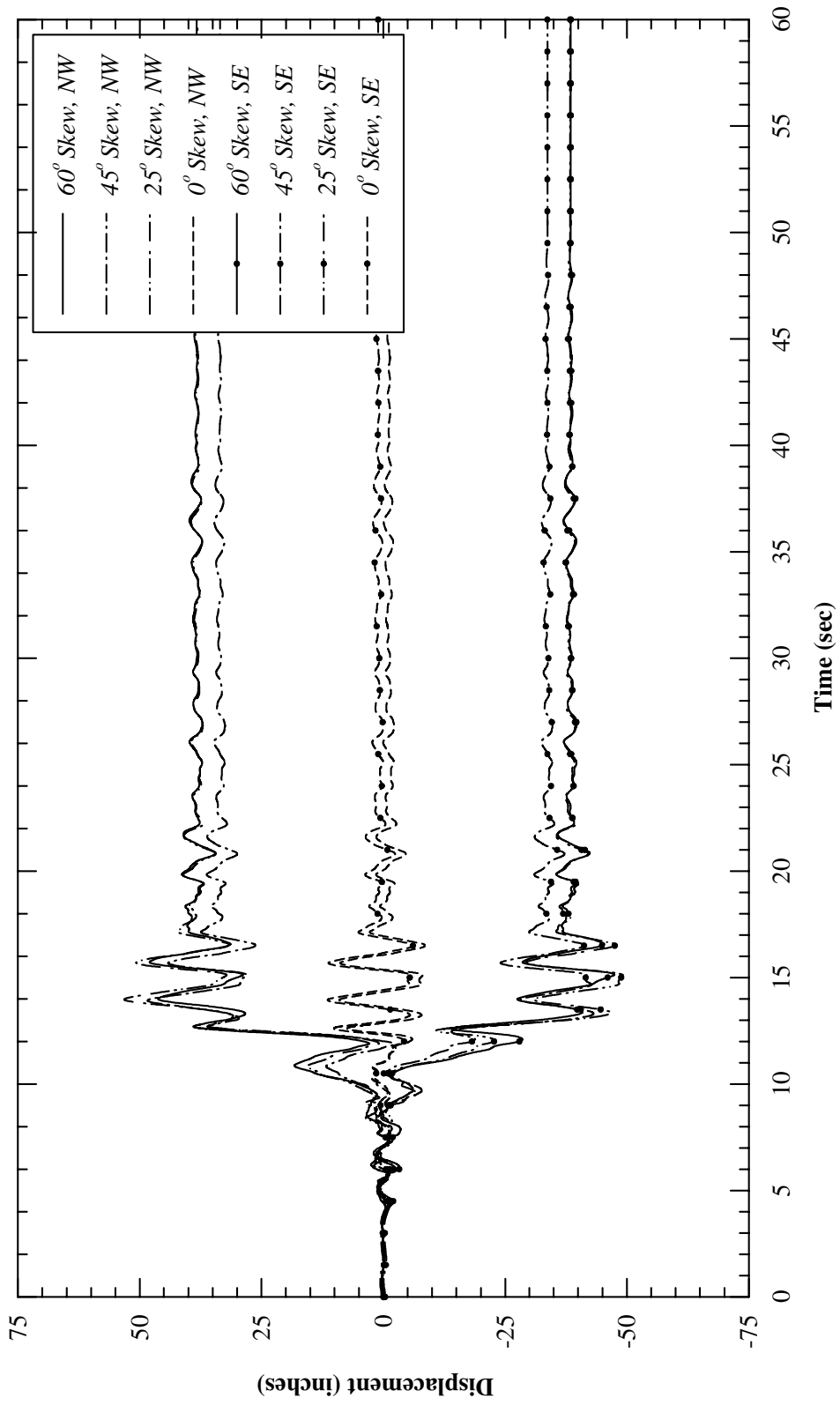


Figure 5.53: Transverse Displacement Due Motion 3 For a Two-Span Single-Column Bridge

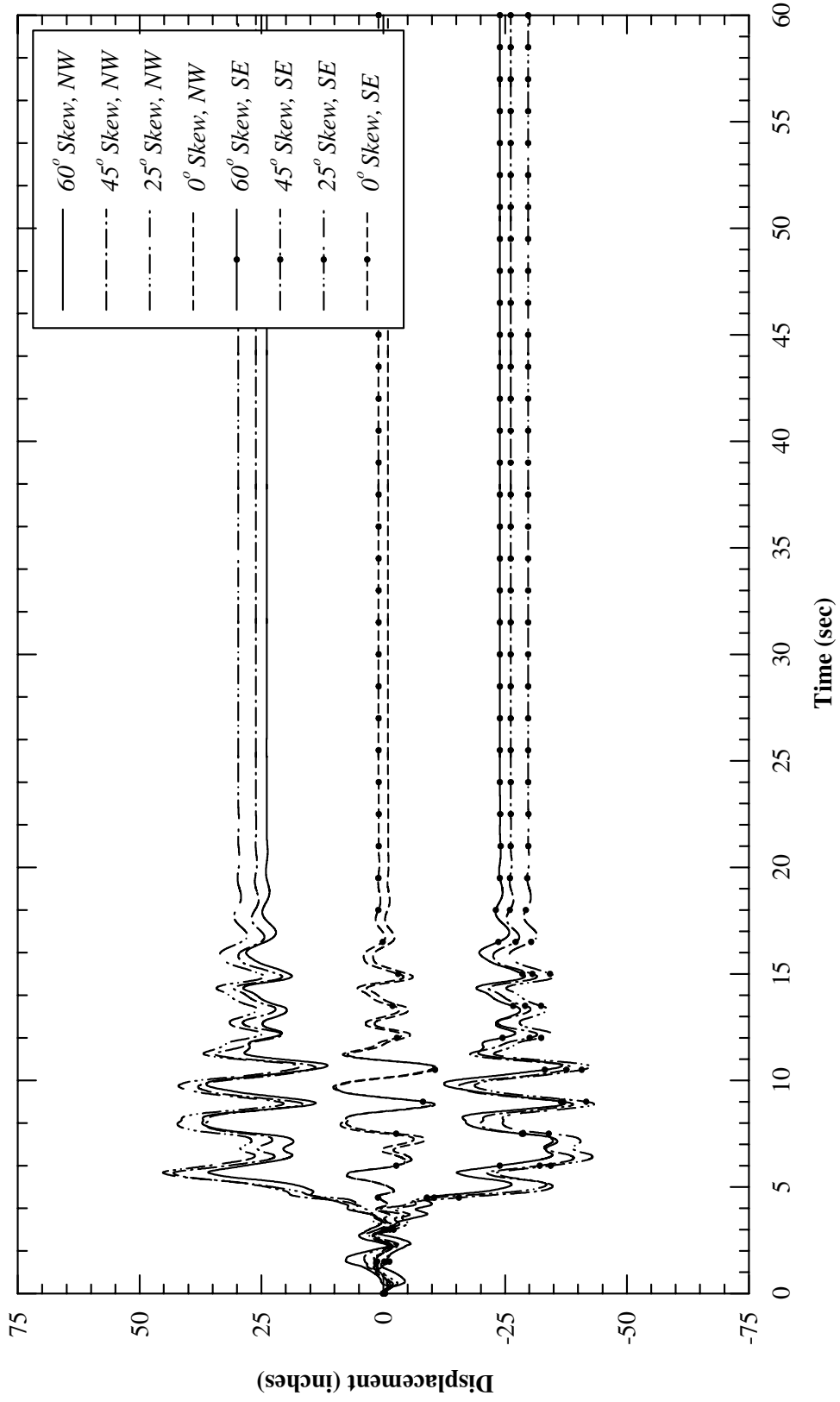


Figure 5.54: Transverse Displacement Due Motion 4 For a Two-Span Single-Column Bridge

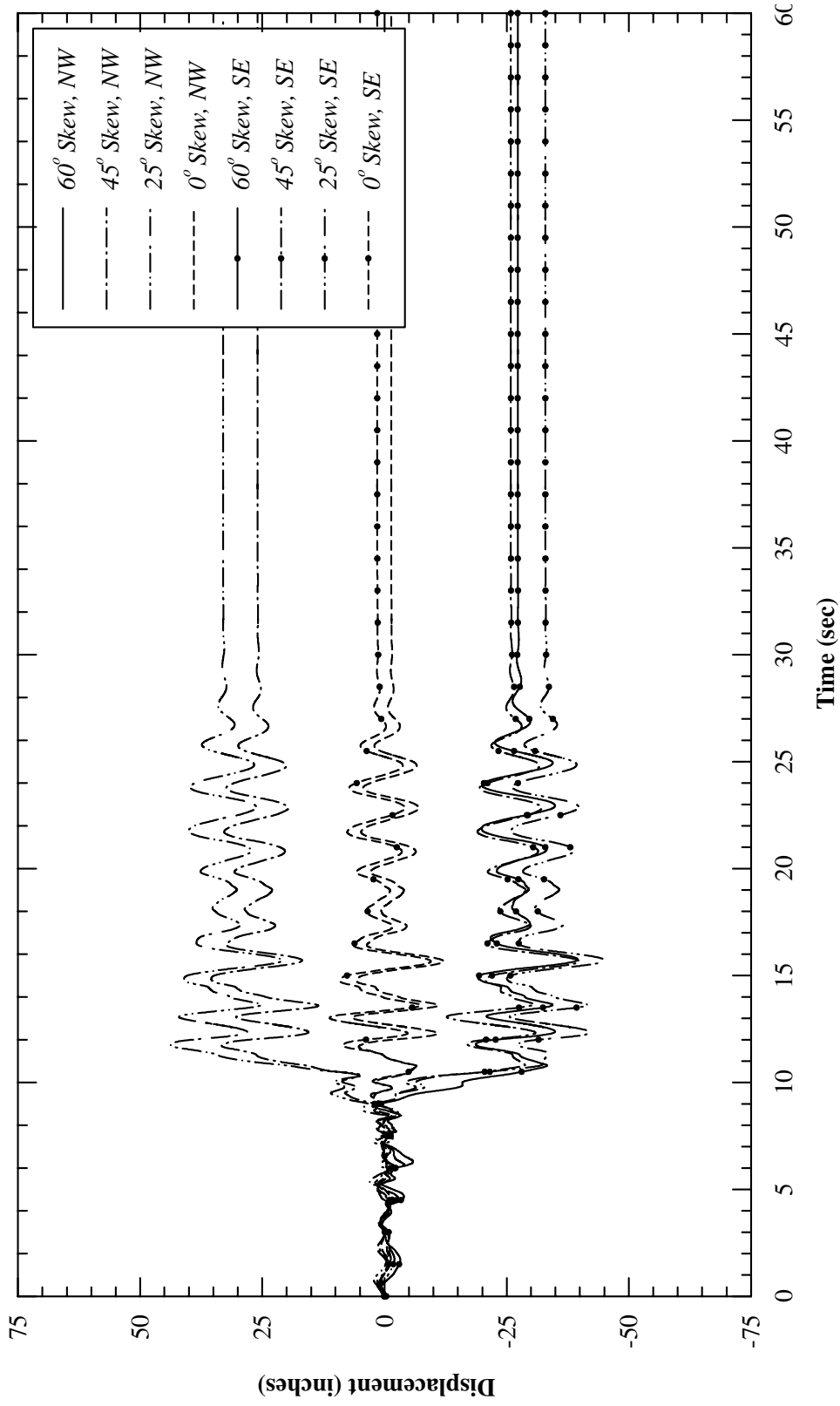


Figure 5.55: Transverse Displacement Due Motion 5 For a Two-Span Single-Column Bridge

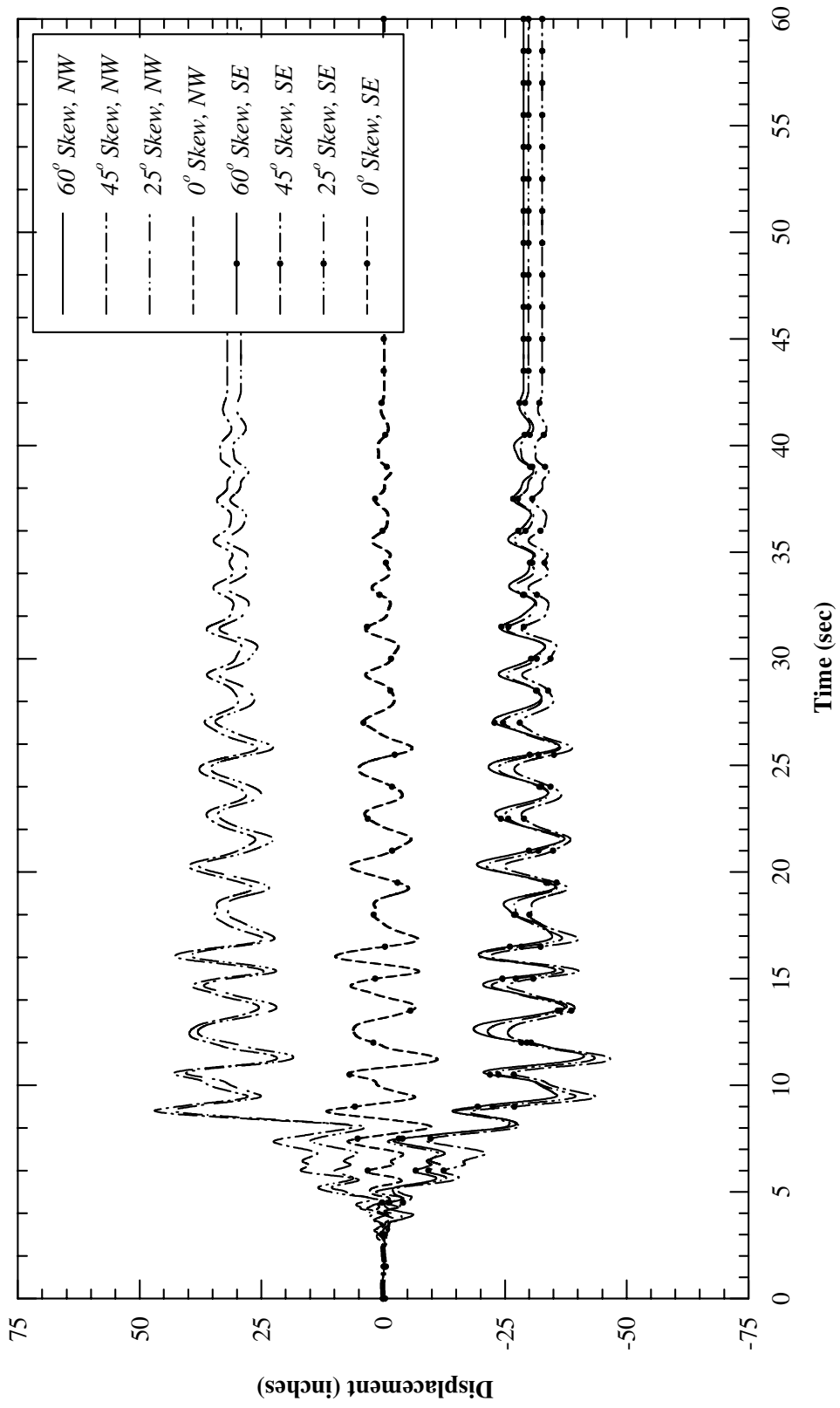


Figure 5.56: Transverse Displacement Due Motion 6 For a Two-Span Single-Column Bridge

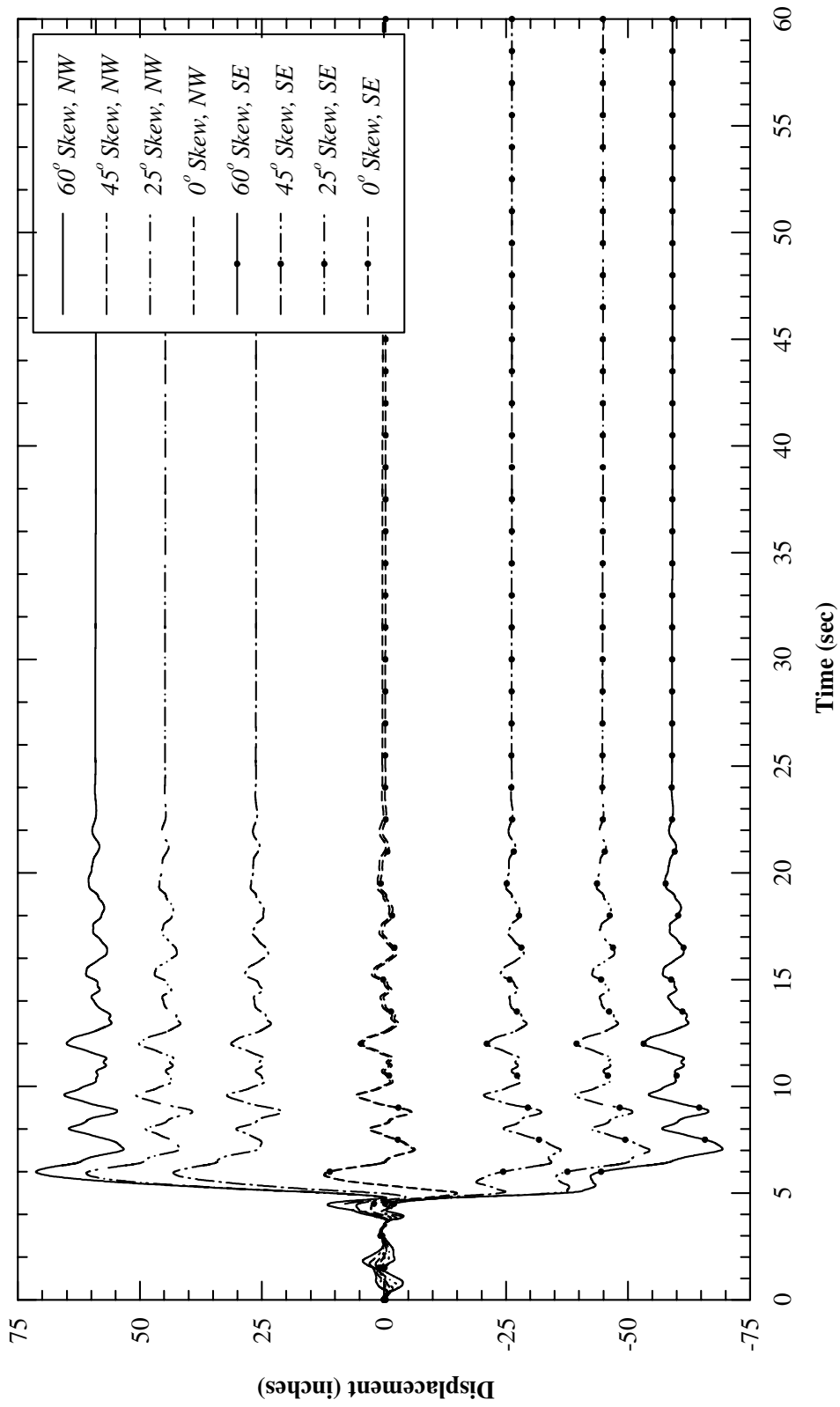


Figure 5.57: Transverse Displacement Due Motion 7 For a Two-Span Single-Column Bridge

5.9.1 Abutment Behavior in the Longitudinal Direction

Figure 5.58 through Figure 5.60 show the hysteretic behavior of the abutment backfill at the acute and obtuse corners west abutment (for 0, 25 and 60-degree skew) due to set number 3 input motion. Figure 5.58 shows the backbone curve and the hysterical behavior of non-skewed abutment –backfill. It can be observed that the backfill has been fully engaged during the seismic loading and the ultimate abutment force has been fully mobilized and is uniformly distributed along the backwall.

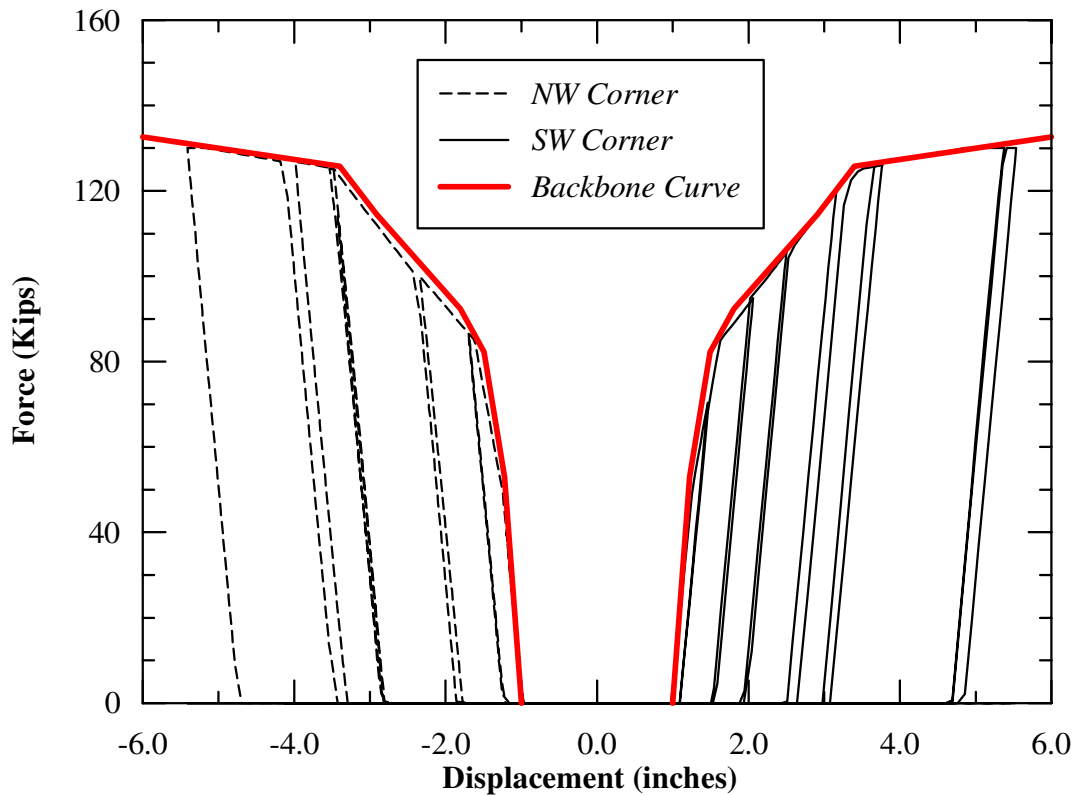


Figure 5.58: Hysteretic Abutment Backfill Response For a Two-Span Single-Column Bridge with 0° Skew Angle

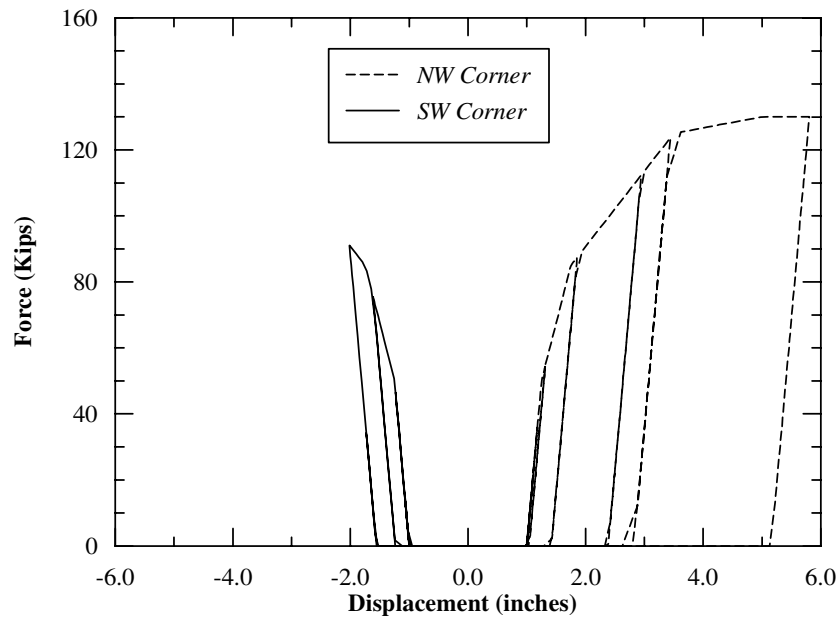


Figure 5.59: Hysteretic Abutment Backfill Response For a Two-Span Single-Column Bridge with 25° Skew Angle

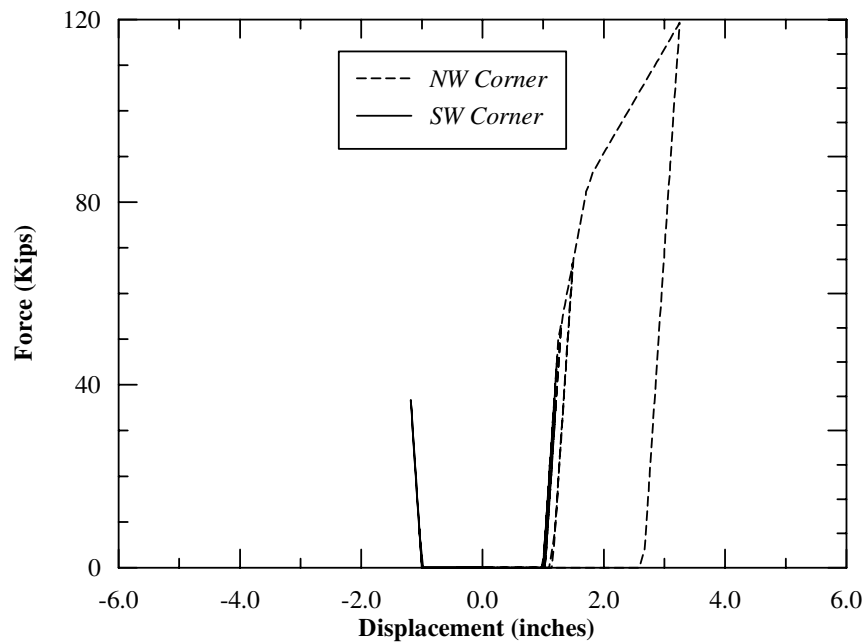


Figure 5.60 Hysteretic Abutment Backfill Response For a Two-Span Single-Column Bridge with 60° Skew Angle

However, Figure 5.59 and Figure 5.60 demonstrate that the abutment hysteretic force-displacement response differ for the skewed abutments due to clockwise rotation. As the result of bridge rotation similar to the single-span bridge structures, the obtuse corners of the bridge deck have been pushed into the abutment backfill and the passive force is fully mobilized, while the acute corners have moved away from the abutment backfill and the passive wedge has been mobilized only partially. It was observed that as the skew angle increased the abutment participation becomes less at both the acute and obtuse corners. This behavior reflects the influence of skew angle on abutment participation during a major seismic event.

The results of the analytical model revealed the important role of ground motion characteristics on the bridge abutment hysteretic behavior. The most unique aspect of the calculated response was the presence of high residual rotation of the bridge deck. Figure 5.59 and Figure 5.60 show that the combination of skew angles and the presence of one-sided high velocity pulse in the input ground motion caused the hysteretic response of the abutment to be biased in one direction similar to the shake table test conducted at University of Nevada Reno (Phan et al., 2005) as shown Figure 5.59 and Figure 5.60.

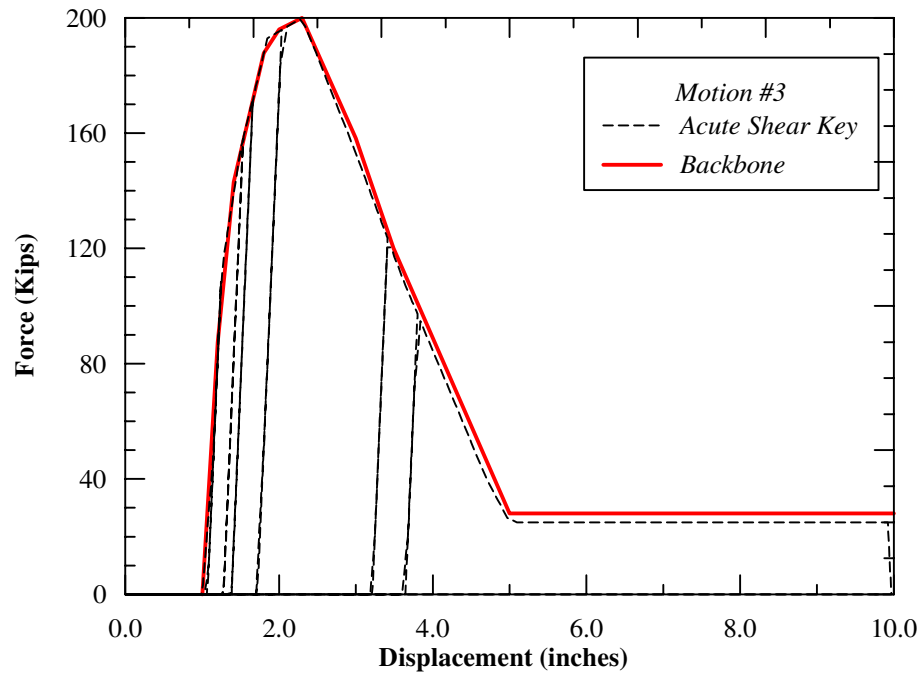
5.9.2 Abutment Behavior in the Transverse Direction

Reconnaissance reports after earthquakes such as the 1994 Northridge Earthquake indicated many bridge abutment shear keys failure as a result of deck rotations and lateral movements. Figure 5.61 shows an example of the shear key failure due to deck rotation at the east side of abutment 1 during the 1994 Northridge

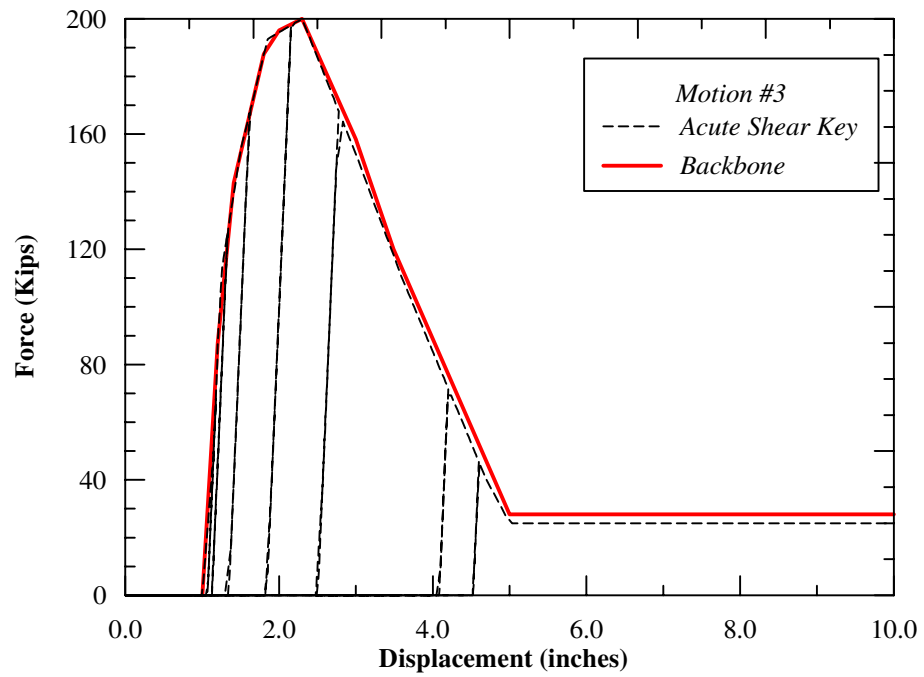
earthquake. The shear key on the west side of the abutment did not experience any significant damage. An analytical example of the hysteretic behavior of the transverse abutment shear keys of bridge model with 45 degree skew angle is shown in Figure 5.62 and Figure 5.63 for the acute and obtuse corners deck. The abutment shear keys were modeled using a nonlinear plasticity link element. Figure 5.23 shows the expansion gap and the nonlinear shear key backbone curve used in the model. As shown in Figure 5.62 the shear keys located on the acute corners are observed to approach their ultimate structural capacities during the shaking. This result suggests that these keys could potentially fail when subjected to stronger shaking, which could allow the bridge to rotate and cause the deck to become unseated from the abutment due to lateral movement. The first impact between the abutment-shear keys and the bridge deck took place after the gap closure. Hysteretic behavior of the shear keys indicates that there is less damage at the obtuse corners than the acute corners due to deck rotation. As shown in Figure 5.63 the deformations of the shear keys on the obtuse corners are in the order of couple of inches including the 1 inch expansion gap opening while the deformations on the acute corners are in excess of several inches.



Figure 5.61: Shear Key Failure Due to Deck Rotation 1994 Northridge Earthquake

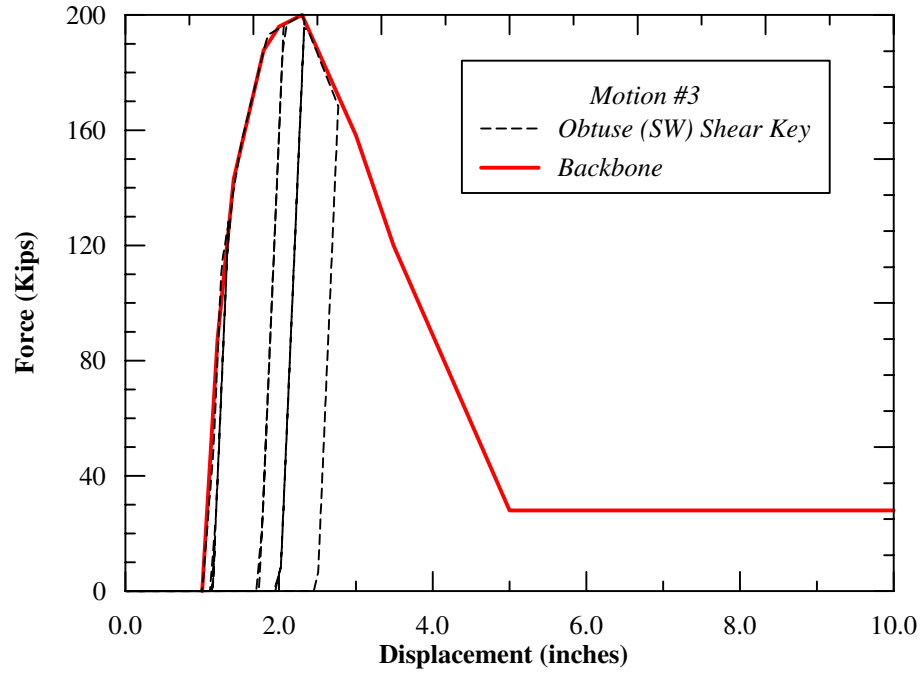


(a)

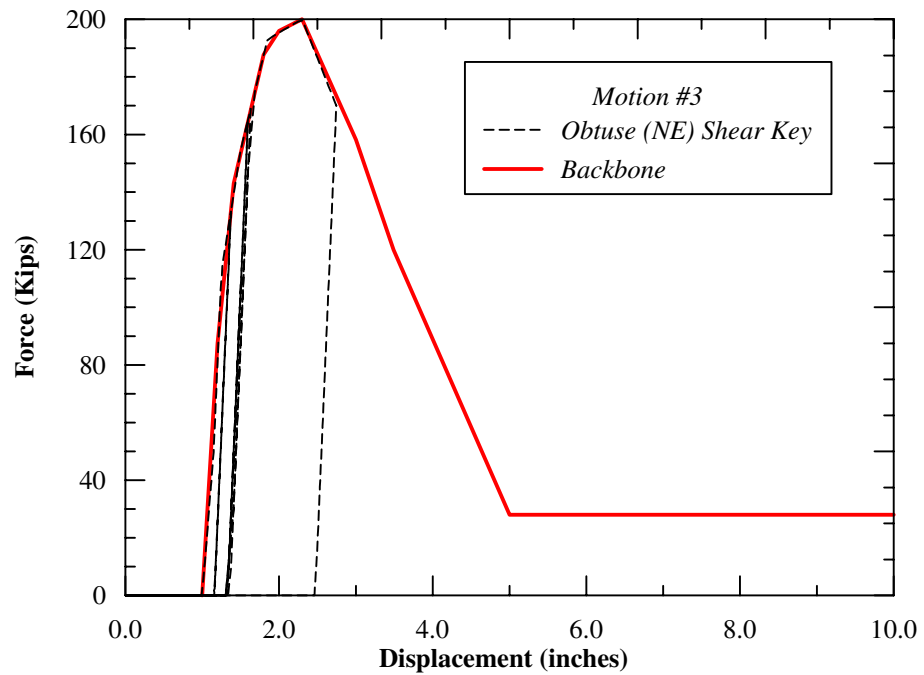


(b)

Figure 5.62: Hysteretic Abutment Shear Key Response at the Acute Corners For a Two-Span Single-Column Bridge with 0° Skew Angle



(a)



(b)

Figure 5.63 Hysteretic Abutment Shear Key Response at the Obtuse Corners For a Two-Span Single-Column Bridge with 45° Skew Angle

5.10 Results of the Analysis for All Bridge Models

In the previous sections various components and global behavior of a single-span and a two-span-single-column bent was investigated the mechanism of the problem. The purpose of the following sections is to investigate global response for all five bridge configurations due to rotation of various skew angles using seven sets of ground motions.

5.10.1 Rotational Response

Figure 5.64 to Figure 5.81 show that the deck rotation for the 25, 45 and 60-degree skew built up during the initial peak cycles of shaking of all seven ground motions. The time histories for the non-skewed configurations are not shown since the rotations were insignificant. The results of analysis indicate that once this large rotation had occurred, the deck did not return to its original position for all three skewed configurations. In contrast, the non-skewed bridge deck experienced neither significant rotation nor permanent transverse displacement despite the large velocity pulses in the input motions. From these analyses, the following observations are made for all bridge structures in this chapter:

- The bridge dynamic behavior is dependent on the characteristics of the input ground motions. The magnitude of permanent rotation varies among all seven input motions, particularly for Bridges No. 1 to 3, and all bridge skew configurations (Figure 5.64 to Figure 5.72).

- The bridges experienced significant amounts of rotation about the vertical axis during seismic ground shaking when the abutments are skewed, whereas the non-skewed bridge showed little or no rotation.
- The decks experienced significant amount of rotation which builds up during initial peak cycles shortly after the velocity pulses occurred (about 3 to 13 seconds). None of the decks returned to their original position. Bridge No. 1 (single-span without column) and No. 2 (with one single-column bent) experienced the largest magnitudes of rotation.
- The bridge decks then rotated back in a reverse direction by a small amount. The amount of this rotation was largest for Bridges No. 1 and 2. Bridges No. 3 to 5, which consist of more rigid bridge structure systems, showed little or no significant reverse rotation.
- Subsequent deck rotations were small for Bridges No. 1 and 2. The response is observed to undergo more and more oscillation for the more rigid Bridges No. 3 to 5 (with multiple-column bents and more spans).

Figure 5.82 and Figure 5.85 show the three-dimensional histogram depicting maximum and the average residual deck rotations developed from the seven response time histories motions for a single-span, two-span-single-column bent and three-span-single-column bent bridge models (Bridge No. 1, Bridge No. 2 and Bridge No. 3) for three skew configurations. It is also observed that there is a clear trend between the magnitude of deck rotation and skew angle among all seven input

motions. As the number of spans increases the deck rotation decreases due to presence of the bridge columns.

Figure 5.84 is a three-dimensional histogram depicting maximum deck rotations due to the seven input ground motions for a two-span-single-column bent and two-span-two-column bent bridge models (Bridge No. 2, and Bridge No. 4) for three skew configurations. The results of the analysis indicate that as the number of column per bent increase the deck rotation decreased due to column rigidity.

Figure 5.85 shows the results of the maximum rotation for a three-span-single-column bent and three-span-two-column bent bridge models (Bridge No. 3, and Bridge No. 5). The results of the analysis indicate that as the number of column per bent increase the deck rotation decreased due to column rigidity. However, the magnitude of the deck rotations for all three skew angles is similar (25, 45, and 60 degree skew). As a matter of fact the magnitude of the deck rotation for a 45 degree skew angle is slightly higher than the deck rotation for the 60 degree skew angle.

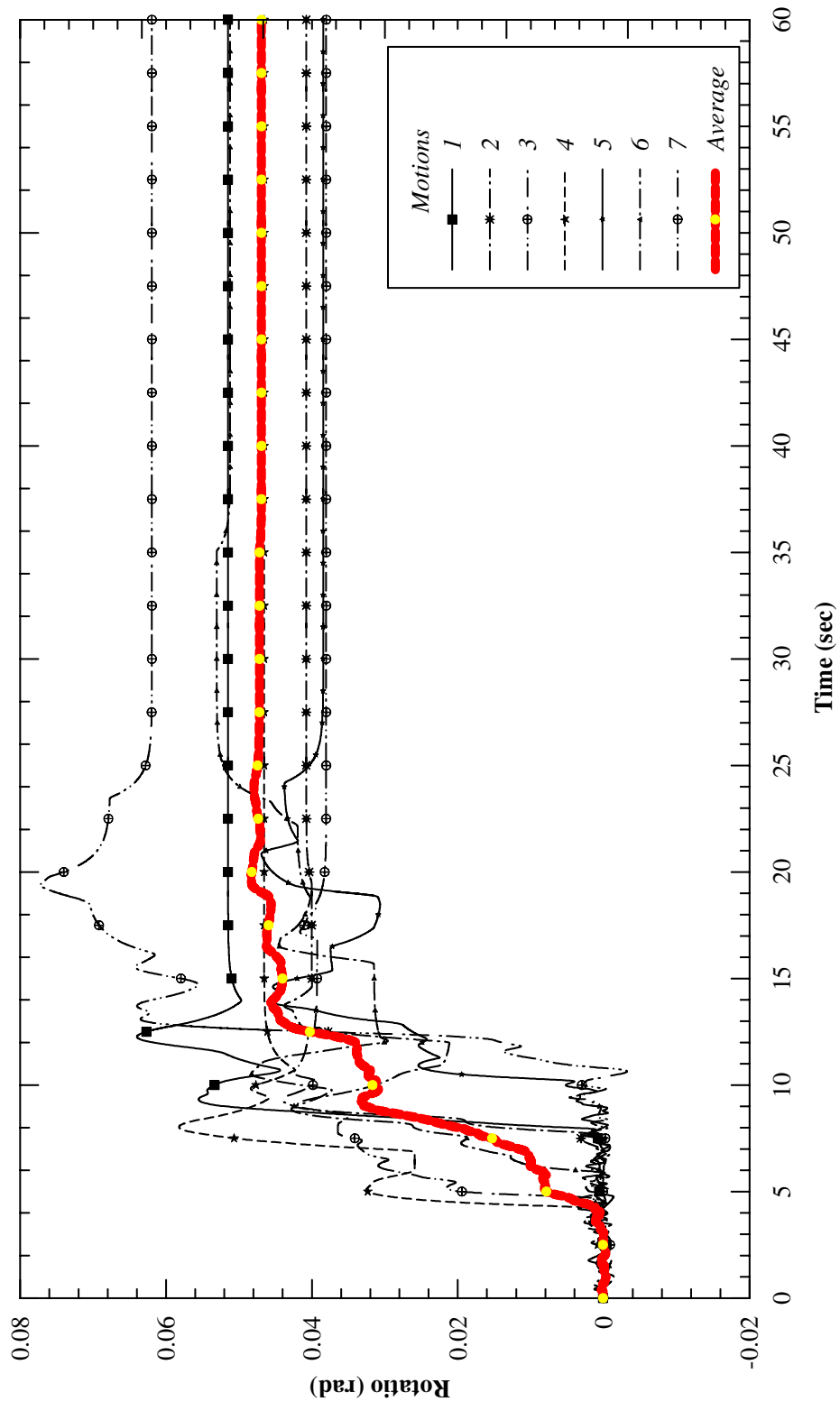


Figure 5.64 :Rotation Time History of Single Span Bridge With 25° Skew Angle (Length =102')

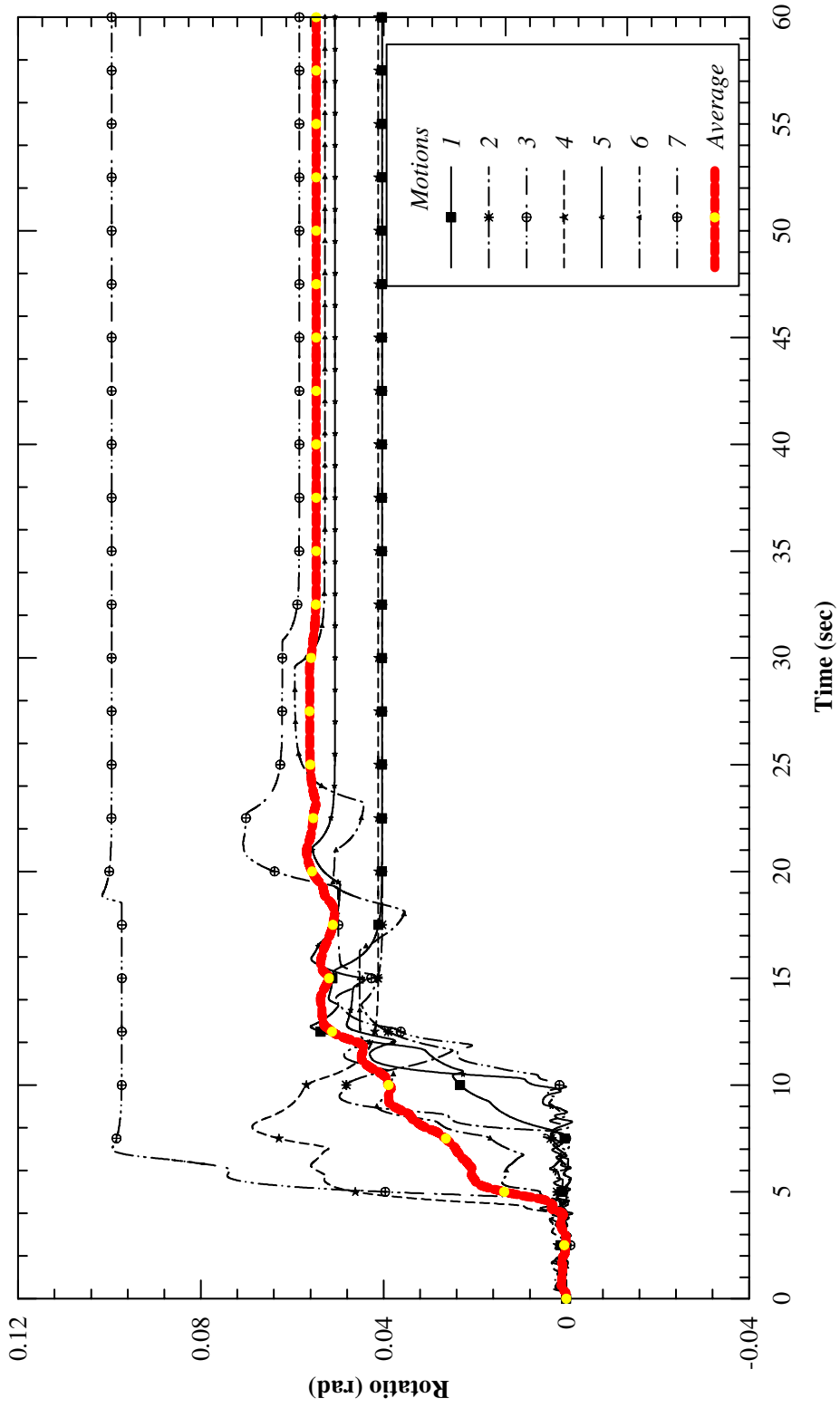


Figure 5.65: Rotation Time History of Single Span Bridge With 45° Skew Angle (Length = 102')

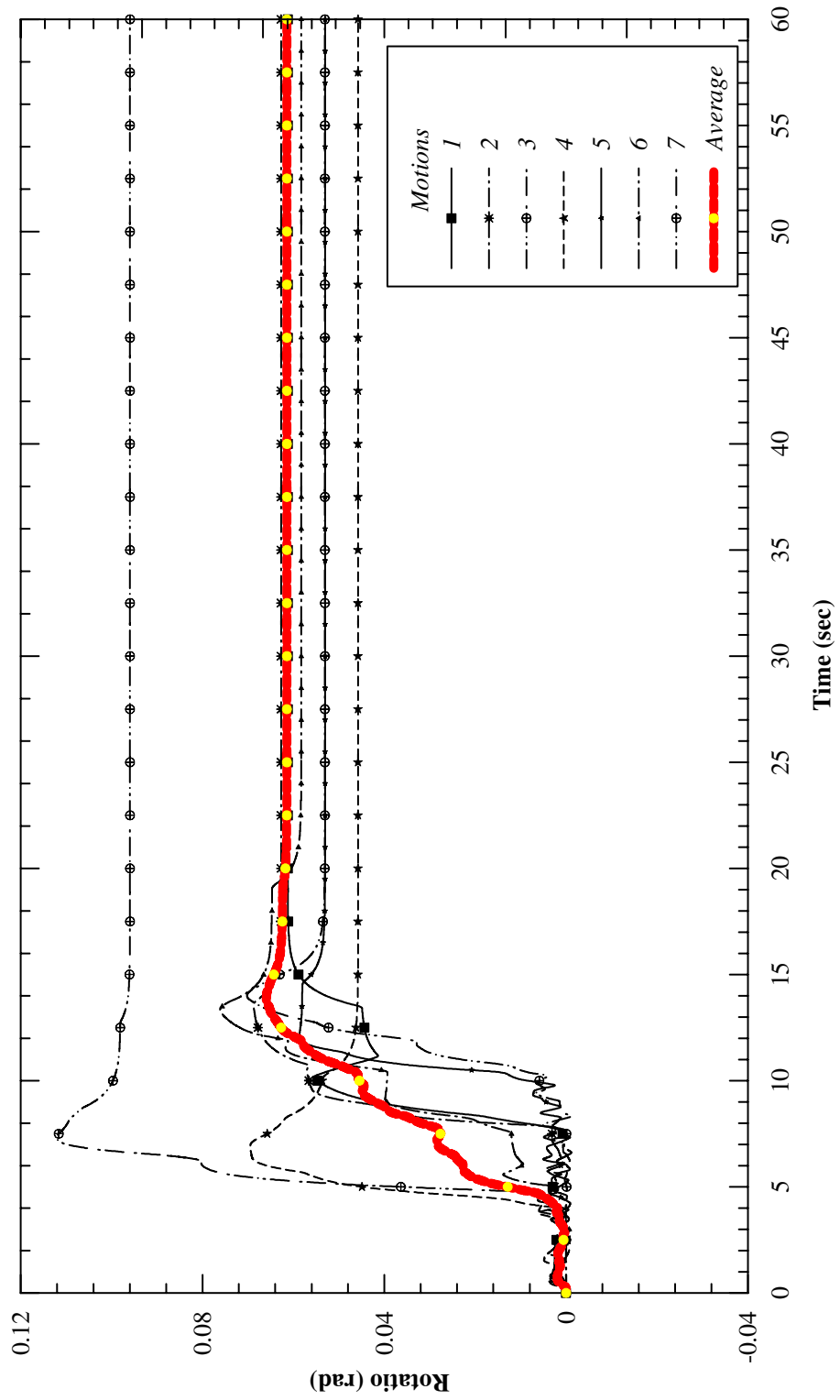


Figure 5.66: Rotation Time History of Single Span Bridge With 60° Skew Angle (Length = 102')

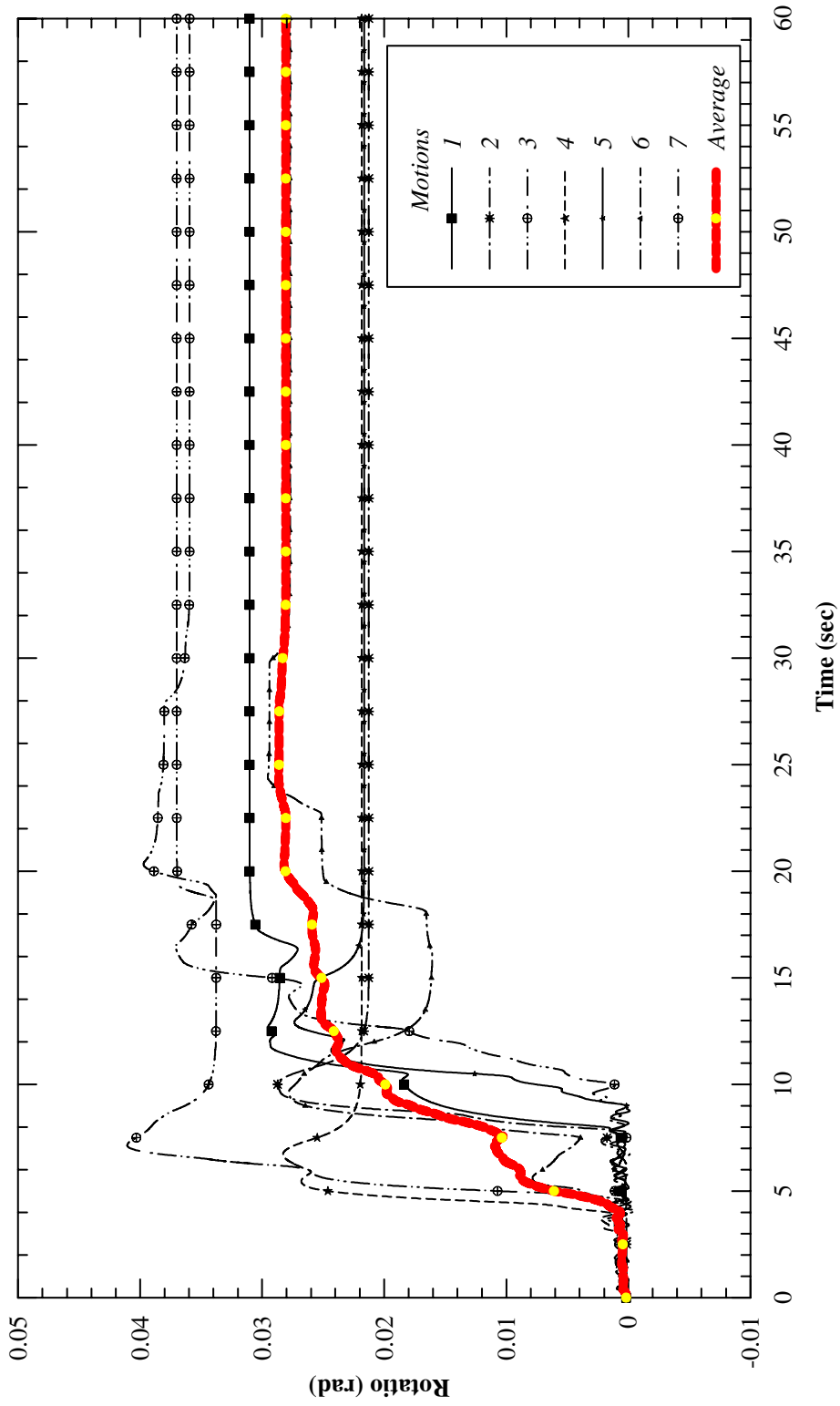


Figure 5.67: Rotation Time History of Single Span Bridge With 25° Skew Angle (Length =204')

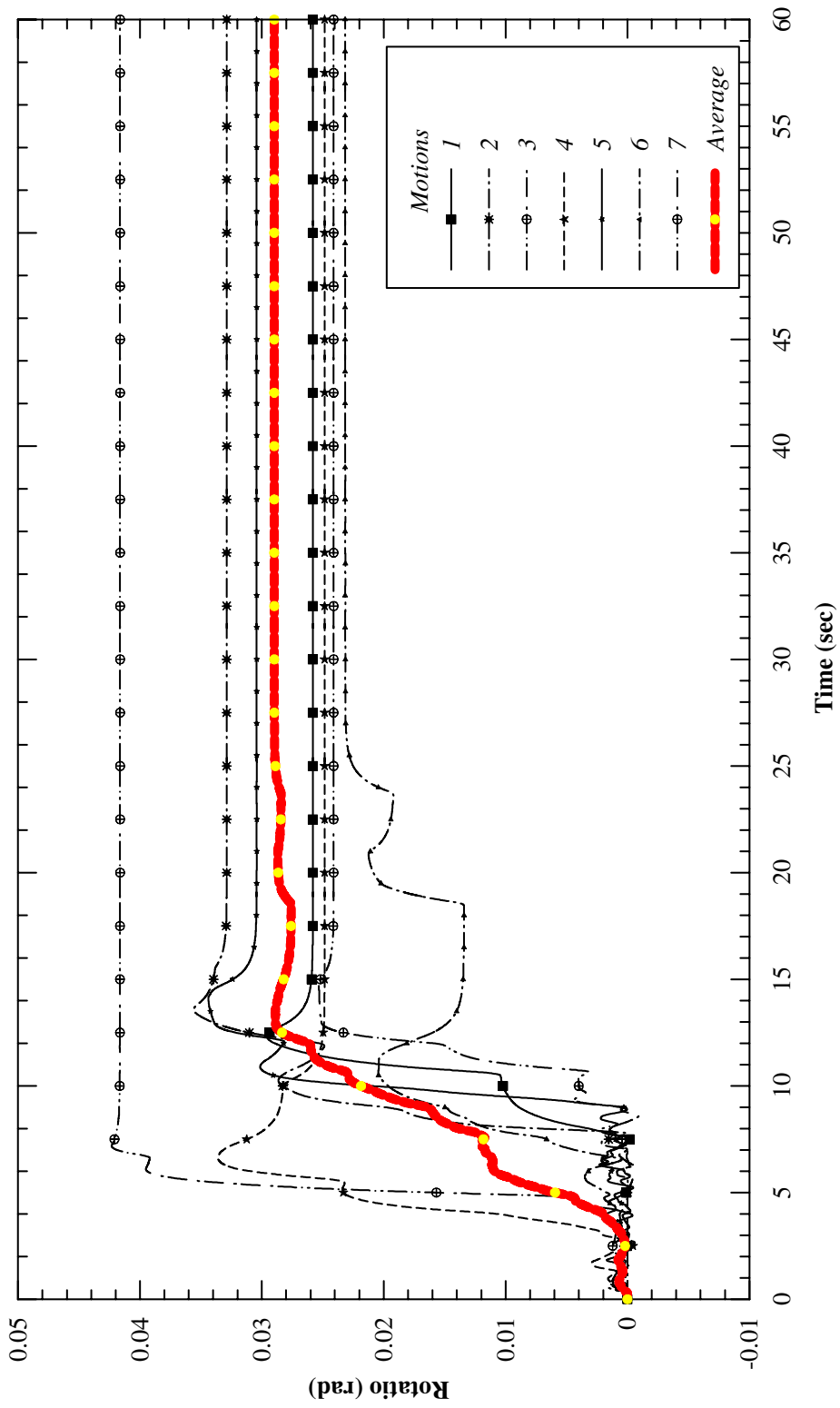


Figure 5.68: Rotation Time History of Single Span Bridge With 45° Skew Angle (Length =204')

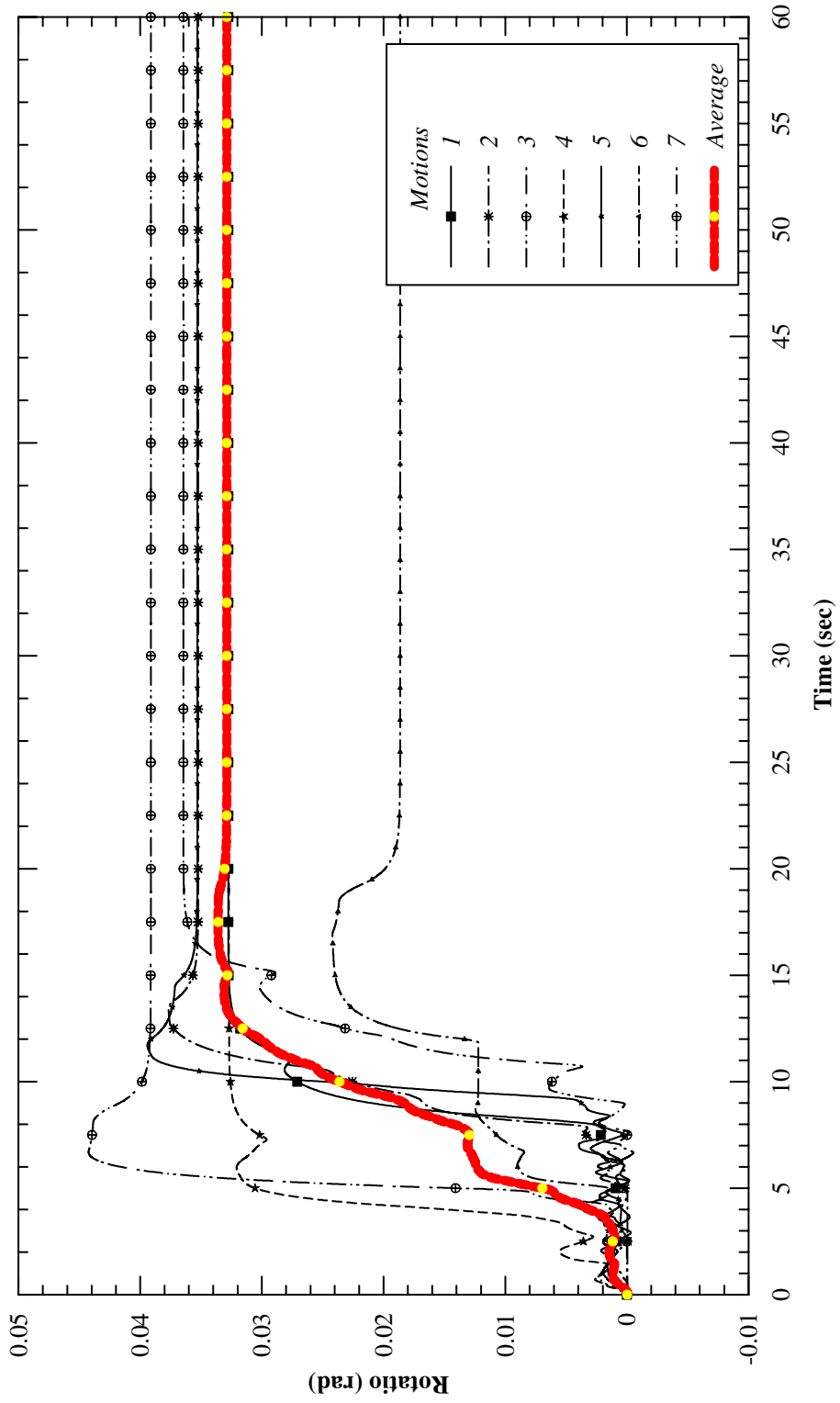


Figure 5.69: Rotation Time History of Single Span Bridge With 60° Skew Angle (Length =204')

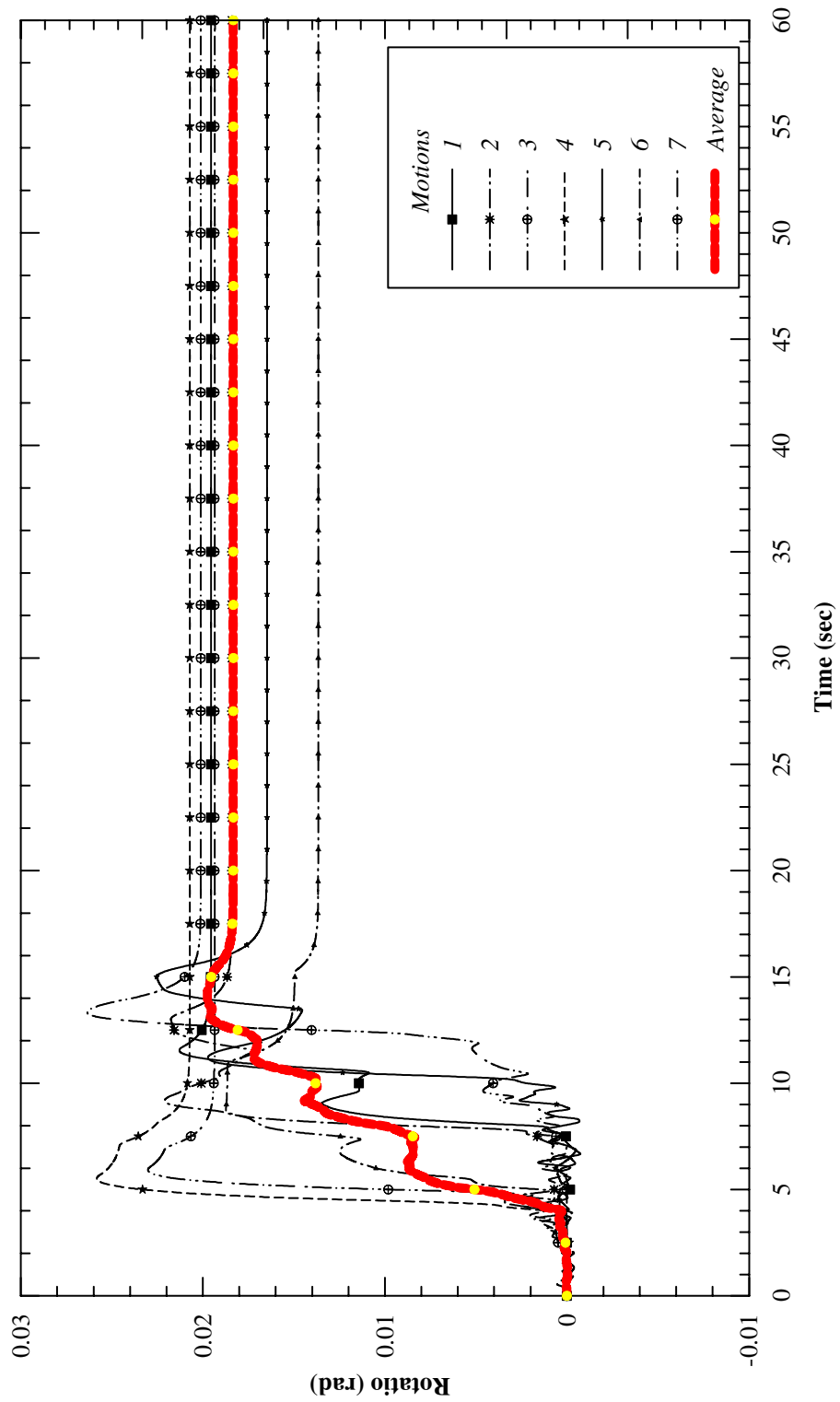


Figure 5.70: Rotation Time History of Two-Span Single-column Bridge With 25° Skew Angle

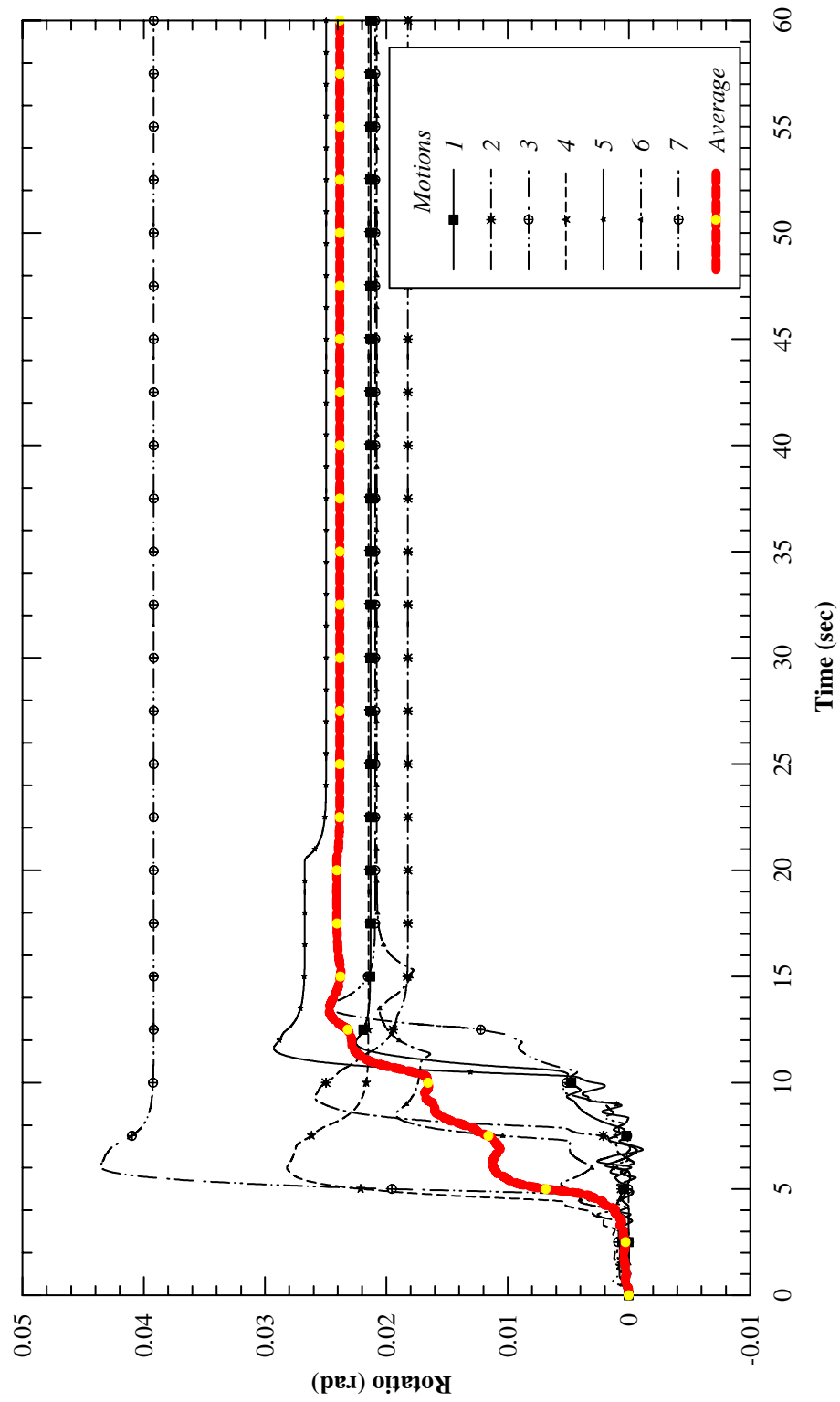


Figure 5.71: Rotation Time History of Two-Span Single-column Bridge With 45° Skew Angle

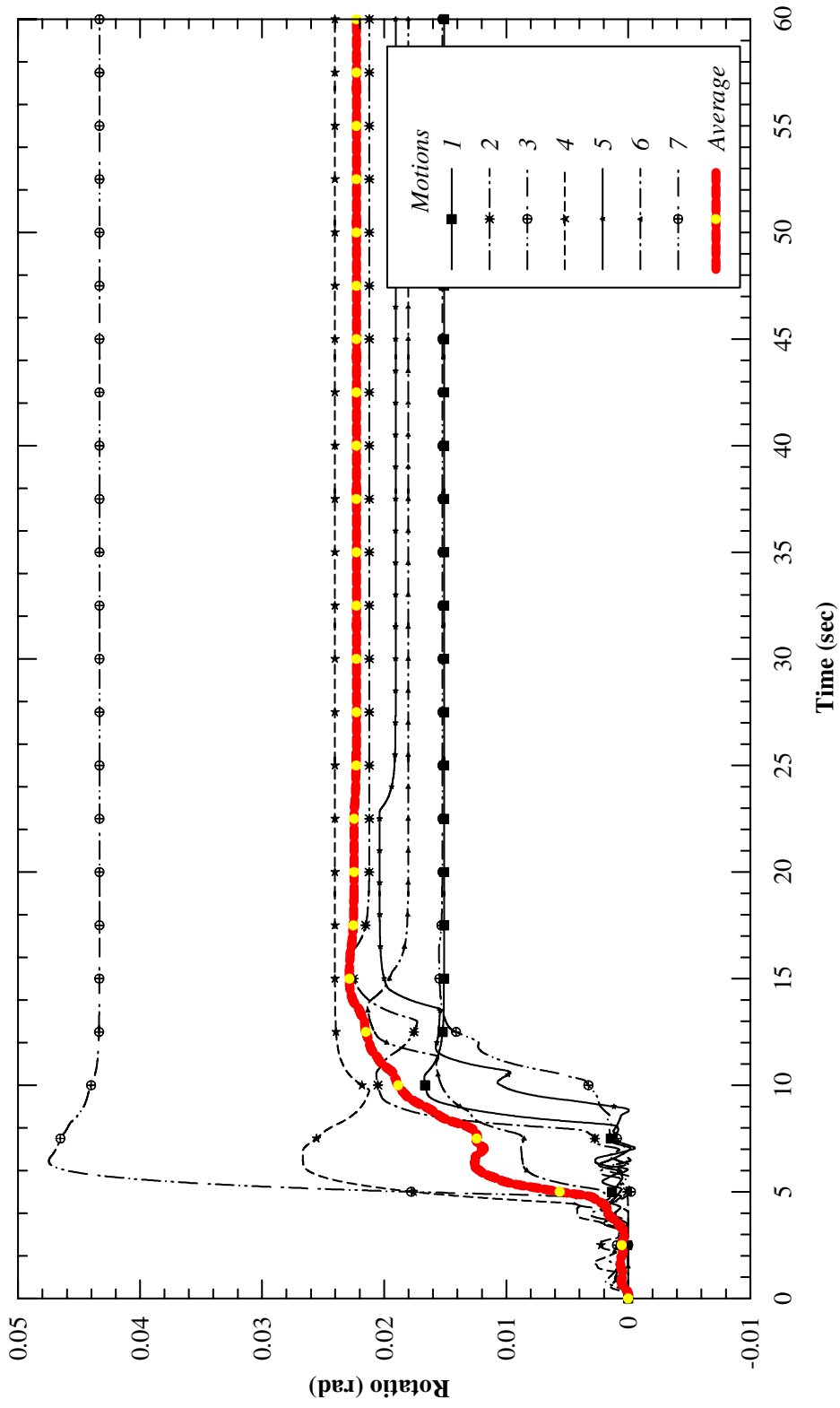


Figure 5.72 : Rotation Time History of Two- Span Single-column Bridge With 60° Skew Angle

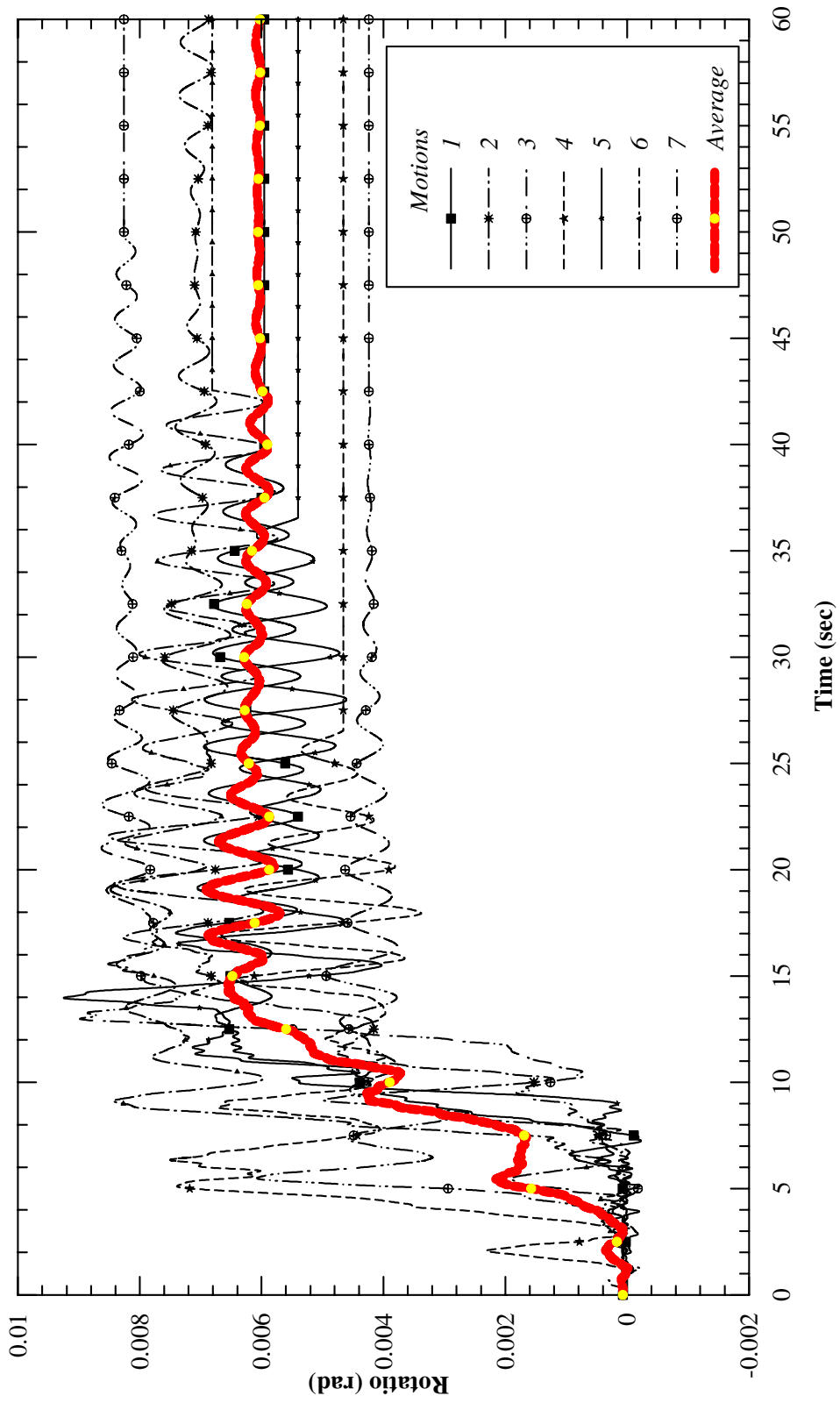


Figure 5.73: Rotation Time History of Three- Span Single-column Bridge With 25° Skew Angle

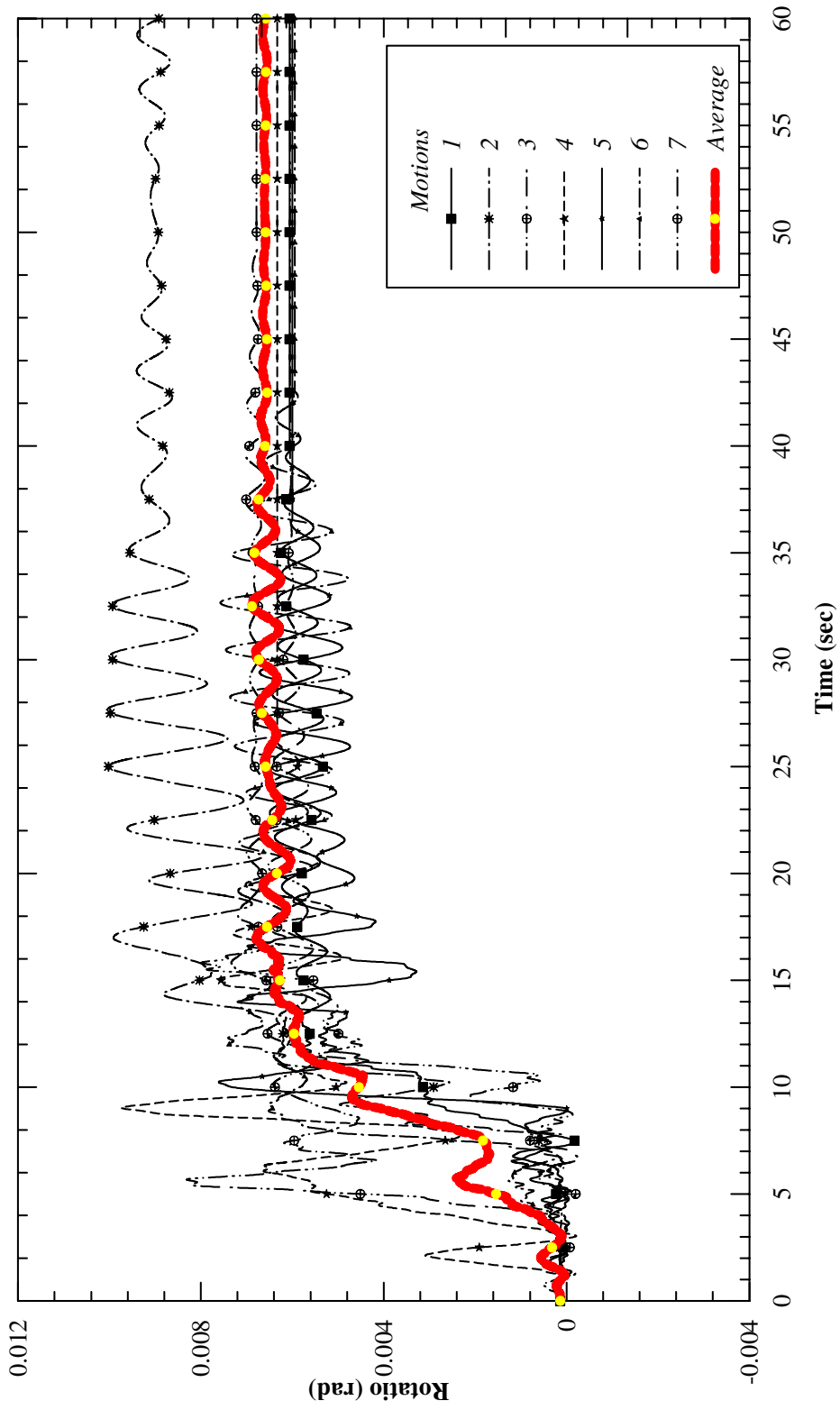


Figure 5.74: Rotation Time History of Three- Span Single-column Bridge With 45° Skew Angle

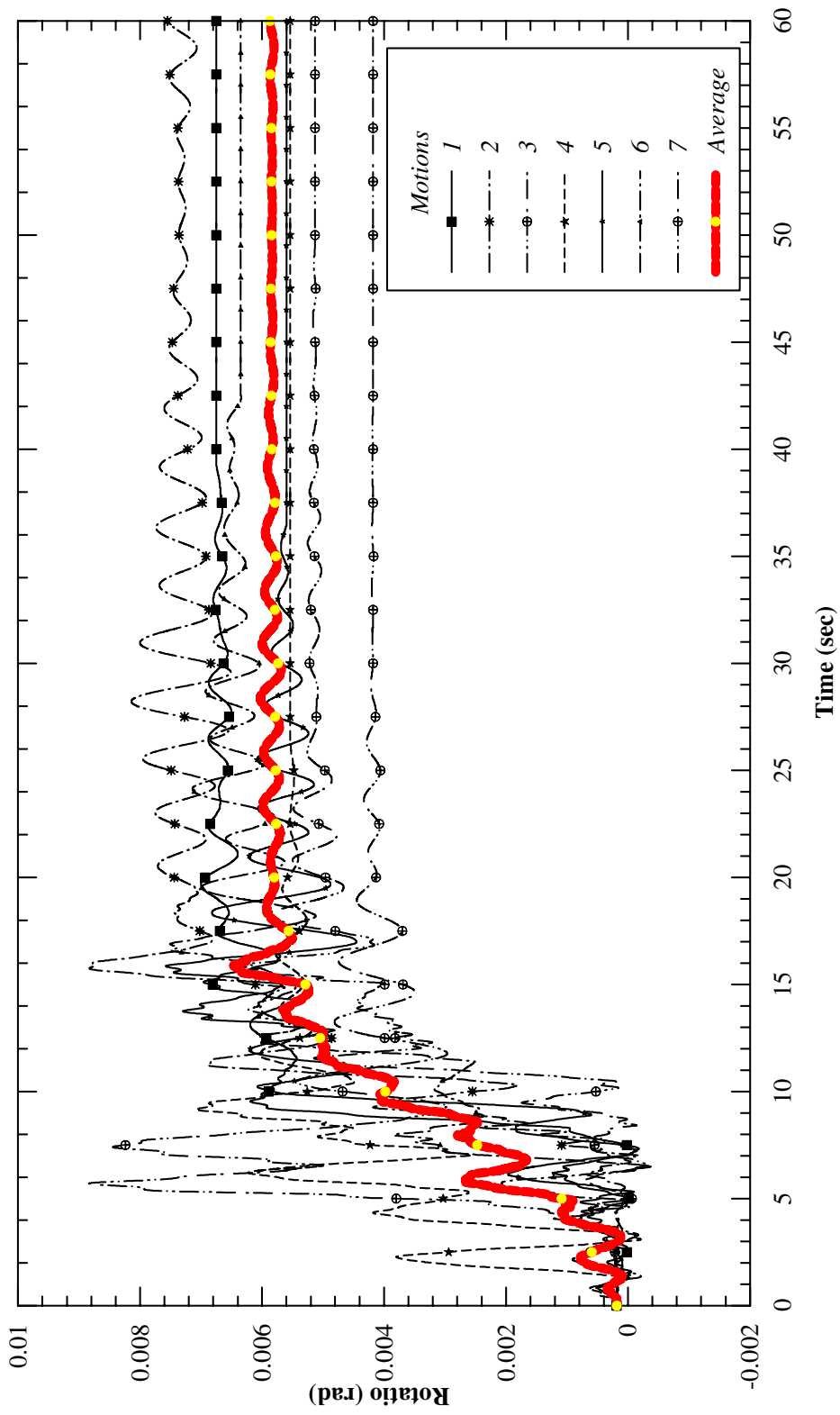


Figure 5.75: Rotation Time History of Three-Span Single-column Bridge With 60° Skew Angle

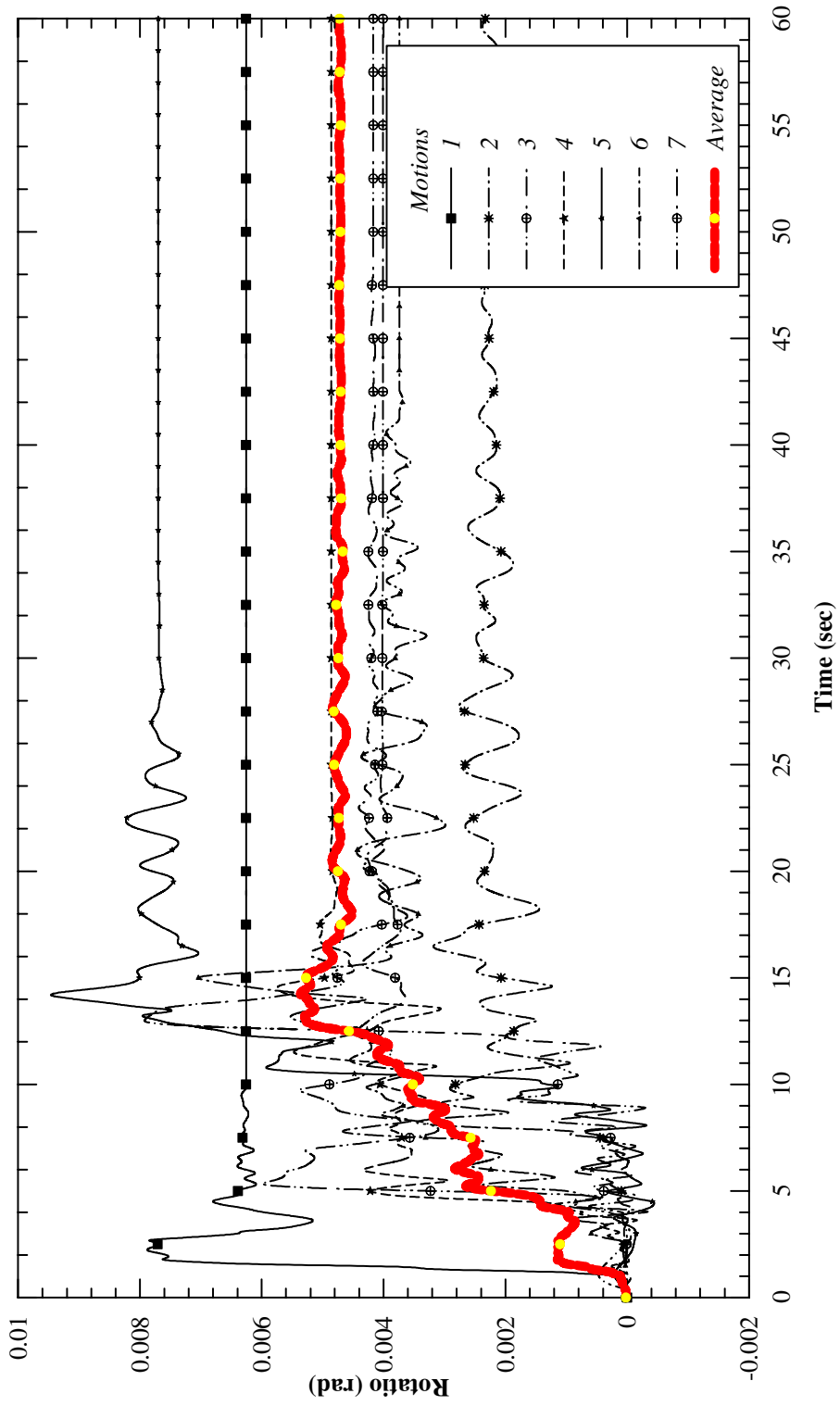


Figure 5.76: Rotation Time History of Two-Span Two-column Bridge With 25° Skew Angle

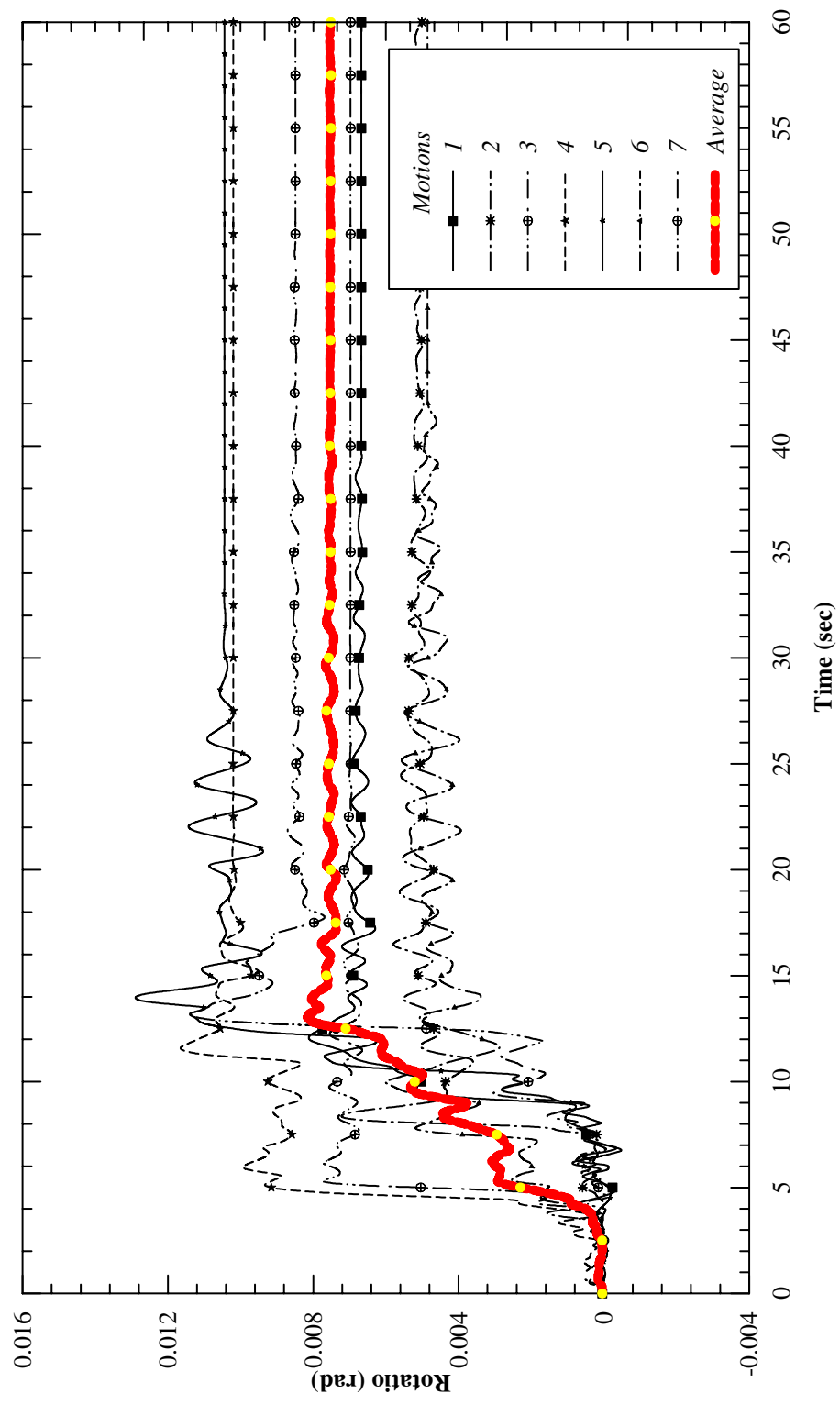


Figure 5.77: Rotation Time History of Two-Span Two-column Bridge With 45° Skew Angle

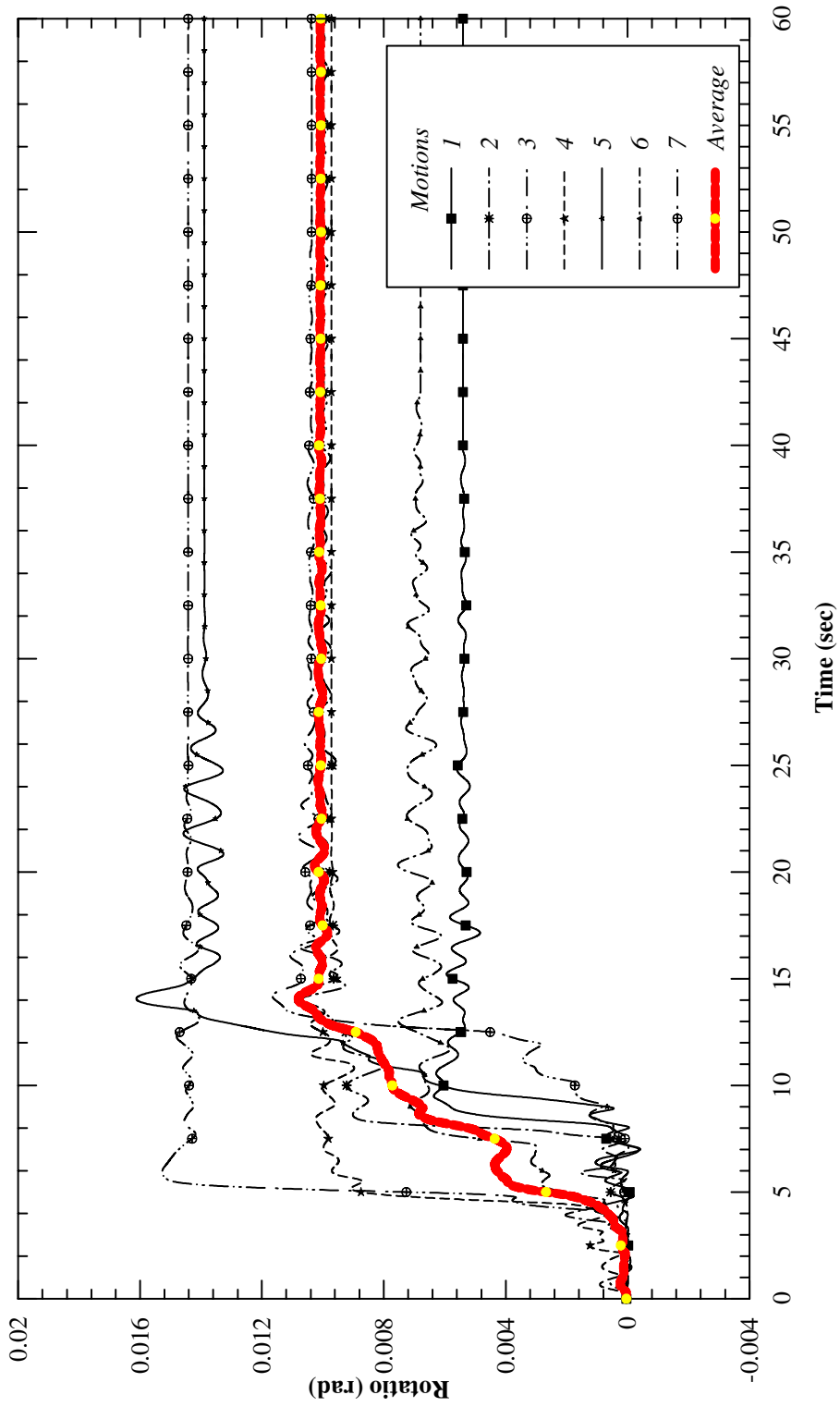


Figure 5.78: Rotation Time History of Two-Span Two-column Bridge With 60° Skew Angle

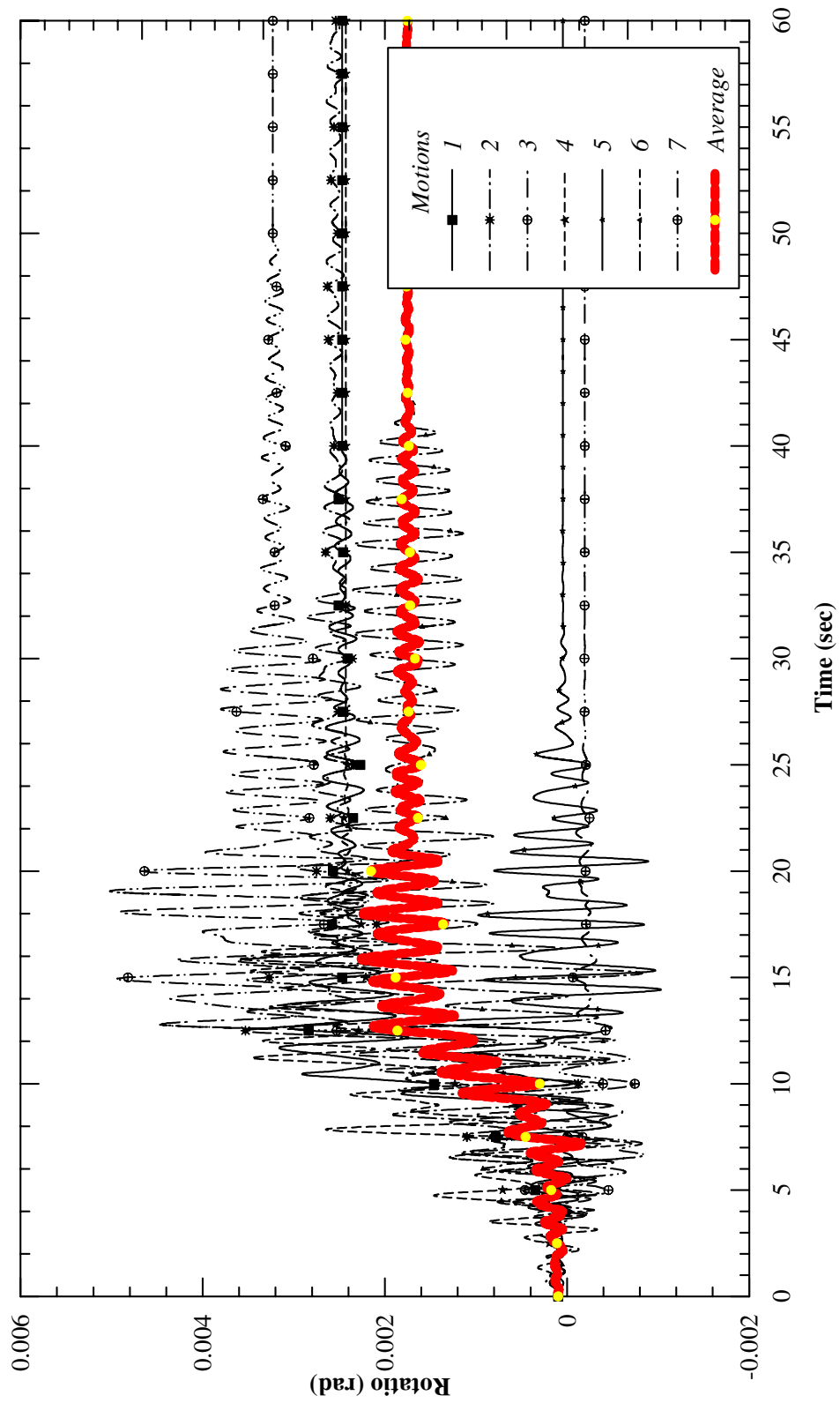


Figure 5.79: Rotation Time History of Three-Span Two-column Bridge With 25° Skew Angle

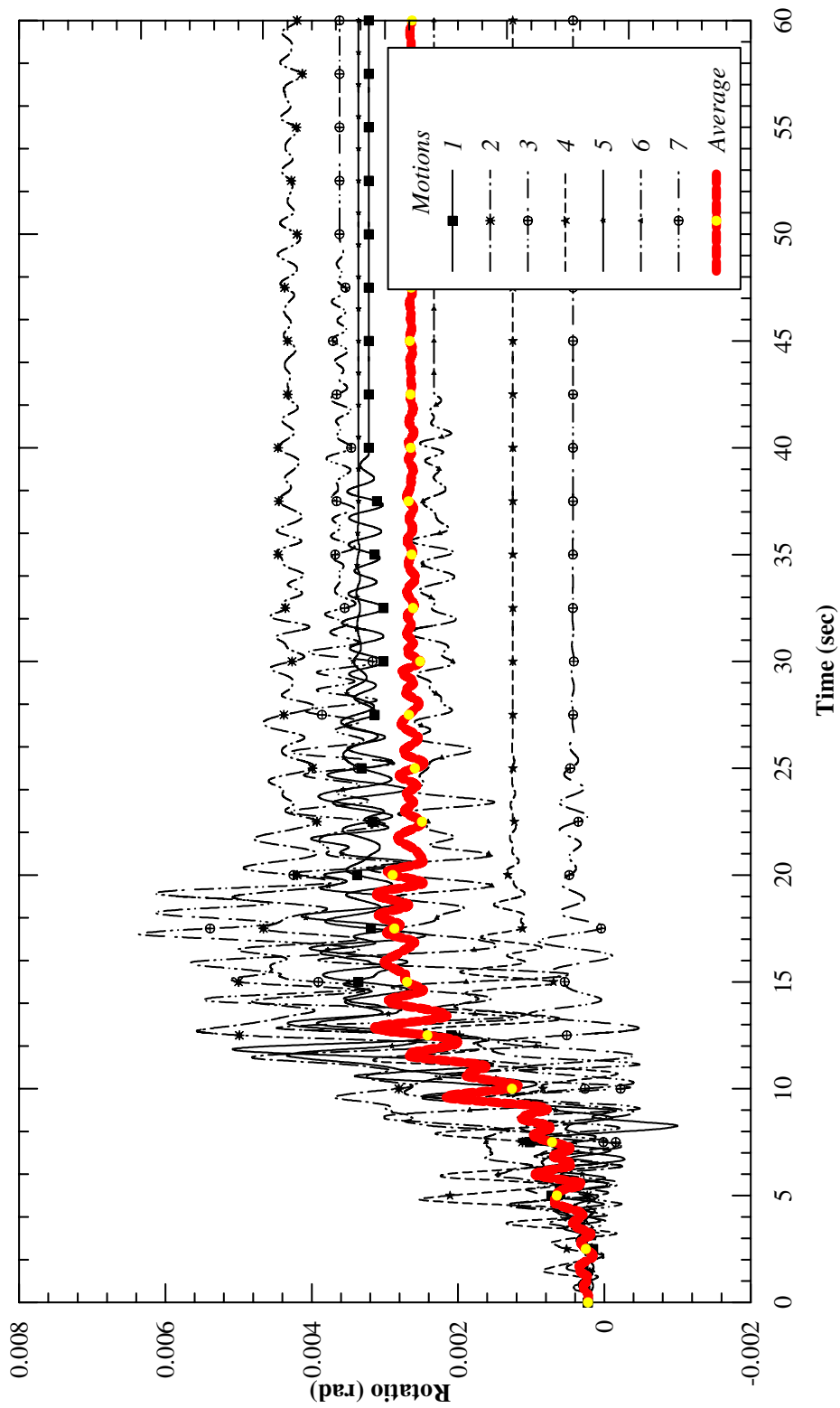


Figure 5.80: Rotation Time History of Three-Span Two-column Bridge With 45° Skew Angle

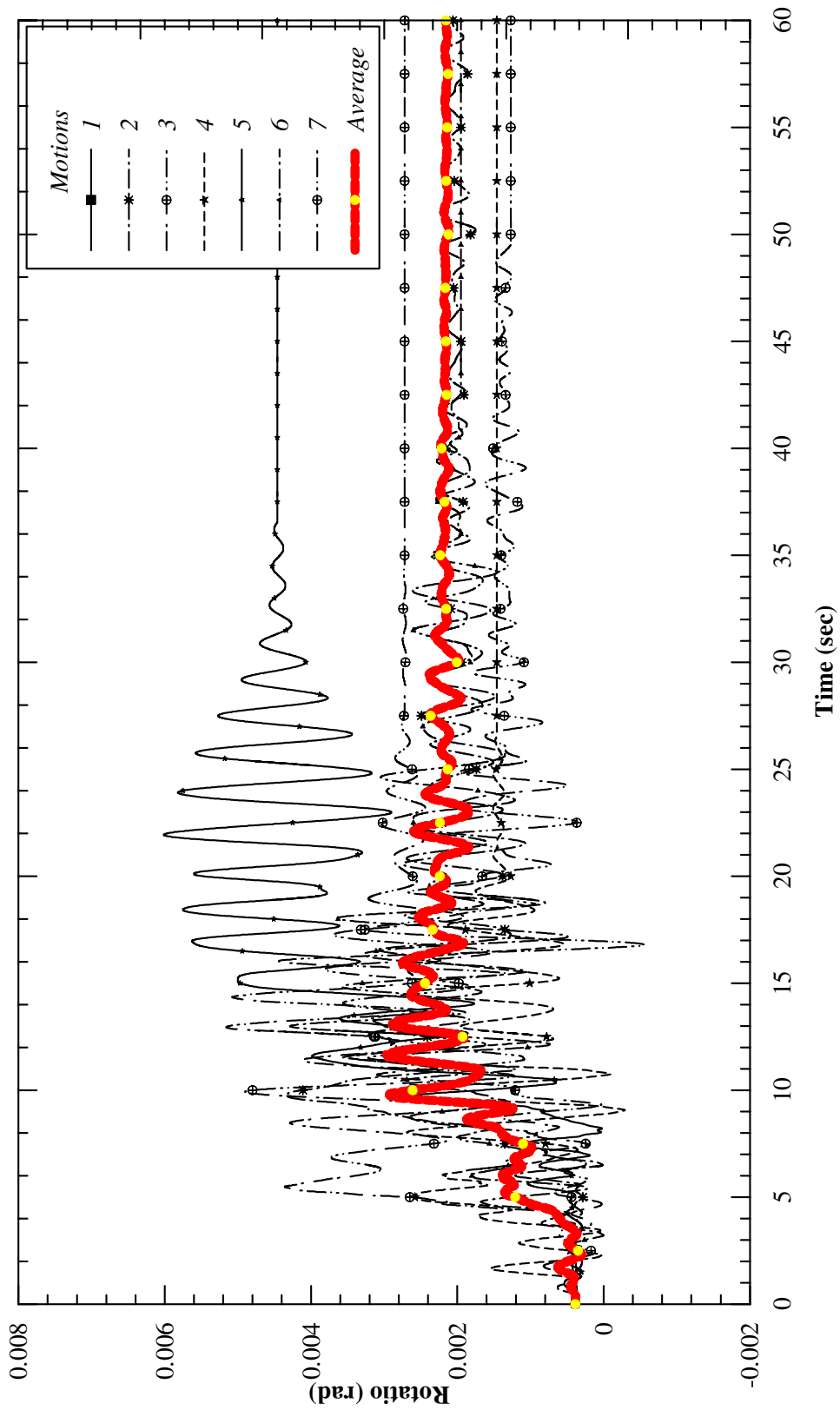


Figure 5.81: Rotation Time History of Three-Span Two-column Bridge With 60° Skew Angle

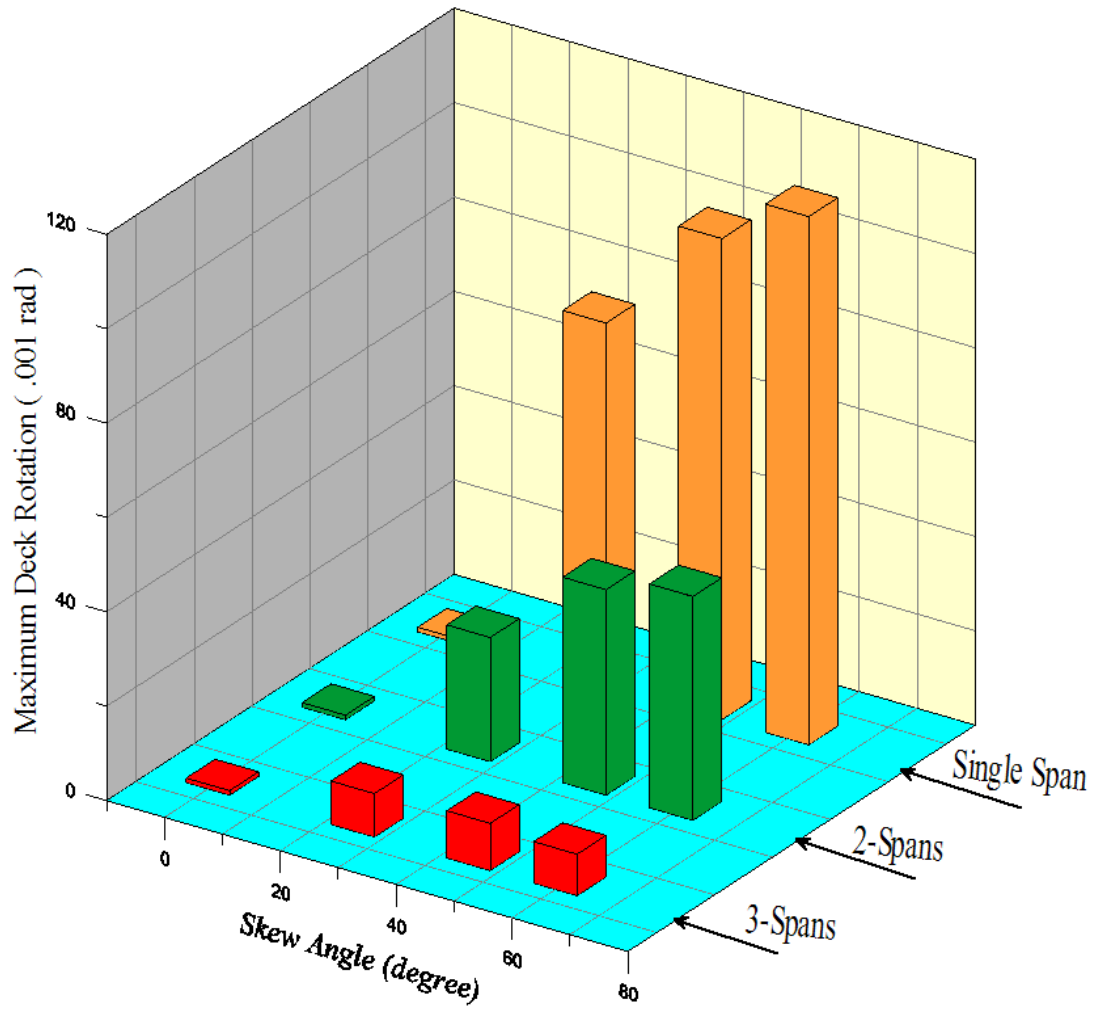


Figure 5.82: Maximum Deck Rotations

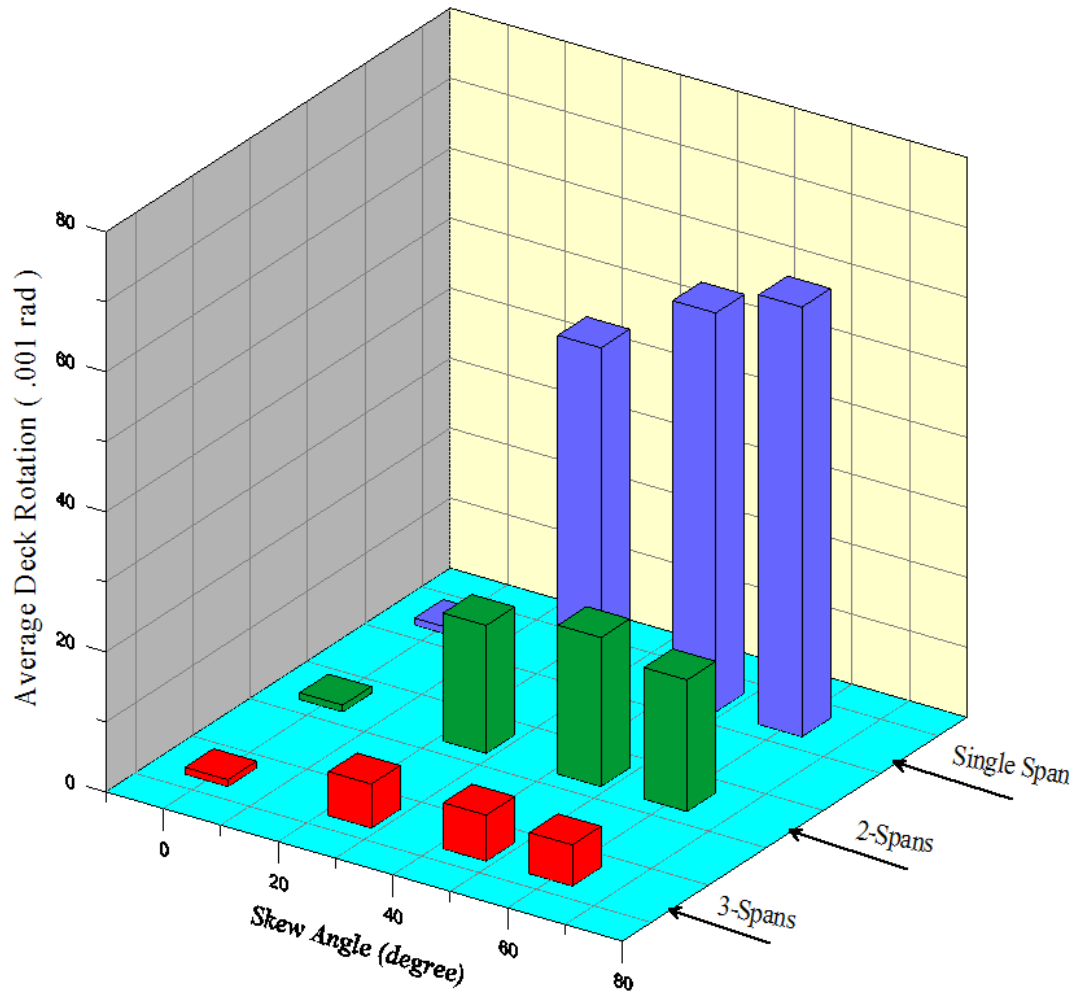
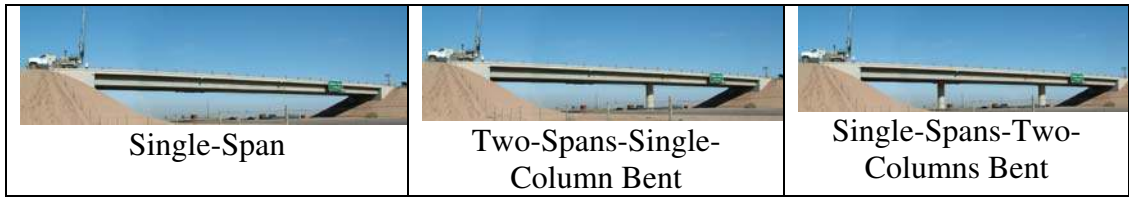


Figure 5.83: Average Residual Deck Rotations

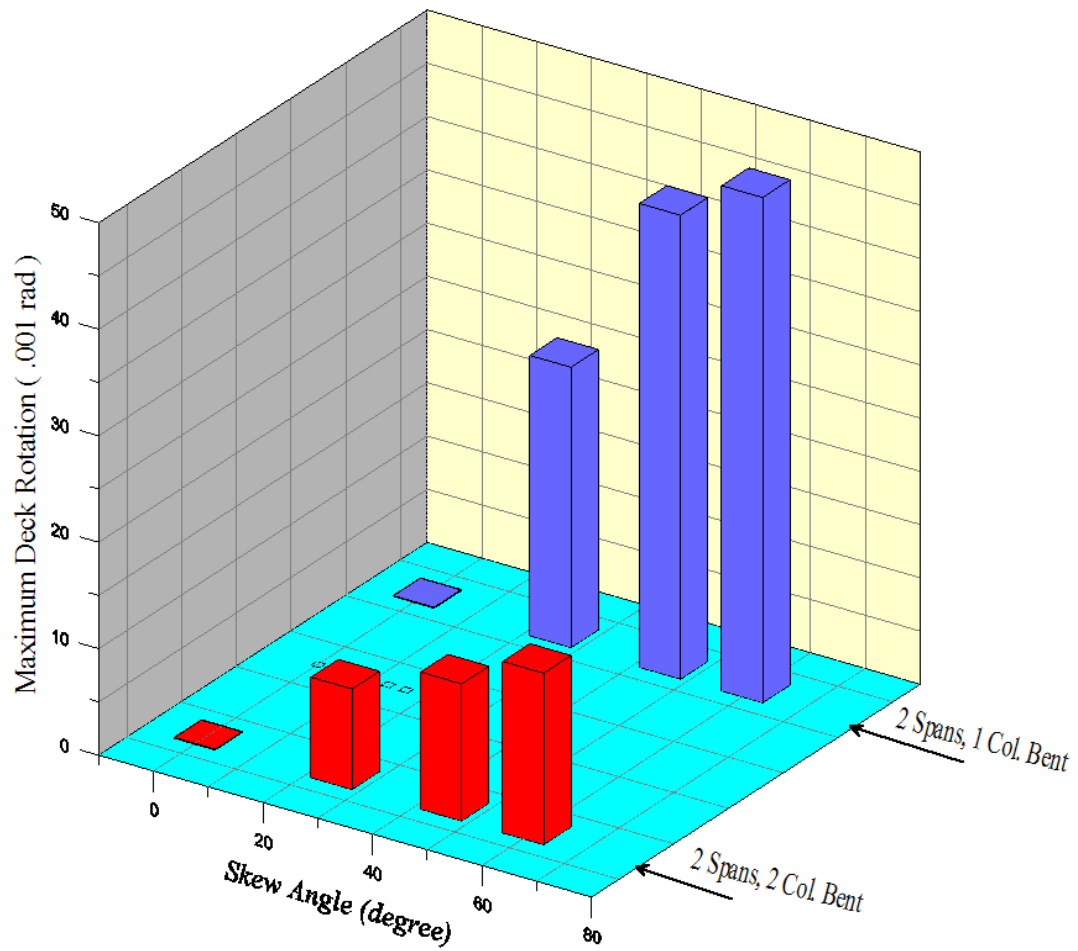


Figure 5.84: Two-Span Bridge Maximum Residual Deck Rotations

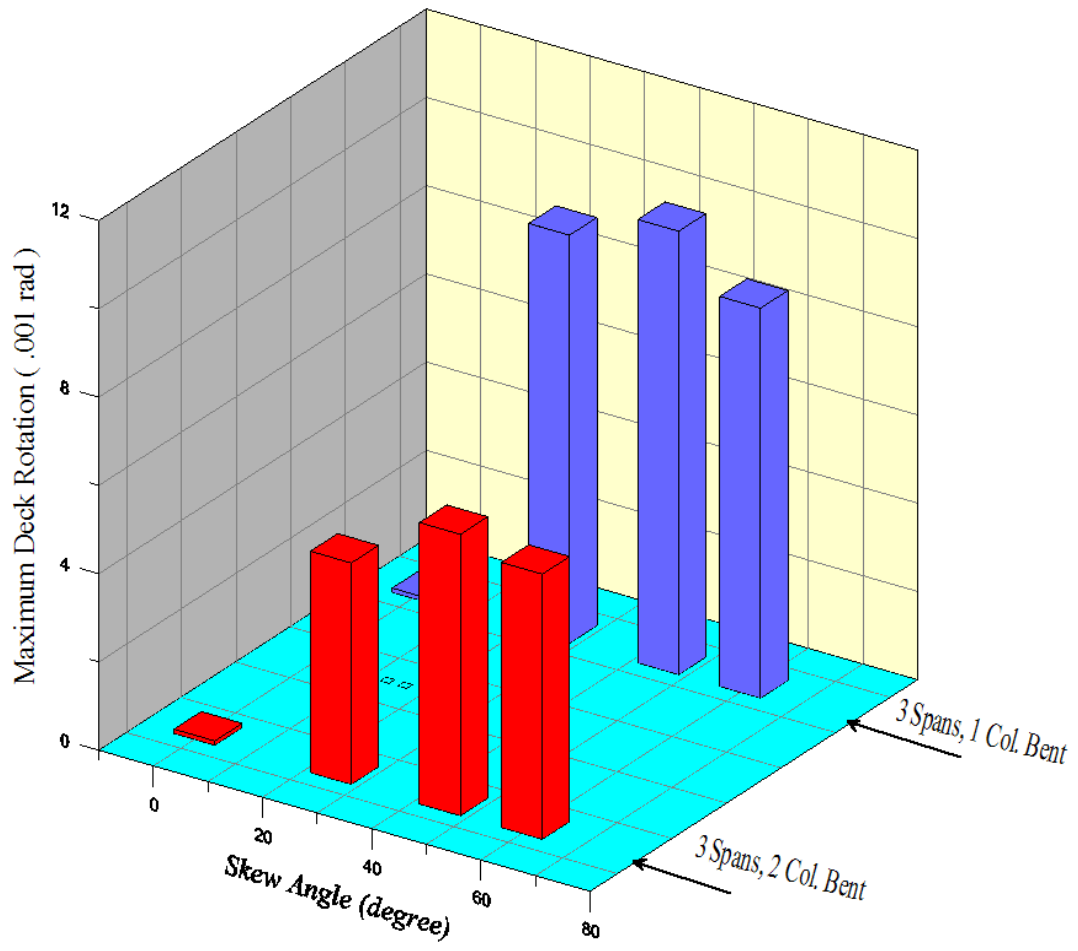


Figure 5.85: Three-Span Bridge Maximum Residual Deck Rotations

5.11 Conclusions

Three-dimensional models of a various bridge configurations were developed incorporating 0° , 25° , 45° and 60° skew angles. Nonlinear force-deformation relationship was used to model the interaction between bridge deck and the abutment backfill. The abutment shear keys were modeled using combination of the UCSD experimental backbone curves and contribution of the soil capacity in the transverse direction of the abutment. Nonlinear time-history analyses using a total of seven sets of two-component response-spectra-compatible time history input motions were performed to evaluate the seismic response of the abutments and the superstructure as a function of skew angle. All motions exhibited velocity pulses to characteristic of near-field effects.

From the results, it was found that the skewed-bridge decks undergo significant rotations about the vertical axis during seismic ground events and are permanently displaced from the original location by the end of shaking. The non-skewed bridge decks did not experience significant rotation or permanent transverse displacement despite the large velocity pulses in the input motions. Depending on the intensity of the velocity pulses, this may cause the deck to become unseated at the abutments. The deck rotation is due to development of a non-uniform passive soil wedge behind the abutment wall that results in asymmetric soil reactions between the acute and obtuse corner of the wall. The width and capacity of this passive wedge depends on a number of factors, particularly abutment (embankment) width, skew angle and ground motion characteristics. Such behavior has been

observed at existing skew abutments during the recent earthquakes. Most of the permanent rotation (transverse deck offset) was observed to build up during the initial peak cycles of shaking by all seven ground motions.

CHAPTER SIX

CASE STUDY OF AN INSTRUMENTED SKEWED BRIDGE

6.1 Introduction

Nonlinear soil-abutment-structure interaction analysis of typical ordinary highway bridge structures subjected to seismic ground motions with high velocity pulses was discussed in the previous chapter. The purpose of this chapter is to investigate the seismic Soil-Abutment-Foundation-Structure Interaction (SAFSI) analysis of ordinary highway bridge structures. The numerical methods used for SAFSI of highway bridge structures can be classified into direct approach and substructure approach. In the direct approach, nonlinear soil and foundation behaviors are explicitly included in the global model to account for geotechnical and structural behavior of foundations. The substructure approach divides the system into two subsystems, a superstructure that includes the bridge columns, bridge deck and bridge abutments and a substructure that includes the foundations and the surrounding soil media.

Many bridges are supported on pile foundations that may penetrate multiple soil layers with varying stiffness and shear strength properties. For a deep pile foundation, ground motion excitation with depth is felt along the pile length. Hence, seismic loading criteria must account for the variation in ground motion with depth, rather than merely adopting surface motion as the basis for the earthquake design. The effects of depth-varying ground motion can rigorously be addressed by modeling the global bridge

including representation of each individual pile, with distributed soil springs, extending from ground surface to the pile tip. The depth-varying ground motions from a free-field site response analysis can be used to excite the soil-pile structure system; whereby, the depth varying soil-pile properties and ground motions are rigorously taken into account. Such an analysis is referred as a complete system or direct approach. The advantage of employing the complete system approach includes possible implementation of non-linear soil-foundation supports arising from either material or geometric non-linearity.

Alternatively, a substructure system can be used to reduce the size of the problem in the complete structural model. This approach establishes the structural model without the complete foundation element. The foundation substructure is modeled by a linear stiffness matrix representing the entire soil-pile system and a set of kinematic ground motion representing effective shaking arising from the depth-varying motions acting along the piles. The substructuring technique to compute the stiffness matrix and kinematic motion involves modeling each individual pile to a convenient interface with the superstructure. Then static condensation is used to derive the condensed foundation substructure stiffness and the effective ground excitation (kinematic motion) transmitted to the superstructure.

While the detailed structural bridge models consisting of a complete foundation system are frequently used in high profile projects where plenty of resources are available, this kind of bridge model becomes economically not feasible for many ordinary bridges where resources are limited. The substructure foundation system serves

as an alternative to the complete foundation system for the structure bridge model and yet provides reasonably accurate representation.

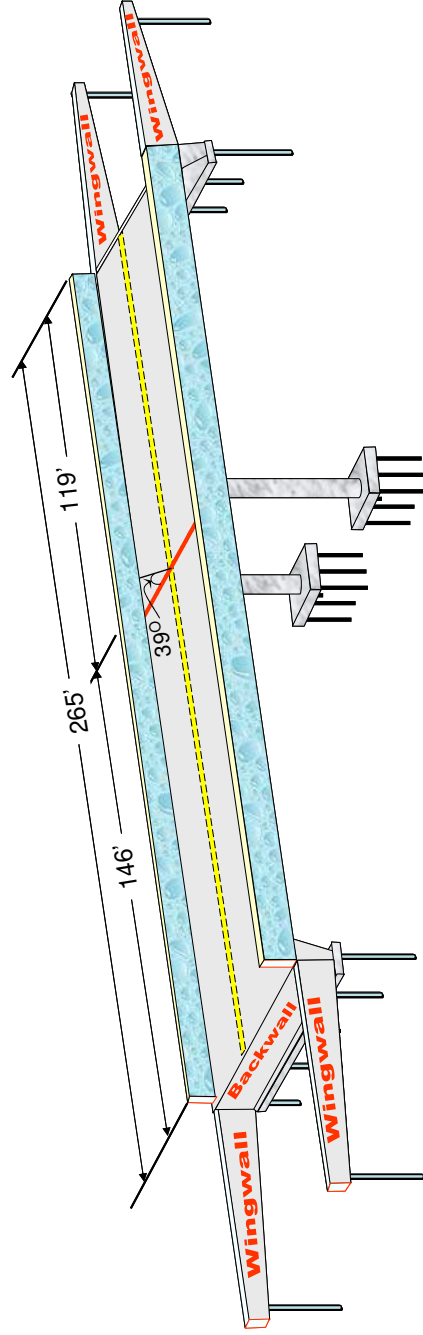
The objective of this chapter is to compare the results of the direct approach with those of the substructure approach through a case study of an instrumented bridge structure.

6.2 Bridge Description

The Painter Street Overpass is located in Rio Dell, California. The structure is a two-span cast-in-place prestressed reinforced concrete box-girder bridge supported on two-column bents and integral abutments, as shown in Figure 6.1 and Figure 6.2. The bridge is approximately 265 feet long and 52 feet wide with spans measuring 146 and 119 feet with a 39° skew angle, as shown in Figure 6.2. The depth of the deck is 5.67 feet. The average height of the columns is approximately 24 feet and each is supported on 4 x 5 driven 45-ton concrete piles, as shown in Figure 6.3. The average height of the monolithic abutment backwall is approximately 12 feet. The west abutment backwall rests on a neoprene bearing strip lubricated with grease to allow thermal movement between the abutment wall and the backfill. There is a 1-inch gap between the abutment wall and the abutment backfill. The west abutment is supported on a single row of 16 concrete piles. The east abutment backwall is monolithic, e.g., the wall is cast to the deck and the pile cap and it is supported on a single row of 14-ton driven concrete piles. As a result, the west abutment is more flexible than the east abutment.

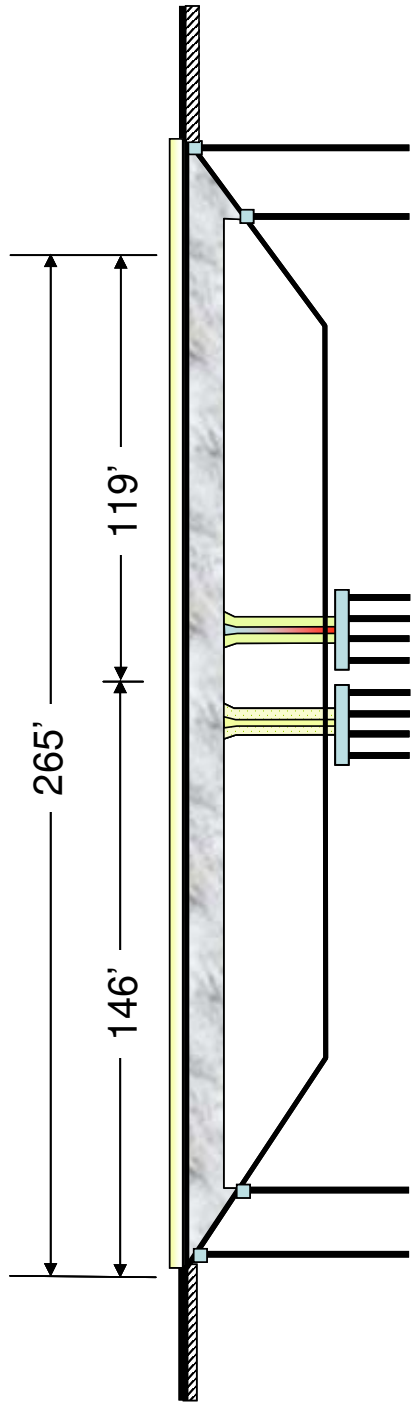


(a) General View

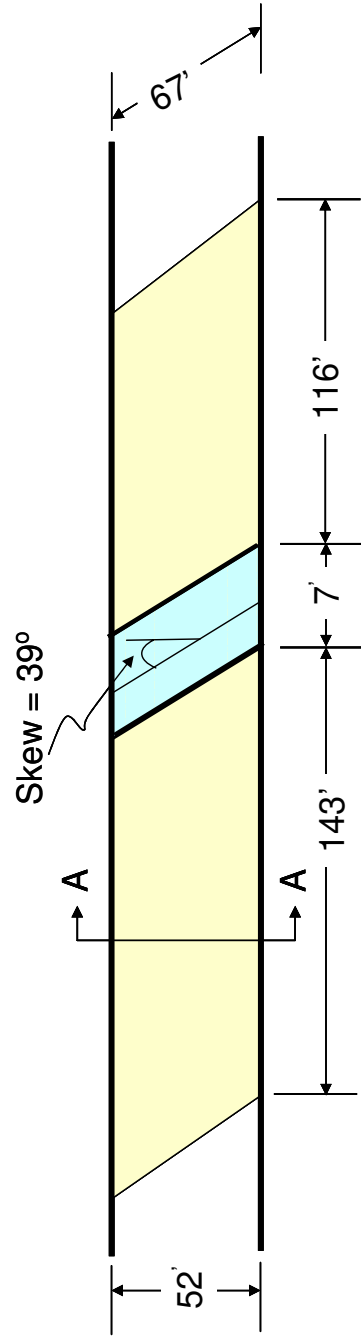


(b) Structural components

Figure 6.1: 3-D View of the Painter Street Bridge



(a) Elevation



(b) Plan

Figure 6.2: Elevation and Plan Views of the Painter Street Bridge

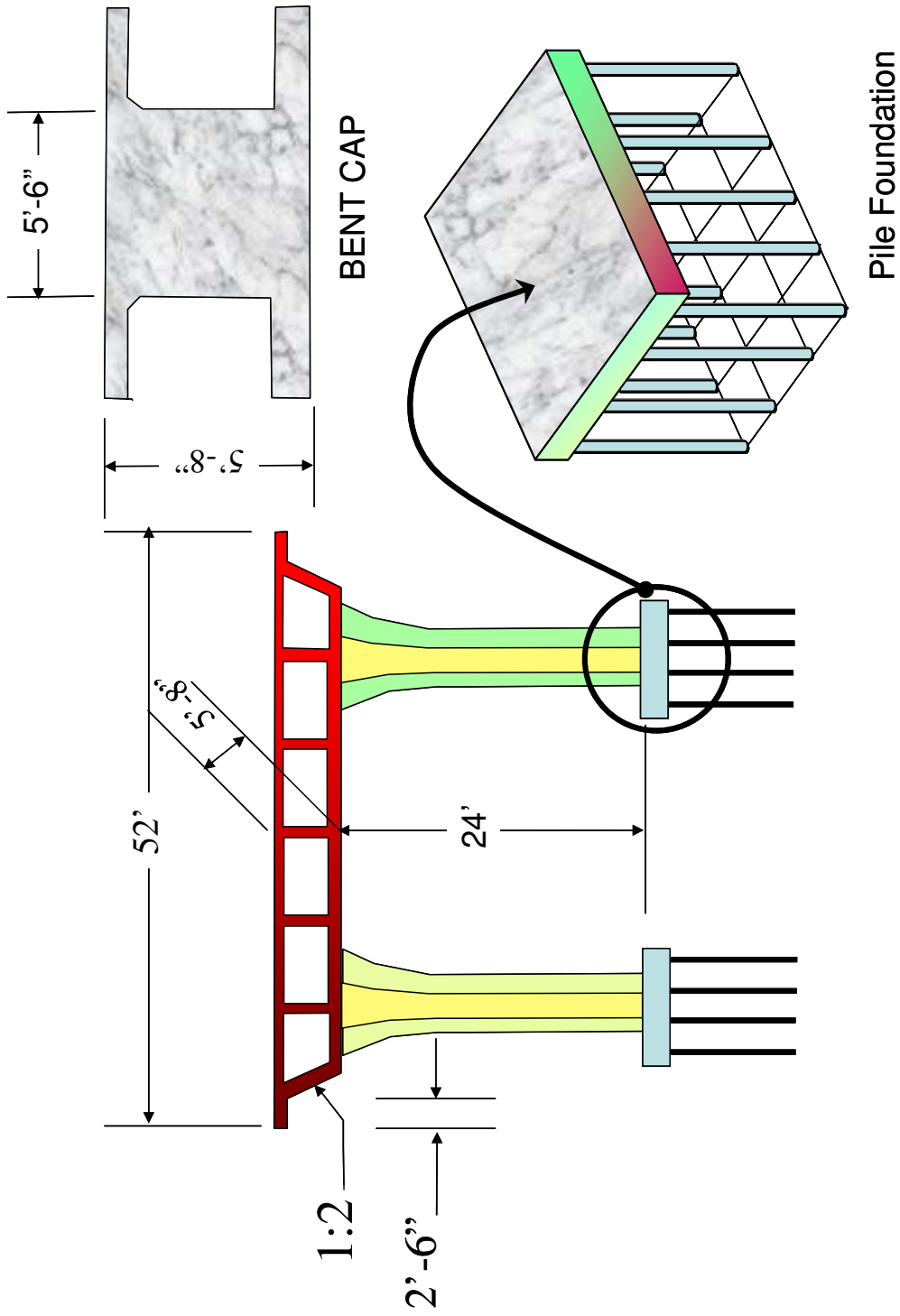


Figure 6.3: Cross Section of Superstructure and Pile Foundation of the Painter Street Bridge

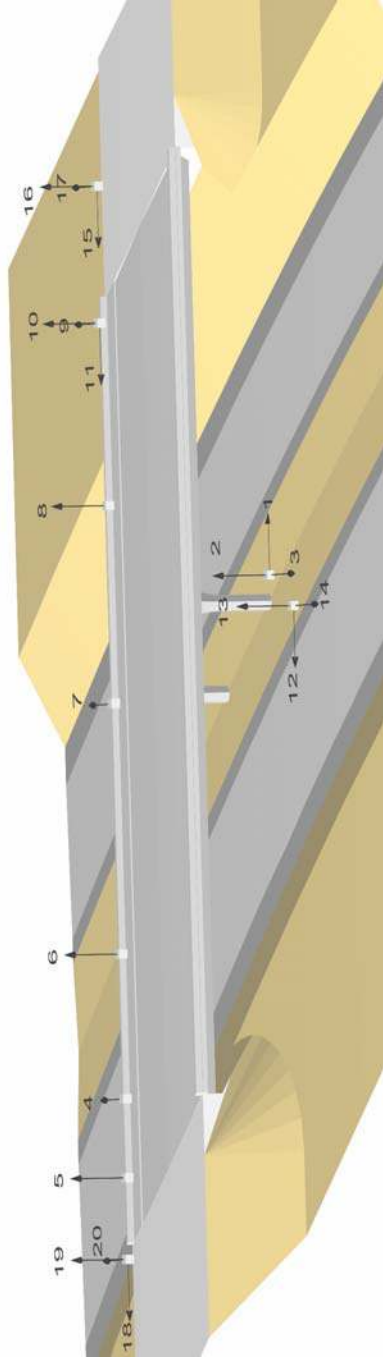
6.3 Seismic Instrumentation and Input Ground Motion

The Painter Street Overpass is seismically instrumented and has been shaken by several earthquakes for which records are available. The largest earthquake that shook the structure is the 6.9 magnitude 1992 Cape Mendocino/Petroliia earthquake. The location of the instruments that measured the free-field (Channels 12, 13 and 14) motions and structure accelerations (all other channels) are shown in Figure 6.4.

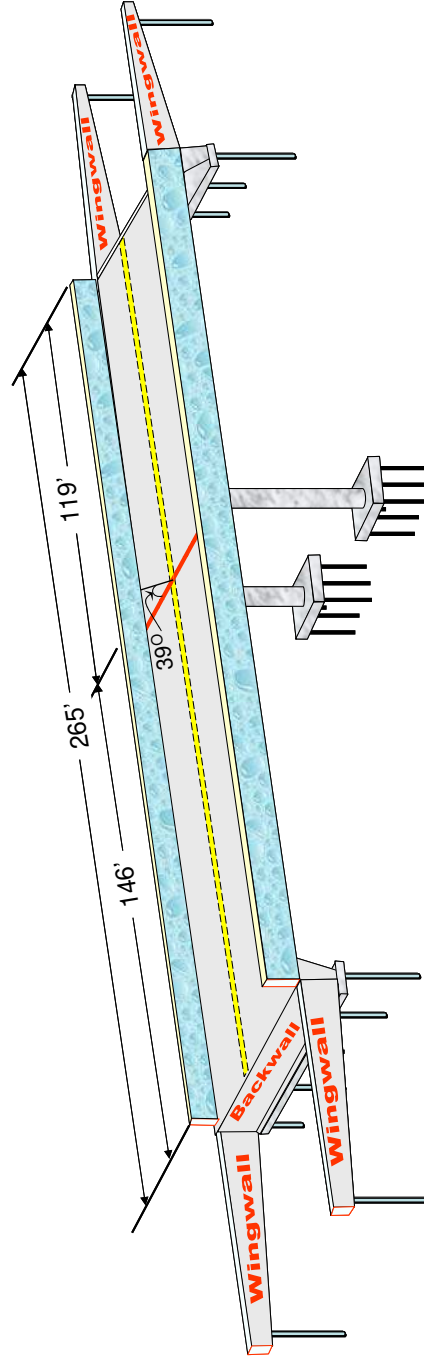
For performing dynamic analyses with a time-domain approach, the unscaled recorded free-field acceleration-time histories of the Cape Mendocino/Petroliia earthquake were used as input motions to excite the bridge. The strongest component of the input motion was in the bridge transverse direction. The acceleration, velocity and displacement time histories of the recorded and the input motions are shown in Figure 6.5, Figure 6.6 and Figure 6.7. The peak ground accelerations, velocities and displacements of the three input motions are summarized in Table 6.1.

Table 6.1 Characteristics of the Input Motions of the Painter Street Bridge

Bridge Direction	Peak Acceleration (g)	Peak Velocity (in/sec)	Peak Displacement (in)
Transverse (N-S)	0.54	18.30	2.06
Longitudinal (E-W)	0.38	14.61	2.97
Vertical	0.20	3.85	0.84



(a) Seismic Instrumentations



(b) 3-D Structural Configuration

Figure 6.4: Seismic Instrumentation at the Painter Street Bridge

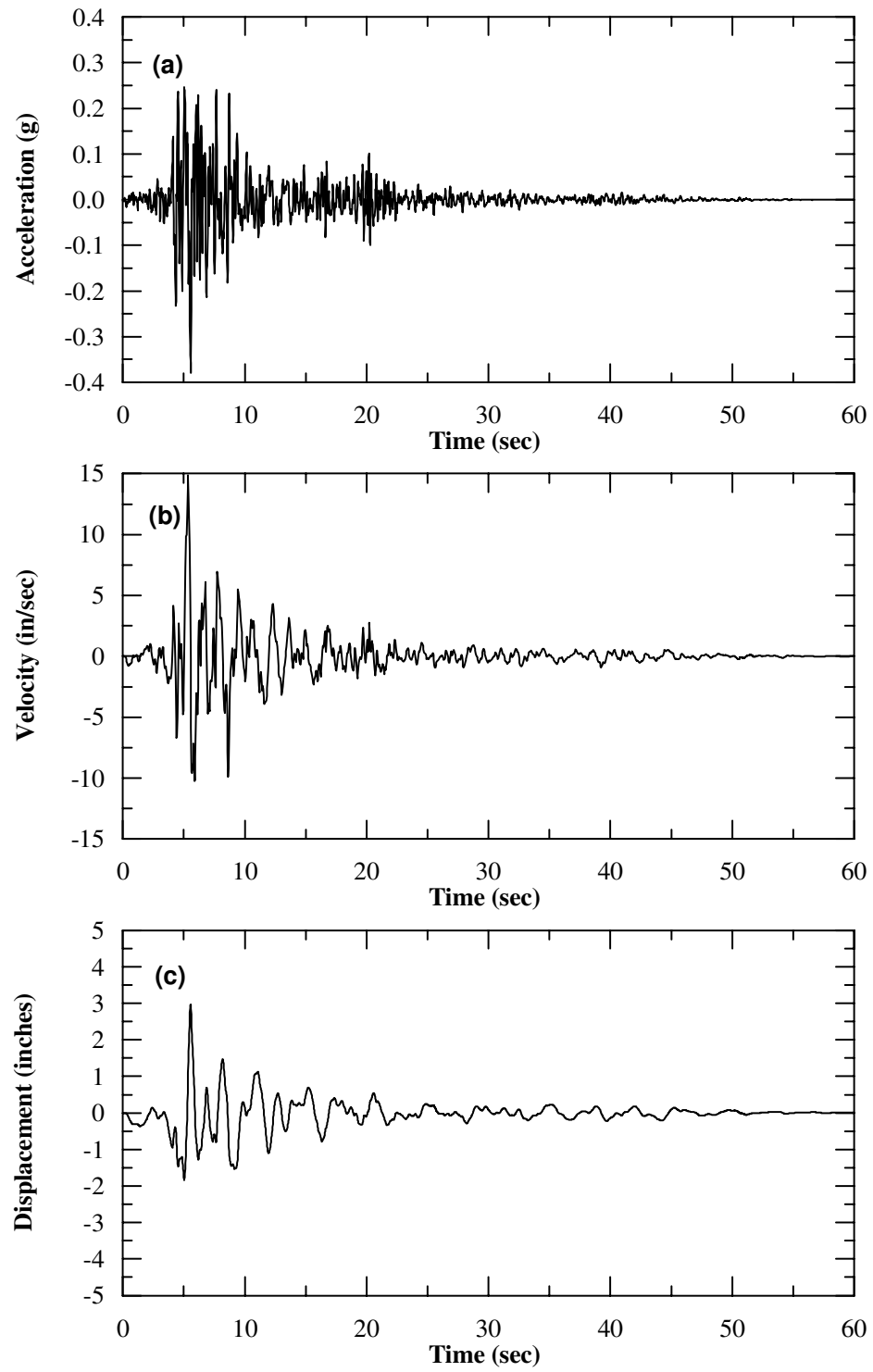


Figure 6.5: Input Motion in Longitudinal Direction (Channel 12)

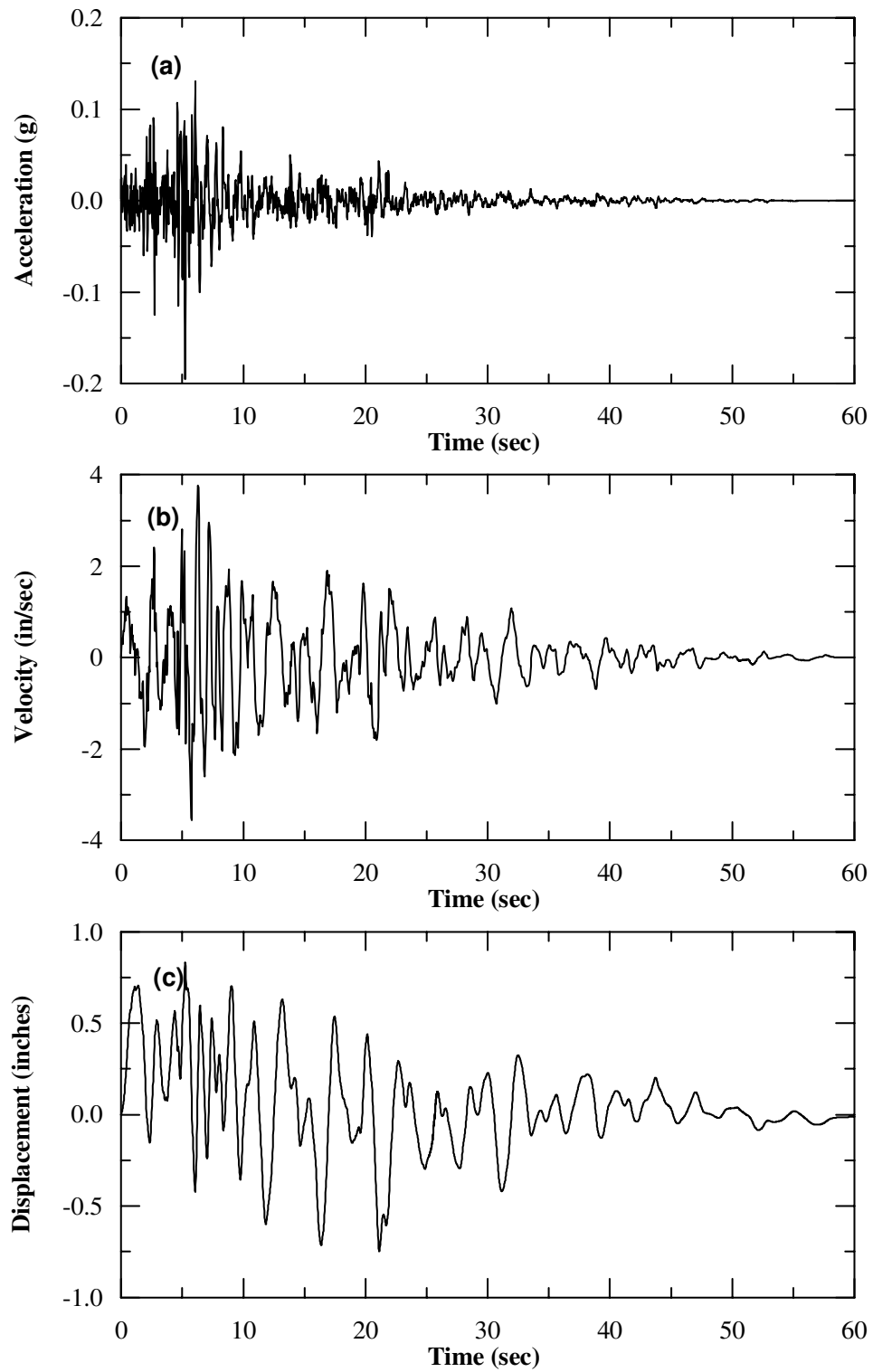


Figure 6.6: Input Motion in Vertical Direction (Channel 13)

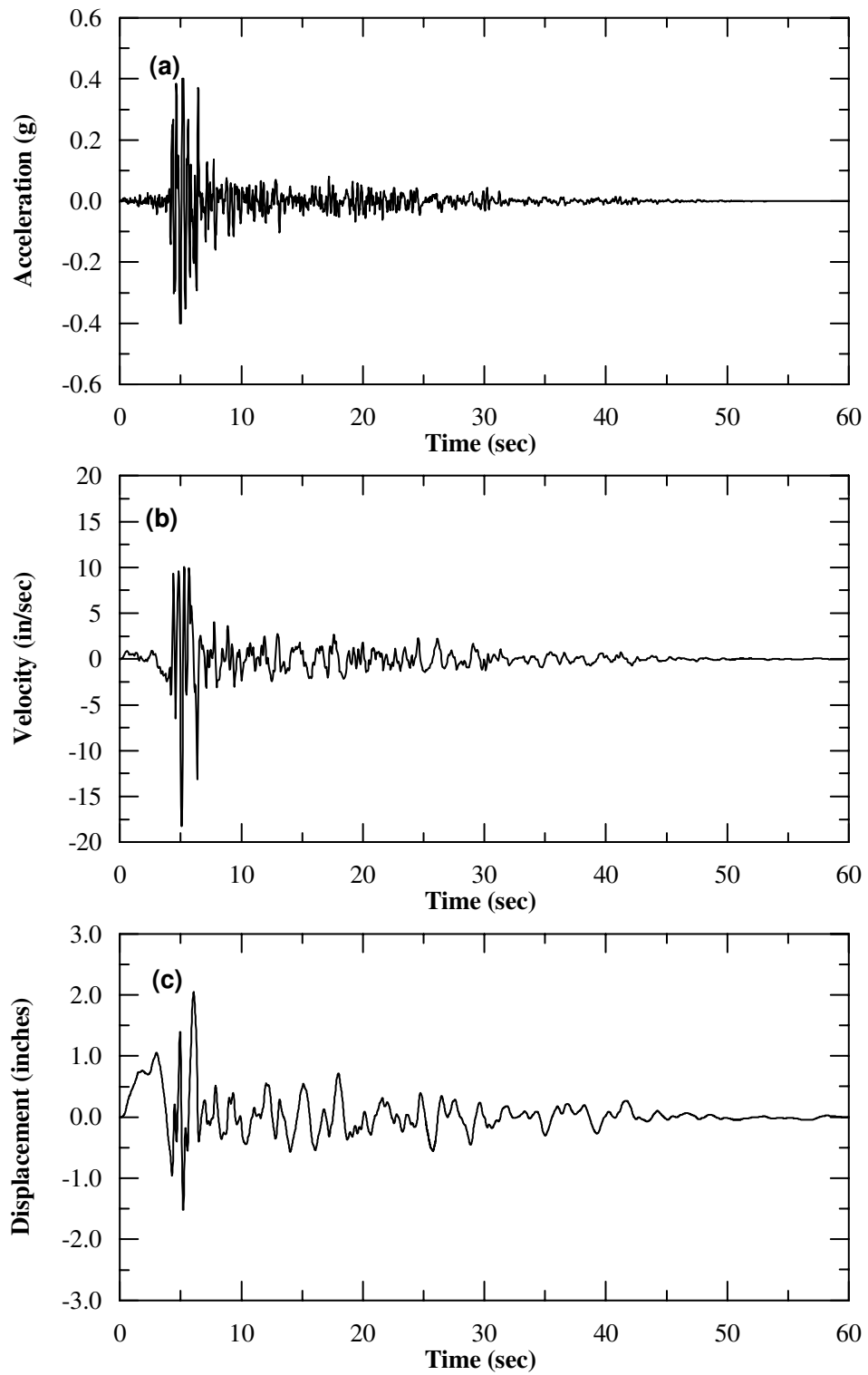


Figure 6.7: Input Motion in Transverse Direction (Channel 14)

6.4 Geotechnical Information

The As-built Plans from 1973 for Painter Street Bridge include a Log of Test Boring Sheet which shows a soil boring that was drilled at Bent 2 to a depth of 55 feet. The log displays soil type and strength descriptions and Standard Penetration Test (SPT) blowcounts at 5-ft depth intervals. As shown in Figure 6.8, the recent site investigation (EMI, 2004) consisted of two soil borings, two in-hole pressuremeter tests, and two seismic cone penetrometer soundings in the eastbound lane behind both abutments near the approach slabs, a small distance behind the abutment walls. The depth of interest in that study was in the upper few feet of the abutment backwalls where the backwall engages (pushes into) the backfill soils and the passive wedge are expected to mobilize. Two eight-inch diameter shallow dry auger borings were drilled through the embankment fills at each abutment down to 12.5 and 14 feet depth below existing road grade. No groundwater was encountered in these borings. Geotechnical soil sampling consisted of relatively “undisturbed” ring samples collected using a Modified California sampler and disturbed bag samples collected with a SPT sampler at 2.5 and 5-foot depth intervals. The Drive sampler is a split-barrel sampler (2.5-inch ID) with a tapered cutting tip and lined with a series of brass rings. The standard split-spoon sampler has a 1.4-inch ID and 2-inch OD. At each depth, the samplers were alternated and driven either 18 inches into virgin soil or until refusal using a 140-lb hammer free-falling from a height of 30 inches.

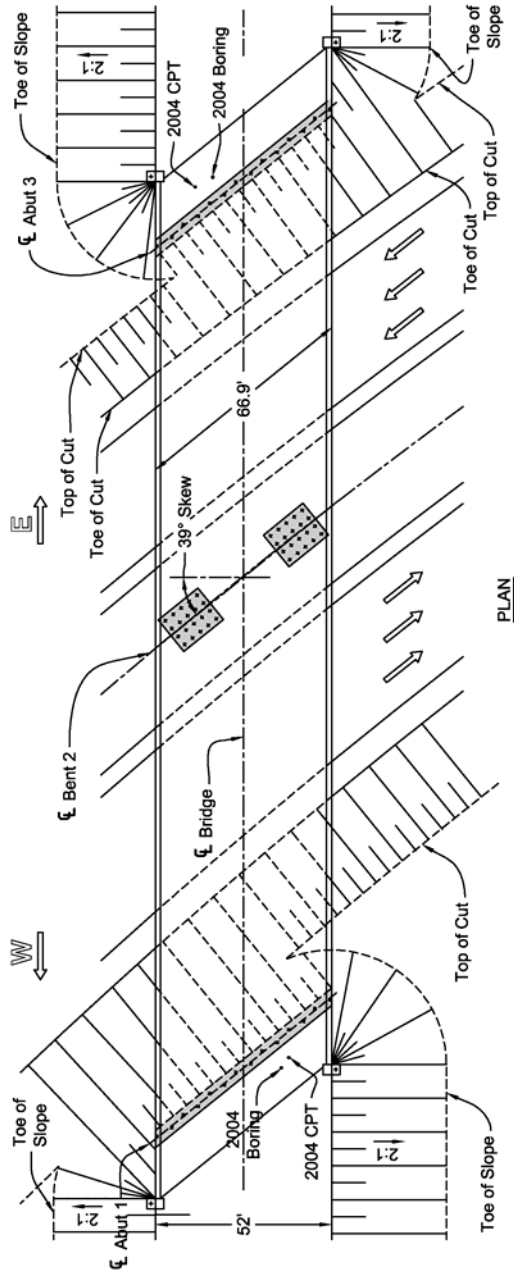
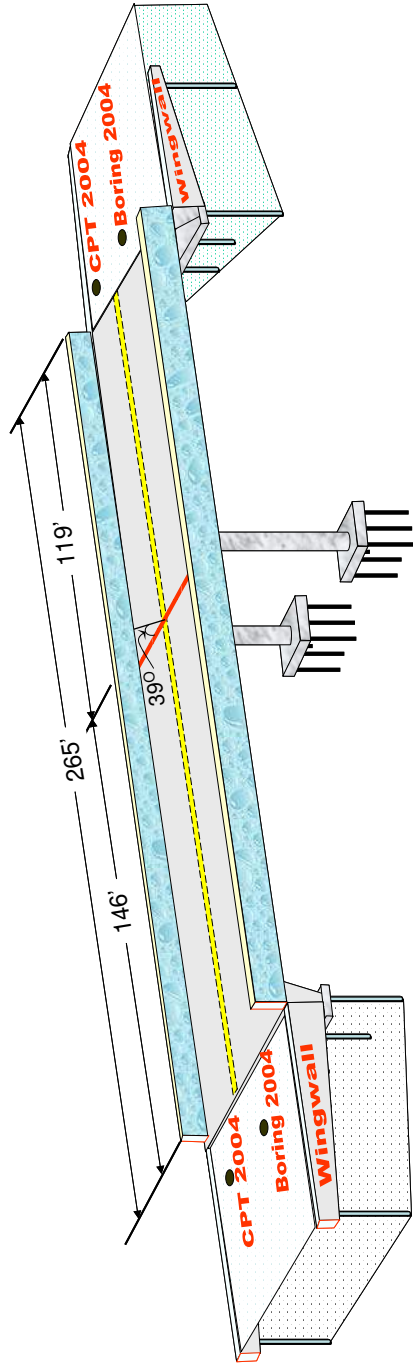


Figure 6.8: Layout of Abutment Backfill Borings at the Painter Street Bridge Site

The blowcounts for the last 12 inches of penetration were recorded on the boring logs. Selected soil samples were tested in a soils laboratory to determine backfill properties such as grain size distribution and soil strength tests. Large bulk samples of near-surface soils were collected to determine for properties such as gravel and silts contents, plasticity and expansion potential.

Two pressuremeter tests were performed near each soil boring to determine in-situ soil resistance. Two probe holes were drilled adjacent to the soil borings and a 70-mm-diameter mechanical RocTest Texam Pressuremeter probe placed tight in virgin soil using an NX drill bit at 5 feet and 7.5 feet depth below existing road grade. The test consists of inflating a rubber membrane enclosed in a flexible metal shield with water to exert lateral pressure on the backfill soil with cycles of unloading and reloading. The test measures the in-situ nonlinear lateral stress-strain behavior and stiffness (modulus) of the backfill.

The two conventional CPT soundings (denoted as CPT-1 and CPT-2) were conducted next to the borings to allow correlation with the soil type and measured soil strength with the shear wave velocity measurements. The soundings used a standard cone with 10 cm² area using a 25-ton truck with on-board data acquisition. During penetration of the cone, the cone tip resistance and sleeve friction is continually measured. This data was correlated to soil behavior type, undrained shear strength and friction angle. Shear wave and compression wave velocities were measured every 2.5 feet depth using the seismometer built into the cone. Shear

waves were generated by impacting a wooden beam that is coupled to the ground surface by the truck dead weight. The sledgehammer impact triggers the electronic recording of the wave arrival time measured by the seismic cone in the ground.

6.5 Idealized Soil Profile and Properties

Figure 6.9 shows an idealized soil profile with design properties based on the available geotechnical data and the bridge foundation configuration. The strata are as follows:

- The fill embankments at the Abutments consist of compacted dense to very dense, damp, fine to coarse sand with some silt and gravel up to 1 inch size down to about 6.5 feet depth below road grade. Sand equivalent (SE) is a measure of the amount of fines and coarse fractions in predominantly granular samples and a large bulk sample tested as 43, satisfying Caltrans' standard abutment backfill specification of 20.
- The natural soils below consist of stiff to very stiff low-plasticity clayey silt to plastic silty clay with traces of fine to medium sand, subrounded gravel up to ½ inch in size, and organic material down to about El. 102 feet.
- A layer of medium dense sands and silts down to about El. 87 feet
- A dense to very dense sand with silt and gravel that serves as a bearing stratum for the pile foundations down to at least El. 64 feet explored.

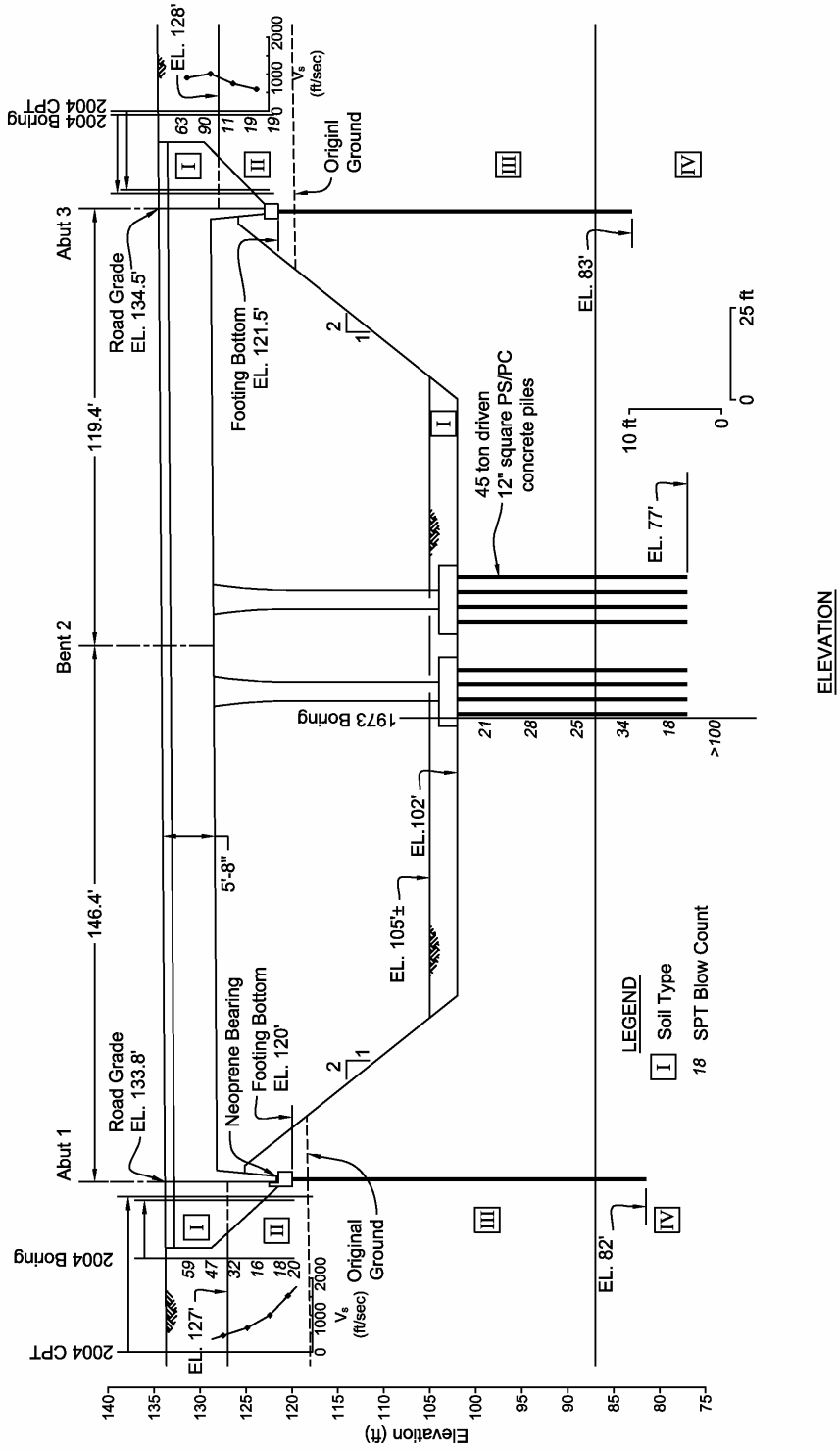


Figure 6.9: Geometry and Idealized Soil Profile at the Painter Street Bridge Site

High groundwater was encountered in 1973 and then was lowered below the bottom of the existing roadcut. Current groundwater levels are not known, but are assumed at the bottom of the present roadway base fills. Figure 6.9 also shows graphs of uncorrected field SPT blowcounts, CPT measurements and shear wave velocities. Non-standard blowcounts were converted to SPT-equivalent blowcounts. The SPT value is widely used in geotechnical design practice to correlate soil strengths and other parameters. Table 6.2 and Table 6.3 summarize the properties of the existing backfills and natural soils for use in our computer model. These values were derived as follows:

- *Field soil densities* were measured in the laboratory directly from carefully preserved ring samples per ASTM D-2937 and D-2216 methods. The maximum density and optimum moisture content was determined on shallow bulk samples using the Modified Proctor Test in a 4-inch diameter mold (ASTM D-1557) using four trial points to develop a dry density versus moisture curve.
- *Gradation* of sandy soils was determined by standard sieve tests per Caltrans Test Methods 202/203. The grain size curves show the presence of fines and coarse fractions.
- *Plasticity* of cohesive samples was determined from laboratory Atterberg limits (plasticity index, liquid limit and plastic limits) using Caltrans Test Method 204. The plastic limit determines whether a soil is a silt or clay, and the degree of plasticity (e.g., low or high).

- *Shear Strength Parameters* (total-stress friction angles and cohesion strengths) were determined from load-displacement curves and Mohr circles obtained from cyclic unconsolidated undrained (UU) triaxial tests at failure and residual (large displacement) values from direct shear tests. The triaxial tests were performed on extruded ring samples per ASTM D-2850. Sand samples were screened through a #4 sieve (to remove large gravel) and placed in a rubber membrane. Specimens were then consolidated and tested in a Geomatic triaxial apparatus to failure under unconsolidated undrained conditions at three different confining pressures and three unloading and reloading cycles. Direct shear tests were conducted using ASTM-D3080 on ring samples of sandy soils subjected to three vertical pressures near the overburden pressure.
- *Shear wave velocities (SV)* were measured using the seismic cone soundings. Caltrans BDS indicates a presumptive shear wave velocity of 800 feet per second for compacted backfills.
- *Soil Moduli* were determined from the pressuremeter and triaxial tests from stress-strain curves for initial monotonic loading (Young's modulus), secant modulus E_{50} (50% of the failure stress), and the modulus for unloading and reloading. These moduli are representative of the strain range (up to 25%) expected in the subsequent engineering application and are much lower than very-small-strain moduli calculated from shear wave velocity.

Table 6.2 Idealized Soil Parameters for Painter Street Bridge Site

Unit	Soil Type (USCS Symbol)	Soil Properties			
		γ' (pcf)	ϕ (deg)	c (psf)	v_s (fps)
1	Compacted Sandy Fill (SP, GP)	130	38	50	670
2	Stiff Silt and Clay (ML/CL)	128	11	3,300	1,000
3	Medium dense Sand (SP)	57	34	0	NA
4	Dense Sand with Gravel (SP)	63	36	0	NA

Notes: γ' = Effective Unit Weight, ϕ = Friction Angle ' c = Cohesion,
 v_s = Shear wave velocity

Table 6.3 Idealized Stiffness Parameters to Develop p-y Springs for Painter Street Bridge Site

Unit	Soil Type	p-y Curve Parameters			Soil Stiffness	
		K (pci)	ϵ_{50}	E_s (ksf)	E_{50} (ksf)	E_r (ksf)
1	Compacted Sandy Fill	60	-	NA	NA	NA
2	Stiff Silt and Clay)	-	.005	90	110	300
3	Medium dense Sand	60	-	NA	NA	NA
4	Dense Sand with Gravel	80	-	NA	NA	NA

Notes:
 ϵ_{50} = Strain Parameter for p-y curve, J = Empirical Coefficient for p-y curve
 k = Modulus of subgrade reaction
 E_{50} = Stiffness at 50% of Ultimate Stress, E_r = Unloading/ Reloading modulus

6.6 Global Bridge Model

The skewed bridge abutment foundations and the surrounding soils constitute a strongly-coupled system. The complete soil-abutment-foundation-structure interaction of the Painter Street bridge system, is separated into two substructures separated by a foundation interface: (1) superstructure (2) pile foundation and surrounding soils. Two approaches, namely the direct method and the substructure method are used for analyzing the global bridge response as shown Figure 6.10.

In the direct approach all structural components, all foundation components and all the soil support springs are explicitly included in the bridge model. A more feasible alternative is to use substructuring concept to reduce the structuring modeling and analysis to a manageable size. The concept of substructuring can be applied either to a single pile or a pile group foundation. On the other hand, the substructure system simplifies the foundation to a reduced degree-of-freedom system by using a substructuring technique. The choice between substructuring of the individual pile or the entire pile group depends on the application. For example, if plastic hinge behavior of the pile is to be considered in the global bridge model, substructuring of individual piles would be used in which case individual pile head loads (shear and moment) can be obtained directly from the global analysis. If substructuring of the entire pile group is adopted, the individual pile loads would be available only after a back-substitution process is carried out on the foundation substructure, common known as pushover analysis.

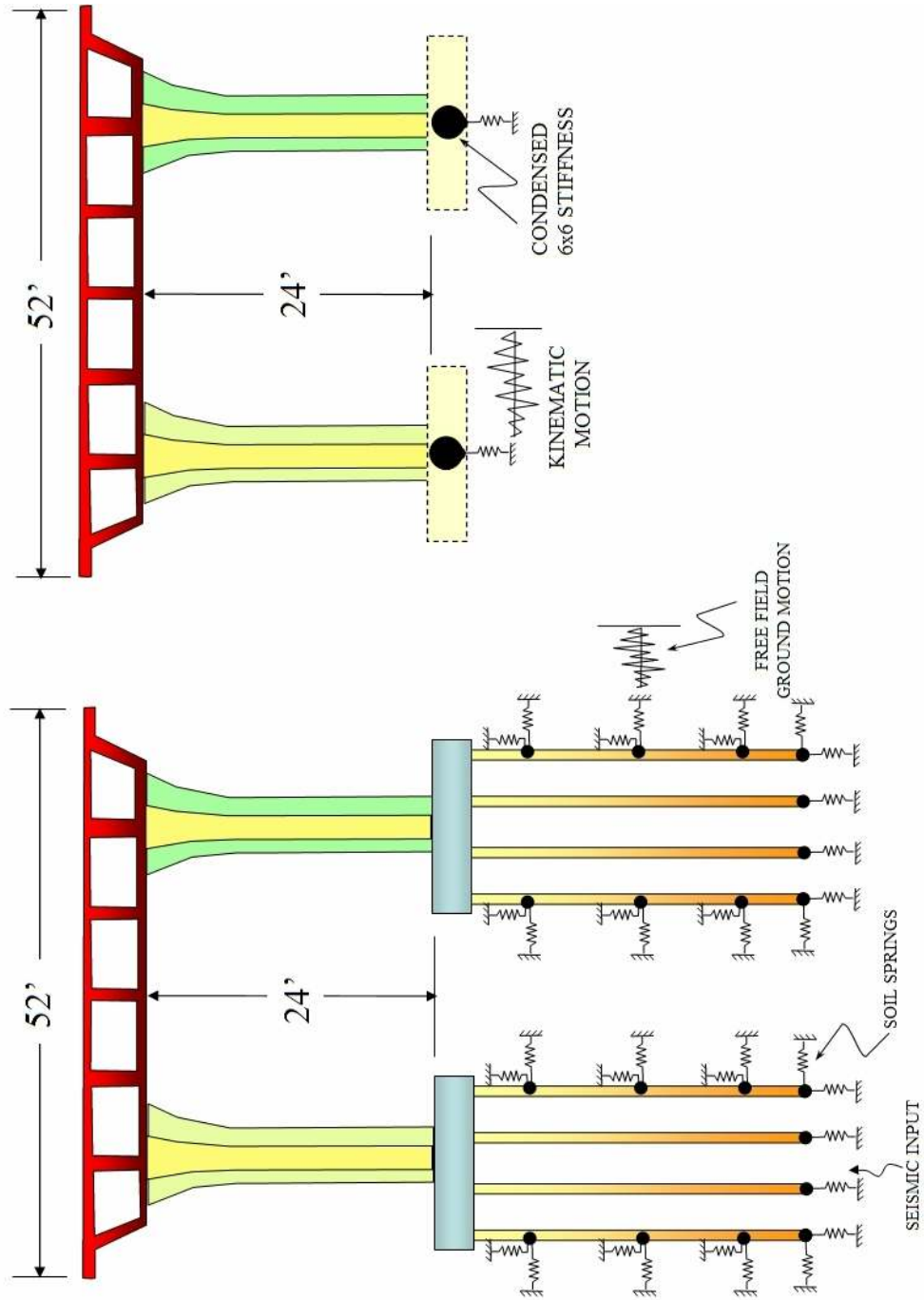


Figure 6.10: Total System Versus Substructure System

For the direct method the foundation system, non-linear soil springs were developed using the site specific geotechnical data. The soil springs were not only non-linear but also inelastic upon unloading to allow for a hysteretic behavior. When the substructuring technique was used to simplify the foundation in the global bridge model, the pile group was represented by a 6x6 linear stiffness matrix. Since soil springs were nonlinear, the first step towards developing the foundation stiffness matrix involved linearization of the non-linear soil springs by performing a lateral pushover analysis on a single pile to a representative displacement level expected during the design earthquake. Once the non-linear soil springs were linearized on the basis of the lateral pushover analysis, the problem became analogous to beams on elastic springs, and the method of substructuring was used to obtain a condensed stiffness matrix.

6.7 Global Bridge Modeling Using Direct Method

For the complete detailed fully-coupled three-dimensional nonlinear dynamic finite-element (FE) model considering soil-abutment-foundation-structure interaction (SAFSI) bridge was developed using the site specific geotechnical data. The global bridge structure and foundation was modeled using the computer program SAP2000 as shown Figure 6.11 to perform nonlinear time history analysis to obtain the “exact” response of the bridge as a function of time. The gravity load was applied to the bridge system prior to the time history analysis. The displacements due to gravity load were removed from the calculated displacement.

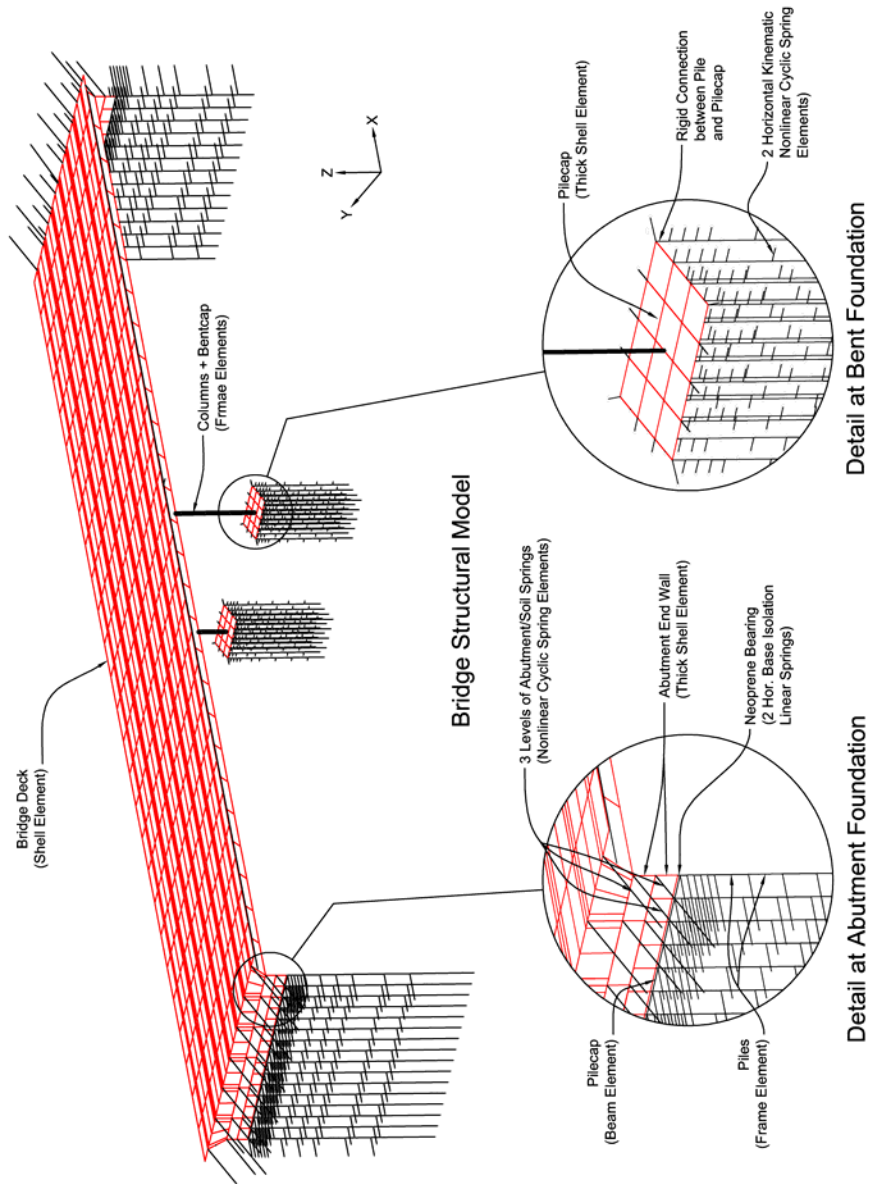
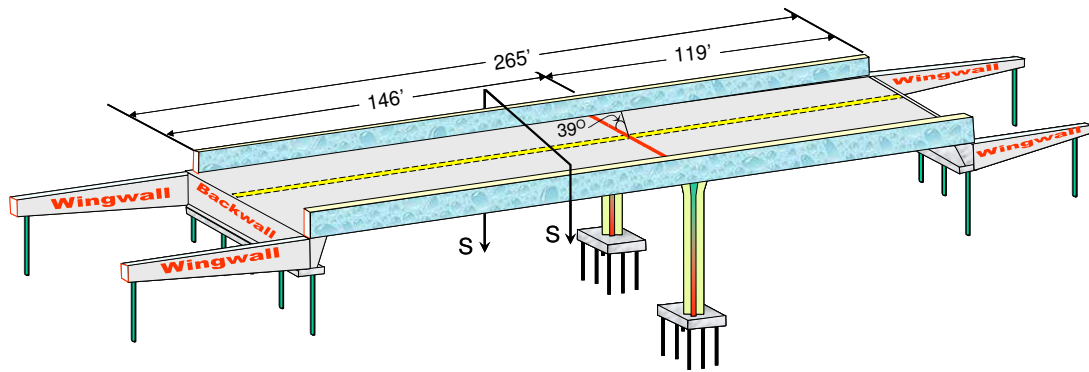
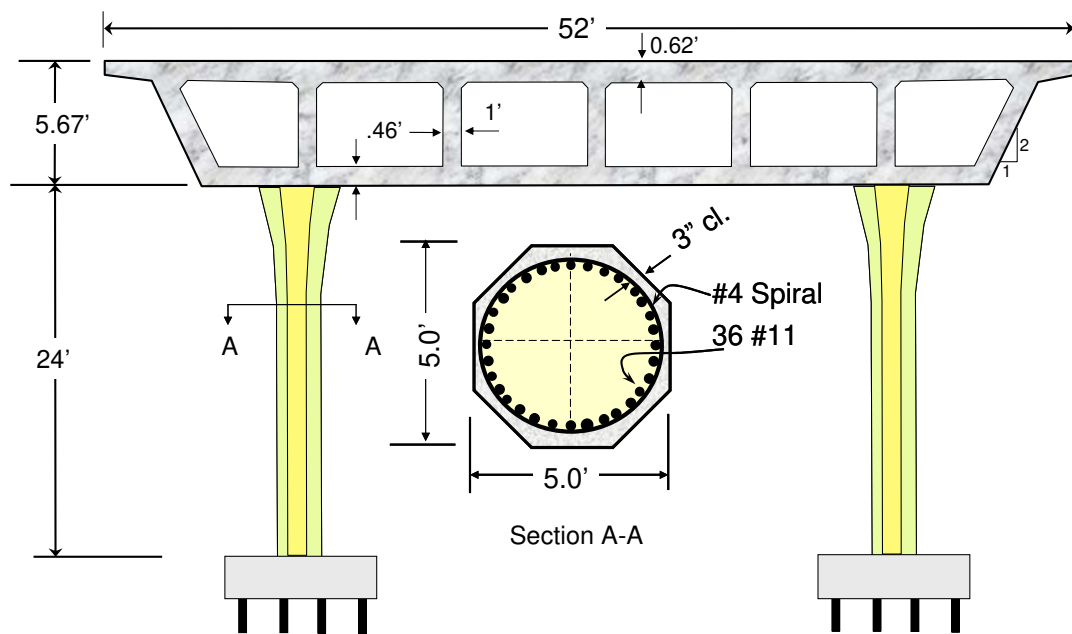


Figure 6.11: Painter Street Bridge Model for Direct Method

The bridge deck and the abutments wall were modeled as shell elements with applicable structural properties. The support provided by the west abutment was modeled using a friction isolator to simulate the neoprene pad and to decouple the superstructure and abutment backwall from the pile cap. The isolator was fixed in the vertical direction only. The support provided by the east abutment was fixed to the pile cap. At the west abutment, lateral sliding friction of the endwall on the concrete pile cap was incorporated in the model. Using a frictional coefficient of 0.45 and assuming one-half of each the span dead weight contributes to the weight at each abutment, a total linear frictional stiffness of 420 kips per inch of displacement was estimated following Section 14 of the Caltrans Bridge Design Specifications (2000). This was distributed using a total of 14 lateral springs applied between the bottom the wall and the pile heads. The structural behavior of the piles and columns was modeled using frame elements. The transverse section of the bridge structure and the cross section of the column used in the analysis are shown in Figure 6.12. SAP2000 computer program was used to develop the moment-curvature relationship of the column cross-section as shown in Figure 6.13.



3D View



Section S-S

Figure 6.12: Bent and columns Sections for Painter Street Bridge

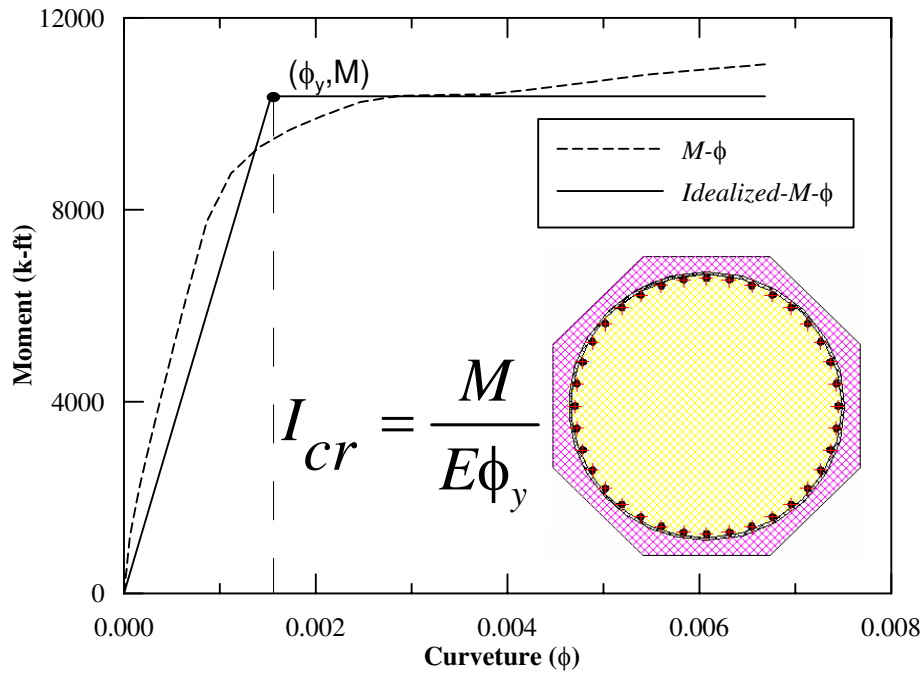


Figure 6.13: Moment Curvature Relationship for Painter Street Bridge

The pile cap at the west abutment has one longitudinal and two transverse shear keys. When the bottom of the abutment endwall pushes toward the keys, the pile cap and underlying foundation are engaged. A nonlinear plasticity model was used to simulate the abutment shear key behavior as observed during a prior Caltrans-UCSD field experiment (Bozorgzadeh et al. 2003). The nonlinear backbone curve was scaled to produce the structural shear key capacity of the abutment as a function of displacement between bridge deck and abutment pile cap. In addition, the curve was offset to incorporate the 1-inch expansion gap. At the tail end of the curve, a fourth segment was added to account for the tangential component of the abutment-backfill passive capacity due to deck rotation and the passive capacity

contribution of the exterior embankment soil. The longitudinal abutment-backfill was modeled by a series of nonlinear link elements distributed along each abutment backwall. One transverse key was applied at the north end and one at the south end of each abutment. The nonlinear backbone curves for each shear key (four in the transverse direction) and soil springs (twenty one in the normal direction) are shown in Figure 6.14.

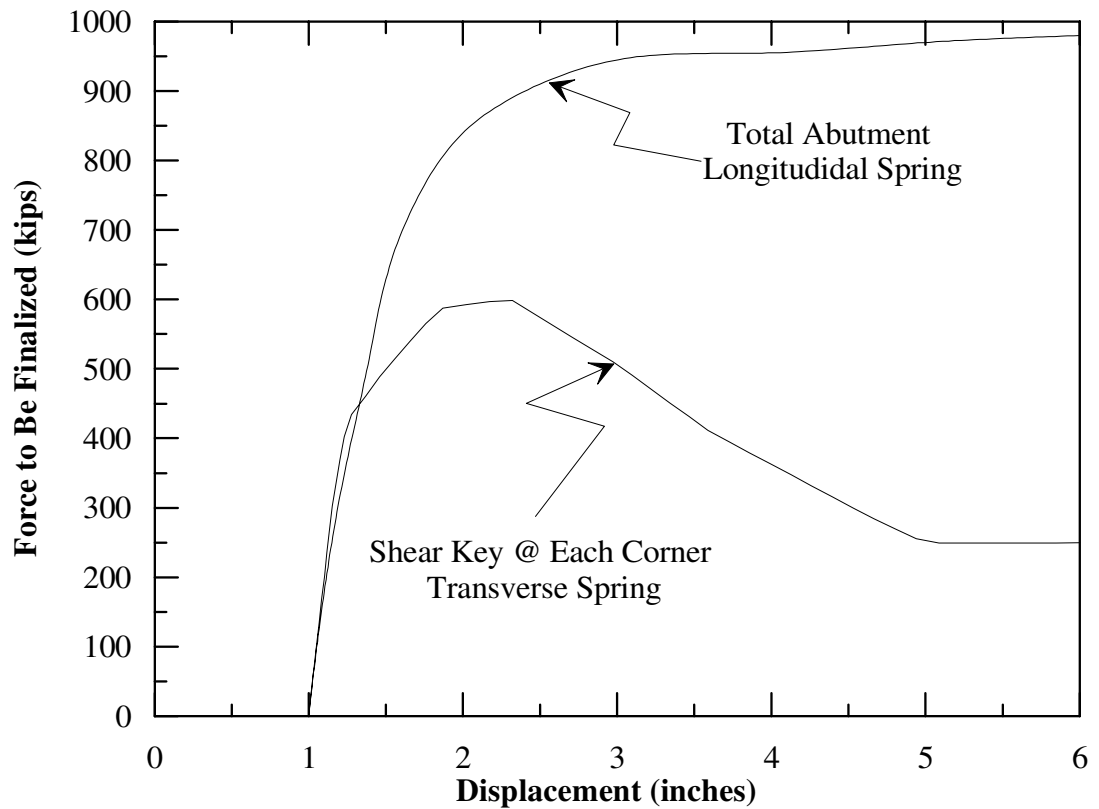


Figure 6.14: Shear Key Capacities at West Abutment for Painter Street Bridge

The nonlinear backbone curves at each abutment was divided into 21 nonlinear discrete backbone curves longitudinal direction perpendicular to the skew angle to represent the backfill distributions at the abutment stem walls.

6.7.1 Pile Foundations

The pile foundations were modeled as beam elements with nonlinear springs to represent interaction between the piles with the surrounding soil as shown in Figure 6.15. Lateral pile-soil support curves were generated according to API criteria (API, 1993) using the parameters given in Table 6.3. For the abutment piles, p-y curves were generated at depths of 1, 2, 3, 5, 10, 15, 20, and 30 feet from pile top and at the pile tip at 37.5 ft. For the bent piles, p-y curves were calculated at depths of 1, 2, 3, 5, 10, 15, 20 feet, below pile top and pile tip at 25 ft. The p-y soil resistance springs are omni-directional, e.g. they can be thought of as “rotating” around the pile axis into the direction of the soil resistance during seismic loading. In the pile foundation model, two nonlinear horizontal springs (one in the bridge longitudinal and one in the bridge transverse direction) were applied along each pile and at each of the above depths.

6.7.2 Abutment Soil-Structure Interaction

The dynamic interaction between the deck, abutment wall and the embankment soil in the direction perpendicular to the abutment wall was modeled by a gap element between the bridge deck and the abutment backfill and a nonlinear spring. The dynamic deck-abutment interaction along the skew-angle in the

transverse direction was model by a gapping element, nonlinear shear key and nonlinear soil springs. The detailed model to the abutment is shown in Figure 6.17.

Gapping at the west abutment, a 1-inch structural expansion gap exists between the structural and the soil backfill. Gapping elements were incorporated to simulate these gaps between the soil and the bridge deck in the longitudinal and transverse directions. The initial opening was set to one inch. The east abutment is monolithic abutment and in direct contact with backfill. Gap elements with zero initial opening were incorporated to disallow tension in the backfill.

The nonlinear spring represents the near-field load-deformation behavior at the longitudinal abutment-embankment soil interface. A separate continuum finite-element model was developed using PLAXIS (2005) with a strain-hardening-soil model to develop this load-deformation relationship (backbone curve) as shown schematically in Figure 6.17. This model incorporates the combined response of the two soil layers behind the abutment backwall. The hysteretic behavior of the backbone curve is modeled using the multi-linear plasticity model with the tension side of the curve set to zero. The behavior is essentially that of a gap element in series with a compressive plastic spring at the west abutment and only compression spring at the east abutment. Upon load reversal, the spring unloads elastically until zero force is reached, with net permanent deformation present. Further loading in the tension direction acts as an open gap, with no force exhibited. Reloading in the compressive direction remains at zero force until the gap is closed at a deformation

equal to the permanent plastic deformation. The spring loads elastically until the backbone curve is reached, then follows the backbone with increasing plastic deformation as shown in Figure 6.16.

The soil mass contribution from the passive wedge is attached at each end of nonlinear spring as shown in Figure 6.17. McCallen and Romstad (1994) showed that dynamic behavior of a bridge system is relatively insensitive to variation of abutment-embankment soil mass when the soil is undergoing small strains. However, the system dynamics becomes more sensitive to the soil mass when the abutment-embankment soil becomes softer as would be expected due to soil softening during strong shaking. In fact, for any soil-structure interaction problem there are two mechanisms affect energy dissipation during seismic loading: the strain-dependent energy dissipation mechanism (material damping) associated with nonlinear hysteretic behavior of the soil and radiation damping (geometric damping) associated with dissipation of elastic wave energy away from the bridge. When proper nonlinear inelastic abutment springs are implemented allowing for hysteretic behavior, the strain-dependent energy dissipation mechanism is automatically simulated, accounting for material damping in the abutment. Due to highly nonlinear nature of the abutment-backfill in the vicinity of the abutment the contribution of the damping associated with radiation damping is insignificant and was not considered in this study.

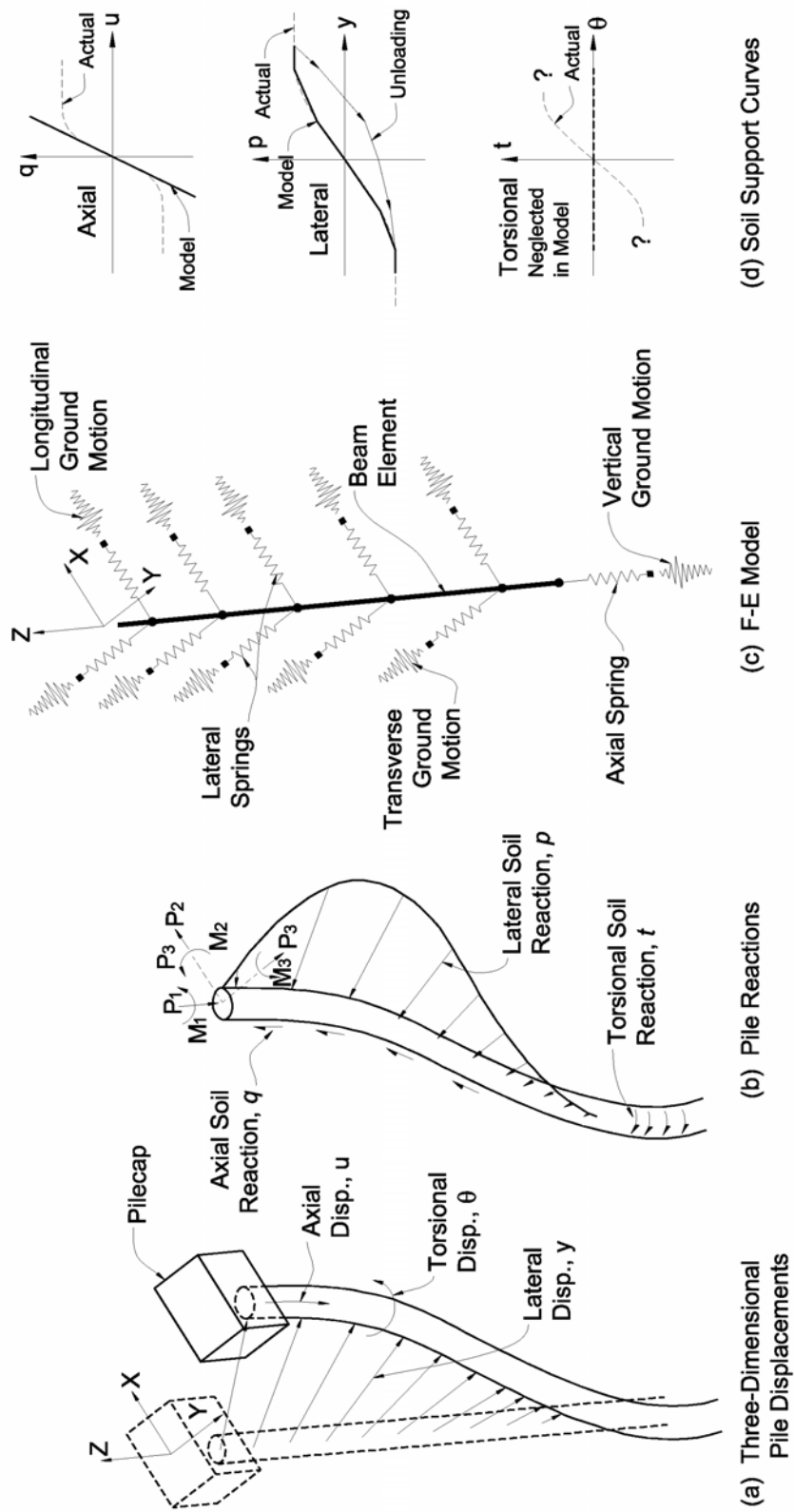


Figure 6.15: Bridge Pile Foundation Model

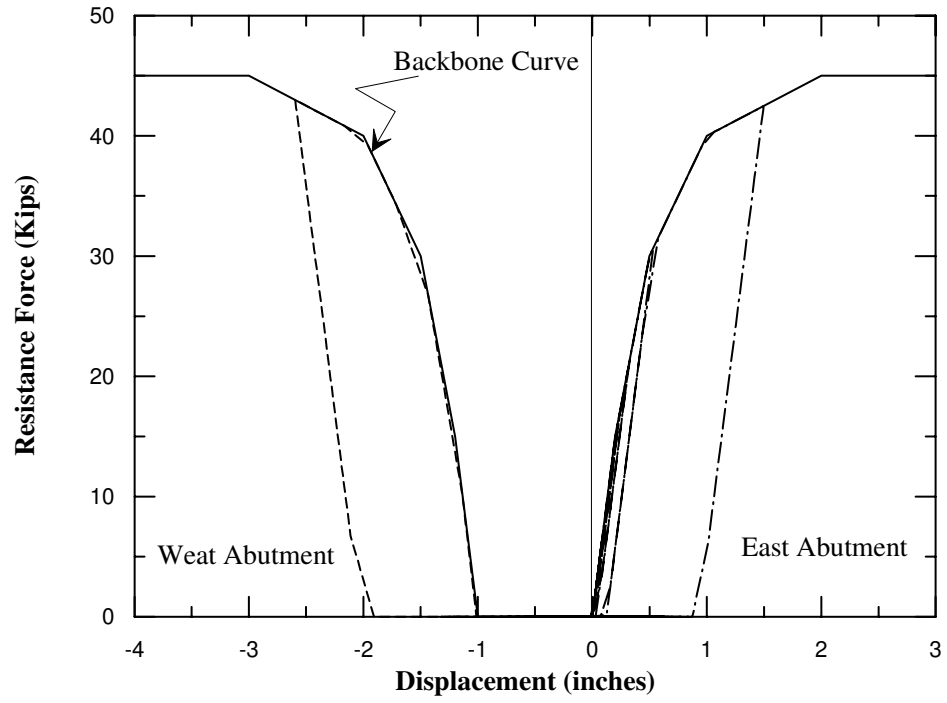


Figure 6.16: Longitudinal Abutment-Soil Loading-Unloading Curves

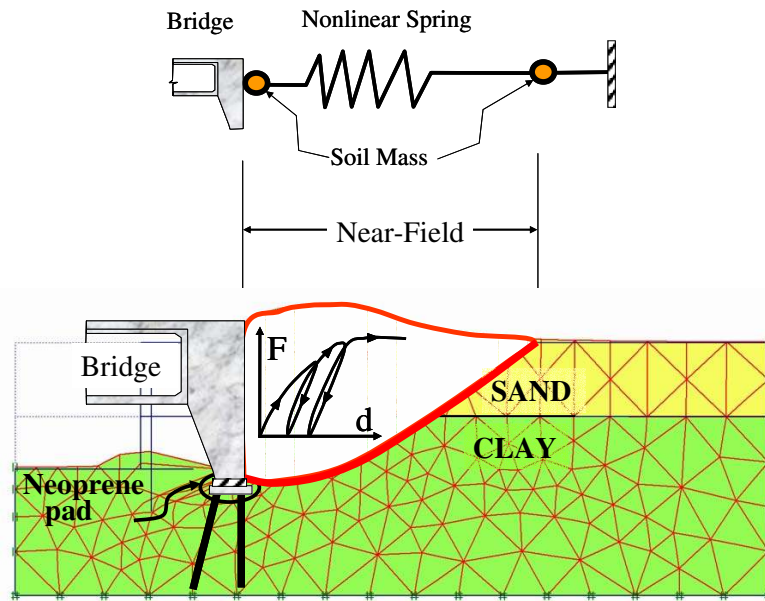


Figure 6.17: Bridge Monolithic Abutment Model

6.7.3 Global Bridge Displacement Response

Figures 6.18 through 6.27 show a comparison of the calculated displacement response of the analytical model with those obtained from the acceleration records for major points and directions on the bridge. The results of the model match the records remarkably well, particularly the longitudinal response at both abutments. It should be noted that the model used did not formally include wingwalls and thus did not allow comparisons with recorded wingwall motions (Channels 15 through 20).

Since the west span of the bridge is larger than the east span and the bridge deck has much more flexibility than at the west abutment, the center of rigidity of the bridge system is closer to the east abutment. As a result, the bridge is expected to rotate about its vertical axis during seismic shaking. The fact that recorded transverse peak ground accelerations at the west abutment was about 1.5 times higher than at the east abutment indicates that the bridge must have undergone such rotation during the earthquake. Figure 6.28 presents the transverse displacement-time histories results from the analytical model at opposing far corners of the bridge deck (shown as “NW” and “SE” in Figure 6.4). Figure 6.29 presents the deck rotation time histories results from the analytical model. From these comparisons, the superstructure underwent significant rotations during the earthquake and returned to its original position by the end of ground shaking. Inspection of the concrete barrier rails and curbs and the pavement striping during EMI’s field investigation (EMI, 2004) did not show any permanent lateral offset at either abutment.

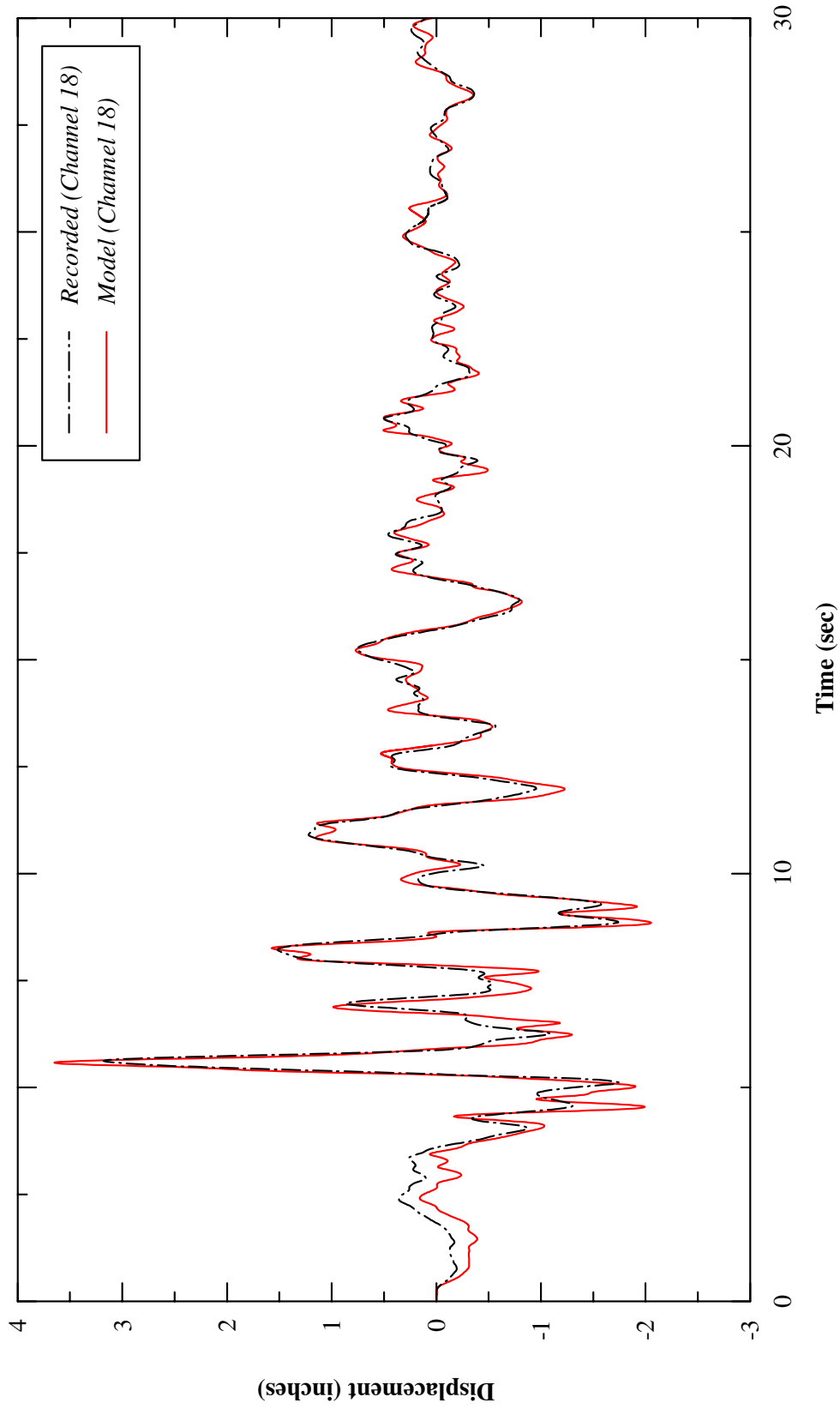


Figure 6.18: Recorded Response Versus Analytical Response of the Direct Method (Channel 18)

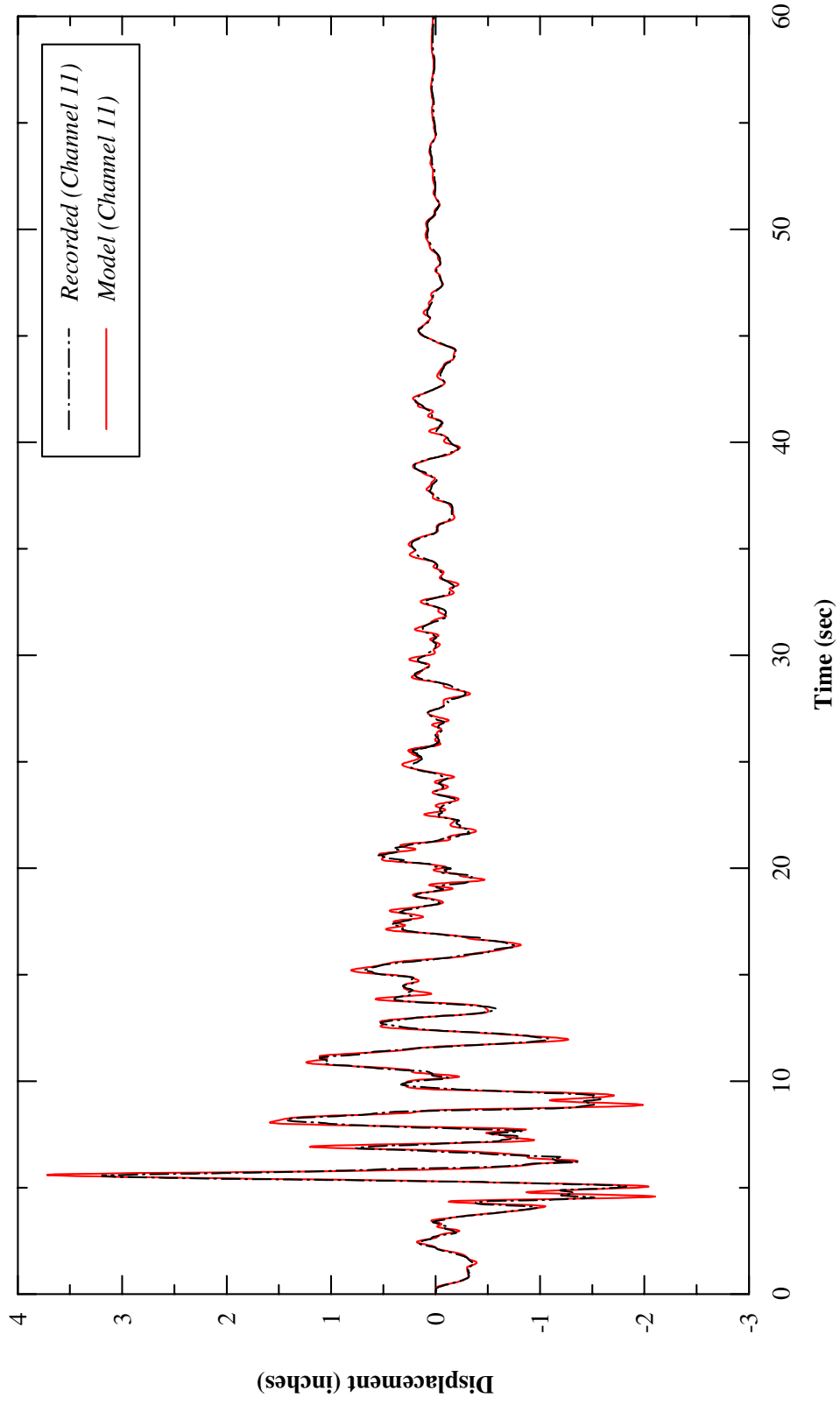


Figure 6.19: Recorded Response Versus Analytical Response of the Direct Method (Channel 11)

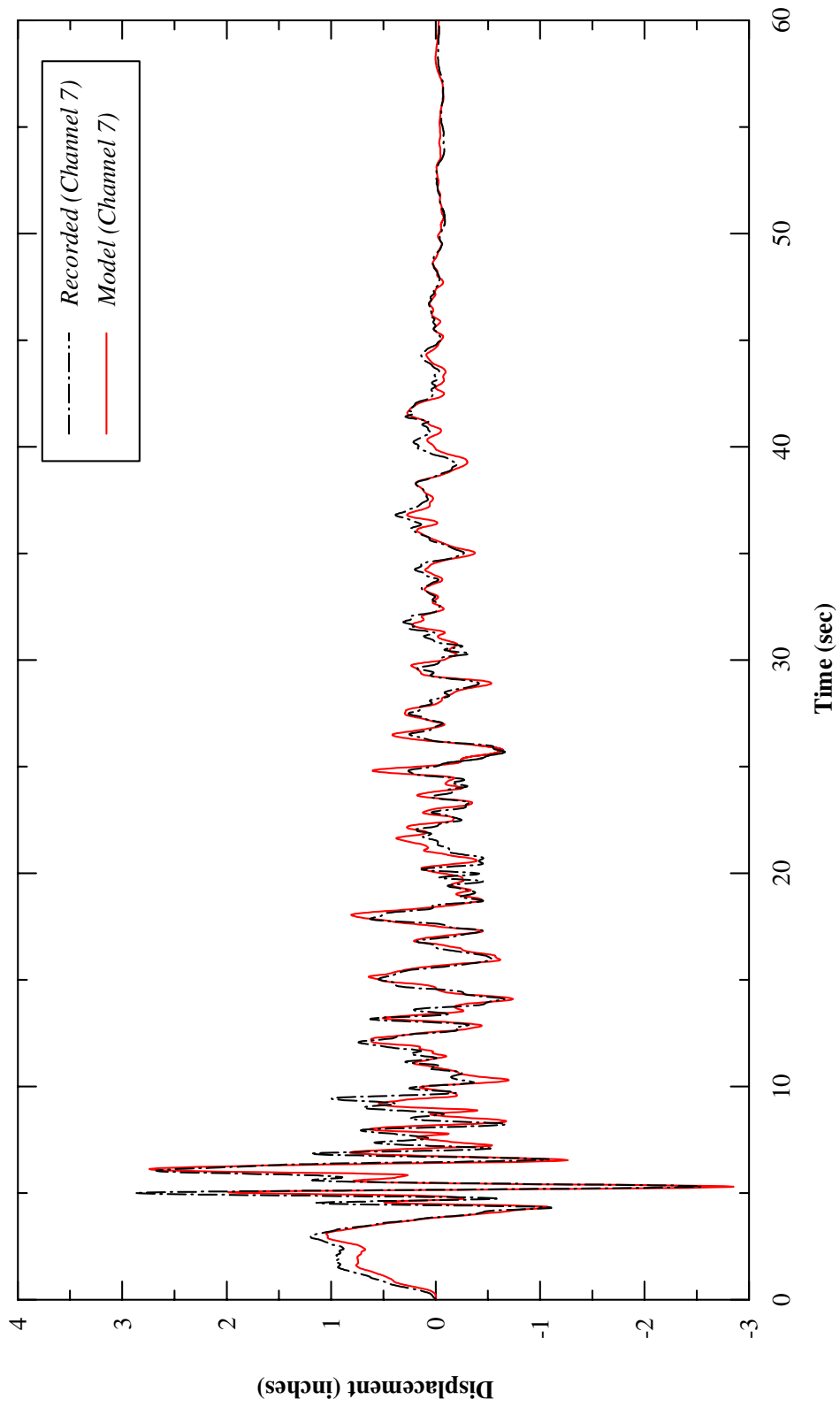


Figure 6.20: Recorded Response Versus Analytical Response of the Direct Method (Channel 17)

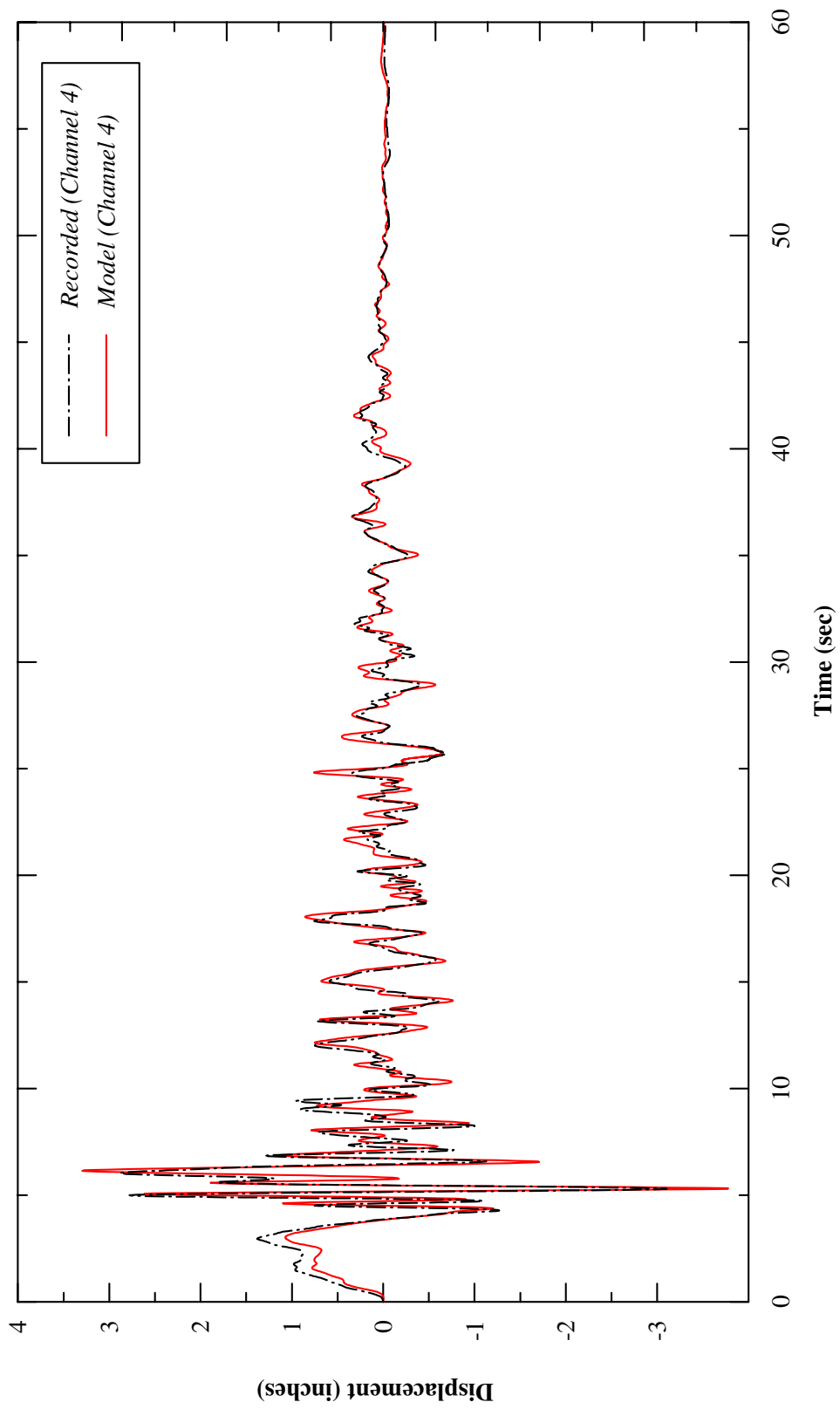


Figure 6.21: Recorded Response Versus Analytical Response of the Direct Method (Channel 4)

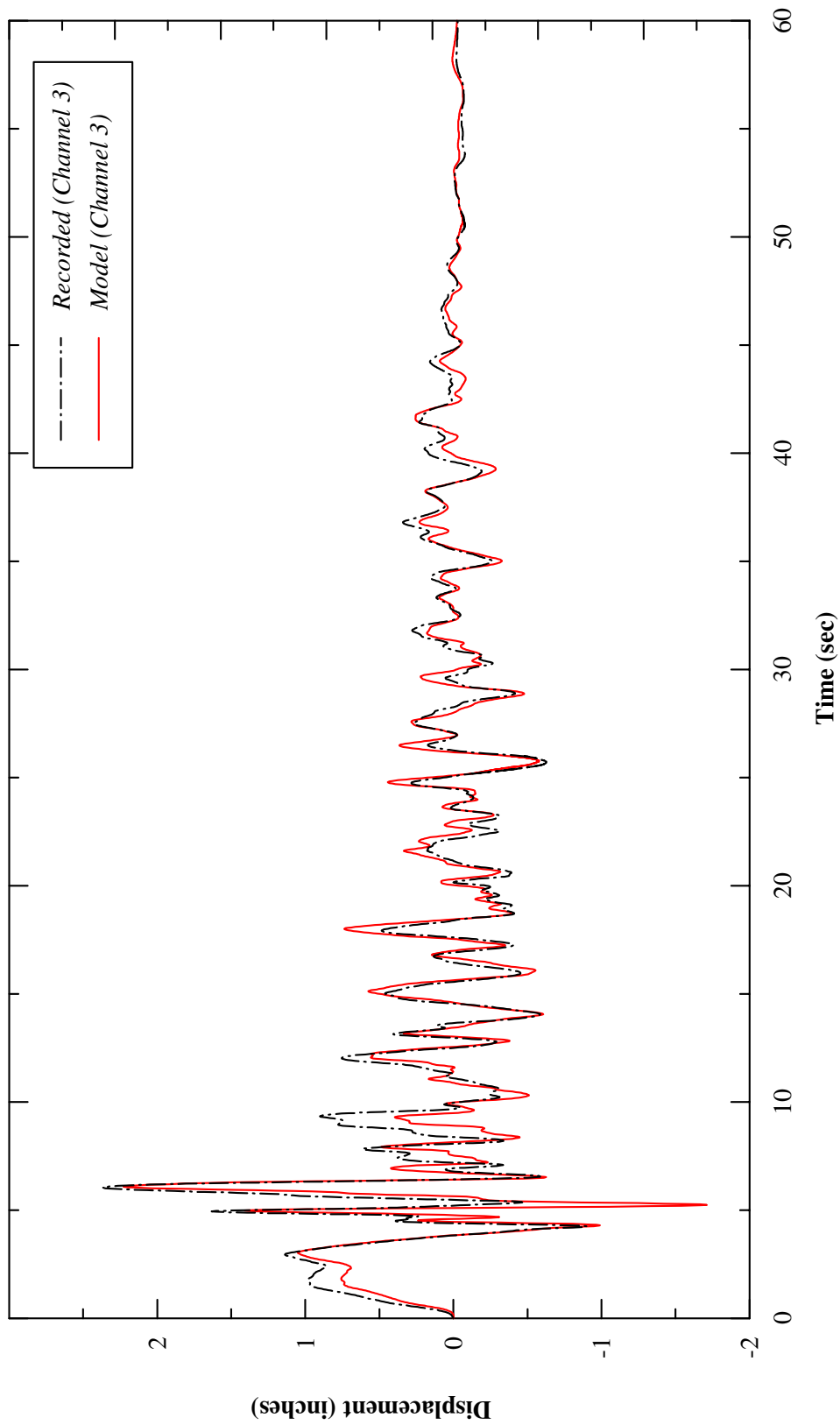


Figure 6.22: Recorded Response Versus Analytical Response of the Direct Method (Channel 3)

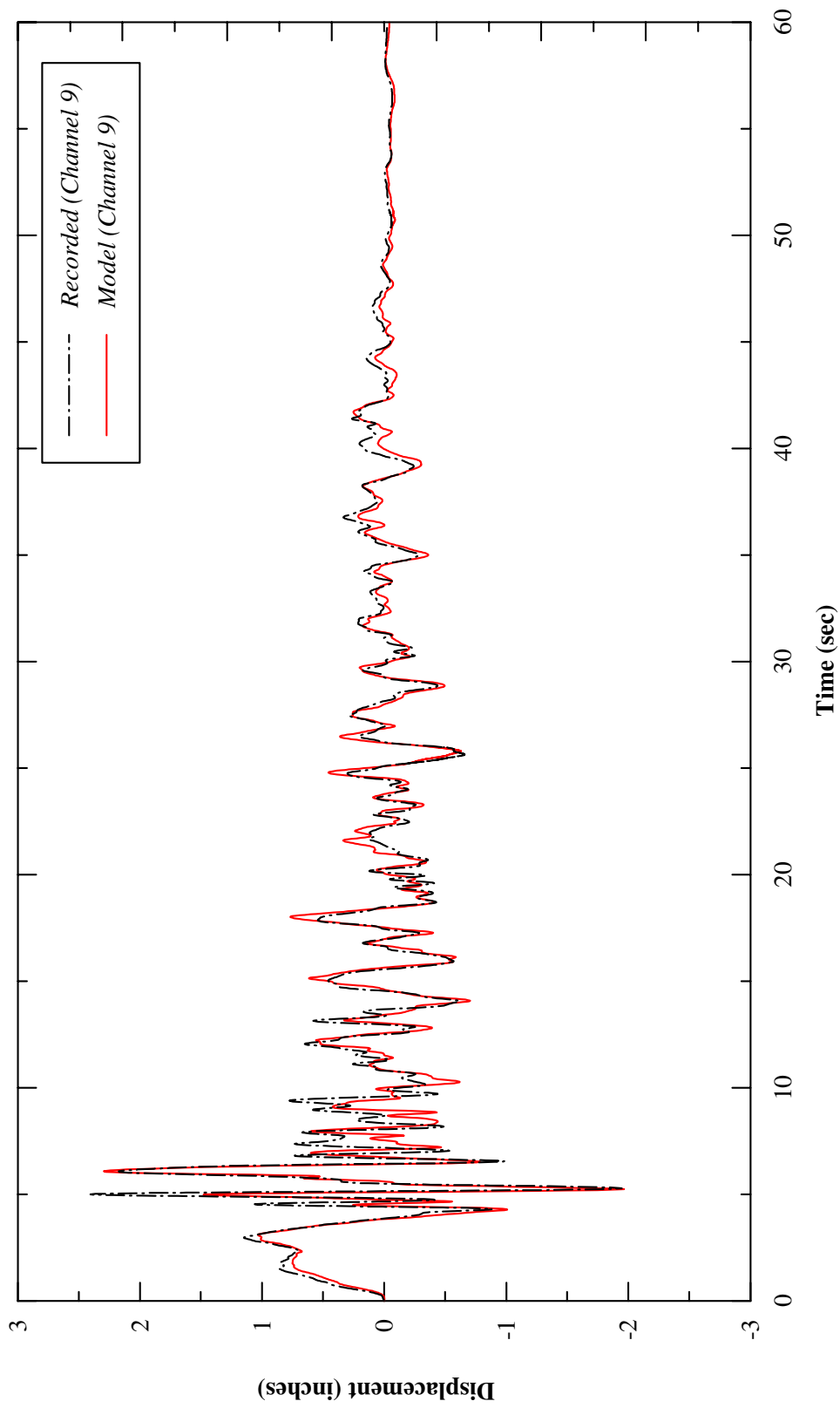


Figure 6.23: Recorded Response Versus Analytical Response of the Direct Method (Channel 9)

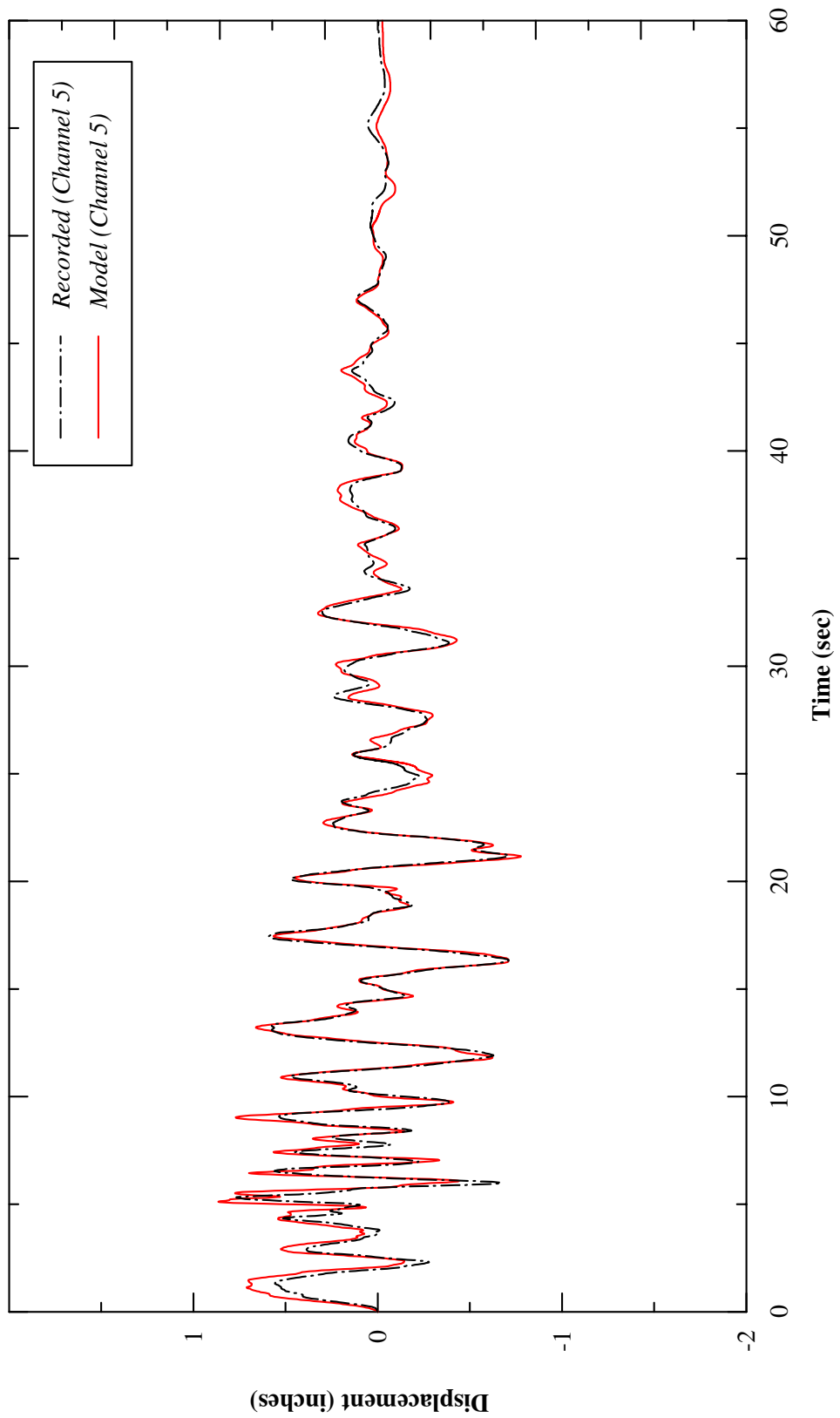


Figure 6.24: Recorded Response Versus Analytical Response of the Direct Method (Channel 5)

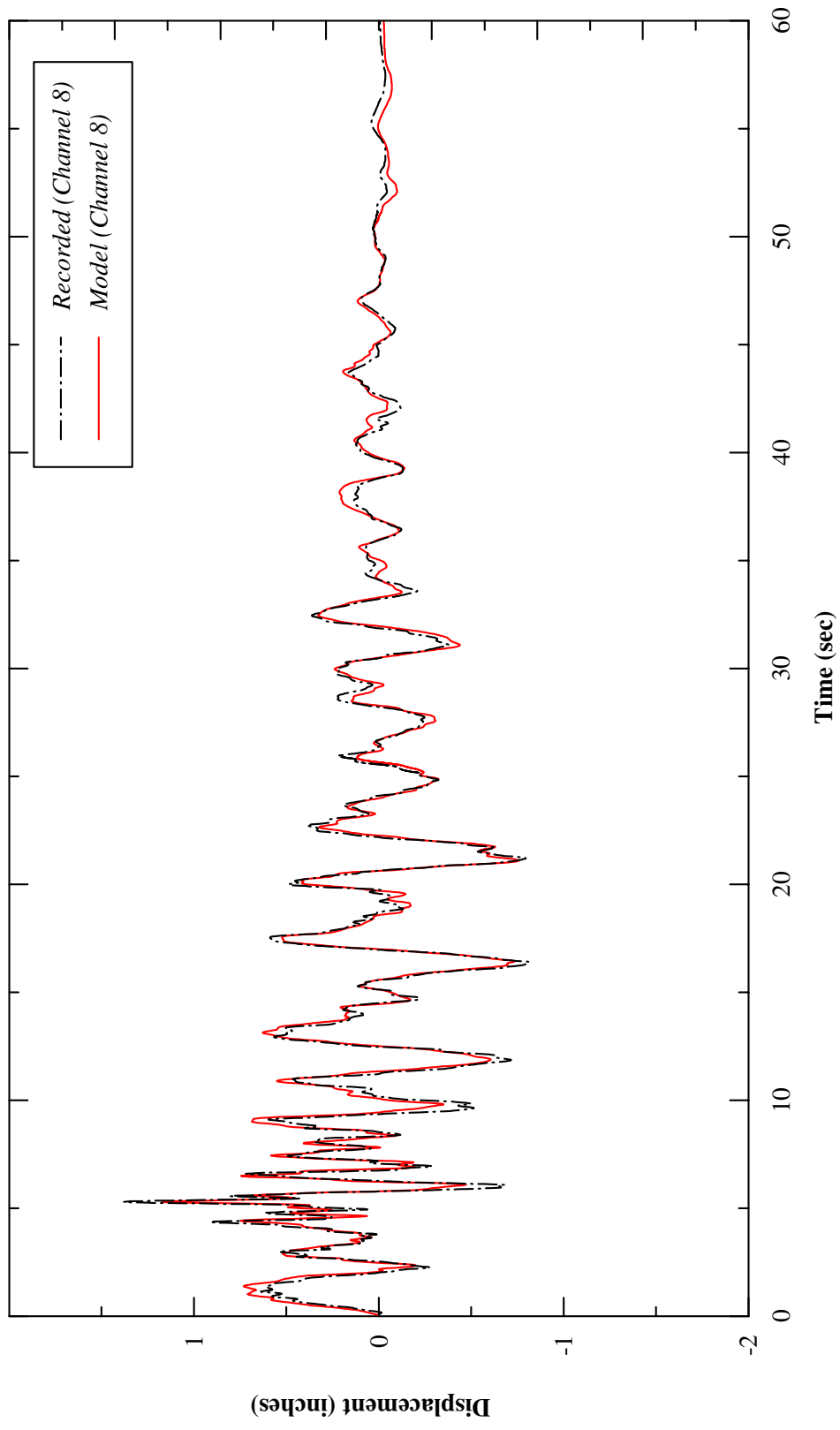


Figure 6.25: Recorded Response Versus Analytical Response of the Direct Method (Channel 8)

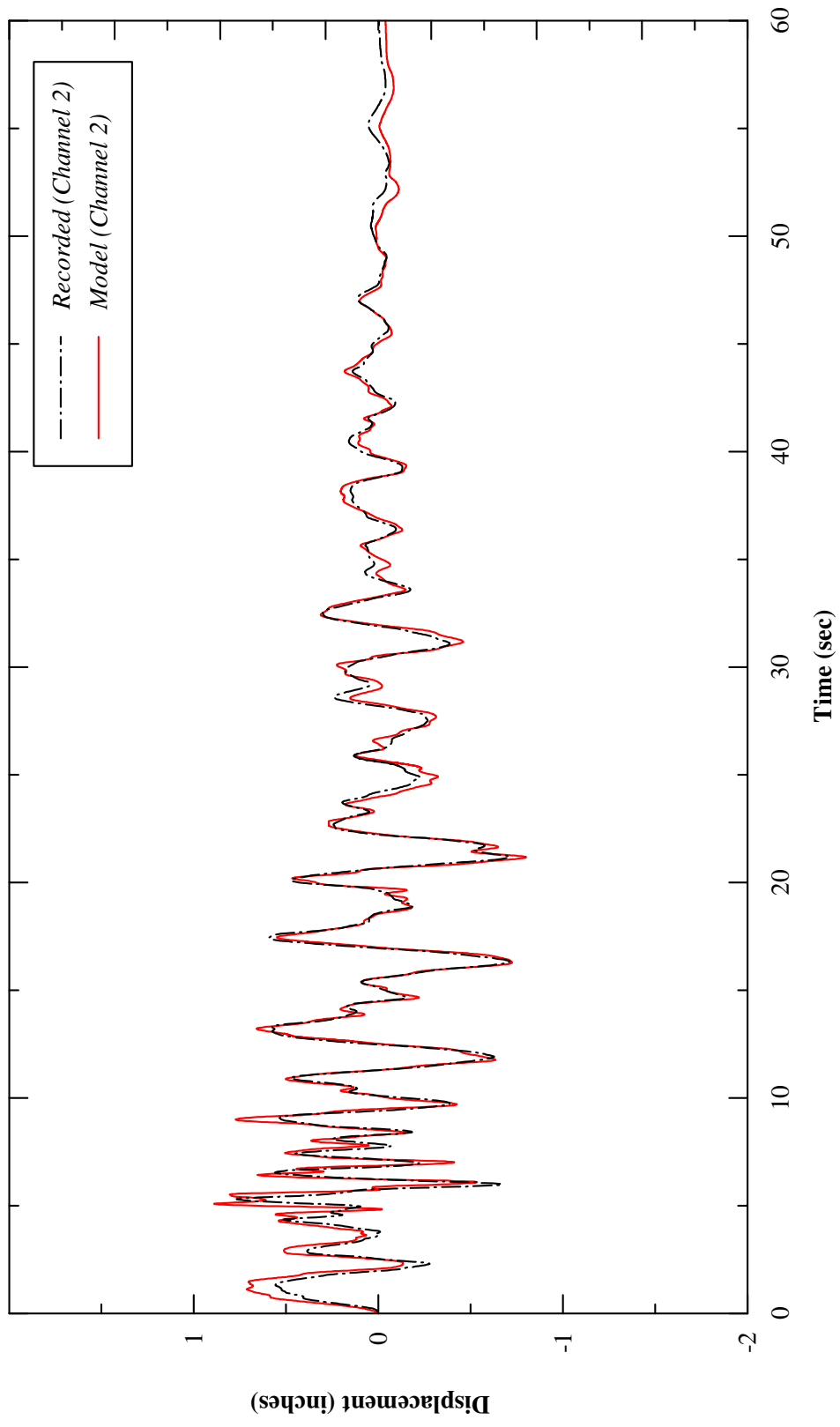


Figure 6.26: Recorded Response Versus Analytical Response of the Direct Method (Channel 2)

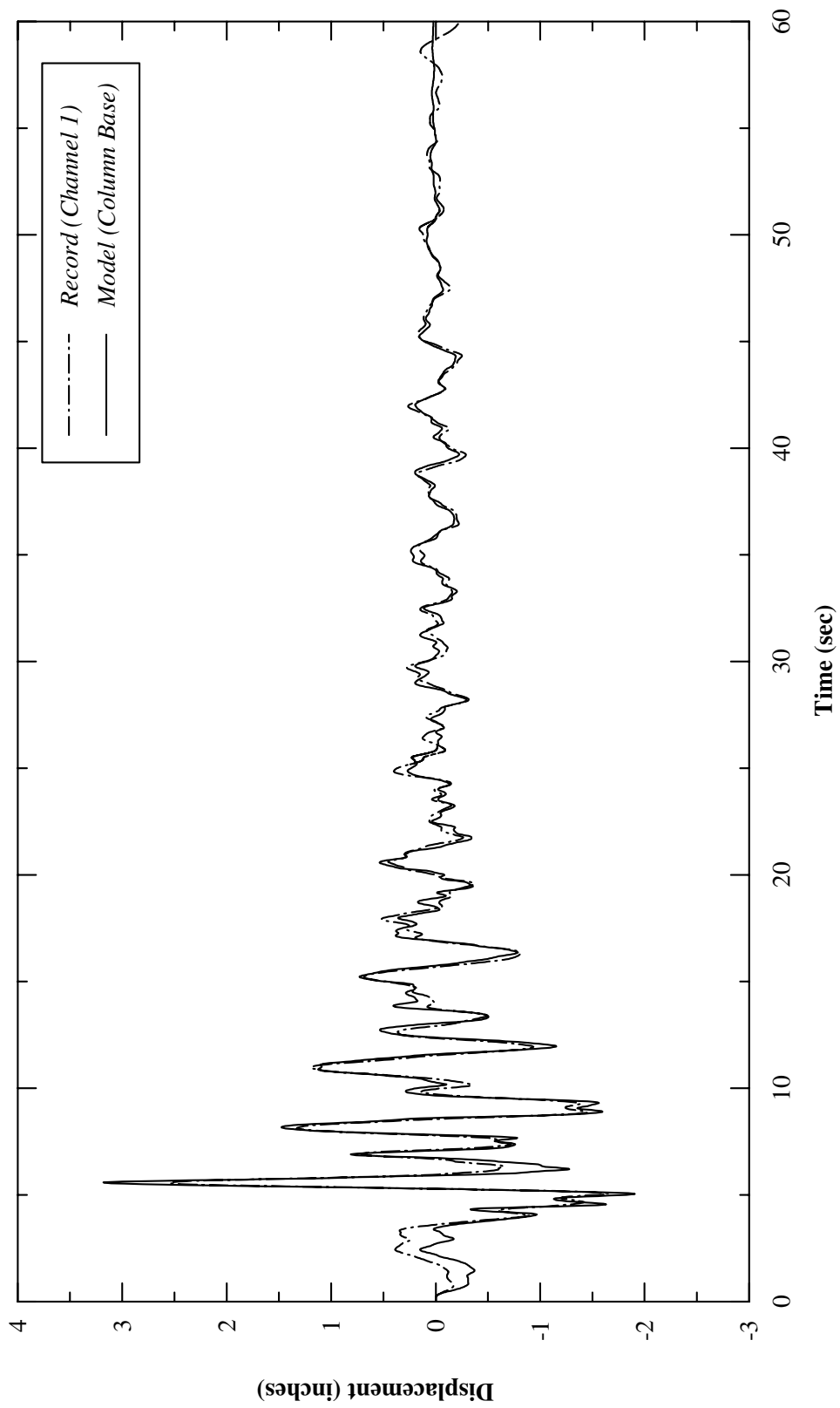


Figure 6.27: Channel 1 Transverse at Column base of the Direct Method

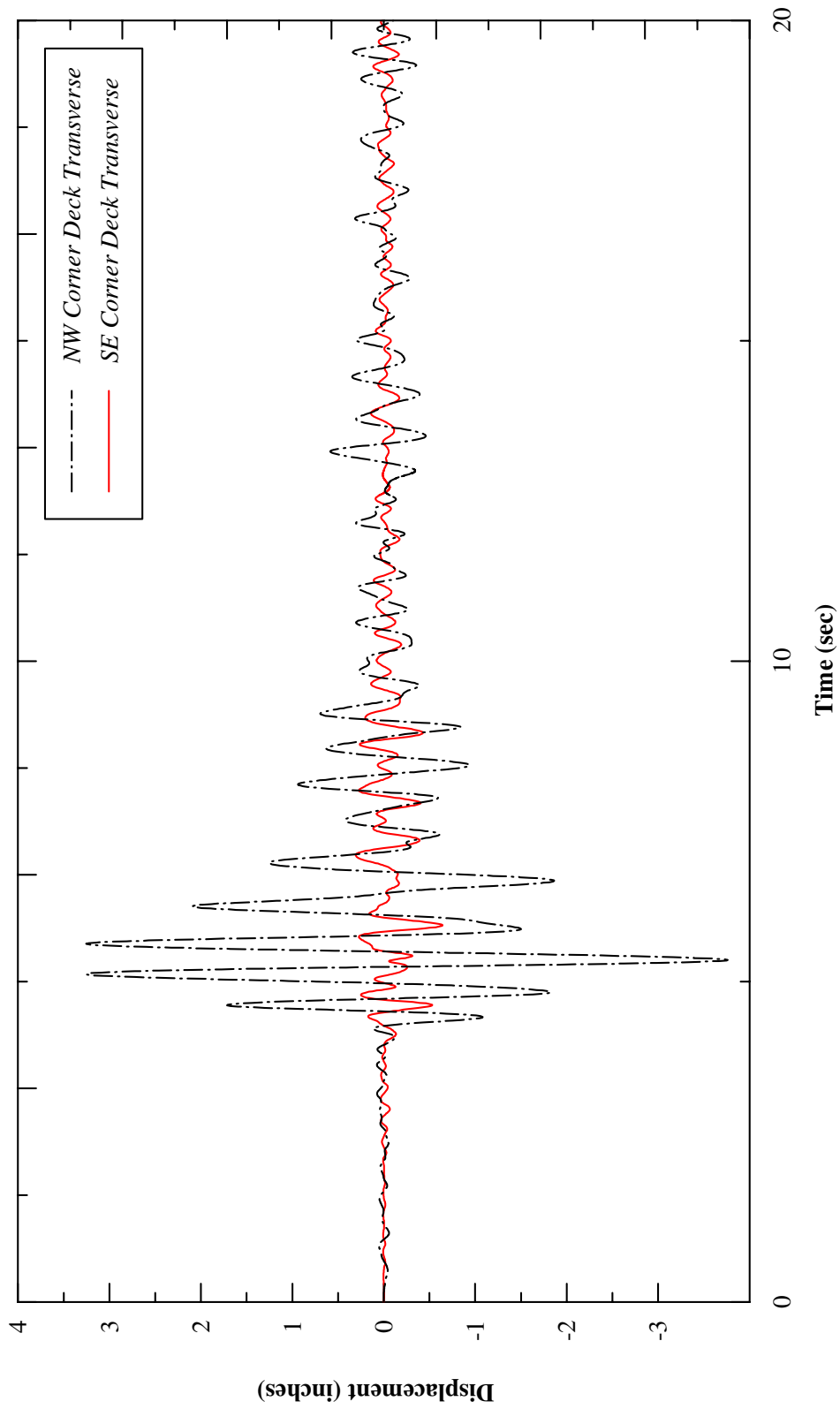


Figure 6.28: Comparisons of the Northwest and Southeast Corners Displacement Response in the Transverse Directions Using Direct Method

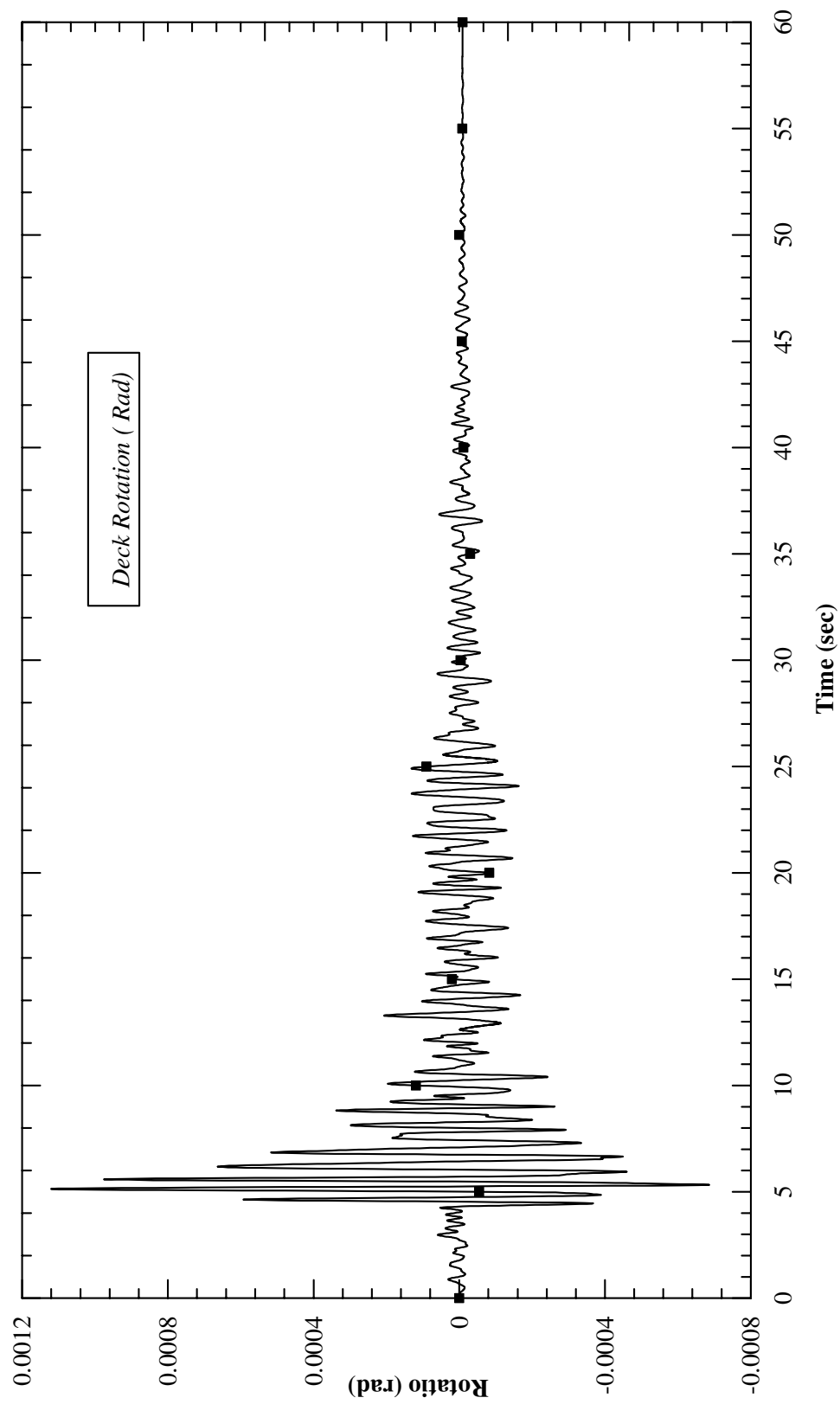
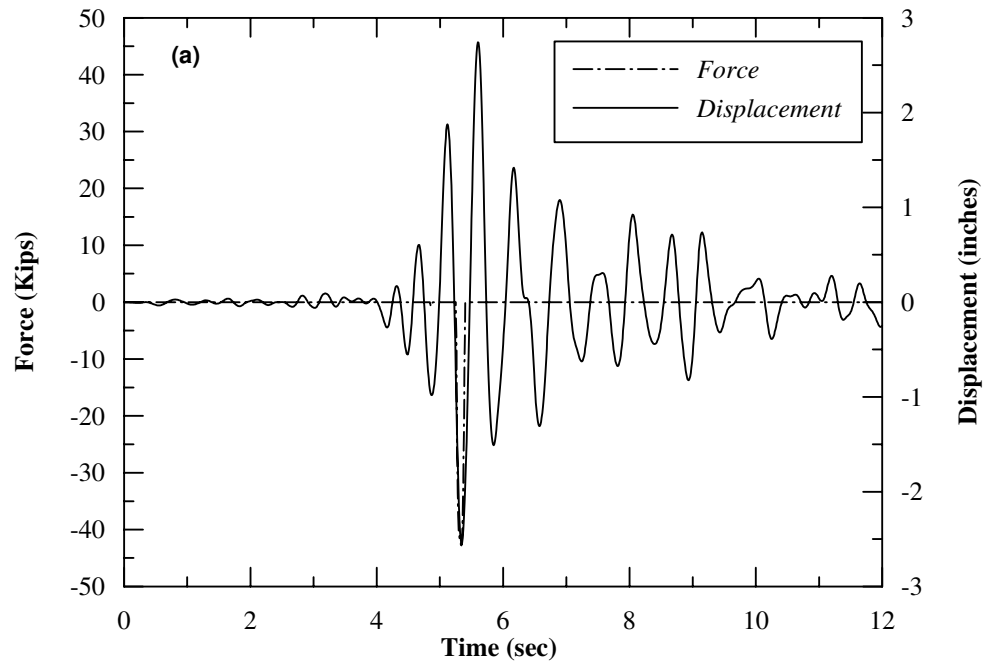


Figure 6.29: Deck Rotational Response Using Direct method

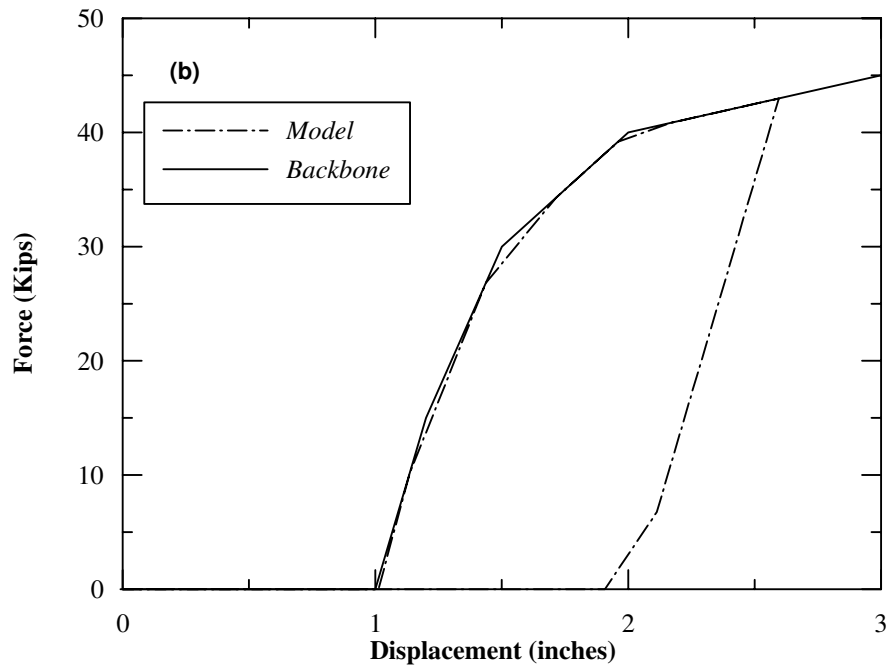
6.7.4 Abutment Force and Displacement Response

Figure 6.30 and Figure 6.31 show the average force-displacement response of the abutments. At the West Abutment, the backfill participates to resist seismic forces after 4.5 seconds of shaking following closure of the 1-inch expansion gap. At the East Abutment (where there is no gap), the backfill begins to resist lateral forces at the instance the bridge moves eastward.

Figure 6.32 shows the transverse displacement response between the abutment (pile cap) and the bridge deck. The difference between these two time histories corresponds to transverse offset of the deck relative to the seat of up to about 2 inch and illustrates the bridge deck rotation in time. The hysteretic behavior of the north and south transverse shear keys at the west abutment are shown in Figure 6.33 and Figure 6.34. The two shear keys are observed to approach their ultimate structural capacities. This result suggests that these keys could potentially fail when subjected to stronger shaking, which could allow the bridge to rotate and cause the deck to become unseated at the east abutment due to lateral movement.

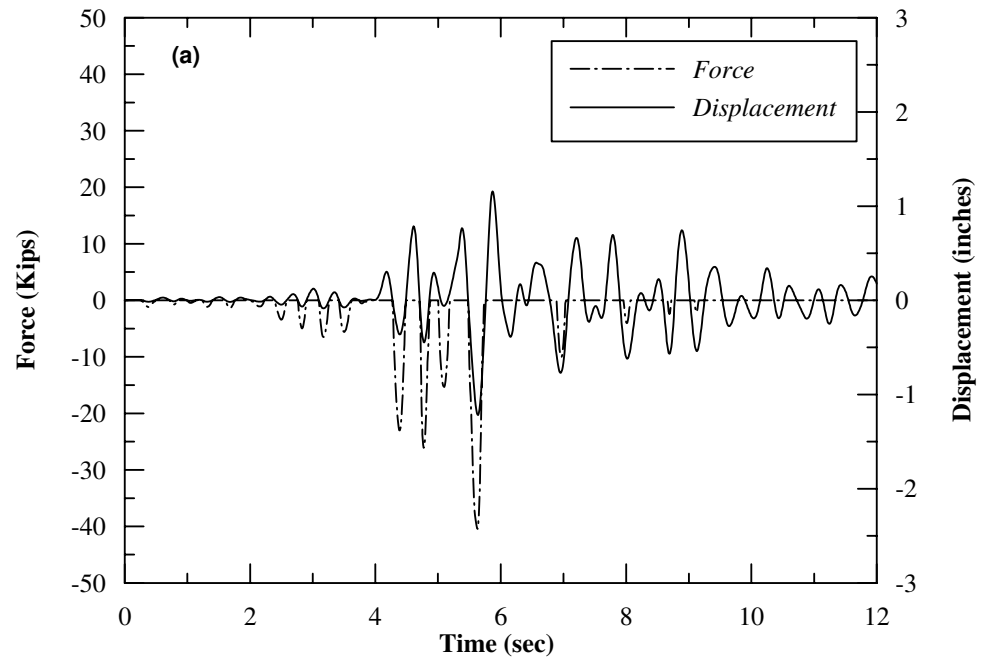


(a)

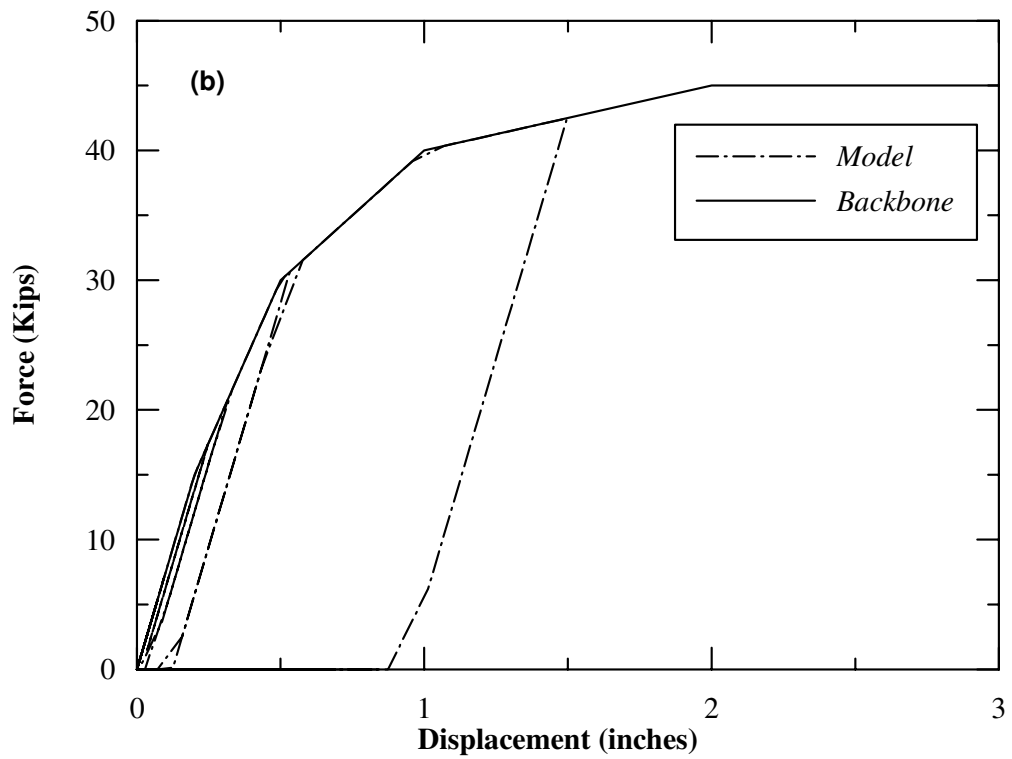


(a)

Figure 6.30: Force-Displacement Response at The West Abutments Using Direct method



(a)



(b)

Figure 6.31: Force-Displacement Response at The East Abutments Using Direct method

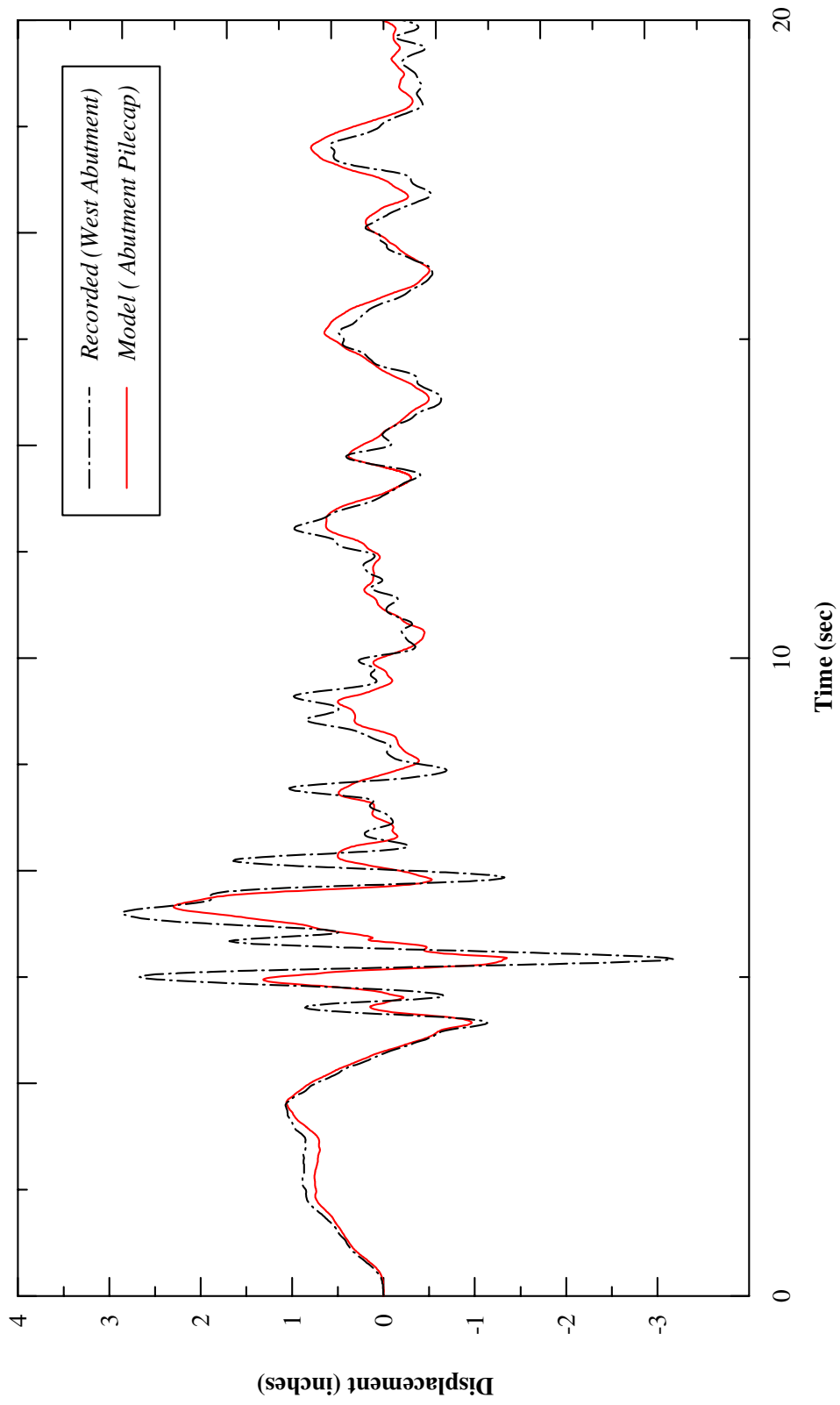
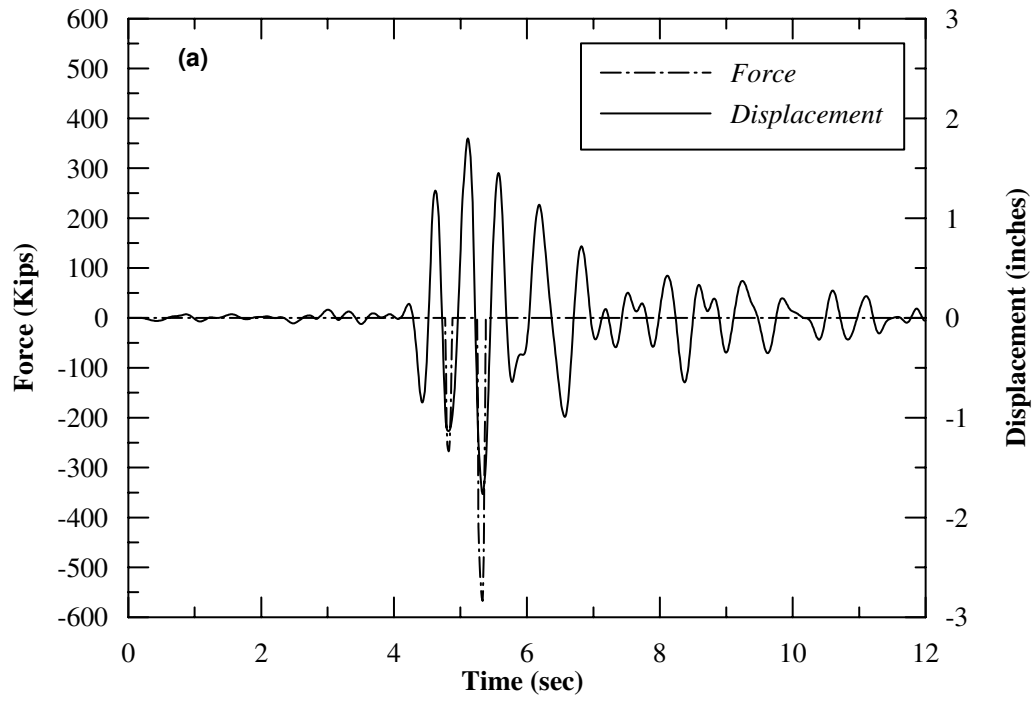
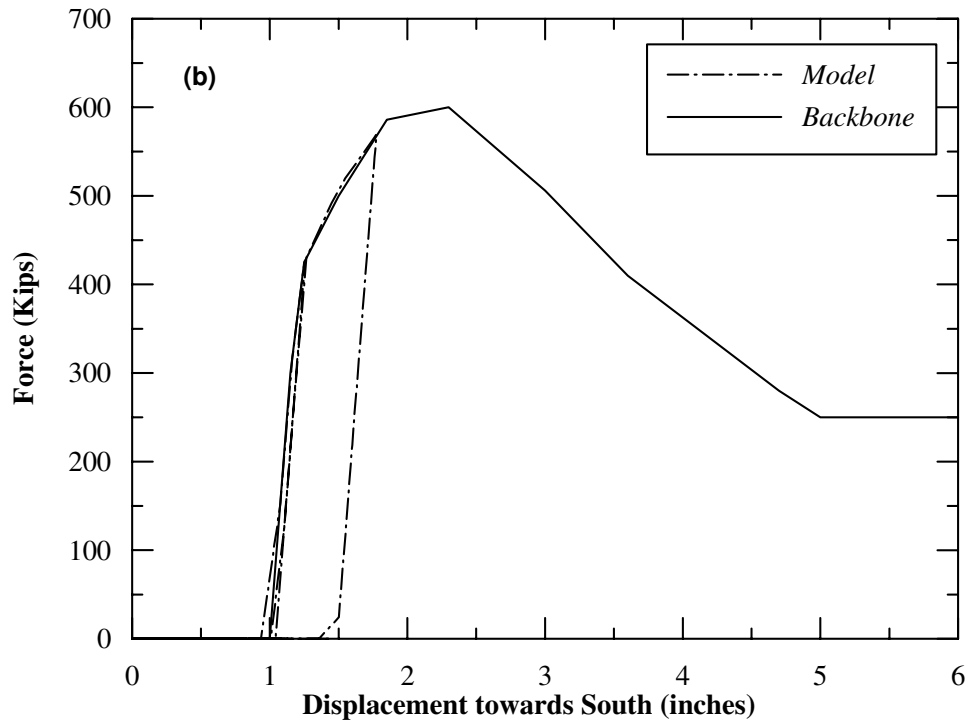


Figure 6.32: Displacement response at the West Abutment Seat Using Direct method

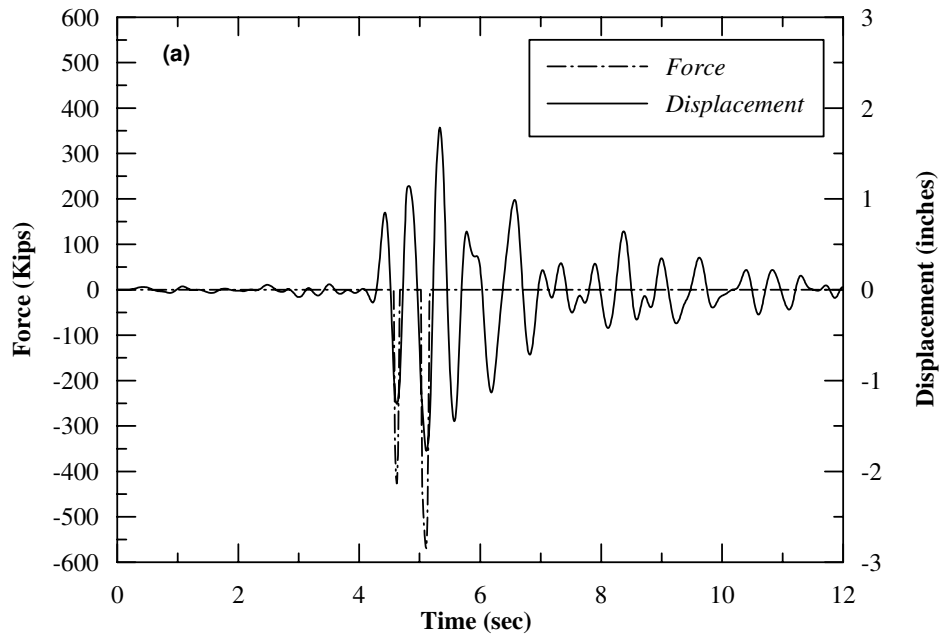


(a)

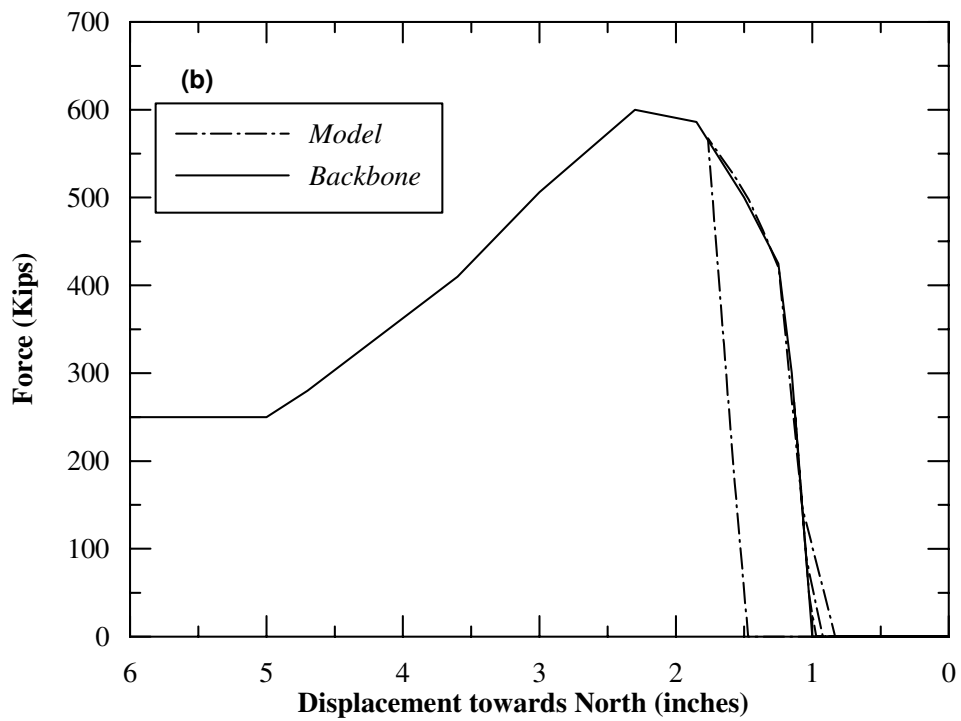


(b)

Figure 6.33: Force-Displacement Capacity of Shear Key at West Abutment Using Direct method



(a)



(b)

Figure 6.34: Force-Displacement Capacity of Shear Key at West Abutment Using Direct method

6.8 Substructuring Technique

The concept of the substructuring system and foundation impedance can be explained using equation of motion in the frequency domain. Several researches have developed numerous procedures to determine dynamic impedance of pile foundation. The purpose of this section is to explain why substructuring technique is the most efficient way to represent the bridge foundation for seismic global analysis of the bridge structure. Figure 6.35 shows a linear pile foundation system of mass M , Lateral stiffness K and damping C subjected to a horizontal ground excitation force.

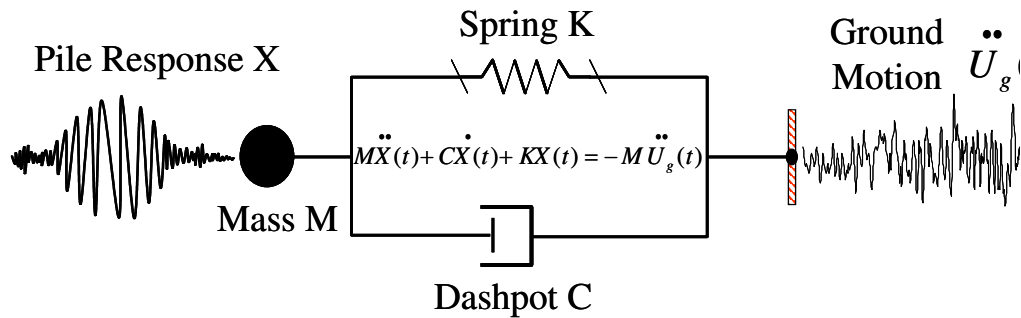


Figure 6.35: Schematic of soil-pile interaction

At each instant of time t , the equation of motion from the free body shown in Figure 6.35 can be expressed in a general form as shown in Eq. (6.1).

$$M\ddot{X}(t) + C\dot{X}(t) + KX(t) = -M\ddot{U}_g(t) \quad (6.1)$$

where

$$\begin{aligned}\ddot{X} &= i^2 \omega^2 X \\ \dot{X} &= i \omega X\end{aligned}\tag{6.2}$$

Substituting Eq. (6.2) into Eq. (6.1), then

$$Mi^2 \omega^2 X(t) + Ci \omega X(t) + KX(t) = -M \ddot{U}_g(t)\tag{6.3}$$

In which M, C and K are mass, damping and stiffness matrix respectively, of a single degree freedom of the structure, (X) is the total displacement vector of the system, and U_g is the acceleration vector of the free-field ground motion.

Let

$$-M \ddot{U}_g(t) = F(t)$$

Where F(t) is the free field excitation force due to ground acceleration therefore, Eq. (6.2) can be expressed as follow:

$$Mi^2 \omega^2 X(t) + Ci \omega X(t) + KX(t) = F(t)\tag{6.4}$$

Then

$$\frac{F(t)}{K - M\omega^2 + Ci\omega} = X(t)\tag{6.5}$$

where

$$[K] - [M]\{\omega^2\} + [C]\{i\omega\} = \bar{K} + i\omega C$$

Let

$$K - M\omega^2 = \bar{K}$$

K is the static stiffness,

\bar{K} is the dynamic stiffness.

$\bar{K} + i\omega C$ is the dynamic impedance.

The dynamic impedance is a complex stiffness which is consisted of real part and imaginary part. The real part is the dynamic stiffness \bar{K} is a function of static stiffness K and the circular frequency ω . The imaginary part of the stiffness is a function of frequency and viscous damping C and the circular frequency ω .

Figure 6.36 shows a general plot of the dynamic impedance versus frequency of the system. It can be seen that as the frequency increases the dynamic stiffness decreases, however, in the frequency range of interest for bridge structure the dynamic stiffness is practically the same as the static stiffness. That is the main reason substructuring technique using static condensation can be used to develop 6x6 foundation stiffness matrix.

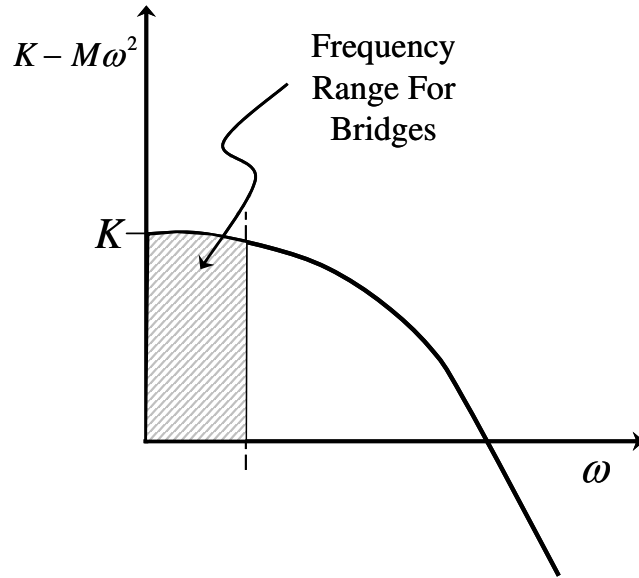


Figure 6.36: Dynamic Impedance Versus frequency

The substructuring technique using static condensation is used to develop the foundation stiffness matrices for the each pile group at the bent and at the each abutment as shown below.

$$\mathbf{K}_{Pile} = \begin{bmatrix} K_{11} & 0 & 0 & 0 & 0 & -K_{16} \\ 0 & K_{22} & 0 & 0 & 0 & 0 \\ 0 & 0 & K_{33} & K_{34} & 0 & 0 \\ 0 & 0 & K_{43} & K_{44} & 0 & 0 \\ 0 & 0 & 0 & 0 & K_{55} & 0 \\ -K_{61} & 0 & 0 & 0 & 0 & K_{66} \end{bmatrix}$$

where:

k_{11}, k_{22}, k_{33} are corresponding to translational degrees of freedom

k_{44}, k_{55}, k_{66} are corresponding to rotational degrees of freedom

$k_{16}, k_{34}, k_{61}, k_{43}$ are corresponding to cross coupling degrees of freedom

As shown in Figure 6.37 each column is supported on 20 concrete piles and the west and the east abutments are supported on a single row of 16 and 14 concrete piles respectively. The pile group supporting each individual column and the surrounding soil are represented by a 6x6 stiffness matrix and individual pile and the surrounding soil supporting the bridge abutments are represented by a 6x6 matrix.

6.8.1 Procedures To Develop Stiffness Matrix

The soil-foundation-structure interaction of a bridge system depending on the soil profile and structural integrity of the piles and pile cap system could be highly nonlinear. In order to represent the foundation nonlinearity using a linear 6x6 stiffness matrix, equivalent linear foundation stiffness matrices were developed based on the average recorded displacement obtained from channel 1,2 and 3 located close to the bottom of the column at bent number 2. The piles were pushed at the top for the given displacement. The soils reactions along the soil profile were divided by the deformation along the pile length in order to calculate the linear subgrade reactions. The subgrade reactions were multiplied by each tributary length in between the nodal points to calculate the linear springs at each nodal point along the pile length. To model the soil pile interaction effect, the stiffness of the soil surrounding each pile were modeled using lumped generalized spring elements attached to pile at discrete nodal points located along the centerline of the pile. The linear translational spring elements, namely longitudinal and transverse springs acting parallel and perpendicular to the bridge centerline, respectively, were used at

each pile nodal point for modeling the lateral soil stiffness and a linear vertical spring was attached at the tip of each pile for modeling vertical pile stiffness. The combination of the linear springs at the nodal points and the stiffness of the piles were condensed to a full 6x6 matrix at the pile caps. Using the above procedures as an example the full 6x6 matrix for the pile group at the bent is given in Table 6.4.

Table 6.4 Bent Foundation Stiffness Matrix(kips, inch and radian)

3.21E+03	0	0	0	0	0
0	3.21E+03	0	0	0	0
0	0	3.03E+03	0	0	0
0	0	0	7.87E+7	0	0
0	0	0	0	4.92E+7	0
0	0	0	0	0	1.35E+7

6.9 Bridge Response Using Substructuring Technique

Figure 6.39 through Figure 6.45 shows comparisons of the calculated displacement time history response versus recorded response of the bridge superstructure using a substructure technique. The comparison between the recorded motions and the computed motions using substructure approach is remarkably close.

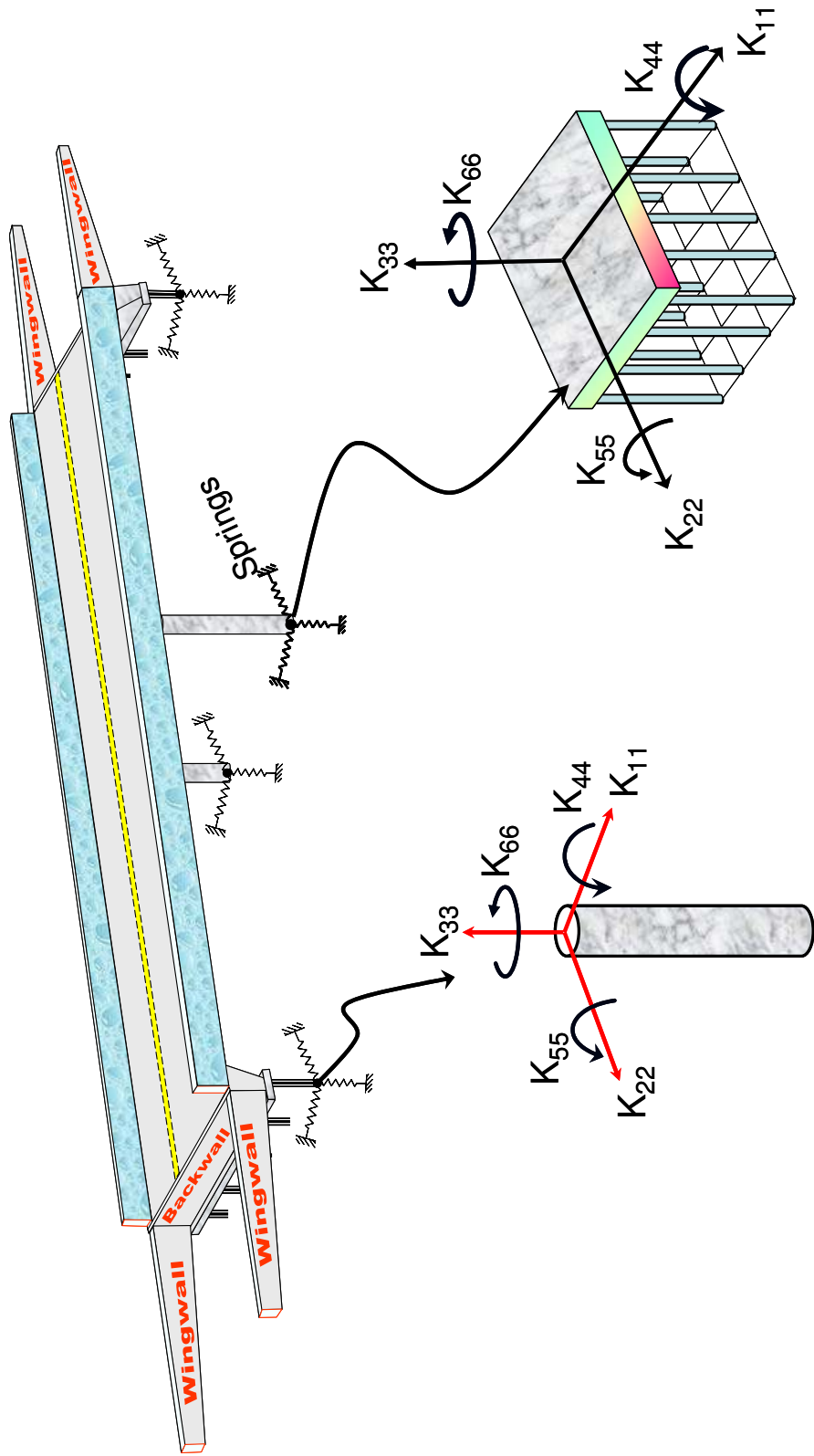


Figure 6.37: Substructuring Approach For Abutments and Bent

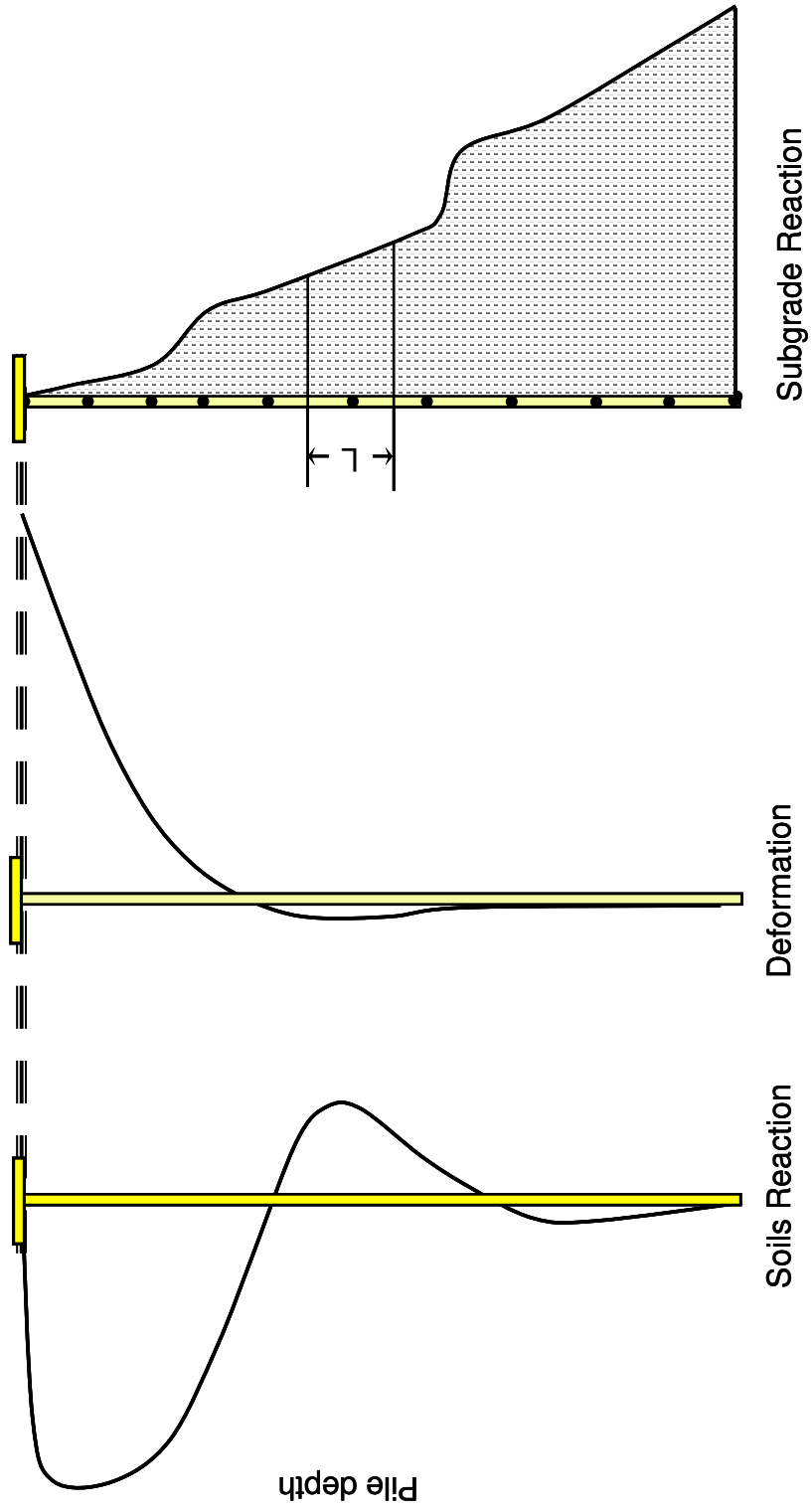


Figure 6.38: Soil-Pile Interaction

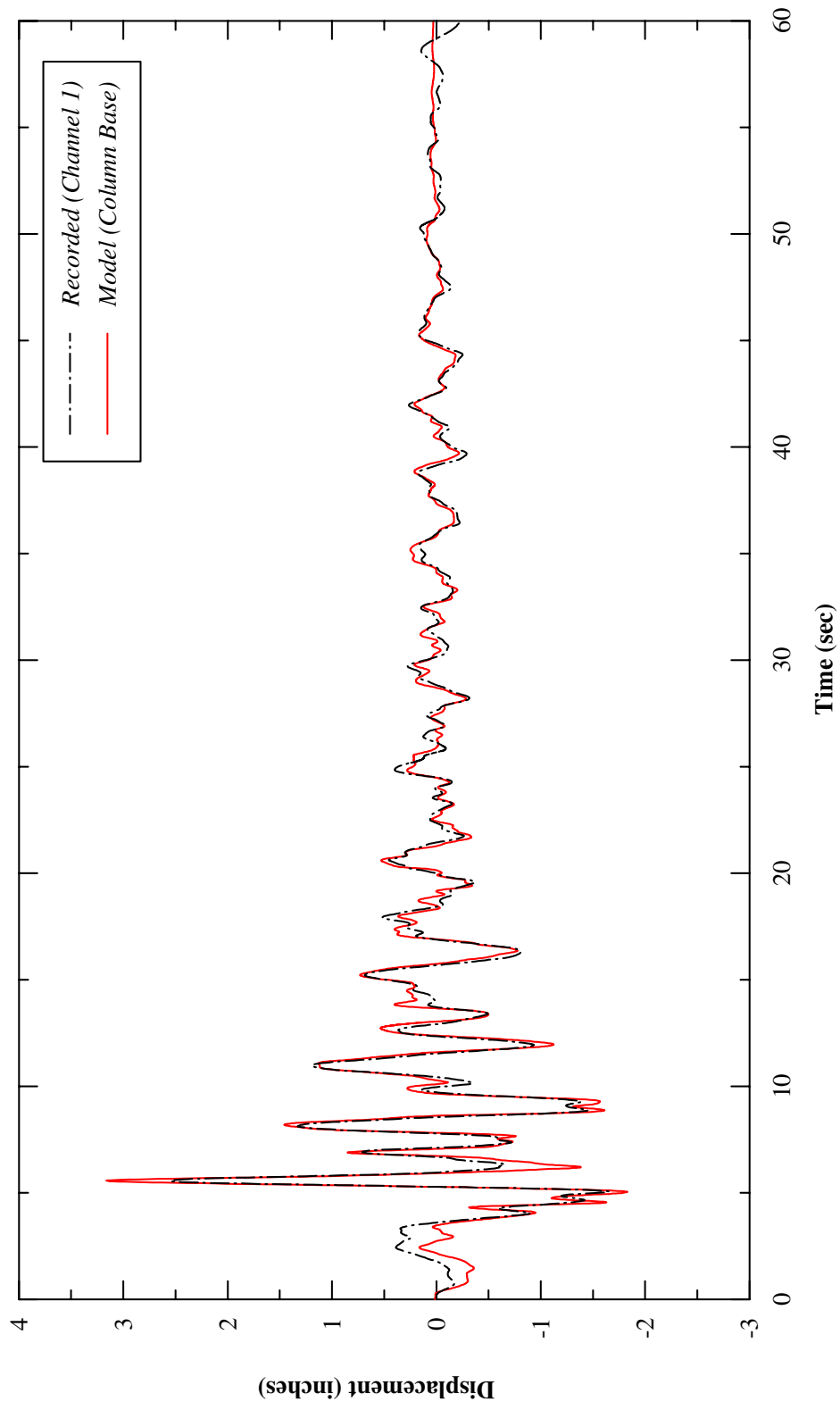


Figure 6.39: Recorded Response Versus Analytical Response Using Substructure Method (Channel 1)

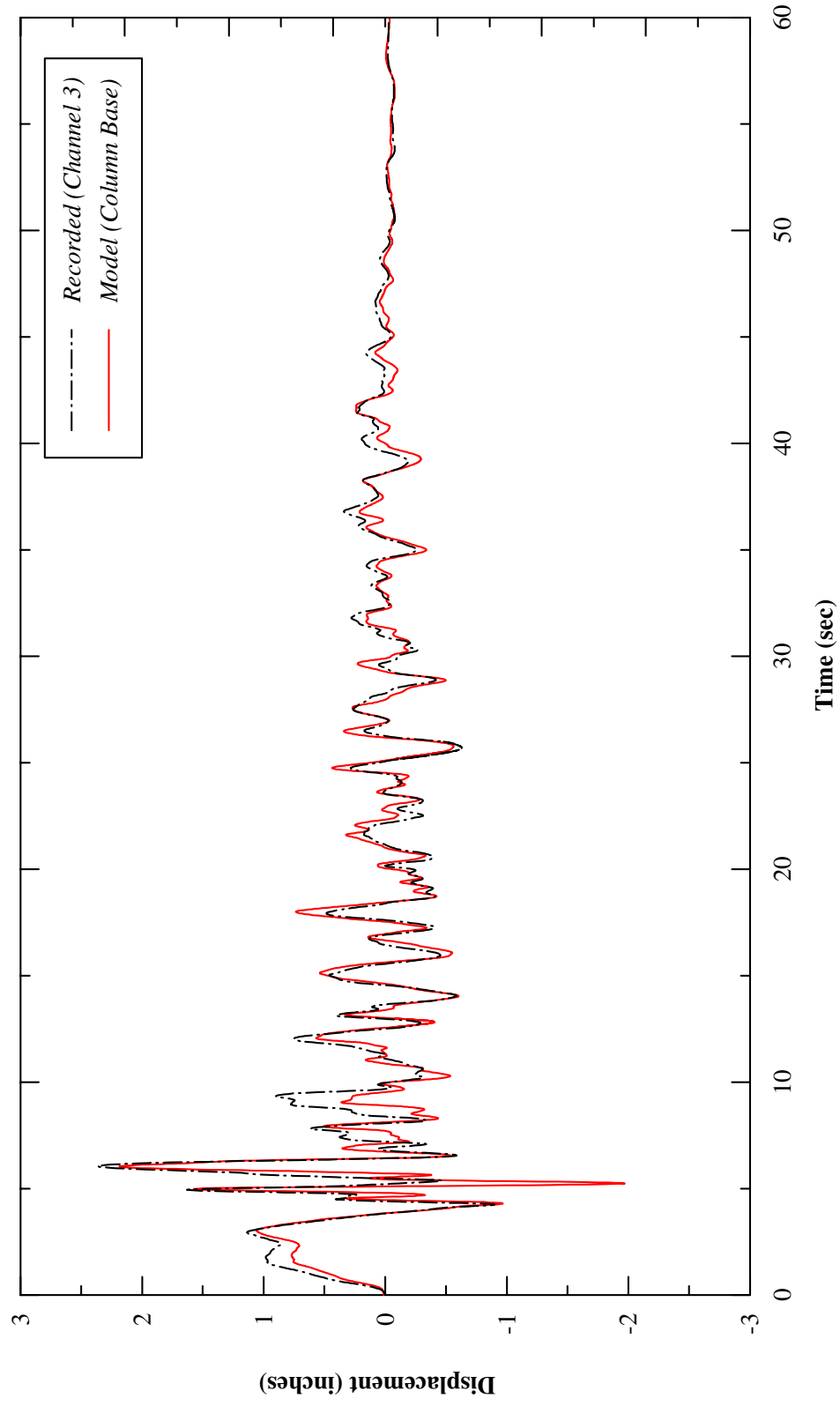


Figure 6.40: Recorded Response Versus Analytical Response Using Substructure Method (Channel 3)

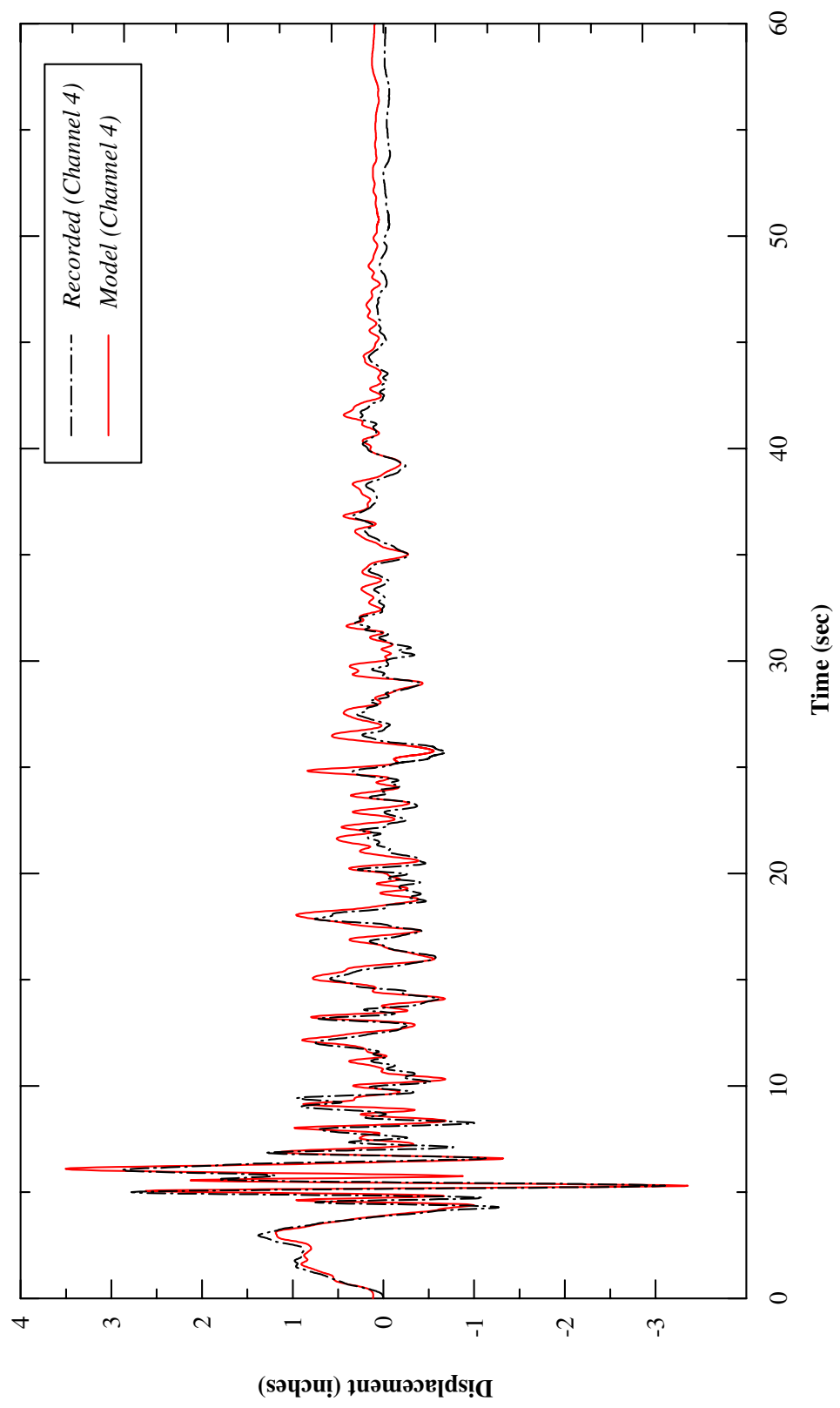


Figure 6.41: Recorded Response Versus Analytical Response Using Substructure Method (Channel 4)

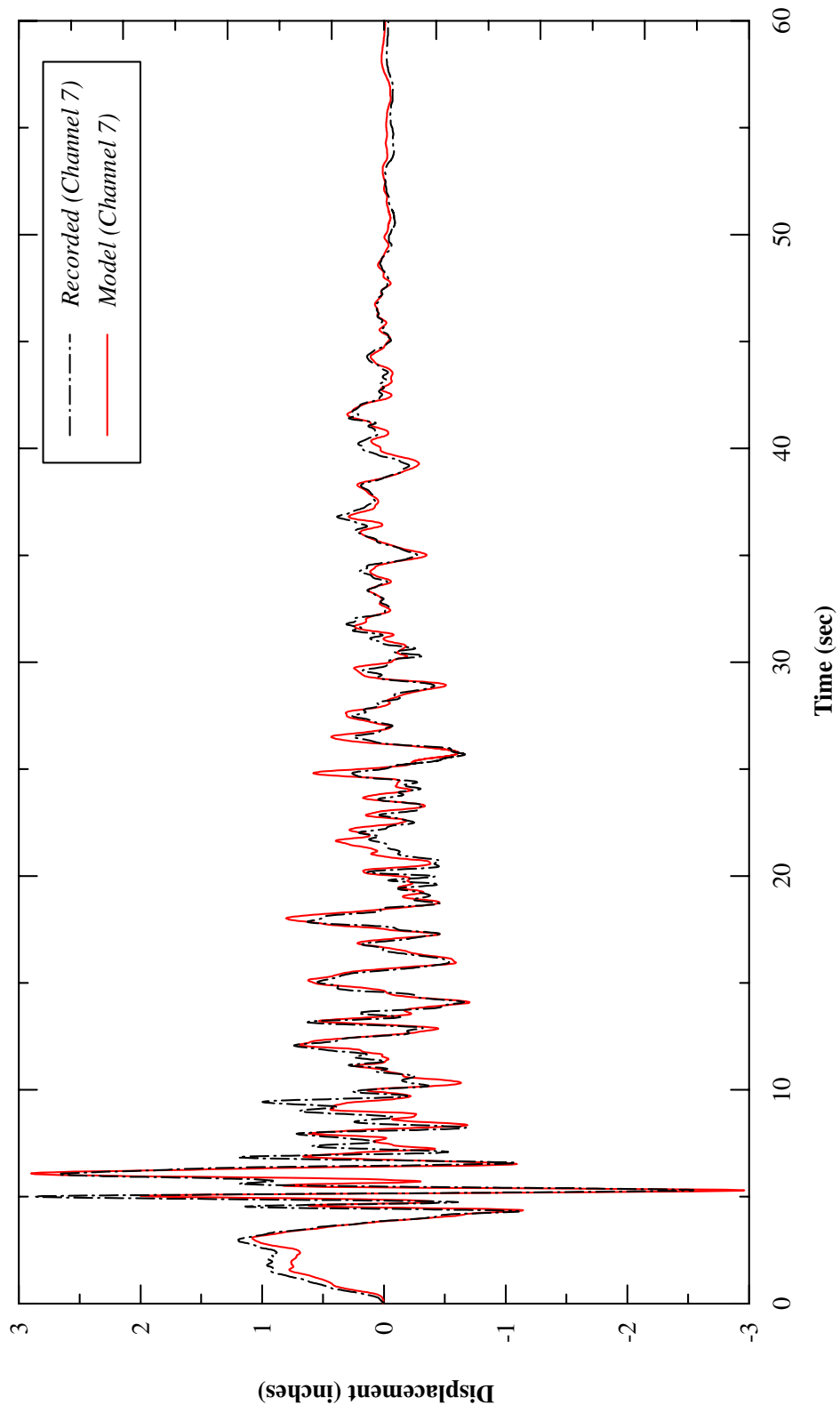


Figure 6.42: Recorded Response Versus Analytical Response Using Substructure Method (Channel 7)

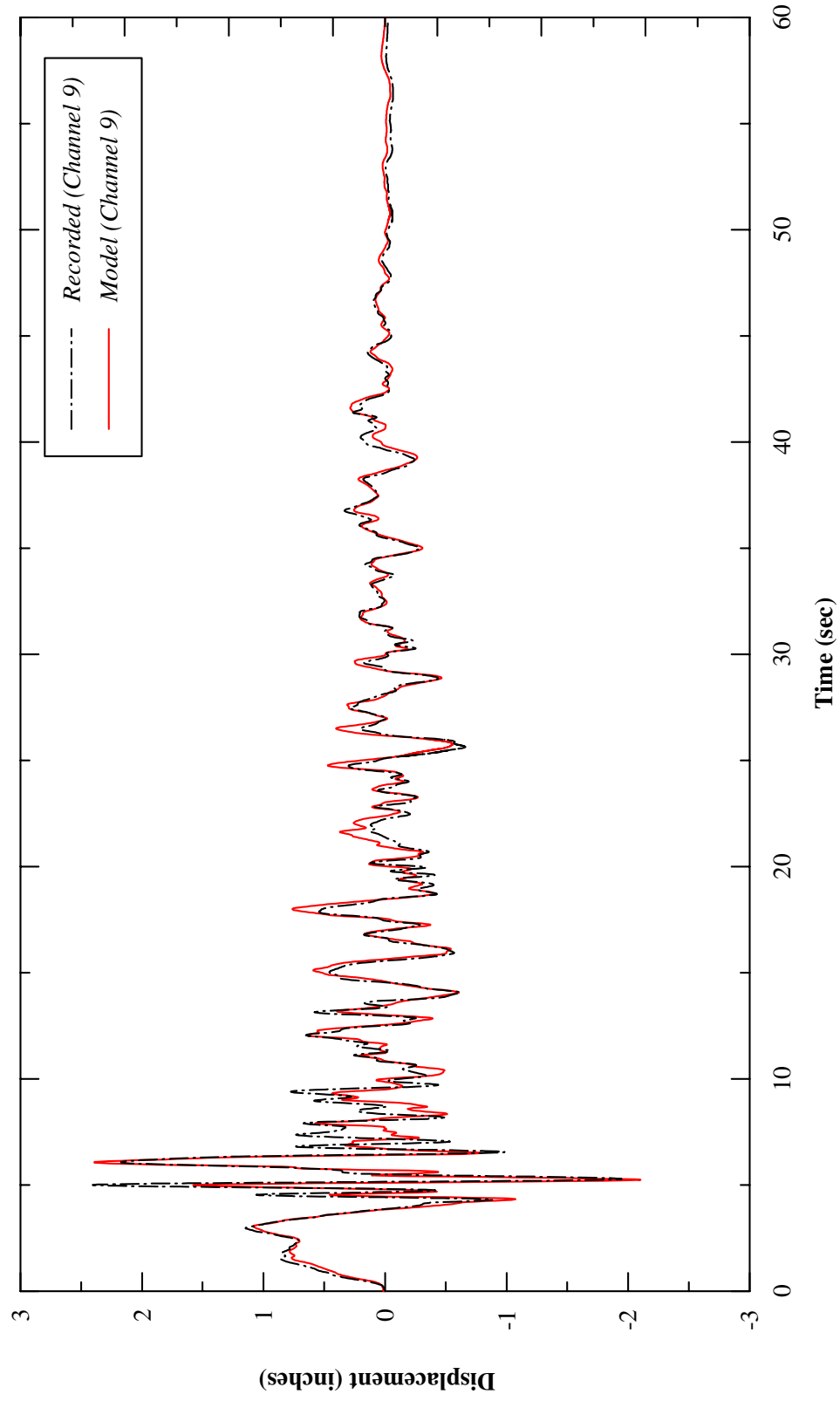


Figure 6.43: Recorded Response Versus Analytical Response Using Substructure Method (Channel 9)

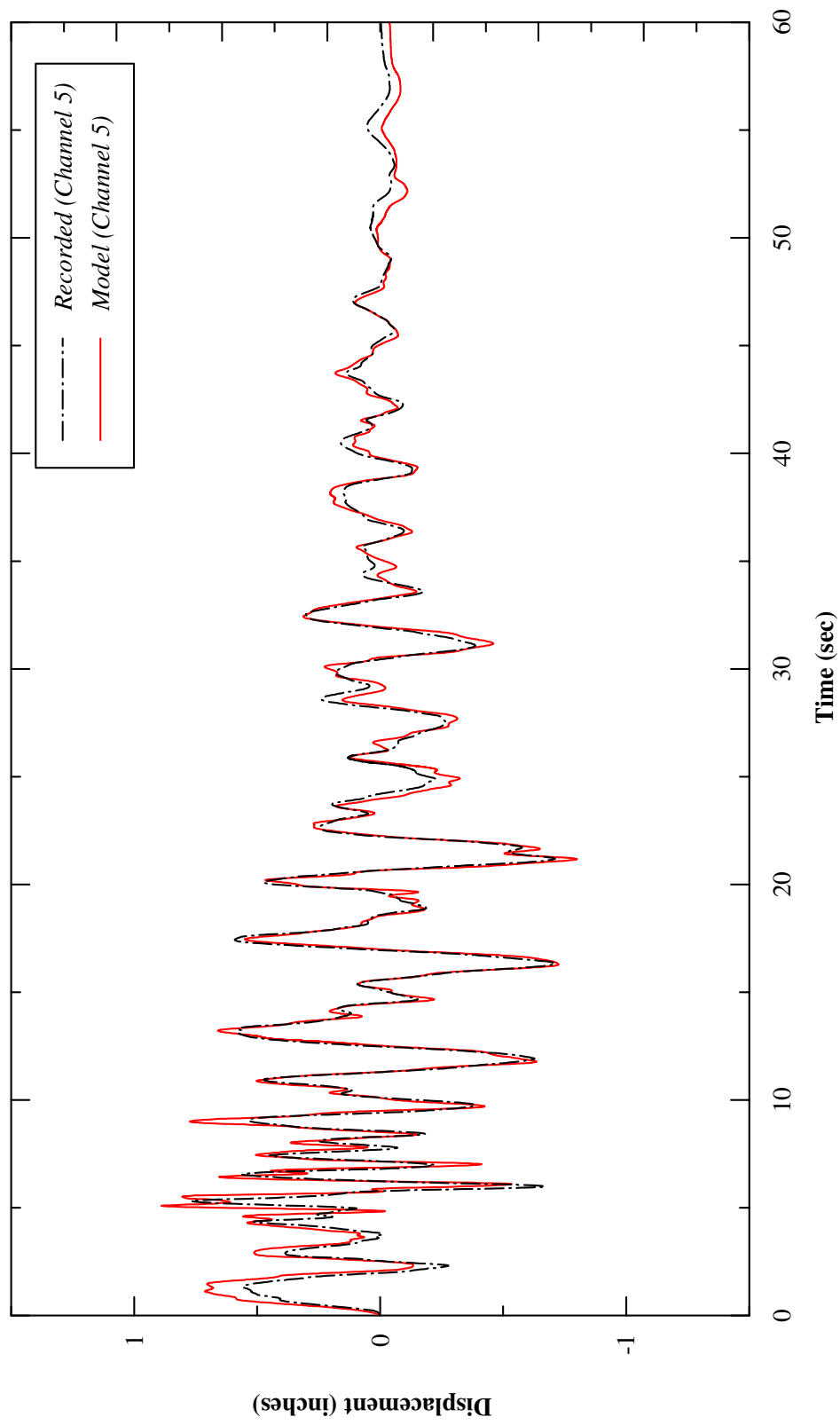


Figure 6.44: Recorded Response Versus Analytical Response Using Substructure Method (Channel 5)

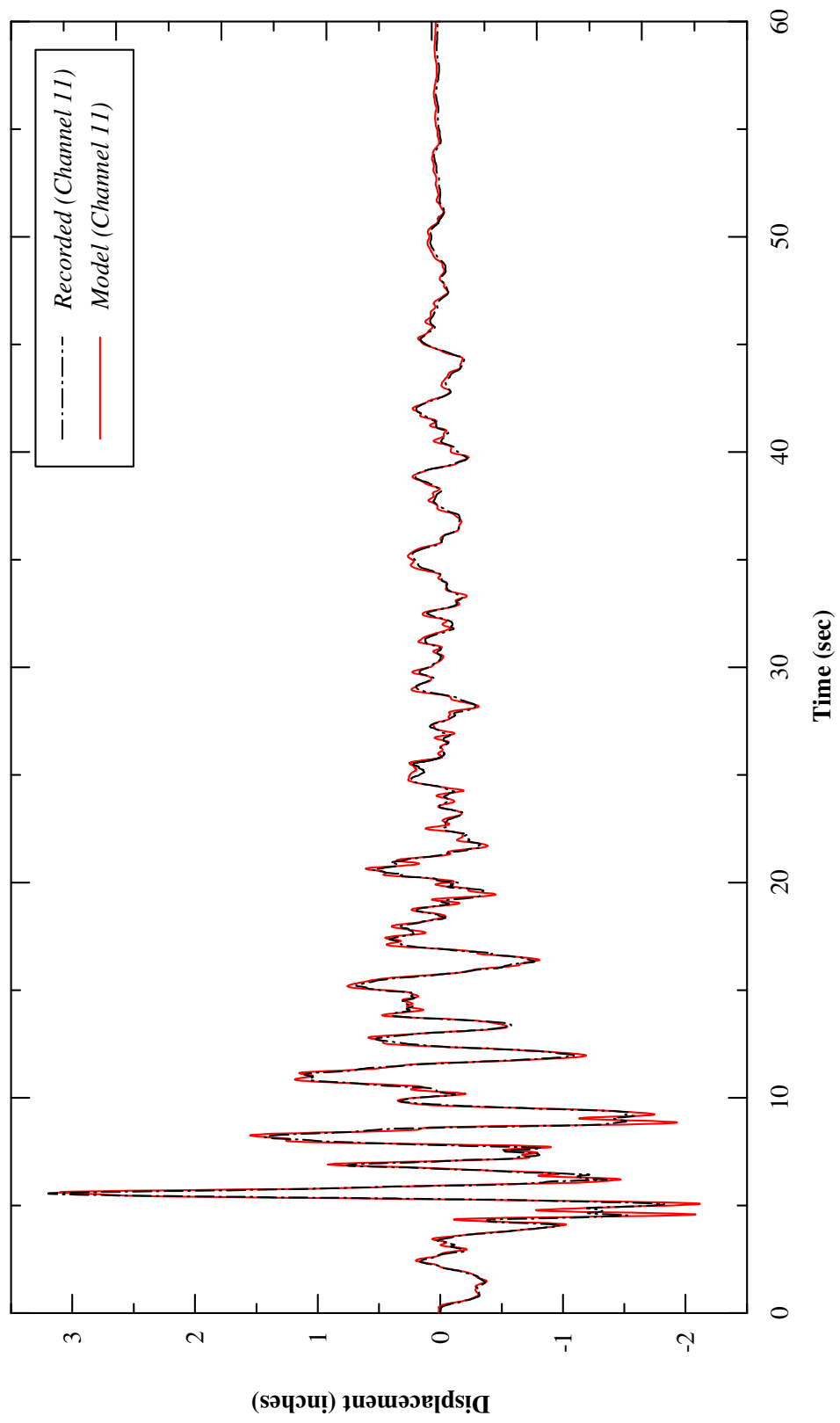


Figure 6.45: Recorded Response Versus Analytical Response Using Substructure Method (Channel 11)

6.10 Conclusions

A global, three-dimensional finite-element structural model of Painter Street Overpass Bridge which is seismically instrumented was developed to investigate using two different approaches. The remarkable match achieved between models and the recorded motions is due to additional steps taken to realistically estimate passive soil and shear key capacities at the abutment walls. The quality of the structural bridge evaluations depends directly on the magnitude of soil properties and capacities. The soil-abutment-foundation-structure interaction model parameters were based on actual engineering soil properties. The abutment-backfill interaction was modeled separately (using PLAXIS) and this requires an understanding of earth pressure theories; the pile-soil interaction was developed using pile design criteria which are based on pile load tests. The comparison between the recorded motions and the computed motions is also very favorable for the both foundation modeling approaches. The study led to conclusions that both the complete foundation system and the substructure foundation system can offer reasonable solutions. The results are very encouraging for the geotechnical engineers as significant time saving can be realized if the foundation substructure can be simplified in seismic response studies. While the complete foundation system is the most desirable modeling approach, it may not be required for simple ordinary bridges. Reasonably accurate solutions can be obtained by the substructure foundation system.

CHAPTER SEVEN

CONCLUSIONS AND RECOMMENDATIONS

7.1 Summary and Conclusions

The purpose of this dissertation is to investigate the nonlinear global seismic soil-abutment-foundation-structure interaction behavior of typical highway skewed-bridge structures subjected to near-fault ground motions with high velocity pulses.

Three-dimensional nonlinear finite element models of typical box girder bridges for various skew angles were developed. The bridge decks were modeled using both three-dimensional shell elements and frame elements. Moment-curvature relationships were developed to model the nonlinear behavior of the reinforced concrete columns. Nonlinear link elements were used to model the abutment-backfill and the expansion gaps in the longitudinal directions and the shear keys and the expansion gaps in the transverse directions. The structural models were excited using seven sets of bilateral response-spectra-compatible time history ground motions with the near fault effects.

A practical and simplified design tool was developed and calibrated with all available experimental data to predict the nonlinear force displacement capacity of the abutment backfill. In addition advanced three-dimensional nonlinear finite element models were developed to simulate the skew abutment-backfill nonlinear behavior and to understand the mechanism of the problem. A nonlinear closed form hyperbolic force-deformation relationship which takes the backfill stiffness and

ultimate capacity of the backfill into account is developed as a powerful and effective tool for practicing bridge engineers. Parametric studies were carried out to better understand the mechanics of skewed bridge behavior. The parameters included nonlinear wide ranges of skew angle, bridge width, span length, number of columns per bent, number of actual earthquakes recorded motions and response spectra-compatible time history ground motions. All the motions have near-source ground motion characteristics with high velocity pulses. Case study based on the recorded response of a skewed-two-span reinforced concrete box girder under strong shaking was performed to validate the modeling techniques developed in this dissertation.

Chapter 3 describes the limit-equilibrium method using mobilized Logarithmic-Spiral failure surfaces coupled with a modified Hyperbolic soil stress-strain behavior referred here as the “LSH” model to capture the nonlinear abutment-backfill force-displacement relationship. A nonlinear closed form hyperbolic force-deformation relationship referred here as the “HFD” model is developed as a powerful and effective tool for practicing bridge engineers.

Chapter 4 presents the applications of the two- and three-dimensional finite-element analysis to investigate the mechanism of the abutment-backfill behavior in particular bridge abutments with high skew angles. Three-dimensional finite-element analysis indicates that the total resistance of the mobilized passive wedge is maximum for the zero skew angle and decreases as the magnitude of skew angles are increased.

Chapter 5 discusses the mechanics and the behavior of the three-dimensional dynamic behavior of bridges with wide ranges of skew angles, implementation of the nonlinear abutment-structure interaction into the bridge global model, parametric studies and discussion regarding the impact ground motions with high velocity pulses. It was concluded that seismic response of the bridge structure depends on many factors such as nonlinear abutment springs, column ductility, skew angles and characteristics of the ground motions.

Chapter 6 presents a three-dimensional nonlinear finite-element model of an instrumented bridge structure for the validation of the modeling technique applied in this dissertation. Both direct model and substructure model were implemented. The direct model included the superstructure, nonlinear columns, nonlinear bridge abutments and pile foundations with full coupling between structure and foundation soils. For the substructure model the pile foundations were represented by condensed stiffness matrices. The bridge system was subjected to the three-component recorded free-field earthquake motions. The modeling techniques were calibrated and verified using the recorded response of the bridge structures at various locations.

7.2 Recommendations

The simple HFD relationship shown in Figure 7.1 is recommend to develop longitudinal nonlinear abutment springs for seismic design of typical highway bridge when no geotechnical data is available. Eq. (7.1) and Eq. (7.2) may be used to develop abutment springs for the cohesionless and cohesive backfill respectively.

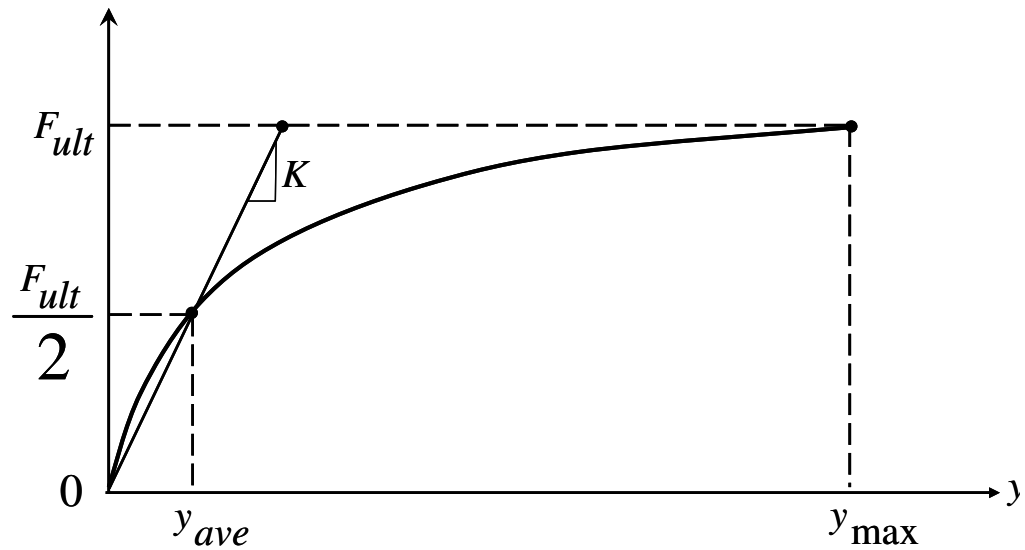


Figure 7.1 Abutment Seat Width Requirements

$$F(y) = \frac{8y}{1+3y} H^{1.5} \quad (y \text{ in inches, } F \text{ in kips per ft of wall}) \quad (7.1)$$

$$F(y) = \frac{8y}{1+1.3y} H \quad (y \text{ in inches, } F \text{ in kips per ft of wall}) \quad (7.2)$$

The expansion gaps may be model as part of the abutment backbone curve for computational efficiency.

7.3 Further Research

Although the results of the analysis illustrated that with proper bridge boundary conditions and suitable bridge components parameters, it is possible to capture the global seismic behavior of the bridge structures, additional research studies and verification testing is recommended. Additional research includes nonlinear dynamic analyses and centrifuge and shaking table tests of skewed bridge

structures systems, under earthquake excitations with high velocity pulses. Shaking table tests of reasonably scaled complete systems, and centrifuge tests of complete systems are of particular priority. Regarding the analytical research, more parametric studies should be carried on various components of the bridge structures as listed below to analyze:

- (1) The contribution of the far field geometric damping (which was neglected in this investigation) along with the nonlinear force-deformation relationship of the bridge abutment.
- (2) The variation of nonlinear abutment backbone curves in both transverse and longitudinal directions.
- (3) Modeling of a realistic representation of the elastomeric pads.
- (4) Variations of span length and depth of the superstructure, number of columns per bent and columns ductility.
- (5) The seismic response of bridges with modern column-shaft construction.
- (6) Switching the ground motion in the transverse and longitudinal direction.

Regarding the experimental research the following studies is recommended to validate the analytical models and to develop guidelines and procedures for the seismic performance based-design of bridge structures:

- (1) Conduct large-scale field experiments in the longitudinal direction of the abutment-embankment bridge approaches constructed with mechanically stabilized earth (MSE) walls to develop nonlinear abutment backbone curve.

- (2) Conduct large-scale field experiments on a skew abutment to develop nonlinear abutment backbone curves for skewed abutments.
- (3) Conduct shaking table tests of reasonably scaled complete systems using 2-component motions to investigate the global behavior of the bridge-abutment-structure interaction system.
- (4) Conduct geotechnical-structural centrifuge tests including a bridge soil-abutment-pile-foundation-structure with various bridge geometries and skew angles using 2-component ground motions with and without velocity pulses to investigate the global behavior of the bridge system.

REFERENCES

- AASHTO (1992). Standard Specifications for Highway Bridges, Fifteenth Edition, Washington, D.C.
- Applied Technology Council (1996), Seismic Evaluation and Retrofit of Concrete Buildings, ATC-40, Report No. SSC 96-01, November.
- Ashour, M., Norris, G., and Pilling, P. (1998). Lateral Loading of a Pile in Layered Soil Using the Strain Wedge Model. *Journal of Geotechnical and Geoenvironmental Engineering*, ASCE, Vol. 124, No. 4, pp. 303-315.
- American Society for Testing and Materials (ASTM) (2003). "Annual Book of Standards," Soil and Rock; Dimension Stone; Geosynthetics, Vol. 04.08.
- Bardet, J. P. (1997). *Experimental Soil Mechanics*, Prentice Hall, Upper Saddle River, New Jersey 07458.
- Bardet, J. P., and S.M. Mortazavi, (1987). "simulation of shear band formation in overconsolidated clay" *Proc. 2d Int. Conf. Const, Laws for Engr. Mat., Tuscon*, 805-812.
- Bhatia, S. K., and Bakeer, R. M. (1989). "Use of the finite element method in modeling a static earth pressure problem." *International Journal for Numerical and Analytical Methods in Geomechanics*, 13, 207-213.
- Bozorgzadeh, A., Megally, S., Restrepo, J., and Ashford, S., 2005. Seismic Response and Capacity Evaluation of Sacrificial Exterior Shear Keys of Bridge Abutments, Dept. of Structural Engineering, UC San Diego.
- Bransby, P. L., and Smith, I. A. A. (1975). "Side friction in model retaining-wall experiments." *Journal of the Geotechnical Engineering Division, Proc. of ASCE*, 101(GT7), July, 615-632.
- Caltrans (1989). *Bridge Design Aids*, Division of Structures, October, 14-1-14-7.
- Caltrans *Seismic Design Criteria* (2004).
- Caquot, A., and Kerisel, J. (1948). *Tables for the Calculation of Passive Pressure, Active Pressure and Bearing Capacity of Foundations*, Gauthier-Villars, Paris.

- Chen, W. F., and Mizuno, E. (1990). *Nonlinear Analysis in Soil Mechanics, Developments in Geotechnical Engineering Vol. 53*, Elsevier.
- Chu, S.-C., and Su, J.-J. (1994). "A method for passive earth pressure computation on sands." *Proc. of the Eighth International Conference on Computer Methods and Advances in Geomechanics, Morgantown, West Virginia, USA, 22-28 May 1994*, Siriwardane and Zaman (eds), Balkema, Rotterdam, Vol. III, 2441-2445.
- Clough, G. W., and Duncan, J. M. (1991). "Earth pressures." *Foundation Engineering Handbook, 2nd Edition*, Fang (ed), van Nostrand Reinhold, New York.
- Craig, R. F. (1992). *Soil Mechanics, Chapter 6, 4th Edition*, Chapman & Hall.
- Crouse, C. B., and Hushmand, B. (1987). "Estimate of bridge foundation stiffnesses from forced vibration data." *Proc. of the Third International Conference on Soil Dynamics and Earthquake Engineering, Princeton University, June*.
- Crouse, C. B., Hushmand, B., and Martin, G. R. (1987). "Dynamic soil-structure interaction of a single-span bridge." *Earthquake Engineering and Structural Dynamics*, 15, 711-729.
- Crouse, C. B., Hushmand, B., Liang, G., Martin, G. R., and Wood, J. (1985). "Dynamic response of bridge - abutment-backfill systems." *Proc. Joint U.S.-New Zealand Workshop on Seismic Resistance of Highway Bridges, San Diego, CA, May 8-10*.
- Cutillas, A. M., Lera, M. S. C., and Alarcon, E. (1994). "Dynamic soil-structure interaction in bridge abutments." *Proc. of the Eighth International Conference on Computer Methods and Advances in Geomechanics, Morgantown, West Virginia, USA, 22-28 May 1994*, Siriwardane and Zaman (eds), Balkema, Rotterdam, 3, 905-910.
- Das, B. M. (1996). *Principles of Geotechnical Engineering, 3rd Edition*, PWS-KENT Publishing Company, Boston.
- Desai, C. S., and Christian, J. T. (1977). *Numerical Methods in Geomechanics*, McGraw-Hill, New York.

- Desai, C. S., and Siriwardane, H. J. (1984). *Constitutive Laws for Engineering Materials with Emphasis on Geologic Materials*, Prentice-Hall, Inc., Englewood Cliffs, NJ 07632.
- Duncan, J. M., Byrne, P., Wong, K. S., and Mabry, P. (1980). *Strength, Stress-Strain and Bulk Modulus Parameters for Finite Element Analyses of Stresses and Movements in Soil Masses*, Report No. UCB/GT/80-01, August, Department of Civil Engineering, University of California, Berkeley, California.
- Duncan, J. M., and Chang, C. Y. (1970). "Non-linear analysis of stress and strain in soils." *Journal of Soil Mechanics and Foundations Division, ASCE*, 96 (SM5), 1629-1653.
- Dubrova, G. A. (1963). *Interaction of Soil and Structures*. Izd. Rechnoy Transport, Moscow, U.S.S.R.
- Earth Mechanics, 2005. *Field Investigations Report for Abutment Backfill Characterization, Response Assessment of Bridge Systems – Seismic, Live, and Long Term Loads, Task 3, RTA Contract No. 59, Report to Dept. of Structural Engineering, University of San Diego, La Jolla, January 18.*
- El-Gamal, M. E.-S. (1992). *Optimum Design for Bridge Abutments Subjected to Strong Seismic Excitation*, M.S. Degree Thesis, University of Nevada, Reno.
- Fang, Y.-S., Chen, T.-J., and Wu, B.-F. (1994). "Passive earth pressures with various wall movements." *Journal of Geotechnical Engineering, ASCE*, 120(8), 1307-1323.
- Faraji, S. Ting, J.M., Crovo, D.S. and Ernst, H. (2001). "Nonlinear analysis of integral bridges; finite-element model." *Journal of Geotechnical and Geoenvironmental Engineering*, ASCE, Vol. 127, No. 5, 454-461.
- Gadre, A. (1997). *Lateral Response of Pile-Cap Foundation Systems and Seat-Type Bridge Abutments in Dry Sand*, Ph. D. Thesis, Rensselaer Polytechnic Institute, August.
- Goel, R. K., and Chopra, A. K. (1995). "Evaluation of abutment stiffness in a short bridge overcrossing during strong ground shaking." *Proc. of the Fourth U. S. Conference on Lifeline Earthquake Engineering, Technical Council on Lifeline Earthquake Engineering Monograph No. 6, August.*

- Griffiths, D. V. (1990). "Failure criteria interpretation based on Mohr-Coulomb friction." *Journal of Geotechnical Engineering, ASCE*, 116(6), 986-999.
- Griffiths, D. V., and J. H. Prevost, J. H. (1990). "Stress-strain curve generation from simple triaxial parameters." *International Journal for Numerical and Analytical Methods in Geomechanics*, 14, 587-594.
- Griggs, M. N. (1992). *Experimental and Analytical Investigation of Laterally Loaded Piles*, M.S. Thesis, Department of Civil and Environmental Engineering, University of California, Davis.
- Hardin, B. O., and Drnevich, V. P. (1972). "Shear modulus and damping in soils: design equations and curves." *Journal of Soil Mechanics and Foundations Division, ASCE*, 98 (SM7), 667-692.
- Hausmann, M. R. (1990). *Engineering Principles of Ground Modification*, McGraw-Hill Publishing Company.
- Hill, R. (1950). *The Mathematical Theory of Plasticity*, Oxford University Press, Ely House, London.
- James, R.G. and Bransby, P.L. (1971). *Experimental and Theoretical Investigations of a Passive Earth Pressure Problem*, *Geotechnique*, Vol. 20, No. 1, pp. 17-36, London, England.
- Janbu, N. (1957). *Earth Pressure and Bearing Capacity Calculations by Generalized Procedure of Slices*. Proc., 4th Int. Conf. on Soil Mechanics and Foundation Eng., Vol. 2, pp. 207-213.
- Joyner, W. B. (1975). "A method for calculating of nonlinear seismic response in two dimensions." *Bulletin of the Seismological Society of America*, October, 65(5), 1337-1357.
- Joyner, W. B., and Chen, A. T. F. (1975). "Calculation of nonlinear ground response in earthquakes." *Bulletin of the Seismological Society of America*, October, 65(5), 1315-1337.
- Kondner, R. L. (1963). "Hyperbolic stress-strain response: cohesive soils." *Journal of Soil Mechanics and Foundations Division, ASCE*, 89 (SM1), 115-143.
- Kumar, J., and Subba Rao, K. S. (1997). "Passive pressure coefficients, critical failure surface and its kinematic admissibility." *Geotechnique*, 47(1), 185-192.

- Lam, I. P., Martin, G. R., and Imbsen, R. (1991). "Modeling bridge foundations for seismic design and retrofitting." The Third Bridge Engineering Conference, Denver, Colorado, March 10-13.
- Lambe, T. W., and Whitman, R. V. (1969). Soil Mechanics, John Wiley & Sons, New York.
- Larkin, T. J., and Marsh, E. J. (1992). "Two dimensional nonlinear site response analysis." Proc. Pacific Conference on Earthquake Engineering, 3, 217-227, Auckland, November.
- Levine, M. B., and Scott, R. F. (1989). "Dynamic response verification of simplified bridge-foundation model." Journal of Geotechnical Engineering, ASCE, 115(2), February, 246-260.
- Mace, N., and Martin, G. R. (1996). "Ground remediation - aspects of the theory and approach to compaction grouting." Proc. of the Sixth Japan-US Workshop on Earthquake Resistant Design of Lifeline Facilities and Countermeasures Against Soil Liquefaction, Tokyo, Japan.
- Maciejewski, J. and Jarzebowski, A. (2004), Application of Kinematically Admissible Solutions to Passive Earth Pressure Problems, ASCE Journal of Geomechanics, June, Vol. 127.
- Malvern, L. E. (1969). "Introduction." Mechanics of a Continuous Medium, Prentice Hall, Englewood Cliffs, New Jersey.
- Maragakis, E. (1985). A Model for the Rigid Body Motions of Skew Bridges, Report No. EERL 85-02, Earthquake Engineering Research Laboratory, Caltech, Pasadena.
- Maragakis, E., Thornton, G., Saiidi, M., and Siddharthan, R. (1989). "A simple non-linear model for the investigation of the effects of the gap closure at the abutment joints of short Bridges." Earthquake Engineering and Structural Dynamics, 10, 1163-1178.
- Maroney, B., and Chai, Y. H. (1994). "Bridge abutment stiffness and strength under earthquake loadings." Proc. of the Second International Workshop on the Seismic Design of Bridges, Queenstown, New Zealand, August 9-12.

- Maroney, B., Kutter, B., Romstad, K., Chai, Y. H., and Vanderbilt, E.(1994). "Interpretation of large scale bridge abutment test results." Proc. of the Third Caltrans Seismic Research Workshop, Sacramento, June 27-29.
- Martin, G. R., Lam, I. P., Yan, L.-P., Kapuskar, M., and Law, H. (1996). "Bridge abutments - modelling for seismic response analysis." Proc. of the 4th Caltrans Seismic Research Workshop, Sacramento, July 9-11.
- Martin, G. R., Yan, L.-P., and Lam, I. P. (1997). Development and Implementation of Improved Seismic Design and Retrofit Procedures for Bridge Abutments, Final Report on a Research Project Funded by the California Department of Transportation, September.
- Matsuo, M., Kenmochi, S., and Yagi, H. (1978). "Experimental study on earth pressure of retaining wall by field tests." *Soils and Foundations*, 18 (3), 27-41.
- Meyerhof, G. G. (1963). "Some recent research on the bearing capacity of foundations." *Canadian Geotechnical Journal*, 1 (1), 16-26.
- Mokwa, R. L. and Duncan, J. M. (2001). Experimental Evaluation of Lateral-Load Resistance of Pilecaps. *Journal of Geotechnical and Geoenvironmental Eng.*, ASCE, Vol. 127, No. 2, pp. 185-192.
- Naval Facilities Engineering Command (NAVFAC, 1986). *Foundation & Earth Structures, Design Manual 7.02*, U.S. Government Printing Office.
- Norris, G.M. (1977). The drained shear strength of uniform quartz sand as related to particle size and natural variation in particle shape and surface roughness. Ph.D. Thesis, University of California, Berkeley, CA.
- Norris, G.M. (1998). Lateral Loading of a Pile in Layered Soil Using the Strain Wedge Model, *Journal of Geotechnical and Geoenvironmental Eng.*, ASCE, Vol. 124, No. 4, pp. 303-315.
- Ovesen, N.K., 1964, *Anchor Slabs, Calculation Methods, and Model Tests*. Danish Geotechnical Institute, Bulletin No. 16, Copenhagen.
- Ovesen, N.K., and Stromann, H. (1972). Design Methods for Vertical Anchor Slabs in Sand. *ASCE, Proc., Spec. Conf. Perf. Earth and Earth-Supp. Struct.*, Vol. 2.1, pp. 1481-1500.

- Pastor, M., Zienkiewicz, O. C., and Chan A. H. C. (1990). "Generalized plasticity and the modelling of soil behaviour." *International Journal for Numerical and Analytical Methods in Geomechanics*, 14, 151-190.
- Prevost, J. H. (1985). "A simple plasticity theory for frictional cohesionless soils." *Soil Dynamics and Earthquake Engineering*, 4(1), 9-17.
- Prevost, J. H., and Popescu, R. (1996). " Constitutive relations for soil materials." *Electronic Journal of Geotechnical Engineering*, October.
- Richart, F. E., Jr., Hall, J. R., Jr., and Woods, R. D. (1970). *Vibrations of Soils and Foundations*, Prentice-Hall, Englewood Cliffs, NJ.
- Rollins, K.M., and Cole, R.T. (2005). *Cyclic Lateral Load Behavior of a Pile Cap and Backfill*. Accepted for Publication, *Journal of Geotechnical and Geoenvironmental Engineering*.
- Rollins, K.M., and Sparks, A. (2002). *Lateral Resistance of Full-Scale Pilecap with Gravel Backfill*. ASCE, *Journal of Geotechnical and Geoenvironmental Engineering*, Vol. 128, No. 9, pp. 711-723.
- Romstad, K., Kutter, B., Maroney, B., Vanderbilt, E., Griggs, M., and Chai, Y. H. (1995). *Experimental Measurements of Bridge Abutment Behavior*. Dept. of Civil and Environmental Eng., University of California, Davis, Report No. UCD-STR-95-1, Sept.
- Romstad, K., Kutter, B., Maroney, B., Vanderbilt, E., Griggs, M., and Chai, Y. H. (1995). *Experimental Measurements of Bridge Abutment Behavior*, Department of Civil and Environmental Engineering, University of California, Davis, Report No. UCD-STR-95-1, September.
- Rowe, P. W., and Peaker, K. (1965). *Passive Earth Pressure Measurements*. Geotechnique, Vol. 15, No. 1, pp. 22-52, London, England.
- Scott, R. F. (1985). "Plasticity and constitutive relations in soil mechanics." *Journal of Geotechnical Engineering*, ASCE, 111(5), 563-605.
- Seed, H. B., and Idriss, I. M. (1970). *Soil Moduli and Damping Factors for Dynamic Response Analysis*, Report No. EERC 70-10, University of California, Berkeley.
- SAP 2000 (2005). *Integrated Finite Element Analysis and Design of Structures*. by Computers and Structures, Inc., Berkeley, CA.

- Schanz, T., Vermeer, P.A., and Bonnier, P.G. (1999). Formulation and Verification of the Hardening-Soil Model. in Brinkgreve, R.B.J., Beyond 2000 in Computation. Geotechnics, Balkema, pp. 281-290.
- Shamsabadi, A., Rollins, K., and Kapuskar, M., 2007. "Nonlinear Soil-Abutment-Bridge Structure Interaction for Seismic Performance-Based Design," Journal of Geotechnical and Geoenvironmental Engineering, ASCE (under publication).
- Shamsabadi, A., Law, L., and Martin, G. (2006) Comparison of direct method versus substructure method for seismic analysis of a skewed bridge," Proceedings, 5th National Seismic Conference for Bridges and Highways, San Francisco, Sept.
- Shamsabadi, A., Nordal, S. (2006) "Modeling passive earth pressures on bridge abutments for nonlinear seismic soil-structure interaction using PLAXIS." PLAXIS Bulletin issue 20.
- Shamsabadi, A., Law, L., and Martin, G. (2006) Comparison of direct method versus substructure method for seismic analysis of a skewed bridge," Proceedings, 5th National Seismic Conference for Bridges and Highways, San Francisco, Sept.
- Shamsabadi, A., Kapuskar, M., and Zand, A., 2006. "Three-Dimensional Nonlinear Finite-Element Soil-Abutment Structure Interaction Model for Skewed Bridges," Proceedings, 5th National Seismic Conference for Bridges and Highways, San Francisco, Sept.
- Shamsabadi, A., and Kapuskar, M. (2006), "Practical Nonlinear Abutment Model for Seismic Soil-Structure Interaction Analysis," 4th Int'l Workshop on Seismic Design and Retrofit of Transportation Facilities, San Francisco, March 13-14.
- Shamsabadi, A., Ashour, M., and Norris, G. (2005). Bridge Abutment Nonlinear Force-Displacement-Capacity Prediction for Seismic Design. Journal of Geotechnical and Geoenvironmental Engineering, ASCE, Vol. 131, No. 2, pp. 151-161.
- Shamsabadi, A., Yan, L., and Martin, G. (2004). Three Dimensional Nonlinear Seismic Soil-Foundation-Structure Interaction Analysis of a Skewed Bridge Considering Near Fault Effects. Proceedings, US-Turkey Soil-Structural Interaction Workshop, Oct.

- Shamsabadi, A., Yan, L., and Law, H. K. (2002a). Nonlinear Abutment-Backfill-Structure Interaction Behavior for Seismic Design of Bridges. Proceedings, 3rd International Workshop on Performance-Based Seismic Design and Retrofit of Transportation Facilities, Tokyo, Japan, July 9-11.
- Shamsabadi, A., Yan, L., Martin, G. R., Lam, I. P., Tsai, C.-F., and Law, H. K. (2002b). Effects of Abutment Modeling on Seismic Response of Ordinary Standard Bridges. Proceedings, Transportation Research Board Road Builders' Clinic, March.
- Shen, J., and Lopez, M. (1997). "Seismic performance of integral abutment bridges." *Seismic Analysis and Design for Soil-Pile-Structure Interactions*, Geotechnical Special Publication No. 70, ASCE, 111-125.
- Shields, D. H., and Tolunay, A. Z. (1973). "Passive pressure coefficients by method of slices." *Journal of the Soil Mechanics and Foundation Division*, Proc. of ASCE, 99(SM12), December, 1043-1053.
- Siddharthan, R. El-Gamal, M., and Maragakis, E. A. (1995). "Influence of free-field strains on nonlinear lateral abutment stiffnesses." Proc. of the Seventh Canadian Conference on Earthquake engineering, Montreal, June.
- Stewart, J., Tacirogla, E., and Wallace, J. (2006). "Full Scale Large Deflection Testing of Foundation Support Systems for Highway Bridges." UCLA Draft Report on a Research Project Funded by the California Department of Transportation, December.
- Taylor, P. W., Bartlett, P. E., and Wiessing, P. R. (1981). "Foundation rocking under earthquake loading." Proc. of the Tenth International Conference on Soil Mechanics and Foundation Engineering, 3, 313-322.
- Terzaghi, K. (1943). *Theoretical Soil Mechanics*, John Wiley & Sons, Inc., New York, N.Y.
- Welsh, A. K. (1967). "Discussion on dynamic relaxation." Proc. of Institute of Civil Engineers. 37, 723-750.
- Wiessing, P. R. (1979). *Foundation Rocking on Sand*, M. E. Thesis, University of Auckland, School of Engineering Report No. 203, November.

- Wilkins, M. L. (1964). "Fundamental methods in hydrodynamics." *Methods in Computational Physics*, Alder et al. Eds., New York, Academic Press, 3, 211-263.
- Wilson, J. C. (1988). "Stiffness of non-skew monolithic bridge abutments for seismic analysis." *Earthquake Engineering and Structural Dynamics*, 16, 867-883.
- Wilson, J. C., and Tan, B. S. (1990a). "Bridge abutments: formulation of simple model for earthquake response analysis.." *Journal of Engineering Mechanics*, ASCE, 116(8), 1828-1837.
- Wilson, J. C., and Tan, B. S. (1990b). "Bridge abutments: assessing their influence on earthquake response of Meloland Road Overpass." *Journal of Engineering Mechanics*, ASCE, 116(8), 1838-1856.
- Wong, K. S., and Broms, B. B. (1994). "Analysis of retaining walls using the hyperbolic model." *Soil-Structure Interaction: Numerical Analysis and Modeling*, Chapter 17, Bull, J. W. (editor), E & FN SPON.